Winter 12-15-2022

Toward Enhancing the Synthesis of Renewable Polymers: Feedstock Conversions and Functionalizable Copolymers

Tedd Casey Wiessner
Washington University in St. Louis

WASHINGTON UNIVERSITY IN ST. LOUIS

Department of Chemistry

Dissertation Examination Committee:
John Bleeke, Chair
Jonathan Barnes
Kevin Moeller
William B. Tolman
Bess Vlaisavljevich

Toward Enhancing the Synthesis of Renewable Polymers: Feedstock Conversions and Functionalizable Copolymers

By
Tedd C. Wiessner

A dissertation presented to
The Graduate School
of Washington University in
partial fulfillment of the
requirements for the degree
of Doctor of Philosophy

August 2022
St. Louis, Missouri

Table of Contents

List of Figures iv

List of Schemes xiii

List of Tables xix

Abbreviations xxi

Acknowledgements xxiv

Abstract xxvi

Chapter 1: Catalytic Processes for the Conversion of Carboxylic Acid Derivatives to Olefins 1

1.1 Introduction 2
1.2 Homogeneous Catalysis: Ethenolysis 7
1.3 Homogeneous Catalysis: Decarboxylative Routes from Carboxylic Acids 8
1.3.1. Decarboxylation: Kolbe electrolysis 9
1.3.2. Decarboxylation: Lead 10
1.3.3. Decarboxylation: Silver 11
1.3.4. Decarboxylation: Ruthenium 13
1.3.5. Decarboxylation: Photocatalysis 16
1.3.6. Decarboxylation: Biocatalysis 21
1.3.6A. $OleT_{JE}$ peroxygenase/decarboxylase 22
1.3.6B. UndA and UndB Decarboxylases 26
1.3.6C. Ols (Olefin Synthase) 28
1.3.6D. Phenolic acid decarboxylase 29
1.3.6E. Other enzymatic systems 29
1.4 Homogeneous Catalysis: Dehydrative Decarbonylation Methods 30
1.4.1. Dehydrative Decarbonylation from Acyl Halides 31
1.4.2. Dehydrative Decarbonylation from Anhydrides 32
1.4.3. Dehydrative Decarbonylation from *p*-nitrophenyl esters 47
1.4.4. Dehydrative Decarbonylation from Carboxylic Acids 49
1.4.5. Dehydrative Decarbonylation from Amides 51
1.4.6. Dehydrative Decarbonylation from Methyl Esters 52
1.4.7. Mechanistic Insights to Dehydrative Decarbonylation Reactions 53
1.5. Heterogeneous Catalysts 62
1.6. Future Prospects and Outlook 71
1.7. References 74

Chapter 2. Ligand Effects on Pd-acyl Complexes 94

2.1. Introduction 95
2.2. Results and Discussion 100
2.2.1 Experimental results 100
2.2.2 Theoretical results 114
2.3. Conclusion 121

2.4. Experimental 124
2.4.1. Synthesis of Palladium-Acyl Species 125
2.4.2. Reactivity Studies of Palladium-Acyl Complexes 141
2.4.3. Synthesis of Protonated Phosphine 148
2.5. Theory 151
2.6. References 153

Chapter 3. Statistical Incorporation of Olefin-containing Caprolactones into Polylactide for Copolymer Post-polymerization Modification 160
3.1. Introduction 161
3.2. Results and Discission 174
3.2.1. Statistical Copolymerization Development 174
3.2.2. Post-polymerization Modifications 188
3.3. Conclusions and Outlook 200
3.4. Experimental 202
3.4.1. Synthesis of monomers 204
3.4.2. Copolymerization reactions 214
3.4.3. Copolymer post-polymerization modification procedures 227
3.5. References 248

Appendix A. Directing group strategy for the dual catalytic transesterification and dehydrative decarbonylation of fatty acid methyl esters 268
A.1. Introduction 269
A.2. Results and Discussion 272
A.3. Conclusions 277
A.4. Experimental 278
A.5 Appendix A References 283

Appendix B. Graphs and Tables for Chapter 2 285

Appendix C. Polymer characterization (size exclusion chromatography, distribution plots) for Chapter 3 290

Appendix D. X-ray Crystallographic Data 306

Appendix E: Extra Computational/Theory details 326
E.1. Computational details 327
E.2. Oxidative addition (DFT) 328
E.3. Supplemental schemes for figure 2.13 329
E.4. DFT optimized geometries 331
E.5. DFT relative energies for different coordination numbers in select species 333
E.6. DFT functional choice 337
E.7. Coordinates and total energies for calculated structures presented in the manuscript 338
E.8 Appendix E References 342

List of Figures

Figure 1.1 Drop-in strategy for replacing fossil fuels with biomass sources 3

Figure 1.2 Synthesis of commodity chemicals from fossil or biomass resources 4

Figure 1.3 Deoxygenation reactions of fatty acids and ethenolysis of unsaturated fatty acids into α-olefins 5

Figure 1.4 Substrate effects on reactivity of $Ru_3(CO)_{12}$ 14

Figure 1.5 General photocatalytic mechanism, based off of Ir/Cobaloxime system 16

Figure 1.6 Phthalimide esters and examples of photocatalysts and dehydrogenative catalysts in discussed reports 17

Figure 1.7 Photocatalytic mechanism for the conversion of phthalimide esters to olefins with an organic photocatalyst 18

Figure 1.8 Mechanism for $OleT_{JE}$ converting acids into olefins 23

Figure 1.9 $OleT_{JE}$ and lipase immobilized on a cellulose matrix for improved biocatalytic performance 25

Figure 1.10 Photobiocatalytic decarboxylation of fatty acids into olefins 26

Figure 1.11 Proposed mechanism of UndA decarboxylase 27

Figure 1.12 Dehydrative decarbonylation mechanism for the conversion of fatty acid derivatives into olefins 31

Figure 1.13 Proposed mechanism for the transition metal catalyzed dehydrative decarbonylation of mixed anhydrides (acetic or pivalic anhydride) 35

Figure 1.14 Amide bonds: (a) amide resonance structures (b) Types of amide bond distortion, with example molecules 51

Figure 1.15 Mechanism for the dual catalytic conversion of methyl palmitate to olefins 53

Figure 1.16 Mechanistic elucidations of hydrocinnamic acid to styrene via the combination of $PdCl_2$, PPh_3 and pivalic anhydride 55

Figure 1.17 Comparison of polar solvents for dehydrative decarbonylation of stearic acid 57

Figure 1.18 Effects of Xantphos and IPr on most energetically demanding steps for olefin synthesis 59

Figure 1.19 (a) oxidative addition process of Pd and Rh complexes. (b) β-H elimination starting from the decarbonylation intermediate (1) to form propene coordinated to the catalyst (2) and subsequent catalyst regeneration (3) 61

Figure 1.20 Stearic anhydride reaction pathways with varied concentrations 63

Figure 1.21 Conversion of heptanoic acid to alkanes, alkenes and other products via Pd and Pt nanoparticles at low conversions (<5%) 65

Figure 1.22 Use of heterogeneous catalysts with DPEphos and acetic anhydride and comparison of yields for stearic acid 66

Figure 1.23 Hydrogenation/dehydration strategy for hexene synthesis over Cu/Al_2O_3 67

Figure 1.24 Mechanism for deoxygenation of fatty acids over $PtSn/SiO_2$ bimetallic catalyst and select yields for products of substrates 68

Figure 1.25 $PtSnK/SiO_2$ reactions with esters and triglycerides 69

Figure 2.1 Generally proposed mechanism of dehydrative decarbonylation of fatty acids 95

Figure 2.2 Dual catalytic cycle for conversion of fatty acid methyl esters to olefins 96

Figure 2.3 Multidentate directing groups screened in comparison to 2-pyridine methanol 97

Figure 2.4 X-ray crystal structures of Pd-acyl complexes 2 and 3 101

Figure 2.5 Thermolysis of complex 1 in CD_3CN NMR 103

Figure 2.6 Example ^1H NMR for halide abstraction of Pd-acyl 1 105

Figure 2.7 Kinetic plot for halide abstraction of Pd-acyl 1, k_{obs} vs $[NaBAr^f]$ 106

Figure 2.8 X-ray crystal structures of Pd-acyl complex $2(SbF_6)$ 107

Figure 2.9 ^1H NMR of $2^+(I)$ 109

Figure 2.10 Reactions of Pd-acyl $2^+(I)$ with stacked ^1H NMR spectra 110

Figure 2.11 ^1H NMR of complex $3^+(BF_4)$ 112

Figure 2.12 ^1H NMR monitoring decay of complex 4^+ over time 113

Figure 2.13 DFT computed reaction Pd-catalyzed decarbonylation 115

Figure 2.14 Computed reaction profile for chloride abstraction, CO deinsertion, β-H elimination and styrene formation stages of complexes 1-3 116

Figure 2.15 Deinsertion and β-H elimination optimized transition state geometries 117

Figure 2.16 DFT optimized geometries of complex 3 intermediate and transition states 119

Figure 2.17 ^{1}H NMR Spectrum of 2 (CD_2Cl_2) 128

Figure 2.18 ^{13}C NMR of 2 (CD_2Cl_2) 128

Figure 2.19 ^{31}P NMR Spectrum of 2 (CD_2Cl_2) 129

Figure 2.20 ^{1}H NMR Spectrum of $2^{+}(BF_4)$ (CD_3CN) 131

Figure 2.21 ^{13}C NMR Spectrum of $2^{+}(BF_4)$ (CD_3CN) 132

Figure 2.22 ^{31}P NMR Spectrum of $2^{+}(BF_4)$ (CD_3CN) 132

Figure 2.23 ^{1}H NMR Spectrum of $2^{+}(SbF_6)$ (CD_3CN). 0.5:1 diethyl ether: complex solvate 133

Figure 2.24 ^{13}C NMR Spectrum of $2^{+}(SbF_6)$ (CD_3CN) 133

Figure 2.25 Portion of HR ESI-MS showing experiment (top) and simulation (bottom) for $2^{+}(BF_4)$ monomer 134

Figure 2.26 Portion of HR ESI-MS showing experiment (top) and simulation (bottom) for $2^{+}(BF_4)$ dimer. 134

Figure 2.27 Portion of HR ESI-MS showing experiment (top) and simulation (bottom) for $2^{+}(SbF_6)$ monomer. 135

Figure 2.28 Portion of HR ESI-MS showing experiment (top) and simulation (bottom) for $2^{+}(SbF_6)$ dimer 135

Figure 2.29 ^{1}H NMR Spectrum of 3 (CD_2Cl_2) 137

Figure 2.30 ^{13}C NMR Spectrum of 3 (CD_2Cl_2) 138

Figure 2.31 ^{31}P NMR Spectrum of 3 (CD_2Cl_2) 138

Figure 2.32 ^{1}H NMR $2^{+}(I)BAr^{f}$ (CD_2Cl_2) 140

Figure 2.33 ^{13}C NMR $2^{+}(I)$ BAr^{f} (CD_2Cl_2) 140

Figure 2.34 ^{31}P NMR of 2^{+}(I) BAr^{f} (CD_2Cl_2) 141

Figure 2.35 COSY NMR 2^{+}(I) BAr^{f} (CD_2Cl_2) 141

Figure 2.36 ^{1}H NMR spectrum of thermolysis reaction with complex 1, CD_3CN, 46 °C 143

Figure 2.37 ^{1}H NMR spectra of thermolysis reactions of 1 (A), 2 (B), 2^{+} (C) and 3 (D) in THF-D_8 at 54 °C 143

Figure 2.38 ^{1}H NMR of $3^{+}BF_4$ a (CD_3CN) 146

Figure 2.39 ^{1}H NMR of 4^{+} BF_4 (CD_2Cl_2) 147

Figure 2.40 ^{13}C NMR of complex 4^{+} BF_4 (CD_2Cl_2) 147

Figure 2.41 ^{31}P NMR of 4^{+} BF_4 (CD_2Cl_2) 148

Figure 2.42 COSY NMR of 4^{+} BF_4 (CD_2Cl_2) 148

Figure 2.43 ^{1}H NMR of H-P$^{t}Bu_3^{+}$ (Cl^{-}) (CD_3CN) 150

Figure 2.44 ^{31}P NMR Spectrum of H-P$^{t}Bu_3^{+}$ (Cl^{-}) (CD_3CN) 150

Figure 2.45 ^{31}P NMR Spectrum of D-P$^{t}Bu_3^{+}$ (Cl^{-}).....151

Figure 3.1 Synthesis of lactide from lactic acid 162

Figure 3.2 Tacticities of polylactide that can arise from the three monomers 162

Figure 3.3 Coordination-insertion mechanism for the ring-opening copolymerization of lactide and ε-caprolactone 163

Figure 3.4 Different microstructures for the copolymerization of lactide with caprolactone 165

Figure 3.5 Monomers synthesized and tested for statistical copolymerization with *rac*-lactide 168

Figure 3.6 Coordination-insertion mechanism for Ring-opening Polymerization of Olefin-containing Caprolactones.....170

Figure 3.7 Uninhibited insertion of alkoxide into unsubstituted caprolactone versus potential coordination/insertion modes of inhibition.....171

Figure 3.8 Primary and secondary alkoxides generated from the last inserted monomer of ε-caprolactone 171

Figure 3.9 Overarching project goals of copolymerization project.....173

Figure 3.10 Aluminum-salen catalysts bearing bulky silyl groups 175

Figure 3.11 Catalysts tested for copolymerization ability.....177

Figure 3.12 $^{13}C\{^{1}H\}$ NMR of copolymerization between A and *rac*-LA using benzoic acid (10%) as catalyst.....182

Figure 3.13 Copolymerization of C with lactide under optimized conditions 185

Figure 3.14 ^{13}C NMR of carbonyl region of *rac*-LA and monomer C copolymerizations at varied ratios.....186

Figure 3.15 Attempts at molecular weight control of copolymers, where X represents the % of aluminum catalyst and the % of initiating benzyl alcohol.....187

Figure 3.16 Post-polymerization modification type reactions performed and copolymers of *rac*-LA and C 189

Figure 3.17 Thiol-ene reaction where R = octane, and the copolymer of C and *rac*-LA is made up of a 1:8 ratio 190

Figure 3.18 Mercaptopropyl terminated PDMS and [2-3% (mercaptopropyl)methylsiloxane-dimethylsiloxane copolymer reagents 190

Figure 3.19 Thiol-ene reaction of copolymer with mercapto-terminated PDMS..... 191

Figure 3.20 DOSY NMR of PDMS containing copolymer after thiol-ene reaction.....192

Figure 3.21 Crosslinked copolymer using 1,6-hexanedithiol as a crosslinking agent 193

Figure 3.22 Copolymer 22:1 *rac*-LA:C, hydroboration/oxidation and ROP grafting from....195

Figure 3.23 ^{1}H NMR spectra of ROP graft from reactions varying caprolactone amounts....196

Figure 3.24 ^{1}H NMR spectra graft from reactions using photo-initiating conditions and methacrylate.....197

Figure 3.25 ^{1}H NMR 3-vinyl caprolactone (C).....208

Figure 3.26 ^{13}C NMR of 3-vinyl caprolactone (C) 209

Figure 3.27 COSY NMR 3-vinyl caprolactone (C) 209

Figure 3.28 HSQC NMR 3-vinyl caprolactone (C) 210

Figure 3.29 Catalysts screened for the copolymerization of alkene-caprolactones and *rac*-lactide 211

Figure 3.30 ^{1}H NMR Poly(6-allyl caprolactone-co-*rac*-LA) (1:1 feed ratio) 215

Figure 3.31 ^{13}C NMR Poly(6-allyl caprolactone-co-*rac*-LA) (1:1 feed ratio) 216

Figure 3.32 COSY NMR Poly(6-allyl caprolactone-co-*rac*-LA) (1:1 feed ratio.....216

Figure 3.33 HSQC NMR Poly(6-allyl caprolactone-co-*rac*-LA) (1:1 feed ratio) 217

Figure 3.34 ^{1}H NMR Poly(2-allyl caprolactone-co-*rac*-LA) (1:1 monomer feed) 218

Figure 3.35 ^{13}C NMR Poly(2-allyl caprolactone-co-*rac*-LA) (1:1 monomer feed) 219

Figure 3.36 COSY NMR Poly(2-allyl caprolactone-co-*rac*-LA) (1:1 monomer feed) 219

Figure 3.37 HSQC NMR Poly(2-allyl caprolactone-co-*rac*-LA) (1:1 monomer feed) 220

Figure 3.38 ^{1}H NMR Poly(3-vinyl caprolactone-*stat*-*rac*-LA) (1:1 monomer feed).....223

Figure 3.39 ^{13}C NMR Poly(3-vinyl caprolactone-*stat*-*rac*-LA) (1:1 monomer feed).....223

Figure 3.40 COSY NMR Poly(3-vinyl caprolactone-*stat*-*rac*-LA) (1:1 monomer feed). With select coupled protons labeled 224

Figure 3.41 HSQC NMR Poly(3-vinyl caprolactone-*stat*-*rac*-LA) (1:1 monomer feed) 224

Figure 3.42 ^{1}H NMR of poly(3-vinyl caprolactone) 225

Figure 3.43 ^{13}C NMR of poly(3-vinyl caprolactone) 225

Figure 3.44 COSY NMR of poly(3-vinyl caprolactone) homopolymer 226

Figure 3.45 HSQC NMR of poly(3-vinyl caprolactone) 226

Figure 3.46 ^{1}H NMR of 3-vinyl caprolactone/*rac*-LA (1:8) copolymer with 1-octane thiol..228

Figure 3.47 ^{13}C NMR of 3-vinyl caprolactone/*rac*-LA (1:8) copolymer with 1-octane thiol.228

Figure 3.48 COSY NMR of 3-vinyl caprolactone/*rac*-LA (1:8) copolymer with 1-octane thiol 229

Figure 3.49 DOSY NMR of thiol-ene of poly(3-vinyl caprolactone-co-*rac*-LA) overlapped with mercapto-terminated PDMS 229

Figure 3.50 ^{1}H NMR hydroboration-oxidation product 3-vinyl caprolactone/*rac*-LA (1:13) copolymer 232

Figure 3.51 ^{13}C NMR hydroboration-oxidation product 3-vinyl caprolactone/*rac*-LA (1:13) copolymer 232

Figure 3.52 ^{1}H NMR ROP graft from reaction example. 20 equivalents of ε-caprolactone...234

Figure 3.53 ^{13}C NMR ROP graft from reaction example. 20 equivalents of ε-caprolactone..234

Figure 3.54 COSY NMR ROP graft from reaction. 20 equivalents of ε-caprolactone.....235

Figure 3.55 DOSY NMR ROP graft from reaction. 20 equivalents of ε-caprolactone.....235

Figure 3.56 ^{1}H NMR of graft from ROP copolymers (caprolactone: initiator = 20:1) 5 equivalents caprolactone.....236

Figure 3.57 DOSY NMR of graft from ROP copolymers (caprolactone: initiator alcohol = 20:1) 20 equivalents caprolactone 236

Figure 3.58 ^{1}H NMR grafting from radical polymerization of poly(3-vinyl caprolactone-co-lactide.....237

Figure 3.59 ^{1}H NMR of graft from ROP copolymers (caprolactone: initiator alcohol = 50:1) 237

Figure 3.60 DOSY of graft from ROP copolymers (caprolactone initiator alcohol = 50:1)...238

Figure 3.61 ^{1}H NMR radical polymerization graft from reactions with methacrylate (50 equivalents 240

Figure 3.62 COSY NMR of radical polymerization graft from reactions with methacrylate.240

Figure 3.63 DOSY NMR of graft from radical polymerization with methacrylate 241

Figure 3.64 Comparison of poly(**C**-co-*rac*-LA) and its graft from products with methacrylate 241

Figure 3.65 ^{1}H NMR of the metathesis reaction of copolymer with PEG-O-allyl 243

Figure 3.66 DOSY NMR of metathesis reaction between poly(3-vinyl caprolactone-co-*rac*-LA) with PEG-O-allyl.....243

Figure 3.67 ^{1}H NMR of bromination product of poly(3-vinyl caprolactone-co-*rac*-lactide) .245

Figure 3.68 Stacked spectra of parent copolymer and the brominated product 245

Figure 3.69 ^{1}H NMR of epoxidation product of poly(3-vinyl caprolactone-co-*rac*-lactide) .247

Figure 3.70 Stacked spectra of parent copolymer and the epoxidized product.....247

Figure A.1 Dual catalytic cycle for the conversion of fatty acid methyl esters into olefins ..269

Figure A.2 Stepwise process for the conversion of fatty methyl ester into olefins.....270

Figure A.3 Ligands used for the dual catalytic reactions.....271

Figure B.1 k_{obs} versus [$NaBAr^{f}$] 288

Figure B.2 All values of k_{obs} generated over three trials.....288

Figure C.1 SEC (light-scattering) of poly(6-allyl caprolactone-co-*rac*-lactide).....295

Figure C.2 Poly(6-allyl caprolactone-co-*rac*-lactide) conventional analysis 295

Figure C.3 Poly(2-allyl caprolactone-co-*rac*-lactide) conventional analysis 296

Figure C.4 Poly(2-allyl caprolactone-co-*rac*-lactide) light scattering.....296

Figure C.5 Poly(3-vinyl caprolactone-co-*rac*-lactide) (1:5) conventional analysis 297

Figure C.6 Poly(3-vinyl caprolactone-co-*rac*-lactide) (1:5) light scattering analysis 297

Figure C.7 Poly(3-vinyl caprolactone-co-*rac*-lactide) (1:9); Monomer: Initiator = 20:1. Light Scattering Analysis 298

Figure C.8 Poly(3-vinyl caprolactone-co-*rac*-lactide) (1:9); Monomer: Initiator = 20:1. conventional analysis.....298

Figure C.9 Poly(3-vinyl caprolactone-co-*rac*-lactide) (1:9); Monomer: Initiator = 100:1. light scattering analysis.....299

Figure C.10 Poly(3-vinyl caprolactone-co-*rac*-lactide) (1:9); Monomer: Initiator = 100:1. conventional analysis.....299

Figure C.11 Poly(3-vinyl caprolactone-co-*rac*-lactide) (1:9 Monomer: Initiator = 200:1. Light scattering analysis.....300

Figure C.12 Poly(3-vinyl caprolactone-co-*rac*-lactide) (1:9); Monomer: Initiator = 200:1. conventional analysis.....300

Figure C.13 Poly(3-vinyl caprolactone-co-*rac*-lactide) (1:9); Monomer: Initiator = 300:1. light scattering analysis.....301

Figure C.14 Poly(3-vinyl caprolactone-co-*rac*-lactide) (1:9 Monomer: Initiator = 300:1. conventional analysis 301

Figure C.15 Distribution Plot (copolymer 1:22 C:*rac*-LA) 302

Figure C.16 Distribution plot of thiol-ene product. (C: *rac*-LA = 1:8) 303

Figure C.17 Distribution Plot hydroboration-oxidation product (copolymer 1:22 C:*rac*-LA) 304

Figure C.18 Distribution Plot ROP grafting-from product (copolymer 1:22 C:*rac*-LA) 20 equivalents of caprolactone per alcohol. 305

Figure D.1 Crystal Structure of complex 2 313

Figure D.2 Crystal Structure of complex $2^{+}(SbF_6)$ 320

Figure D.3 Crystal Structure of complex 3 325

Figure E.1 DFT optimized geometries of the dppe 333

List of Schemes

Scheme 1.1 General ethenolysis of unsaturated fatty acid derivative. Two step conversion of oleic acid into 1-decene and 1-nonene through a decarboxylation/ethenolysis sequence ...7

Scheme 1.2 Kolbe electrochemistry example ...9

Scheme 1.3 Reactions of butyric acid isomers with $Pb(OAc)_4$ and their products ...10

Scheme 1.4 Silver catalyzed oxidative decarboxylation of fatty acid derivatives by Ag(II). (a) mechanistic steps proposed for the conversion of carboxylic acids into alkyl cation (b) reactions of alkyl cation generated by Ag-oxidation with various solvents (c) selective conversion of acid to alkanes or alkenes with or without Cu(II) ...12

Scheme 1.5 Reaction sequence for the isomerization/decarboxylation of unsaturated fatty acids into olefins by $Ru_3(CO)_{12}$ ...13

Scheme 1.6 $Ru_3(CO)_{12}$ decarboxylation of fatty acids to complicated mixtures of alkenes, alkanes, and alkyl aromatics ...15

Scheme 1.7 Dual ligand photocatalytic system ...18

Scheme 1.8 Cobaloxime/Iridium photocatalytic method for olefins ...19

Scheme 1.9 Cobaloxime/acridine photocatalytic system for conversion of triglycerides into LAOS and subsequent polymerization to poly(α-olefins) ...21

Scheme 1.10 $OleT_{JE}$ reactions. (a) Peroxide shunt method. (b) Use of O_2 as an oxidant and NADPH as an electron shuttle ...24

Scheme 1.11 UndA and UndB conversion of fatty acids into olefins with O_2 as the oxygen donor ...27

Scheme 1.12 Olefin synthase (Ols) conversion mechanism for α-olefins formation ...28

Scheme 1.13 Phenolic acid decarboxylase catalyzed conversion of cinnamic acid variants to styrene derivatives ...29

Scheme 1.14 (a) Conversion of acyl-bromides to olefins. (b) Synthesis of oxidative addition products with acyl chlorides and their subsequent reactivity with I_2 or under heating ...32

Scheme 1.15 Transformation of stearic acid into olefins, by means of an *in-situ* generated anhydride ...33

Scheme 1.16 General formation of dimer and mixed anhydrides and their subsequent conversion to olefins, acids, and CO ...34

Scheme 1.17 Reactions of lauric acid derivatives with Pd and Rh catalysts.....36

Scheme 1.18 $PdCl_2$ catalyzed synthesis of alkyl acrylates, styrene, and acrylonitrile.....38

Scheme 1.19 Dehydrative decarbonylation of carboxylic acids using Pd(II) with bidentate DPEphos 38

Scheme 1.20 4-phenylbutyric acid conversion to olefins with solvent determined selectivity...39

Scheme 1.21 Portion-wise addition of anhydride with acidic additive under distillation condition for high selectivity and TON of fatty acids 40

Scheme 1.22 Use of Pd-DPEphos precatalysts for carboxylic acid conversion with acetic anhydride.....41

Scheme 1.23 Use of quinoline scaffolded phosphine as a bulky monodentate ligand for fatty acid and vegetable distillate conversions to olefins.....42

Scheme 1.24 Selectivity switch observed with anhydride use and temperature, catalyzed by Vaska's complex 43

Scheme 1.25 Expansion of Ir catalysts to unsaturated olefins. (a) use of PPh_3 as ligand, showing high conversions in five hours. (b) NPh_3 as ligand, requiring 8-16 hours for high conversion.....44

Scheme 1.26 Iron-catalyzed production of olefins under CO pressure.....45

Scheme 1.27 Ni high-throughput experimentation. A) initial screenings of metal salts and ligands for the conversion of hydrocinnamic acid into styrene. B) Applying high-throughput best reactions to nonanoic acid for the synthesis of 1-octene 46

Scheme 1.28 Pre-functionalization of fatty acids as *p*-nitrophenyl esters for activation towards dehydrative decarbonylation and subsequent Heck-cross coupling 47

Scheme 1.29 Dual ligand approach with IPr and Xantphos for the conversion of *p*-nitrophenyl esters into olefins 48

Scheme 1.30 NiI_2 dual catalyzed system with stoichiometric or catalytic PPh_3.....49

Scheme 1.31 Ni and Rh catalyzed conversion of saturated fatty acids into olefins using liquid triphenylphosphine as solvent.....50

Scheme 1.32 Amides as activated substrates for the synthesis of linear olefins 52

Scheme 1.33 Dual catalytic conversion of methyl palmitate to olefins using a transient directing group 2-pyridine methanol.....52

Scheme 1.34 Formation of hydrocinnamic anhydrides and their conversion to styrene.....54

Scheme 1.35 Lactone and fatty acid conversion to olefins over γ and tungstated alumina 64

Scheme 1.36 Three step procedure for light olefins from FAMEs 70

Scheme 2.1. Synthesis of Pd-acyl complexes.....100

Scheme 2.2. Halide abstraction of Pd-acyl 2 to form 2^+ or 2^+(I).....108

Scheme 2.3 Halide abstraction reactions of Pd-acyl 3 111

Scheme 2.4 Effect of different ligand environments and explicit 118

Scheme 2.5 Isomerization of solvated cationic intermediate, 2^+.....119

Scheme 2.6 Effect of different ligand environments on β-H elimination transition state energy barriers in complex 2 120

Scheme 2.7 Effect of different ligand environments on β-H elimination transition state energy barriers in complex 3 121

Scheme 2.8 Synthesis of Complex 1 126

Scheme 2.9 Synthesis of Complex 2 126

Scheme 2.10 Synthesis of complex 2^+.....129

Scheme 2.11 Synthesis of complex 3 through ligand exchange of PPh_3 of 2 with dppe 136

Scheme 2.12 Halide abstraction of 2 forms either the isolated complex 2^+.....139

Scheme 2.13 Thermolysis of Pd-acyl complexes.....142

Scheme 2.14 Halide abstraction of 3 145

Scheme 3.1 Synthesis of 6-allyl and 2-allyl caprolactone 174

Scheme 3.2 Degradation of PLA to methyl lactate 179

Scheme 3.3 Synthesis of 3-vinyl caprolactone monomer.....184

Scheme 3.4 Three step synthesis of 3-vinyl caprolactone.....194

Scheme 3.5 Metathesis grafting-from reaction using polyethylene glycol monomethyl ether capped with an allyl group (PEG-O-allyl) 198

Scheme 3.6 Bromination and epoxidation of 3-vinyl caprolactone copolymers.....198

Scheme 3.7 Two-step synthesis of 6-allyl caprolactone (monomer A).....204

Scheme 3.8 Synthesis of 2-allyl caprolactone (monomer B) 205

Scheme 3.9 Three-step synthesis of 3-vinyl caprolactone (monomer C).....205

Scheme 3.10 Synthesis of poly(ethylene glycol) methyl allyl ether 208

Scheme 3.11 Synthesis of salen-type ligands bearing bulky silyl groups (*tert*-butyldimethylsilyl (TBDMS) and triisopropylsilyl (TIPS)) 213

Scheme 3.12 Metalation of bulky silyl group-containing ligands with triethylaluminum.....214

Scheme 3.13 Copolymerization reaction of 6-allyl caprolactone with *rac*-lactide 214

Scheme 3.14 Copolymerization reaction of 2-allyl caprolactone with *rac*-lactide 217

Scheme 3.15 Copolymerization of 3-vinyl caprolactone with *rac*-lactide to form poly(3-vinyl caprolactone-*stat*-*rac*-lactide).....220

Scheme 3.16 Thiol-ene reaction of poly(3-vinyl caprolactone-stat-*rac*-lactide) 227

Scheme 3.17 Crosslinking reactions of poly(3-vinyl caprolactone-stat-*rac*-lactide) 230

Scheme 3.18 Hydroboration-oxidation of poly(3-vinyl caprolactone-stat-*rac*-lactide) 231

Scheme 3.19 Ring-opening polymerization grafting-from reaction with ε-caprolactone 233

Scheme 3.20 Free-radical polymerization grafting from reaction with methacrylate with poly(3-vinyl caprolactone-stat-*rac*-lactide) 238

Scheme 3.21 Metathesis grafting-from reaction with monomethyl monoallyl ether polyethylene glycol.....242

Scheme 3.22 Bromination of poly(3-vinyl caprolactone-stat-*rac*-lactide) with elemental bromine 244

Scheme 3.23 Epoxidation of poly(3-vinyl caprolactone-stat-*rac*-lactide) using *m*CPBA 246

Scheme A.1 Synthesis of directing group A by Ni-catalyzed cross coupling.....272

Scheme A.2 Synthesis of directing group B through multi-route syntheses 273

Scheme A.3 Synthesis of directing group A by Ni-catalyzed cross coupling 278

Scheme A.4 Synthesis of directing group A via multistep synthesis 278

Scheme A.5 Synthesis of directing group B through multi-route syntheses 279

Scheme A.6 Synthesis of directing group C by two different routes 280

Scheme A.7 Synthesis of directing group esters 280

Scheme A.8 Transesterification of methyl palmitate with directing groups with $ZnCl_2$ 281

Scheme A.9 Dehydrative decarbonylation reactions starting from directing group esters 281

Scheme A.10 Dual catalytic conversion of methyl palmitate to olefins under catalytic conditions 281

Scheme A.11 Dual catalytic conversion of methyl palmitate to olefins with metal pre-stirring of catalyst and directing group 282

Scheme E.1 Oxidative addition steps for the reaction of 3-PPCl and $Pd(P^tBu_3)_2$ to form 1 ...329

Scheme E.2 Oxidative addition steps for 3-PPCl and $Pd(PPh_3)_4$.....329

Scheme E.3 The DFT computed reaction mechanism for Pd-catalyzed CO deinsertion of 3-phenylpropionyl chloride 329

Scheme E.4 The DFT computed reaction mechanism for Pd-catalyzed CO deinsertion of 3-phenylpropionyl chloride starting from with 2 330

Scheme E.5 The DFT computed reaction mechanism for Pd-catalyzed CO deinsertion of 3-phenylpropionyl chloride starting from with 3 330

Scheme E.6 The isomerization of the solvated cationic intermediate, 2^+, prior to CO deinsertion 331

Scheme E.7 Effect of explicit solvent molecule on the CO deinsertion transition state energy barriers in P^tBu_3 Pd-acyl complexes 333

Scheme E.8 Effect of different ligand environments and explicit solvent on the CO deinsertion transition state energy barriers in PPh_3 Pd-acyl complexes 334

Scheme E.9 Effect of explicit solvent molecule on the CO deinsertion transition state energy barriers in dppe Pd-acyl complexes 334

Scheme E.10 Effect of different ligand environments and explicit solvent on the β-hydride elimination transition state energy barriers in P^tBu_3 Pd-acyl complexes 335

Scheme E.11 Effect of different ligand environments on β-hydride elimination transition state energy barriers in PPh_3 Pd-acyl complexes 336

Scheme E.12 Effect of different ligand environments and explicit solvent on the β-hydride elimination transition state energy barriers in dppe Pd-acyl complexes 337

List of Tables

Table 1.1 Comparison of various functional groups of lauric acid with $(Ph_3P)_2PdCl_2$ and PPh_3 36

Table 1.2 Comparison of various functional groups of lauric acid with $(Me_2PhP)_2Rh(CO)Cl$ 36

Table 2.1 Select thermolysis reactions of Pd-acyl complexes 102

Table 2.2 Conversions of Pd-acyl complexes to styrene, various additives 104

Table 3.1 Conversion of monomers in homopolymerizations 178

Table 3.2 Conversion of monomers during 1:1 copolymerization between *rac*-LA and **A** 180

Table 3.3 Copolymerizations of 3-vinyl caprolactone and *rac*-LA (1:9 ratio) while varying the amount of initiating alcohol and catalyst 188

Table A.1 Transesterification of methyl palmitate with varied DG's conversions 274

Table A.2 Decarbonylation of pre-synthesized DG-esters under catalytic conditions 275

Table A.3 Dual catalytic reactions performed under previously optimized conditions 276

Table A.4 Results of pre-stir studies 276

Table B.1 Reactions of complex 1 286

Table B.2 Reactions of complex 2 287

Table B.3 Reactions of complex 2^+ 287

Table B.4 Reactions of complex 3 287

Table B.5 Slopes, errors and R^2 values for kinetic studies of chloride abstraction from 1 ..291

Table C.1 Size exclusion chromatography data for attempts at molecular weight control during the statistical copolymerization of 3-vinyl caprolactone with *rac*-lactide 294

Table C.2 Size exclusion chromatography data for select poly(3-vinyl caprolactone-*rac*-lactide) copolymers 302

Table C.3 Size exclusion chromatography data for select poly(3-vinyl caprolactone-*rac*-lactide) copolymers functionalized by 1-octane thiol 303

Table C.4 Size exclusion chromatography data for select poly(3-vinyl caprolactone-*rac*-lactide) copolymers functionalized by hydroboration/oxidation 304

Table C.5 Size exclusion chromatography data for select poly(3-vinyl caprolactone-*rac*-lactide) copolymers functionalized by a ROP grafting from reaction with caprolactone 305

Table E.1 Selected bond distances (Å) and angles (°) for crystal structure and corresponding DFT-optimized geometry for complex 1. 331

Table E.2 Selected bond distances (Å) and angles (°) for crystal structure and corresponding DFT-optimized geometry for complex 2 332

Table E.3 Selected bond distances (Å) and angles (°) for crystal structure and corresponding DFT-optimized geometry for complex 3 332

Table E.4 Selected bond distances (Å) and angles (°) for crystal structure and corresponding DFT-optimized geometry for complex 2^{+}.....332

Table E.5 Optimized geometries using different functionals for the $P^{t}Bu_3$ Pd-acyl complex 338

Table E.6 The total energies for the Pd compounds shown in Figure 3 reported in a.u. 339

Table E.7 The total energies for the Pd compounds shown in Schemes S1-S5 reported in a.u 340

Table E.8 The total energies for the small molecules involved in the reactions reported in a.u. 341

List of Abbreviations

Ac: acetic

ADI: α-diimine

ATRP: atom transfer radical polymerization

Bipy: 2,2'-bipyridineCOD: 1,5-cyclooctadiene

Đ: polydispersity (M_w/M_n)

DBA: Dibenzylideneacetone

DBU: 1,8-Diazabicyclo[5.4.0]undec-7-ene

DFT: Density Functional Theory

DMAP: 4-(dimethylamino)pyridine

DMPA: dimethoxyphenylacetophenone

DMPU: N,N'-dimethylpropyleneurea

DOSY: Diffusion-ordered spectroscopy

Dppe: 1,2-bis(diphenylphosphino) ethane

Dppf: 1,2-bis(diphenylphosphino) ferrocene

Dppp: 1,2-bis(diphenylphosphino) propane

DPP: diphenyl phosphate

FRP: Free-radical polymerization

GC: Gas chromatography

GVL: γ-valerolactone

HAA: Hydrogen atom abstraction

HMPA: Hexamethylphosphoramide

IMes: 1,3-Bis(2,4,6-trimethylphenyl) imidazolazolium chloride

IPr: 1,3-Bis(2,6-diisopropylphenyl) imidazol-2-ylidene

LDA: Lithium diisopropylamide

LAO: Linear α-olefin

LIO: Linear internal olefin

LO: Linear olefin

*m*CPBA: *meta*-chloroperoxybenzoic acid

MW: Molecular Weight

NADPH: Nicotinamide adenine dinucleotide phosphate

n-BuLi: *n*-butyl lithium

NMR: Nuclear magnetic resonance

Nomura-TBDMS: tert-butyldimemethylsilyl-salen ligand

N-MI: *N*-methylimidazole

Nomura-TIPS: triisopropylsilyl-salen ligand

PLA: polylactide

PCL: polycaprolactone

PDMS: Poly(dimethylsiloxane)

PEG: poly(ethylene glycol)

Ph: phenyl

PhBI: phenyl bis(imine)

Phen: phenanthroline

Piv: pivaloyl

pyrBI: pyridyl bis(imine)

pyrox: pyridine-oxazoline

rac-LA: racemic lactide

RAE: Redox active ester

ROP: ring opening polymerization

rt: room temperature, 24˚C

Salen Ligand: A class of ligands made up of two salicylaldehyde units bridged by a diamine (e.g., ethylene diamine, 2,2-dimethyl-1,3-propanediamine)

TBD: triazabicyclodecene

TBDMS: *tert*-butyldimethylsilyl

T_g: Glass transition temperature

TIPS: triisopropylsilyl

TMEDA: tetramethylethylene diamine

TMS: Trimethylsilyl

TOF: Turnover frequency

TON: turnover number

UV: Ultraviolet

Acknowledgements

There are more people than I can name who deserve recognition in getting me here today. First, I would like to express my gratitude to my Ph.D. advisor, Professor William Tolman for his endless support, help and guidance over these five years that have helped shape me as a chemist. The additional support, understanding and flexibility he exhibited in my last year as I navigated cancer treatment as well as a graduate program are beyond anything I could have hoped for.

I would also like to thank the two members of my Ph.D. advisory committee, Professors Kevin Moeller and John Bleeke for their constructive comments and invaluable insights over the years. Additionally, I would like to thank Professors Bess Vlaisavljevich and Jonathan Barnes for being members of my dissertation defense committee. I would like to further thank Samuel Asiedu Fosu, Dr. Riffat Parveen and Profressor Bess Vlaisavljevichv for the opportunity to collaborate and all of the great insights they provided during our work together.

I would like to acknowledge and thank Elizabeth Kellstedt and Professor Marc Hillmyer at the University of Minnesota-Twin Cities for providing me with size exclusion chromatography data.

Thank you to all the members of the Tolman group for being great colleagues and making even the mundane days of purifications enjoyable. I hope you all find success in the future. In addition, thank you to the entire chemistry department and administrative staff for their help and guidance over the last five years.

The work I did during my Ph.D. would not have been possible without the funding provided by the Center for Sustainable Polymers as a part of the National Science Foundation (CHE-1901635), thank you for your support.

A special thank you is necessary to all of the amazing doctors and nurses at Siteman Cancer Center whose positive attitudes and dedication to their patient's wellbeing allows me to be here today.

Finally, thank you to all of the amazing friends and family in my life, without whom I would not have been able to get to this point today. The endless love and support you all have given me has been immeasurable and can never be repaid.

Tedd C. Wiessner

Washington University in St. Louis

August 2022

ABSTRACT OF THE DISSERTATION

Toward Enhancing the Synthesis of Renewable Polymers: Feedstock Conversions and Functionalizable Copolymers
by

Tedd C. Wiessner

Doctor of Philosophy in Chemistry

Washington University in St. Louis, 2022

Professor William B. Tolman, Principal Investigator

This thesis describes research under the rubric of the Center for Sustainable Polymers that is aimed at two separate goals. The goal of the first project (Chapters 1 and 2) was to develop a deeper mechanistic understanding of a method for the synthesis of linear α-olefins, while the second aimed at synthesizing statistical copolymers that incorporate olefin-containing monomers through ring-opening transesterification polymerization and showing that these copolymers could be functionalized.

In Chapter 1, published methods for the conversion of fatty acids to linear α-olefins are reviewed to provide context for the mechanistic work we accomplished (Chapter 2). In Chapter 2 the dehydrative decarbonylation mechanism is investigated with the hopes of identifying factors that may lead to better catalyst design. A series of Pd-acyl complexes were synthesized with hydrocinnamoyl chloride and phosphine ligands. The three different ligands (P^tBu_3, PPh_3, and dppe) were chosen for their ability to induce differing coordination environments around Pd to examine what role the steric environment has specifically on the decarbonylation and β-hydride

elimination steps. Experimental work was informed by theory to better understand the various thermodynamic differences between ligands and upon chloride abstraction from Pd. A reactivity trend, as determined by the formation of styrene, was observed in the order of P^tBu_3 > dppe > PPh_3. Key findings include: the β-hydride elimination step has the highest impact from ligand choice, the low coordination number induced by P^tBu_3 lowers reaction barriers for all steps of the catalytic cycle and the *trans* coordination of the Pd complex with two PPh_3 ligands contributes to a low efficiency for styrene production.

In Chapter 3, a series of olefin-containing caprolactone monomers were statistically copolymerized with racemic-lactide to create a new class of copolymers. The new copolymers, bearing uniformly distributed pendant olefins, underwent a series of post-polymerization modification reactions to convert the alkenes into numerous functionalities such as hydroxyl, bromo and epoxide units. Furthermore, small, and large molecules, such as 1-octanethiol, polyethylene glycol, polycaprolactone, polydimethylsiloxane and polymethacrylate were fused with the copolymers through grafting-to and grafting-from reactions by thiol-ene, metathesis, ring-opening polymerization and free radical polymerization reactions.

Chapter 1.

Catalytic Processes for the Conversion of Carboxylic Acid Derivatives to Olefins

1.1 Introduction

Fossil fuel feedstocks are essential for the production of goods used in everyday life, from clothing to medical applications to materials necessary for vehicles and transportation.[1] These products have led to drastic improvements in our quality of life. The growing use of petroleum resources in manufacturing, however, has led to increasing environmental concerns as resources are limited, their use contributes extensively to greenhouse gas emissions, and often there are environmental consequences that derive from their extraction.[2] These combined issues have led to a greater investment in finding alternative, renewable, options for various petroleum-based materials.

The conversion of biomass and their derivatives to commodity chemicals, traditionally produced from fossil fuels, has therefore become of great interest. Biomass, which is broadly defined as the total mass of organic matter within a given area, includes wood and wood processing wastes, biogenic material (paper, cotton, and food), animal/human sewage, and most commonly agricultural crops and waste materials (i.e., corn, soybeans, algae, and byproducts of their production). Biomass materials are produced on scales upwards of one billion metric tons annually and offer readily available and abundant opportunities to replace petroleum as source materials.[3] One of the major barriers for replacing petroleum with alternative sources is often the requirement for extensive optimization of supply chains and production lines, especially when the bio-available resource differs significantly from the traditionally produced one. In this regard, it is advantageous to find alternative resources that share common intermediates along the production line to produce the same end target product, often described as a drop-in strategy (Figure 1.1).[4] By employing a drop-in strategy, replacing fossil fuels with renewable sources becomes increasingly economically viable, as new production lines do not have to be fully

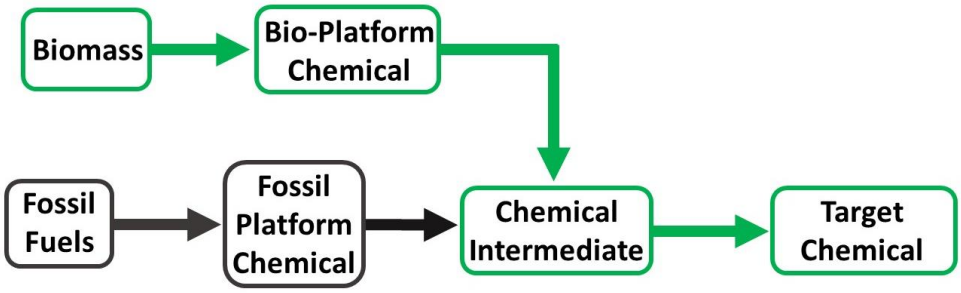

Figure 1.1. Drop-in strategy for replacing fossil fuels with biomass sources.

redeveloped and constructed, and the processes are no longer competitive, but complementary.[4a] One example is the production of chemical intermediates known as linear olefins (LOs). Traditionally, LOs have been produced from fossil fuel resources in one of two ways (Figure 1.2). Ethylene gas, obtained from petroleum by fractional distillation and cracking, can be oligomerized by a metathesis reaction to generate LOs. Alternatively, *n*-alkanes are made through the Fischer-Tropsch process from syngas (CO, H_2 and H_2O), and then undergo a dehydrogenation reaction to produce LOs. Both processes exclusively yield even-numbered chains that initially form linear α-olefins (LAOs) but under catalytic conditions can isomerize into mixtures of LAOs and linear internal olefins (LIOs). Both ethylene oligomerization and the Fischer-Tropsch process are nonselective with respect to chain length, producing even-numbered chains of LOs in a Flory-Schulz type distribution, which ultimately hampers their efficiency.[5]

Two of the most abundant and feasible forms of biomass for replacing petroleum reserves are lignocellulosic biomass and triglycerides in the form of animal fats and vegetable oils. Animal fats and vegetable oils contain numerous varieties of fatty acids or triglycerides that can be readily converted into long-chain fatty acids of varied length through hydrolysis under acidic or basic conditions.[6] These oils are typically saturated carbon chains, but can often contain alkene units along the carbon chain that can be broken ("cracked") directly via ethenolysis to

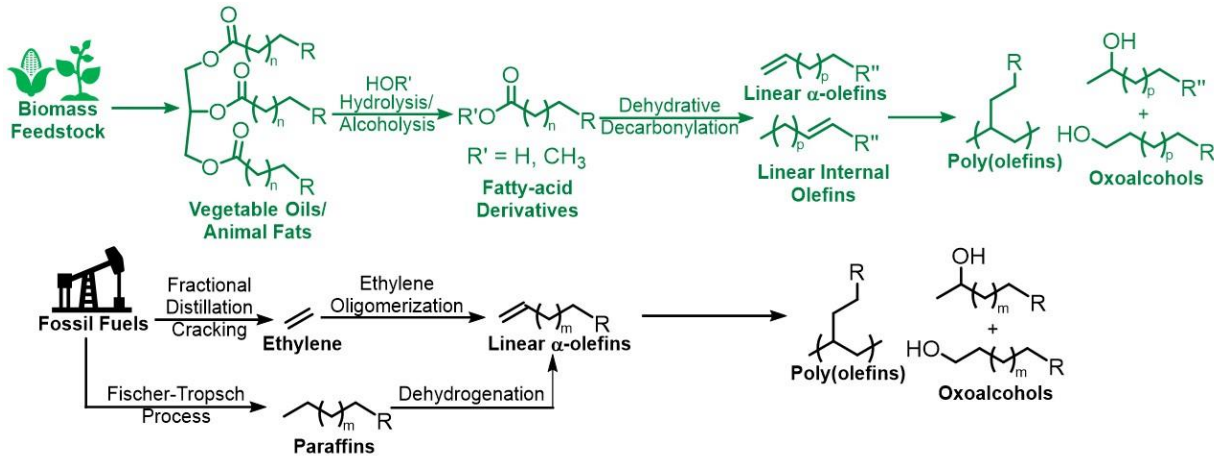

Figure 1.2. Synthesis of commodity chemicals from fossil fuel or biomass resources

LAOs (Figure 1.3).[7] Furthermore, fatty acids and their derivatives can undergo a series of other deoxygenation reactions to produce paraffins, and ketones used as biodiesel (Figure 1.3a). Several deoxygenation reactions have been implemented for the conversion of fatty acid derivatives. Hydrodeoxygenation involves the use of H_2 gas to remove oxygen from the fatty acid in order to create a saturated alkane usually of equal carbon chain length to the starting material, while producing water as a byproduct. However, during the process carbon monoxide may also be lost, resulting in a saturated carbon chain one unit shorter than the starting material. Dehydrative decarboxylation produces ketones, CO_2, and H_2O, whereas decarboxylation and dehydrative decarbonylation processes produce a mixture of linear alkanes and olefins along with CO_2 or CO/H_2O, respectively. Linear alkanes are valuable products used as various forms of biodiesels, whereas LOs can be used for lubricants as is or may enter existing markets (through the drop-in strategy) as chemical intermediates for further derivation into target chemicals.

The plethora of opportunities for sourcing and producing fatty acids makes them a unique bio-platform for linear olefins, (LOs), and provides an alternative to fossil resources as chemical intermediates. LOs are attractive commodity chemicals as they are currently produced on scales

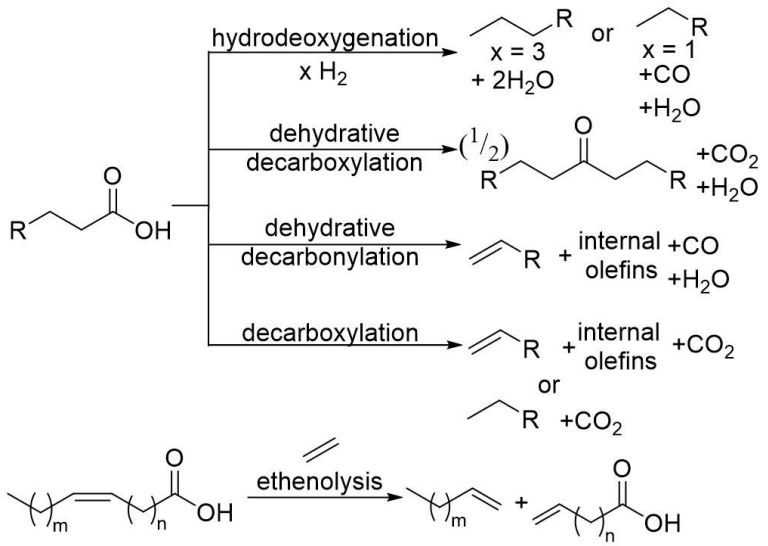

Figure 1.3. Deoxygenation reactions of fatty acids (top). Ethenolysis (bottom) of unsaturated fatty acids to α-olefins

of over 100,000 metric tons/year with a global market value estimated between $9.2 and 10.1 billion as of 2020 (up from 7.54 billion in 2014) with an expectation to grow in value at a rate of 6.5% between 2021-2026.[8] LOs, which contain at least one olefin group at an internal position (LIO) or at the α-position (LAO), have a wide range of industrial uses on their own as lubricants, but further modification to target chemicals has been established (Figure 1.2). Although LIOs can be used as lubricants their uses are limited and LAOs are much more desirable. LAOs are intermediates in the production of oxo-alcohols by hydroformylation/reduction, used as detergents, can be reduced to paraffins for biofuels, and as comonomers in the copolymerization with ethylene to make valuable poly(α-olefins) for synthetic lubricants and surfactants.[9]

Numerous different strategies have been explored for converting fatty acid derivatives into olefins by varied deoxygenation routes including homogeneous, heterogeneous, bio- and photocatalytic methods.[10] Homogeneous methods are wide ranging but proceed via the deoxygenation reactions of either decarboxylation or dehydrative decarbonylation. Photo- and bio-catalytic methods operate almost exclusively under decarboxylative conditions, while

heterogeneous catalysts exhibit much more complicated reactivity and can form LAOs through either deoxygenation route or other means due to the requirement for H_2 gas in many reactions set ups.

In this chapter, past works aimed at synthesizing LAOs from fatty acid derivatives, current state of the art methods, our current mechanistic understanding of these processes and potential future routes will be discussed. The discussion is separated into three main categories: homogeneous catalysis via decarboxylation, homogeneous catalysis via dehydrative decarbonylation and heterogeneous methods. An additional initial commentary on ethenolysis, which is not a deoxygenation reaction but remains relevant, is also provided. A key goal of this discussion is to set the stage for my work, which was focused on developing a detailed understanding of a catalytic dehydrative decarbonylation process, ultimately to inform efforts to enhance the synthesis of LAOs from biomass.

1.2. Homogeneous Catalysis: Ethenolysis

Ethenolysis is a catalytic chemical transformation whereby an olefin metathesis reaction with ethylene and an internal olefin react (Scheme 1.1a).[11] Ethenolysis of long chained compounds is commonly referred to as "cracking" as it breaks apart the chain to create a 1:1 mixture of two new α-olefins, whose length is determined by the location of the double bond within the starting material. The overall chemical reaction is atom economical, with 100% of the reagents being incorporated into the end products (not including the catalyst, which may be reused). Those end products are themselves short ($\leq C_5$) to medium (C_6-C_{12}) chain alkenes. For example, ethenolysis of oleic acid (C_{18}), which has a carbon chain length of 18 and an internal olefin at the 9-position, using a Hoyveda-Grubbs catalyst leads to two products, 1-decene and 1-nonenoic acid. Alternatively, a two-step procedure has been developed to first decarboxylate fatty acids to internal olefins and subsequently crack the double bond, which yields two LAOs (Scheme 1.1b).[12] In the case of oleic acid, which is first converted into (*Z*)-8-heptadecane, cracking produces 1-nonene and 1-decene (96% yield, 96% α-selectivity).

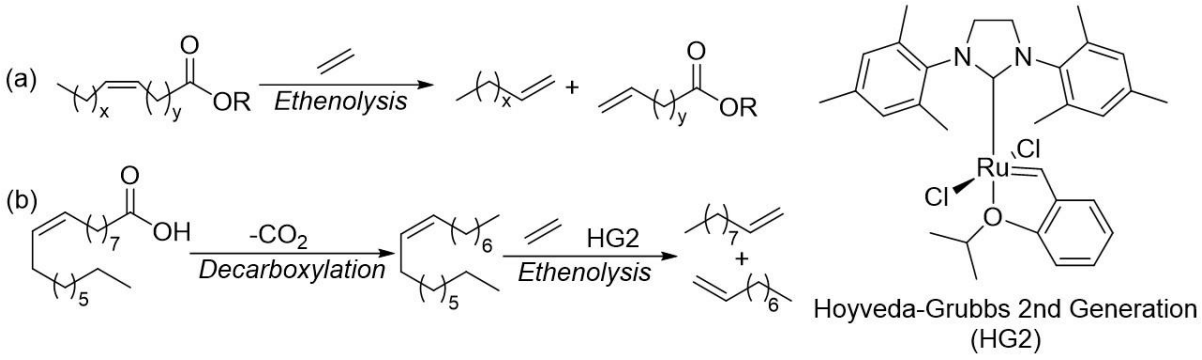

Scheme 1.1. (a) General ethenolysis of unsaturated fatty acid derivative. (b) Two step conversion of oleic acid into 1-decene and 1-nonene through a decarboxylation/ethenolysis sequence. x + y must equal 14.

1.3. Homogeneous Catalysis: Decarboxylative Routes from Carboxylic Acids

Several different routes exist for transforming carboxylic acid derivatives into LAOs. Two main deoxygenation type reactions are typically employed in homogeneous catalysis: decarboxylation and dehydrative decarbonylation. In decarboxylation the fatty acid is typically directly converted into olefins or other products without the requirement for activating the acid moiety by means of an additional functional group. Exceptions to this are with the use of redox active esters (RAEs) used in some photochemical transformations (discussed below). In decarboxylation reactions CO_2 is lost, often with concomitant removal of H_2 gas, depending on the presence of basic species in the reaction. Dehydrative decarbonylation, on the other hand, forms CO and H_2O and requires the activation of the C-O acyl bond of the acid derivative via an anhydride, electron withdrawing ester or other means. Both homogeneous methods have been accomplished with an array of transition metals, either in the form of simple commercially available salts or more elaborate complexes. They offer the benefits of performing highly reproducible reactions and are currently the most abundant and active catalysts for deoxygenation reactions of acids into LAOs. However, limited recyclability and often low catalyst stability have led to limited TONs, hampering their ability to replace current routes of production for LAOs from fossil fuels. Homogeneous methods have focused on metals such as Pb, Ag, Ru, Pd, Rh, Ni, Fe, Co, and Ir and will be discussed within.

1.3.1. Decarboxylation: Kolbe electrolysis

Kolbe electrolysis is the first reported method for converting acids into olefins, predating other strategies such by nearly a century to 1848.[13] The method traditionally used a sodium or potassium salt of fatty acids to form alkanes or alkenes through a decarboxylative dimerization event (Scheme 1.2). The reaction proceeds through a radical-induced decarboxylation of a carboxylate to form an alkyl radical, which then recombines with another radical in solution, gets further oxidized to the cation or undergoes disproportionation. The combination of radical species leads to a variety of products based on kinetic and thermodynamic factors, showing a lack of selectivity for alkanes, alkenes, esters, or ethers.[14] More recent developments have shown some promise for electrocatalytic methods being strong alternatives for LAO synthesis as an environmentally friendly methodology that follows green principles such as using nontoxic solvents, e.g., water, under mild conditions, and using electrons as an immaterial reagent.[15]

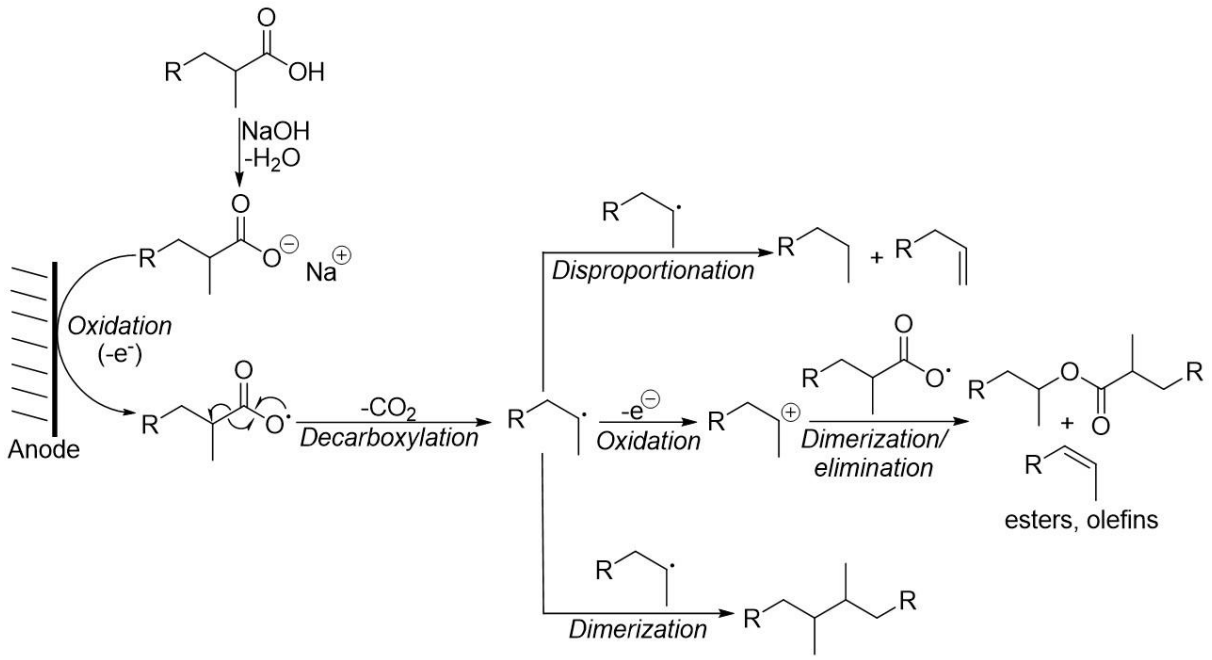

Scheme 1.2. Kolbe electrochemistry

Furthermore, little to no waste is produced (assuming byproducts find a purpose) and triglycerides (plant oils) can be converted directly to olefins without the need for an intermediate hydrolysis to fatty acids. Selectivity to produce LAOs without ether, alkane, or ester side products currently limit the electrocatalytic methodology, however, use of such mixtures could still be of benefit for biofuel production.

1.3.2. Decarboxylation: Lead (Pb)

One of the classic examples of the catalytic production of alkenes from carboxylic acids involved the use of stoichiometric amounts of lead tetraacetate ($Pb(OAc)_4$) to induce an oxidative decarboxylation reaction. Substrates included the short aliphatic acids *n*-valeric, isovaleric and 2-methylbutyric acid, which were converted into a mixture of olefins, ketones, esters, and butyl benzenes (Scheme 1.3).[16] $Pb(OAc)_4$ was proposed to operate through a radical chain mechanism that was strongly inhibited by the presence of O_2. Various additives, including pyridine, valeryl peroxide and Cu(II) salts were used to increase the efficiency of the reactions,

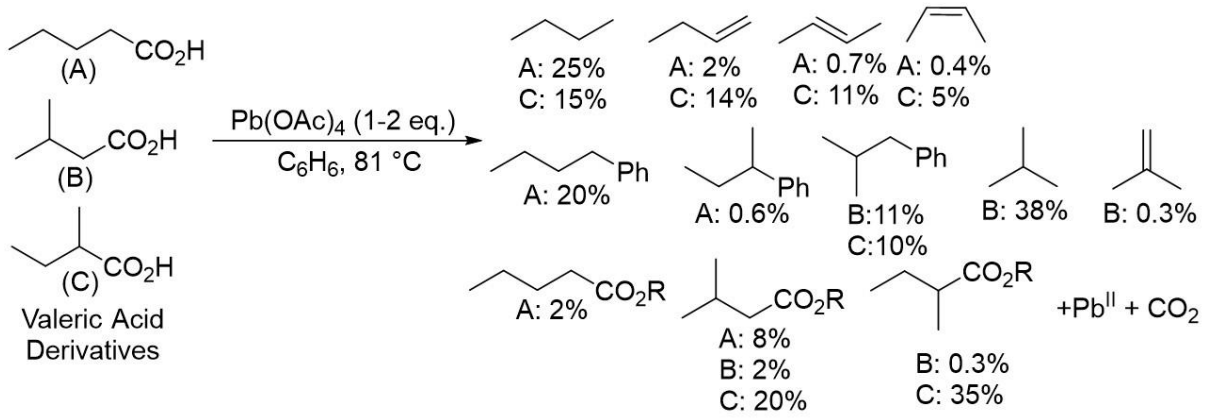

Scheme 1.3. Reactions of butyric acid isomers with $Pb(OAc)_4$ and their products. Note: when Cu(II) salts are used under the same reaction conditions 1-alkene products are formed exclusively along with CO_2 and stoichiometric Pb(II) waste. R = acetate for A, valerate for B and butyrate for C. Other trace products include *sec*-butyl acetate and *n*-butyl acetate.

with Cu(II) salts leading to selective production of 1-alkenes. The procedure was ultimately hindered by overall low yields from byproducts and the use of stoichiometric amounts of toxic lead reagents raising environmental and toxicity concerns.

1.3.3. Decarboxylation: Silver (Ag)

In 1970 the use of silver salts in tandem with peroxydisulfate ($S_2O_8^{2-}$) , a strong oxidizing agent, was first reported to be capable of oxidative decarboxylation of carboxylic acids.[17] The combination of silver and oxidant was proposed to form a Ag(II) species capable of converting simple acids (e.g. acetic, *n*-butyric, isobutyric and pivalic acids) into olefins.[18] Initial reactions required excess carboxylic acids, used as solvents, with study being focused on the overall mechanistic process. An oxidative decarboxylation process was proposed to be initiated by Ag(II) and occurs via two discrete oxidation steps (Scheme 1.4a).[19] To initiate the reaction Ag(II) was first generated *in situ* by oxidation with the peroxydisulfate salt (Scheme 1.4a(I)). The fatty acids' carboxylate group then undergoes an oxidative event with Ag(II), losing a proton in the process and forming an acyloxy radical and Ag(I). Rapid decarboxylation fragmentation of the radical species forms an alkyl radical with concomitant loss of CO_2. The alkyl radical can either abstract a hydrogen atom from solvent to form an alkane or be further oxidized by a second equivalent of Ag(II) to generate an alkyl cation that is susceptible to further transformations (see Scheme 1.4b).[20] More recently, Ag(II)-catalyzed oxidative decarboxylation converted unsaturated fatty acids and diglycerides into LAOs (with Cu salts) or alkanes (without Cu salts) (Scheme 1.4c).[21] Using $CuSO_4$ alkenes could be selectively produced over alkanes, albeit in moderate yields (<40%), with notable primary alcohol by products. No chain walking or

isomerization of the starting material was observed during the process, producing at the time of publication (2011) some of the first examples of LAOs from unsaturated fatty acids.

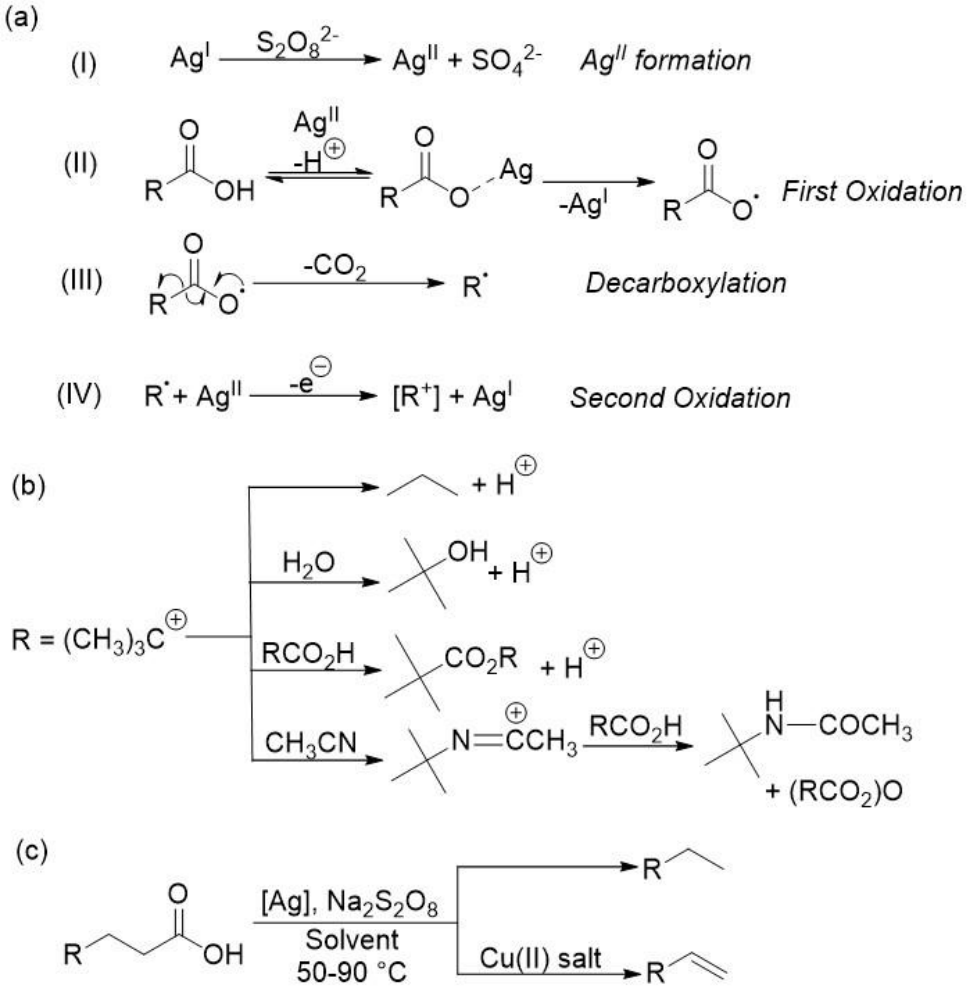

Scheme 1.4. Silver catalyzed oxidative decarboxylation of fatty acid derivatives by Ag(II). (a) mechanistic steps proposed for the conversion of carboxylic acids into alkyl cation (b) reactions of alkyl cation generated by Ag-oxidation with various solvents (c) selective conversion of acid to alkanes or alkenes with or without Cu(II)

1.3.4 Decarboxylation: Ruthenium (Ru)

Unlike most other transition metals, ruthenium can catalyze direct decarboxylation of fatty acids without an activating group. Commercially available $Ru_3(CO)_{12}$ has been used to transform a wide arrangement of saturated and unsaturated fatty acids into mixtures of alkanes and alkenes. One of the first examples came in 2014, where a tandem isomerization-decarboxylation procedure was demonstrated with unsaturated fatty acids such as oleic and undecylenic acid using Ru precursors $[Ru(CO)_2EtCO_2]_n$ or $Ru_3(CO)_{12}$ at 250 °C.[22] The study determined that Ru serves two functions. First, it coordinates to the double bond of an unsaturated fatty acid and isomerizes it through a series of Ru-hydride insertions and β-hydride eliminations (chain walking) until it reaches the position adjacent to the carboxylic acid moiety (Scheme 1.5). After isomerization Ru can induce decarboxylation of the acid, though it is currently unclear if a radical or ionic pathway is operational. Upon decarboxylation, the Ru can further isomerize the double bond(s) of the fatty acid to create mixtures of LIOs.

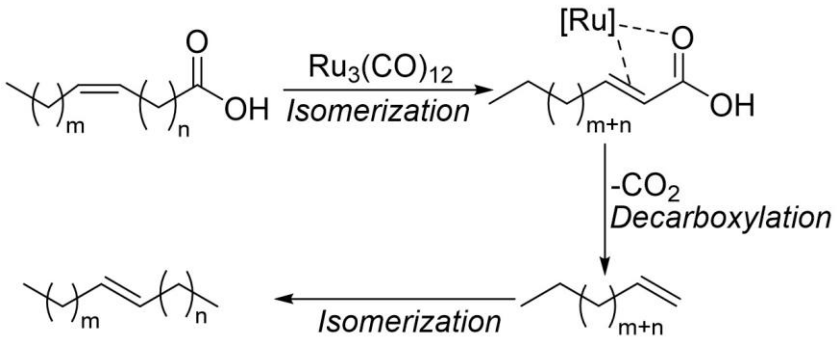

Scheme 1.5. Reaction sequence for the isomerization/decarboxylation of unsaturated fatty acids into olefins by $Ru_3(CO)_{12}$

The dual role of the Ru catalyst for both isomerization and decarboxylation was investigated by altering the substrate from oleic acid to the ester methyl oleate. During the reaction rapid isomerization of the alkyl chain's double bond was observed, but no decarboxylation occurred (Figure 1.4). By comparison, stearic acid, which is the fully saturated

analog to oleic acid and so cannot isomerize, was 28 times less reactive than oleic acid, implying an enhancement in reactivity from alkene coordination. Cinnamic acid possesses a double bond adjacent to the carboxylic acid and cannot isomerize but maintained high rates of decarboxylation like oleic acid. Meanwhile, *trans*-7-tetradecene, was isomerized to a mixture of isomers under the conditions. The enhanced rates for unsaturated substrates indicated that coordination to the double bond of the starting material plays a significant role in the reaction, perhaps acting as a directing group. With the proclivity of Ru to rapidly isomerize alkenes, no LAO selectivity was observed, and products were mixtures of alkenes, alkanes and even alkyl benzenes.

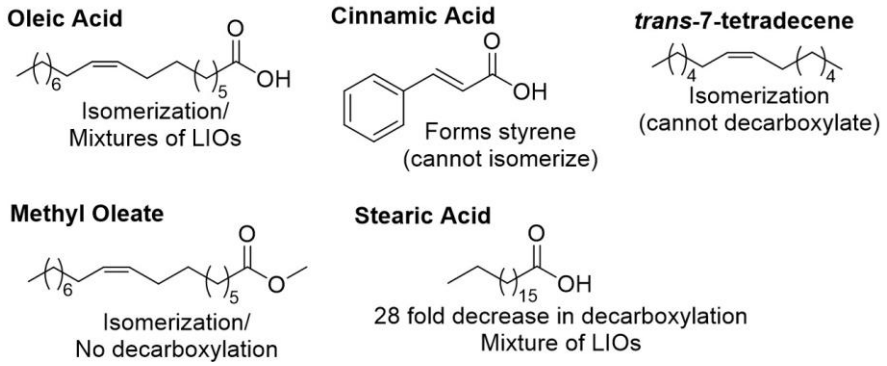

Figure 1.4. Substrate effects on reactivity of $Ru_3(CO)_{12}$

Subsequent work with $Ru_3(CO)_{12}$ expanded the substrate scope of the original procedure to a wider range of saturated and unsaturated carboxylic acids.[23] All substrates, other than monounsaturated fatty acids, which produced majority alkanes, showed product distributions of alkenes, alkanes, and alkyl benzenes, with alkenes being the major product (Scheme 1.6). The complex reaction mixtures emphasized the multifaceted role of the $Ru_3(CO)_{12}$ catalyst that operates under a series of competing processes. For example, to explain the variety of products identified within the reaction mixtures, Ru must be able to perform isomerization, decarboxylation, desaturation, hydrogenation and even cyclization (aromatization) processes,

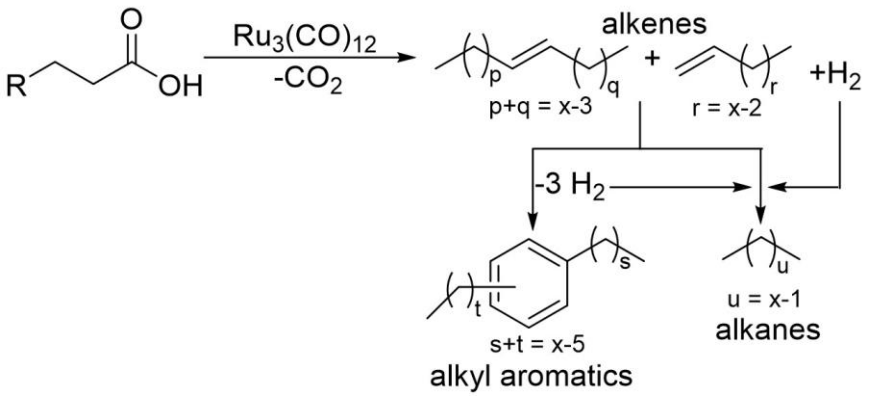

Scheme 1.6. $Ru_3(CO)_{12}$ decarboxylation of fatty acids to complicated mixtures of alkenes, alkanes, and alkyl aromatics. x = n-2, n = number of carbons in a fatty acid chain. X = 10, 12, 14,16, with y +z = x-2

that compete with each other, thus limiting the availability to selectively create LAOs from the process. Under the reaction conditions (250 °C, neat, 0.5 mol% Ru, 24 hr) isomerization of unsaturated starting materials was determined to be the first step of the reaction. Decarboxylation follows with a calculated barrier of 249 kJ/mol (for oleic acid) to form a mixture of heptadecenes (LIOs and LAO).[24] In the reported process, occurring within a closed reaction vessel, H_2, was formed via dehydrogenation leading to side reactions such as hydrogenation of the alkene to form alkanes. Alternatively, heptadecenes could be dehydrogenated by Ru to form polyunsaturated compounds prone to cyclization reactions, producing mixtures of alkyl benzenes. The ruthenium ($Ru_3(CO)_{12}$) precatalyst's propensity to perform chain walking before or after a dehydrogenation underscores its complicated reactivity, where Ru can also transform alkenes into alkadienes and subsequently lead to cyclization reactions to create aromatics. The lack of selectivity in the reaction creates a diverse array of products making it inefficient for sustainable production of LAOs. However, it should be mentioned that linear alkanes as well as alkylaromatics are useful components of biodiesel and jet fuel. Further work would be needed to control product distributions.

1.3.5. Decarboxylation: Photocatalysis

The high temperatures often required for the synthesis of LAOs from fatty acid derivatives are energy intensive and typically lead to rapid isomerization of LAOs to the more thermodynamically stable LIOs. Therefore, alternative routes that operate at lower temperatures and can avoid isomerization are attractive. In this regard, photocatalysis has offered an alternative strategy, operating at or near room temperature. Photocatalysts operate under several mechanisms depending on if they are oxidative or reductive in their excited state. A general photocatalytic mechanism is outlined in Figure 1.5 based on a recent report using an Ir photocatalyst, where the photoexcited Ir complex acts as an oxidant.[28] To begin, the photocatalyst is irradiated by blue or UV light to put it in an excited state (denoted by "*"). At the same time the acid substrate is primed by deprotonation by a base or metal hydride to generate the carboxylate anion. A single electron transfer (SET) between the excited photocatalyst and substrate leads to rapid radical decarboxylation to generate an alkyl radical.

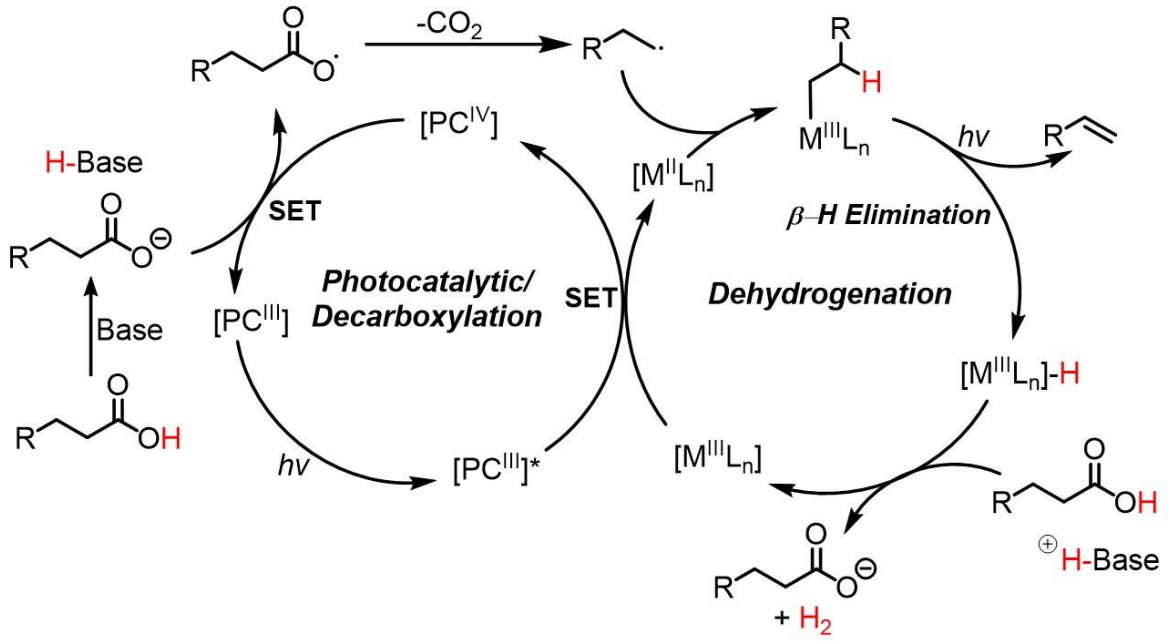

Figure 1.5. General photocatalytic mechanism, based off Ir/Cobaloxime system. SET: single electron transfer. M = metal catalyst, L = ligand, n = number of ligands and PC = photocatalyst

Trapping of the alkyl radical by a metal catalyst and subsequent β-H elimination generates the desired α-olefin. H_2 gas is typically irreversibly extruded from the system by deprotonation of a new fatty acid, or regeneration of the initiating base. The production of H_2 limits the ability of metal hydrides to reinsert into LAOs and prevents isomerization, leading to high LAO selectivities.

Photocatalytic methods in general require radical generation, either by means of a photocatalyst alone or in tandem with an activating group such as phthalimide esters (Figure 1.6).[25] A 2018 report described how phthalimide esters, also referred to as redox active esters (RAEs), of a wide range of carboxylic acids were converted to olefins with high levels of selectivity by using an organic photocatalyst to generate alkyl radicals through reduction of the phthalimide group (Figure 1.7). Loss of CO_2 and a phthalimide anion generates an alkyl radical that gets trapped by a Cu(II) catalyst. The transient Cu(III)-alkyl species is deprotonated by a phthalimide anion to form the olefin and a Cu(I) intermediate via an oxidative elimination process.[26] The catalytic cycle closes by single electron transfer between photocatalyst and Cu(I) to regenerate Cu(II). Mechanistic studies showed light and Cu are necessary for successful olefin formation. Radical clock experiments supported intermediacy of a radical species, whereas

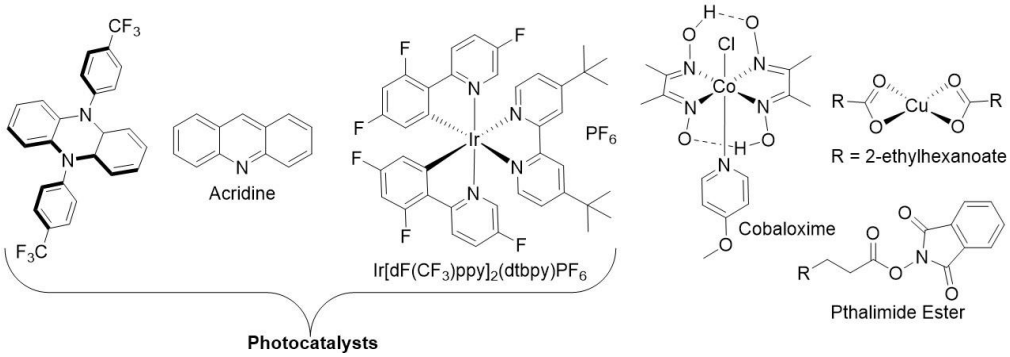

Figure 1.6. Phthalimide esters and examples of photocatalysts and dehydrogenative catalysts in discussed reports.

experiments with other trapping agents implied carbocation intermediates were not operative. Quantum yields were low (Φ = 0.01), requiring continuous photoirradiation during the reaction and indicating a radical chain was not operative.

A second example of work using phthalimide esters demonstrated the use of a dual ligand

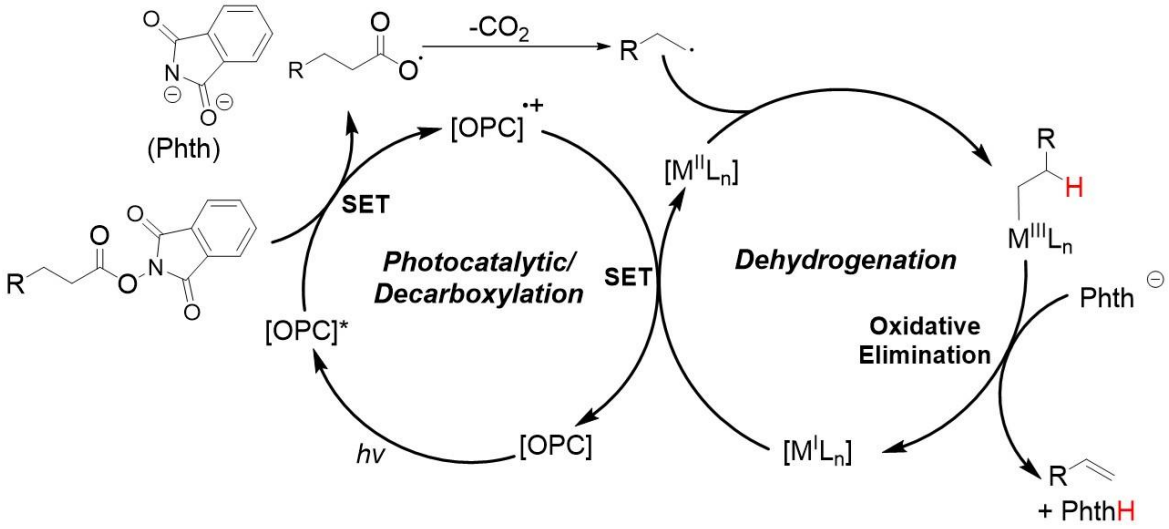

Figure 1.7. Photocatalytic mechanism for the conversion of phthalimide esters to olefins with an organic photocatalyst (OPC)

system with Pd.[27] Under blue light irradiation (440 nm), $PdCl_2$ in the presence of Xantphos, CyJohnPhos, and 2,4,6-collidine (as base) catalyzes a decarboxylative desaturation of alkane based carboxylic acids (Scheme 1.7). The dual-ligand nature was key to reaction efficiency, with Xantphos being the only effective bidentate ligand screened, likely due to its large bite angle and a conjugated backbone that is apparently necessary for photoactivity. Likewise, the monodentate

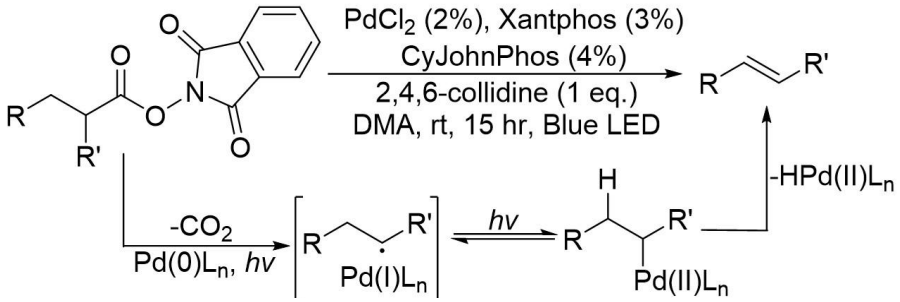

Scheme 1.7. Dual ligand photocatalytic system.

ligand's cone angle was crucial to high yields, with smaller PPh_3 almost completely suppressing the reaction, whereas bulkier ligands such as P(*t*-Bu)$_3$ effectively promoting the reaction, but to a lesser degree (54% vs 93% with CyJohnPhos). The choice of monodentate phosphine impacted the yield of the alkenes but had no effect on the selectivity for β-H elimination over other potential side reactions (e.g., radical induced cyclization), suggesting the ligand dissociates from the metal center prior to the olefin formation step. Mechanistic studies implied Xantphos played a major role in photoexcitation of the Pd species as the Pd-Xantphos species effectively absorbed light (UV-Vis and Stern-Volmer analysis). The bulkiness of CyJohnPhos was crucial for the monodentate ligand to have the appropriate ability to coordinate/dissociate from Pd at various times throughout the catalytic cycle, offering catalyst stability and tuning the reactivity of the system.

Further utility of photoredox methods was developed using cobaloxime catalysts with Ir photosensitizers and carbonate bases, all of which could be used in catalytic amounts (Scheme 1.8).[28] Both saturated and unsaturated fatty acids, as well as several medicinally important substrates, underwent successful conversion to α-olefins, without any isomerization in either the positioning or *E*/*Z* conformation of the double bonds. However, scalability was a notable issue

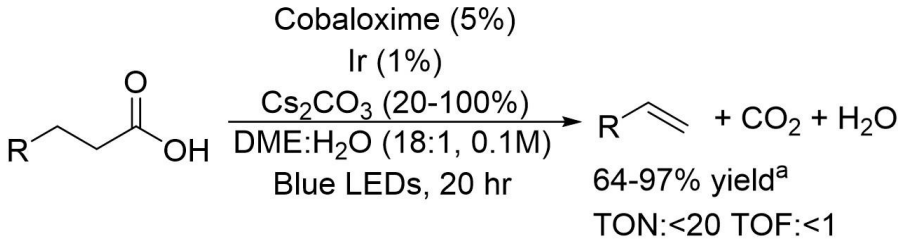

Scheme 1.8. Cobaloxime/Iridium photocatalytic method for olefins. DME: dimethoxyethane, Ir: Ir[dF(CF_3)ppy]$_2$(dtbpy)PF_6 where ppy = 5-(trifluoromethyl)-2-pyridinyl-*N*]phenyl and dtbpy = di-*tert*-butylbipyridine. Cobaloxime as seen in Figure 1.6.

that must be overcome, one detrimental influence being CO_2 induced acidification of the reaction medium that would have to be addressed in engineering efforts (i.e. flow reactors).

Cobaloxime type catalysts have more recently shown success in tandem with acridine based photocatalysts.[29] Even with a higher loading of photocatalyst when compared to previous cobaloxime methods (6-20% acridine vs. 1% Ir) the switch from Ir to an organic PC has the potential to drastically reduce costs and increase sustainability. A large array of fatty acid and medicinally relevant small molecules substrates were converted to LAOs without isomerization and in high yields. Most importantly, the direct conversion of biomass in the form of triglycerides was performed by using a tricatalytic system of lipase, acridine and cobaloxime (Scheme 1.9). In the system, a bacterium-derived lipase enzyme first converts the triglyceride, such as tristearin, into fatty acids (stearic acid for tristearin). The acid then gets converted to the LAO by acridine/cobaloxime catalysis forming LAOs in yields of 62-85%. Furthermore, with one of the major uses of LAOs being polymerization to make poly(α-olefins), triglycerides converted to saturated LAOs were used in a chain-walking polymerization procedure with a Ni catalyst and diethylaluminum chloride cocatalyst. For example, 1-tridecene was synthesized from palmitin derived from corn, soybean, sunflower, and hydrogenated canola oils, and then polymerized to polyethylene-type polymers in yields of 76-99%. These results demonstrated the feasibility of the procedure. Further practicality to the approach was demonstrated by gram scale synthesis of LAOs from acids and triglycerides.

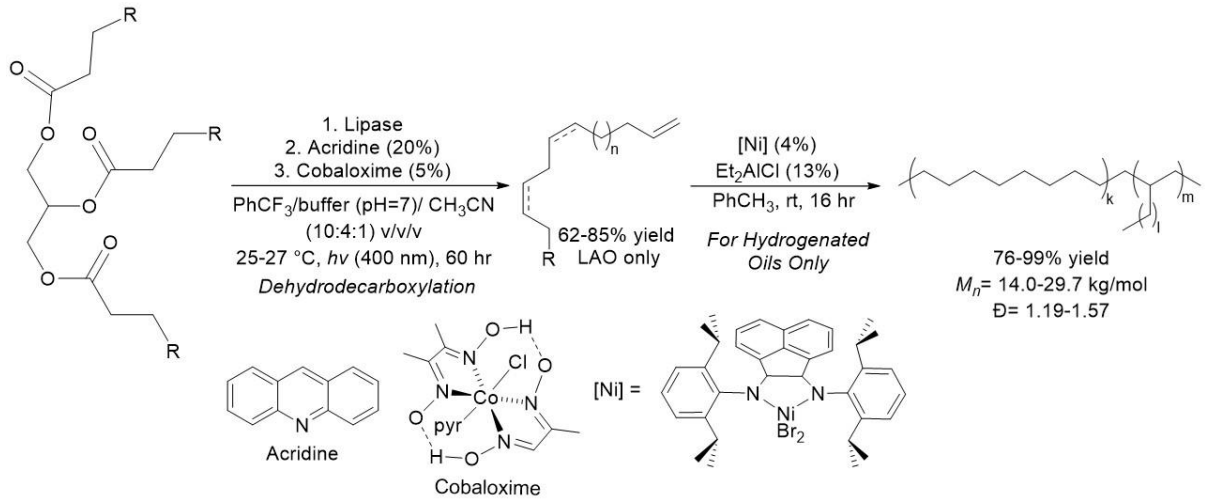

Scheme 1.9. Cobaloxime/acridine photocatalytic system for conversion of triglycerides into LAOS and subsequent polymerization to poly(α-olefins). Acridine as seen in figure 1.6. Lipase derived from *Burkholderia cepacian* (Amano Lipase PS). Pyr: pyridine, R = saturated or unsaturated alkyl chain.

1.3.6. Decarboxylation: Bio-catalytic

From an environmental perspective bio-catalysis offers one of the most sustainable routes for chemical production.[30] Biocatalytic methods operate at or near ambient conditions (room temperature, physiological pH, 1 atm), limiting energy consumption while also utilizing water as an environmentally benign solvent. From a green perspective these attributes put these methods far above conventional ones that require highly polar and/or toxic solvents that are often not recycled, costly additives that produce stoichiometric waste such as anhydrides/acids, or precious metals that require extensive mining to acquire. Like all methods discussed thus far, the efficacy of bio-catalysis can vary, but unlike other methodologies it can exclusively produce α-olefins via a decarboxylation pathway only. On the flip side, drawbacks to bio-catalytic methods are the sensitivity of the enzymes used as catalysts to environmental changes (i.e., temperature and pH must be well maintained) as well as the need for dilute reaction conditions, measured in titers.

Nonetheless, several different classes of enzymes have been reported for the synthesis of LAOs from fatty acids, as discussed below.

1.3.6A. $OleT_{JE}$ peroxygenase/decarboxylase

$OleT_{JE}$ is a cytochrome P450 enzyme from *Jeotgalicoccus* sp. ATCC 8456, a member of the CYP152 peroxygenase family. $OleT_{JE}$ acts as a fatty acid decarboxylase and produces LAOs from long chain fatty acids, diacids and hydroxy fatty acids with the aid of an oxidant (H_2O_2 or O_2).[31] The enzyme reacts with a range of long chain fatty acids and elucidated structures have shown that its active site is made up of a Fe-heme that is preformed specifically for fatty acid binding.[32] Like other P450s, Fe is the responsible metal for the catalyzed reaction, however, an oxidant in the form of H_2O_2 or O_2 is required to access the high-valent Fe(IV) species necessary for the decarboxylation pathway.

$OleT_{JE}$ catalyzed decarboxylation is proposed to occur via a high valent Fe(IV)-oxo radical cation species whereby the key step is a hydrogen atom abstraction (HAA) from the β-position of the fatty acid. Subsequently the instability of the aliphatic radical leads to rapid decarboxylation, either via a radical or anionic pathway, to generate the olefin (Figure 1.8). The hydroxy-Fe(III) species generated from HAA is protonated to form water, which is released to create a resting state Fe(III) porphyrin. To reenter the catalytic cycle an oxidant converts the Fe(III) to regenerate the active Fe(IV) moiety. Mechanistic studies of $OleT_{JE}$ have helped support some key aspects of the decarboxylation/olefination mechanism, most notably that decarboxylation does not proceed through an oxygen insertion reaction.[33] DFT computations also suggest that solvent polarity plays a critical role in whether decarboxylation/olefination or

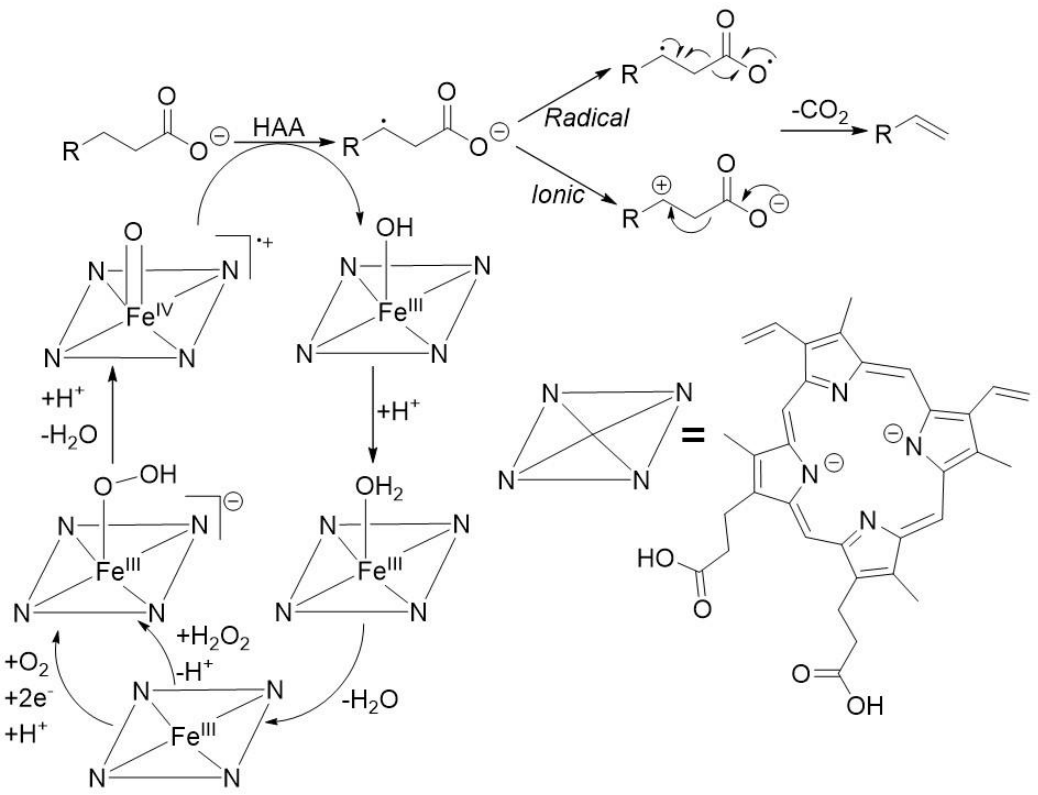

Figure 1.8. Mechanism for $OleT_{JE}$ converting acids into olefins. HAT (hydrogen atom abstraction) at the β-position radical or ionic decarboxylation pathways are possible to generate LAOs

hydroxylation reactions occur.[34] Using a solvent with more accessibility to the substrate within the binding pocket of the enzyme leads to an enhanced selectivity for decarboxylation.

In a 2011 report, using H_2O_2 as an oxygen source, $OleT_{JE}$ catalyzed decarboxylation of fatty acids of length C_{16}-C_{20} into LAOs with a TON of 36 and a TOF of 420/ hr was described (Scheme 1.10).[35] Use of H_2O_2, or other oxygen donors, is referred to as a "peroxide shunt" which drives P450 enzymes forward without using O_2.[36] Although often an effective strategy to increase TOF, it can be problematic because the peroxide causes oxidative damage to the heme that supports the Fe active site, eventually leading to catalyst degradation.

One method to avoid degradation is to switch oxygen atom donors from H_2O_2 to O_2, which has been accomplished in tandem with NADPH (nicotinamide adenine dinucleotide phosphate). In 2014 it was reported that fatty acids of length C_{12}-C_{20} were converted into LAOs using NADPH as an electron donor (Scheme 1.10).[37] However, side reactions were common, producing a mixture of hydroxylated products, which hampered yields and overall reaction efficacy. Improvements with NADPH were identified when it was used in tandem with the

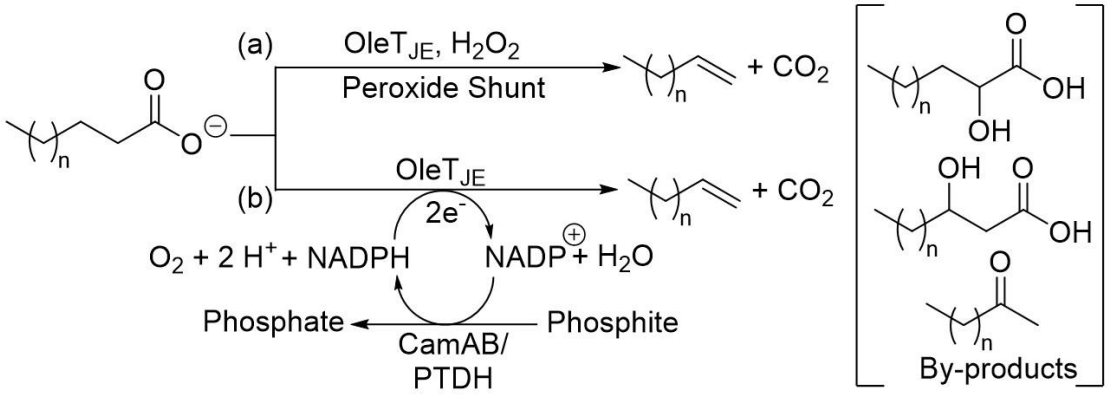

Scheme 1.10. OleT$_{JE}$ reactions. (a) Peroxide shunt method. (b) Use of O_2 as an oxidant and NADPH as an electron shuttle. NADPH (nicotinamide adenine dinucleotide phosphate). PTDH (phosphite dehydrogenase).

enzyme putidaredoxin CamAB reductase, leading to a highly efficient system for regenerating NADPH as the electron donor, with loadings of only 0.06 mol% of enzyme (catalyst).[38] TON and TOF were improved for converting acids to olefins from 194 and 66, respectively, in the previous system (O_2/NADPH only) to 2000 and TOF 90/ hr.[37,38] Hydroxylation side reactions were also successfully minimized, with olefin formation reaching between 86-99% yields.

OleT$_{JE}$ was further optimized by fusing it with a reductase domain of P450BM3 to create a self-sufficient protein, OleT-BM3R.[39] Under aqueous conditions with O_2 as the oxidant and NADPH as electron donor the fusion protein was able to operate without the need for any auxiliary redox partners, while expanding substrate scope to include both aromatic and long

chain fatty acids at only a 0.02 mol% catalyst loading. Further utility was demonstrated with the fused protein remaining active after two months of storage (-20 °C) and through a gram scale conversion of stearic acid to 1-heptadecene in 60% yield. $OleT_{JE}$ has also been successfully immobilized on a cohesion-cellulose binding module in tandem with a lipase enzyme to create a new multienzyme complex (Figure 1.9).[40] The new complex exhibited enhanced stability in terms of pH, temperature and solvents when compared to its individual components. Repeated use of the complex (10 batches) showed minimal loss in reactivity, while exhibiting a 9.2-fold increase in reactivity over the separated enzymes. Increases in yields for LAO of 72 and 69% for waste cooking oils and microalgal oils versus 24 and 25% when the two enzymes were not immobilized into a single complex further demonstrated the superiority of the immobilization.

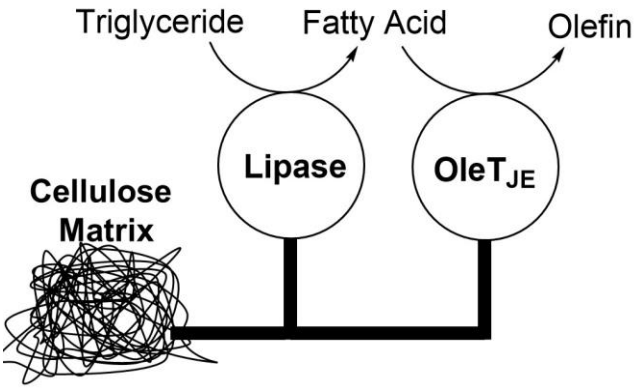

Figure 1.9. $OleT_{JE}$ and lipase immobilized on a cellulose matrix for improved biocatalytic performance

A dual photobiocatalytic system of $OleT_{JE}$, generated H_2O_2 *in situ* from O_2 and H_2O creating a self-sustainable means of oxidant formation (Figure 1.10).[41] The use of flavin mononucleotide (FMN) as photocatalyst with a sacrificial electron donor ethylenediaminetetraacetate (EDTA) converted medium to long chain fatty acids to olefins in typically modest yields (<40% yield) and good selectivity for LAOs over β-hydroxy acid byproducts (≤79%) but was notably inhibited by unsaturated acids. Further development of such

methods could offer cost advantages to current homogeneous methods relying on expensive noble metals.

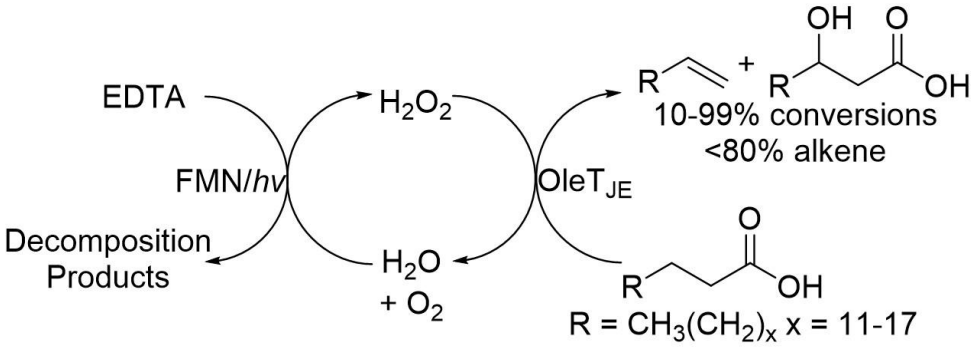

Figure 1.10. Photobiocatalytic decarboxylation of fatty acids into olefins. EDTA = ethylenediaminetriacetate, FMN = flavin mononucleotide.

1.3.6.B. UndA and UndB Decarboxylases

Two other decarboxylase enzymes, UndA and UndB, are members of the *Pseudomonas* genus. UndA is a small enzyme that is made up of only 261 amino acids with an Fe(II) center coordinated by three amino acids as the active site. It is proposed to initiate catalysis by first binding acids in the carboxylate form along with a single H_2O molecule. UndA has a limited substrate scope, only showing reactivity with medium chain fatty acids (C_{10}-C_{14}). It is proposed to proceed via a radical decarboxylation pathway like other biocatalytic methods, but with some mechanistic differences (Scheme 1.11). In particular, an Fe(III) superoxide species is proposed to abstract the β-hydrogen of the substrate (Figure 1.11).[42] A single electron transfer event follows to make the LAO, while generating an Fe(IV)-oxo species that gets reduced by an external reductant back to Fe(II). One of the main limiting factors on the reactivity of UndA has been finding suitable reducing agents for catalysis, that are both active enough and don't lead to degradation of the enzyme. Key differences between UndA and $OleT_{JE}$ include the fact that

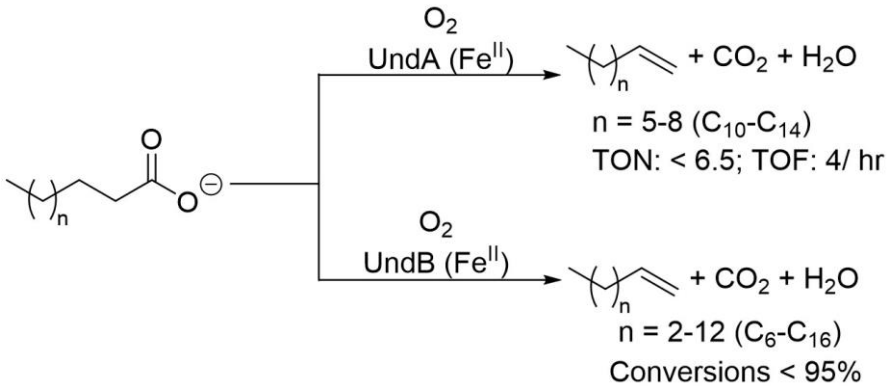

Scheme 1.11. UndA and UndB conversion of fatty acids into olefins with O_2 as the oxygen donor.

UndA abstracts the β-hydrogen by means of an Fe(III)-superoxide instead of an Fe(IV) site, and the requirement for UndA to use a reducing agent for turnover, whereas $OleT_{JE}$ requires oxidation to create the active catalyst.

When compared to UndA, UndB has a larger substrate scope and is able to react with fatty acids with 6-16 carbon atoms, but like UndA, it is most active for C_{10}-C_{14} fatty acids. To date, the mechanistic understanding of UndB is limited, but it is currently hypothesized to operate under a similar mechanism to UndA. When comparing decarboxylase enzymes, UndB

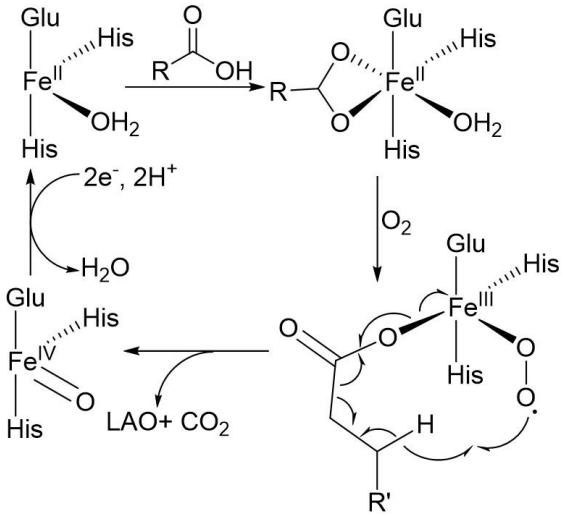

Figure 1.11. Proposed mechanism of UndA decarboxylase

has the highest *in vivo* activity relative to UndA and $OleT_{JE}$ for the synthesis of 1-decene, but lacks the titer (maximum concentration where the reaction remains efficient) of $OleT_{JE}$. Out of the three decarboxylase enzymes $OleT_{JE}$, UndA and UndB, $OleT_{JE}$ remains dominant in terms of its versatility and overall reactivities. Analysis of maximum titers (for any substrate) also show $OleT_{JE}$ to reign supreme at 97 mg/L versus 6 mg/L for UndA and 55 mg/L for UndB. Ideally, a biocatalytic method would be able to operate under highly concentrated conditions to minimize solvent, however, loss of CO_2 acidifies aqueous media, requiring dilute conditions for mitigation.

1.3.6.C. Ols (Olefin Synthase)

Ols is a multienzyme olefin synthase derived from cyanobacteria *Lyngbya majuscide*. Ols can convert long chain acids and operates under a distinctly different mechanism than those proposed for $OleT_{JE}$, UndA and UndB (Scheme 1.12).[43] To convert fatty acids into LAOs, the fatty acid is acylated and attached to an acyl carrier protein (ACP). Next, a sulfotransferase (ST) enzyme sulfonates an installed β-hydroxy group from a sulfonate dimer (3'phosphoradenosine 5'phosphosulfate). A thioesterase (TE) then hydrolyzes the β-sulfonate part of the fatty acid, which is followed by decarboxylation and elimination of the sulfate to produce a LAO.

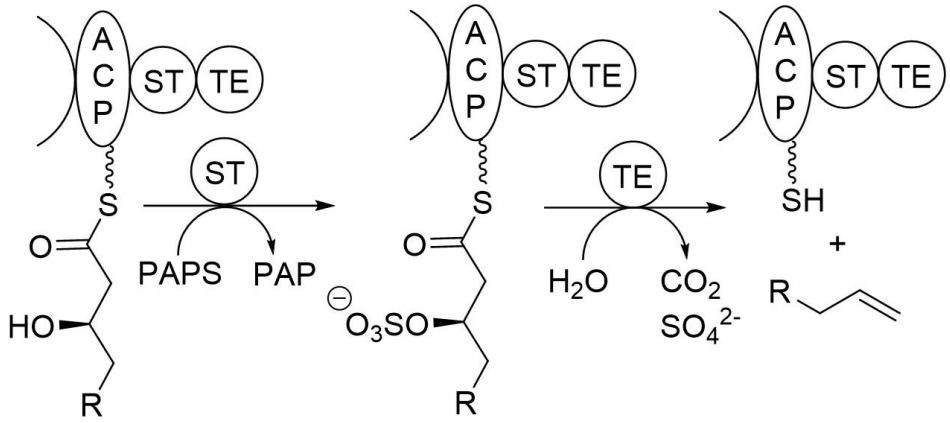

Scheme 1.12. Olefin synthase (Ols) mechanism for α-olefins formation.

1.3.6.D. Phenolic acid decarboxylase

In contrast to $OleT_{JE}$, UndA, UndB and Ols, phenolic acid decarboxylases can convert certain aromatic carboxylic acids into olefins (Scheme 1.13).[44] There are two classes of phenolic acid decarboxylases, one of which requires a cofactor and one that does not. Both phenolic acid decarboxylases only convert aromatic acids into their olefin counterparts. The cofactor dependent version is highly efficient for the conversion of substrates such as cinnamic acid into styrene, but it does not function with aliphatic acids.[45] Cofactor free enzyme acts exclusively on *p*-hydroxy aromatic fatty acids such as ferulic and coumaric acids but will not catalyze reactions of substrates such as cinnamic acid that the cofactor-dependent enzyme does. Due to the limited substrate scopes of phenolic acid decarboxylases, they are not readily employed outside of very specific circumstances and are currently most applicable to styrene production.

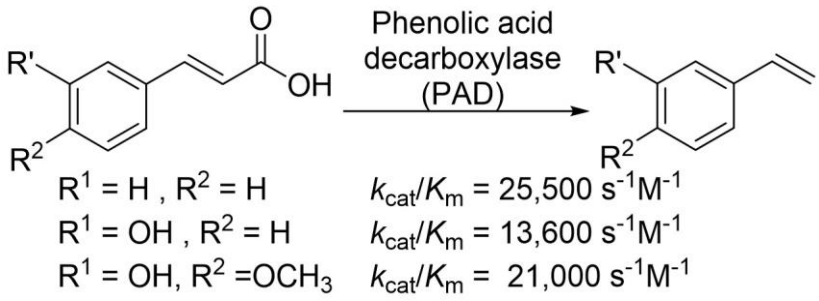

Scheme 1.13. Phenolic acid decarboxylase catalyzed conversion of cinnamic acid variants to styrene derivatives. R^1/ R^2 = H (cinnamic acid) requires cofactor. R^1= OH, R^2 = H (coumaric acid); R^1= OH, R^2 = OCH_3 (ferulic acid) does not require a cofactor.

1.3.6.E. Other enzymatic systems

Other enzymatic systems worth mentioning, but that won't be further discussed, include OleA and the newly discovered photoenzymatic decarboxylase *Chlorella variabilis NC64A* (*CvFAP*). OleA is a decarboxylase that exclusively produces internal olefins from fatty acids and has no ability to produce LAOs.[46] *CvFAP*, on the other hand, is efficient at producing linear

alkanes and does not generate olefins.[47] However, *CvFAP* can decarboxylate fatty acids that may already possess internal or terminal olefins with high selectivity, and thus has potential for use in the synthesis of LIO and LAOs if the unsaturation originates from the starting materials.

1.4. Homogeneous Catalysis: Dehydrative Decarbonylation Methods

In contrast to early work necessitating thermally induced radical pathways and stoichiometric Pb or Ag that suffer from low yields and selectivity, LAOs can be synthesized using numerous transition metals via homogeneous methods via a different dehydrative decarbonylation pathway (Figure 1.12). Distinct from the decarboxylative pathways discussed above, dehydrative decarbonylation produces a unit of CO in tandem with H_2O. The catalytic cycle is proposed to begin with oxidative addition into the activated C-X acyl bond. Decarbonylation, also referred to as CO deinsertion, follows, to create a metal-alkyl species. The olefin forming step, β-hydride elimination, occurs next, at which point the olefin can dissociate and the metal complex reductively eliminate a unit of HX to complete the catalytic cycle. Alternatively, the olefin can rotate 180° and the metal-hydride may reinsert through hydrometallation and subsequently perform further iterations of β-hydride elimination and reinsertion to generate mixtures of linear internal olefins. Over the years a broad range of different transition metals have been used for this reaction, including but not limited to Rh, Ru, Ni, Mn, Fe, Ir, and most commonly Pd. Fatty acid derivatives have included carboxylic acids, esters, aldehydes, and acyl halides.

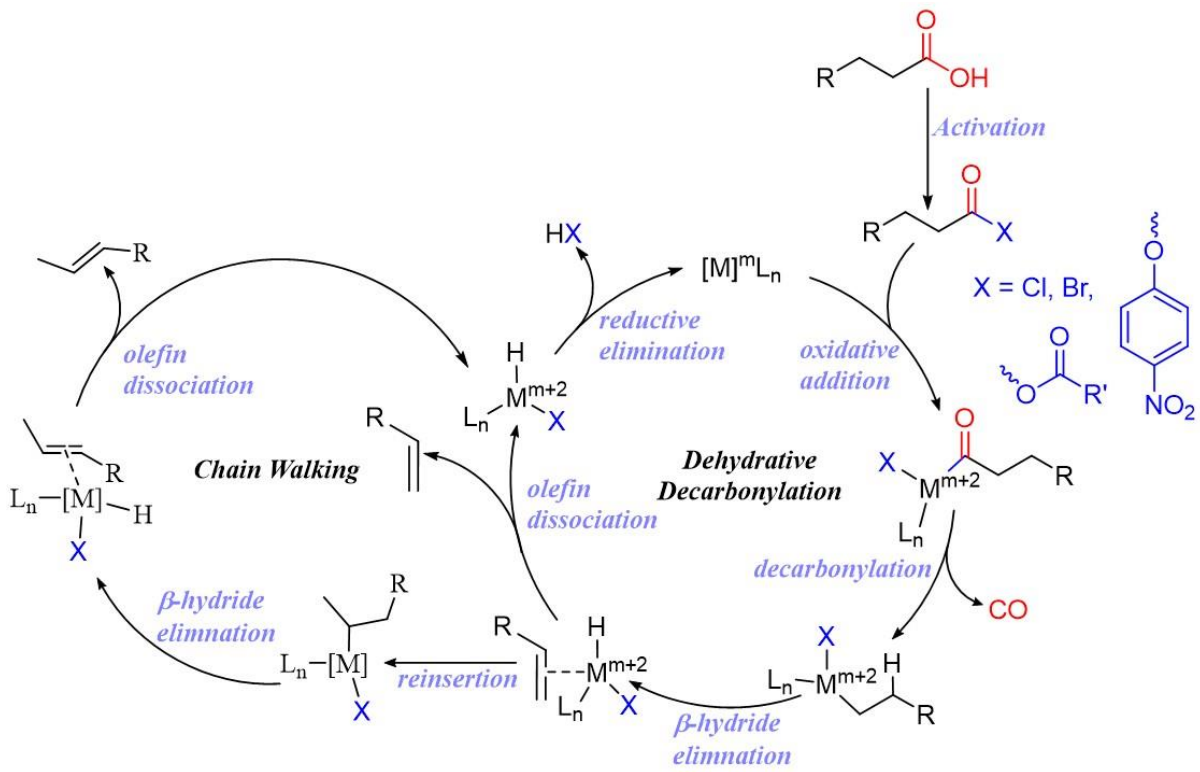

Figure 1.12. Dehydrative decarbonylation mechanism for the conversion of fatty acid derivatives into olefins.

1.4.1. Dehydrative Decarbonylation from Acyl Halides

Owing to the difficulties in direct oxidative addition into the C-O bond of carboxylic acids, various routes of activation have been investigated. An illustrative activated substrate is an acyl halide, which is carboxylic acid derivatives activated through conversion of the C-O acyl bond into a C-X bond (X = Cl, Br).[48] Early reports demonstrated success with $RhCl(PPh_3)_3$ as catalyst, readily producing alkenes from acyl-chlorides and bromides, but requiring high reaction temperatures (~200 °C) and generating a mixture of products (Scheme 1.14a).[48a] Noticeable in these initial reports was the reversibility of the decarbonylation step, with Rh catalysts showing the ability to insert CO back into alkyl-Cl/Br bonds, which may have hampered the overall

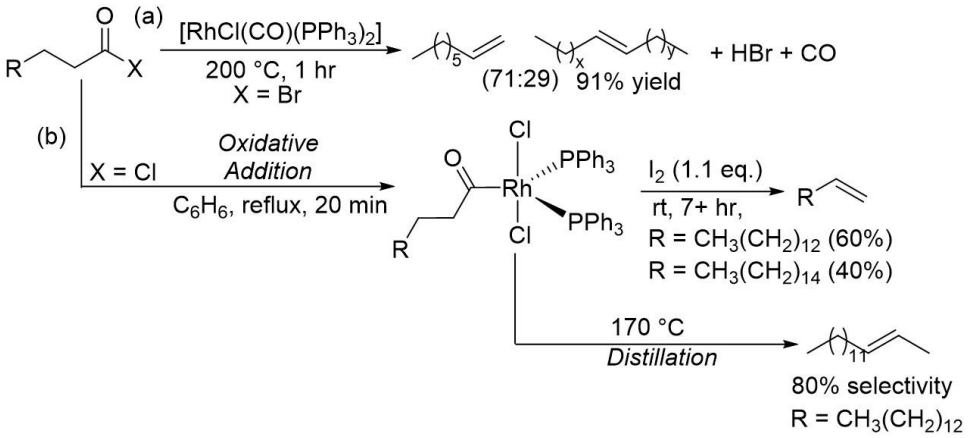

Scheme 1.14. (a) Conversion of acyl-bromides to olefins. (b) Synthesis of oxidative addition products with acyl chlorides and their subsequent reactivity with I_2 or under heating.

efficiency of the reactions. Upon reaction of a stoichiometric amount of acyl chloride (e.g., palmitoyl chloride, stearoyl chloride) and $RhCl(PPh_3)_3$ a five-coordinate acyl-Rh complex was isolated. The Rh-acyl species formed alkenes with the addition of I_2 or upon heating, indicating it may be an intermediate in the catalytic process, formed via oxidative addition (Scheme 1.14b). Reactions with I_2 at rt produced mostly LAOs, but upon heating the Rh-acyl complexes formed mixtures of LIOs. A mixture of LIOs was also reported when Rh was replaced by $PdCl_2$ under the same reaction conditions (200 °C).

1.4.2. Dehydrative Decarbonylation from Anhydrides

A 1976 report described how $RhCl_3$ in the presence of excess triphenylphosphine converted stearic acid into a mixture of isomeric heptadecenes with an α-selectivity of 45% and near quantitative conversion (99%; Scheme 1.15).[49] The nature of the catalyst was crucial to the success of the reaction, with anhydrous and hydrated $RhCl_3$ showing differing selectivity for which isomers form and the latter being significantly more efficient. The active catalyst was determined spectroscopically to be $(Ph_3P)_2Rh(CO)Cl$ in both cases, but anhydrous $RhCl_3$ was

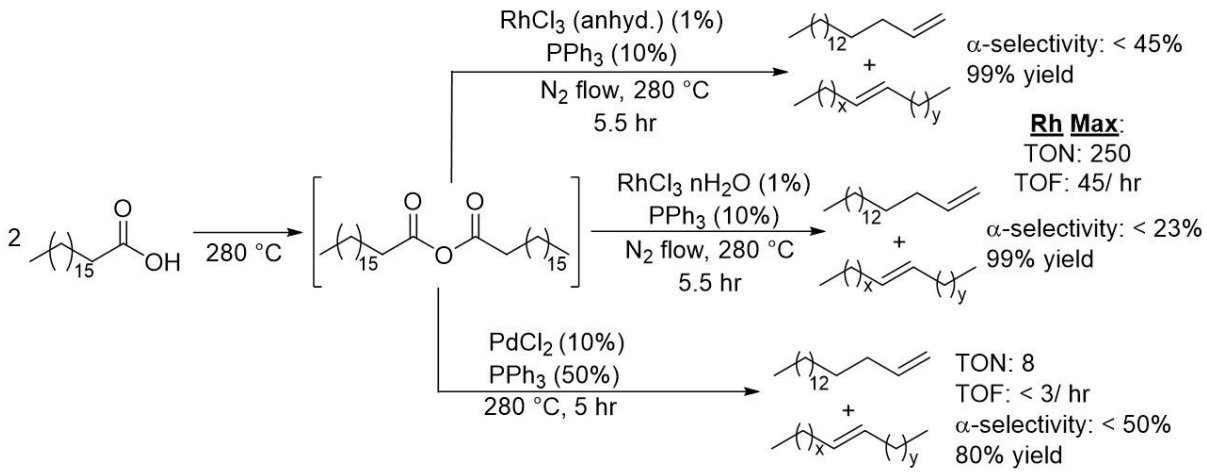

Scheme 1.15. Transformation of stearic acid into olefins, by means of an *in-situ* generated anhydride. Anhyd: anhydrous.

postulated to start off as larger polymeric nanoparticles with reduced surface area, inhibiting formation of active catalytic species. On the other hand, hydrated $RhCl_3$ (3 H_2O) begins as a monomeric, hexacoordinate, compound that can exchange PPh_3 for H_2O and readily form the active catalyst. Stearic acid was used as a model substrate with a ratio of acid: $RhCl_3$: PPh_3 of 100: 1: 10 at 280-285 °C leading to a catalyst TON of up to 250 moles of alkene per mole of $RhCl_3$. High ratios of phosphine ligand were proposed to aid in the formation of the dimeric anhydride from stearic acid, which was a necessary activation step to enable oxidative addition of the C-O acyl bond. The reaction required a constant purge of N_2 gas to remove CO formed from decarbonylation, otherwise potentially poisoning the active catalyst. High reaction temperatures were postulated to be crucial to two aspects of the reaction. Firstly, formation of stearic anhydride through dimerization of two units of stearic acid only occurs at elevated temperatures. The oxidative addition to the C-O acyl bond of acids is notoriously difficult and without formation of an anhydride no reaction occurred. Second, high temperatures help remove CO from the Rh catalyst, allowing open coordination sites to form a 4 or 3-coordinate Rh species active towards oxidative addition. As a minor aspect of the report, it was noted that $PdCl_2$ also

converted stearic acid to olefins, but with a significantly lowered reaction efficiency. $PdCl_2$ required high excesses of PPh_3 (50 equivalents relative to Pd), with 10 mol% of Pd and still only had a TON of <10 and TOF of <3/ hr but had a comparable selectivity for LAOs (α-selectivity <50%) as $RhCl_3$.

Successful realization of the activation of the acyl C-O bond by an *in-situ* dimeric anhydride formation paved the way for the use of sacrificial anhydrides as activating groups to create mixed-anhydride systems (Scheme 1.16). Mixed anhydrides formed between fatty acids and acetic or pivalic anhydride are attractive due to their formation at or near room temperature. On the other hand, the use of sacrificial anhydrides leads to stoichiometric amounts of acid waste, with one equivalent of acetic or pivalic acid being generated upon mixed anhydride formation and a second equivalent being produced upon reductive elimination to regenerate the active catalyst.

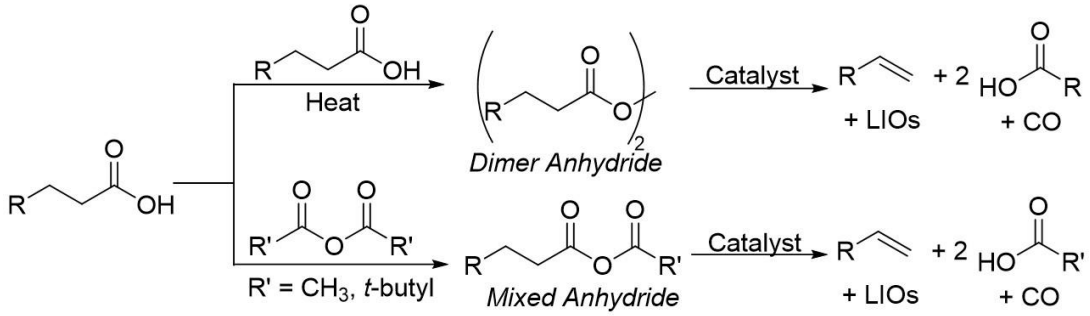

Scheme 1.16. General formation of dimer and mixed anhydrides and their subsequent conversion to olefins, acids, and CO.

Substrates activated by as mixed anhydrides have been proposed to follow a mechanism with four main steps (Figure 1.13). After *in situ* formation of the mixed anhydride, oxidative addition ensues with the metal catalyst. Decarbonylation (CO deinsertion) then occurs to form a metal-alkyl species. β-H elimination forms the olefin and subsequent reductive elimination regenerates the active catalyst and a unit of acid (typically acetic or pivalic acid).

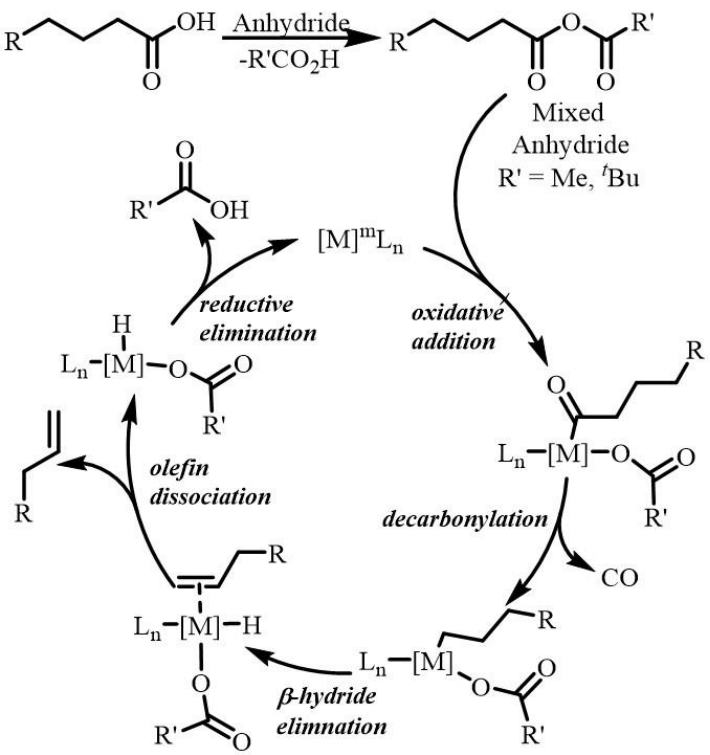

Figure 1.13. Proposed mechanism for the transition metal catalyzed dehydrative decarbonylation of mixed anhydrides (acetic or pivalic anhydride)

One of the first examples of a mixed anhydride system involves an equimolar mixture of a fatty acid, decanoic acid, and acetic anhydride combined at 250 °C with either a Pd or Rh catalyst, which selectively produces the α-olefin 1-nonene.[50] Selectivity for LAOs and reaction TON were strongly dependent on what type of fatty acid derivative was used and whether acetic anhydride was present in the reaction mixture (Scheme 1.17, Tables 1.1, 1.2). Use of the combination of carboxylic acid and anhydride together proved superior to reactions with a pre-synthesized dimeric anhydride, carboxylic acid (forms dimeric anhydride *in situ*), the acyl chloride, or aldehyde, both in terms of TON and selectivity for LAOs. As in previously reports with acyl halides (see above), a flow of N_2 gas was crucial to remove CO at temperatures above 180-190 °C for the transformation to achieve high yields.[49] *In situ* distillation was also

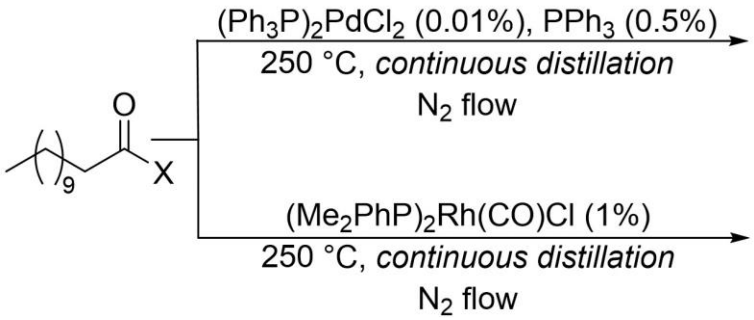

Scheme 1.17. Reactions of lauric acid derivatives with Pd and Rh catalysts.[50]

X =	α-selectivity	TON
OH	No reaction	N/A
Cl	76%	50
H	[a]	20
$CH_3(CH_2)_8CO_2$ (dimer)	84%	1260
OH + Acetic Anhydride	94%	7350

Table 1.1. Comparison of various functional groups of lauric acid with $(Ph_3P)_2PdCl_2$ and PPh_3. [a] mixture of ≥95:5 undecane: 1-undecene was observed. N/A = not applicable.

X =	α-selectivity	TON
OH	79%	60
Cl	28%	1330
H	[a]	240
$CH_3(CH_2)_8CO_2$ (dimer)	87%	280
OH + Acetic Anhydride	97%	700

Table 1.2. Comparison of various functional groups of lauric acid with $(Me_2PhP)_2Rh(CO)Cl$ [a] mixture of ≥95:5 undecane: 1-undecene was observed

implemented to avoid isomerizing via chain walking and is credited for the high α-selectivity (97%). Studies using Rh catalysts (e.g., $(Me_2PhP)_2Rh(CO)Cl$, 1 mol%) with lauroyl chloride exhibited a more rapid decarbonylation reaction versus other substrates, but these reactions showed a substantial decrease in selectivity for α-olefins when compared to the combination of lauric acid and acetic anhydride (28% vs 97%). Notably, although Pd showed no reactivity to the free acid, Rh was able to convert it to LAO with 79% selectivity. At this point it is unclear whether Rh was capable of decarboxylating the fatty acid directly or if it reacted with the acid anhydride dimer through the decarbonylative process.

When compared to Rh, the Pd catalysts used were highlighted as more efficient. A low loading of Pd catalyst (0.01 mol%), in the form of $(Ph_3P)_2PdCl_2$, accomplished the transformation with a TON of 12,370, which remains one of the highest TON reported for homogeneous dehydrative decarbonylation processes even today. Large excesses of PPh_3 (50:1 PPh_3: Pd) were required as PPh_3 strongly influenced catalyst stability. The switch from $(Ph_3P)_2PdCl_2$ to $Pd(PPh_3)_4$ also showed a decrease in TON from 12,370 to 1,550 (while maintaining near equal α-selectivity), indicating Pd(II) precursors may be superior to Pd^0. When the ratio of Pd:PPh_3 was changed from 50:1 to 25:1, while maintaining high temperatures >200 °C, continuous distillation, and using acetic anhydride as an activating group, a maximum TON of 10,000, TOF 10,000/ hr and α-selectivity >97% for $Pd(PPh_3)_4$ at (0.1 mol%) was reported. [51] .

Thereafter, Pd^{II} salts became one of the most popular metals of choice for the synthesis of LAOs. The broad applicability of $PdCl_2$ was shown by its ability to convert various bio-derived carboxylic acid into alkyl acrylates, acrylonitrile, and styrene (Scheme 1.18).[52] Neat conditions were used by switching from acetic (bp = 140 °C) to pivalic anhydride (bp = 193 °C), enabling higher reaction temperatures of 190 °C to be used in a mixed-anhydride system. Both DPEphos and Xantphos successfully facilitated the conversion to olefins, but PPh_3 showed equal success, having the additional benefit of being a cheaper ligand option (Sigma Aldrich as of 6/10/2022 DPEphos $6/g, Xantphos $24/g, PPh_3 $1.20/g; 25g container). Furthermore, styrene was prepared on a preparative scale of 25 g (57% yield) from hydrocinnamic acid under open air conditions, demonstrating the utility of the procedure for deriving important commodity alkenes from bio-sources.

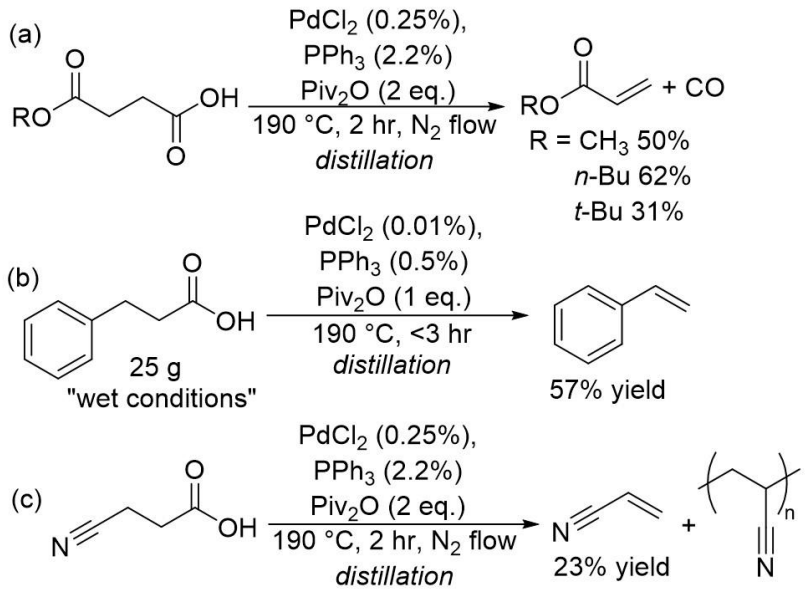

Scheme 1.18. $PdCl_2$ catalyzed synthesis of alkyl acrylates, styrene, and acrylonitrile.[52]

Using the bidentate ligand bis[(2-diphenylphoshpino)phenyl] ether (DPEphos), instead of PPh_3, with $PdCl_2$ in a 3:1 (ligand: Pd) ratio enabled successful dehydrative decarbonylation at a reduced temperature of 110 °C (vs. 250 °C) with high α-selectivity of 83% (selectivity was only reported for the substrate 4-phenylbutyric acid) using two equivalents of pivalic anhydride (Scheme 1.19).[53] The lower temperature disallowed distillation so isomerization was prevented by halting the reaction prior to completion (~80% conversion). The lowered temperature also resulted in the need for a highly polar solvent, *N*,*N*'-dimethylpropyleneurea (DMPU), which soon after became one of the main solvents of choice for LAO chemistry. However, even with

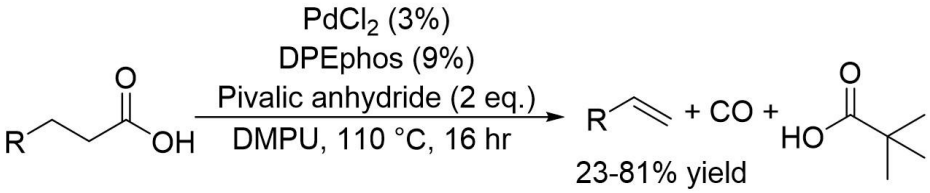

Scheme 1.19. Dehydrative decarbonylation of carboxylic acids using Pd^{II} with bidentate DPEphos. R = saturated and unsaturated carbon chains, aromatics, cyclohexane, etc.[53] TON/TOF were not determined due to reactions being stopped prior to completion.

low activities, a versatile substrate scope was demonstrated for both saturated and unsaturated fatty acids. Of note, the switch from $PdCl_2$ to $PdBr_2$ precatalysts led to a complete reversal of selectivity, exclusively producing internal olefins, for reasons that are unclear.

Further work on the same $PdCl_2$/ DPEphos system showed that the choice of anhydride (acetic vs. pivalic) plays little role in affecting oxidative addition of fatty acid mixed anhydrides. Instead, reaction temperature was identified as the most important factor if the dimerized acid-anhydride is to become the activated species.[54] Trialkylamine bases, such as NEt_3, were introduced and exhibited a drastic effect on the stability of the catalytic species and in avoiding isomerization of the olefins during the reaction, and DMPU was reported necessary to achieve the highest activities. Unfortunately, the tradeoff of lower temperatures likely led to the need for higher loadings of Pd, while giving low TON (<33) and TOF (~2/ hr). A novel selectivity switch for the substrate 4-phenyl butyric acid was identified, favoring α- or internal olefins simply by altering the solvent of the reaction mixture (Scheme 1.20). Reactions in DMPU led to high α-selectivity while those in CH_3CN led to near exclusive internal olefin product, likely due to CH_3CN outcompeting DPEphos for coordination to Pd, generating a bis(acetonitrile)$PdCl_2$ complex.

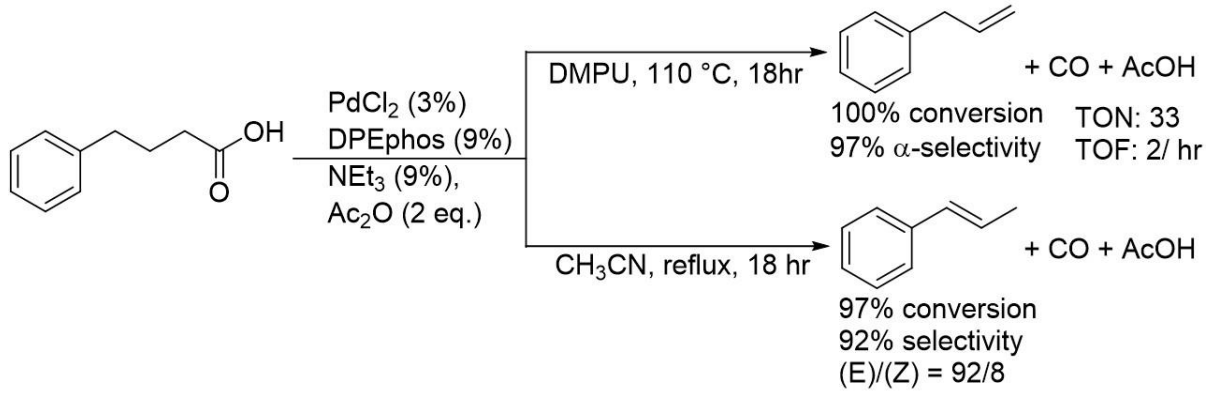

Scheme 1.20. 4-phenylbutyric acid conversion to olefins with solvent determined selectivity. Pd TON: ≤ 33, TOF: 2/ hr.[54]

Other bidentate ligands such as Xantphos (4,5-bis(diphenylphosphino)-9,9'-dimethylxanthene) were examined.[55] Initial work demonstrated that using an acidic additive such as (*t*-Bu)$_4$biphenol in tandem with portion-wise addition of acetic anhydride (1.53 equivalents added over six portions) could convert a diverse array of carboxylic acids into olefins with loadings of $PdCl_2(PPh_3)_2$ and Xantphos of only 0.05 and 0.06 mol%, respectively. Low temperatures were maintained, while under vacuum, also avoiding the need for a polar solvent such as DMPU (Scheme 1.21).

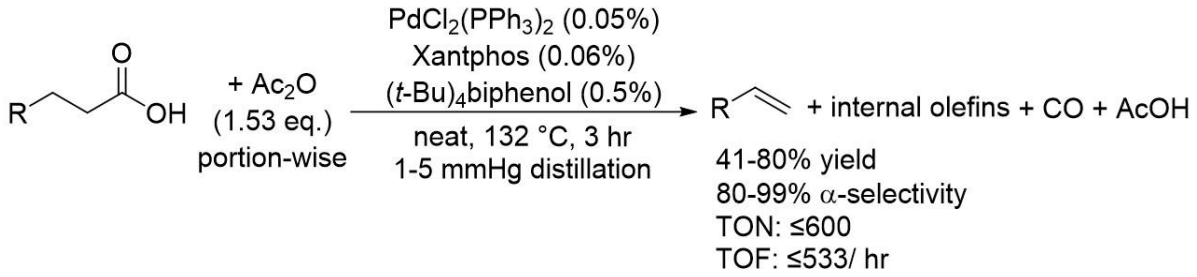

Scheme 1.21. Portion-wise addition of anhydride with acidic additive under distillation condition for high selectivity and TON of fatty acids

Further development of bidentate phosphines and Pd was reported with the synthesis of a series of well-defined Pd^{II}-precatalysts.[56] In doing so the requirement for excess phosphines was eliminated, while still producing LAOs at high levels of selectivity (>95%) for a large variety of substrates using a mild reaction temperature of 110 °C and without the need for continuous distillation (Scheme 1.22).[56a] When $PdCl_2$ and DPEphos were used *in situ* 3 mol% of Pd and 9 mol% of phosphine were required to reach high yields (~100%), versus only 0.5 mol% for DPEphos-Pd precatalysts. However, high levels of selectivity were observed even at lower loadings of Pd (0.5 or 1%, for 10 and 35% conversion, respectively) for the *in situ* system. Furthermore, the precatalysts exhibited TON and TOF eight times that of the corresponding $PdCl_2$/DPEphos *in situ* reaction (TON: 176 vs. 22, TOF: 11.7 vs. 1.3/ hr). Computations suggested the use of discrete precatalysts may lower energy barriers created by excess

phosphines binding to the metal center, making Pd precatalysts more efficient at lower loading, while maintaining an α-selectivity of 96%. Subsequent work with the Pd-precatalysts showed switching from toxic DMPU to an environmentally sourced solvent, such as γ-valerolactone, offers near equal efficiency for the reaction.[56b]

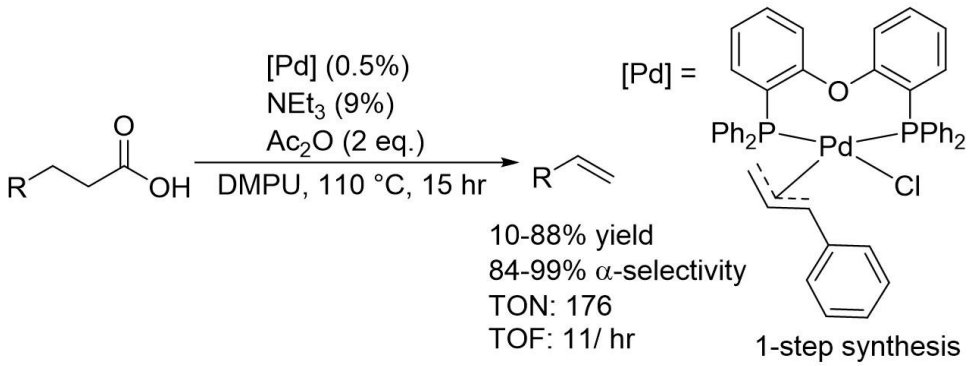

Scheme 1.22. Use of Pd-DPEphos precatalysts for carboxylic acid conversion with acetic anhydride.

Variation of Pd-precatalysts was pursued in efforts to optimize the catalytic reactions. An investigation into quinoline scaffolded monophosphine ligands as structurally similar, monodentate, analogs to reported diphosphines such as DPEphos and Xantphos was reported in 2021.[57] Though no mechanistic work was done to establish the overall role of the bulky monodentate ligand, good to moderate yields and α-selectivities were reported, with TON and TOF of 20 and 3, respectively (Scheme 1.23). Vegetable oil deodorizer distillate, a byproduct created by the vegetable oil refinery process, that is high in free fatty acids was also successfully converted to alkenes in a 70% (gas chromatography) yield.

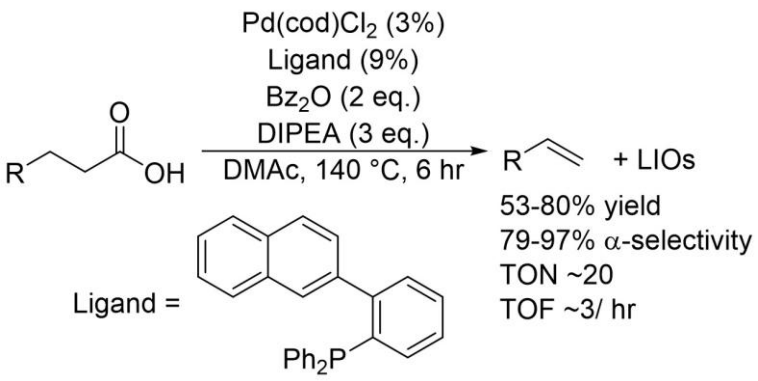

Scheme 1.23. Use of quinoline scaffolded phosphine as a bulky monodentate ligand for fatty acid and vegetable distillate conversions to olefins. Bz = benzoate, DIPEA = diisopropylethylamine, DMAc = dimethylacetamide

Outside of Pd and Rh, Ir is another noble metal that has proven capable of activating anhydrides through a dehydrative decarbonylation mechanism. In 2011 Vaska's complex ($IrCl(CO)(PPh_3)_2$), without additional ligand added, was reported to provide distinct selectivities for LAOs or LIOs dependent on both temperature and anhydride addition (Scheme 1.24).[58] At 160 °C in the presence of KI and acetic anhydride a high selectivity for α-olefins was observed, whereas without anhydride and at increased temperatures of 250 °C mixtures of internal olefins were the major products. Without the use of exogenous anhydride, higher temperatures are required to form a dimerized form of the acids as a symmetric anhydride before the substrate is activated enough for oxidative addition. KI was postulated to play a role in ligand exchange with Cl on Ir, creating a more active catalyst that can operate under reduced temperatures. Overall, acetic anhydride was a sufficient promotor to facilitate the reaction at lowered temperatures, while maintaining high selectivities, but when KI is the sole promoter of the reaction higher temperatures are required to form an activated substrate, which also promotes isomerization to internal olefins.

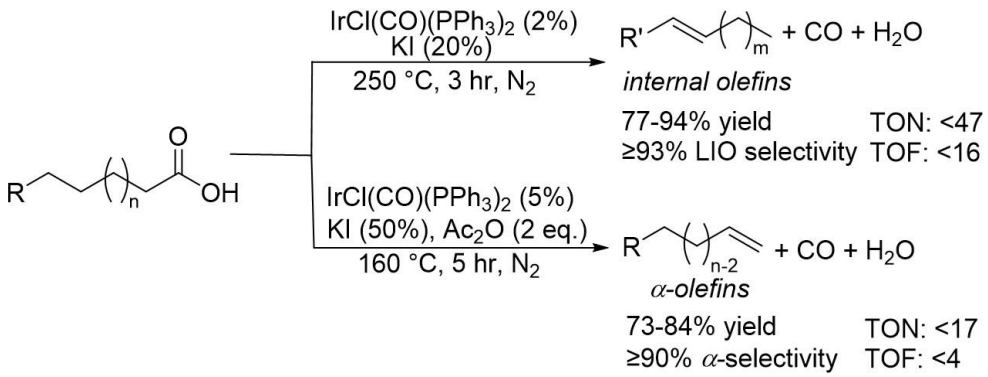

Scheme 1.24. Selectivity switch observed with anhydride use and temperature, catalyzed by Vaska's complex.

The substrate scope for Ir catalysts was expanded later to a diverse array of unsaturated and diacid molecules.[59] Unlike work with Vaska's complex, the Ir catalyst was generated in situ from the commercially available dimer $[Ir(cod)Cl]_2$ (2.5 mol%) and PPh_3 (15 mol%), in the presence of KI (Scheme 1.25a). Notably, under the same conditions, $PdCl_2$ and $RhCl_3$ provided no catalytic activity. Conversions of >65% and α-selectivity >80% for all substrates was accomplished, but no mention of isomerization of starting materials was disclosed (i.e., chain walking on unsaturated substrates prior to decarbonylation or *E/Z* isomerization) and overall, the complex was less selective than Vaska's complex.[63] Under otherwise identical conditions, PPh_3 was later replaced by its amine derivative NPh_3 for several saturated and unsaturated fatty acids to give comparable yields (Scheme 1.25b).[60] Unlike the reactions with PPh_3, NPh_3 reactions offer the ability to operate under air as N-C bonds are less susceptible than P-C to degradation, but use of NPh_3 led to lowered LAO selectivities. As has been observed in previous works, the selectivity between LAO and LIO could be somewhat manipulated based on reaction conditions, with higher temperatures (180 vs 160 °C) and reaction times (16 vs. 8 hr) preferring more thermodynamically stable LIOs. This effect was noticeably enhanced when switching from NPh_3

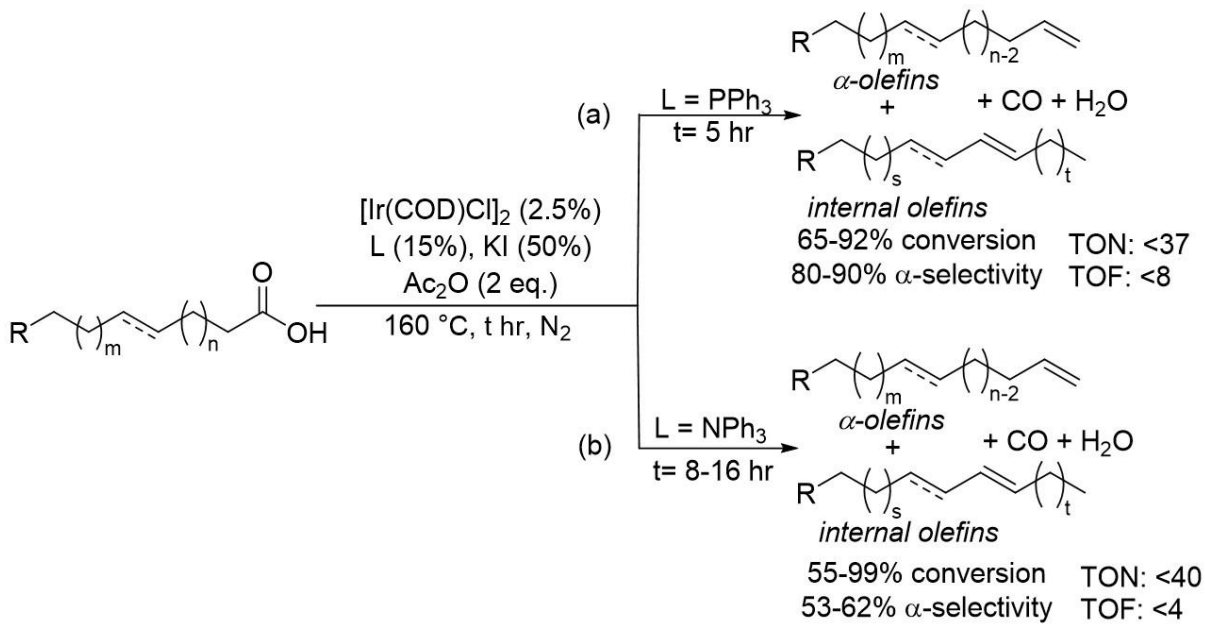

Scheme 1.25. Expansion of Ir catalysts to unsaturated olefins. (a) use of PPh_3 as ligand, showing high conversions in five hours. (b) NPh_3 as ligand, requiring 8-16 hours for high conversion.

to bidentate *N,N'*-tetramethylpropylenediamine (LAO/LIO switches from 63/37 to 5/95 for oleic acid as substrate).

Transitioning from noble metals to base metals is attractive as a means to decrease cost of operation and to enhance availability. Of the few examples of dehydrative decarbonylation by base metals, iron complexes were examined in 2012 (Scheme 1.26).[61] A simple iron salt, $FeCl_2$, in the presence of KI, bidentate phosphine ligand DPPPent (1,5-diphenylphosphino)pentane), and CO (20 atm) created an active catalyst, $Fe(CO)_mL_n$, *in situ* for reactions of fatty acid mixed-anhydrides. Modest yields (60-80%) but high selectivity for LAOs >91% were reported, with the acetic anhydride stoichiometry of 1:1 with acid being a crucial factor. Mechanistic work interrogated the ability of the Fe complex to operate under multiple different mechanisms of catalysis, such as single electron or two electron processes. No effects from radical scavengers (TEMPO, galvinoxyl and 1,1-diphenylethylene) were observed, implying a single electron

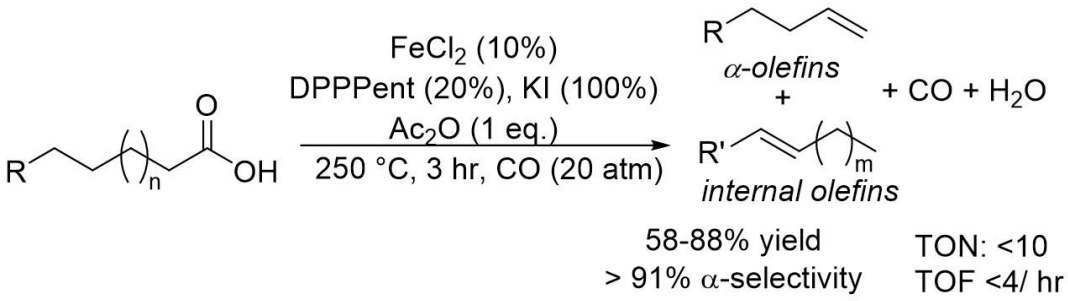

Scheme 1.26. Iron-catalyzed production of olefins under CO pressure.

radical process was not operative. Analysis of the reaction headspace identified the presence of CO (GC), even when it was not added artificially, supporting a decarbonylative mechanism. Although yields are slightly diminished when compared to reactions reported with Pd, the switch to an inexpensive metal such as Fe is promising.

The drive for less expensive, more sustainable options to noble metal catalysts led to an extensive investigation using high-throughput screening methods with base metal salts, ligands and hydrocinnamic acid (Scheme 1.27a).[62] During the study over 20 base metal precursors were tested for their ability to transform hydrocinnamic acid into styrene in the presence of pivalic anhydride at 190 °C with upwards of 20 different ligands, including mono and bidentate phosphines, *N*-heterocyclic carbenes and others. Ni(0) (e.g. $Ni(cod)_2$ and $Ni(PPh_3)_4$) and Ni(II) (e.g., NiI_2) compounds showed the highest levels of productivity over other base metals (Fe, Co, Cu, Zn, Mn) in tandem with phosphine ligands. Reactions with simple phosphines such as PPh_3 were equally productive relative to their more elaborate counterparts (e.g., DPEphos, dppb, DavePhos). Analysis of reaction mixtures showed styrene dimerization likely accounted for the low yields (~30%). Mechanistic studies identified high temperatures as a key parameter necessary to remove CO, which otherwise poisoned the catalyst, forming a stabile $Ni(CO)_2(PPh_3)_2$ species after two catalytic turnovers that could no longer react with substrate.

Upon catalyst screening with hydrocinnamic acid, the best yielding Ni derivatives and ligands were used to convert nonanoic acid ($CH_3(CH_2)_7CO_2H$) to the LAO 1-octene (Scheme 1.27b). The combination of $Ni(cod)_2$ and DPEphos or Xantphos led to high levels of α-selectivity (94%) comparable to previously discussed Pd, Ir, and Fe systems (see above), though with slightly diminished yields (56%).

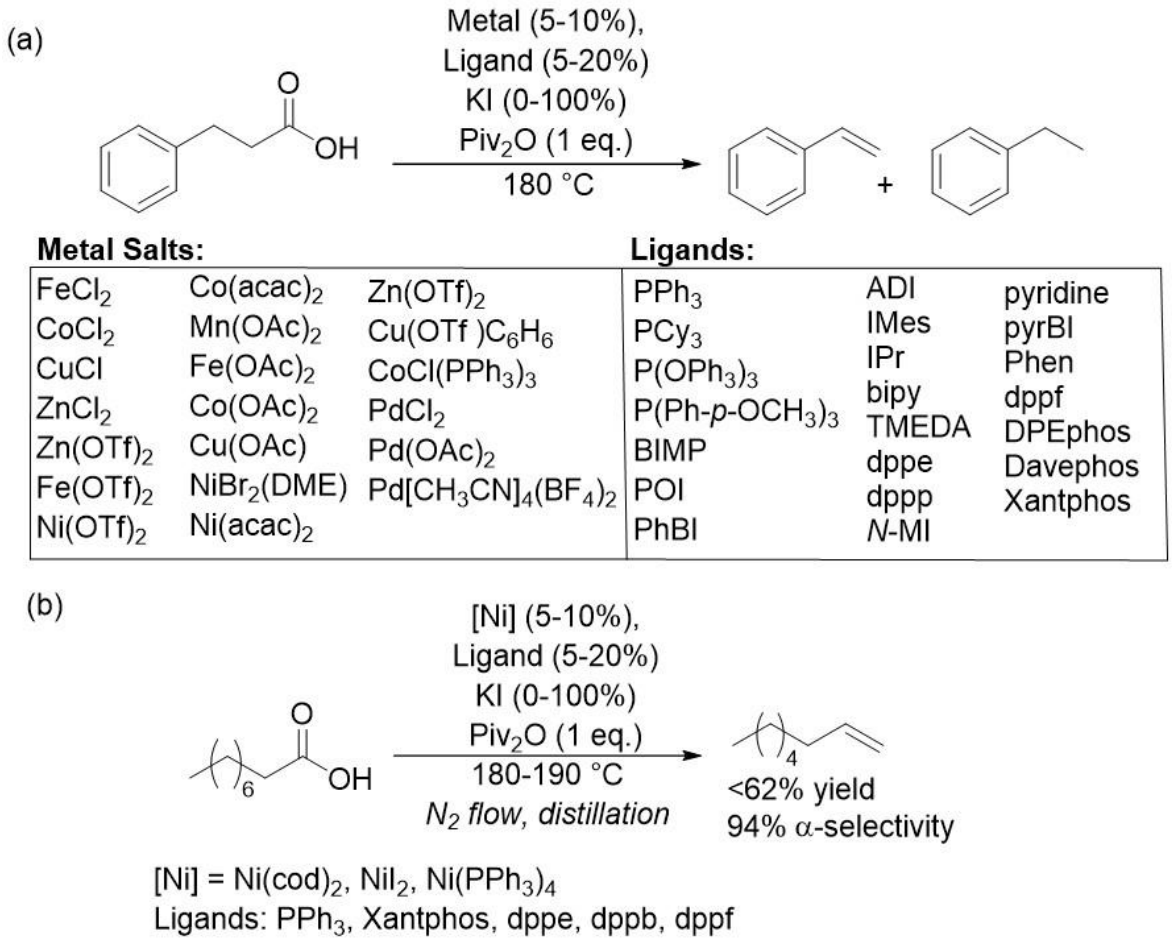

Scheme 1.27. Ni high-throughput experimentation. A) initial screenings of metal salts and ligands for the conversion of hydrocinnamic acid into styrene. B) Applying high-throughput best reactions to nonanoic acid for the synthesis of 1-octene

1.4.3. Dehydrative Decarbonylation from *p*-nitrophenyl esters

Even with mixed-anhydride systems showing great success in activating fatty acid derivatives they have several drawbacks. These include low efficiencies in terms of catalytic turnover, the frequent need for high catalyst loadings or excess phosphines, but most notably the requirement for stoichiometric (1-2 equivalents) amounts of acetic or pivalic anhydride for activation, which generates two to four equivalents of acetic or pivalic acid byproduct upon reaction. Even when sacrificial anhydrides could be avoided, reactions typically required temperatures upwards of 200 °C to generate the dimerized acid anhydride necessary for C-O bond activation. These drawbacks have inspired searches for alternative methods of activation.

In one such strategy, aromatic fatty acids were first converted into activated *p*-nitrophenyl esters.[63] Using $PdCl_2$ with LiCl at 160 °C in DMPU without any additional ligand converted such esters into internal olefins, with little to no observed α-selectivity. A subsequent Heck-type cross coupling then demonstrated the utility of incorporating biomass derived chemicals into synthetic opportunities (Scheme 1.28). Further development of the catalytic system aimed at improving selectivity showed that a dual ligand approach with Xantphos and the *N*-heterocyclic carbene, 1,3-diisopropylphenylimidazo-2-ylidene (IPr), was highly effective for

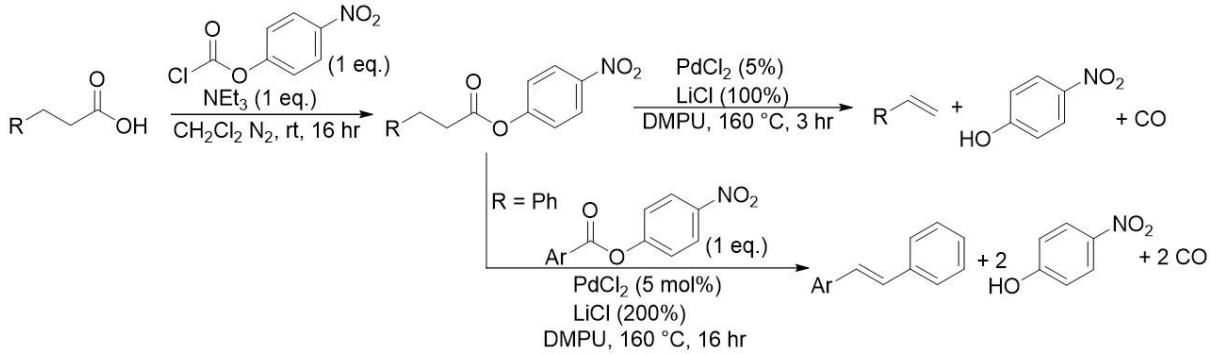

Scheme 1.28. Pre-functionalization of fatty acids as *p*-nitrophenyl esters for activation towards dehydrative decarbonylation and subsequent Heck-cross coupling.

converting *p*-nitrophenyl esters into olefins with conversions >90% and selectivities of >98% at a 2.5 mol% Pd loading (Scheme 1.29).[64] A LiCl additive was crucial for improving reaction efficiency and it was postulated that chloride served as a transient ligand that helped stabilize the metal center upon partial decoordination of the Xantphos ligand. The high levels of α-selectivity were attributed to Xantphos, which led to a α-selectivity up to 82% when it was the sole ligand but increased to 92% by using a mixture comprising 10 mol% each of Xantphos/PPh_3 and 5 mol% $PdCl_2$. Replacing PPh_3 with IPr improved the LAO selectivity (>98%) for a series of long chain fatty acids ($CH_3(CH)_nCO_2H$, n = 7, 9, 10, 12, 14, 16). When IPr was omitted, but Xantphos included, under optimized conditions ($PdCl_2$ (2.5 mol%), DMPU, 190 °C, LiCl (20%)) conversion of *p*-nitrophenyl palmitate (C_{16}) to 1-pentadecene was reported at 46% yield, with α-selectivity of >98%. However, when Xantphos was omitted instead conversions reached 95%, but LAO selectivity dropped to <5%. Taken together, the use of two different ligands was necessary to create a system that was both highly selective and maintained high reactivities.

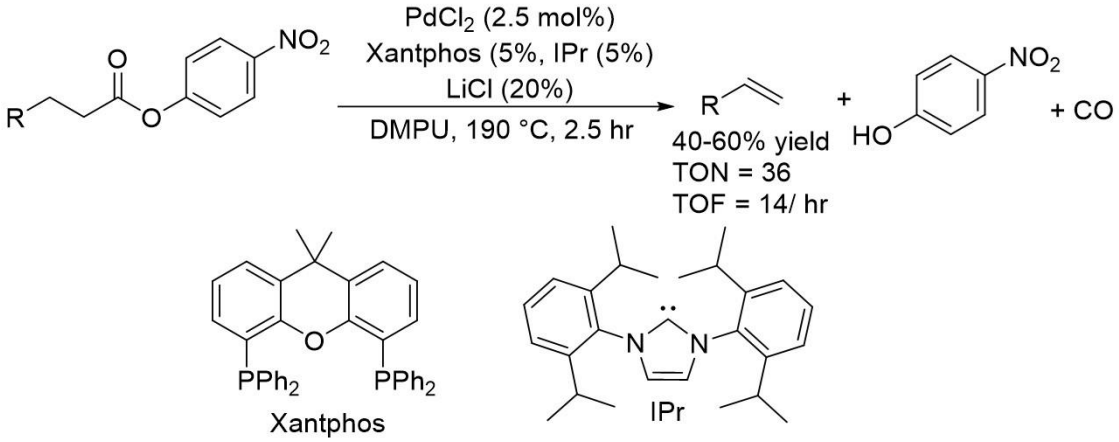

Scheme 1.29. Dual ligand approach with IPr and Xantphos for the conversion of *p*-nitrophenyl esters into olefins. IPr: 1,3-Bis(2,6-diisopropylphenyl) imidazol-2-ylidene

1.4.4. Dehydrative Decarbonylation from Carboxylic Acids

In a 2017 report, a dual catalytic system using Ni(II) salts, $Cu(OTf)_2$ (OTf = trifluoromethanesulfonate), PPh_3 and 1,1,3,3,-tetramethyldisiloxane (TMDS) at 190 °C was described that converted fatty acids to LOs without the use of prefunctionalized or *in situ* activating groups (Scheme 1.30).[65] To this day, this method remains one of the only reports for anhydride-additive free conversion of fatty acids to olefins by Ni or any first row transition metal. In the reported procedure, LAO selectivity reached up to 70%, with yields of up to 82% with $Ni(acac)_2$ or $Ni(OAc)_2$. PPh_3 had a dual role in the procedure, acting as either a ligand or a reductant, generating quantitative amounts of $OPPh_3$ over the course of the reaction. By addition of a copper catalyst, e.g. $Cu(OTf)_2$, and a terminal reductant, 1,1,3,3-tetramethyldisiloxane (TMDS), PPh_3 could be added in catalytic quantities as the $OPPh_3$ formed is reduced *in situ*. In the absence of Cu/TMDS olefin yields were only as high as PPh_3 loadings, and no olefin was produced without PPh_3 present. Unfortunately, when the reaction was performed as a dual catalytic system very little LAO selectivity was observed (<5%). The drop in LAO selectivity was attributed to the requirement of volatile TMDS to be handled within a closed reaction vessel,

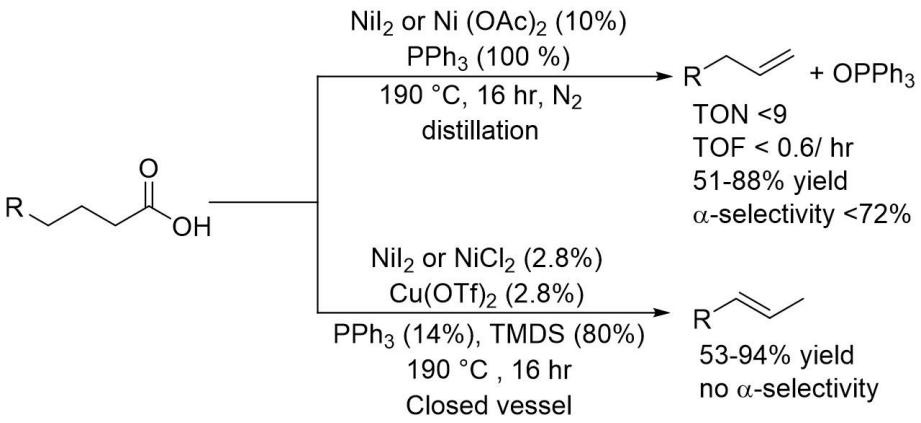

Scheme 1.30. NiI_2 dual catalyzed system with stoichiometric or catalytic PPh_3

which allowed for repeated interactions between the catalyst and olefin, typically prevented by *in situ* distillation. Low LAO selectivities when distillation is not operationally available again shows that catalytic systems rapidly isomerize LAOs to LIOs under standard reaction conditions. Although the current mechanism remains unclear, analysis of the headspace of the reaction vessel showed that CO was present, but not CO_2, suggesting that a decarbonylative pathway is operational.

A later report described how acids were directly converted to olefins without activating groups with either Ni or Rh catalysts while in liquid PPh_3 (Scheme 1.31).[66] Commercially available $(PPh_3)_2NiCl_2$ and Wilkinson's catalyst ($(PPh_3)_3RhCl$) demonstrated differing selectivities for LAO/LIOs for a series of saturated fatty acids. Most notably, the medium chain length lauric acid (C_{12}) was converted in a highly selective fashion to LAO with >95% α-selectivity in 71% yield using Rh with no other byproducts detected (GCMS/Raman spectroscopy). When switching to Ni a drop in selectivity to 79% occurred, with some alkanes present, but near quantitative conversions were achieved. Spectroscopic evidence and the observation of water, CO and $OPPh_3$ supported the likelihood of a dehydrative decarbonylation mechanism, matching the previous dual catalytic reaction discussed above and the likely crucial involvement of PPh_3.[65]

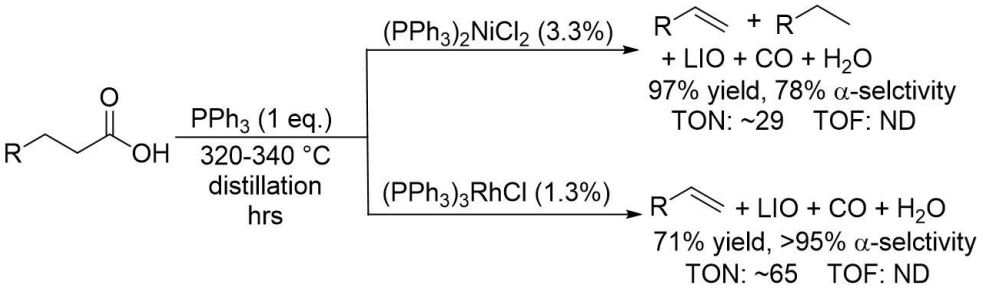

Scheme 1.31. Ni and Rh catalyzed conversion of saturated fatty acids into olefins using liquid triphenylphosphine as solvent. Specific times were not provided for reactions so TOF could not be determined. ND: not determined.

1.4.5. Dehydrative Decarbonylation from Amides

Amides have traditionally been recognized as one of the most stable functional groups in chemistry due to the resonance stabilization between the nitrogen lone pair and the carbonyl.[67] However, by altering the functional groups on the nitrogen atom, the C-N bond can be forced to rotate, disrupting the C(O)-N planarity and the amide resonance, thus weakening the C-N bond and activating it (Figure 1.14).[68]

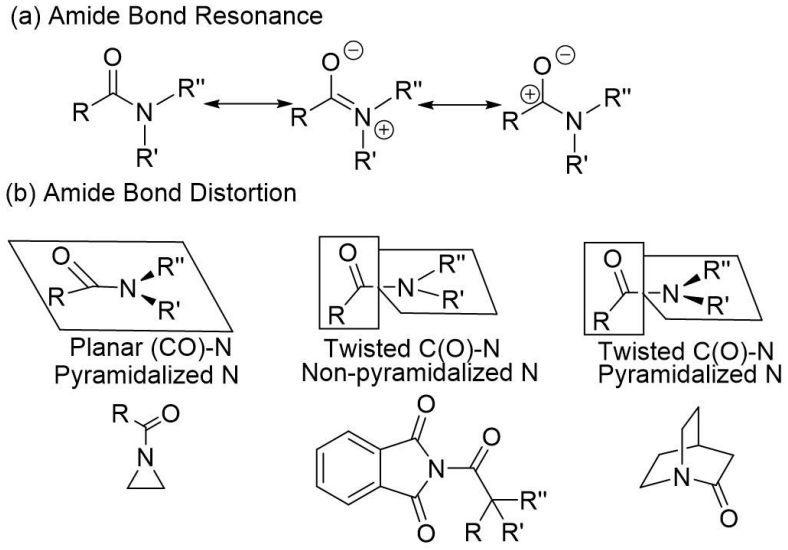

Figure 1.14. (a) amide resonance structures. (b) Types of amide bond distortion, with example molecules

Amide conversion to olefins was first reported in 2015 during substrate scope screenings of a Pd cross coupling reaction with a naphthalene derivative (Scheme 1.32a).[69] The strategy was later expanded to include a larger array of substrates, activated through addition of a Boc (*tert*-buytloxycarbonyl) protecting group, while using $Ni(cod)_2$ and a bulky NHC ligand (ICy) (Scheme 1.32b). A large array of fatty acids and small molecules were converted in moderate to good yields, but with little to no LAO selectivity for fatty acid substrates. The lack of selectivity was largely attributed to the highly reactive nature of Ni-H intermediates.[62]

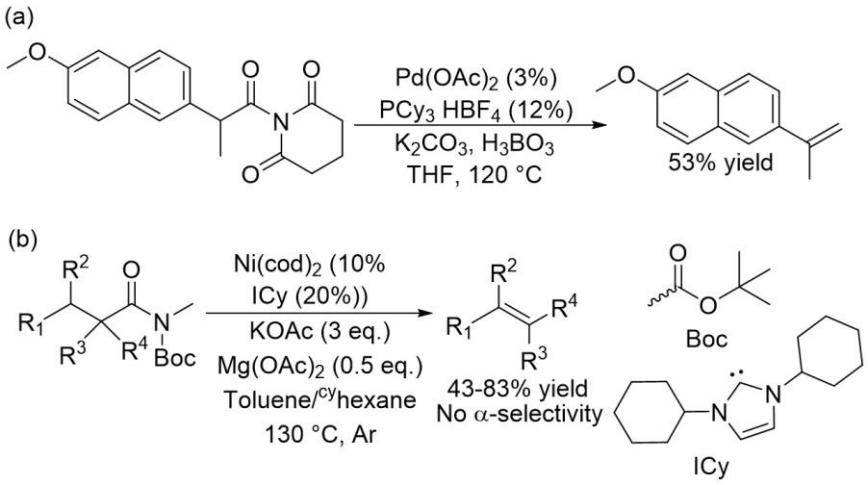

Scheme 1.32. Amides as activated substrates for the synthesis of linear olefins.

1.4.6. Dehydrative Decarbonylation from Methyl Esters

Like amides, methyl esters have proven notoriously difficult to activate due to their strong C-OR acyl bond. In this regard, reports on their conversion to olefins are limited. Activation of the C-O acyl bond was accomplished in a dual-catalytic method involving the transesterification of the methyl ester with a directing group, 2-pyridine methanol, to create a new mixed ester, followed by dehydrative decarbonylation with a Ru catalyst (Scheme 1.33).[70] The mechanism was proposed to involve an initial transesterification event between methyl ester and the pyridine of the directing group, catalyzed by $ZnCl_2$ as a Lewis Acid (Figure 1.15). The nitrogen of the pyridine is thought to coordinate to $Ru_3(CO)_{12}$, which places it within proximity to the C-O acyl bond of the new ester, facilitating oxidative addition. Control experiments

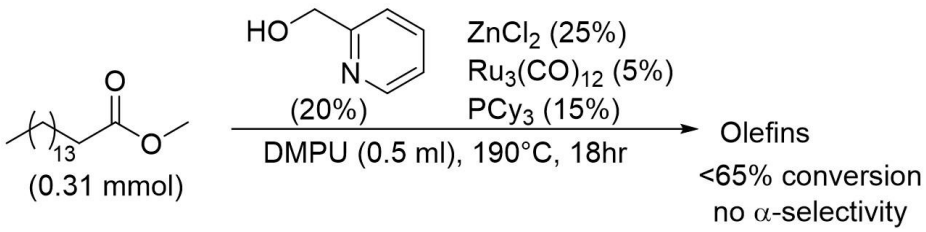

Scheme 1.33. Dual catalytic conversion of methyl palmitate to olefins using a transient directing group 2-pyridine methanol

showed that switching 2-pyridine methanol to benzyl alcohol led to a complete loss of reactivity, supporting the crucial role of coordination of the pyridine N atom to Ru, similar to how the double bonds of unsaturated fatty acids were thought to direct and accelerate decarboxylation reactions as discussed above.[22] After oxidative addition the remainder of the dehydrative decarbonylation reaction proceeds to produce a mixture of olefins. No LAO selectivity was observed even with extensive optimizations, and conversions achieved a maximum value of 66%.

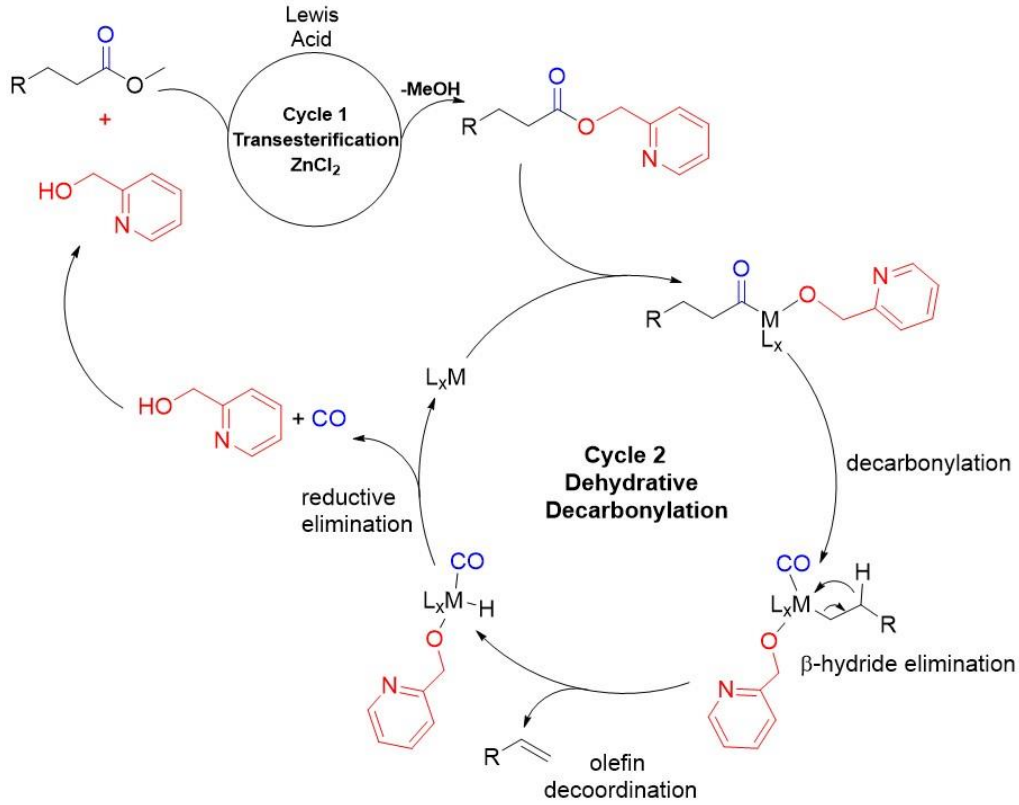

Figure 1.15. Mechanism for the dual catalytic conversion of methyl palmitate to olefins

1.4.7. Mechanistic Insights to Dehydrative Decarbonylation Reactions

With so much experimental work having been developed to produce LAO and LIOs from fatty acid derivatives, surprisingly little mechanistic understanding has accrued in a field dating

back to the 1970's. It was not until 2016 that density functional theory (DFT) was first employed as a tool for mechanistic study in these systems.[62] Initially DFT provided insights, in tandem with experiment, for the conversion of hydrocinnamic acid to styrene using $Ni(PPh_3)_4$ as a catalyst. The DFT calculations elucidated why high temperatures are so often a requirement for dehydrative decarbonylation processes, to remove CO from the catalyst. In the reported system (*vide supra*, Scheme 1.27) hydrocinnamic acid was first activated into a symmetric (dimer) or mixed anhydride in the presence of pivalic anhydride and showed a temperature dependence on the ratio between anhydrides, with the dimeric anhydride being favored at 180 °C, but the mixed anhydride species favored at room temperature (Scheme 1.34). Experimentally, the elementary steps of the reaction (oxidative addition to the C-O bond, decarbonylation, and β-H elimination to form styrene) are all facile processes at room temperature, and the amount of styrene produced equaled the amount of $Ni(PPh_3)_4$ added to the solution (no catalytic turnover). The complexes $(CO)Ni(PPh_3)_3$ and $(CO)_2Ni(PPh_3)_2$ were isolated upon reactions with butyric anhydride at room temperature and at 100 °C, indicating their potential intermediacy in the catalytic process. When the reaction of hydrocinnamic acid/anhydride was initiated with $(CO)_2Ni(PPh_3)_2$, no conversion

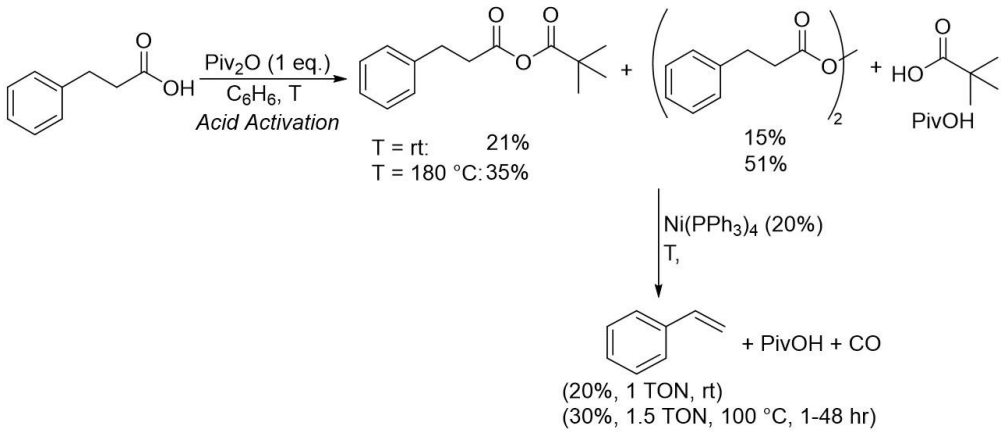

Scheme 1.34. Formation of hydrocinnamic anhydrides and their conversion to styrene

of starting material was observed, indicating it is not an active species in the process. Combined, these results implied that loss of CO from the Ni-center may be turnover limiting during the catalytic process and that the ligation of CO to Ni must be overcome (CO removed) to achieve catalysis. DFT calculations indicated the formation of $(CO)Ni(PPh_3)_3$ to be highly exergonic (-24.0 kcal/mol), showing that phosphine ligand coordination to the Ni-center readily displaces styrene upon β-H elimination (olefin generation). Most importantly the turnover limiting step was determined to be an energy intensive regeneration of the catalyst through loss of CO (26.2 kcal/mol). The high barriers for CO extrusion help explain why high temperatures are so often required for dehydrative decarbonylation processes, even when activation via mixed anhydride formation occurs readily near room temperature. The high barriers also give justification as to why many catalytic processes see enhancements while under vacuum distillation or N_2 flow to help with CO removal.

In other DFT studies, reactions of hydrocinnamic acid using pivalic anhydride, $PdCl_2$ and PPh_3 were explored.[52,71] The turnover determining step was calculated to involve the bis-phosphine acyl intermediate converting via a metal-assisted deprotonation transition state that had a Gibbs free energy of 34.6 kcal/mol (Figure 1.16). When various carboxylates were investigated no clear correlation was found between the pKa of their corresponding acids and the

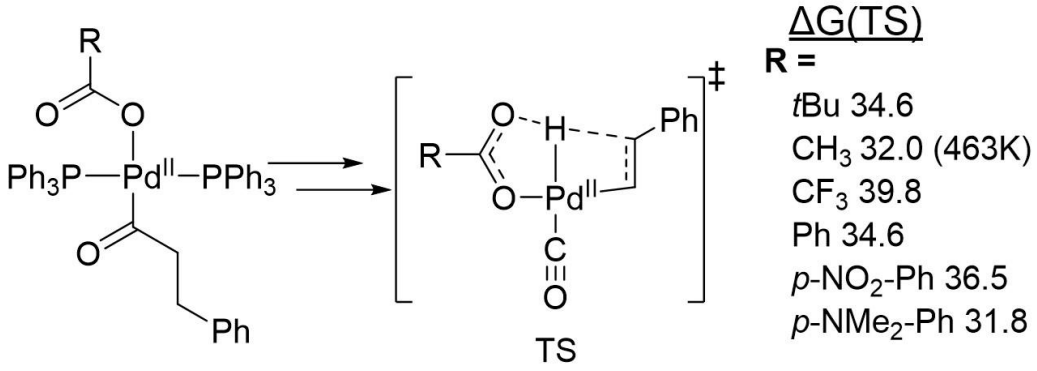

Figure 1.16. Mechanistic elucidations of hydrocinnamic acid to styrene via the combination of $PdCl_2$, PPh_3 and pivalic anhydride

energy of activation, indicating little impact of carboxylate structure on the rate determining step of the reaction. Although it is apparent that carboxylates play a crucial role in their ability to stabilize the Pd center through switching between κ^2 and κ^1 binding modes during the catalytic process, this rules out further optimization of the carboxylate moiety to improve reaction efficiency.

PPh_3 ($V_{\%buried}$ = 29.6%, cone angle = 145°), the ligand of choice in the experimental work being investigated, was compared to two other monodentate ligands, P(*o*-tolyl)$_3$ ($V_{\%buried}$ = 41.4%, cone angle = 194°) and P(*p*-tolyl)$_3$ ($V_{\%buried}$ = 28.2%, cone angle = 145°) in efforts to assess increasing sterics (P(*o*-tolyl)$_3$) or enhancing electronic donating abilities (P(*p*-tolyl)$_3$).[72] No effect was observed from the slight modification of electronics on any aspect of the catalytic cycle, but switching from PPh_3 to the bulkier P(*o*-tolyl)$_3$ decreased the overall energetic barriers of the process from 34.6 to 26.0 kcal/mol, most notable during the rate determining alkene formation step. One potential explanation was that the bulkier phosphine helps accelerate the reaction, while preventing decomposition and poisoning of the catalyst that occurs from CO generation, and aiding in the removal of both CO and alkene from the Pd. The observed benefits of using a bulky ligand are exemplified in other experimental work with bulky ligands that have proven successful, such as those with DPEphos, Xantphos and IPr.[27,53,55,64]

Catalytic reactions of fatty acid derivatives, either activated through a dimeric or mixed anhydride system, have been exclusively performed under neat or highly polar aprotic conditions. High temperatures >200 °C required for neat reactions or the requirement for toxic, expensive solvents (e.g., DMPU) are typically not thought about as favorable from a practical or industrially relevant standpoint. Thus, the pursuit for a green solvent was investigated using DFT and in the process solvent effects were examined for the dehydrative decarbonylation process.[56b]

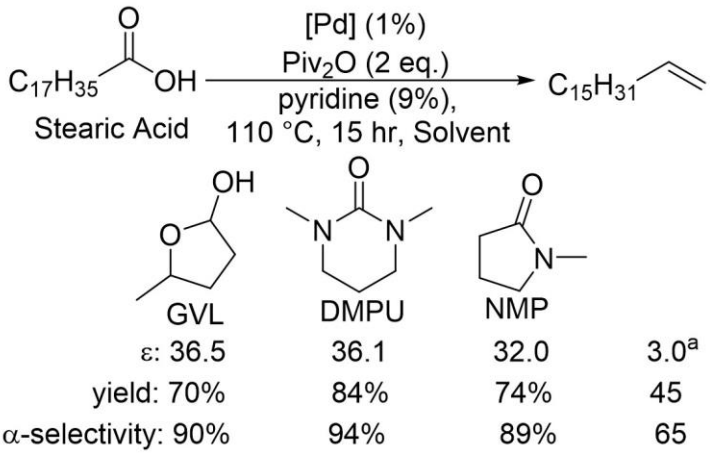

Figure 1.17. Comparison of polar solvents for dehydrative decarbonylation of stearic acid

In particular, an alternative to DMPU was found to be γ-valerolactone (GVL), which has a similar dielectric constant (36.5 vs. 36.1 for DMPU) and was similarly effective for converting stearic acid into olefins (70% yield, 90% LAO vs. 84% yield and 94% LAO for DMPU) (Figure 1.17). Calculations determined that GVL and DMPU achieve high levels of LAO selectivity and conversions by combining properties of high aprotic polarity and a high boiling point (207 °C for GVL) without side reactions with the catalyst, substrate, or any intermediates of the reactions. Three main factors were identified as crucial to the solvent choice. First, dipolar solvents are required for the carboxylate of the anhydride to dissociate from the metal center during the reaction. The dissociation of carboxylate allows the bidentate ligand DPEphos to remain bonded to the metal center without completely blocking all coordination sites, which is crucial for the catalyst to maintain its activity and selectivity throughout catalysis, and to prevent degradation. Second, apolar solvents can provide moderate levels of activity, but the reaction pathway was calculated to be suboptimal due to partially blocked actives sites or competing coordination with the phosphine ligand, which leads to both decreased selectivity for LAOs and catalyst decomposition. Third, protic solvents were shown to be unsuitable due to the reduction in

basicity of the carboxylate unit, which hampers the olefin-forming hydrogen transfer step. To summarize key findings, the superiority of polar solvents to stabilize the rate determining transition state in the olefin-forming β-H transfer step is key to their success. This effect is enabled by means of creating steric and electronic room on the catalyst by ligand (solvent) dissociation, whereas apolar solvents compete with phosphine coordination leading to catalyst degradation.

Further mechanistic study on the effect of ligand choice helped provide initial understanding of potential structure-activity relationships, which outside of the use of a couple Pd-precatalysts (discussed above) have not been thoroughly investigated for dehydrative decarbonylation processes.[56a] In a dual ligand system discussed above with Xantphos and IPr, both ligands were necessary to achieve the high yields and LAO selectivity.[64] IPr has a buried volume of 47.6% and cone angle of 172° making it an extremely bulky monodentate ligand, while also acting as a strong σ-donor.[73] DFT calculations suggested that IPr remains bonded to Pd throughout the catalytic cycle, while its steric bulk plays a critical role in preventing chain walking (Figure 1.18). For isomerization to occur after the olefin forming β-H elimination step the olefin must either rotate 180° or dissociate from Pd and reassociate prior to hydride reinsertion. The most energy demanding influence of IPr was calculated to be the alkene rotation (5.4 kcal/ mol) necessary for isomerization to occur effectively preventing it, which leads to an increase in LAO selectivity. Xantphos, on the other hand, is a *trans*-spanning ligand that can bind in both bidentate (κ^2) and monodentate (κ^1) fashion. The ability is thought to be crucial for the success of dehydrative decarbonylation reactions on Pd, allowing there to be room around Pd during alkene formation by dissociating one phosphine, while recoordination rapidly dissociates the LAO and prevents it from further interacting with the Pd catalyst. DFT calculations

determined the most energetically demanding step with Xantphos to be hydride reinsertion (8.4 kcal/mol). While alkene decoordination would initially lead to a three coordinate Pd species, Xantphos switching from κ^1 to κ^2 is a crucial rationale for high LAO selectivity. Together, the dual ligand system allowed no viable alkene rotation transition states to be found as the coordination sphere around Pd was too crowded.

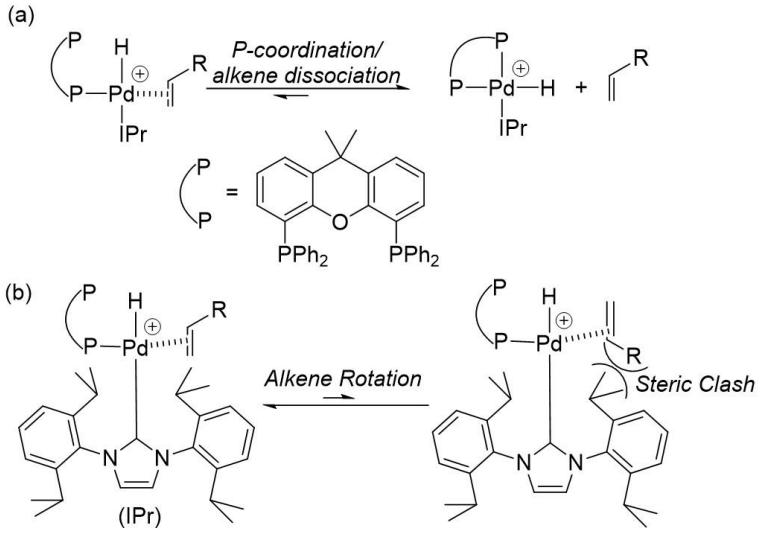

Figure 1.18. Effects of Xantphos and IPr on most energetically demanding steps for olefin synthesis.

DPEphos, which has shown similar success in dehydrative decarbonylation reactions to Xantphos and is structurally similar, was investigated for its role in supporting Pd-precatalysts discussed above.[56] Calculations point to the hemilability of DPEphos being a critical feature to the decreased thermodynamic barrier and high α-selectivity achieved using the ligand.[74] In particular, the initially bidentate ligand is able to facilitate decarbonylation by switching to a monodentate binding mode, creating space for CO to deinsert from the acyl unit and bind to Pd. Subsequent rapid recoordination of the second phosphine arm back to Pd displaces the CO unit from Pd. By displacing CO early in the catalytic cycle and achieving a bidentate mode of binding the Pd can have room for β-H elimination to produce the LAO. Bidentate binding of DPEphos

also provides the appropriate amount of steric crowding around Pd to rapidly dissociate the newly formed olefin and preventing isomerization from occurring, leading to high levels of α-selectivity, similar to Xantphos, while allowing a H-transfer event to occur to the anhydride carboxylate and regenerate the catalyst.

Mechanistic studies that compare multiple metal catalyst systems are rare. One recent study comparing Rh and Pd catalysts has offered some useful insights that may aid in future reaction design.[75] Two catalytic systems were investigated: Pd/PPh_3 and $(PPh_3)_2Rh(CO)Cl$, each of which had been previously used in dehydration decarbonylation processes (the substrate was altered for computational simplicity to butyric acid).[75] Overall, the Pd catalyst was calculated to offer a much more facile reaction with barriers for decarbonylation of 19.3 vs. 30.6 kcal/mol and alkene formation of 25.3 and 33.4 kcal/mol, which matched experimental observations. Several notable differences in the two catalysts play into the differences in reaction barriers, but perhaps none is larger than the influence CO has as a ligand. In most reports it is assumed that $PdCl_2$ first gets reduced by excess phosphine *in situ* to a Pd(0) species with subsequent coordination of PPh_3, prior to catalysis. In contrast, the active Rh catalyst is postulated to be the initial complex $(PPh_3)_2Rh(CO)Cl$, making Pd more electron rich and more primed for oxidative addition than the Rh(I) center. During oxidative addition Pd goes from a likely coordination number of two to four, whereas Rh increases from three to six, as Rh(III) species prefer a hexacoordinate octahedral geometry (Figure 1.19).

Oxidative addition is followed by decarbonylation, calculated to be more facile with Pd, in part because a lower valent Pd(II)-CO species exhibits enhanced stability versus a Rh(III)-CO species. The third step of the catalytic cycle, β-H elimination/alkene formation, again shows a major difference in barriers between metals, where Pd has a $\Delta G^{\ddagger}$ of 25.3 and Rh of 33.4

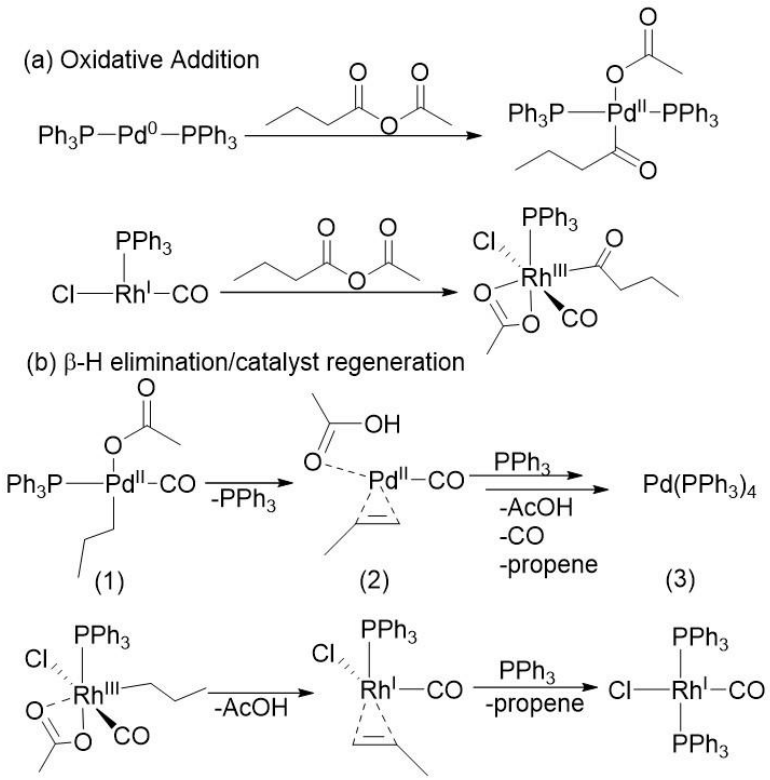

Figure 1.19. (a) oxidative addition process of Pd and Rh complexes. (b) β-H elimination starting from the decarbonylation intermediate (1) to form propene coordinated to the catalyst (2) and subsequent catalyst regeneration (3).

kcal/mol. One of the major factors accounting for this difference is that Pd can dissociate both PPh_3 ligands prior to β-H transfer, decreasing steric crowding around the metal, whereas loss of phosphines is unfavorable for Rh, which instead must lose one of its CO ligands, likely occurring immediately after decarbonylation. Both metals require a CO ligand for reductive elimination of the pivalic acid to be a favorable process to stabilize the low valent Pd(0)or Rh(I) generated during the reaction.

Taken together, the computational work provides key insights into why Pd is superior to Rh, and likely many other metals, matching experimental observations that have made it the workhorse of dehydrative decarbonylation reactions over the past several decades. The transient nature of PPh_3 on Pd offers an explanation as to why it is often required in excess with Pd, but

hinders other metals, like Rh, where it cannot readily dissociate during catalysis. Although further mechanistic work is necessary to elucidate key differences between specific reported systems (i.e., Pd vs. Ni, ligand design etc.) initial studies may aid in better future reaction design.

1.5. Heterogeneous Catalysis

Heterogeneous catalysis is often thought of as a more industrially relevant means of catalysis than its homogeneous counterpart due to enhanced thermal stability, avoidance of costly ligands, and ease of separation of catalyst and products.[76] However, when it comes to converting fatty acid derivatives into olefins several drawbacks have been noted. These include low activities (TON/TOF), rapid catalyst poisoning/deactivation or the need for pre-activation with hydrogen gas and heightened temperatures. Product selectivity has also been a major issue for heterogeneous methods, not only for producing LAOs over LIOs, but heterogeneous catalysts often lead to mixtures of ketones, esters, paraffins and partially hydrogenated products due to the presence of H_2.[77]

Stearic acid (C_{18}) has been one of the most explored fatty acids for heterogeneous catalysis to date. With 17 carbons in its aliphatic chain (18 total), it is one of the longest fatty acids available commercially and in nature. In 2011 stearic acid was converted to LAOs at 523 K (250 °C) over a Pd/Al_2O_3 catalyst in the absence of H_2 gas.[78] It was suggested that stearic acid dimerizes to form stearic anhydride in the rate limiting step. The initial feed concentration was found to be a determining factor in what reaction pathways were dominant during operation (Figure 1.20). At very low acid feeds decarboxylation was dominant, forming paraffins almost exclusively, but as feed concentrations increased stearic anhydride became a more prominent intermediate leading to decarbonylation of the anhydride, generating olefins. On the other hand,

when substrate concentrations increased further, decarboxylation of the anhydride to generate ketones was the dominant reaction. In order to achieve high selectivity of olefins (>99% LAO + LIOs), the conversion of stearic acid had to remain low (<20%), but no specific α-selectivity was observed.

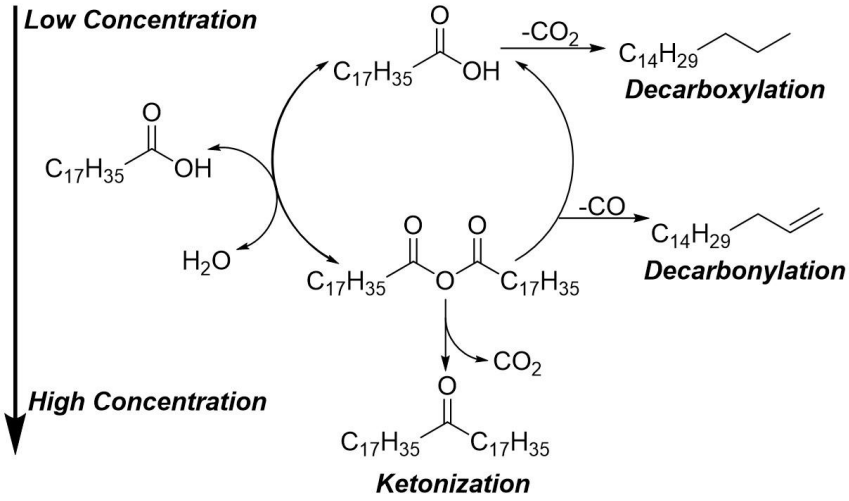

Figure 1.20. Stearic anhydride reaction pathways with varied concentrations

LAOs were produced in a highly selective fashion in a 2013 report, when a series of four different lactones and unsaturated acids were transformed into olefins over gamma-alumina and tungstated alumina at 648 K (375 °C).[79] The reaction was proposed to proceed via decarboxylation of unsaturated fatty acids generated *in situ* by ring opening lactones with water used as solvent (Scheme 1.35). Interestingly, no transition metal catalyst was required for this transformation, instead only using heterogeneous Lewis acid catalysts. An α-selectivity of 99% was reported for γ-butyrolactone, but only when the reaction was at ≤10% conversion. LAO selectivity decreased to 92% at 43% total butene yield (substrate conversion) after which point isomerization became rapid. During the course of study, water was identified as a means to inhibit isomerization of α-olefins over Lewis acid sites, whereas the isomerization was rapid over Bronsted acid sites regardless of water's presence.

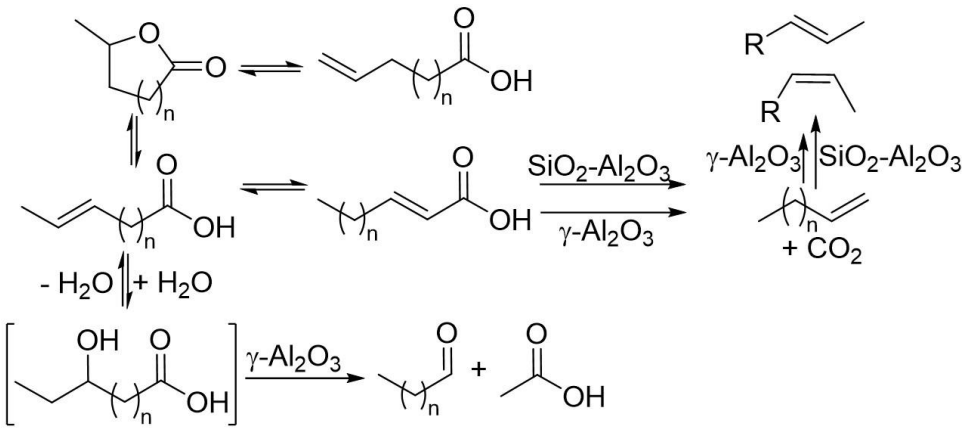

Scheme 1.35. Lactone and fatty acid conversion to olefins over γ- and tungstated alumina

Studies of Pt or Pd nanoparticles supported on carbon in a fixed bed reactor showed conversion of heptanoic acid to hexenes through decarbonylation pathways.[80] Temperatures of 573 K (300 °C) were required, but both liquid (37 bar) and gas phase (1 bar) reactions were investigated in their role for product selectivity. Liquid phase reactions showed low TOF of 18/ hr for Pt and 2.6/ hr for Pd systems. Low TOF was thought to be due to sintering of the catalysts or through deposition of carbonaceous species, limiting the amount of surface area available for catalysis. Conversions of heptanoic acid had to remain low to keep the reaction operating under the decarbonylation pathway and generating olefins, as it was observed that when going from 1 to 5% conversion with Pt nanoparticles in liquid phase there was an increase in the amount of hexane and CO_2 formed (Figure 1.21). Hexane and CO_2 were likely generated through secondary side reactions such as the water-gas shift reaction which creates H_2 used for hydrogenation of olefins. Switching to the gas phase (1 bar), a maximum of 57% α-selectivity (at <11% total conversion) for the Pt system was achieved. The low pressure of the system in the gas phase likely prevented repeat interactions of 1-hexene with the metal catalysts, averting isomerization. Overall, the processes were only effective at synthesizing LAO or LIOs when conversion of acids remained very low.

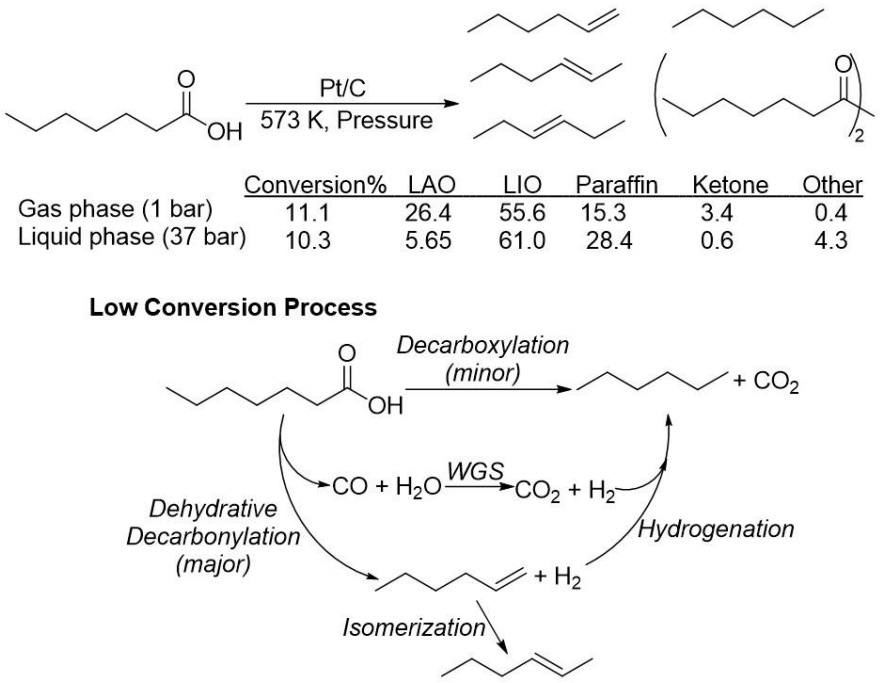

Figure 1.21. Conversion of heptanoic acid to alkanes, alkenes, and other products via Pd and Pt nanoparticles at low conversions (<5%).

Use of mixed anhydrides has led to successful routes to LAOs under homogeneous catalysis (see above), but it was not until 2016 that they were reported to be used with heterogeneous catalysts for activating fatty acids.[81] Combining Pd/C (1%) with the bidentate phosphine ligand, DPEphos (10%), and acetic anhydride (1 equivalent) at 250 °C for 15 minutes showed a marked improvement in yields, selectivities and substrate scope over previously reported heterogeneous methods (Figure 1.22). TOF of 420/ hr and α-selectivities of >95% were achieved without the requirement of H_2 gas, solvent or *in situ* distillation. Unlike most reported systems that focused as proof of concepts on a single substrate, a range of medium to long chained fatty acids were successfully converted (39-70% to olefins with high levels of α-selectivity >95%). Aromatic fatty acids showed moderate α-selectivities of 60-66% and

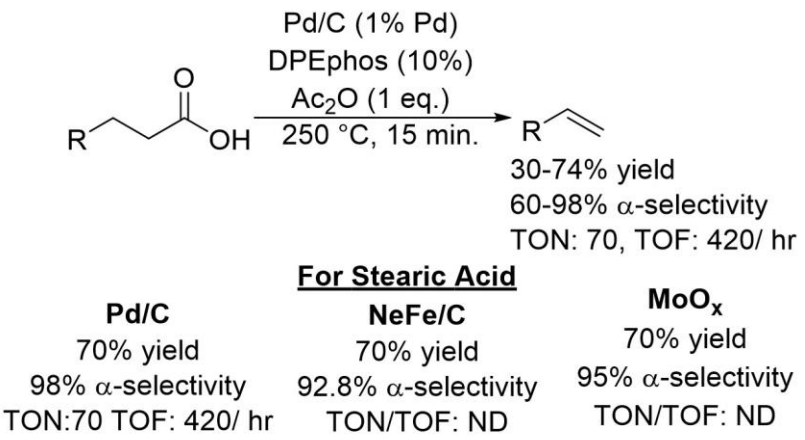

Figure 1.22. Use of heterogeneous catalysts with DPEphos and acetic anhydride and comparison of yields for stearic acid. ND = not determined, due to number of active sites or metal loading not being disclosed.

selectivity for LAOs remained high even at >20% conversion of acids, without hydrogenated products. The catalytic system was stable for three sets of reactions before showing decreased catalytic activity due to agglomeration of Pd clusters. It was proposed that the stalling of conversions derived from CO poisoning from the decarbonylation mechanism, coking and olefin absorption. Mechanistic investigations support the role of a heterogeneous catalyst that operates in similar fashion to homogenous Pd in the activation of an *in situ* generated mixed anhydride species.

In the quest to move away from noble metals to more abundant base metals comparative work was reported in 2020 using either a NiFe/C alloy or a mixed valent MoO_x catalyst.[82] Stearic acid was used as the sole substrate of comparison, while also using the ligand DPEphos and acetic anhydride as the activating agent (mol % of reagents was not provided) while a notable decrease in temperature from 250 to 190 °C was reported. Both NiFe/C and MoO_x efficiently converted stearic acid (70% conversion) to olefins with high levels of LAO selectivity (~95%). The limited conversion was regarded as due to the coordination of olefins to the active sites of the metal catalysts due to the reactions taking place in the liquid phase, similar to with Pd/C.

As with homogeneous catalysis, the desire to avoid stoichiometric anhydride reagents has led to the development of alternative methods. Unfortunately, in terms of heterogeneous catalysis that omission leads to a limitation in LAO selectivity, here thought of as the formation of any/all olefin products versus paraffins, ketones, esters, alcohols, or other materials. A tandem hydrogenation/dehydration reaction of hexanoic acid in a fixed bed reactor at 210 °C under 5 bar of H_2 with a Cu catalyst dispersed on Al_2O_3/ SiO_2 was developed.[83] The strategy avoided an oxidative addition event to the C-O acyl bond, which is the case with mixed anhydride systems, and instead began by first reducing the acid moiety to an alcohol with Cu/H_2 (Figure 1.23). The Lewis Acidic Al_2O_3/ SiO_2 sites then facilitated dehydration of the alcohols to olefins. In this strategy a 92% selectivity was observed for olefin products as a mixture of 1, 2 or 3-hexene, but no specific LAO selectivity was reported. A selectivity switch from akene to alkane occurred upon complete conversion of heptanoic acid, indicating hydrogenation reactions become dominant at high conversions. Spectroscopic studies indicated that during the reaction small

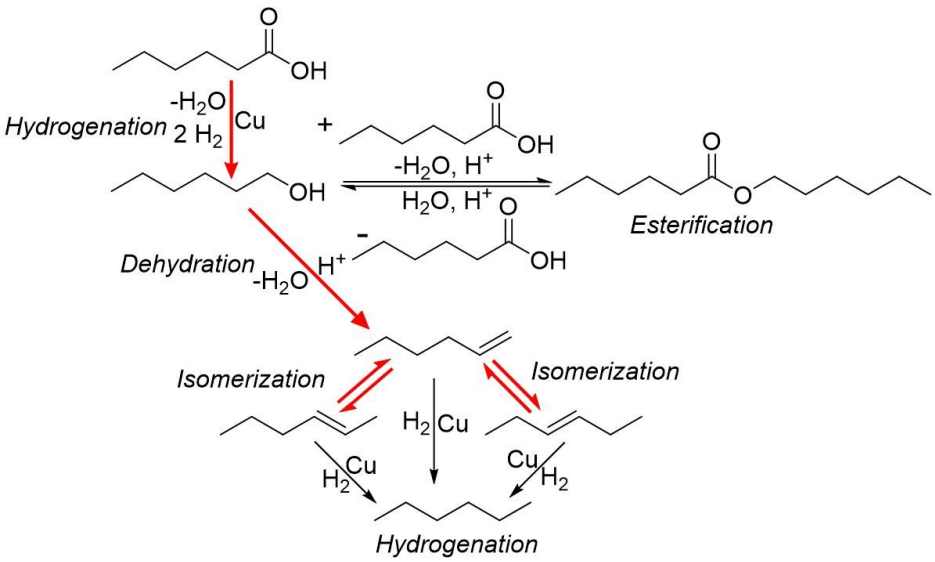

Figure 1.23. Hydrogenation/dehydration strategy for hexene synthesis over Cu/Al_2O_3. Main pathways are shown in red.

amounts of acid bind to the catalyst surface, inhibiting hydrogenation of olefins (which don't bind to the Cu/Al particles), but once the acid was consumed a 99.8% selectivity for hexane (hexene hydrogenation) occurred.

A 2021 report described how a $PtSn/SiO_2$ catalyst quantitatively converted stearic acid with a ~73% selectivity for heptadecene at 320 °C, without H_2.[84] Kinetic and spectroscopic investigations suggested a direct decarbonylation of the acid was the primary reaction (Figure 1.24). IR spectroscopy showed the acids adsorbed onto the SnO_x surface prior to dissociating into acyl and hydroxide ions over the catalysts' oxygen vacancies. The breaking of a C-C bond on the PdSn alloy yields CO and an alkyl cation that then gets deprotonated by the hydroxide to yield alkene and water. A wide array of feedstocks were examined, including the methyl esters and triglycerides of palmitic and stearic acid (tripalmitin and tristearin, respectively). Further

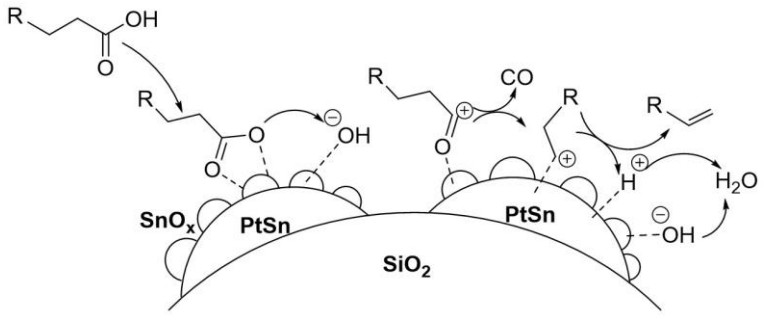

Feedstock (%)	Conversion (%)	Alkene (%)	Alkane (%)	Aldehyde/Alcohol (%)
Stearic Acid	100	72.0	19.2	1.9
Palmitic Acid	100	72.8	26.2	0.2
Methyl Stearate	97.6	75.8	20.1	1.6
Methyl Palmitate	82.4	61.6	13.6	2.9
Palm oil	48.0	21.0	6.0	21
Tristearin	67.4	45.4	12	10

Figure 1.24. Mechanism for deoxygenation of fatty acids over Pt_1Sn_1/SiO_2 bimetallic catalyst and select yields for products of substrates

analysis showed no loss of reactivity over four batch reactions with quantitate conversions and >72% olefin selectivity (LIO + LAO) of palmitic and stearic acids.

Even with the many limitations found in heterogeneous catalysis, it does offer a distinct advantage over homogeneous methods for converting fatty esters and triglycerides. Methyl esters, palm kernel and coconut oils have been demonstratively deoxygenated into α-olefins and diesel components over a $PtSnK/SiO_2$ catalyst with continuous distillation (Figure 1.25).[85] Helium carrier gas aided in the removal/purification of products while increasing α-selectivity and limiting hydrogenation side reactions. Even so, yields of LAOs were modest in reactions of triglycerides (e.g., 28% LAO vs 51% LIO for trilaurin), but were improved upon to decent selectivities with coconut and palm kernel oils (47 and 53% LAO, respectively).

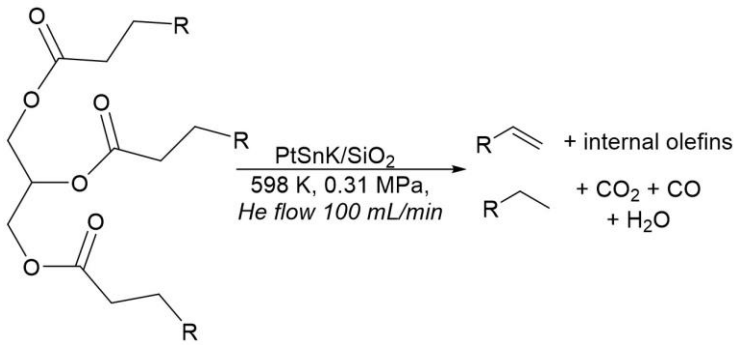

Substrate	Conversion (%)	LAO (%)	LIO (%)	Alkane (%)
Trilaurin	96	28	51	11
Trimyristin	93	25	58	1.3
Palm Kernel Oil	78	47	25	12
Coconut Oil	46	53	19	15

Figure 1.25. $PtSnK/SiO_2$ reactions with esters and triglycerides. R = saturated or unsaturated alkyl chain

Fatty acid methyl esters (FAMEs) are one of the major components of waste cooking oils, making their use as a chemical feedstock highly attractive. A combination of Ni_3Al alloy and $NiMoS/Al_2O_3$ catalysts in tandem with steam cracking generated a series of light olefins

from FAMEs in three distinct steps (Scheme 1.36).[86] Ni_3Al first hydrogenates unsaturated FAMEs, which was crucial to prevent degradation of the catalyst bed and led to smooth hydroprocessing of the saturated FAMEs for periods of up to 1,000 hr. The second step, hydrodeoxygenation, occurred by $NiMoS/Al_2O_3$ with the hydrogenated FAMEs, thereby creating paraffins, which have their own uses as biofuels. The following paraffin products underwent steam cracking to create a mixture of olefins: ethylene, propylene, and 1,3-butadiene in a total yield of 61.9%, which was a significant gain when compared to fossil naphtha cracking under identical conditions (52.9%). Although only short-chained olefins are produced through this procedure, the bio-derived ethylene and propylene gases could in theory be used in oligomerization procedures to make longer chain LAOs under identical processes to those currently used from fossil fuel sources.

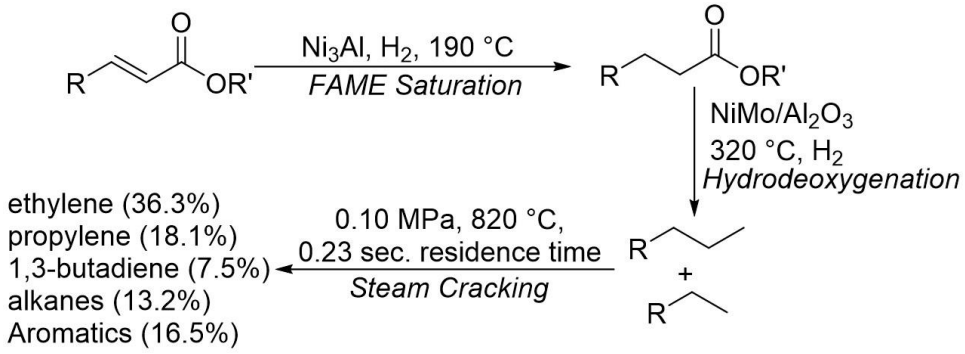

Scheme 1.36. Three step procedure for light olefins from FAMEs

For mixed anhydride systems with heterogeneous catalysts DFT calculations suggest that the success of the bidentate ligand DPEphos used in multiple reports is likely due to its ability to create a series of cavities within the metal surface that enhance the selectivity for olefins, while also preventing catalyst deactivation.[87] The flexibility of the DPEphos ligand also aids in the desorption of CO upon decarbonylation, an important factor in preventing catalyst deactivation.

Monodentate phosphines such as PPh_3 do not offer such an enhancement because they form monolayers that completely passivate the metal surface, blocking substrate interaction.

Another study of hydrodeoxygenation of fatty acids on MoS_2 predicts a stepwise reaction that forms paraffins of equal carbon chain length to the starting material.[88] The reaction begins by C-O hydrogenolysis into an aldehyde followed by hydrogenation to the alcohol. A dehydration reaction leads to the 1-alkene, and a subsequent hydrogenation results in the alkane (paraffin). Nickel containing catalysts (e.g., Ni_3S_2 and Ni-MoS_2), however, lead to a highly favorable loss of carbon by decarbonylation in the reaction, which is attributed to the presence of Ni(II). A key difference between the Mo and Ni based catalysts is that a common aldehyde or alcohol intermediate is not shared between the hydrodeoxygenation and decarbonylation type pathways that they operate under, respectively. Instead decarbonylation of fatty acids can occur through a sequential dehydration-decarbonylation where a ketene intermediate is key for C-C bond cleavage.

Heterogeneous catalytic methods show promise in many aspects to successfully provide linear olefin chemical feedstocks from fatty acid derivatives, especially for triglycerides and esters that are difficult to active. However, their often nonexistent selectivity for LAOs and low TOF/TON have hampered their use. Nevertheless, progress has been made over the last decade and they could offer a promising or complimentary means in switching from fossil fuel sources to biorenewable ones in LAO production.

1.6. Future Prospects and Outlook

Overall, tremendous progress has been made over the last 50 years for the conversion of fatty acids into LAOs with several ground-breaking works within the last decade. Triglycerides,

fatty acids, and their derivatives, currently available on large scales, may offer an economical and abundant alternative to fossil fuel resources for the production of LAOs. However, major limitations to current procedures first need to be addressed before any of the discussed methods could be made feasible as replacements to current methods that use fossil fuels. Even though α-selectivities of >95% are commonplace, catalysts often exhibit low activities (TON/TOF) that would make their implementation on a large scale difficult. The estimate for a commercially viable industrial process would require catalysts to have TON upwards of 50,000, far exceeding current standards that commonly have TON <100.[89]

Currently homogeneous catalysts show the highest activities and selectivities for LAOs, but the requirement for activated substrates severely limits their practicality. Biocatalytic and photocatalytic systems may offer solutions to these problems as they have proven capable of directing activating carboxylic acids with near perfect selectivities for LAOs under "green" reaction media (near room temperature, water as solvent/cosolvent). Scalability issues are notable for both methods as biocatalysts currently must operate under dilute conditions and both bio- and photocatalytic processes are susceptible to acidification of aqueous reaction media by CO_2 released via decarboxylation. Engineering solutions such as the use of a flow reactors may be necessary to overcome these limitations.

Heterogeneous catalysts are attractive over homogeneous variants due to their enhanced thermal stability and their demonstrative ability to undergo repeat use, but the near complete lack of LAO selectivity at high conversions is currently a major limitation. The requirement for H_2 to ensure reasonable catalyst activity for many systems complicates product distributions, producing esters, ketones, and alkanes in tandem with LOs. Although low TON have been reported thus far, heterogeneous variants have been much less explored than their homogenous

counterparts. Already heterogeneous methods have demonstrated the ability to convert waste oils and triglycerides directly into LOs, skipping the need for a hydrolysis step to first make fatty acids prior to LO synthesis. Furthermore, the demonstrated ability to convert triglycerides into short olefins such as ethylene and propene could offer a green approach to replacing fossil resources typically used for LAO synthesis from ethylene oligomerization.

To achieve an industrially viable catalyst creative approaches are needed. It may be that a combination of differing catalysts is required to convert fatty acid derivatives to LAOs at an adequate activity/yield. One such method was recently reported combining enzyme and heterogeneous catalysts to product LAOs starting from glucose.[90] Improvements in engineering will also aid in the use of multiple catalysts to stepwise convert bioderived feedstocks into valuable commodity chemicals. Flow reactors offer the opportunity to overcome certain limitations currently experienced by byproduct contamination, such as acidification of reaction media by CO_2 during photocatalysis. Alternatively, rational catalyst design has been limited and although some experimental and computational mechanistic studies have been performed to help explain current methods, little work has been performed to understand structure-activity relationships of current systems. The structurally similar and commercially available Xantphos and DPEphos ligands have been perhaps the most successful in dehydrative decarbonylation reactions, but synthetic modifications to improve their reactivity/LAO selectivity have not been made. Nor has ligand design been reported in general as a means of further reaction optimization. Therefore, rationally exploring the effects of ligands on the overall deoxygenation processes or discrete mechanistic steps within them, perhaps with computational input, is needed to better understand how catalyst structure can be improved.

1.7 References

1. Andrady, A. L., & Neal, M. A. (2009). Applications and societal benefits of plastics. *Philosophical Transactions of the Royal Society B: Biological Sciences*, *364*(1526), 1977–1984

2. (a) Jambeck, J., Geyer, R., Wilcox, C., Siegler, T. R., Perryman, M., Andrady, A., Narayan, R., & Law, K. L. (2015). Plastic waste inputs from land into the ocean. *Science*, *347*(6223), 768-771. (b) Sharma, R. (2015). Environmental Issues of Deep-Sea Mining. *Procedia Earth and Planetary Science*, *11*, 204–211. (c) Dontala, S. P., Reddy, T. B., & Vadde, R. (2015). Environmental Aspects and Impacts its Mitigation Measures of Corporate Coal Mining. *Procedia Earth and Planetary Science*, *11*, 2–7. (d) Carvalho, F. P. (2017). Mining industry and sustainable development: Time for change. *Food and Energy Security*, *6*(2), 61–77.

3. (a) Zakzeski, J., Bruijnincx, P. C. A., Jongerius, A. L., & Weckhuysen, B. M. (2010). The catalytic valorization of lignin for the production of renewable chemicals. *Chemical Reviews*, *110*(6), 3552–3599. (b) Dhepe, P., Tomishige, K., & Wu, K. C. W. (2017). Catalytic Conversion of Biomass to Monofunctional Hydrocarbons and Targeted Liquid-Fuel Classes. *ChemCatChem*, *9*(14), 2613–2614. (c) Dodds, D. R., & Gross, R. a. (2007). Chemicals from Biomass. *Science*, *318*, 1250–1251. (d) John, A. (2022). Chpt. 11. Dehydrative Decarbonylation. In *Organometallic chemistry in industry : a practical approach* (pp. 283–303).

4. (a) Vennestrøm, P. N. R., Osmundsen, C. M., Christensen, C. H., & Taarning, E. (2011). Beyond petrochemicals: The renewable chemicals industry. *Angewandte Chemie - International Edition*, *50*(45), 10502–10509. (b) Luis, F., & Moncayo, G. (n.d.). *Biorefinery: from biomass to chemicals and fuels*. (c) van Dyk, S., Su, J., Mcmillan, J. D., & Saddler, J. (John). (2019). Potential synergies of drop-in biofuel production with further co-processing at oil refineries. *Biofuels, Bioproducts and Biorefining*, *13*(3), 760–775. (d) Sheldon, R. A. (2014). Green and sustainable manufacture of chemicals from biomass: State of the art. *Green Chemistry*, *16*(3), 950–963. (e) Carus, M., Dammer, L., Puente, Á., Raschka, A., & Arendt, O. (2017). Bio-based drop-in, smart drop-in and dedicated chemicals. *Renewable Carbon*, *745623*, 1–3. (f) Edward L. Kunkes, Dante A. Simonetti, Ryan M. West, Juan Carlos Serrano-Ruiz, Christian A. Gärtner, J. A. D. (2008). Catalytic Conversion of Biomass to Monofunctional Hydrocarbons and Targeted Liquid-Fuel Classes. *Science*, *322*, 417–421.

5. The Flory-Schulz distribution is a probability distribution describing the relative ratios of polymers of different lengths that occur in an ideal step-growth polymerization (such as ethylene oligomerization). (a) Flory, B. P. J. (1936). Molecular Size Distribution in Linear Condensation Polymers. *Journal of the American Chemical Society*, *1*(7), 1877–1885. (b) Britovsek, G. J. P., Malinowski, R., McGuinness, D. S., Nobbs, J. D., Tomov, A. K., Wadsley, A. W., & Young, C. T. (2015). Ethylene Oligomerization beyond Schulz-Flory Distributions. *ACS Catalysis*, *5*(11), 6922–6925.

6. (a) Chen, B. S., Zeng, Y. Y., Liu, L., Chen, L., Duan, P., Luque, R., Ge, R., & Zhang, W. (2022). Advances in catalytic decarboxylation of bioderived fatty acids to diesel-range alkanes. *Renewable and Sustainable Energy Reviews*, *158*(January), 112178. (b) Yao, X., Strathmann, T. J., Li, Y., Cronmiller, L. E., Ma, H., & Zhang, J. (2021). Catalytic hydrothermal deoxygenation of lipids and fatty acids to diesel-like hydrocarbons: a review. *Green Chemistry*, *23*(3), 1114–1129. (c) Di Vito Nolfi, G., Gallucci, K., & Rossi, L. (2021). Green diesel production by catalytic hydrodeoxygenation of vegetables oils. *International Journal of Environmental Research and Public Health*, *18*(24). (d) Rogers, K. A., & Zheng, Y. (2016). Selective Deoxygenation of Biomass-Derived Bio-oils within Hydrogen-Modest Environments: A Review and New Insights. *ChemSusChem*, *9*(14), 1750–1772.

7. (a) Britovsek, G. J. P., Malinowski, R., McGuinness, D. S., Nobbs, J. D., Tomov, A. K., Wadsley, A. W., & Young, C. T. (2015). Ethylene Oligomerization beyond Schulz-Flory Distributions. *ACS Catalysis*, *5*(11), 6922–6925. (b) Higman, C. S., Lummiss, J. A. M., & Fogg, D. E. (2016). Olefin Metathesis at the Dawn of Implementation in Pharmaceutical and Specialty-Chemicals Manufacturing. *Angewandte Chemie - International Edition*, *55*(11), 3552–3565. (c) Chikkali, S., & Mecking, S. (2012). Refining of plant oils to chemicals by olefin metathesis. *Angewandte Chemie - International Edition*, *51*(24), 5802–5808. (d) van der Klis, F., Le Nôtre, J., Blaauw, R., van Haveren, J., & van Es, D. S. (2012). Renewable linear alpha olefins by selective ethenolysis of decarboxylated unsaturated fatty acids. *European Journal of Lipid Science and Technology*, *114*(8), 911–918. (e) Bidange, J., Fischmeister, C., & Bruneau, C. (2016). Ethenolysis: A Green Catalytic Tool to Cleave

Carbon–Carbon Double Bonds. *Chemistry - A European Journal*, *22*(35), 12226–12244. (f) Spekreijse, J., Sanders, J. P. M., Bitter, J. H., & Scott, E. L. (2017). The Future of Ethenolysis in Biobased Chemistry. *ChemSusChem*, *10*(3), 470–482.

8. (a) *Linear Alpha Olefin Market Report, Trends and Forecast 2021-2026*. (n.d.). Retrieved June 5, 2022, from https://www.imarcgroup.com/linear-alpha-olefins-market (b) *Linear Alpha Olefin Market Size, Share, Analysis, Report 2022-2027*. (n.d.). Retrieved June 5, 2022, from https://www.expertmarketresearch.com/reports/linear-alpha-olefin-market (c) *Linear Alpha Olefins Market Size, Share, Opportunities & Forecast*. (n.d.). Retrieved June 5, 2022, from https://www.verifiedmarketresearch.com/product/linear-alpha-olefins-market

9. Franke, R.; Selent, D.; Börner, A. Applied Hydroformylation. *Chem. Rev.* **2012**, *112* (11), 5675–5732.

10. (a) Chatterjee, A.; Hopen Eliasson, S. H.; Jensen, V. R. Selective Production of Linear α-Olefins: Via Catalytic Deoxygenation of Fatty Acids and Derivatives. *Catalysis Science and Technology*. 2018, pp 1487–1499. (b) Zhang, X.; Jordan, F.; Szostak, M. Transition-Metal-Catalyzed Decarbonylation of Carboxylic Acids to Olefins: Exploiting Acyl C-O Activation for the Production of High Value Products. *Org. Chem. Front.* **2018**, *5* (16), 2515–2521. (c) Haque, F. M.; Ishibashi, J. S. A.; Lidston, C. A. L.; Shao, H.; Bates, F. S.; Chang, A. B.; Coates, G. W.; Cramer, C. J.; Dauenhauer, P. J.; Dichtel, W. R.; Ellison, C. J.; Gormong, E. A.; Hamachi, L. S.; Hoye, T. R.; Jin, M.; Kalow, J. A.; Kim, H. J.; Kumar, G.; Lasalle, C. J.; Liffland, S.; Lipinski, B. M.; Pang, Y.; Parveen, R.; Peng, X.; Popowski, Y.; Prebihalo,

E. A.; Reddi, Y.; Reineke, T. M.; Sheppard, D. T.; Swartz, J. L.; Tolman, W. B.; Vlaisavljevich, B.; Wissinger, J.; Xu, S.; Hillmyer, M. A. Defining the Macromolecules of Tomorrow through Synergistic Sustainable Polymer Research. *Chem. Rev.* **2022**, *122* (6), 6322–6373. (d) Pattanaik, B. P.; Misra, R. D. Effect of Reaction Pathway and Operating Parameters on the Deoxygenation of Vegetable Oils to Produce Diesel Range Hydrocarbon Fuels: A Review. *Renew. Sustain. Energy Rev.* **2017**, *73*, 545–557. (e) Tabandeh, M., Cheng, C. K., Centi, G., Show, P. L., Chen, W. H., Ling, T. C., Ong, H. C., Ng, E. P., Juan, J. C., & Lam, S. S. (2022). Recent advancement in deoxygenation of fatty acids via homogeneous catalysis for biofuel production. *Molecular Catalysis*, *523*(June 2020), 111207.

11. (a) Bidange, J.; Fischmeister, C.; Bruneau, C. Ethenolysis: A Green Catalytic Tool to Cleave Carbon–Carbon Double Bonds. *Chem. - A Eur. J.* **2016**, *22* (35), 12226–12244. (b) Spekreijse, J.; Sanders, J. P. M.; Bitter, J. H.; Scott, E. L. The Future of Ethenolysis in Biobased Chemistry. *ChemSusChem* **2017**, *10* (3), 470–482.
12. van der Klis, F.; Le Nôtre, J.; Blaauw, R.; van Haveren, J.; van Es, D. S. Renewable Linear Alpha Olefins by Selective Ethenolysis of Decarboxylated Unsaturated Fatty Acids. *Eur. J. Lipid Sci. Technol.* **2012**, *114* (8), 911–918.
13. (a) Id, C. R. E. F. Zersetzung Der Valeriansäure Durch Den Elektrischen Strom. *Justus Liebigs Ann. Chem.* **1848**, *64* (3), 339–341. (b) Kolbe, H. Untersuchungen Über Die Elektrolyse Organischer Verbindungen. *Justus Liebigs Ann. Chem.* **1849**, *69* (3), 257–294.

14. Sanderson, J. E.; Levy, P. F.; Cheng, L. K.; Barnard, G. W. The Effect of Pressure on the Product Distribution in Kolbe Electrolysis. *J. Electrochem. Soc.* **1983**, *130* 9), 1844–1848. (b) Levy, P. F.; Sanderson, J. E.; Cheng, L. K. Kolbe Electrolysis of Mixtures of Aliphatic Organic Acids. *J. Electrochem. Soc.* **1984**, *131* (4), 773–777.

15. Dos Santos, T. R.; Harnisch, F.; Nilges, P.; Schröder, U. Electrochemistry for Biofuel Generation: Transformation of Fatty Acids and Triglycerides to Diesel-Like Olefin/Ether Mixtures and Olefins. *ChemSusChem* **2015**, *8* (5), 886–893. (b) Meyers, J.; Kurig, N.; Gohlke, C.; Valeske, M.; Panitz, S.; Holzhäuser, F. J.; Palkovits, R. Intramolecular Biradical Recombination of Dicarboxylic Acids to Unsaturated Compounds: A New Approach to an Old Kolbe Reaction. *ChemElectroChem* **2020**, *7* (24), 4873–4878.

16. (a) Bacha, J. D., & Kochi, J. K. (1968). Alkenes from acids by oxidative decarboxylation. *Tetrahedron*, *24*(5), 2215–2226. (b) Kochi, J. K. (1965). Oxidations with Lead (IV). I. Mechanism of the Decarboxylation of Pentanoic Acids. *Journal of the American Chemical Society*, *87*(16), 3609–3619. (c) Bacha, J. D.; Kochi, J. K.; Bethea III, T. W. Free Radicals in Thermal and Photochemical Oxidative Decarboxylation with Lead (IV). *J. Am. Chem. Soc.* **1967**, *3172* (25), 6538–6547.

17. Anderson, J. M., & Kochi, J. K. (1970). Silver (I) -Catalyzed Oxidative Decarboxylation of Acids by Peroxydisulfate. The Role of Silver (II). *Journal of the American Chemical Society*, *92*(6), 1651–1659.

18. Anderson, J. M., & Kochi, J. K. (1970). Silver(II) Complexes in Oxidative Decarboxylation of Acids. *Journal of Organic Chemistry*, *35*(4), 986–989.

19. Mentasti, E., Baiocchi, C., & Coe, J. S. (1984). Mechanistic aspects of reactions involving Ag(II) AS AN oxidant. *Coordination Chemistry Reviews*, *54*, 131–157.

20. Fristad, W. E., Fry, M. A., & Klang, J. A. (1983). Persulfate / Silver Ion Decarboxylation of Carboxylic Acids. Preparation of Alkanes, Alkenes and Alcohols. *Journal of Organic Chemistry*, *48*(5), 3575–3577.

21. Van Der Klis, F., Van Den Hoorn, M. H., Blaauw, R., Van Haveren, J., & Van Es, D. S. (2011). Oxidative decarboxylation of unsaturated fatty acids. *European Journal of Lipid Science and Technology*, *113*(5), 562–571.

22. Murray, R. E., Walter, E. L., & Doll, K. M. (2014). Tandem isomerization-decarboxylation for converting alkenoic fatty acids into alkenes. *ACS Catalysis*, *4*(10), 3517–3520.

23. Knothe, G., Steidley, K. R., Moser, B. R., & Doll, K. M. (2017). Decarboxylation of fatty acids with triruthenium dodecacarbonyl: Influence of the compound structure and analysis of the product mixtures. *ACS Omega*, *2*(10), 6473–6480.

24. (a) Doll, K. M., Bantchev, G. B., Walter, E. L., Murray, R. E., Appell, M., Lansing, J. C., & Moser, B. R. (2017). Parameters governing ruthenium sawhorse-based decarboxylation of oleic acid. *Industrial and Engineering Chemistry Research*, *56*(4), 864–871. (b) Moser, B. R., Knothe, G., Walter, E. L., Murray, R. E., Dunn, R. O., & Doll, K. M. (2016). *Analysis*

and Properties of the Decarboxylation Products of Oleic Acid by Catalytic Triruthenium Dodecacarbonyl.

25. Tlahuext-Aca, A., Candish, L., Garza-Sanchez, R. A., & Glorius, F. (2018). Decarboxylative Olefination of Activated Aliphatic Acids Enabled by Dual Organophotoredox/Copper Catalysis. *ACS Catalysis*, *8*(3), 1715–1719.

26. (a) De La Mare, H. E.; Kochi, J. K.; Rust, F. F. The Oxidation of Free Radicals By Metal Ions. *J. Am. Chem. Soc.* **1961**, *8*, 2013. (b) Kochi, J. K. Mechanisms of Organic Oxidation and Reduction by Metal Complexes. *Science* **1967**, *155* (3761), 415–424. (c) Kochi, J. K.; Bemis, A.; Jenkins, C. L. Mechanism of Electron Transfer Oxidation of Alkyl Radicals by Copper (II) Complexes. *J. Am. Chem. Soc.* **1968**, *90* (17), 4616–4625.

27. Cheng, W.-M., Shang, R., & Fu, Y. (2018). Irradiation-induced palladium-catalyzed decarboxylative desaturation enabled by a dual ligand system. *Nature Communications*, *9*(1), 5215.

28. Sun, X., Chen, J., & Ritter, T. (n.d.). Catalytic dehydrogenative decarboxyolefination of carboxylic acids. *Nature Chemistry*, *2*, 1–5.

29. Nguyen, V. T., Nguyen, V. D., Haug, G. C., Dang, H. T., Jin, S., Li, Z., Flores-Hansen, C., Benavides, B. S., Arman, H. D., & Larionov, O. V. (2019). Alkene Synthesis by Photocatalytic Chemoenzymatically Compatible Dehydrodecarboxylation of Carboxylic Acids and Biomass. *ACS Catalysis*, *9*(10), 9485–9498.

30. (a) Wohlgemuth, R. Biocatalysis-Key to Sustainable Industrial Chemistry. *Curr. Opin. Biotechnol.* **2010**, *21* (6), 713–724. (b) Sheldon, R. A.; Woodley, J. M. Role of Biocatalysis in Sustainable Chemistry. *Chem. Rev.* **2018**, *118* (2), 801–838. (c) Bicas, J. L.; Molina, G.; Cavalcante Barros, F. F.; Pastore, G. M. *White Biotechnology for Sustainable Chemistry*; 2015; Vol. 2016-Janua.

31. (a) A. Alcasabas, P. I. Darley and P. Pir, U.S. Pat., 0206057, 2014. (b) S. Schaffer, J. Gielen, N. Decker, N. Kirchner, T. Haas, M. Potter and H. Hager, WO2013024111A1, 2013.

32. Liu, Y., Wang, C., Yan, J., Zhang, W., Guan, W., Lu, X., & Li, S. (2014). Hydrogen peroxide-independent production of α-alkenes by OleT JE P450 fatty acid decarboxylase. *Biotechnology for Biofuels*, *7*(1), 1–12.

33. (a) Grant, J. L., Hsieh, C. H., & Makris, T. M. (2015). Decarboxylation of fatty acids to terminal alkenes by cytochrome P450 compound i. *Journal of the American Chemical Society*, *137*(15), 4940–4943. (b) Wang, J. B., Lonsdale, R., & Reetz, M. T. (2016). Exploring substrate scope and stereoselectivity of P450 peroxygenase OleTJE in olefin-forming oxidative decarboxylation. *Chemical Communications*, *52*(52), 8131–8133. (c) Hsieh, C. H., Huang, X., Amaya, J. A., Rutland, C. D., Keys, C. L., Groves, J. T., Austin, R. N., & Makris, T. M. (2017). The Enigmatic P450 Decarboxylase OleT Is Capable of, but Evolved to Frustrate, Oxygen Rebound Chemistry. *Biochemistry*, *56*(26), 3347–3357.

34. Faponle, A. S., Quesne, M. G., & De Visser, S. P. (2016). Origin of the Regioselective Fatty-Acid Hydroxylation versus Decarboxylation by a Cytochrome P450 Peroxygenase: What Drives the Reaction to Biofuel Production? *Chemistry - A European Journal*, *22*(16), 5478–5483.

35. Rude, M. A.; Baron, T. S.; Brubaker, S.; Alibhai, M.; Del Cardayre, S. B.; Schirmer, A. Terminal Olefin (1-Alkene) Biosynthesis by a Novel P450 Fatty Acid Decarboxylase from Jeotgalicoccus Species. *Appl. Environ. Microbiol.* **2011**, *77* (5), 1718–1727.

36. Munro, A. W., Girvan, H. M., Mason, A. E., Dunford, A. J., & McLean, K. J. (2013). What makes a P450 tick? *Trends in Biochemical Sciences*, *38*(3), 140–150.

37. Liu, Y., Wang, C., Yan, J., Zhang, W., Guan, W., Lu, X., & Li, S. (2014). Hydrogen peroxide-independent production of α-alkenes by OleT JE P450 fatty acid decarboxylase. *Biotechnology for Biofuels*, *7*(1), 1–12.

38. Dennig, A., Kuhn, M., Tassoti, S., Thiessenhusen, A., Gilch, S., Bülter, T., Haas, T., Hall, M., & Faber, K. (2015). Oxidative Decarboxylation of Short-Chain Fatty Acids to 1-Alkenes. *Angewandte Chemie - International Edition*, 2015, *54*(30), 8819–8822.

39. Lu, C., Shen, F., Wang, S., Wang, Y., Liu, J., Bai, W. J., & Wang, X. (2018). An Engineered Self-sufficient Biocatalyst Enables Scalable Production of Linear Alpha Olefins from Carboxylic Acids. *ACS Catal*, 2018, 8, 5794–5798.

40. Li, F., Yang, K., Xu, Y., Qiao, Y., Yan, Y., & Yan, J. (2019). A genetically-encoded synthetic self-assembled multienzyme complex of lipase and P450 fatty acid decarboxylase for efficient bioproduction of fatty alkenes. *Bioresource Technology*, *272*(September 2018), 451–457.

41. Zachos, I.; Gaßmeyer, S. K.; Bauer, D.; Sieber, V.; Hollmann, F.; Kourist, R. Photobiocatalytic Decarboxylation for Olefin Synthesis. *Chem. Commun.* **2015**, *51* (10), 1918–1921.

42. Zhang, S.; Liu, Y. Mechanism of Fatty Acid Decarboxylation Catalyzed by a Non-Heme Iron Oxidase (UndA): A QM/MM Study. *Org. Biomol. Chem.* **2019**, *17* (45), 9808–9818.

43. (a) Gehret, J. J.; Gu, L.; Gerwick, W. H.; Wipf, P.; Sherman, D. H.; Smith, J. L. Terminal Alkene Formation by the Thioesterase of Curacin A Biosynthesis: Structure of a Decarboxylating Thioesterase. *J. Biol. Chem.* **2011**, *286* (16), 14445–14454. McCarthy, J. G.; Eisman, E. B.; Kulkarni, S.; Gerwick, L.; Gerwick, W. H.; Wipf, P.; Sherman, D. H.; Smith, J. L. Structural Basis of Functional Group Activation by Sulfotransferases in Complex Metabolic Pathways. *ACS Chem. Biol.* **2012**, *7* (12), 1994–2003. (c) Liu, Q.; Wu, K.; Cheng, Y.; Lu, L.; Xiao, E.; Zhang, Y.; Deng, Z.; Liu, T. Engineering an Iterative Polyketide Pathway in Escherichia Coli Results in Single-Form Alkene and Alkane Overproduction. *Metab. Eng.* **2015**, *28*, 82–90. (d) Mendez-Perez, D.; Begemann, M. B.; Pfleger, B. F. Modular Synthase-Encoding Gene Involved in α-Olefin Biosynthesis in Synechococcus Sp. Strain PcC 7002. *Appl. Environ. Microbiol.* **2011**, *77* (12), 4264–4267.

44. (a) Gómez Baraibar, Á.; Reichert, D.; Mügge, C.; Seger, S.; Gröger, H.; Kourist, R. A One-Pot Cascade Reaction Combining an Encapsulated Decarboxylase with a Metathesis Catalyst for the Synthesis of Bio-Based Antioxidants. *Angew. Chemie - Int. Ed.* **2016**, *55* (47), 14823–14827. (b) Frank, A.; Eborall, W.; Hyde, R.; Hart, S.; Turkenburg, J. P.; Grogan, G. Mutational Analysis of Phenolic Acid Decarboxylase from Bacillus Subtilis (BsPAD), Which Converts Bio-Derived Phenolic Acids to Styrene Derivatives. *Catal. Sci. Technol.* **2012**, *2* (8), 1568–1574. (c) McKenna, R.; Nielsen, D. R. Styrene Biosynthesis from Glucose by Engineered E. Coli. *Food, Pharm. Bioeng. Div. - Core Program. Top. 2011 AIChE Annu. Meet.* **2011**, *1* (5), 340–350. (d) Payer, S. E.; Pollak, H.; Schmidbauer, B.; Hamm, F.; Juričić, F.; Faber, K.; Glueck, S. M. Multienzyme One-Pot Cascade for the Stereoselective Hydroxyethyl Functionalization of Substituted Phenols. *Org. Lett.* **2018**, *20* (17), 5139–5143.

45. Lin, F.; Ferguson, K. L.; Boyer, D. R.; Lin, X. N.; Marsh, E. N. G. Isofunctional Enzymes PAD1 and UbiX Catalyze Formation of a Novel Cofactor Required by Ferulic Acid Decarboxylase and 4-Hydroxy-3-Polyprenylbenzoic Acid Decarboxylase. *ACS Chem. Biol.* **2015**, *10* (4), 1137–1144.

46. Beller, H. R., Goh, E. B., & Keasling, J. D. (2010). Genes involved in long-chain alkene biosynthesis in micrococcus Luteus. *Applied and Environmental Microbiology*, 2010, *76*(4), 1212–1223.

47. (a) Huijbers, M., Zhang, W., & Hollmann, F. (2018). Light-driven enzymatic decarboxylation of fatty acids. *Angewandte Chemie International Edition*, 2018, 13648–

13651. (b) Zhang, W., Ma, M., Huijbers, M. M. E., Filonenko, G. A., Pidko, E. A., Van Schie, M., De Boer, S., Burek, B. O., Bloh, J. Z., Van Berkel, W. J. H., Smith, W. A., & Hollmann, F. (2019). Hydrocarbon Synthesis via Photoenzymatic Decarboxylation of Carboxylic Acids. *Journal of the American Chemical Society*, 2019, *141* (7), 3116–3120.

48. (a) Tsuji, J. (1967). Organic Syntheses by Means of Noble Metal Compounds. *Tetrahedron Letters*, *50*, 4565–4568. (b) Tsuji, J., & Ohno, K. (1968). Organic syntheses by means of noble metal compounds. XXXIV. Carbonylation and decarbonylation reactions catalyzed by palladium. *Journal of the American Chemical Society*, *90*(1), 94–98. (c) Tsuji, J., & Ohno, K. (1968). Organic syntheses by means of noble metal compounds. XXXIV. Carbonylation and decarbonylation reactions catalyzed by palladium. *Journal of the American Chemical Society*, *90*(1), 94–98.

49. Foglia, T. A., & Barr, P. A. (1976). Decarbonylation dehydration of fatty acids to alkenes in the presence of transition metal complexes. *Journal of the American Oil Chemists Society*, *53*(12), 737–741.

50. Miller, J. A., Nelson, J. A., & Byrne, M. P. (1993). A Highly Catalytic and Selective Conversion of Carboxylic Acids to 1-Alkenes of One Less Carbon Atom. *Journal of Organic Chemistry*, *58*(1), 18–20.

51. Kraus, G. A., & Riley, S. (2012). A Large-Scale Synthesis of α-Olefins and α,ω-Dienes. *Synthesis*, *44*, 3003–3005.

52. Miranda, M. O., Pietrangelo, A., Hillmyer, M. A., & Tolman, W. B. (2012). Catalytic decarbonylation of biomass-derived carboxylic acids as efficient route to commodity monomers. *Green Chemistry*, *14*(2), 490–494.

53. Gooßen, L. J., & Rodríguez, N. (2004). A mild and efficient protocol for the conversion of carboxylic acids to olefins by a catalytic decarbonylative elimination reaction. *Chemical Communications*, *4*(6), 724–725.

54. Nôtre, J. Le, Scott, E. L., Franssen, M. C. R., & Sanders, J. P. M. (2010). Selective preparation of terminal alkenes from aliphatic carboxylic acids by a palladium-catalysed decarbonylation-elimination reaction. *Tetrahedron Letters*, *51*(29), 3712–3715.

55. (a) Liu, Y., Kim, K. E., Herbert, M. B., Fedorov, A., Grubbs, R. H., & Stoltz, B. M. (2014). Palladium-catalyzed decarbonylative dehydration of fatty acids for the production of linear alpha olefins. *Advanced Synthesis and Catalysis*, *356*(1), 130–136. (b) Liu, Y., Virgil, S. C., Grubbs, R. H., & Stoltz, B. M. (2015). Palladium-Catalyzed Decarbonylative Dehydration for the Synthesis of α-Vinyl Carbonyl Compounds and Total Synthesis of (-)-Aspewentins A, B, and C. *Angewandte Chemie - International Edition*, *54*(40), 11800–11803.

56. (a) Chatterjee, A., Hopen Eliasson, S. H., Tï¿½rnroos, K. W., & Jensen, V. R. (2016). Palladium Precatalysts for Decarbonylative Dehydration of Fatty Acids to Linear Alpha Olefins. *ACS Catalysis*, *6*(11), 7784–7789. (b) Hopen Eliasson, S. H., Chatterjee, A.,

Occhipinti, G., & Jensen, V. R. (2019). Green Solvent for the Synthesis of Linear α-Olefins from Fatty Acids. *ACS Sustainable Chemistry and Engineering*, *7*(5), 4903–4911.

57. Lee, H. W.; Yung, K. F. Synthesis of Alpha Olefins: Catalytic Decarbonylation of Carboxylic Acids and Vegetable Oil Deodorizer Distillate (Vodd). *Catalysts* **2021**, *11* (8).

58. Maetani, S.; Fukuyama, T.; Suzuki, N.; Ishihara, D.; Ryu, I. Efficient Iridium-Catalyzed Decarbonylation Reaction of Aliphatic Carboxylic Acids Leading to Internal or Terminal Alkenes. *Organometallics* **2011**, *30* (6), 1389–1394.

59. Ternel, J., Lebarbé, T., Monflier, E., & Hapiot, F. (2015). Catalytic decarbonylation of biosourced substrates. *ChemSusChem*, *8*(9), 1585–1592.

60. Ternel, J.; Léger, B.; Monflier, E.; Hapiot, F. Amines as Effective Ligands in Iridium-Catalyzed Decarbonylative Dehydration of Biosourced Substrates. *Catal. Sci. Technol.* **2018**, *8* (15), 3948–3953.

61. Maetani, S., Fukuyama, T., Suzuki, N., Ishihara, D., & Ryu, I. (2012). Iron-catalyzed decarbonylation reaction of aliphatic carboxylic acids leading to α-olefins. *Chemical Communications*, *48*(19), 2552–2554.

62. John, A., Miranda, M. O., Ding, K., Dereli, B., Ortuno, M. A., Lapointe, A. M., Coates, G. W., Cramer, C. J., & Tolman, W. B. (2016). Nickel Catalysts for the Dehydrative Decarbonylation of Carboxylic Acids to Alkenes. *Organometallics*, *35*(14), 2391–2400.

63. John, A., Hogan, L. T., Hillmyer, M. A., & Tolman, W. B. (2015). Olefins from biomass feedstocks: Catalytic ester decarbonylation and tandem Heck-type coupling. *Chemical Communications*, *51*(13), 2731–2733.

64. John, A., Dereli, B., Ortunȉo, M. A., Johnson, H. E., Hillmyer, M. A., Cramer, C. J., & Tolman, W. B. (2017). Selective Decarbonylation of Fatty Acid Esters to Linear α-Olefins. In *Organometallics* (Vol. 36, Issue 15, pp. 2956–2964).

65. John, A., Hillmyer, M. A., & Tolman, W. B. (2017). Anhydride-Additive-Free Nickel-Catalyzed Deoxygenation of Carboxylic Acids to Olefins. *Organometallics*, *36*(3), 506–509.

66. Cataldo, F. Synthesis of Linear Olefins from Fatty Acids: A Comparison of Nickel(I) and Rhodium(I) Catalysts in Liquid Triphenylphosphine. *Eur. Chem. Bull.* **2019**, *8* (3), 88–95.

67. (a) Marochkin, I. I.; Dorofeeva, O. V. Amide Bond Dissociation Enthalpies: Effect of Substitution on NC Bond Strength. *Comput. Theor. Chem.* **2012**, *991*, 182–191. (b) Mucsi, Z.; Chass, G. A.; Viskolcz, B.; Csizmadia, I. G. Quantitative Scale for the Extent of the Amide Bond. Amiditity Percentage as a Chemical Driving Force. *J. Phys. Chem. A* **2007**, *111*, 13245–13254.

68. (a) Liu, C.; Szostak, M. Twisted Amides: From Obscurity to Broadly Useful Transition-Metal-Catalyzed Reactions by N−C Amide Bond Activation. *Chem. - A Eur. J.* **2017**, *23* (30), 7157–7173. (b) Shi, S.; Nolan, S. P.; Szostak, M. Well-Defined Palladium(II)-NHC Precatalysts for Cross-Coupling Reactions of Amides and Esters by Selective N-C/O-C

Cleavage. *Acc. Chem. Res.* **2018**, *51* (10), 2589–2599. (c) Meng, G.; Shi, S.; Szostak, M. Cross-Coupling of Amides by N-C Bond Activation. *Synlett* **2016**, *27* (18), 2530–2540. (d) Shi, S.; Szostak, M. Decarbonylative Cyanation of Amides by Palladium Catalysis. *Org. Lett.* **2017**, *19* (12), 3095–3098. (e) Lei, P.; Meng, G.; Ling, Y.; An, J.; Nolan, S. P.; Szostak, M. General Method for the Suzuki-Miyaura Cross-Coupling of Primary Amide-Derived Electrophiles Enabled by [Pd(NHC)(Cin)Cl] at Room Temperature. *Org. Lett.* **2017**, *19* (24), 6510–6513. (f) Meng, G.; Szostak, M. General Olefin Synthesis by the Palladium-Catalyzed Heck Reaction of Amides: Sterically Controlled Chemoselective N-C Activation. *Angew. Chemie - Int. Ed.* **2015**, *54* (48), 14518–14522. (g) Bourne-branchu, Y.; Gosmini, C.; Gr, Ø. N -Boc-Amides in Cross-Coupling Reactions. *Chem. - A Eur. J.* **2019**, *25*, 2663–2674.

69. Meng, G.; Szostak, M. Sterically Controlled Pd-Catalyzed Chemoselective Ketone Synthesis via N-C Cleavage in Twisted Amides. *Org. Lett.* **2015**, *17* (17), 4364–4367.

70. Fieser, M. E.; Schimler, S. D.; Mitchell, L. A.; Wilborn, E. G.; John, A.; Hogan, L. T.; Benson, B.; LaPointe, A. M.; Tolman, W. B. Dual-Catalytic Decarbonylation of Fatty Acid Methyl Esters to Form Olefins. *Chem. Commun.* **2018**, *54* (55), 7669–7672.

71. Ortuño, M. A., Dereli, B., & Cramer, C. J. (2016). Mechanism of Pd-Catalyzed Decarbonylation of Biomass-Derived Hydrocinnamic Acid to Styrene following Activation as an Anhydride. *Inorganic Chemistry*, *55*(9), 4124–4131.

72. (a) Bilbrey, J. A.; Kazez, A. H.; Locklin, J.; Allen, W. D. Exact Ligand Cone Angles. *J. Comput. Chem.* **2013**, *34* (14), 1189–1197. (b) Clavier, H.; Nolan, S. P. Percent Buried Volume for Phosphine and N-Heterocyclic Carbene Ligands: Steric Properties in Organometallic Chemistry. *Chem. Commun.* **2010**, *46* (6), 841–861.

73. (a) Clavier, H., Correa, A., Cavallo, L., Escudero-Adán, E. C., Benet-Buchholz, J., Slawin, A. M. Z., & Nolan, S. P. (2009). [Pd(NHC)(allyl)Cl] complexes: Synthesis and determination of the NHC percent buried volume (%Vbur) steric parameter. *European Journal of Inorganic Chemistry*, *13 SPEC. ISS.*, 1767–1773. (b) Fantasia, S.; Nolan, S. P. A General Synthetic Route to Mixed NHC-Phosphane Palladium(O) Complexes (NHC = N-Heterocyclic Carbene). *Chem. - A Eur. J.* **2008**, *14* (23), 6987–6993.

74. Hopen Eliasson, S. H.; Jensen, V. R. Benefit of a Hemilabile Ligand in Deoxygenation of Fatty Acids to 1-Alkenes. *Faraday Discuss.* **2019**, *220*, 231–248.

75. Eliasson, S., Chatterjee, A., Occhipinti, G., & Jensen, V. (2017). The Mechanism of Rh-Catalyzed Transformation of Fatty Acids to Linear Alpha olefins. *Inorganics*, *5*(4), 87.

76. Schlögl, R. Heterogeneous Catalysis. *Angew. Chemie - Int. Ed.* **2015**, *54* (11), 3465–3520.

77. (a) Lestari, S.; Päivi, M. A.; Bernas, H.; Simakova, O.; Sjöholm, R.; Beltramini, J.; Max Lu, G. Q.; Myllyoja, J.; Simakova, I.; Murzin, D. Y. Catalytic Deoxygenation of Stearic Acid in a Continuous Reactor over a Mesoporous Carbon-Supported Pd Catalyst. *Energy and Fuels* **2009**, *23* (8), 3842–3845. (b)

78. Hollak, S. A. W.; Bitter, J. H.; Van Haveren, J.; De Jong, K. P.; Van Es, D. S. Selective Deoxygenation of Stearic Acid via an Anhydride Pathway. *RSC Adv.* **2012**, *2* (25), 9387–9391.

79. Wang, D.; Hakim, S. H.; Martin Alonso, D.; Dumesic, J. A. A Highly Selective Route to Linear Alpha Olefins from Biomass-Derived Lactones and Unsaturated Acids. *Chem. Commun.* **2013**, *49* (63), 7040–7042.

80. (a) Lopez-Ruiz, J. A.; Davis, R. J. Decarbonylation of Heptanoic Acid over Carbon-Supported Platinum Nanoparticles. *Green Chem.* **2014**, *16* (2), 683–694. (b) Lopez-Ruiz, J. A.; Pham, H. N.; Datye, A. K.; Davis, R. J. Reactivity and Stability of Supported Pd Nanoparticles during the Liquid-Phase and Gas-Phase Decarbonylation of Heptanoic Acid. *Appl. Catal. A Gen.* **2015**, *504*, 295–307.

81. Chatterjee, A.; Jensen, V. R. A Heterogeneous Catalyst for the Transformation of Fatty Acids to α-Olefins. *ACS Catal.* **2017**, *7* (4), 2543–2547.

82. (a) Zhang, Z.; Lin, W.; Li, Y.; Okejiri, F.; Lu, Y.; Liu, J.; Chen, H.; Lu, X.; Fu, J. Heterogeneous Non-Noble Catalyst for Highly Selective Production of Linear α-Olefins from Fatty Acids: A Discovery of NiFe/C. *ChemSusChem* **2020**, *13* (18), 4922–4928. (b) Zhang, Z.; Li, Y.; Okejiri, F.; Liu, M.; Chen, H.; Liu, J.; Chen, K.; Lu, X.; Ouyang, P.; Fu, J. Highly Selective Production of Linear 1-Heptadecene from Stearic Acid over a Partially Reduced MoO: X Catalyst. *Chem. Commun.* **2020**, *56* (32), 4456–4459.

83. Yeap, J. H.; Héroguel, F.; Shahab, R. L.; Rozmyslowicz, B.; Studer, M. H.; Luterbacher, J. S. Selectivity Control during the Single-Step Conversion of Aliphatic Carboxylic Acids to Linear Olefins. *ACS Catal.* **2018**, acscatal.8b03370.

84. Zhao, L.; Li, B.; Zhao, C. Selective Decarbonylation of Fatty Acids to Long-Chain Alkenes via PtSn/SnOx-Induced C-O Activation. *ACS Sustain. Chem. Eng.* **2021**, *9* (38), 12970–12977.

85. Chiappero, M.; Do, P. T. M.; Crossley, S.; Lobban, L. L.; Resasco, D. E. Direct Conversion of Triglycerides to Olefins and Paraffins over Noble Metal Supported Catalysts. *Fuel* **2011**, *90* (3), 1155–1165.

86. Sun, P.; Liu, S.; Zhou, Y.; Zhang, S.; Yao, Z. Production of Renewable Light Olefins from Fatty Acid Methyl Esters by Hydroprocessing and Sequential Steam Cracking. *ACS Sustain. Chem. Eng.* **2018**, *6* (10), 13579–13587.

87. Ortuño, M. A.; López, N. Creating Cavities at Palladium-Phosphine Interfaces for Enhanced Selectivity in Heterogeneous Biomass Conversion. *ACS Catal.* **2018**, *8* (7), 6138–6145.

88. Wagenhofer, M. F.; Baráth, E.; Gutiérrez, O. Y.; Lercher, J. A. Carbon-Carbon Bond Scission Pathways in the Deoxygenation of Fatty Acids on Transition-Metal Sulfides. *ACS Catal.* **2017**, *7* (2), 1068–1076.

89. Schrodi, Y.; Ung, T.; Vargas, A.; Mkrtumyan, G.; Lee, C. W.; Champagne, T. M.; Pederson, R. L.; Hong, S. H. Ruthenium Olefin Metathesis Catalysts for the Ethenolysis of Renewable Feedstocks. *Clean - Soil, Air, Water* **2008**, *36* (8), 669–673.

90. (a) Wang, Z. Q.; Song, H.; Koleski, E. J.; Hara, N.; Park, D. S.; Kumar, G.; Min, Y.; Dauenhauer, P. J.; Chang, M. C. Y. A Dual Cellular–Heterogeneous Catalyst Strategy for the Production of Olefins from Glucose. *Nat. Chem.* **2021**, *13* (12), 1178–1185. (b) Chowdhury, S.; Peralta-Yahya, P. Two Steps to Sustainable Polymers. *Nat. Chem.* **2021**, *13* (12), 1157–1158.

Chapter 2.

Ligand effects on the reactivity of palladium-acyl complexes[1]

[1] Portions of the work within chapter 2 were previously published: Wiessner, T. C.; Fosu, S. A.; Parveen, R.; Rath, N. P.; Vlaisavljevich, B.; Tolman, W. B *Organometallics* **2020**, *39* (22), 3992–3998.

2.1. Introduction

The dehydrative dehydration of fatty acid derivatives to olefins typically requires activation of the acid by means of acyl halides,[1] anhydrides[2] or *p*-nitrophenyl esters (X groups; Figure 2.1).[3] Complexes of palladium[2,4] have been the most commonly used for this transformation, but success also has been demonstrated for complexes of Rh,[5] Ru,[6] Ir,[7] Fe[8] and Ni.[9] Alternatively, recent reports using photoredox methods describe a different, single electron, mechanism whereby olefins can be directly generated from the carboxylic acid through decarboxylation.[10]

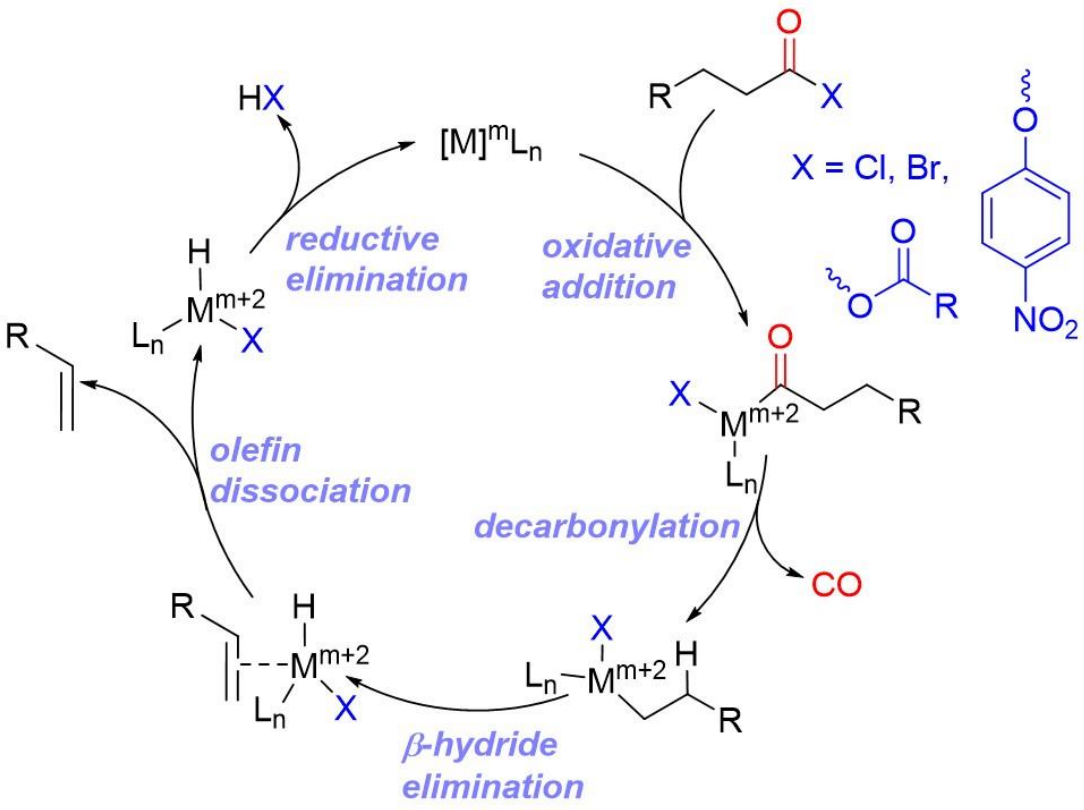

Figure 2.1. Generally proposed catalytic cycle of the dehydrative decarbonylation of fatty acid derivatives to olefins. X is an activating group that can be added during or prior to catalysis, 'm' represents the initial oxidation state of the metal (M), R is an alkyl chain or aromatic unit, and R' is either a CH_3 or *tert*-butyl group of anhydride.

Avoiding the need for acid activation inspired recent work in our group whereby fatty acid methyl esters (FAMEs) were converted to a mixture of internal and alpha olefins (LAOs).[11] Our strategy was to use a transient directing group, 2-pyridine methanol, with a Lewis Acid cocatalyst, $ZnCl_2$, that would *in situ* create a new ester, thus facilitating the coordination of a Ru catalyst for a decarbonylation dehydration sequence (Figure 2.2). Inspired by these initial results we questioned whether a directing group of increased denticity would provide benefits to the reactivity for the dehydrative decarbonylation of FAMEs to LAOs. We hypothesized that a multidentate directing group would offer a few benefits versus the weakly coordinating 2-pyridine methanol. Namely, a multidentate ligand may strengthen coordination to Ru, perhaps facilitating the decarbonylation step upon transesterification because the Ru-center would be in

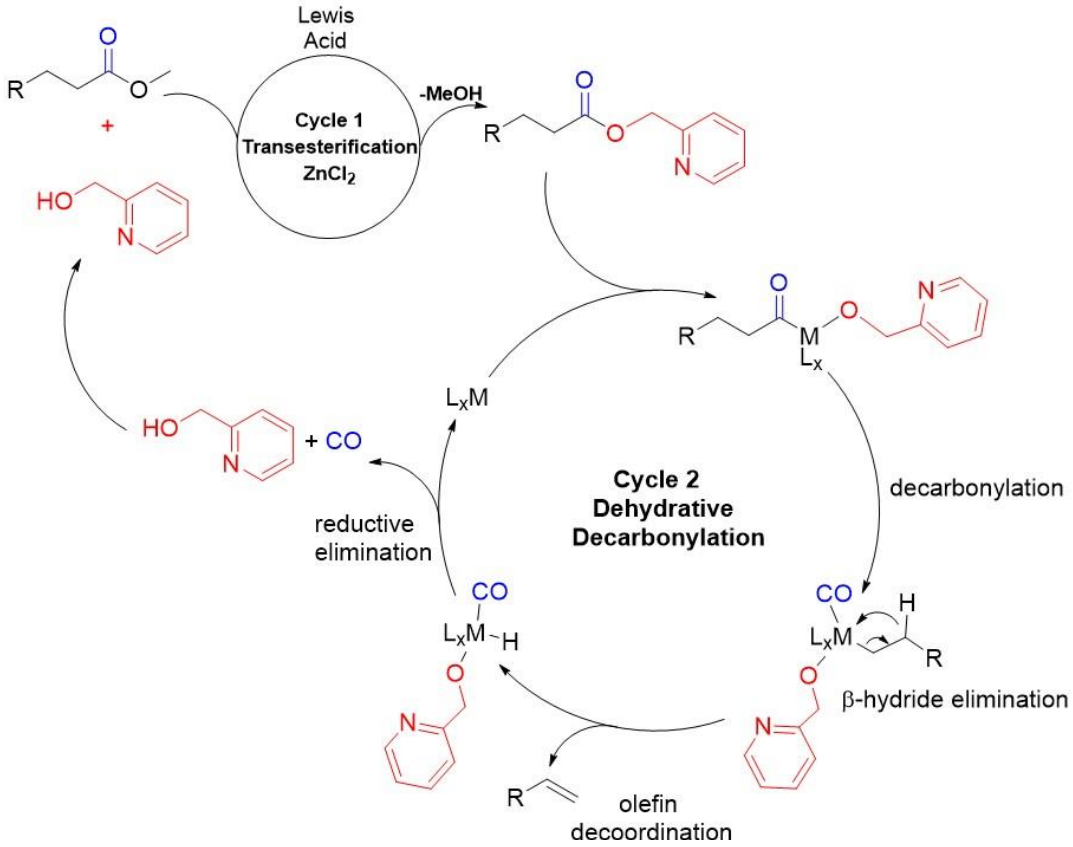

Figure 2.2. Dual catalytic cycle for the conversion of fatty acid methyl esters into olefins, where cycle 1 is a transesterification event between directing group, 2-pyridine methanol and cycle 2 is the dehydrative decarbonylation sequence enabled by $Ru_3(CO)_{12}$ as M and PCy_3 as L. 'x' is the number of ligands on M.

immediate proximity to the ester C-O acyl bond. A multidentate directing group might also alter the electronics around the Ru-center during the dehydrative decarbonylation cycle, potentially making for a more active catalyst by altering elementary steps such as oxidative addition or reductive elimination. With our initial conditions producing a maximum of 64% conversion from methyl palmitate to linear internal olefins, we also anticipated that a multidentate ligand would have increased steric bulk versus 2-pyridine methanol and may prevent the Ru from undergoing a chain-walking process, thus enhancing the selectivity of the overall process for α-olefins.

Surprisingly, initial reaction sets of two different bidentate ligands (**A** and **B**) and one tridentate ligand (**C**) of similar electronics showed a large decrease in efficiency for this process when compared to 2-pyridine methanol (Figure 2.3). A full discussion of these experiments is provided in Appendix A. In brief, both the transesterification and decarbonylation steps were individually investigated and showed very little conversion to the directing group ester or olefins, respectively. Furthermore, dual catalytic reactions were performed under the previously optimized conditions ($Ru_3(CO)_{12}$ (5 mol%), PCy_3 (15 mol%), $ZnCl_2$ (25 mol%), and 2-pyridine methanol (20 mol%), 190 °C, DMPU (0.6 M), 18 hr) but showed only minor conversion to olefins for **A**, while **B** and **C** were unsuccessful. Overall, our studies indicated that increasing the denticity of the directing group impacted the dual-catalytic process negatively, hampering its overall efficiency.

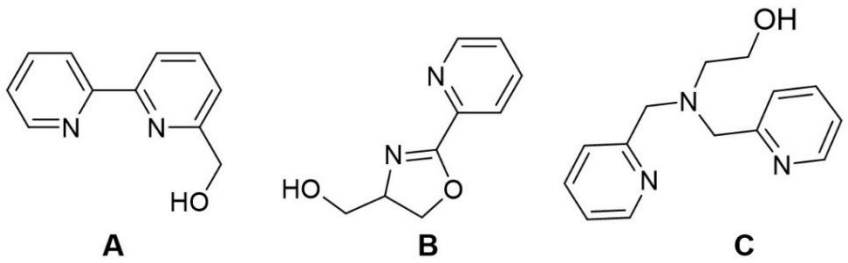

Figure 2.3. Multidentate directing groups screened for comparison to 2-pyridine methanol

Due to the multidentate directing group ligands' surprisingly negative impact on the dehydrative decarbonylation reaction, we questioned what influence ligand choice may have on the overall mechanism. We decided to undertake a more detailed study to better understand the underlying mechanism and how catalyst structure effects catalytic reactivity for the formation of olefins.[12] Based on previous reports, in which oxidative addition to the fatty acid derivative is unlikely to be rate-determining, we chose to investigate hydrocinnamoyl chloride as a substrate, from which styrene could be the only olefin formed, thus avoiding the possibility of chain-walking.[13] We aimed to investigate steps subsequent of oxidative addition in the catalytic cycle: decarbonylation (CO deinsertion) and β-H elimination (olefin formation) through stoichiometric reactions to determine what effect the ligand/steric environment has. Palladium was chosen as it is the metal historically used most for conversion of fatty acids to olefins (see chapter 1). To this end we synthesized three different Pd-acyl species and subjected them to reactions with a series of chemical additives and reaction conditions.

Three ligands were chosen for our Pd-acyl complexes based on their different influences on the steric environment around Pd: P^tBu_3, PPh_3, and 1,2-bis(diphenylphosphino) ethane (dppe). P^tBu_3 has been reported to induce a three-coordinate geometry in Pd-acyl species due to its large cone angle (θ) of 182° and buried volume ($V_{\%burr}$) of 29.6%.[14] On the other hand, PPh_3 is significantly smaller (θ=145°, $V_{\%burr}$=26.7%) and forms four-coordinate *trans*-phosphine complexes.[15] The bidentate ligand, dppe (θ=217°, $V_{\%burr}$=51.4%) is of similar size to two PPh_3 ligands, but is constrained to adopt a *cis*-coordination.[16] With the goal of evaluating how these differences effected the decarbonylation and β-hydride elimination steps of the dehydrative decarbonylation mechanism we synthesized the three Pd-acyl species and subjected them to reactivity studies. Our experimental results were informed by theory in collaboration with

Samuel Asiedu Fosu, Riffat Parveen and Bess Vlaisavljevich at University of South Dakota. Herein, we report the clear influences of phosphine structure and steric environment on the mechanism of decarbonylation (deinsertion) and β-hydride elimination, with potential implications for future catalyst design.

2.2. Results and Discussion

2.2.1 Experimental.

The Pd-hydrocinnamoyl complexes **1-3** were prepared as shown in Scheme 2.1. Compound **1** was identified by comparison of its ^{1}H and ^{13}C NMR spectra and X-ray crystal structure to data previously reported.[14a] Complexes **2** and **3** are new and were characterized by ^{1}H, $^{13}C\{^{1}H\}$, and ^{31}P NMR spectroscopy and X-ray crystallography (Figure 2.4). While **1** adopts a slightly distorted T-shaped geometry with the phosphine ligand *trans* to chloride, **2** and **3** are square planar with either *trans* or *cis* phosphine ligands, respectively. The $^{31}P\{^{1}H\}$ NMR spectra are consistent with retention of the solid-state coordination environments in solution, as **2** exhibits only one peak at 19.6 ppm for two equivalent phosphine ligands and **3** shows two coupled doublets, indicating inequivalent P atoms in a *cis* geometry (37.7 and 20.5 ppm, J_{PP} = 44 Hz). Comparison of the hydrocinnamoyl methylene peaks in the ^{1}H NMR spectra for the three complexes shows a trend in δ of **2** (1.51/2.19 ppm) < **3** (2.43/2.76 ppm) < **1** (2.89/3.54 ppm) that we attribute to *trans* influences that may be important in the reactivity of the complexes (*vide infra*). Thus, a *trans* chloride in **2**

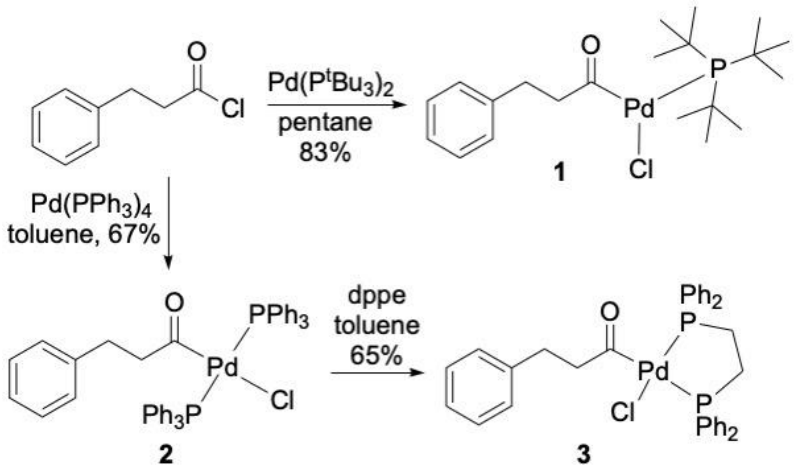

Scheme 2.1. Syntheses of complexes **1, 2** and **3**

induces the most upfield chemical shift, a *trans* -$PRPh_2$ (R = methylene) moiety in **3** has an intermediate effect, and the absence of a *trans* ligand in **1** results in the most downfield peaks.

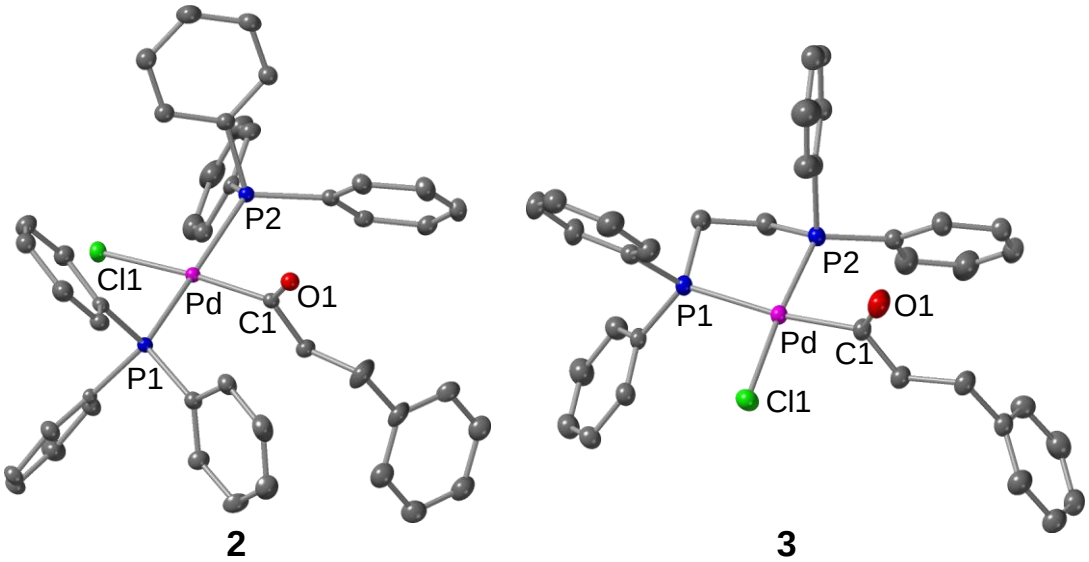

Figure 2.4. Representations of the X-ray crystal structures of **2** and **3** showing all nonhydrogen atoms as 50% thermal ellipsoids. Selected bond distances (Å) and angles (deg): **2**: Pd-C(1): 1.983(2), Pd-P(1): 2.3486(5), Pd-P(2): 2.3393(5), Pd-Cl(1): 2.4291(5), O(1)-C(1): 1.191(2). P1-Pd-Cl: 94.150(17), P2-Pd-C1: 88.034(17) P1-Pd-P2: 177.592(18), C1-Pd-C1: 175.40(6), C1-Pd-P1: 89.38(6), C1-Pd-P2: 88.37(6). **3**: Pd-C(1): 2.033(2) , Pd-P(1): 2.3956(5), Pd-P(2): 2.2331(5), Pd-Cl(1): 2.3693(5), O(1)-C(1): 1.201(3). P1-Pd-C1: 173.53(7) , P2-Pd-C1: 89.59(6), P1-Pd-P2: 84.997(18), Cl-Pd-C1: 85.73(6), Cl-Pd-P1: 99.716(19), Cl-Pd-P2: 175.27(2),

The complexes **1**-**3** are stable at room temperature, even under air for several days. In initial studies of their reactivity, solutions of the complexes in various solvents were heated (T = 40-65 °C) in attempts to induce decarbonylation and identify intermediates. In every case, the starting material decayed gradually (12-24 h) and some styrene was observed (most effectively by **1**, 40 °C for 12 h, Table 2.1). Interestingly, **2** showed the second highest production of styrene, which we anticipated might be facilitated not by the *trans* nature of the phosphines, but rather the ability for the monodentate ligands to more readily dissociate from Pd, versus the bidentate dppe. We also anticipated that the chloride ligand would not dissociate as readily as the phosphine ligands.

Accordingly, **2** should be better able to open the necessary coordination site *cis* to the carbonyl moiety and facilitate decarbonylation more readily than **3**.

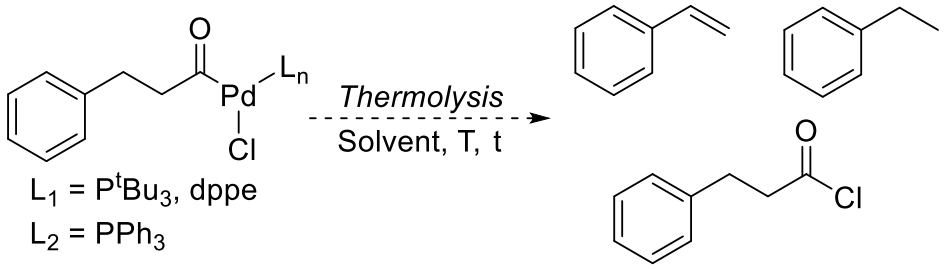

Complex	Solvent (Temperature)	Major Product(s)[a,b]
1	THF (54 °C), 23 hr	66% styrene, 41% hydrocinnamic acid
1	DMSO (54 °C), 23 hr	74% styrene
2	THF (54 °C), 23 hr	42% styrene 42% **2**, 10% ethyl benzene
2	DMSO (54 °C), 23 hr	27% styrene, 60% hydrocinnamic acid
3	THF (54 °C), 23 hr	18% styrene, 19% **3**, Hydrocinnamic acid[c]
3	DMSO (54 °C), 23 hr	21% styrene, 69% **3**
$\mathbf{2}^{+}$	THF (54 °C), 23 hr	86% styrene, 20% Hydrocinnamic Acid
$\mathbf{2}^{+}$	DMSO (54 °C), 23 hr	0% styrene, Hydrocinnamic acid[c]
1	MeCN (46 °C), 22 hr	88% styrene, 2.7% hydrocinnamic acid
1	Benzene (46 °C), 22 hr	72% styrene
1	$CDCl_3$ (46 °C), 22 hr	68% styrene, 43% **1**
1	THF (46 °C), 22 hr	52% styrene, 33% **1**

Table 2.1. Select thermolysis reactions performed in deuterated solvents. [a] Yields of major, identifiable, products were determined by comparison to a standard, 1,3,5-trimethoxybenzene see Table S2 for calculation details. [b]Reactions of **1** show only the presence of styrene and trace amounts of hydrocinnamic acid, whereas, numerous other products form in reactions of **2**, **3** and $\mathbf{2}^{+}$. [c] Yields could not be determined by ^{1}H NMR due to peak overlap.

Unfortunately, complex product mixtures formed during the thermolysis reactions of complexes **2** and **3**, and the components were often challenging to identify due to peak overlap in ^{1}H NMR spectra, whereas **1** showed clean conversion to styrene, with small amounts of hydrocinnamic acid and protonated phosphine (H-P^{t}Bu$_3^+$)(Cl$^-$) (Figure 2.5). Other products observed during thermolysis reactions included hydrocinnamoyl chloride (likely from reductive elimination), hydrocinnamic acid, potentially from nucleophilic attack by adventitious water, ethyl benzene, and others we were unable to identify (Figures 2.36, 2.37). We hypothesize that hydrocinnamoyl chloride may be generated upon reductive elimination of the starting complexes

and hydrocinnamic acid may be formed by nucleophilic attack by adventitious water in the NMR solvent. Ethyl benzene could be formed by one of two pathways. One is reduction of styrene by a Pd-hydride (Pd-H) intermediate generated after β-hydride elimination. Alternatively, after decarbonylation a Pd-ethylbenzene compound could be formed which could then react with Pd-H to give the ethyl benzene product. We were unable to observe or isolate a Pd-H species during thermolysis reactions, but it was observed through alternative means in subsequent reactivity studies (*vide infra*).

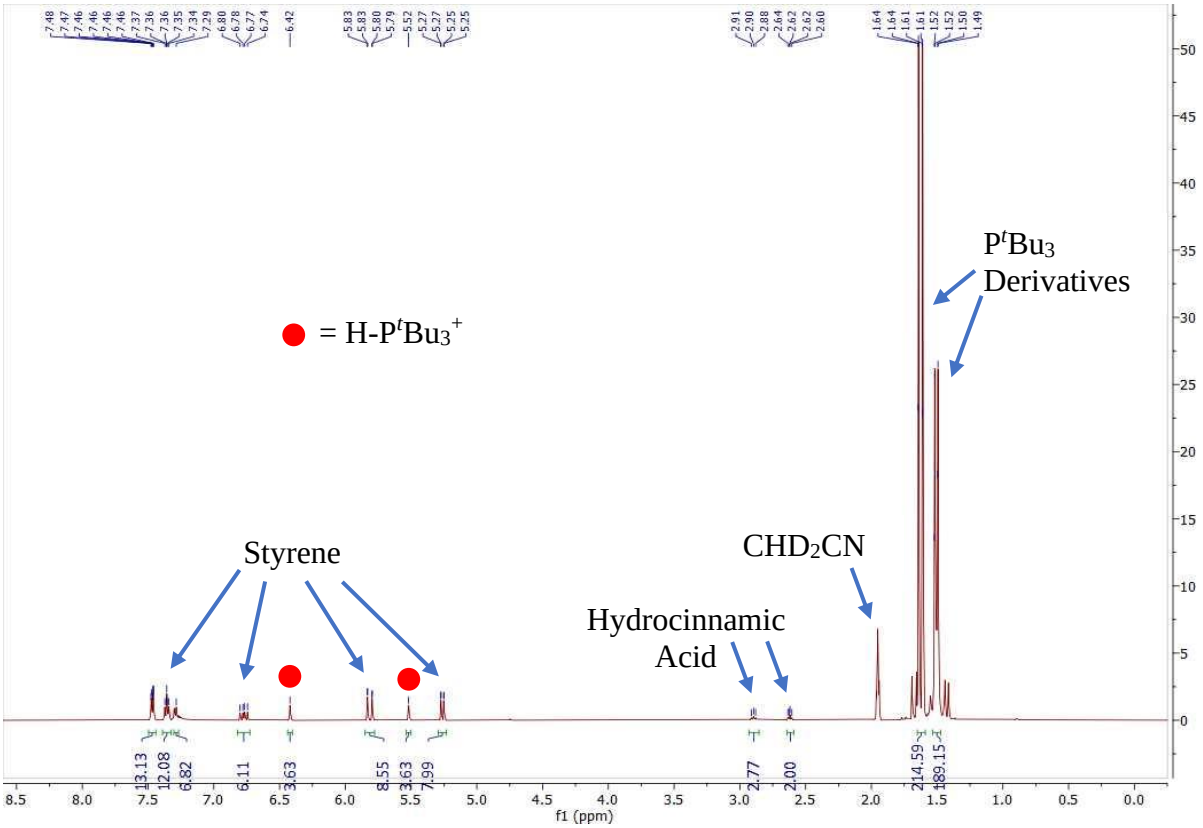

Figure 2.5. Thermolysis of complex **1** in CD_3CN at 40 °C for 12 hours. It is unclear what the nature of the P^{t}Bu$_3$ derivatives are, but it is unlikely that any free ligand is present (1.30 ppm in CD_3CN).

Under our previous hypothesis that decarbonylation would be affected by the decoordination of a ligand *cis* to the carbonyl or enhanced by unsaturation at the metal center (supported by density functional theory (DFT) results described below) we sought to remove the

chloride ligands in the complexes by treating them with various additives such as silver and zinc salts, as well as $NaBAr^F$ (sodium tetrakis[3,5-bis(trifluoromethyl)phenyl]borate) and other Lewis Acids. For comparison of a select number of additive reactions see Table 2.2.

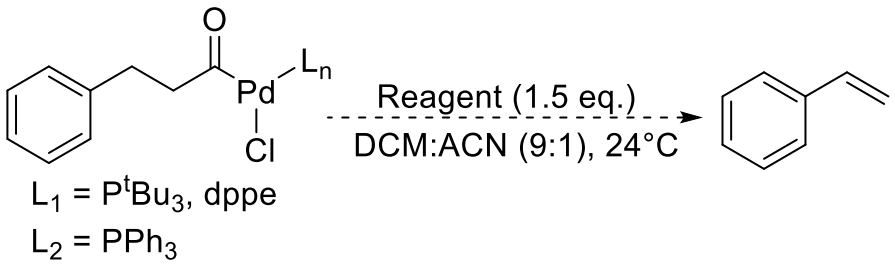

Additive	**1**	**2**	**3**
$AgBF_4$	>99%	< 5% [b]	20% [b,c]
$NaBAr^F$	>99%	< 5% [b]	15% [b,c]
$ZnCl_2$	>99%	7% [b]	19% [b,c]
$Zn(OAc)_2$	90%	< 3%	25%
ZnO	15%	7%	0%
D^IPT	64%	3%	0%

Table 2.2. Conversions of Pd-acyl complexes to styrene. Determined by in situ ^1H NMR spectroscopy. Reagents: AgX (X= BF_4, OTf, SbF_6), NaY (Y= BAr^F, SbF_6, PF_g, BF_4), $ZnCl_2$, $Zn(OAc)_2$, ZnO, 1,3-diisopropyl-2-thiourea (D^IPT). Reactions of **1** performed in acetonitrile-d_3. [b] Cationic complex also formed. [c] 3-phenylpropanal also observed.

In the case of **1**, reactions with silver salts (e.g. $AgBF_4$) were complete within seconds, as noted by rapid precipitation of AgCl, formation of palladium black, full consumption of starting material and quantitative conversion to styrene (^1H NMR). Reactions with $NaBAr^F$ were slower, taking minutes to hours for full consumption of **1** depending on conditions, and were amenable to kinetic analysis (*vide infra*). Reactions with zinc salts also afforded styrene, albeit typically at rates slower than the reactions with silver reagents and not always as cleanly. Thus, treatment of **1** in

acetonitrile with $ZnCl_2$ led to quantitative styrene formation within seconds, even when performed with substoichiometric amounts (33%), but $Zn(OAc)_2$ and ZnO produced styrene in only 92% and 24% yield, respectively, after 22 h.

Monitoring of reactions of **1** and $NaBAr^F$ by ^1H NMR spectroscopy revealed disappearance of the peaks associated with **1** concomitant with formation of styrene and growth of a doublet attributed to the phosphonium $HP^tBu_3^+$ (Figure 2.6). No other species were observed, implying that halide abstraction is rate-determining and all subsequent steps are facile (deinsertion, β-hydride elimination). Consistent with this conclusion and a first-order dependence on **1**, a plot of ln[**1**] vs. time where $[NaBAr^F]_0 = 5.6 \times 10^{-2}$ M and $[\mathbf{1}]_0 = 1.3 \times 10^{-2}$ M is linear (Figure 2.7a). Performing the reaction at various concentrations of $NaBAr^F$ (> [**1**]) and plotting versus the observed rate constants also yields a linear fit, consistent with a first order dependence on $NaBAr^F$

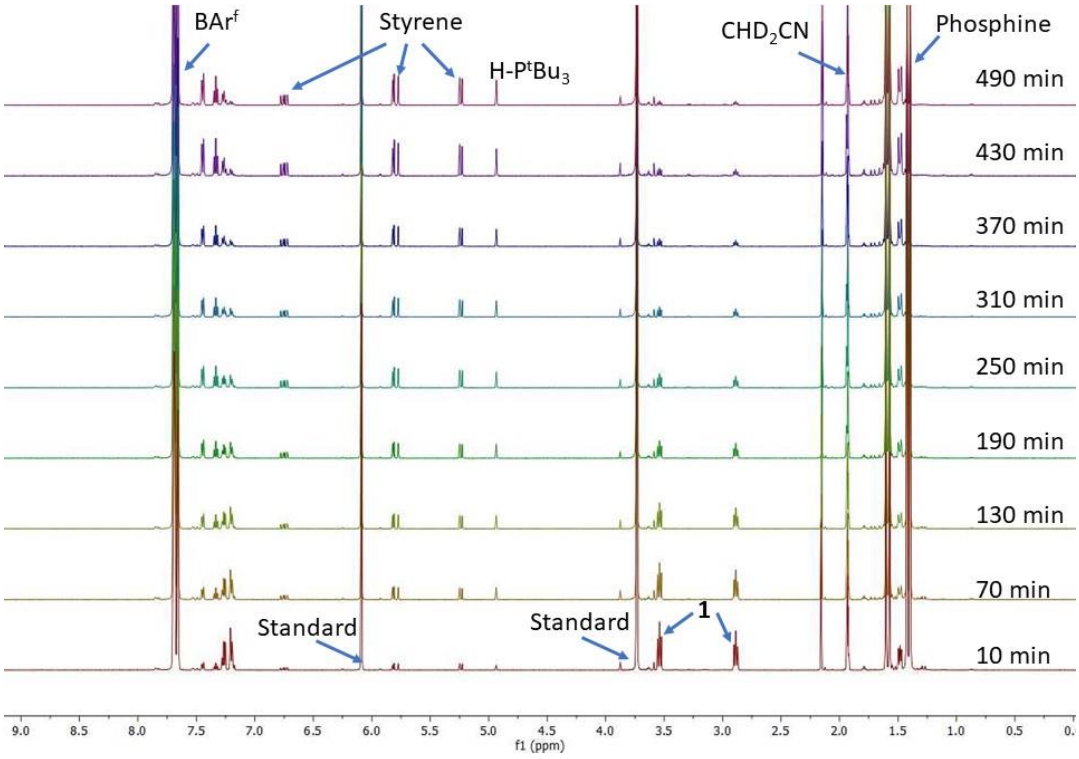

Figure 2.6. Example of ^1H NMR array for the halide abstraction of complex **1** with $NaBAr^f$ (1.5 equivalents) CD_3CN. Spectrum taken every 60 minutes, bottom spectrum is 10 minutes, top spectrum is 490 minutes. $[\mathbf{1}]_0 = 0.013$M, $[NaBAr^f]_0 = 0.028$M.

(Figure 2.7b). Taken together, the data are consistent with rate = k[**1**][$NaBAr^F$], indicative of rate-determining halide abstraction.

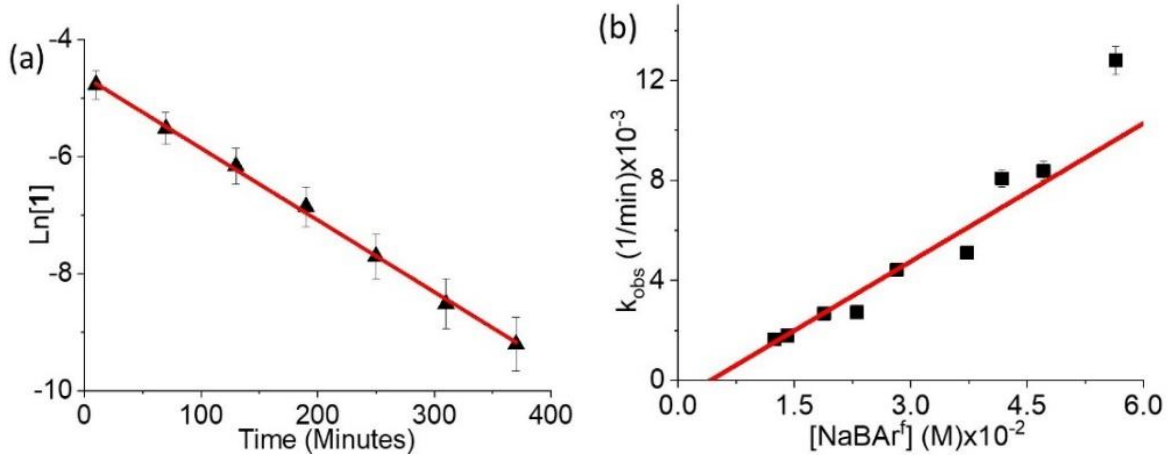

Figure 2.7. (a) Selected example of a kinetic plot for the reaction between **1** and $NaBAr^F$ in acetonitrile-d_3. $[\mathbf{1}]_0$ = 1.3 x 10^{-2} M, $[NaBAr^F]_0$ = 5.6 x 10^{-2} M, k_{obs} = 3.11 x 10^{-3} min^{-1}, R^2 = 0.995. (b) Plot of k_{obs} (avg of triplicate measurements; see Figure S5) vs. [$NaBAr^F$] where $[Pd\text{-}acyl]_0$ = 0.013 M. The indicated linear fit has slope 0.184 M min^{-1} and intercept -7.7x10^{-4} M, R^2=0.953. Full plots of the kinetic data can be found in appendix C.

While the results of the reactions of **1** with silver and zinc salts and $NaBAr^F$ suggest that CO deinsertion is activated by removal of chloride, it is also possible, particularly in the case of the zinc salts, that deinsertion is promoted by binding of the Lewis acid to the carbonyl group. Indeed, 1,3-diisopropyl-2-thiourea, which is known to hydrogen bond and activate carbonyl compounds, induces consumption of **1** to generate styrene, albeit in modest 64% yield after 22 h with formation of side products that could not be easily identified.

In contrast to the reactions of **1**, treatment of **2** with silver and zinc salts and $NaBAr^F$ under the same conditions produced very little styrene (< 10%). Instead, a new species was observed by ^{1}H NMR spectroscopy that we assign as the cationic product of substitution of chloride by CH_3CN, $\mathbf{2}^+$. The species exhibits similar peaks in the ^{1}H NMR spectrum to those of **2**, except the methylene peaks of the hydrocinnamoyl ligand are slightly shifted downfield, from 1.51/2.19 ppm to 1.72/

2.26 ppm (CD_2Cl_2). We conclusively identified $\mathbf{2}^+$ by isolating it as either its BF_4^- or SbF_6^- salt as a white solid and obtaining the X-ray crystal structure for the latter case (Figure 2.8). The complex is square planar, with two *trans* -PPh_3 ligands and an acetonitrile molecule replacing the chloride ligand found in **2**; a single SbF_6^- counterion is present (not shown), consistent with a monocationic Pd(II) species.

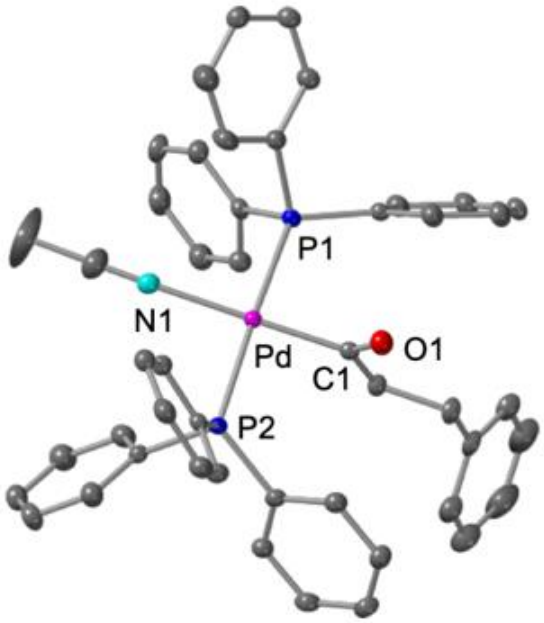

Figure 2.8. Representation of the X-ray crystal structure of **2(SbF$_6$)** showing all nonhydrogen atoms as 50% thermal ellipsoids and SbF_6 counterion omitted for clarity. Selected bond distances (Å) and angles (deg): Pd-C(1): 1.9915(19), Pd-N(1): 2.1606(17), Pd-P(1): 2.3513(5), Pd-P(2): 2.3548(5), O(1)-C(1): 1.199(2). P1-Pd-N1: 91.90(5), P2-Pd-N1: 90.21(5), P1-Pd-P2: 174.869(2), C1-Pd-N1: 178.91(7), C1-Pd-P1: 88.49(5), C1-Pd-P2: 89.48(5).

Isolation of $\mathbf{2}^+$ indicates that decarbonylation is significantly slowed relative to **1**. Consistent with this conclusion, while thermolysis of **1** (65 °C, CD_3CN, 12 h) quantitatively afforded styrene, heating **2(BF$_4$)** under identical conditions produced styrene in only 37% yield with 16% of **2(BF$_4$)** remaining. Treatment of **2(BF$_4$)** with $ZnCl_2$ (1.5 equivalents) in CH_2Cl_2/CH_3CN (9:1) produced a small amount of styrene (10% yield). This result is consistent with some decarbonylation promoted by Lewis Acid coordination to the carbonyl in the cationic

complex. It also suggests that the dissociation of the phosphine ligands may be less favorable for the cationic species. Overall, the sluggish decarbonylation of **2** contrasts with the reactivity observed for **1**, pointing toward significant differences in accessibility of the necessary transition state geometry imposed by the different phosphine ligands (*vide infra*).

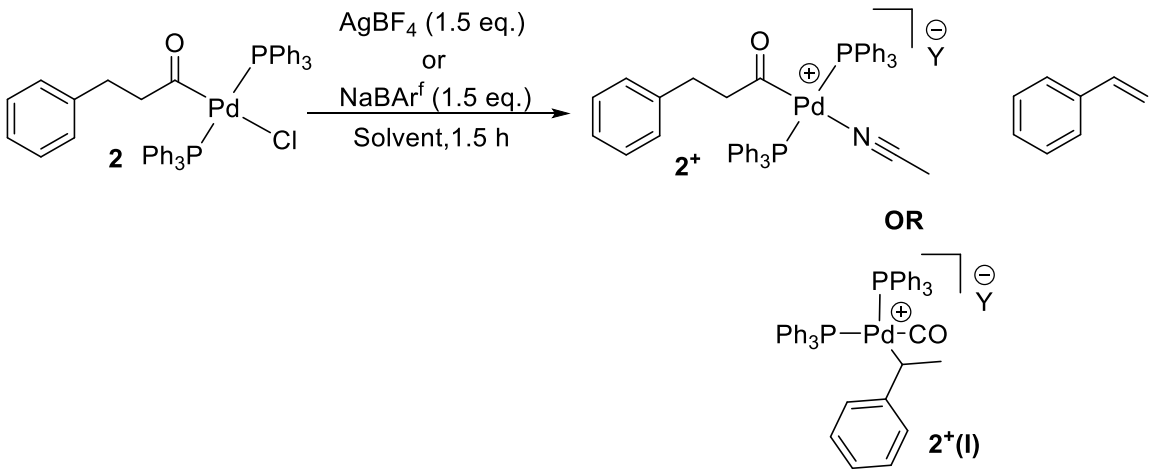

Scheme 2.2. Halide abstraction of **2** forms either the isolated complex $\mathbf{2}^+$ with a small amount of styrene when CH_3CN is present or $\mathbf{2}^+\mathbf{(I)}$ when performed in noncoordinating solvents. Y = BF_4 or $NaBAr^f$

Furthermore, we found that the synthesis of $\mathbf{2(BF_4)}$ was solvent dependent, and without acetonitrile present a new species $\mathbf{2}^+\mathbf{(I)}$ was identified. Without the coordinating ability of CH_3CN in the solution decarbonylation appeared to be facile, resulting in a rapid deinsertion/β-H elimination/ hydropalladation sequence, which resulted in Pd moving adjacent to the phenyl ring, making a 1-pheny-1-Pd-ethyl species (Figure 2.9). We observed this whether using CD_2Cl_2 as the sole solvent or replacing the acetonitrile of the 9:1 (CD_2Cl_2:CD_3CN) mixture initially used in our reactions with a solvent of similar dielectric constant, nitromethane, (CD_3NO_2). Unfortunately, due to the instability of $\mathbf{2}^+\mathbf{(I)}$, we were unable to get confirming data in the forms of high-resolution mass spectrometry, infrared spectroscopy or x-ray crystallography, as crystallization attempts resulted in degradation to styrene and a material, we suspected was palladium black. We do note,

however, that the ^{31}P NMR spectrum shows coupling of phosphine ligands, indicating they are in a *cis* conformation (Figure 2.34). Furthermore, COSY NMR indicates coupling between protons B and C, which are present in the expected 1:3 ratio (Figure 2.35).

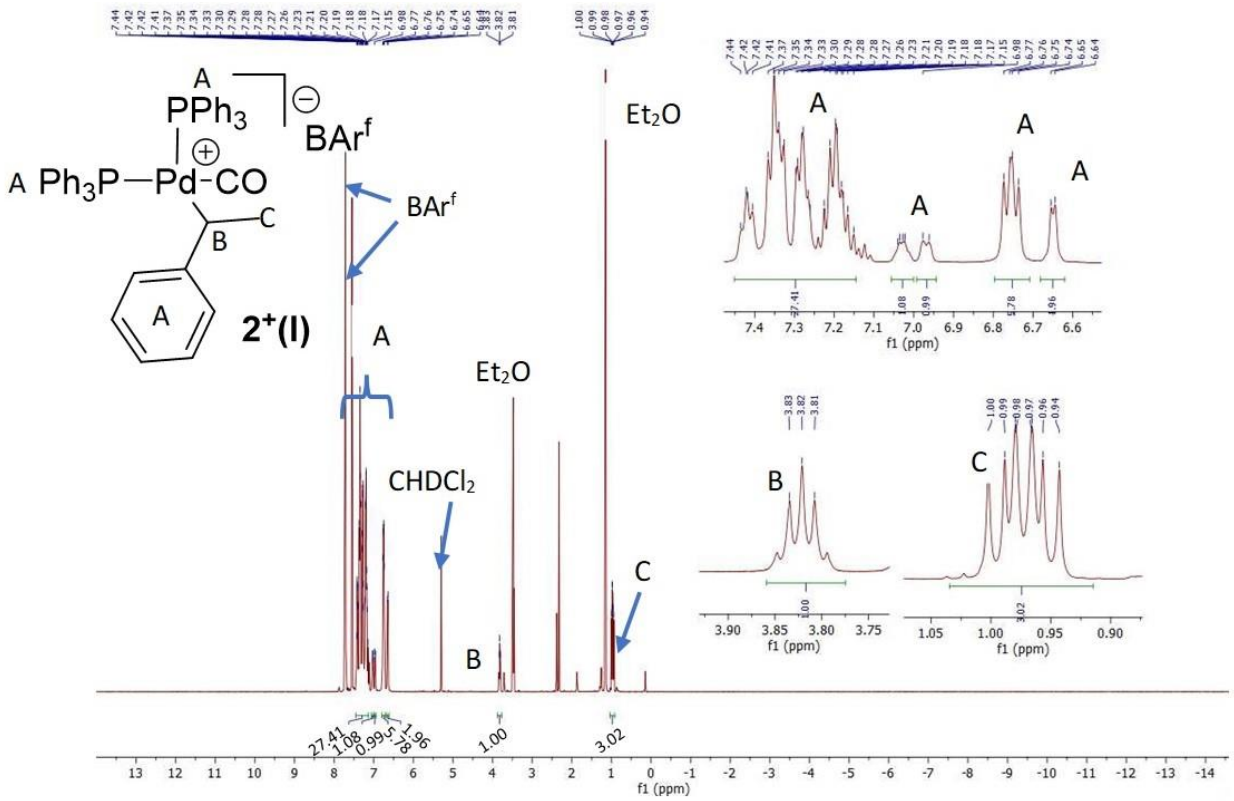

Figure 2.9. ^{1}H NMR **2^{+}(I)BAr^{f}.** [a] (CD_2Cl_2). Note, some residual toluene/benzene from the starting material in aromatic region as noted by the singlet at 2.36 ppm and slight exaggeration of integrations in the aromatic region.

Curious to further investigate the effects of solvent on the stability of **2^{+}(I)** and see if the coordination of acetonitrile facilitates the formation of styrene, we synthesized **2^{+}(I)** through halide abstraction of **2** with $NaBAr^{f}$ (1.5 equivalents) in CD_2Cl_2:CD_3NO_2 (9:1) at room temperature. The solvent was removed yielding a powdery solid that was subsequently redissolved in CD_2Cl_2. Analysis of a ^{1}H NMR spectrum confirmed that no changes occurred through this process. Repeating these steps, but instead adding CD_3CN in place of CD_2Cl_2

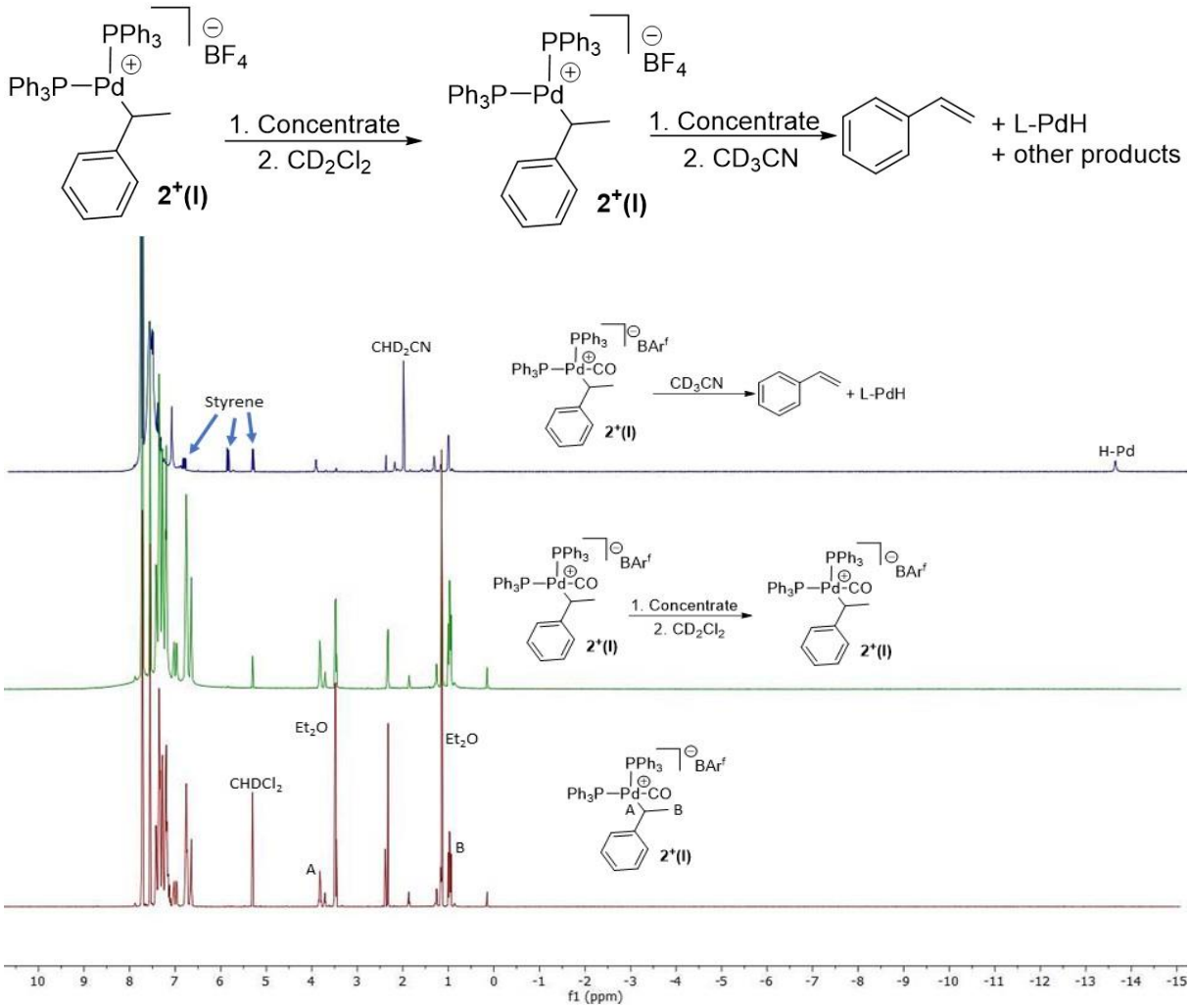

Figure 2.10. Reactions of Complex $\mathbf{2^{+}(I)\ BAr^{f}}$. Bottom spectrum is from initial reaction. Middle spectrum is after concentration and subsequent redissolving in CD_2Cl_2. Top spectra is after a second solvent removal and subsequent addition of CD_3CN causing multiple products to form

showed clear formation of styrene and a Pd-H species (Figure 2.10). Our hypothesis, later supported by theory, indicates the coordination of a molecule of acetonitrile aids in the β-H elimination step. It is unclear as to the nature of the Pd-H species, whether CO and/or CH_3CN are coordinated.

Anticipating that in **3** a *cis* arrangement of the acyl and chloride ligands might lead to enhanced reactivity upon chloride removal, we examined the reactivity of **3** with silver salts. Addition of 1.5 equivalents of $AgBF_4$ to a solution of **3** in CD_2Cl_2/CD_3CN (9:1) revealed formation

of styrene (18%), 3-phenylpropanal (33%) and a new species assigned as $\mathbf{4}^+$ (39%, Scheme 2.3). This assignment was based on ^{1}H, COSY, ^{13}C{^{1}H}, and ^{31}P NMR spectroscopy (Figures 2.32-2.35). Like $\mathbf{2}^+$**(I)**, coupled protons (as determined by COSY) in an integral ratio of 1:3 support the positioning of Pd adjacent to the phenyl ring. Also, coupled, *cis*-phosphines were observed by ^{31}P{^{1}H} NMR spectroscopy (δ_P 41.39 (d), 43.77 ppm (d), J = 45Hz, Figure 2.38).

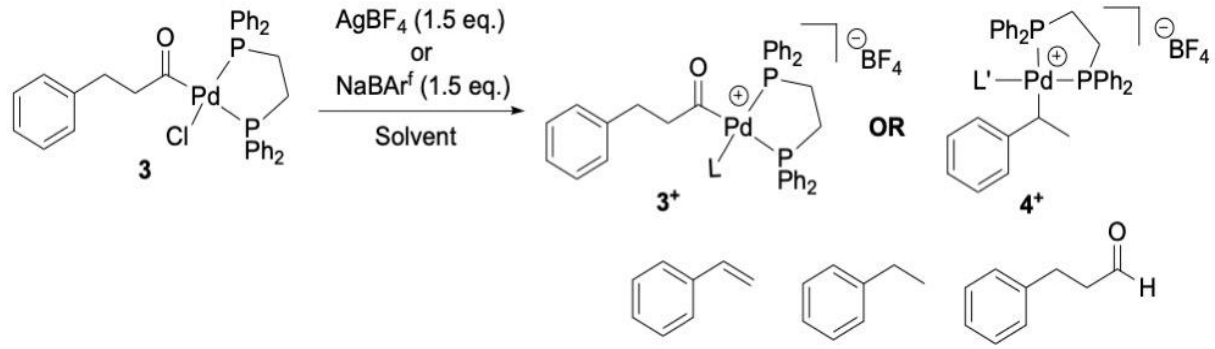

Scheme 2.3. Halide abstraction reactions of **3**. Product mixtures are dependent on solvent conditions. L is postulated as acetonitrile and L' is postulated to be carbon monoxide or an empty coordination site, blocked by the methyl group of the complex, perhaps stabilized by β-agostic interactions.

Attempts to isolate $\mathbf{4}^+$ by filtering the reaction mixture into diethyl ether at -35 °C yielded a yellow solid. Redissolving $\mathbf{4}^+$ in either CD_2Cl_2 or a mixture of CD_2Cl_2 and CD_3NO_2 showed no changes versus the initial spectrum of the yellow solid, but when dissolved in only CD_3CN peaks analogous to those assigned to $\mathbf{2}^+$ were observed, leading to assignment as $\mathbf{3}^+$ (Figure 2.11). We surmise that the ligand denoted as L' bound to $\mathbf{4}^+$ is likely carbon monoxide (CO) as it must remain on Pd in order to generate $\mathbf{3}^+$. Like our hypothesis for the formation of $\mathbf{2}^+$**(I)**, we propose that the coordination of CD_3CN leads to a sequence of β-H elimination/hydropalladation and CO reinsertion, with L now being a coordinating molecule of CD_3CN. Our observations also suggest

that the small fraction of CH_3CN in the initial reaction mixture was insufficient to trap the species $\mathbf{3}^+$ prior to decarbonylation.

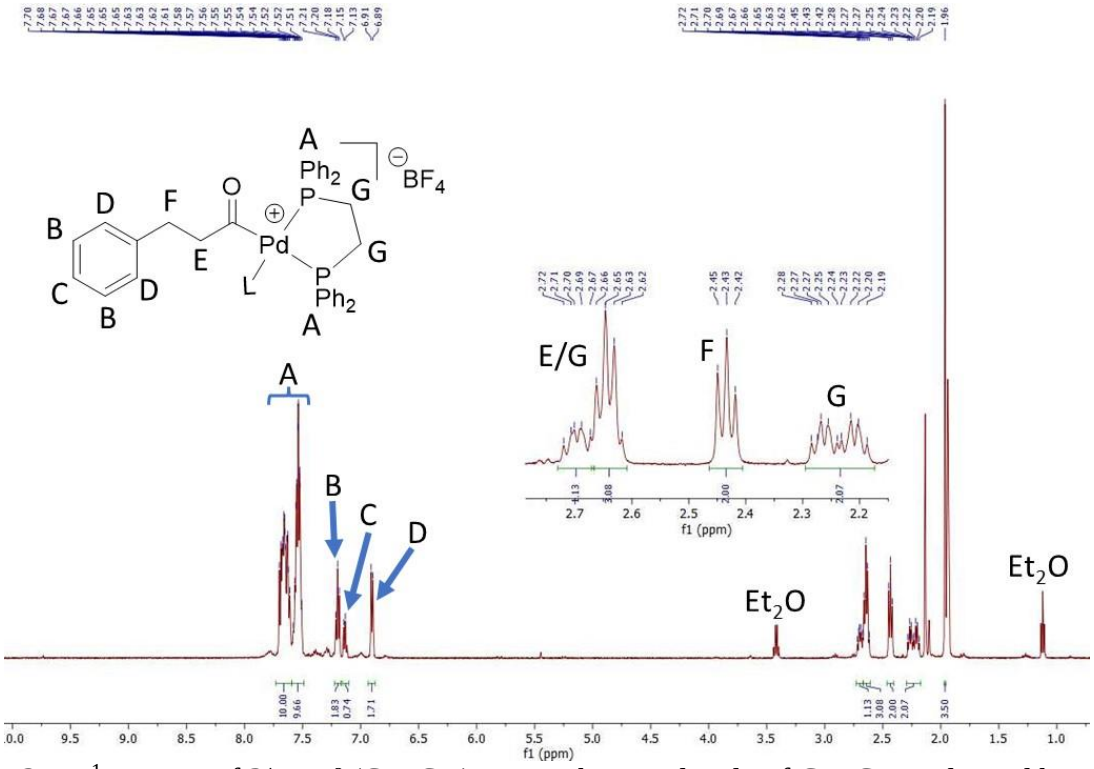

Figure 2.11. ^{1}H NMR of $\mathbf{3}^+\mathbf{BF_4}$ [a] (CD_3CN). L may be a molecule of CD_3CN, indicated by a singlet observed at 2.13 ppm.

Having observed $\mathbf{4}^+$ and its potential to reversibly produce $\mathbf{3}^+$, we were curious to see if it could be an intermediate in styrene production or if longer reaction times would lead to greater yields. Treatment of compound **3** with $NaBAr^F$ (1.5 eq.) in CD_2Cl_2/CD_3CN (9:1) (Figure 2.12) yielded styrene (14%), aldehyde (30%), ethyl benzene (6%) and $\mathbf{4}^+$ (46%). Observing the reaction mixture for several days, we found that the concentration of styrene and aldehyde products remained constant after 12 hours as $\mathbf{4}^+$ gradually decayed to more ethyl benzene and there was no further increase in styrene or aldehyde concentration. From these results we conclude that **3** is more prone to decarbonylation than **2**, but that the subsequent reactions of the initial Pd-ethylbenzene complex are complicated by reversible chain-walking and the possible intermediacy

of a hydride species that would be responsible for aldehyde and ethylbenzene formation. We further note that omitting acetonitrile or replacing it with noncoordinating nitromethane leads to the sole formation of $\mathbf{4}^+$, whereas reactions in only acetonitrile lead to styrene, 3-phenylpropanal and unidentified decomposition products, without observing $\mathbf{4}^+$.

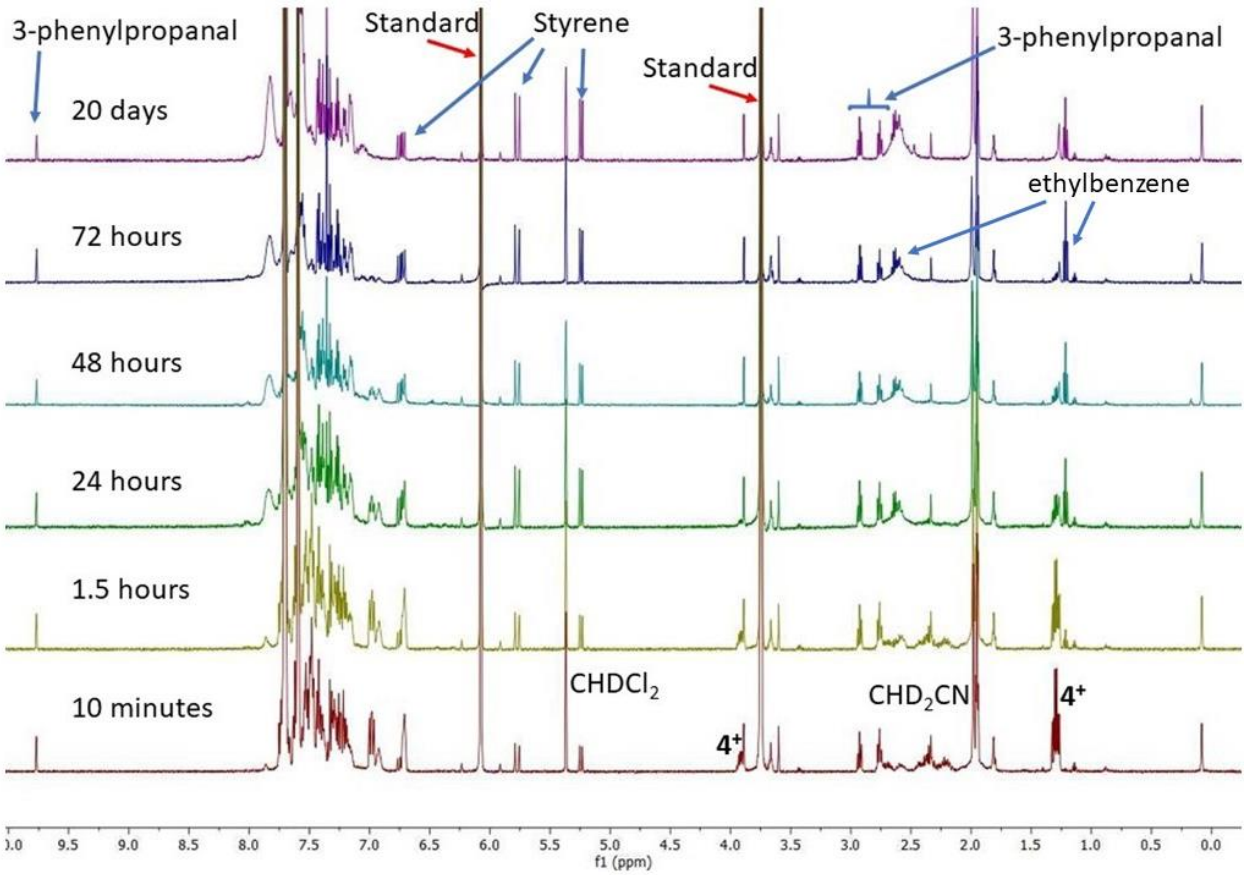

Figure 2.12. Monitoring formation and decay of $\mathbf{4}^+$ over time (CD_2Cl_2).

As in the case of **2**, reactions of **3** with $ZnCl_2$ show the largest amount of styrene (45%), also producing aldehyde (52%) and $\mathbf{4}^+$ (18%). Product yields appear >100%, which we attribute to baseline error in the NMR, measurement of standard in solution and peak overlaps. Reactions with $Zn(OAc)_2$ lead to styrene and 2-phenylpropanal in 24% and 32% yields, respectively, but no $\mathbf{4}^+$, while ZnO and diisopropylthiourea showed no reactivity. The observed increased tendency for

decarbonylation in reactions of **3** is consistent with reports of bidentate ligands facilitating decarbonylation relative to monodentate ligands in decarbonylative cross couplings.[17] Taken together the experimental data suggest the coordination site *cis* to the carbonyl plays a major role in decarbonylation, occurring so fast upon chloride removal in **3** that coordination of CH_3CN at low concentrations cannot prevent it. Thus, a higher reactivity of *cis*, bidentate **3** versus the *trans* monodentate **2** was observed during our additive reactions.

2.2.2 Theory.

All computations were performed by our collaborators Samuel Asiedu Fosu, Riffat Parveen and Bess Vlaisavljevich at University of South Dakota. To gain insight into the reactivity differences observed experimentally, the structures of **1**-**3** and their dehydrogenative decarbonylation reactions were explored by DFT calculations (additional computational details are in Appendix E). They first examined the decarbonylation pathways via thermolysis. The CO deinsertion step for **1** proceeds *via* a transition state with a free energy barrier of 26.1 kcal/mol (Figure 2.13). The equivalent barriers for **2** and **3** are 36.7 and 31.8 kcal/mol, respectively. The lower barrier calculated for **1** is consistent with the experimental observation that upon heating **1** is most effective at producing styrene, albeit slowly.

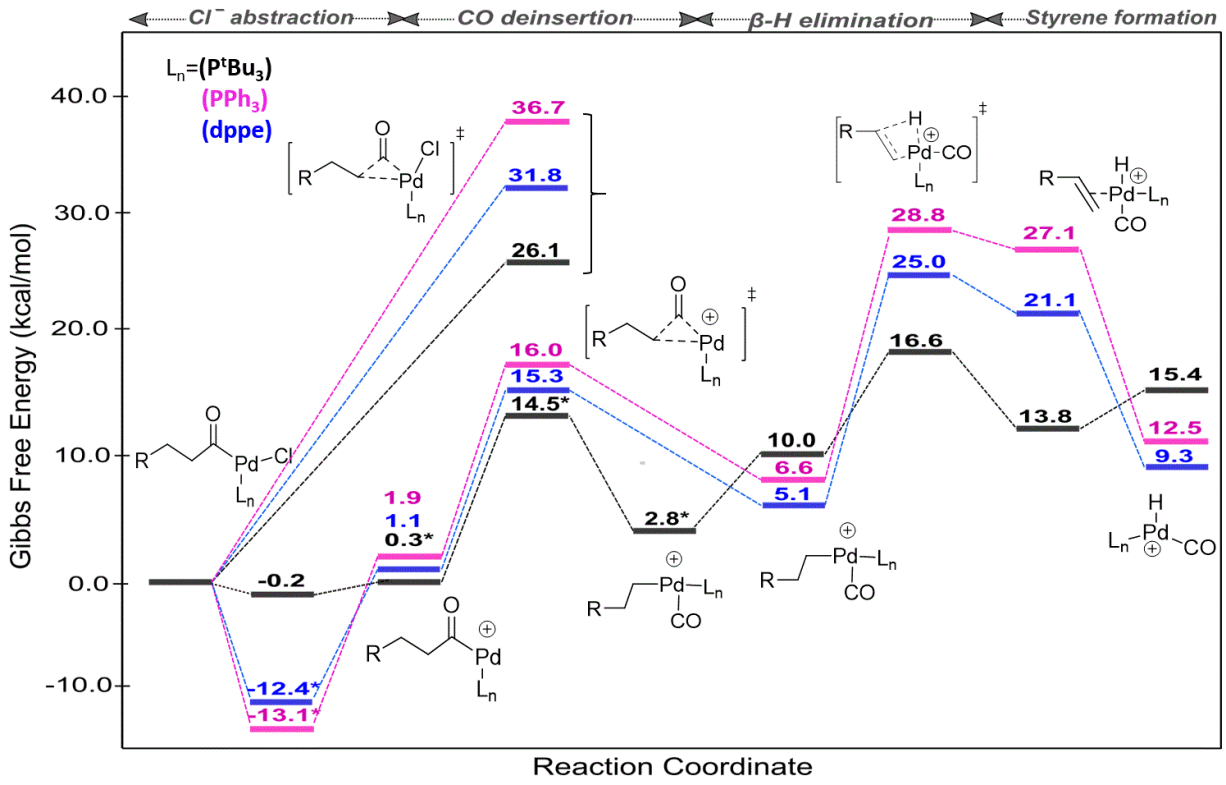

Figure 2.13. DFT computed reaction mechanism for the Pd-catalyzed decarbonylation of 3-phenylpropionylchloride. (*) indicates coordation of explicit acetonitrile (solvent) molecule.

Next, the decarbonylation process was studied including prior halide abstraction. The data reported in the energy profile (Figure 2.13) involve Ag^+ ions as the halide abstracting agent (these results are compared to those obtained using Na^+ ions in Figure 2.14). If chloride is abstracted using Ag^+ followed by explicit solvation of the Pd center by acetonitrile (ΔG = 0.3 kcal/mol), the free energy barrier for the CO deinsertion step for **1** is lowered by 11.4 kcal/mol to $\Delta G^{\ddagger}$ = 14.7 kcal/mol (Figure 3). If the CH_3CN molecule is not explicitly coordinated to Pd, the energy barrier is higher ($\Delta G^{\ddagger}$ = 19.4 kcal/mol).

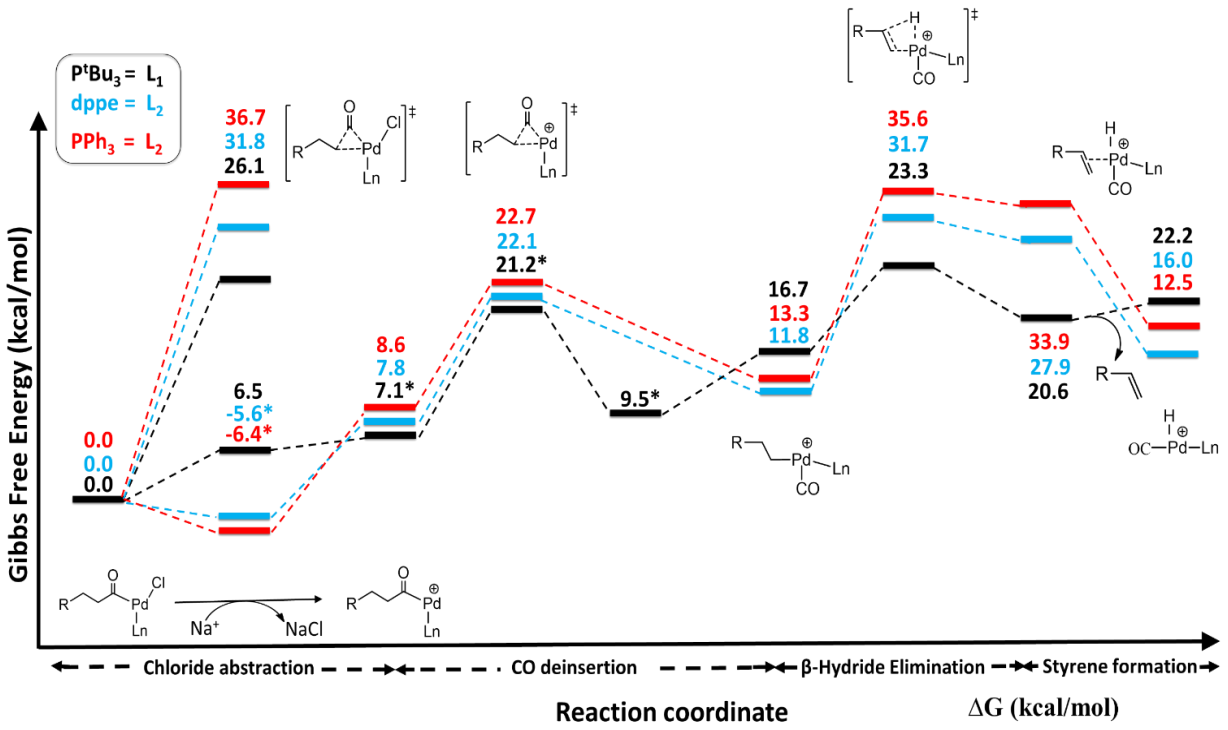

Figure 2.14. Computed reaction profile for chloride abstraction, CO deinsertion, β-hydride elimination and styrene formation stages starting from **1** where L = P^{t}Bu$_3$, **2** where L = PPh$_3$, and **3** where L = dppe.

Both **2** (L_n = PPh$_3$) and **3** (L_n = dppe) undergo similar CO deinsertion reactions to **1** (L_n = P^{t}Bu$_3$; Figure 2.13). The same amount of free energy is required in the bond making and breaking processes in the transition state structures for all three ligands ($\Delta G^{\ddagger}$ = 14.2, 14.1, and 14.2 kcal/mol, respectively). However, coordination by acetonitrile after chloride abstraction in **1** produces a slightly unstable intermediate, which subsequently undergoes CO deinsertion. Explicit solvation facilitates the reaction by allowing the transition state structure to maintain a stable four-coordinate geometry at the Pd(II) center (Figure 2.15). On the other hand, in complexes **2** and **3**, the most favorable transition state structures are not solvated since they are already four-coordinate. The stability of the cationic intermediates, **2**$^+$ (ΔG = -13.1 kcal/mol) and **3**$^+$ (ΔG = -12.4 kcal/mol) leads to higher barriers for CO deinsertion of 29.1 and 27.7 kcal/mol, respectively. Thus, while for **1** CO

deinsertion is significantly hastened after halide abstraction relative to direct thermolysis, for each of **2** and **3** the two routes have similarly high barriers.

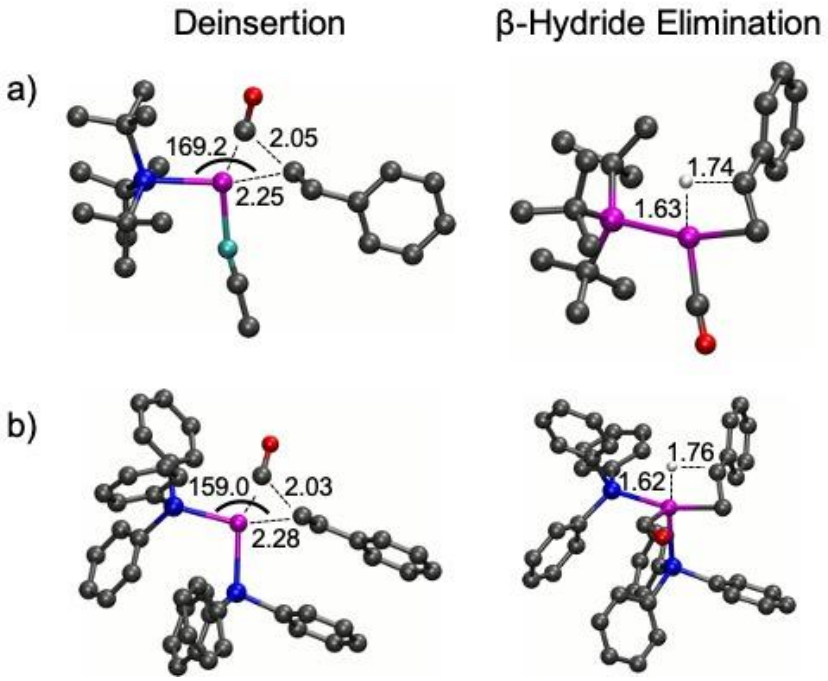

Figure 2.15. Deinsertion and β-hydride elimination optimized transition state geometries for the pathways with the a) P^{t}Bu$_3$ and b) PPh$_3$ ligands. Bond distances in Å and angles in degrees. Hydrogen atoms not involved in β-hydride elimination excluded for clarity. Legend: P = blue, Pd = magenta, C = gray, O = red, N = teal.

Further insight into the CO deinsertion process comes from analysis of the calculated transition state geometries. The respective transition states have P-Pd-C angles ranging from 169.2° with P^{t}Bu$_3$ to 159.0° with PPh$_3$ (Figures 2.15 and 2.16). The structure with P^{t}Bu$_3$ has the shortest distance for the newly formed Pd-C bond (2.25 Å) signifying stronger bonds that stabilize the transition state structure. For the dppe transition state (Figure 2.16), the P-Pd-C angle is 167.6° and the Pd-C bond distance is 2.28 Å.

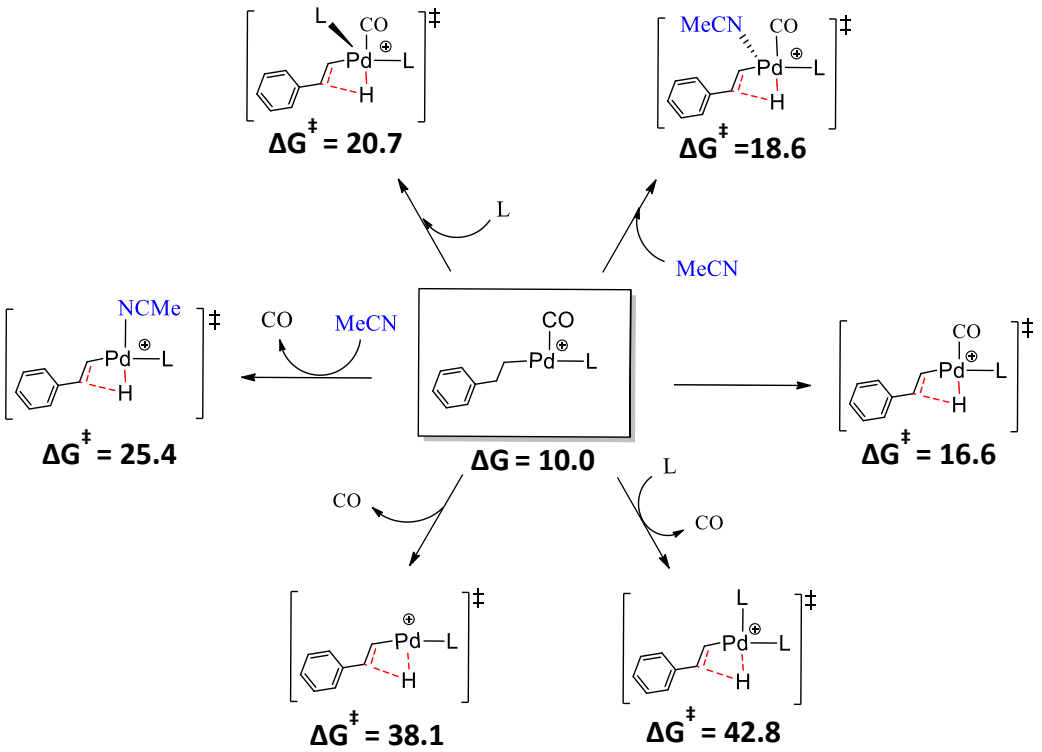

Scheme 2.4. Effect of different ligand environments and explicit solvent on the β-hydride elimination transition state energy barriers in P^{t}Bu$_3$ Pd-acyl complexes. Data reported with reference to **1** in the chloride abstraction pathway with Ag^+ used as halide abstraction agent. Gibbs free energy in kcal/mol.

On the basis of these results it was surmised that the presence of a single P^{t}Bu$_3$ ligand results in more favorable CO deinsertion because of a relative lack of destabilizing steric effects. Also, in the CO deinsertion for the case of PPh$_3$, the *trans* phosphine ligands must rotate to the *cis* position in the transition state, and this requires 3.4 kcal/mol. They speculate that steric effects associated with the *cis* arrangement further add to the energetic cost for CO deinsertion in this case (Scheme 2.5). For the case of the bidentate dppe ligand, the *trans* arrangement is inaccessible, and the transition state exhibits steric characteristics that fall between P^{t}Bu$_3$ and PPh$_3$. The CO deinsertion products are ~10 kcal/mol lower in energy than the TS barriers supporting experimental observations that **3** will more readily undergo CO deinsertion relative to **2**.

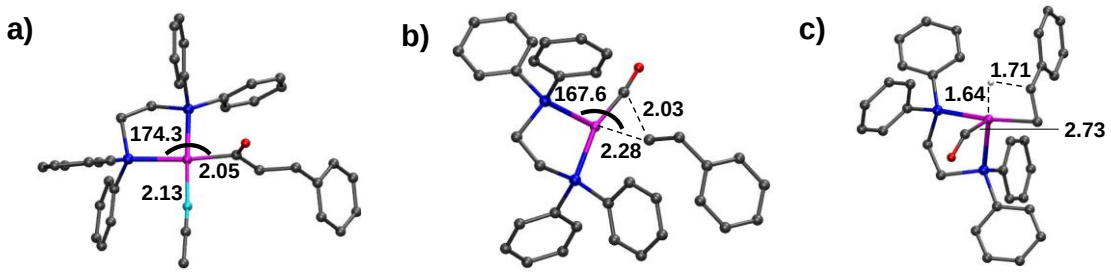

Figure 2.16. DFT optimized geometries of the dppe a) solvated cationic intermediate, b) CO deinsertion transition state structure, and c) β-hydride elimination transition state structure. Bond distances are in Å and angles in degrees. Hydrogen atoms not involved in β-hydride elimination excluded for clarity. Pd in magenta, P in blue, N in cyan, O in red, C in grey.

The findings from the above analysis are in agreement with the results of other studies.[13] For example, it was observed that PPh_3 ligands decoordinate from a Pd catalyst during the decarbonylative dehydration of butanoic acid to maintain four-coordinate complexes, while the ligand remains coordinated to the less active Rh analogue.[13b] Also, in an analysis of the turnover limiting step in the formation of styrene from hydrocinnamic acid by a Pd catalyst with a PPh_3 ligand, it was observed that the four-coordinate transition state structures are more stable than five-coordinate ones.[13a] Furthermore, the use of a bulkier phosphine was predicted to lower the barrier by ~10 kcal/mol.

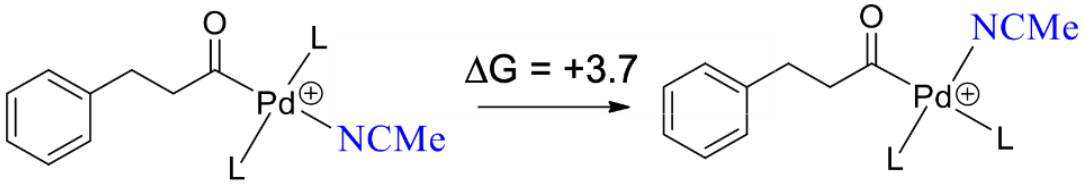

Scheme 2.5. The isomerization of the solvated cationic intermediate, $\mathbf{2}^+$, prior to CO deinsertion. ΔG in kcal/mol.

Turning next to the *β*-hydride elimination step, the transition state with P^tBu_3 has the lowest energy barrier (13.8 kcal/mol) compared to the values of 22.2 and 19.9 kcal/mol for the cases with PPh_3 and dppe, respectively (Figure 2.13, Schemes 2.6 and 2.7). This calculated trend aligns with that seen by experiment, insofar as reactions beginning with **1** produce styrene rapidly and

quantitatively, while **2** and **3** produce smaller yields of styrene. Although solvation stabilizes CO deinsertion when P^tBu_3 is used, *β*-hydride elimination is more favorable without explicit solvation, which allows for a planar, four-coordinate geometry to be maintained in the transition state wherein P^tBu_3 and CO occupy *cis* positions. In contrast, the analogous PPh_3 and dppe TS structures as shown in Figure 3 have square pyramidal geometries with the CO ligand loosely coordinated in the axial position (Pd-CO = 2.60 and 2.70 Å, respectively). However, CO coordination is sufficiently weak with PPh_3 and dppe that its decoordination in the TS alters the energy barriers by only -0.9 or +0.5 kcal/mol, respectively (Schemes S13 and S14), consistent with the preference for a four-coordinate Pd center.

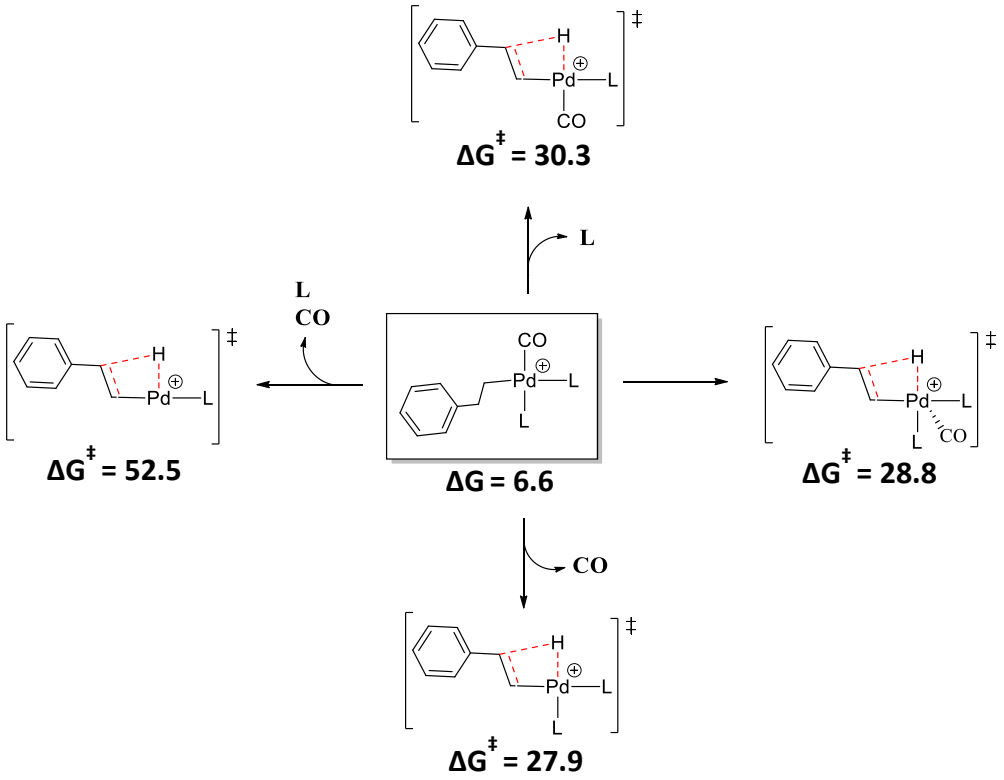

Scheme 2.6. Effect of different ligand environments on β-hydride elimination transition state energy barriers in PPh_3 Pd-acyl complexes. Data reported with reference to **2** in the chloride abstraction pathway with Ag^+ used as halide abstraction agent. Gibbs free energy in kcal/mol.

Overall, the calculations show that *β*-hydride elimination is the rate-determining transition state (RDTS), defined by the highest energy transition state, for all three cases. However, the

presence of the stable halide elimination product for **2** and **3** significantly increases the energy required to form styrene and is not captured by the RDTS alone. The barrier from this determining intermediate to the highest transition state is 16.8, 41.9 and 37.4 kcal/mol for **1**, **2** and **3**, respectively.

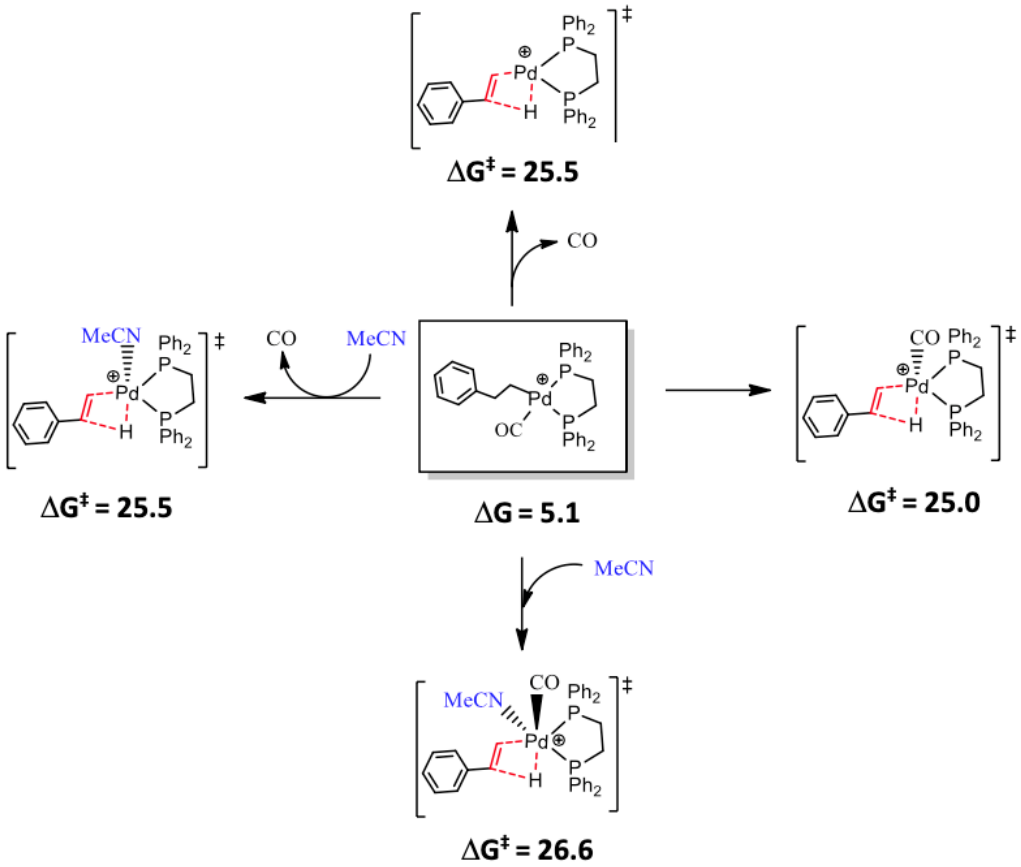

Scheme 2.7. Effect of different ligand environments and explicit solvent on the β-hydride elimination transition state energy barriers in dppe Pd-acyl complexes. Data reported with reference to **3** in the chloride abstraction pathway with Ag^+ used as halide abstraction agent. Gibbs free energy in kcal/mol.

2.3 Conclusion and Outlook

The dehydrative decarbonylation of (L_n)Pd(II)(Cl)-hydrocinnamoyl complexes (L = P^tBu_3, n = 1; L = PPh_3, n = 2; L = dppe, n = 1) was evaluated through experiment and theory with the primary aim of understanding how changes in the nature of the supporting phosphine ligand(s)

influences the efficiency of styrene formation and the energetics of the proposed reaction steps. Removal of the chloride ligand was found to enhance production of styrene, with the complex of P^tBu_3 being the most efficient. A solvento intermediate resulting from chloride abstraction was structurally characterized for the complex of PPh_3 and a related species was implicated on the basis of NMR spectroscopy for the complex of dppe. DFT calculations revealed β-hydride elimination from a stable intermediate formed upon halide abstraction to be rate-determining for the overall dehydrative decarbonylation. The barrier heights for this step and the CO deinsertion step followed the trend P^tBu_3 < dppe < PPh_3, consistent with the experimentally observed dependence of styrene production efficiency on supporting ligand (P^tBu_3 > dppe > PPh_3). A key overall conclusion is that coordinative desaturation through chloride removal and use of the highly sterically hindered P^tBu_3 greatly facilitates dehydrative decarbonylation. In addition, enforcement of a *cis* disposition of phosphine donors in dppe is beneficial relative to the complex comprising PPh_3 ligands.

Under catalytic conditions involving increased temperatures (>110 °C) it has been postulated that phosphine ligands may dissociate from the catalyst at certain points of the catalytic cycle. Although our study was performed at room temperature, and such behavior may not have been accessible, we anticipate studies like ours will aid in future catalyst design. Some of the principles such as coordinative desaturation have been supported by previous computational work that report the necessity for the loss of a ligand prior to decarbonylation or β-hydride elimination, similar to the chloride-abstraction reactions reported herein.[13] Furthermore, bidentate, *trans*-spanning ligands, such as Xantphos or DPEphos, have been postulated to dissociate one phosphine arm at various points in the proposed catalytic cycle, which we hypothesize to be related to the requirement for a vacant coordination site *cis* to the carbonyl motif in order for decarbonylation to occur. This is exemplified in the need for complex **2** to isomerize its PPh_3 ligands from *trans* to

cis prior to decarbonylation and the enhancement in reactivity of the *cis* complex **3**.[3] Given the propensity of bulky ligands to improve the efficiency of the dehydrative decarbonylation process, as seen with complex **1**, we predict that the use of other bulky ligand could improve these processes. One potential area of study would be the comparison of cone angle and buried volume for the conversion of fatty acid derivatives into olefins, which has shown to have major effects on other areas of catalysis. Alternatively, electronic effects have seldom been examined for the conversion of fatty acids to olefins and we foresee the potential to improve these processes upon further study and optimization. We hope that these notions determined through study of a particular Pd-based test system will inform and inspire future efforts to design new catalysts for the generation of olefins from bio-derived carboxylic acids.

2.4. Experimental

Reagents and materials

Unless otherwise reported all procedures were carried out within Vac Glovebox containing a nitrogen atmosphere. All glassware was either flame dried or stored in a 140 °C oven for several hours before use. Solvents were purchased through Fisher Scientific, degassed with argon and dried by an aluminum column prior to use. All reagents that were purchased from commercial sources were used as received, unless stated otherwise. Hydrocinnamoyl chloride (CAS: 645-45-4), 1,2-Bis(diphenylphosphino)ethane (dppe, CAS: 1663-45-2), allylpalladium(II) chloride dimer CAS: 12012-95-2), palladium (π-cinnamyl) chloride dimer (CAS: 12131-44-1), magnesium acetate (anhydrous, CAS: 142-72-3), silver trifluoromethanesulfonate (triflate, CAS: 2923-28-6), silver tetrafluoroborate (CAS: 14104-20-2), silver hexafluoroantimonate (CAS: 26042-64-8) and Schreiner's Thiourea (CAS: 1060-92-0) were purchased from Sigma Aldrich. $Pd(PPh_3)_4$ (CAS: 14421-01-3) was purchased from Strem and Sigma Aldrich. Zinc oxide (anhydrous, CAS: 55204-38-1), Zinc Acetate (anhydrous, CAS: 557-34-6), diisopropylthiourea (CAS: 2986-17-6) were purchased from Fisher Scientific and dried under dynamic vacuum overnight prior to use; aluminum *tert*-butoxide (CAS: 556-91-2) was also purchased from Fisher Scientific. Triazabicyclodecene (TBD, CAS: 5807-14-7), sodium hexafluoroantimonate (CAS: 16925-25-0), sodium tetrafluoroborate (CAS: 13755-29-8) were purchased from Oakwood Chemical and dried under vacuum overnight prior to use. Tri-*tert*-butylphosphine was purchased from Strem. All deuterated solvents were purchased from Cambridge Isotopes. Bis(tri-*tert*-butylphosphine)palladium(0) was synthesized according to a previous report. Sodium and potassium tetrakis[3,5-bis(trifluoromethyl)phenyl]borate salts were synthesized according to a literature report.[18] Nuclear magnetic resonance (NMR) spectroscopy was performed on a 500 MHz

Varian Unity Inova (^{1}H and ^{13}C) or a 300 MHz Varian Unity Plus (^{31}P) instrument. Chemical shifts for ^{1}H NMR spectra were referenced to residual protium in the deuterated solvent, ^{13}C NMR were referenced to the solvent itself and ^{31}P NMR were referenced to phosphoric acid (H_3PO_4). For X-ray crystal structures, preliminary examination and data collection were performed using a Bruker Venture Duo Photon-II single crystal X-Ray diffractometer equipped with an Oxford Cryostream LT device. Data sets were collected using an Incoatec IμS micro-focus source (Cu or Mo) with multi-layer mirror optics. Preliminary unit cell constants were determined from a set of 180 degree fast phi scan frames (typically, 1 secd exposure, 1° scan). Intensity data collections consisted of combinations of ϖ and ϕ scan frames with typical scan width of 0.5° and counting time of 1 to 10 seconds/frame at a crystal-to-detector distance of 3.7 cm. The collected frames were integrated using an orientation matrix determined from the narrow frame scans. Apex II and SAINT software packages (*Bruker Analytical X-Ray, Madison, WI, 2010*) were used for data collection and data integration. Analysis of the integrated data did not show any decay. Final cell constants were determined by global refinement of reflections harvested from the complete data set. Collected data were corrected for systematic errors using SADABS (*Bruker Analytical X-Ray, Madison, WI, 2010*) based on the Laue symmetry using equivalent reflections. Structure solution and refinement were carried out using the SHELXTL- PLUS software package (*Sheldrick, G.M. Acta Cryst.2008, A64,112-122*). The structures were solved by direct methods and refined successfully in the space group indicated in the CIF. Full matrix least-squares refinements were carried out by minimizing $\Sigma w(F_o^2-F_c^2)^2$. The non-hydrogen atoms were refined anisotropically to convergence. All hydrogen atoms were treated using appropriate riding model (AFIX m3). Complete listings of positional and isotropic displacement coefficients for hydrogen atoms and anisotropic displacement coefficients for the non-hydrogen atoms along with the table of calculated and

observed structure factors are available in electronic format (CIF). Funding from the National Science Foundation (MRI, CHE-1827756) for the purchase of the Venture-Duo diffractometer is acknowledged.

2.4.1 Synthesis of Palladium-Acyl Species

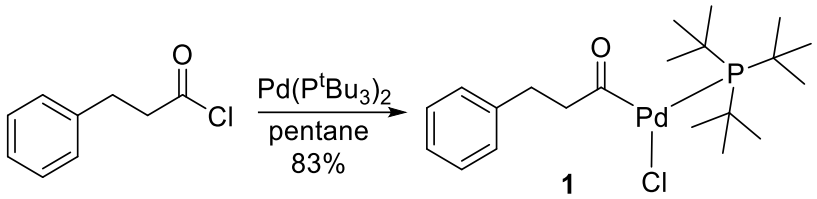

Scheme 2.8. Synthesis of Complex **1**.

Preparation of Complex 1. Complex 1 was synthesized by a previously reported procedure.[19] It was characterized by NMR, matching the reported values. General notes for the synthesis of complex 1: Pd(P^{t}Bu$_3$)$_2$ is soluble in pentane, however, upon addition of hydrocinnamoyl chloride a bright yellow solid crashes out. The solution transitions from bright yellow to colorless once the reaction is complete. Elemental analysis: Theory ($C_{21}H_{36}ClOPPd$): C: 52.84%, H: 7.60%. Experimental: C: 54.63% H: 7.81%. FTIR (neat): ν_{max}/cm^{-1} 1740 cm^{-1} (C=O).

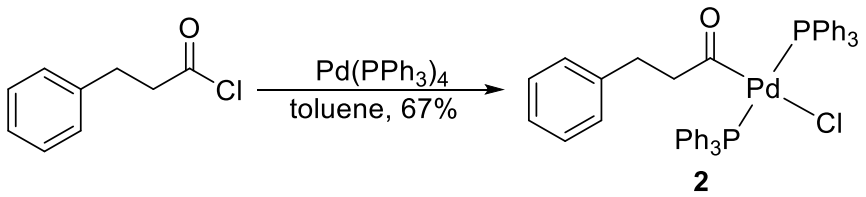

Scheme 2.9. Synthesis of complex **2**.

Preparation of Complex 2. To a 250 mL round bottom flask in a nitrogen filled glovebox Pd(PPh$_3$)$_4$ (5.0 g, 4.33 mmol, 1.0 equivalent) was added, followed by toluene (80 mL) resulting in a cloudy heterogeneous yellow solution. To this solution was added hydrocinnamoyl chloride

(1.30 mL, 8.65 mmol, 2.0 equivalents), resulting in a slightly dirty yellow solution that becomes clear/homogeneous within 5-10 minutes. Within an hour an off-white precipitate forms, and the solution appears yellow/tan. This solution was stirred overnight (~18 hours total) at 24 °C. The white solid was filtered onto a frit and washed with toluene and diethyl ether before being dried under dynamic vacuum (3.08 g, 89%). Even after several days under vacuum ^{1}H NMR shows the presence of toluene in the sample; washes with diethyl ether and pentane help remove residual toluene as does recrystallization. Crystals suitable for X-ray diffraction were isolated by diffusion of pentane into a solution of **2** in benzene. ^{1}H NMR (500MHz, CD_2Cl_2) δ 7.76 ppm (m, 12H), 7.49 ppm (t, 6H, 5Hz), 7.44 ppm (t, 12H, 5Hz), 7.02-7.08 (m, 3H), 6.38 ppm (d, 2H, 5Hz), 2.19-2.22 ppm (2H, dd (or br t)), 1.51-1.54 ppm (2H, dd (or br t)). ^{13}C NMR (126 MHz, CD_2Cl_2): 234.9 (s), 141.6 (s), 135.4 (t), 131.8 (t), 131.0 (t), 128.8 (t), 128.5 (s). 128.4 (s), 125.9 (s), 58.4 (t), 31.4 (s). ^{31}P NMR (121MHz, CD_2Cl_2): 19.6 ppm (s). Elemental analysis: Theory ($C_{45}H_{39}ClOP_2Pd$): C: 67.59%, H: 4.92%. Experimental: C: 66.94% H: 5.03%. FTIR (neat): ν_{max}/cm^{-1} 1673 cm^{-1} (C=O). Notes: More material could also be isolated from the filtrate through addition of pentane or diethyl ether. It was often advantageous, but not necessary for the addition of ethyl ether to the reaction mixture to help precipitate out product ~30 minutes prior to filtration. The quality of $Pd(PPh_3)_4$ varied greatly by supplier and impacts yields significantly.

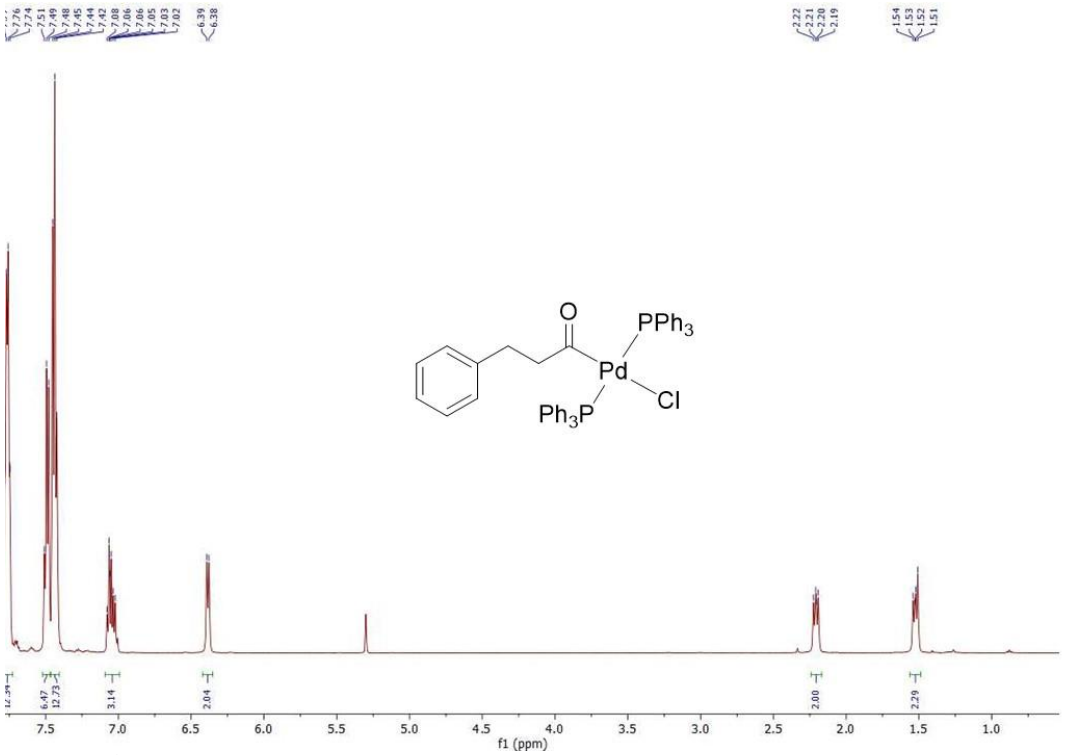

Figure 2.17. ^{1}H NMR Spectrum of **2** (CD_2Cl_2)

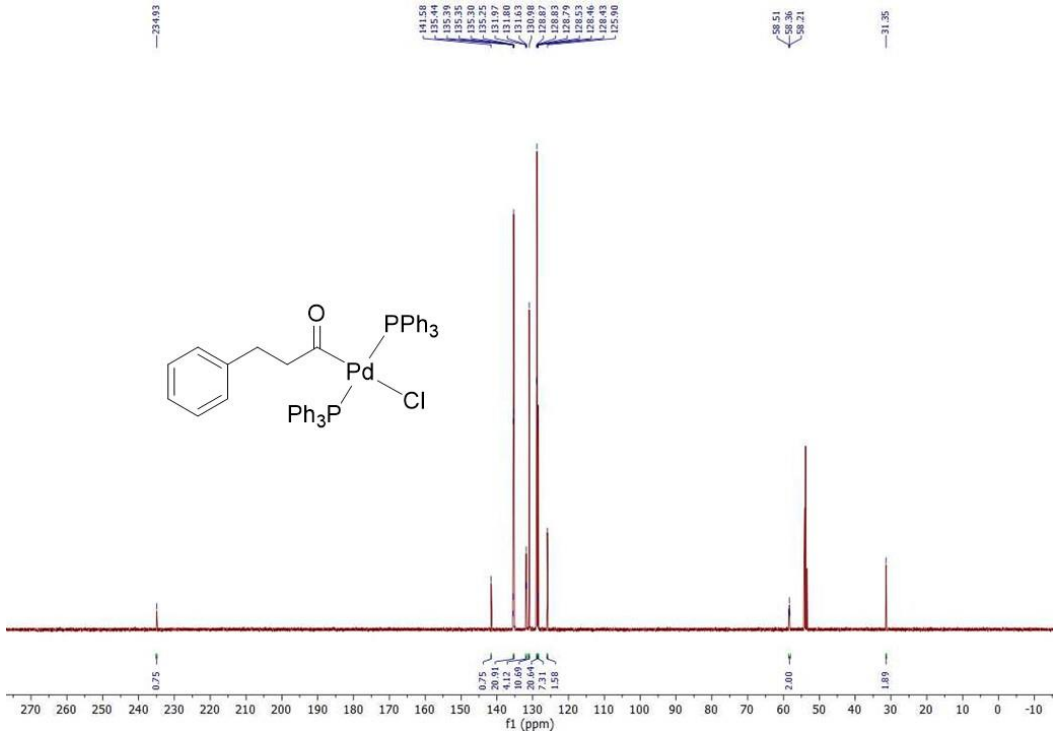

Figure 2.18. ^{13}C NMR of **2** (CD_2Cl_2)

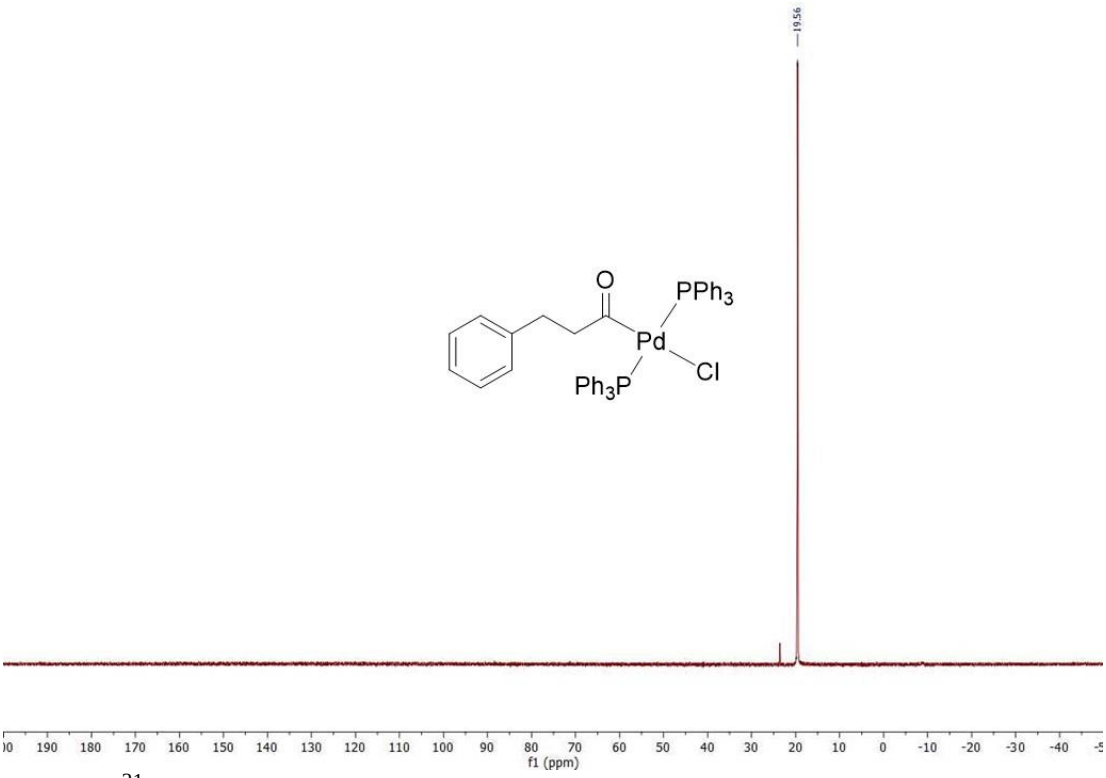

Figure 2.19. ^{31}P NMR Spectrum of **2** (CD_2Cl_2)

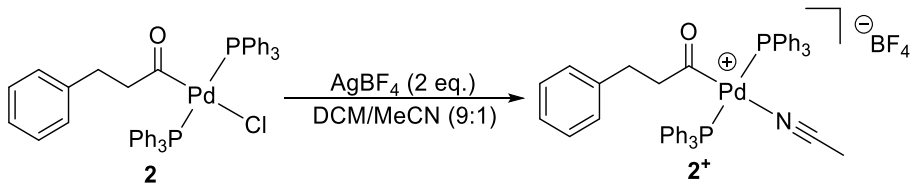

Scheme 2.10. Synthesis of complex $\mathbf{2}^+$.

Preparation of Complex $\mathbf{2^+(BF_4^-)}$. While in a nitrogen filled glovebox, complex **2** (450 mg, 0.56 mmol, 1 equivalent) was dissolved in a mixture of (10:1) CH_2Cl_2/ CH_3CN (3.3 mL) in a 20 mL scintillation vial. To this solution was added $AgBF_4$ (120 mg, 0.62 mmol, 1.1 equivalents) dissolved in a minimum amount of CH_3CN (0.3 mL, the same amount of CH_3CN as in the solution of complex **2**). Upon addition of the $AgBF_4$ solution a white precipitate immediately formed, assumed to be AgCl, however, the solution remains colorless. The mixture was stirred 15 min and

then filtered into an excess of diethyl ether (~15 mL) precooled to -35 °C, yielding a white precipitate. The white precipitate was allowed to continue to crash out of solution for several hours at -35 °C, after which time it was collected on a frit and recrystallized from CH_2Cl_2 (soluble) and diethyl ether (insoluble) in a 1:2 ratio (334 mg, 67%). Crystals suitable for X-ray diffraction were isolated by diffusion of diethyl ether into a solution of **$2^+(BF_4^-)$** in CH_2Cl_2. ^{1}H NMR (500MHz, CD_3CN) δ_H 7.62-7.67 (18H, m), 7.56-7.60 (12H, m), 7.09 (3H, m), 6.40 (2H, m), 2.25-2.28 (2H, dd or br t), 1.72 (2H, dd or br t), 1.96 (3H, s)*. ^{13}C NMR (126 MHz, CD_2Cl_2) δ_c 225.1, 140.1, 134.2, 131.8, 129.4, 128.3, 128.1, 126.0, 117.4, 65.3*, 55.8, 31.0, 14.7*. ^{31}P NMR (121MHz, CD_3CN) δ_P 23.4 ppm. FTIR (neat): ν_{max}/cm^{-1} 1682 cm^{-1} (C=O). NOTE: Other salts studied included AgOTf, $AgSbF_6$, $NaBAr^f$, $NaSbF_6$, $NaBF_4$ and $KBAr^f$ using an identical procedure. *Peak may correspond to a bound molecule of acetonitrile. Although complex **2^+BF_4** was pure by NMR, and the data closely align with that reported for analogous cationic acyl complexes reported previously,[1,5] the results of elemental analysis were poor, which we ascribe to incomplete combustion. High-resolution ESI-MS data (CH_2Cl_2) did not show a parent ion, but included a peak envelope centered at *m/z* 735.1604 (calc: 735.1572) that matches for the decarbonylated cationic species lacking CH_3CN with formula $PdP_2C_{36}H_{30}C_8H_9$. Additional higher mass peaks also were observed, indicating oligomerization under the conditions of the ESI-MS experiment.

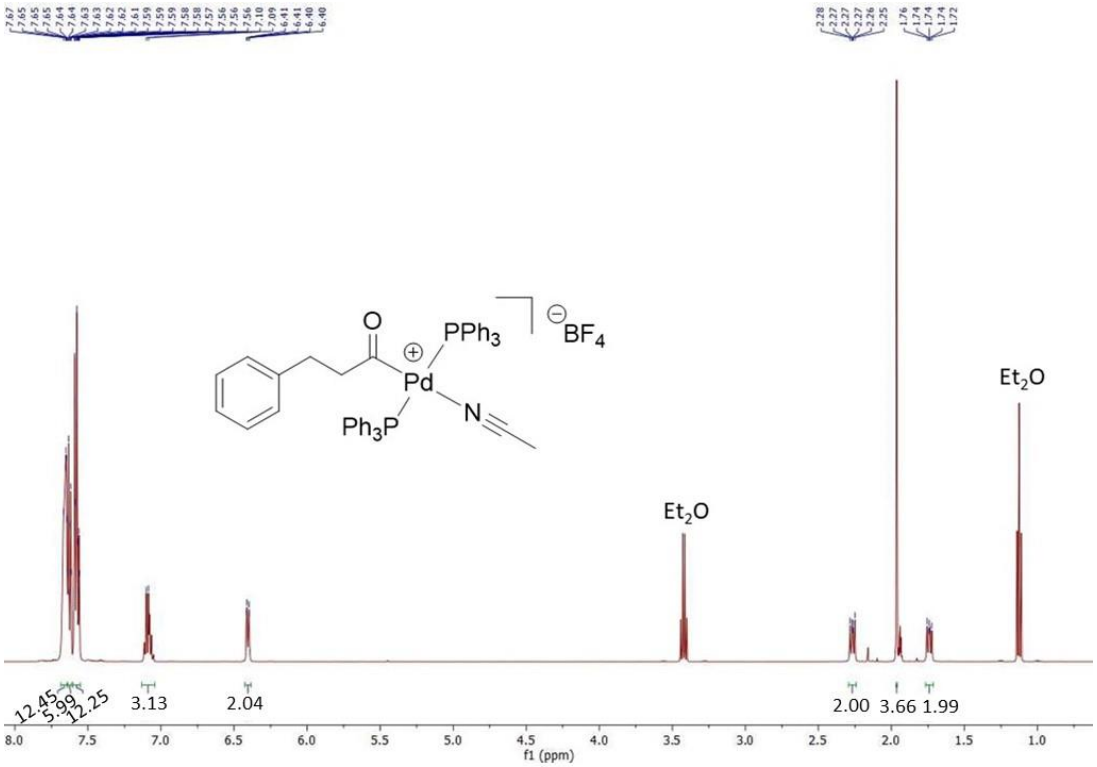

Figure 2.20. ^{1}H NMR Spectrum of $\mathbf{2^{+}(BF_4)}$ (CD_3CN)

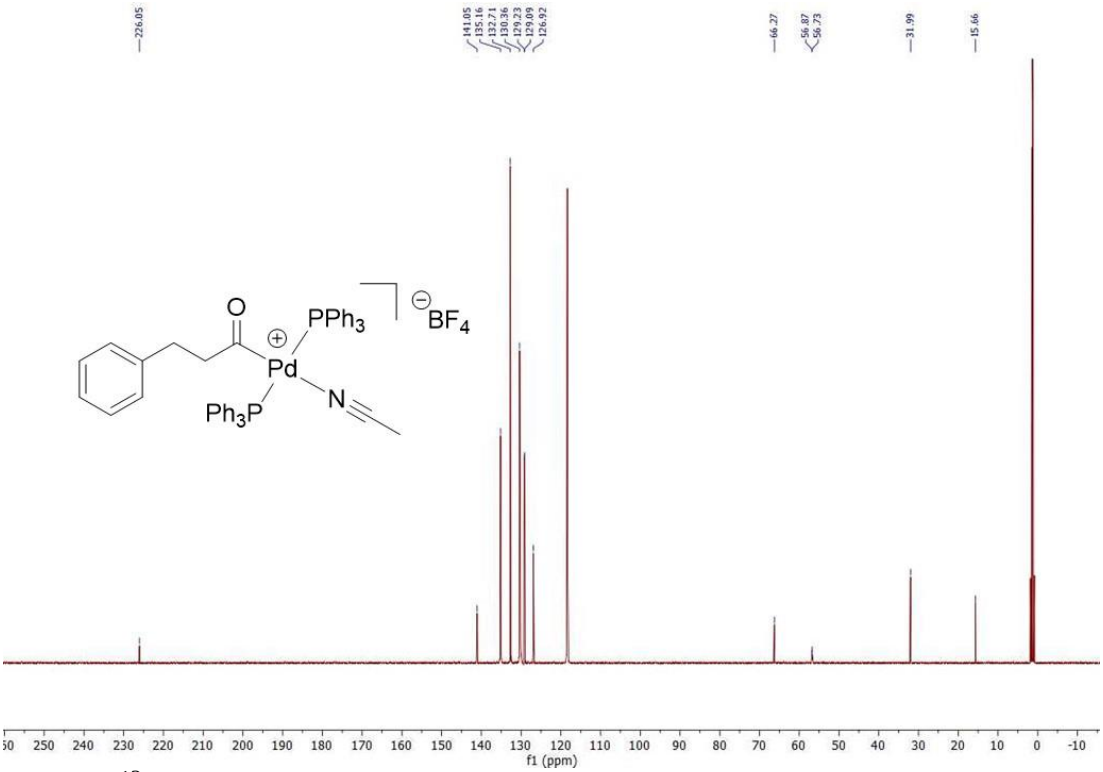

Figure 2.21. ^{13}C NMR Spectrum of **2^{+}(BF$_4$)** (CD_3CN)

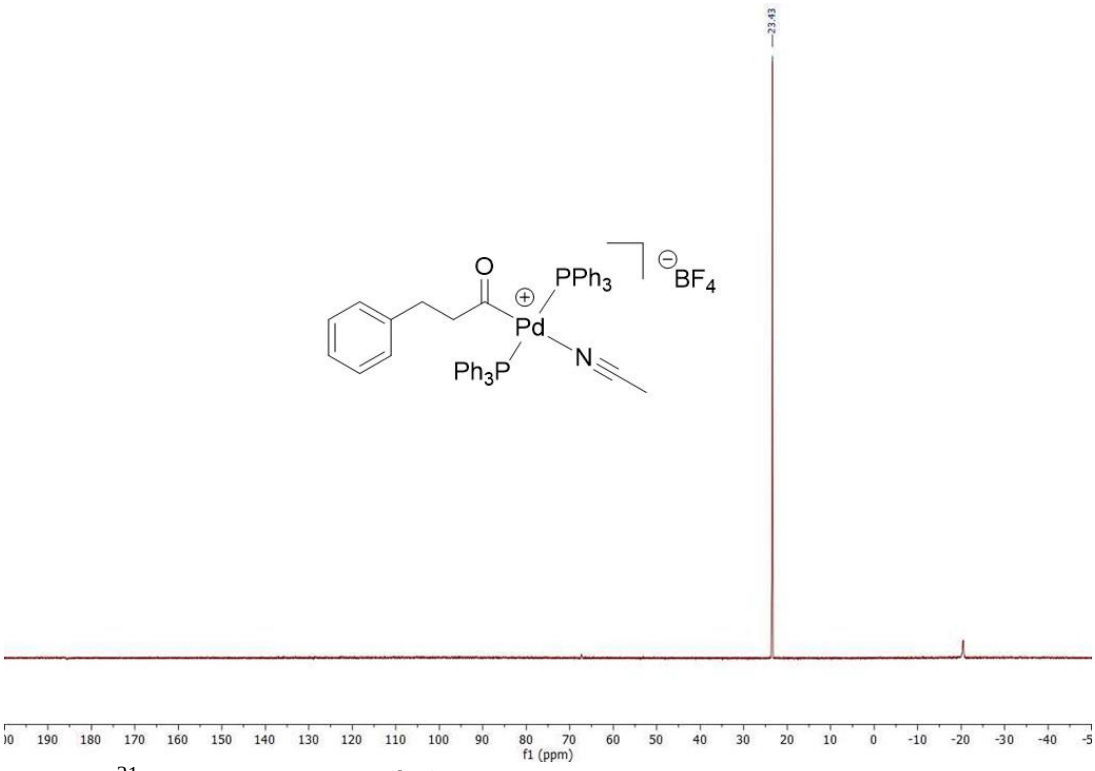

Figure 2.22. ^{31}P NMR Spectrum of **2^{+}(BF$_4$)** (CD_3CN)

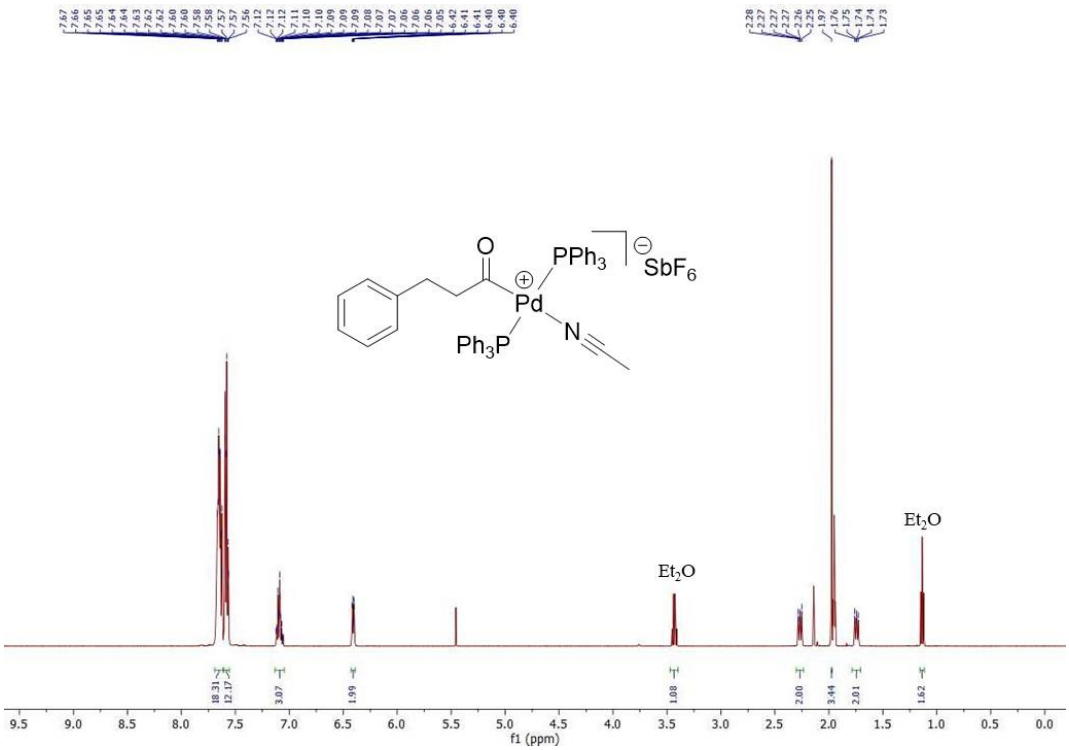

Figure 2.23. ^{1}H NMR Spectrum of **2^{+}(SbF$_6$)** (CD_3CN). 0.5:1 diethyl ether:complex solvate.

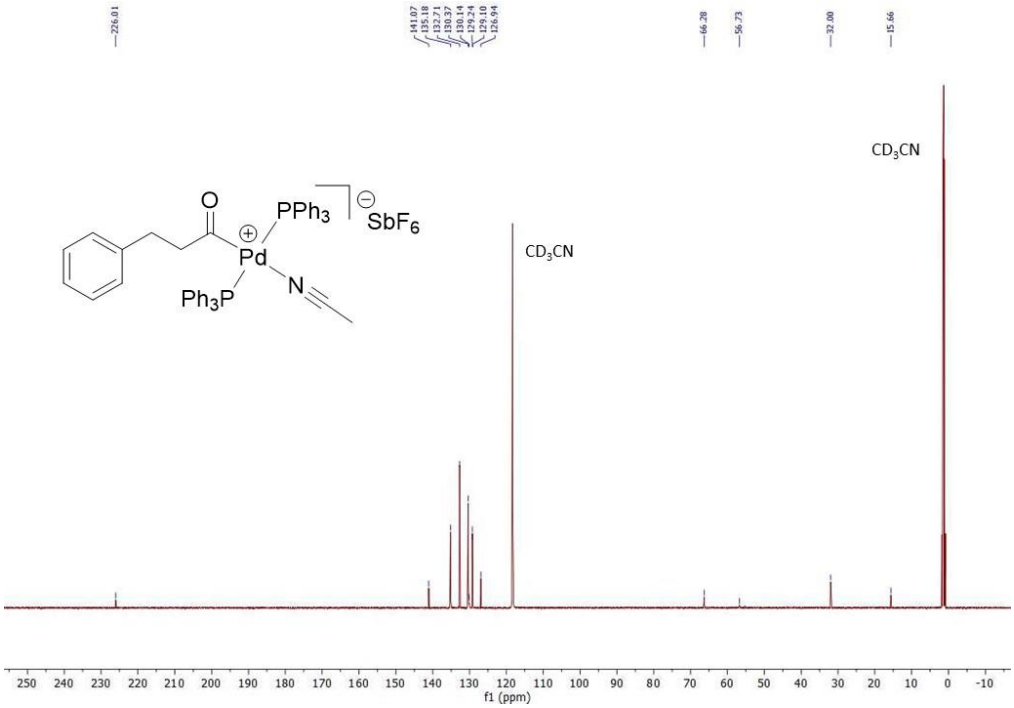

Figure 2.24. ^{13}C NMR Spectrum of **2^{+}(SbF$_6$)** (CD_3CN)

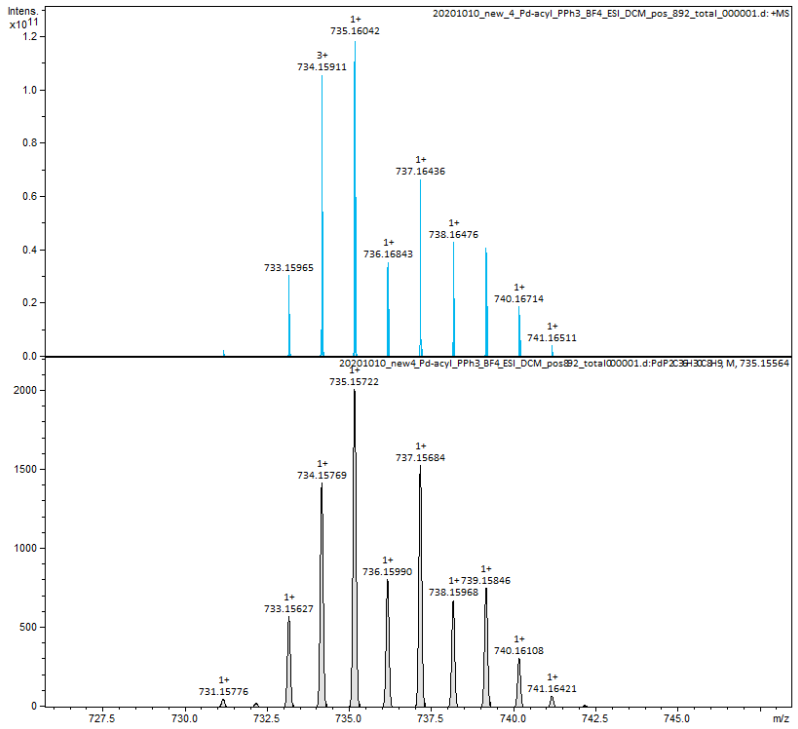

Figure 2.25. Portion of HR ESI-MS showing experiment (top) and simulation (bottom) for **2^{+}(BF$_4$)** monomer.

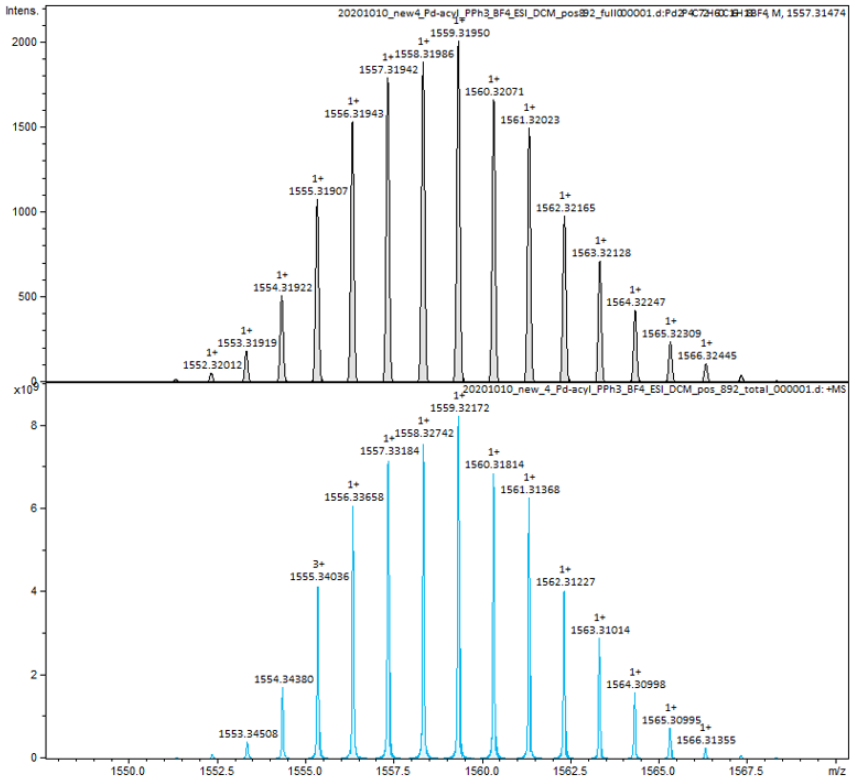

Figure 2.26. Portion of HR ESI-MS showing experiment (top) and simulation (bottom) for **2^{+}(BF$_4$)** dimer.

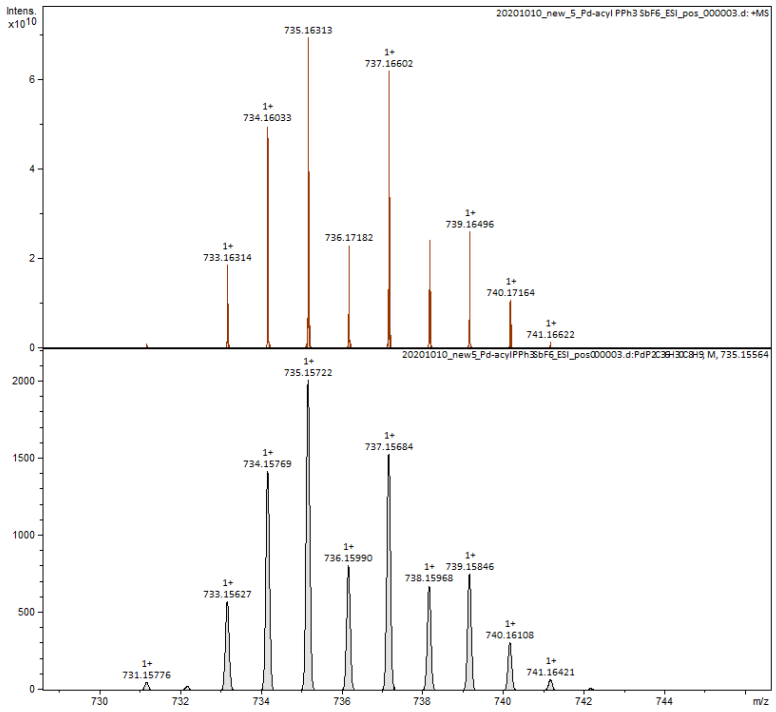

Figure 2.27. Portion of HR ESI-MS showing experiment (top) and simulation (bottom) for **2^{+}(SbF$_6$)** monomer.

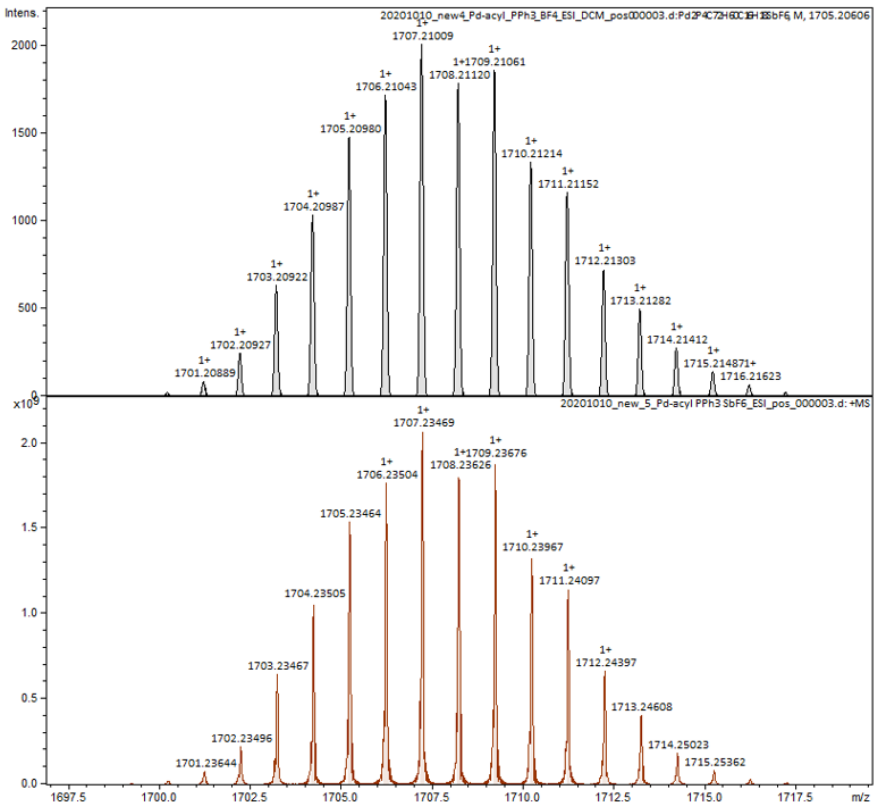

Figure 2.28. Portion of HR ESI-MS showing experiment (top) and simulation (bottom) for **2^{+}(SbF$_6$)** dimer.

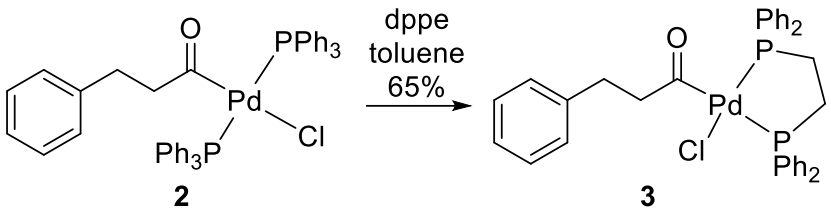

2 **3**

Scheme 2.11. Synthesis of complex **3** through ligand exchange of PPh_3 of **2** with dppe

Complex 3 (dppe). The synthesis of compound **3** was adapted from a previous report.[20] In a 250 mL round bottom flask containing a Teflon stir bar within a nitrogen filled glovebox was added complex **2** (922 mg, 1.15 mmol, 1 equivalent) with toluene (40 mL) resulting in a colorless, heterogeneous mixture. To this mixture was added dppe (919 mg, 2.31 mmol, 2 equivalents), resulting in a shortly lived homogenized solution after ~1 minute of stirring. The solution again becomes heterogeneous within five minutes of the dppe addition, with a white solid forming. The solution was stirred for 30 min at 24 °C, after which time diethyl ether (40 mL) was added to fully precipitate the product and the mixture was stirred an additional 30 min. The mixture was filtered onto a frit and washed with excess diethyl ether and toluene yielding a white solid (679 mg, 86%). Crystals suitable for X-ray diffraction were isolated by diffusion of diethyl ether into a solution of **3** in CH_2Cl_2. ^{1}H NMR (500MHz, CD_2Cl_2) δ_H 7.83 (4H, m), 7.65 (4H, dd, Hz), 7.52 (2H, br t), 7.40-7.47 (10H, m), 7.12 (2H, br t or td), 7.06, (1H, br t or td), 6.82 (2H, br d, 10 Hz), 2.76 (2H, t, 5Hz), 2.51 (1H, m[b]), 2. 44[a] (3H, t), 2.13 (1H, m[b], Hz), 2.08 (1H, m[b]). ^{13}C NMR (CD_2Cl_2, 500MHz) δ_C: 142.3 (s), 133.5 (t), 131.9 (d), 131.4 (dd), 130.3 (d), 129.5 (dd), 128.7 (s), 128.4 (s), 125.8 (s), 54.2 (s), 31.3 (s), 29.1 (dd), 22.6 (dd). ^{31}P NMR (121MHz, CD_2Cl_2) δ_P 37.7 (d, J = 43.6 Hz), 21.0 (d, J = 43.6 Hz). Elemental analysis: Theory ($C_{35}H_{33}ClOP_2Pd$): C: 62.42%, H: 4.94%. Experimental: C: 63.19% H: 4.92%. FTIR (neat): ν_{max}/cm^{-1} 1672 cm^{-1} (C=O). [a]This peak overlaps with a signal corresponding to a methylene proton of the ethyl background of the dppe ligand.

[b] Resembles a broadened quartet

Alternative single step synthesis of 3. To a 20 mL scintillation vial containing a Teflon stir bar within a nitrogen filled glovebox was added $Pd(PPh_3)_4$ (1.41 g, 1.22 mmol, 1 equiv.), dppe (955 mg, 2.44 mmol, 2 equivalents) and toluene (15 mL). Hydrocinnamoyl chloride (0.35 mL, 2.65 mmol, 2 equiv.) was then added. The mixture was then stirred at 24 °C within the glovebox for 24 hr, filtered onto a frit and washed with diethyl ether to produce **3** as a white solid (403 mg, 49%).

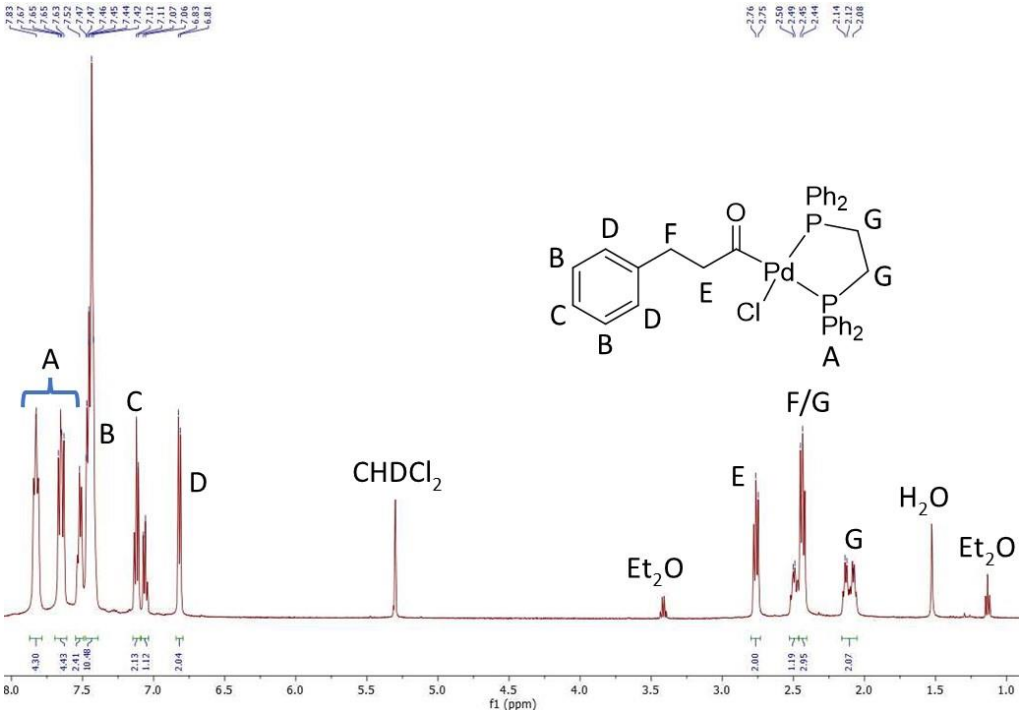

Figure 2.29. ^1H NMR Spectrum of **3** (CD_2Cl_2). H_2O found within the spectrum was found to originate within the NMR solvent.

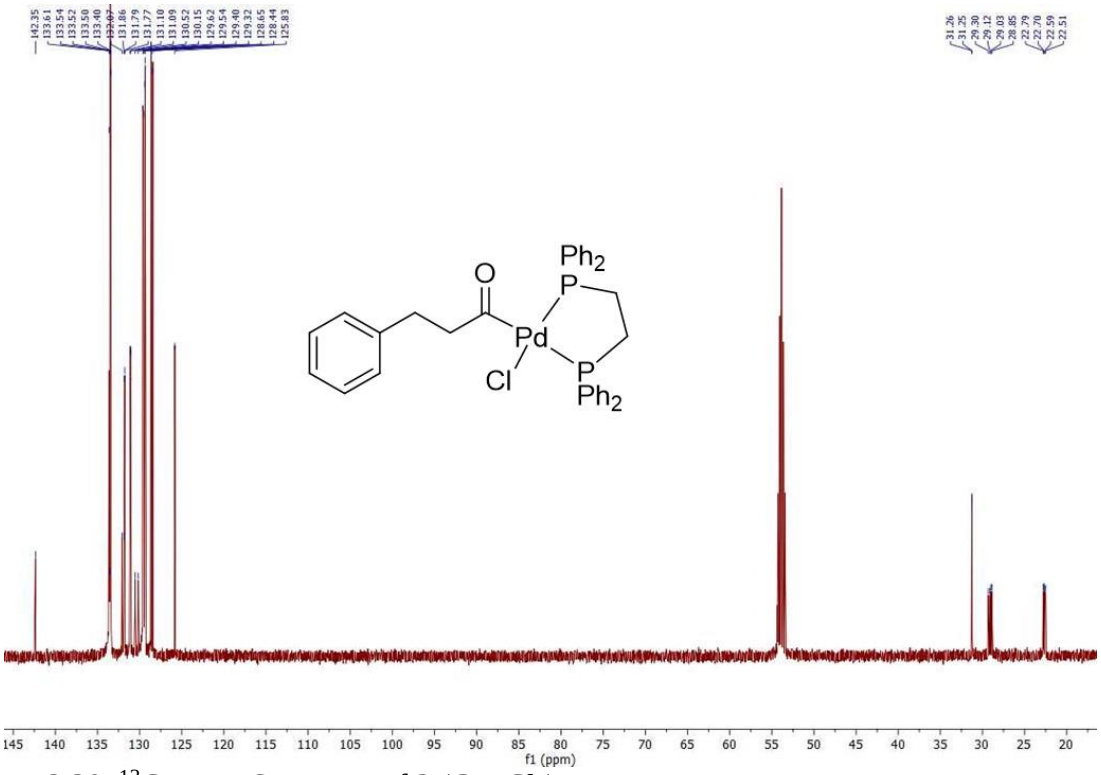

Figure 2.30. ^{13}C NMR Spectrum of **3** (CD_2Cl_2)

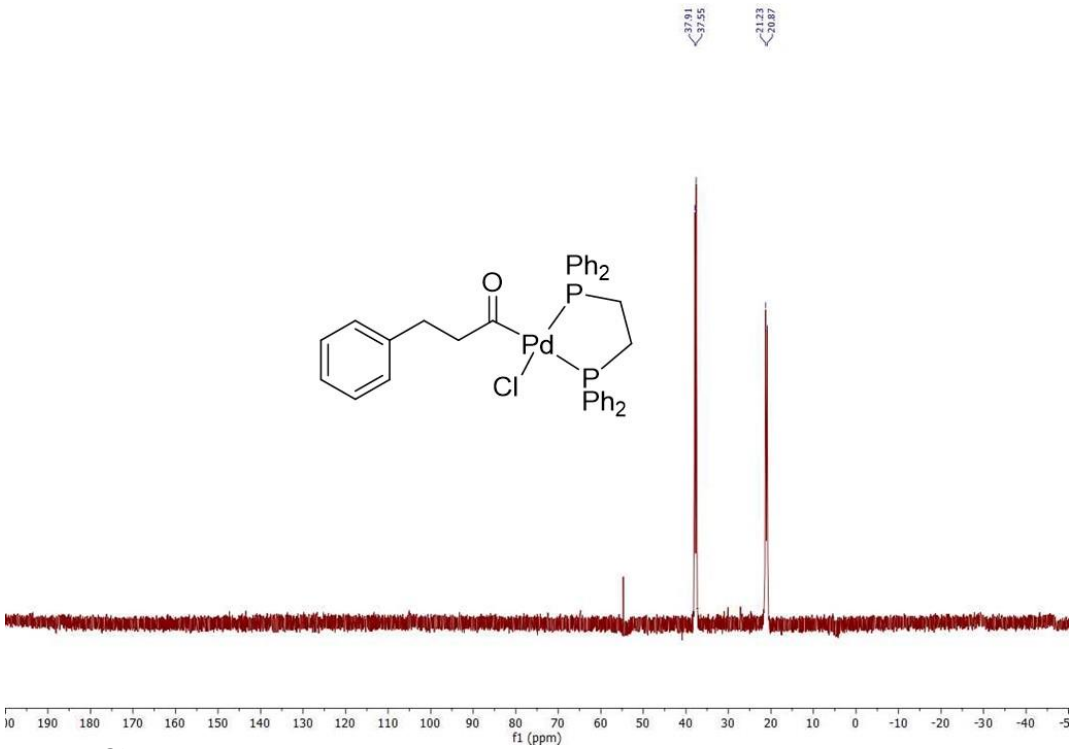

Figure 2.31. ^{31}P NMR Spectrum of **3** (CD_2Cl_2)

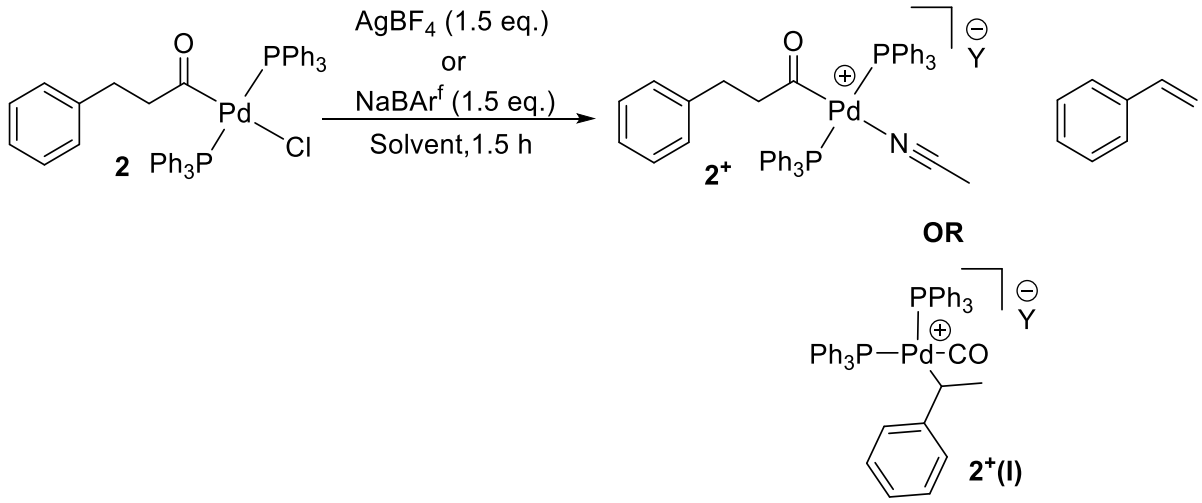

Scheme 2.12. Halide abstraction of **2** forms either the isolated complex $\mathbf{2}^{+}$ with a small amount of styrene when CH_3CN is present or $\mathbf{2}^{+}$**(I)** when performed in noncoordinating solvents. Y = BF_4 or $NaBAr^f$

Synthesis of Complex $\mathbf{2}^{+}$(I)

To a 20 mL scintillation vial containing a Teflon stir bar within a nitrogen glovebox was added **2** (20 mg, 0.025 mmol) and 1 mL of a deuterated noncoordinating solvent (either CD_2Cl_2 or a 9:1 combination of CD_2Cl_2/CD_3NO_2). To this solution was added $AgBF_4$ or $NaBAr^f$ (0.037 mmol, 1.5 equivalents) and the resulting mixture stirred 1.5 hours at 24 °C. The solution was then filtered by syringe and analyzed by ^1H and ^{31}P NMR spectroscopy. Unfortunately, attempts to obtain crystals of complex $\mathbf{2}^{+}$**(I)** led to decomposition as noted by the formation of a black precipitate. $\mathbf{2}^{+}\mathbf{(BAr^f)}$**.** ^1H NMR (500 MHz, CD_2Cl_2) δ_H 7.15-7.44 (25H, m), 7.03 (1H, m), 6.97 (1H, br d), 6.76 (6H, m), 6.64 (2H, br d), 3.82 (1H, m), 0.98 ppm (3H, m). ^{31}P NMR (121 MHz, CD_2Cl_2) δ_P 32.61 (d, 45 Hz), 22.48 ppm (d, 45 Hz)

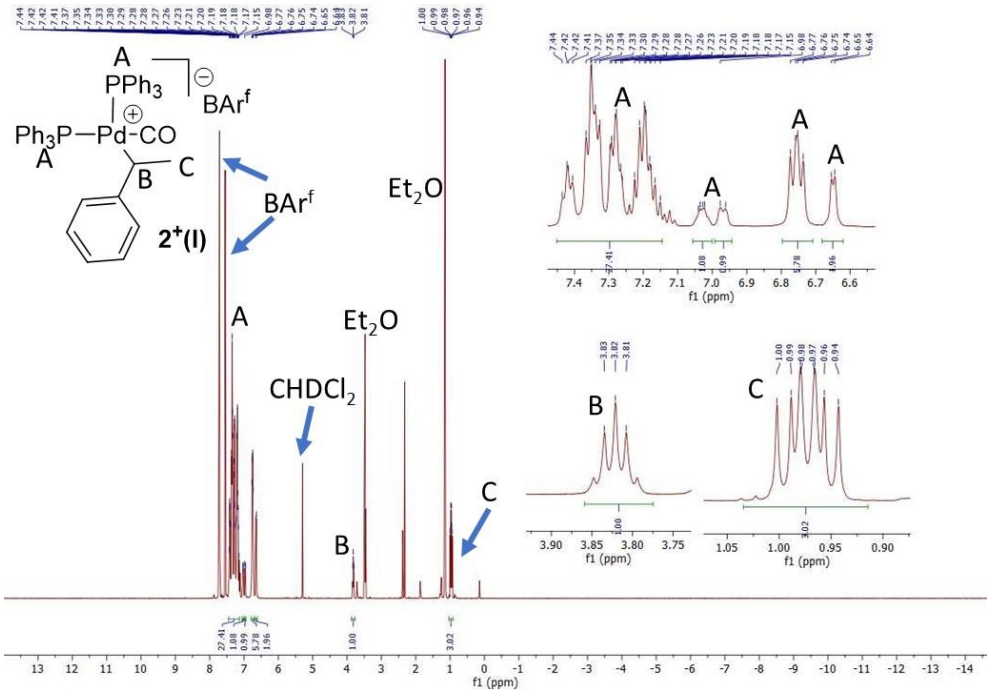

Figure 2.32. ^{1}H NMR **2^{+}(I)BAr^{f}** [a] (CD_2Cl_2). Note: some residual toluene/benzene from the starting material in aromatic region as noted by the singlet at 2.36 ppm and slight exaggeration of integrations in the aromatic region.

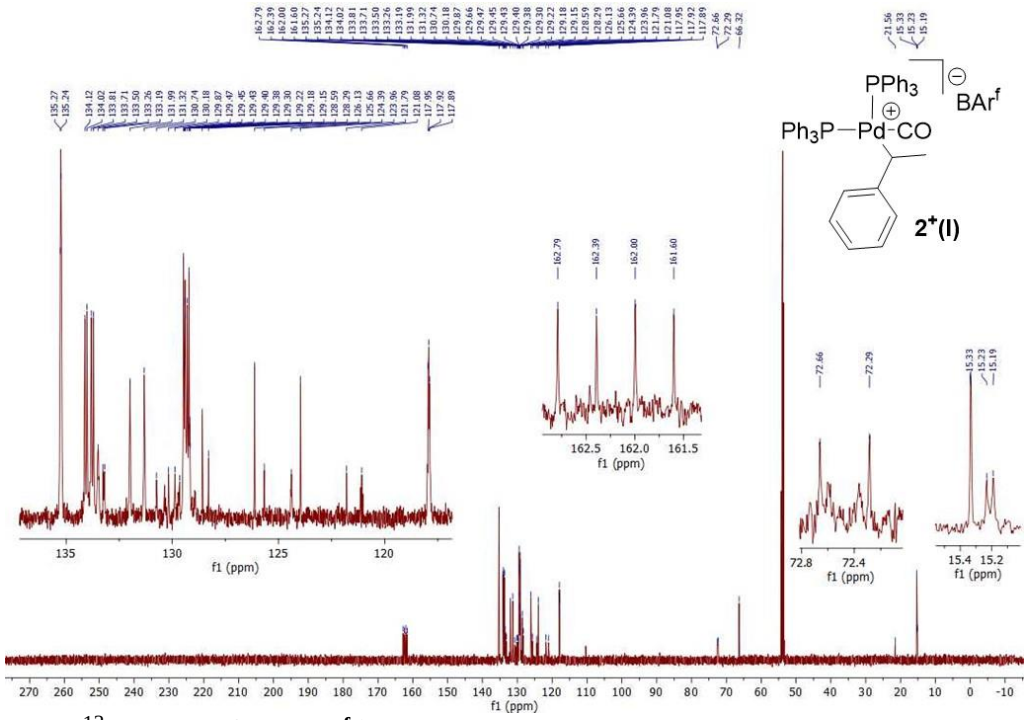

Figure 2.33. ^{13}C NMR **2^{+}(I) BAr^{f}**[a] (CD_2Cl_2).Note: Due to degradation over collection times and likely ^{31}P coupling we did not assign specific carbon peaks for 2^{+}(I)

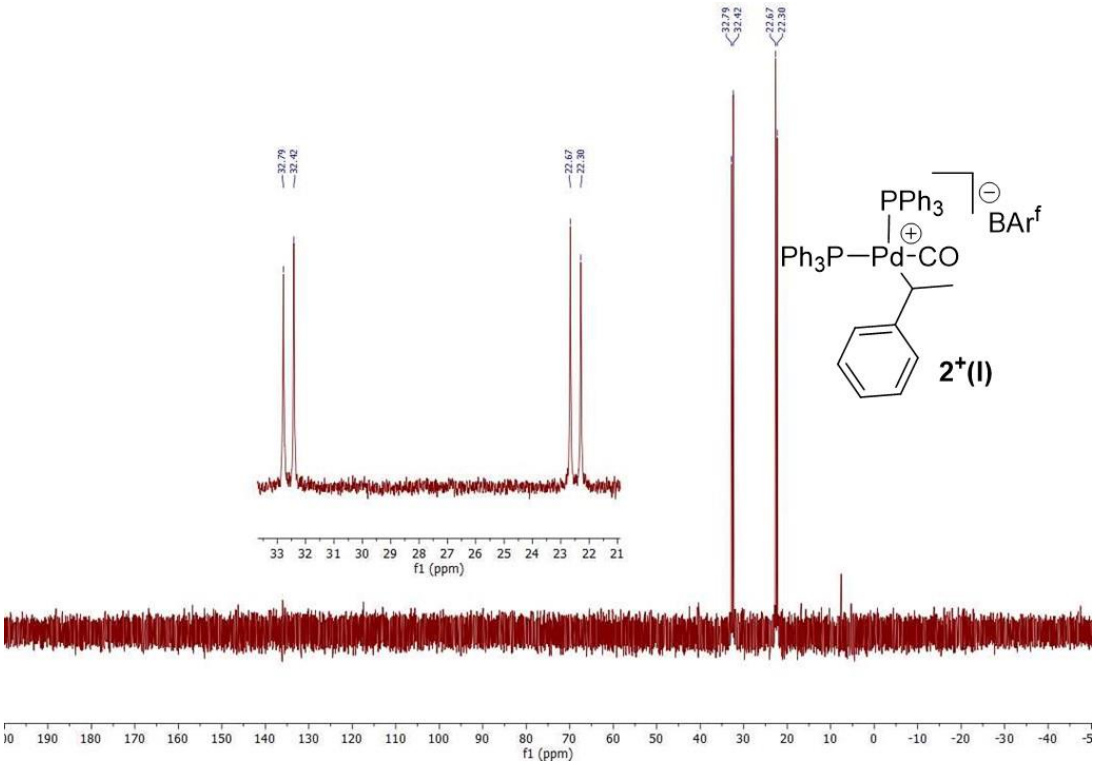

Figure 2.34. ^{31}P NMR of **2^{+}(I) BAr^{f}** (CD_2Cl_2)

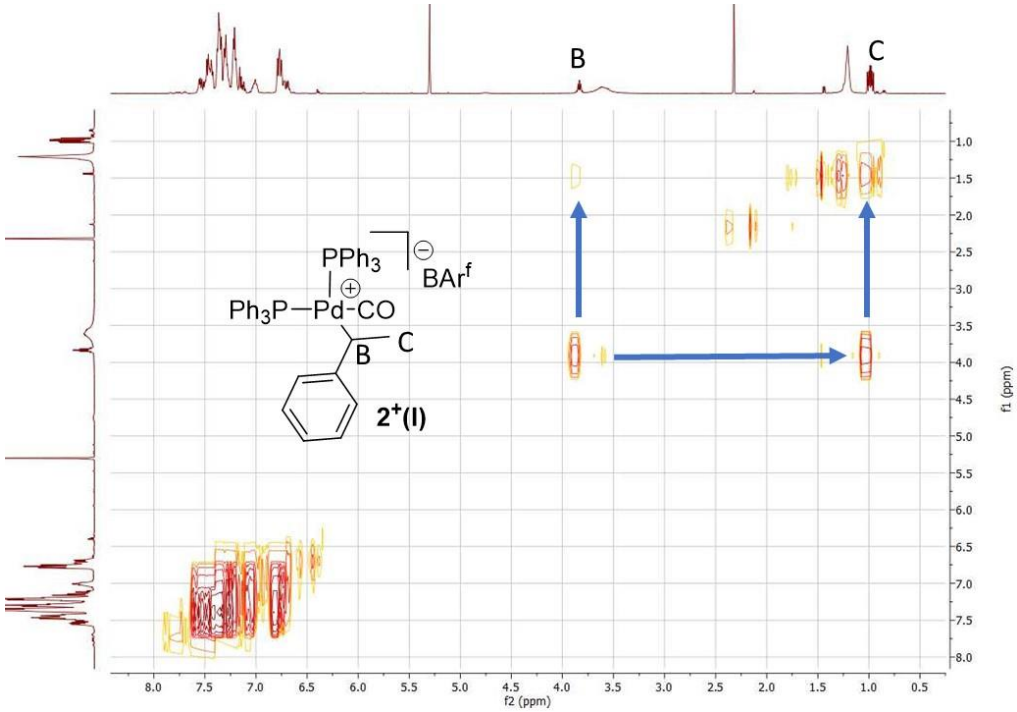

Figure 2.35. COSY NMR **2^{+}(I) BAr^{f}**$^{-a}$ (CD_2Cl_2). Note: COSY NMR shows peak A (methyl) and B (methine) are coupled supporting that they are on adjacent carbon atoms.

2.4.2 Reactivity Studies of Palladium-Acyl Complexes

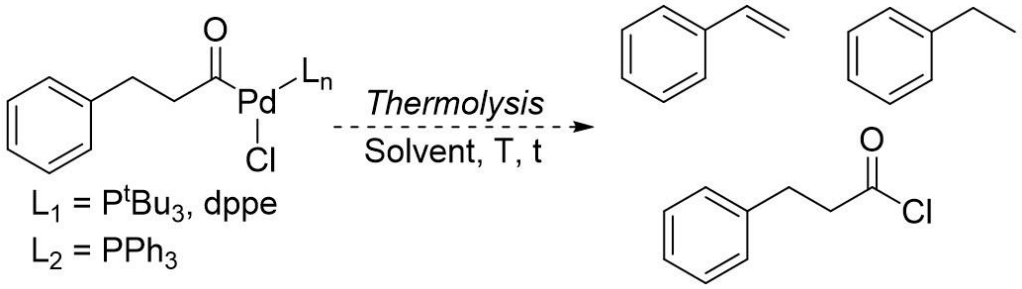

Scheme 2.13. Thermolysis of Pd-acyl complexes.

Thermolysis reactions. While in the glovebox the Pd-acyl complex (0.025 mmol) is dissolved in 1 mL of the solvent of choice in either an 8 mL or 20 mL vial or a 35 mL bomb tube. The sealed container (vial caps were taped with electric tape, bomb tubes contain an O-ring) was taken out of the glovebox and heated in an oil bath or aluminum block for the desired time. Upon cooling, the mixture was brought back into the glovebox and either filtered and analyzed by ^{1}H NMR (if performed in a deuterated solvent) or filtered and concentrated by vacuum. For reactions performed in nondeuterated solvents the concentrated material was then dissolved in a deuterated solvent of choice, typically C_6D_6, filtered to remove any particulates and analyzed by ^{1}H NMR. Note: upon concentration, styrene (bp: 145˚C) is mostly removed from the sample and so the reported yields below are from reactions performed in deuterated solvents.

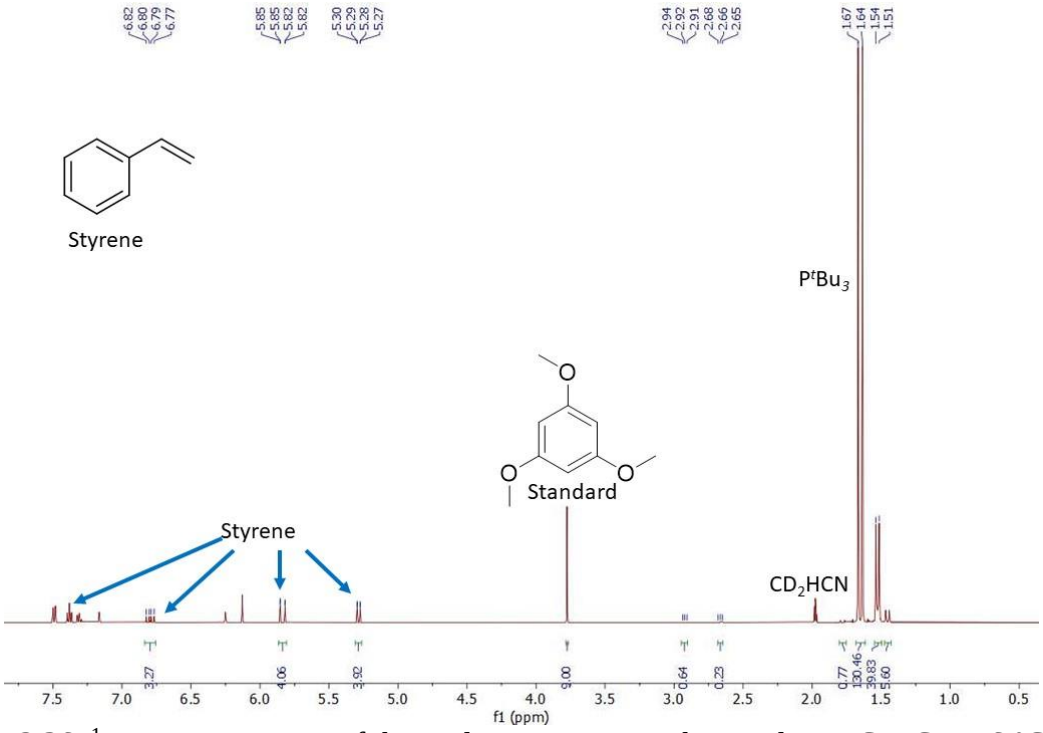

Figure 2.36. ^{1}H NMR spectrum of thermolysis reaction with complex 1, CD_3CN, 46 °C

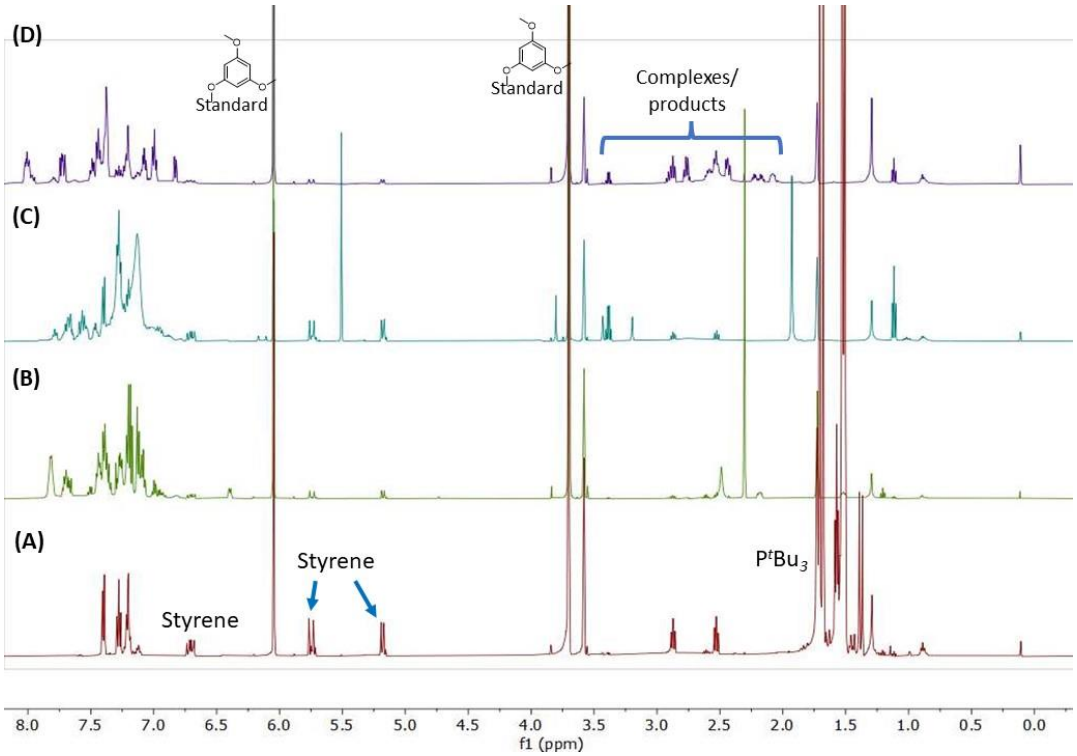

Figure 2.37. Thermolysis of Complexes **1** (A), **2** (B), **2**$^+$ (C) and **3** (D) in THF-D8 at 54 °C. Note that spectra are enlarged to exemplify the baseline products.

Reactions of Complexes 1-3 with Lewis Acids and Additives

Halide abstraction of 1 with Silver Salts. To a 20 mL scintillation vial containing a Teflon stir bar was added complex **1** (12mg, 0.025mmol, 1 equiv.) followed by CD_3CN containing standard (1,3,5-trimethoxybenzene). To this solution was added a silver or sodium salt (AgX, X = BF_4, SbF_6; NaY, Y = BAR^f, SbF_6, BF_4, PF_6) in one portion, leading to the immediate formation of a black precipitate, presumably palladium black. Reaction mixtures were stirred for 22 hours and subsequently filtered by syringe prior to analysis by ^1H NMR.

Reactions of Complexes 1-3 with Lewis Acids and Additives. To a 20 mL scintillation vial within a nitrogen glovebox was added oxidative addition product (0.025 mmol) followed by solvent: 9:1 CD_2Cl_2/ CD_3CN (1 mL) for complexes **2** and **3** or 1ml of CD_3CN for complex **1** and a Teflon stir bar (1,3,5-trimethoxybenzene was used as a standard). To this homogeneous mixture was added the additive chemical (1.5 equiv., 0.0375 mmol). The resulting mixture was stirred for 22 h at 24 °C within the glovebox, filtered by syringe, and analyzed by ^1H NMR. See spreadsheet within the NMR data files for initial concentrations of standard within each reaction mixture. This concentration is expected to increase by the end of the reaction due to the slight evaporation of solvent. Products and analysis of reactions provided in Appendices B and C.

Reaction of Complex 1 with $NaBAr^f$ Array. To a 20 mL scintillation vial in a nitrogen filled glovebox complex **1** (12 mg, 0.025mmol) and 1,3,5-trimethoxybenzene (9mg, 0.054 mmol, 0.027M total,) was dissolved in CD_3CN (2 mL). To this solution was added $NaBAr^f$ (33 mg, 0.037 mmol, 1.5 equiv.) in one portion. The vial was immediately capped and shaken (~5 s), 0.5 mL of the solution transferred to a medium walled 140 mm J-Young NMR tube and the reaction

monitored by ^{1}H NMR. Over the course of the reaction the solution goes from pale yellow to a darker yellow with the formation of a black precipitate on the walls of the vial/ NMR tube.

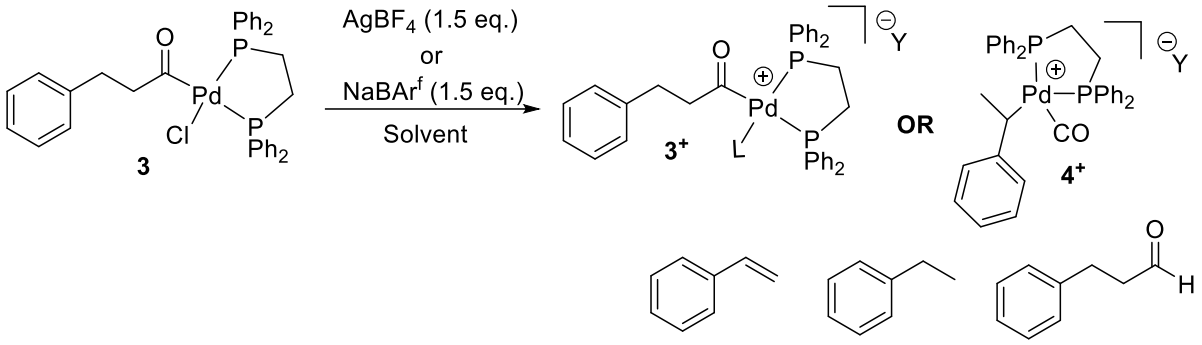

Scheme 2.14. Halide abstraction of **3**. Products formed include either the isolated complex **3$^+$(Y)** with a small amount of styrene when CH_3CN/CD_3CN was present or **4$^+$(Y)** when performed in noncoordinating solvents such as CH_2Cl_2/CD_2Cl_2 or CH_3NO_2/CD_3NO_2. Other notable products are ethyl benzene and 3-phenylpropionaldehyde. COSY NMR shows clear coupling between the proposed methine and methyl protons of **4$^+$(Y)** (Figure 9D)**.** Y = BF_4 or BAr^f. Notably, complex 3

Halide abstraction of Complex 3. While in a nitrogen filled glovebox, complex 3 (400 mg, 0.59 mmol, 1 equivalent) was dissolved in a mixture of (10:1) CH_2Cl_2/ CH_3CN (3.3 mL) in a 20 mL scintillation vial. To this solution was added $AgBF_4$ (173 mg, 0.89 mmol, 1.5 equivalents) or $NaBAr^f$ (788 mg, 0.89 mmol, 1.5 equivalents) dissolved in a minimum amount of CH_3CN (0.3 mL, the same amount of CH_3CN as in the solution of complex **2**). Upon addition of the $AgBF_4/NaBAr^f$ solution a white precipitate formed, assumed to be AgCl/NaCl, however, the solution remains colorless. The mixture was stirred 15 min and then filtered into an excess of diethyl ether (~15 mL) precooled to -35 °C, yielding a white precipitate. **3$^+$ (BF_4)**. ^{1}H NMR (500MHz, CD_2Cl_2) δ_H 7.61-7.71 (10H, m), 7.51-7.58 (10H, m), 7.20 (2H, t), 7.14 (1H, t), 6.90 (2H, d), 2.70 (1H, m), 2.62-2.67 (3H, m), 2.43 (2H, t, J = 10Hz), 2.19-2.28 (2H, m). **4$^+$ (BF_4).** ^{1}H NMR (500MHz, CD_2Cl_2) δ_H 7.59-7.69 (7H, m), 7.44-7.52 (7H, m), 7.40 (2H, td), 7.17-7.25 (5H,

m), 7.10 (1H, br d), 6.92 (2H, m), 6.17 (1H, br t), 3.86 (1H, m), 2.63-2.74 (1H, m), 2.14-2.41 (3H, m), 1.30 (3H, m). ^{31}P NMR (121MHz, CD_2Cl_2) δ_P 41.39 (d, J = 45Hz), 43.77 (d, J = 45Hz).

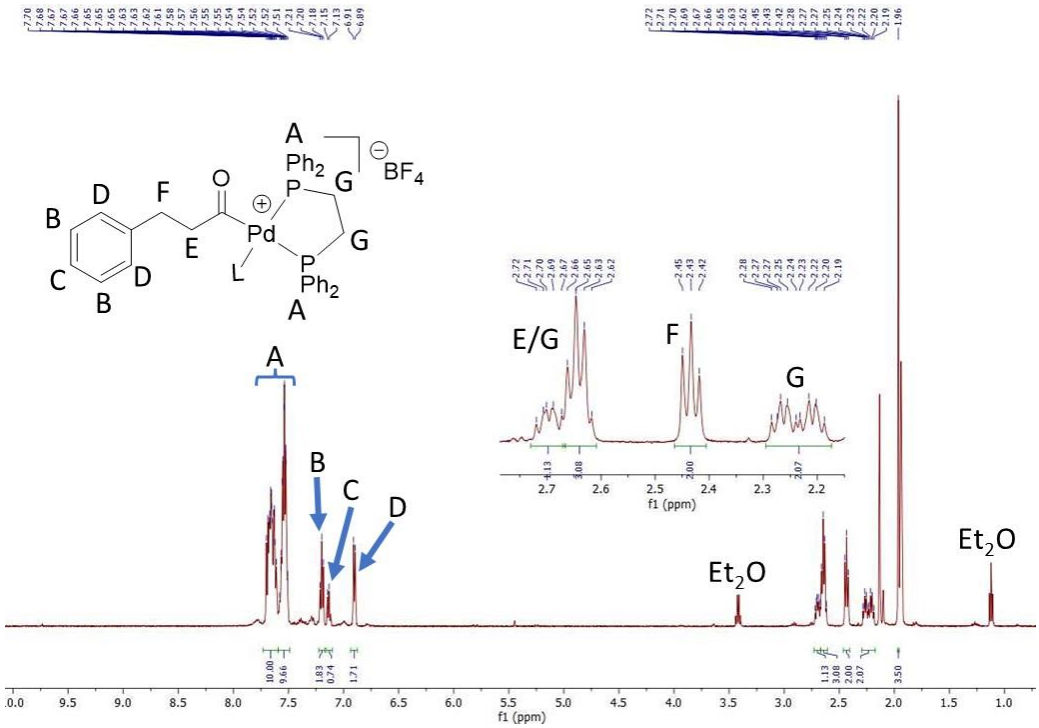

Figure 2.38. ^{1}H NMR of **3^{+}BF$_4$** [a] (CD_3CN). L may be a molecule of CD_3CN, indicated by a singlet observed at 2.13 ppm.

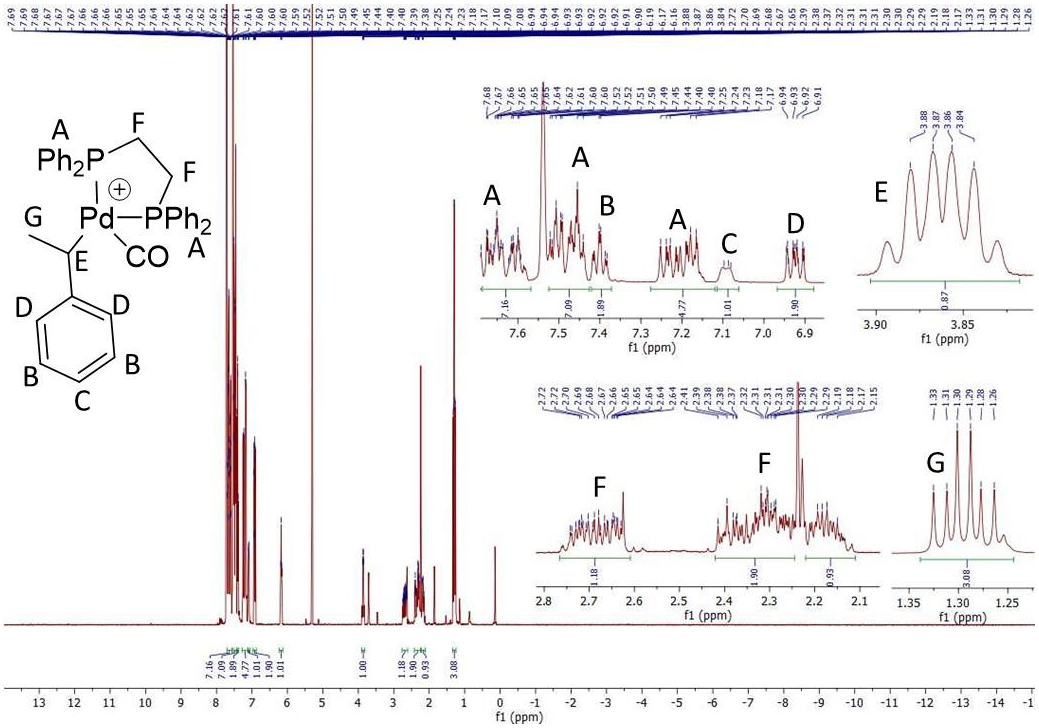

Figure 2.39. ^{1}H NMR of **4^{+} BF$_4$** (CD_2Cl_2)

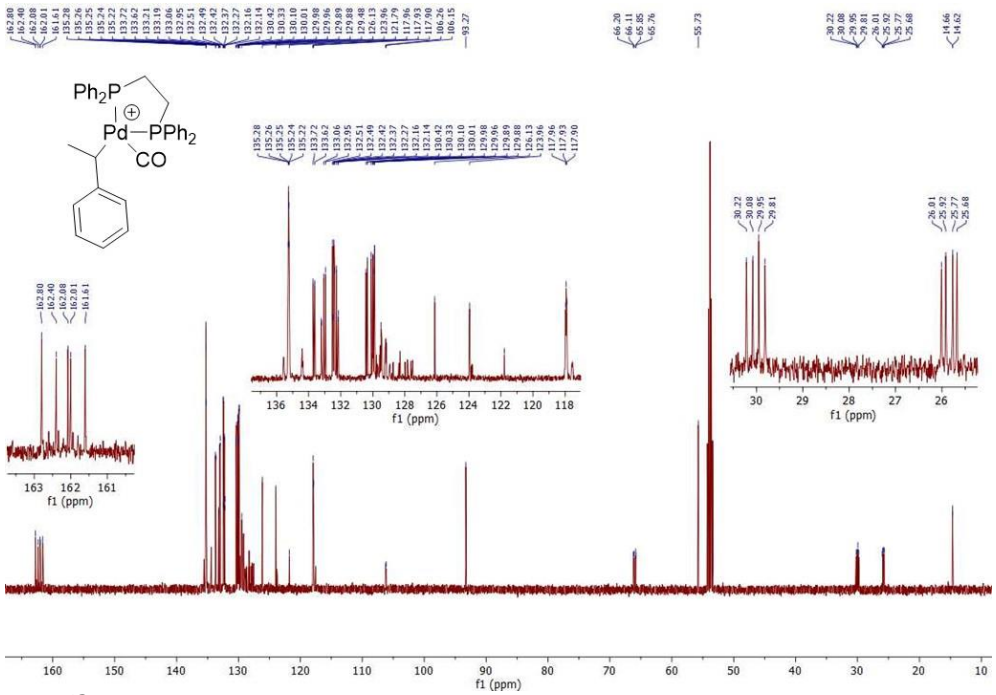

Figure 2.40. ^{13}C NMR of complex **4^{+} BF$_4$** (CD_2Cl_2) Note: Due to degradation over collection times and complex peak overlap we did not assign specific carbon peaks for **4^{+}BF$_4$**

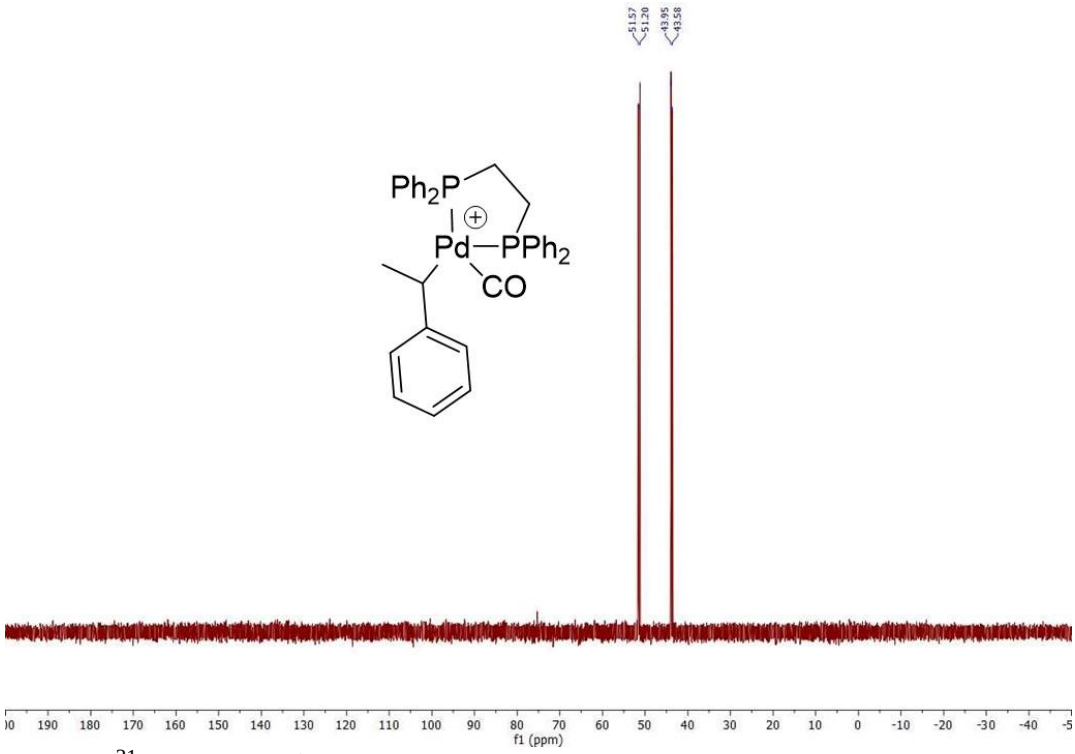

Figure 2.41. ^{31}P NMR of **4**$^{+}$ **BF**$_4$ (CD_2Cl_2)

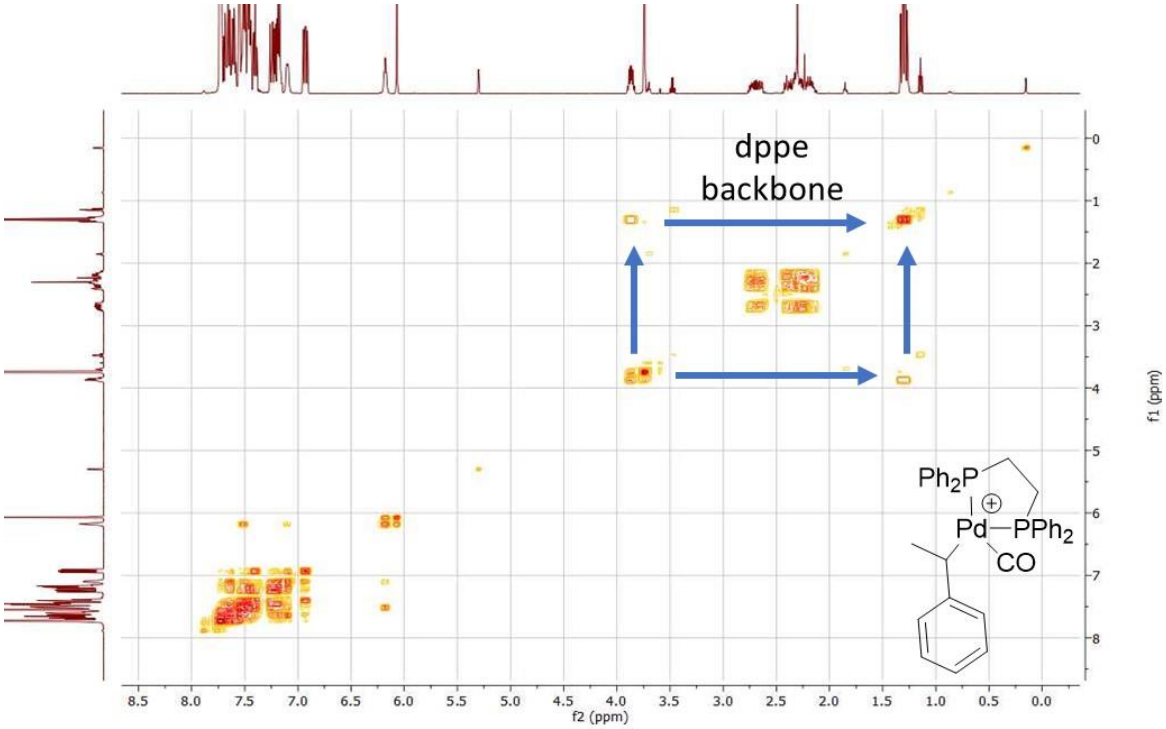

Figure 2.42. COSY NMR of **4**$^{+}$ **BF**$_4$ (CD_2Cl_2). Note**: C**OSY NMR shows peak A (methyl) and B (methine) are coupled supporting that they are on adjacent carbon atoms

2.4.3. Synthesis of Protonated Phosphine

To a 20 mL scintillation vial was added a tertiary phosphine (0.1 mmol) and 1 mL of CD_3CN outside of a glovebox. To this mixture was added either 1 mL of concentrated (37%) HCl in H_2O or DCl in D_2O. The resulting mixture was stirred for two hours. $CDCl_3$ (0.5mL) was added to separate the CH_3CN / water mixture and extract the phosphonium compound. The resulting solution was dried by $MgSO_4$, filtered by syringe, and analyzed by NMR spectroscopy. **H-P^{t}Bu$_3^+$ (Cl$^-$)**. ^{1}H NMR (500MHz, CD_3CN) δ_H 5.70 (1H, d, $J_{P\text{-}H}$ = 107.7 Hz), 1.62 (27H, d, $J_{P\text{-}H}$ = 4.8 Hz); ^{31}P NMR (121MHz, CD_3CN) δ_P 55.0. **D-P^{t}Bu$_3^+$ (Cl$^-$)**. ^{1}H NMR (500MHz, CD_3CN) δ_H 1.62 (27H, d, $J_{P\text{-}H}$ = 4.8 Hz); ^{31}P NMR (121MHz, CD_3CN) δ_P 54.5 (t*, $J_{P\text{-}D}$ = 67.8 Hz). *There is a fourth peak of about half intensity as the main triplet at 55.1 ppm. Based on expected splitting patterns for P-D coupling and differences in calculated J values, this peak appears to not be directly correlated to the desired compound but is likely a singlet peak representing an

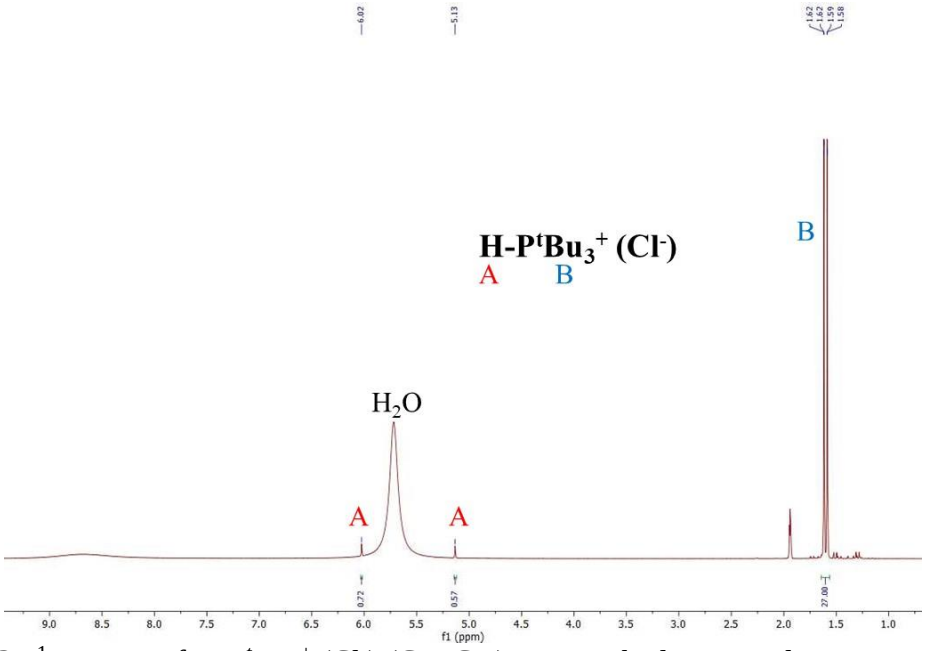

Figure 2.43. ^{1}H NMR of H-P^{t}Bu$_3$$^+$ (Cl$^-$) (CD$_3$CN). Note: The large singlet near 5.70 ppm is likely water within the sample shifted by interaction with H-P^{t}Bu$_3$

impurity or potentially tri-*tert*-butylphosphine oxide.

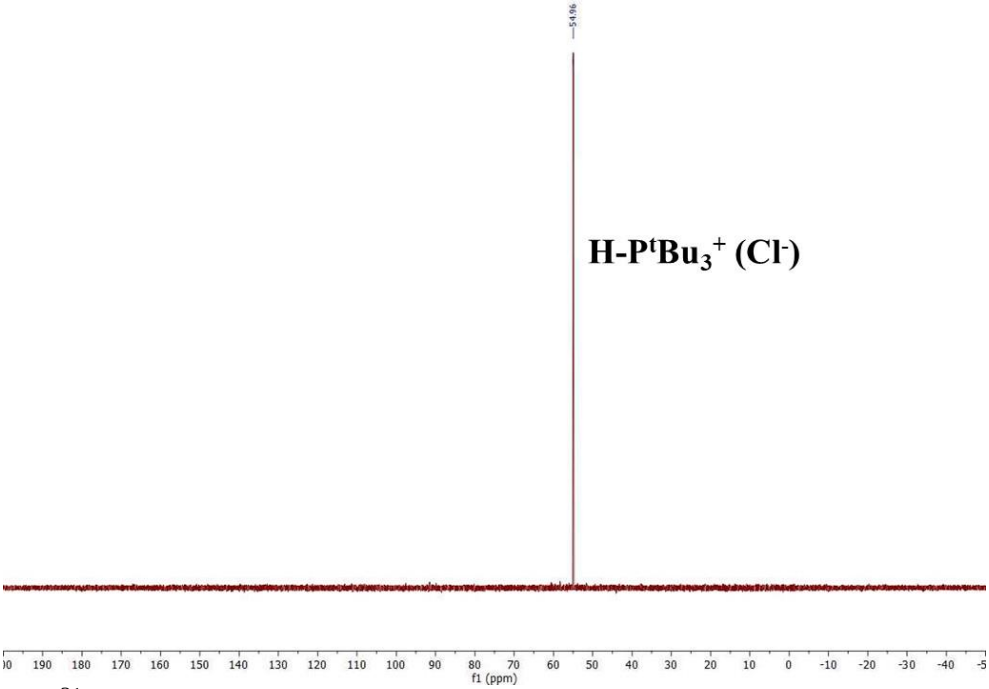

Figure 2.44. ^{31}P NMR Spectrum of H-P^{t}Bu$_3$$^+$ (Cl$^-$) (CD$_3$CN)

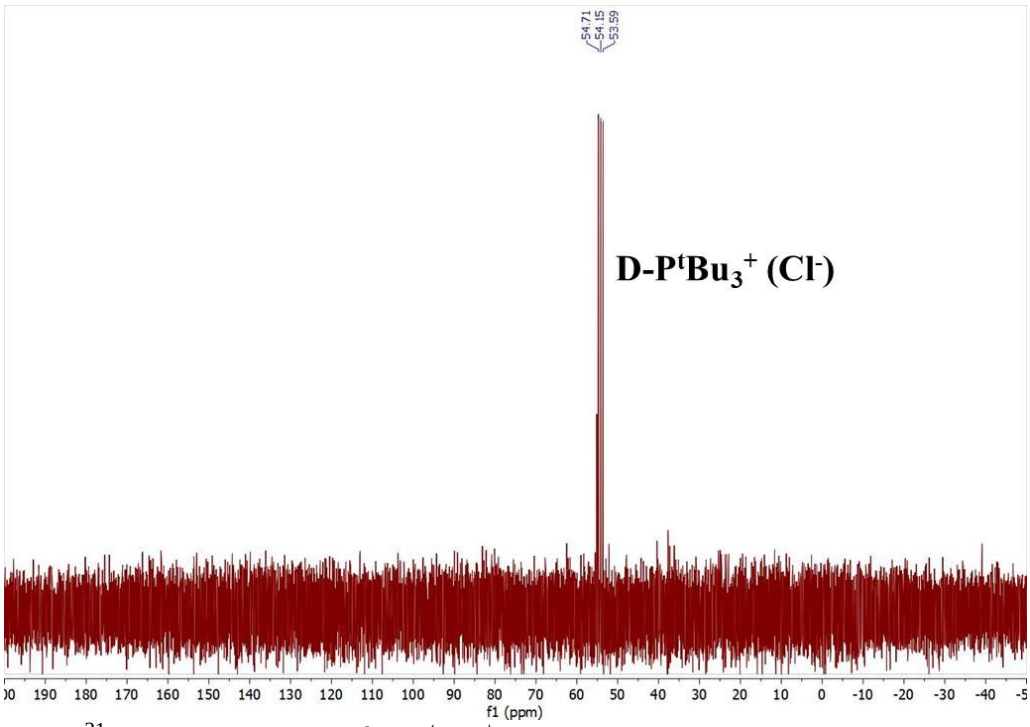

Figure 2.45. ^{31}P NMR Spectrum of D-P^{t}Bu$_3^+$ (Cl$^-$)

2.5. Theory

Preface on computational details. All Density Functional Theory calculations were performed by collaborators Samuel Asiedu Fosu, Dr. Riffat Parveen and Professor Bess Vlaisavljevich at The University of South Dakota.

Computational Details

Density Functional Theory (DFT) calculations were performed with the Gaussian 16 program package.[21] Geometry optimizations of all minima and transition states were performed using the M06-Lfunctional,[22,23] and the nature of all stationary points was verified by harmonic vibrational analysis. The single imaginary frequency for each transition state structure is connected to the reactants and products which was verified by following the intrinsic reaction coordinate (IRC).[24]

Gibbs free energies were computed at 298.15 K. For geometry optimizations and vibrational frequencies, the def2-SV(P) basis set was used for all atoms except for Pd and Ag, where the def2-TZVP basis set and its corresponding effective core potential (ECP) were used.[25] All optimized structures were further subjected to single point calculation using def2-TZVP basis set for all atoms. Solvation effects were included using the continuum solvation model (SMD[26]) for acetonitrile in all calculations. The free energies were corrected to account for the standard state and Grimme's quasiharmonic correction was applied. In the latter correction, all vibrational frequencies lower than 100 cm^{-1} were replaced by a value generated in the GoodVibes[27] program package using the free-rotor approximation as proposed by Grimme. Finally, the sensitivity of the energy barriers to functional choice was tested by performing single point calculations on the M06-L optimized geometries using M06-L, M06,[28] MN15,[29] and ωB97XD.[30] The def2-TZVP basis set was used for all atoms studied. The corresponding ECP was used for Pd and Ag.[31] Finally, the sensitivity of the energy barriers to functional choice was tested by performing a subset of the calculations using M06-L, M06,[32] and ωB97XD.[33] The same basis sets and energy corrections applied to the values in the main text were included here.

2.6. References

1. Tsuji, J.; Ohno, K. Organic Syntheses by Means of Noble Metal Compounds. XXXIV. Carbonylation and Decarbonylation Reactions Catalyzed by Palladium. *J. Am. Chem. Soc.* **1968**, *90*, 94–98.

2. (a) Miranda, M. O.; Pietrangelo, A.; Hillmyer, M. A.; Tolman, W. B. Catalytic Decarbonylation of Biomass-Derived Carboxylic Acids as Efficient Route to Commodity Monomers. *Green Chem.* **2012**, *14*, 490–494. (b) John, A.; Miranda, M. O.; Ding, K.; Dereli, B.; Ortuno, M. A.; Lapointe, A. M.; Coates, G. W.; Cramer, C. J.; Tolman, W. B. Nickel Catalysts for the Dehydrative Decarbonylation of Carboxylic Acids to Alkenes. *Organometallics* **2016**, *35*, 2391–2400. (c) Nôtre, J. Le; Scott, E. L.; Franssen, M. C. R.; Sanders, J. P. M. Selective Preparation of Terminal Alkenes from Aliphatic Carboxylic Acids by a Palladium-Catalysed Decarbonylation-Elimination Reaction. *Tetrahedron Lett.* **2010**, *51*, 3712–3715. (d) Miller, J. A.; Nelson, J. A.; Byrne, M. P. A Highly Catalytic and Selective Conversion of Carboxylic Acids to 1-Alkenes of One Less Carbon Atom. *J. Org. Chem.* **1993**, *58*, 18–20.

3. John, A.; Dereli, B.; Ortunío, M. A.; Johnson, H. E.; Hillmyer, M. A.; Cramer, C. J.; Tolman, W. B. Selective Decarbonylation of Fatty Acid Esters to Linear α-Olefins. *Organometallics* **2017**, *36*, 2956–2964. (b) John, A.; Hogan, L. T.; Hillmyer, M. A.; Tolman, W. B. Olefins from Biomass Feedstocks: Catalytic Ester Decarbonylation and Tandem Heck-Type Coupling. *Chem. Commun.* **2015**, *51*, 2731–2733.

4. (a) Gooßen, L. J.; Rodríguez, N. A Mild and Efficient Protocol for the Conversion of Carboxylic Acids to Olefins by a Catalytic Decarbonylative Elimination Reaction. *Chem.*

Commun. **2004**, *4*, 724–725. (b) Liu, Y.; Kim, K. E.; Herbert, M. B.; Fedorov, A.; Grubbs, R. H.; Stoltz, B. M. Palladium-Catalyzed Decarbonylative Dehydration of Fatty Acids for the Production of Linear Alpha Olefins. *Adv. Synth. Catal.* **2014**, *356*, 130–136. (c) Chatterjee, A.; Hopen Eliasson, S. H.; Törnroos, K. W.; Jensen, V. R. Palladium Precatalysts for Decarbonylative Dehydration of Fatty Acids to Linear Alpha Olefins. *ACS Catal.* **2016**, *6*, 7784–7789. (d) Chatterjee, A.; Hopen Eliasson, S. H.; Jensen, V. R. Selective Production of Linear α-Olefins: Via Catalytic Deoxygenation of Fatty Acids and Derivatives. *Catal. Sci. Technol.* **2018**, *8* (6), 1487–1499.

5. Miller, J. A.; Nelson, J. A.; Byrne, M. P. A Highly Catalytic and Selective Conversion of Carboxylic Acids to 1-Alkenes of One Less Carbon Atom. *J. Org. Chem.* **1993**, *58*, 18–20. Foglia, T. A.; Barr, P. A. Decarbonylation Dehydration of Fatty Acids to Alkenes in the Presence of Transition Metal Complexes. *J. Am. Oil Chem. Soc.* **1976**, *53*, 737–741.

6. (a) Murray, R. E.; Walter, E. L.; Doll, K. M. Tandem Isomerization-Decarboxylation for Converting Alkenoic Fatty Acids into Alkenes. *ACS Catal.* **2014**, *4*, 3517–3520. (b) Fieser, M. E.; Schimler, S. D.; Mitchell, L. A.; Wilborn, E. G.; John, A.; Hogan, L. T.; Benson, B.; LaPointe, A. M.; Tolman, W. B. Dual-Catalytic Decarbonylation of Fatty Acid Methyl Esters to Form Olefins. *Chem. Commun.* **2018**, *54*, 7669–7672.

7. (a) Ternel, J.; Lebarbé, T.; Monflier, E.; Hapiot, F. Catalytic Decarbonylation of Biosourced Substrates. *ChemSusChem* **2015**, *8*, 1585–1592. (b) Maetani, S.; Fukuyama, T.; Suzuki, N.; Ishihara, D.; Ryu, I. Efficient Iridium-Catalyzed Decarbonylation Reaction of Aliphatic Carboxylic Acids Leading to Internal or Terminal Alkenes. *Organometallics* **2011**, *30*, 1389–1394.

8. Maetani, S.; Fukuyama, T.; Suzuki, N.; Ishihara, D.; Ryu, I. Iron-Catalyzed Decarbonylation Reaction of Aliphatic Carboxylic Acids Leading to α-Olefins. *Chem. Commun.* **2012**, *48*, 2552–2554.

9. John, A., Miranda, M. O., Ding, K., Dereli, B., Ortuno, M. A., Lapointe, A. M., Coates, G. W., Cramer, C. J., & Tolman, W. B. (2016). Nickel Catalysts for the Dehydrative Decarbonylation of Carboxylic Acids to Alkenes. *Organometallics*, *35*(14), 2391–2400.

10. (a) Cheng, W.-M.; Shang, R.; Fu, Y. Irradiation-Induced Palladium-Catalyzed Decarboxylative Desaturation Enabled by a Dual Ligand System. *Nat. Commun.* **2018**, *9*, 5215. (b) Tlahuext-Aca, A.; Candish, L.; Garza-Sanchez, R. A.; Glorius, F. Decarboxylative Olefination of Activated Aliphatic Acids Enabled by Dual Organophotoredox/Copper Catalysis. *ACS Catal.* **2018**, *8*, 1715–1719. (c) Sun, X.; Chen, J.; Ritter, T. Catalytic Dehydrogenative Decarboxyolefination of Carboxylic Acids. *Nat. Chem.* **2018**, *10*, 1229–1233. (d) Nguyen, V. T.; Nguyen, V. D.; Haug, G. C.; Dang, H. T.; Jin, S.; Li, Z.; Flores-Hansen, C.; Benavides, B. S.; Arman, H. D.; Larionov, O. V. Alkene Synthesis by Photocatalytic Chemoenzymatically Compatible Dehydrodecarboxylation of Carboxylic Acids and Biomass. *ACS Catal.* **2019**, *9*, 9485–9498.

11. Fieser, M. E., Schimler, S. D., Mitchell, L. A., Wilborn, E. G., John, A., Hogan, L. T., Benson, B., LaPointe, A. M., & Tolman, W. B. (2018). Dual-catalytic decarbonylation of fatty acid methyl esters to form olefins. *Chemical Communications*, *54*(55), 7669–7672.

12. Wiessner, T. C., Fosu, S. A., Parveen, R., Rath, N. P., Vlaisavljevich, B., & Tolman, W. B. (2020). Ligand effects on decarbonylation of palladium-acyl complexes. *Organometallics*, *39*(22), 3992–3998.

13. (a) Ortuño, M. A.; Dereli, B.; Cramer, C. J. Mechanism of Pd-Catalyzed Decarbonylation of Biomass-Derived Hydrocinnamic Acid to Styrene Following Activation as an Anhydride. *Inorg. Chem.* **2016**, *55*, 4124–4131. (b) Eliasson, S.; Chatterjee, A.; Occhipinti, G.; Jensen, V. The Mechanism of Rh-Catalyzed Transformation of Fatty Acids to Linear Alpha Olefins. *Inorganics* **2017**, *5*, 87.

14. (a) Gao, B.; Zhang, G.; Zhou, X.; Huang, H. Palladium-Catalyzed Regiodivergent Hydroaminocarbonylation of Alkenes to Primary Amides with Ammonium Chloride. *Chem. Sci.* **2018**, *9*, 380–386. (b) Clavier, H.; Nolan, S. P. Percent Buried Volume for Phosphine and N-Heterocyclic Carbene Ligands: Steric Properties in Organometallic Chemistry. *Chem. Commun.* **2010**, *46*, 841–861. (c) Bilbrey, J. A.; Kazez, A. H.; Locklin, J.; Allen, W. D. Exact Ligand Cone Angles. *J. Comput. Chem.* **2013**, *34*, 1189–1197.

15. (a) Quesnel, J. S.; Kayser, L. V.; Fabrikant, A.; Arndtsen, B. A. Acid Chloride Synthesis by the Palladium-Catalyzed Chlorocarbonylation of Aryl Bromides. *Chem. - A Eur. J.* **2015**, *21*, 9550–9555. (b) Campos, J.; Nova, A.; Kolychev, E. L.; Aldridge, S. A Combined Experimental/Computational Study of the Mechanism of a Palladium-Catalyzed Bora-Negishi Reaction. *Chem. - A Eur. J.* **2017**, *23*, 12655–12667.

16. Lin, Y. S.; Yamamoto, A. Studies Relevant to Palladium-Catalyzed Carbonylation Processes. Mechanisms of Formation of Esters and Amides from Benzylpalladium and

(Phenylacetyl)Palladium Complexes on Reactions with Alcohols and Amines. *Organometallics* **1998**, *17*, 3466–3478.

17. (a) Masson-Makdissi, J.; Vandavasi, J. K.; Newman, S. G. Switchable Selectivity in the Pd-Catalyzed Alkylative Cross-Coupling of Esters. *Org. Lett.* **2018**, *20* (13), 4094–4098. (b) Chatupheeraphat, A.; Liao, H. H.; Srimontree, W.; Guo, L.; Minenkov, Y.; Poater, A.; Cavallo, L.; Rueping, M. Ligand-Controlled Chemoselective C(Acyl)-O Bond vs C(Aryl)-C Bond Activation of Aromatic Esters in Nickel Catalyzed C(Sp2)-C(Sp3) Cross-Couplings. *J. Am. Chem. Soc.* **2018**, *140* (10), 3724–3735.

18. Martínez-Martínez, A. J.; Weller, A. S. Solvent-Free Anhydrous Li+, Na+ and K+ Salts of [B(3,5-(CF3)2C6H3)4]-, [BArF4]-. Improved Synthesis and Solid-State Structures. *Dalt. Trans.* **2019**, *48* (11), 3551–3554...

19. Gao, B.; Zhang, G.; Zhou, X.; Huang, H. Palladium-Catalyzed Regiodivergent Hydroaminocarbonylation of Alkenes to Primary Amides with Ammonium Chloride. *Chem. Sci.* **2018**, *9* (2), 380–386.

20. Lin, Y. S.; Yamamoto, A. Studies Relevant to Palladium-Catalyzed Carbonylation Processes. Mechanisms of Formation of Esters and Amides from Benzylpalladium and (Phenylacetyl)Palladium Complexes on Reactions with Alcohols and Amines. *Organometallics* **1998**, *17* (16), 3466–3478.

21. Frisch *et al.*, Gaussian 16, Revision A.03. Gaussian, Inc., Wallingford CT, 2016.

22. Zhao, Y.; Truhlar, D. G. A New Local Density Functional for Main-Group Thermochemistry, Transition Metal Bonding, Thermochemical Kinetics, and Noncovalent Interactions. *J. Chem. Phys.* **2006**, *125* (19).

23. Zhao, Y.; Truhlar, D. G. Density Functionals with Broad Applicability in Chemistry. *Acc. Chem. Res.* **2008**, *41* (2), 157–167.

24. Hratchian, H. P.; Schlegel, H. B. Using Hessian Updating to Increase the Efficiency of a Hessian Based Predictor-Corrector Reaction Path Following Method. *J. Chem. Theory Comput.* **2005**, *1* (1), 61–69.

25. Weigend, F.; Ahlrichs, R. Balanced Basis Sets of Split Valence, Triple Zeta Valence and Quadruple Zeta Valence Quality for H to Rn: Design and Assessment of Accuracy. *Phys. Chem. Chem. Phys.* **2005**, *7* (18), 3297–3305.

26. Marenich, A. V.; Cramer, C. J.; Truhlar, D. G. Universal Solvation Model Based on Solute Electron Density and on a Continuum Model of the Solvent Defined by the Bulk Dielectric Constant and Atomic Surface Tensions. *J. Phys. Chem. B* **2009**, *113* (18), 6378–6396.

27. Li, Y. P.; Gomes, J.; Sharada, S. M.; Bell, A. T.; Head-Gordon, M. Improved Force-Field Parameters for QM/MM Simulations of the Energies of Adsorption for Molecules in Zeolites and a Free Rotor Correction to the Rigid Rotor Harmonic Oscillator Model for Adsorption Enthalpies. *J. Phys. Chem. C* **2015**, *119* (4), 1840–1850.

28. Zhao, Y.; Truhlar, D. G. The M06 Suite of Density Functionals for Main Group Thermochemistry, Thermochemical Kinetics, Noncovalent Interactions, Excited States, and Transition Elements: Two New Functionals and Systematic Testing of Four M06-Class Functionals and 12 Other Function. *Theor. Chem. Acc.* **2008**, *120* (1–3), 215–241.

29. Yu, H. S.; He, X.; Li, S. L.; Truhlar, D. G. MN15: A Kohn-Sham Global-Hybrid Exchange-Correlation Density Functional with Broad Accuracy for Multi-Reference and

Single-Reference Systems and Noncovalent Interactions. *Chem. Sci.* **2016**, *7* (8), 5032–5051.

30. Chai, J. Da; Head-Gordon, M. Long-Range Corrected Hybrid Density Functionals with Damped Atom-Atom Dispersion Corrections. *Phys. Chem. Chem. Phys.* **2008**, *10* (44), 6615–6620.

31. Andrae, D.; Häußermann, U.; Dolg, M.; Stoll, H.; Preuß, H. Energy-Adjusted Ab Initio Pseudopotentials for the Second and Third Row Transition Elements. *Theor. Chim. Acta* **1990**, *77* (2), 123–141.

32. Zhao, Y.; Truhlar, D. G. The M06 Suite of Density Functionals for Main Group Thermochemistry, Thermochemical Kinetics, Noncovalent Interactions, Excited States, and Transition Elements: Two New Functionals and Systematic Testing of Four M06-Class Functionals and 12 Other Function. *Theor. Chem. Acc.* **2008**, *120* (1–3), 215–241.

33. Andrae, D.; Häußermann, U.; Dolg, M.; Stoll, H.; Preuß, H. Energy-Adjusted Ab Initio Pseudopotentials for the Second and Third Row Transition Elements. *Theor. Chim. Acta* **1990**, *77* (2), 123–141.

Chapter 3.

Statistical Incorporation of Olefin-containing Caprolactones into Polylactide for Copolymer Post-polymerization Modification

3.1. Introduction

Over the past century plastics made from nonrenewable feedstocks have revolutionized the world and led to a rapid increase in our standard of living. Plastics impact almost every attribute of everyday life including transportation, clothing, packaging, electronics, construction, and others. A large reason for these improvements is the ability to be lighter, more durable, chemically resistant, and cheaper than metal-based materials.[1] Along with the many benefits that plastics bring, however, comes numerous environmental concerns brought on by their use, including pollution and the lack of recyclability.[2] Driven by the desire to create more sustainable materials, alternatives to petroleum-based plastics are being heavily explored.[3] Several biorenewable alternatives are currently being employed, but perhaps none has received as much attention in recent years as polylactide (PLA, also referred to as poly(lactic acid)).

PLA is currently considered to be a possible substitute to fossil-fuel based plastics due to its comparable properties to commercially used polystyrene (PS) and polyethylene terephthalate (PET) while being produced from renewable sources by microbial carbohydrate fermentation, and requiring less energy to produce than oil-based plastics.[4,5,6] The monomer of PLA, lactic acid (2-hydroxypropionic acid), can be produced from any number of polysaccharides found in corn, potatoes, beets and sugarcane, making it a readily sourced bulk material.[6c,7] Lactic acid is abundant as both D- and L- isomers, that can be selected based on the strain of bacteria used during the fermentation process or as a racemic mixture formed upon chemical manufacturing processes. Oligomerization of lactic acid followed by dehydration forms the dimerized cyclic ester lactide, which is available as three different stereoisomers: L-, D- and meso (D-, L-)-lactide (Figure 3.1).[7]

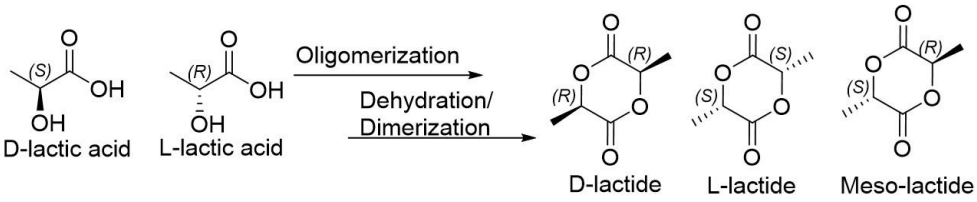

Figure 3.1. Synthesis of lactide from lactic acid

The most common method for the synthesis of PLA is by Ring-Opening Polymerization (ROP), typically achieved through the use of a Lewis Acid metal-based catalyst or an organic catalyst. Due to the chirality of lactide, PLA exists in different forms, which overall impact the macroscopic properties of the polymer (Figure 3.2).[8] Numerous methodologies have thus been developed over recent years to target specific stereo-selective outcomes by altering reaction conditions and ROP initiators.[9,14] However, even with such strategies, PLA is limited in its uses due to its brittleness, low thermal stability, weak elasticity/melt strength, and overall low gas and water permeability, making it almost exclusively used for food packaging, pharmaceuticals, and biomedical uses.[10]

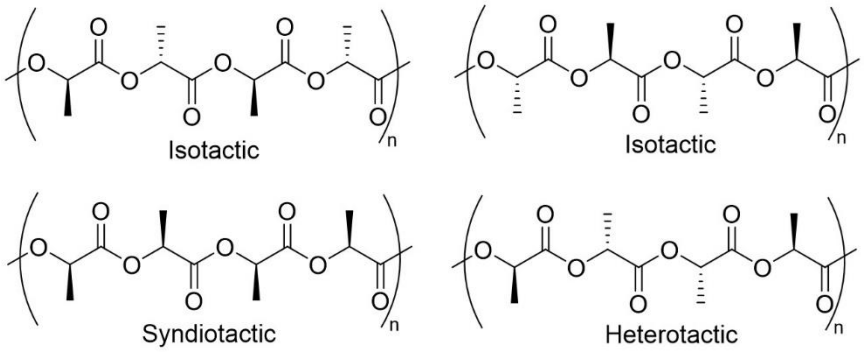

Figure 3.2. Tacticities of polylactide that can arise from the three monomers D-, L- and meso (D-,L-) lactide polymerization

To circumvent the limitations of PLA as a bulk material numerous strategies have been explored. Blending PLA has shown promise to enhancing the toughness vs. strength and heat resistance and has led to a wider birth of applications.[11] Still, strategies involving plasticization

and polymer composites are limited to the properties of the individual components. An alternative strategy to blending is Ring-Opening Copolymerization (ROCOP), which involves polymerizing lactide monomer in tandem with at least one other comonomer (Figure 3.3). In ROCOP the lactide monomer no longer forms a homogeneous polymer but incorporates at least one other comonomer within the polymer chain. This method offers a distinct difference in polymer properties versus blending methods as the two monomers are covalently linked instead of being a heterogeneous mixture of multiple homopolymers or additives. By combining copolymers into a single strand drastic differences in miscibility and thermal stability can occur either in the bulk material or through its ability to offer stabilization to a mixture of homopolymers, allowing for copolymers to be of further use as compatibilizing agents.[12]

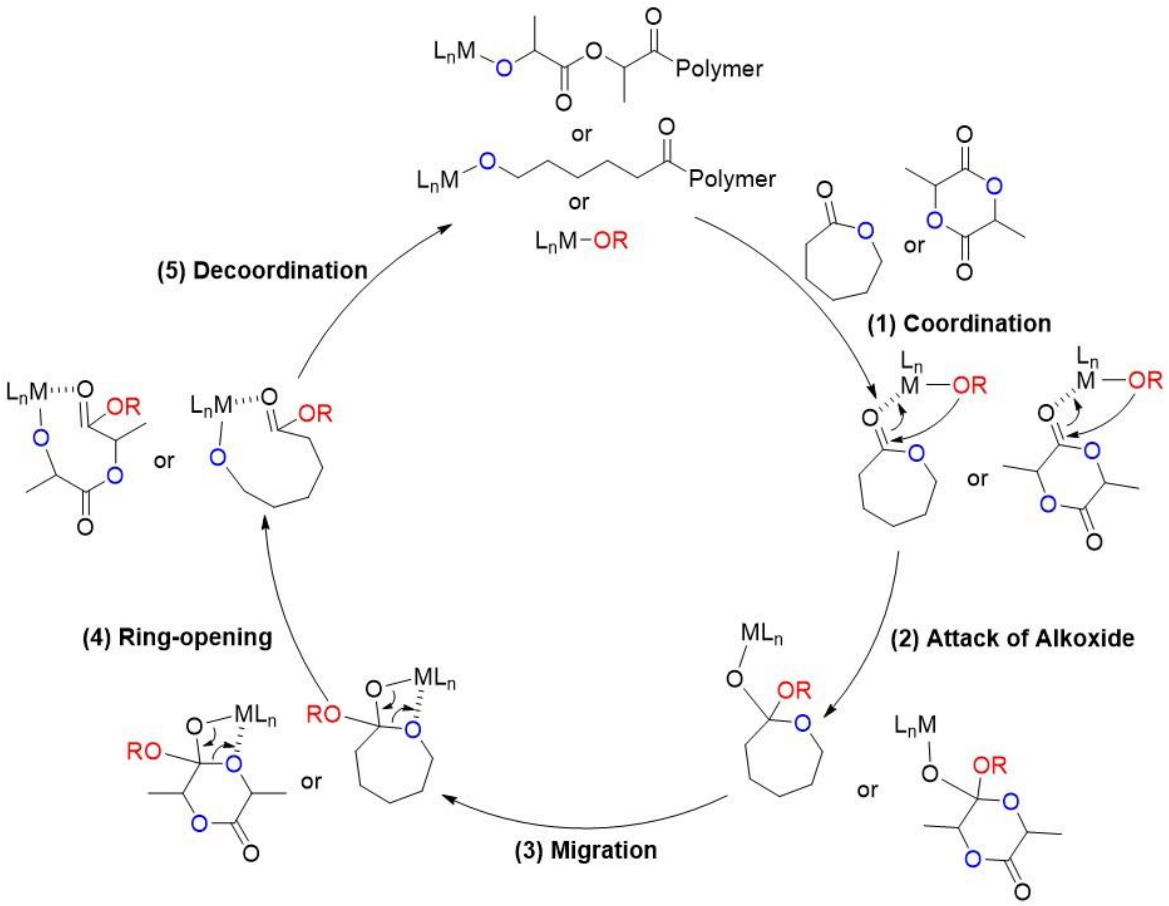

Figure 3.3. Coordination-insertion mechanism for ring-opening copolymerization of lactide with ε-caprolactone. R is either from an initiating alcohol or growing polymer chain.

In a copolymerization process numerous microstructures can be created. The order of addition of reagents, reactivity ratios, and stereoregularity of the monomers are just some of the factors that can be varied. For a standard ROCOP, the reactivity differences between the two monomers controls the defining characteristics of the product polymer as the number of covalent linkages between comonomers and overall microstructure of the copolymer determines the macroscopic properties.[13] For example, if one monomer polymerizes at a much greater rate (k) versus the other ($k_{monomer1} >> k_{monomer2}$) a blocky copolymer is obtained where the copolymer is largely made up of two separate blocks of homopolymers connected through a very small number of covalent linkages between comonomers (Figure 3.4, top). In this scenario the faster reacting monomer will likely polymerize to near completion prior to any incorporation of the second comonomer, essentially proceeding via a sequential addition of monomers. As the rates between comonomers become more similar, a gradient copolymer is formed ($k_{monomer1} > k_{monomer2}$) meaning that as monomer 1 is consumed the concentration of monomer 2 increases, allowing it to compete more readily for incorporation into the copolymer strand (Figure 3.3, middle). At equal reactivities between comonomers ($k_{monomer1} \approx k_{monomer2}$) a statistical copolymer is formed, leading to a polymer chain where the makeup of the copolymer is directly proportional to the feed ratio of the two monomers (Figure 3.4, bottom). In other words, in a statistical copolymerization between two monomers in an equimolar ratio it would be expected that there is a 50% chance of incorporation of either comonomer after each individual insertion. Likewise, upon completion of a copolymerization between two monomers in a 9:1 ratio, there would be nine units of monomer 1 for every monomer 2. Therefore, in a statistical process the overall distribution of the two monomers can be readily tuned based on the feed ratio to alter the distribution of monomers along the copolymer chain and therefore the copolymer's properties.

Although there are numerous monomers of interest for ROCOP with lactide, ε-caprolactone (6-hexalactone) has recently received a great deal of attention.[14] Currently, ε-caprolactone is mostly derived from petroleum and not thought of as a biorenewable material, though recent progress has been made in its derivation from renewable sources.[15] Regardless, ε-caprolactone has shown promise for its copolymerization with lactide as polycaprolactone (PCL) has many differing, but complimentary, properties from PLA that allow for the potential tunability of a copolymer. PCL has a glass transition temperature (T_g) of -60 °C (vs. ≈ 57 °C for PLA, depending on its tacticity, Figure 3.2) has a high thermal stability and elasticity, higher levels of drug permeability and a much slower *in vivo* degradation times of up to one year (vs. weeks for PLA).[16]

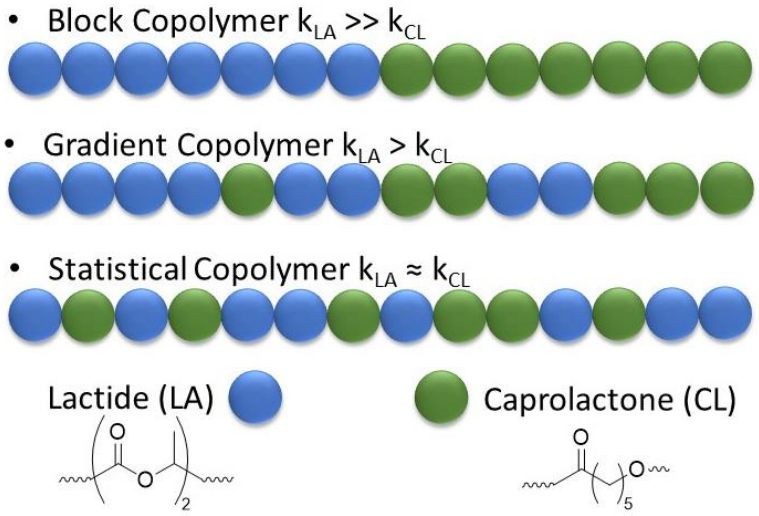

Figure 3.4. Different microstructures for the copolymerization of lactide with caprolactone based on the rates of the two monomers in a copolymerization setting

By combining caprolactone and lactide into a single copolymer a combination of the properties of the two homopolymers can be achieved, giving rise to a new class of copolymers, poly(lactide-co-caprolactone) (PLACL), that can be altered to possess desirable attributes from each monomer. Copolymerization behavior between lactide and ε-caprolactone has been well

documented but presents several obstacles.[14] Initial studies have shown that the rates of polymerization of the two monomers can be drastically different, typically leading to blocky or gradient-like copolymers. Even though under homopolymerizations conditions ε-caprolactone has been often observed to polymerize at rates several orders of magnitude faster than lactide, it often fails to incorporate into the copolymer when both monomers are present.[17] Several factors play into this reversal in reactivities between homo and copolymerization behaviors.

Lactide has two carbonyl groups necessary for coordination to an oxophilic catalyst versus caprolactone only having one, leading to a greater binding to a Lewis acid center of a catalyst and more rapid polymerization. Furthermore, lactide can form chelates between the last lactide unit inserted into the polymer and the active catalyst.[18] So far, no evidence to support ε-caprolactones' ability to form such species has been reported. The observed stabilization created by the formation of the chelate species may inhibit ε-caprolactone from coordinating to an active catalyst center and thus facilitate further lactide incorporation. In fact, in copolymerization studies between ε-caprolactone and lactide using a simple Lewis Acid catalyst, $Al(O^iPr)_3$, it was reported that a growing chain of PCL is equally likely to incorporate either monomer, but a growing chain of PLA incorporates lactide at rates 20-30 times faster than for ε-caprolactone.[17f] Furthermore, the growing chain of PCL was reported to propagate at a rate several orders of magnitude faster than that of the growing PLA chain, meaning that incorporation of lactide severely inhibits the overall kinetics of the copolymerization, while at the same time heavily favoring incorporation of lactide over ε-caprolactone. This behavior has been well documented in the synthesis of block copolymers of lactide and ε-caprolactone poly(LA-block-CL), requiring ε-caprolactone to be polymerized prior to lactide addition.[19]

One of the first methods used to inhibit the preferential incorporation of lactide was to hamper lactide's ability to form stable chelate species. By using catalysts surrounded by bulky ligand frameworks a steric clash can occur between the methyl substituents of lactide and the ligand substituents.[20] The increase in steric hindrance disrupts the chelation effect between the last inserted monomer of lactide with the growing chain, while at the same time interfering with the methyl groups of incoming lactide monomer, allowing ε-caprolactone, which lacks such steric hindrance, to compete more readily for polymerization. The initial success of bulky ligand frameworks has subsequently been replicated in numerous types of active catalyst centers providing a wide range of copolymerization processes, which has opened the door for control of other aspects of copolymerization such as molecular weight (MW), polydispersity (Đ) and tacticity control.[14,21]

As expected, statistical copolymers of lactide and caprolactone (poly(LA-stat-CL) have shown unique properties different from those of blends of the two homopolymers.[22] Nevertheless, potential applications for PLACL are by definition limited by the characteristics of the two monomers and the ratios between them in the copolymer (0-100% of either monomer). We aimed to expand the potential of PLACL materials by creating a new, modifiable class of statistical PLACL copolymers. We envisioned that PLACL copolymers could be tuned, after statistical copolymerization, by making a minor alteration to the ε-caprolactone monomer. The modification of the monomer would entail incorporating a pendant olefin group, in the form of an allyl or vinyl unit, along the aliphatic backbone of caprolactone (Figure 3.5). We chose to incorporate an olefin because of its well-documented versatility in organic transformations, such as thiol-ene, hydroboration-oxidations, and metathesis reactions, which make them ideal candidates for post-polymerization modifications.[23] Key to our design is that by performing

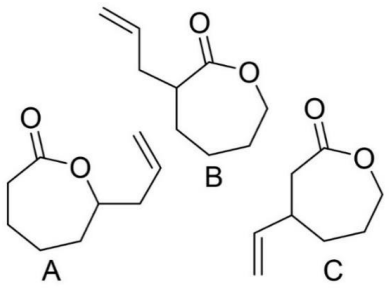

Figure 3.5. Monomers synthesized and tested for statistical copolymerization with *rac*-lactide. 6-allyl caprolactone (**A**), 2-allyl caprolactone (**B**) and 3-vinyl caprolactone (**C**).

statistical copolymerizations between lactide and our modified ε-caprolactone derivatives, the olefin moiety will be uniformly distributed throughout the polymer chain, facilitating creation of PLACL type copolymers that can be readily and evenly manipulated.

Monomers of interest **A** and **B** have been previously reported in limited fashion within the literature, whereas **C** was unknown at the outset of our studies.[24] A single example was reported for the copolymerization of monomer **A** with lactide, whereby tin octanoate was used as catalyst at 110 °C with a benzyl alcohol initiator.[24a] Although it was speculated that a statistical process had taken place, there was not sufficient data to support such a claim. Ultimately, the work was a proof of concept, showing that 6-allyl caprolactone could be homopolymerized or copolymerized with either ε-caprolactone or lactide for the purpose of installing allyl groups along the polymer backbone. Bromination, epoxidation and a hydrosilylation reactions were performed to demonstrate the ability of poly(ε-caprolactone-co-6-allyl caprolactone) to be modified post-polymerization, but no functionalized materials with lactide were reported and material properties were not mentioned. To the best of our knowledge, no examples of copolymers currently exist of **B** with any other monomer than ε-caprolactone. All other literature reports describe only thiol-ene type functionalizations of allyl caprolactone homopolymers, showing the ability for the attachment of sugars, zwitterionic amino groups or PEG for the

purpose of creating water soluble polycaprolactone. Finally, a single example exists of metathesis chemistry for the intramolecular crosslinking of poly(ε-caprolactone-co-6-allyl caprolactone), notably demonstrating changes in the size of single-chain nanoparticles based on the olefin-density of the polymer.[17g]

In our work we aimed to fill the void left by previous reports and focus on copolymerization of ε-caprolactone derivatives with lactide. Upon initiating our studies our first task was to achieve the statistical copolymerization of the selected functionalized ε-caprolactones and lactide. We anticipated the copolymerization reactivity may be heavily influenced by the presence of allyl or vinyl groups on the ε-caprolactone monomer. In particular, the ring opening copolymerization (ROCOP) between *rac*-LA and ε-caprolactone is proposed to work through a coordination-insertion mechanism for metal catalysts that may become disrupted through steric interactions (Figure 3.5). In other words, the addition of an allyl group at the 2 or 6 position on caprolactone could inherently alter the kinetics and thermodynamics of its polymerization, effects that have been previously documented for polymerization of ε-caprolactones with aliphatic substituents, though not well established in copolymerizations with lactide.[25]

For example, the allyl group at the 2 or 6-position of caprolactone (monomer **B**) may interfere with the coordinating ability of the carbonyl motif in step 1, instead favoring coordination to the olefin. While the increased steric hindrance at the 6-position (monomer **A**) could impact the rate or selectivity in propagation of the metal-alkoxide, the increased steric hindrance of the olefin group may also impede the alkoxide insertion into a new monomer (Figures 3.5, 3.6). Both of which may become impediments or change the ability of the functionalized monomers to compete with *rac*-LA in a statistical copolymerization process, which has already been well established to favor *rac*-LA over ε-caprolactone.[26] One reason for

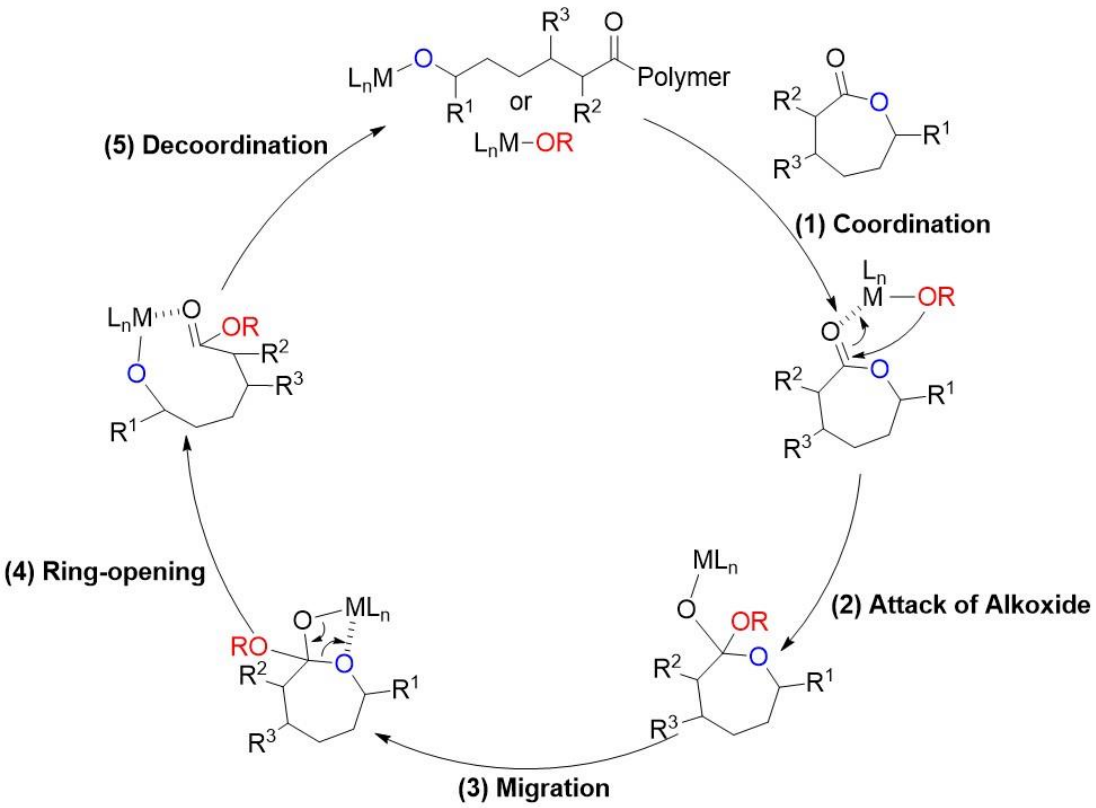

Figure 3.6. Coordination-insertion mechanism for Ring-opening Polymerization of Olefin-containing Caprolactones. 6-allyl caprolactone (A) (R^1 = allyl, R^2 = H, R^3 = H), 2-allyl caprolactone (B) (R^1 = H, R^2 = allyl, R^3 = H), and 3-vinyl caprolactone (C) (R^1 = H, R^2 = H, R^3 = vinyl).

rac-LA's enhanced reactivity is an observable stabilization created by its methyl groups during polymerizations in which Van Der Waals interactions between the protons of the methyl groups and the metal catalyst are able to form a chelate species.[18] ε-Caprolactone lacks methyl groups and does not form such chelate species, leading to a preference of *rac*-LA coordination and insertion into the polymer chain. Although monomers **A** and **B** also lack methyl substituents near the carbonyl and alkoxide group, olefins are well known to coordinate to metal catalysts and so we questioned whether they may provide a similar stabilization or compete for coordination with the carbonyl moiety (Figure 3.7).[10a,27] We also note that for **A** the propagation of the alkoxide (-OR) switches from a primary to secondary alkoxide due to the allyl group's positioning (Figure

3.8). Therefore, in the beginning of our study it was unclear what type of catalyst structure may lead to what reactivities.

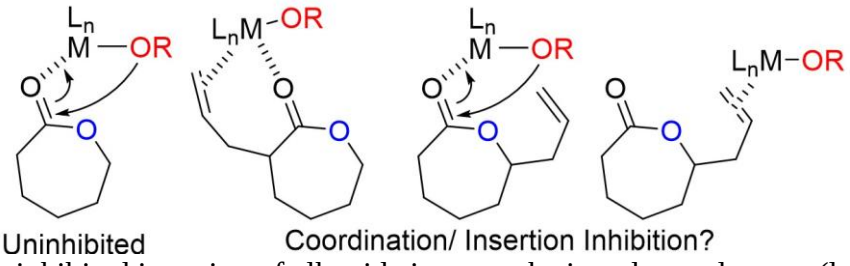

Figure 3.7. Uninhibited insertion of alkoxide into unsubstituted caprolactone (left) versus potential coordination/insertion modes of inhibition.

We decided to focus on synthesizing copolymers with low loadings of monomers **A-C** (< 20%) to maintain some of the biorenewable and degradability aspects of PLA, while offering opportunities for altering the characteristics of the bulk material. In this way we would be focused more on creating a class of PLA-like materials that can undergo post-polymerization modification reactions, but they would be expected to exhibit some material properties of PLACL based on feed ratios. Crucial to our plans was maintaining conditions during copolymerization that statistically incorporate the new monomers with lactide and ensure uniform distribution of the olefin functional handle.

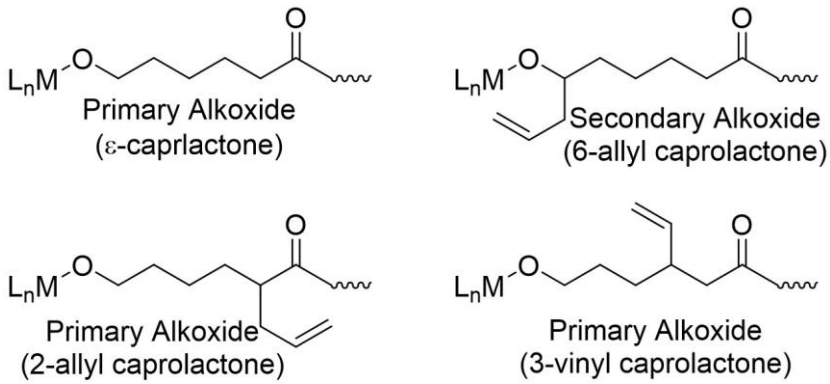

Figure 3.8. Primary and secondary alkoxides generated from the last inserted monomer of ε-caprolactone, 6-allyl caprolactone, 2-allyl caprolactone and 3-vinyl caprolactone

Once methods for the synthesis of the desired statistical copolymers were developed, functionalization of the olefins could be explored. For example, the olefin provides opportunities to add small or large molecules onto the parent copolymer (grafting-to) or grow new polymer chains from the parent (grafting-from) through numerous methodologies. We sought to first demonstrate the highly modifiable behavior of our copolymers through illustrative transformations including thiol-ene reactions, olefin hydroboration-oxidation for conversion to primary alcohols, bromination, epoxidation, free radical polymerization (FRP), ROP, and inter and intramolecular metathesis reactions. Through this approach, we aimed to develop a toolbox of strategies by which our PLACL materials could be readily modified to the user's desire, both in terms of the identity of the modification and the extent provided by varying the monomer feed ratio. We thus aimed to demonstrate the direct covalent attachment of several commercially relevant polymers including PCL, polymethacrylate (PMA), polydimethylsiloxane (PDMS) and polyethylene glycol (PEG), with the opportunity for others.

Herein, we report the synthesis of a series of statistical PLACL copolymers containing pendant olefins and show proof of concept post-functionalization reactions for the modification of these polymers (Figure 3.9). Our focus began on previously reported monomers, **A**/**B**, but difficulties encountered in developing the methodology ultimately led us to create a new monomer, **C**, to accomplish this task. Post-functionalization reactions reported herein include thiol-ene reactions, hydroboration/oxidation followed by ring opening polymerizations, radical

polymerizations, metathesis, bromination, and epoxidation reactions.

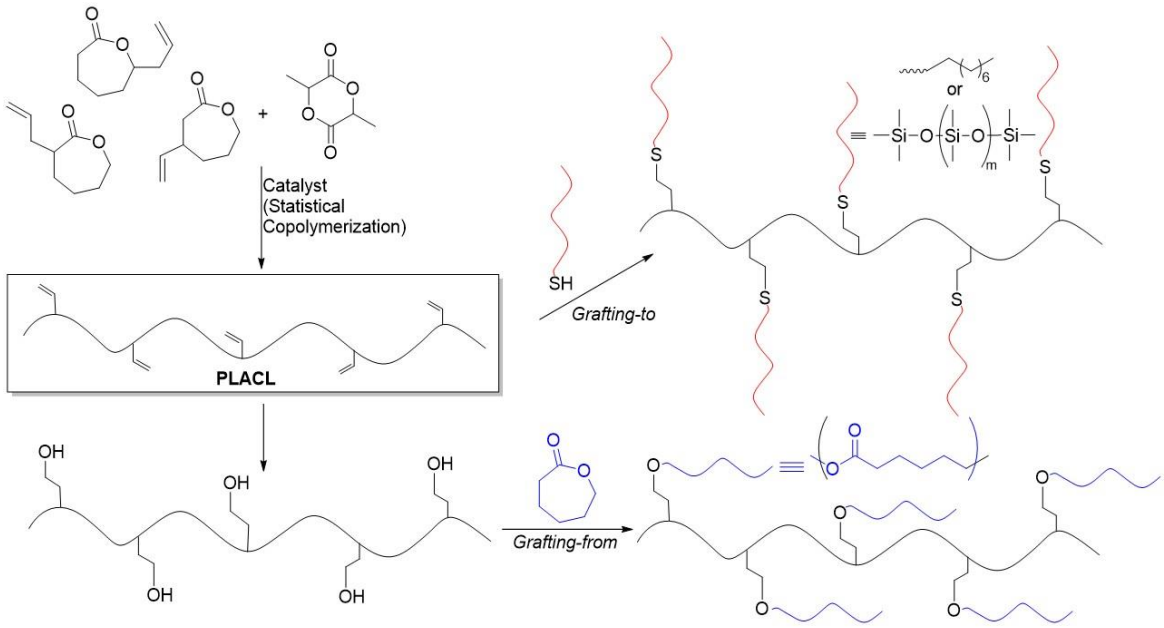

Figure 3.9. Overarching project goals. Olefin-containing caprolactone monomers are first statistically copolymerized with lactide through means of a catalyst. The statistical copolymers (PLACL are then highly modifiable for incorporation of other small or large molecules. Grafting-to approaches include thiol-ene and metathesis chemistry while Grafting-on/from reactions involve growing a polymer chain off of the existing PLACL copolymer.

3.2. Results and Discussion

3.2.1. Statistical Copolymerization Development.

Our studies began with the synthesis of two known monomers, 6-allyl caprolactone (**A**) and 2-allyl caprolactone **(B)** (Scheme 3.1).[3351,52,54] Compound **A** was synthesized from commercially available 1-pyrrolidino-1-cyclohexene via a two-step sequence, beginning with the addition of the allyl group to make 2-allyl cyclohexanone on a 68 g (75%) scale as a yellow oil. The purity and identity of the product was confirmed by ^{1}H NMR spectroscopy, which revealed a match with literature reports and a previously purchased authentic sample from Sigma Aldrich. The Baeyer-Villiger oxidation of 2-allyl cyclohexanone using *meta*-chloroperoxybenzoic acid (*m*CPBA) produced 6-allyl caprolactone (**A**). A mixture of other materials assumed to be epoxidized products also formed, but they were not isolated. Purification by column chromatography, followed by vacuum distillation yielded 20 g (48%) of **A**. Monomer **B** was synthesized directly from ε-caprolactone in a single step using lithium diisopropylamide (LDA),

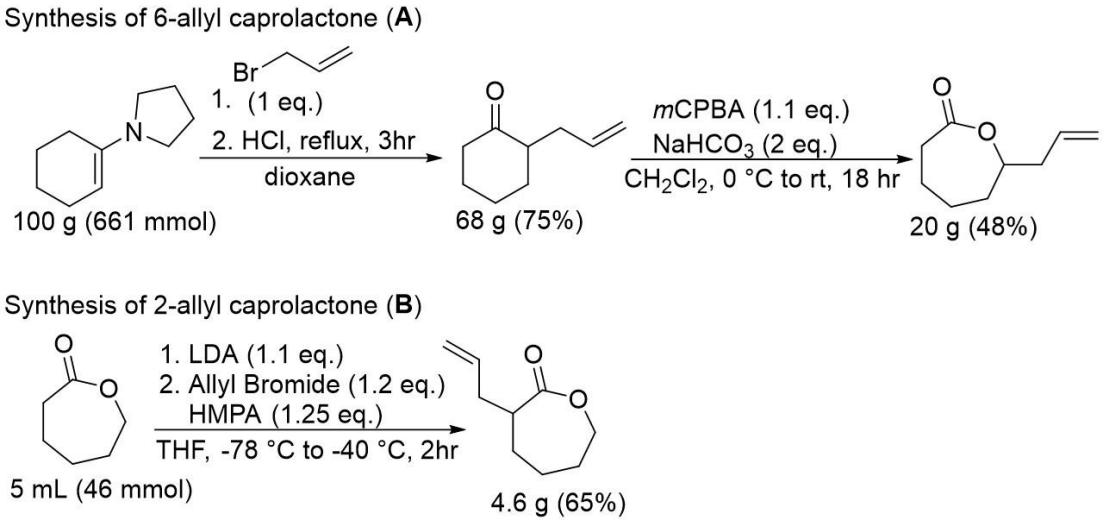

Scheme 3.1. Synthesis of 6-allyl (top) and 2-allyl caprolactone (bottom) derivatives according to published methods, with my yields/scales indicated. HMPA = hexamethylphosphoramide

allyl bromide and hexamethylphosphoramide (HMPA) to give 4.6 g of the product (65%). Although both **A** and **B** were synthesized on gram scale, we were most attracted to **A** at the outset of our studies due to the accessibility of larger amounts (20 g vs. 4.6 g), as well as being able to avoid the copious amounts of pyrophoric *n*-butyl lithium required to generate the LDA necessary for the synthesis of **B**. With purified **A** in hand, we began the search for a catalyst and conditions that would create statistical copolymers with *rac*-LA.

Our screenings began using two of the first catalysts shown to statistically copolymerize ε-caprolactone and racemic-lactide (*rac*-LA), a set of bulky aluminum-salen catalysts bearing a benzyl alkoxide initiating group (Figure 3.10).[9] We chose to investigate both catalysts initially because previous reports had shown that the nature of the copolymerization reaction between ε-caprolactone and lactide is so sensitive to sterics that the change from a *tert*-butyldimethyl silyl (TBDMS) group to a triisopropyl silyl (TIPS) group on the salen ligand greatly impacted the statistical nature of the resulting copolymer.[9] For example, the reactivity ratio of *rac*-LA/caprolactone was reported at 2.6/1 for the TBDMS derivative and 0.73/1 for the TIPS derivative. We were curious to see how such steric interplay would affect the homo/copolymerization behavior of **A**, **B**, and *rac*-LA.

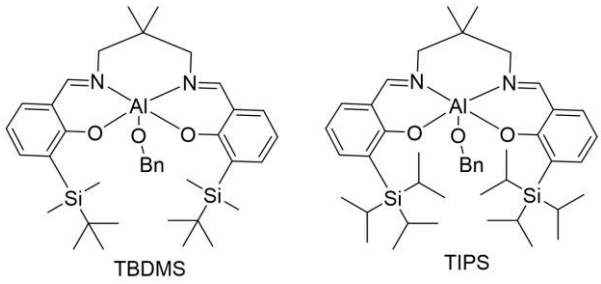

Figure 3.10. Aluminum-salen catalysts bearing bulky silyl groups. TBDMS = *tert*-butyldimethylsilyl and TIPS = triisopropylsilyl. Displayed are aluminum benzyloxide complexes, however, the precursor aluminum-ethyl complexes can be used in tandem with an alcohol initiator in solution.

Monomers **A** and **B** were initially tested for both homopolymerizations and copolymerizations with *rac*-LA using both the TBDMS and TIPS catalysts under the previously reported conditions (90 °C, 1M in toluene, 100:1:1 ratio between total monomer: catalyst: initiator).[9] To a 10 mL scintillation vial in a nitrogen filled glovebox was added either **A** or **B** for homopolymerizations or **A** or **B** and *rac*-LA for copolymerizations for a total monomer amount of 2.0 mmol. Toluene (2 mL) was added to make a 1M solution and one of the two bulky silyl catalysts was added at a 1% loading relative to total monomer concentration. Thus, the overall ratio of monomer: catalyst: initiator was 100:1:1 as the initiating group, benzyl oxide, was built into the starting catalyst. The reaction mixture was then heated at 90 °C for 20 hr, quenched with drops of methanol, volatiles removed *in vacuo* and conversions of monomers to polymers analyzed by ^{1}H NMR spectroscopy.

Intriguingly, under these conditions the two monomers show markedly different reactivities with the two catalysts, as determined by their respective conversions to polymer. The TBDMS derivative homopolymerized both **A** and **B**, showing >95% monomer conversion after 24 hours, but when copolymerization reactions were performed with *rac*-LA (1:1 monomer feed), **A** was polymerized only very slowly, showing low conversions (<40%) after 24 hr. Further analysis by NMR spectroscopy indicated that **A** was not polymerized until after all *rac*-LA was consumed, suggesting formation of a block-type copolymer. Monomer **B**, on the other hand, did not show any polymerization reactivity in the presence of lactide even after all *rac*-LA was consumed, which resulted in a mixture of PLA and monomer **B**. However, the drastic drop in reactivity of both **A** and **B** in copolymerizations with *rac*-LA, which itself maintains high levels of reactivity, show that under the experimental conditions the TBDMS catalyst will not form a statistical copolymer. Holding all conditions constant but switching catalysts to the

bulkier TIPS derivative showed that it was unable to perform even homopolymerizations of **A** (~0% conversion). Monomer **B**, on the other hand, was successfully converted into polymer during homopolymerizations with monomer conversions of >90% after 24 hr. Unfortunately, no conversion of **B** was observed in the presence of *rac*-LA, even while *rac*-LA was converted to > 75% polymer. The lack of success in the copolymerization reactions with the bulky silyl catalysts prompted us to widen our search for other reported catalysts (Figure 3.11).

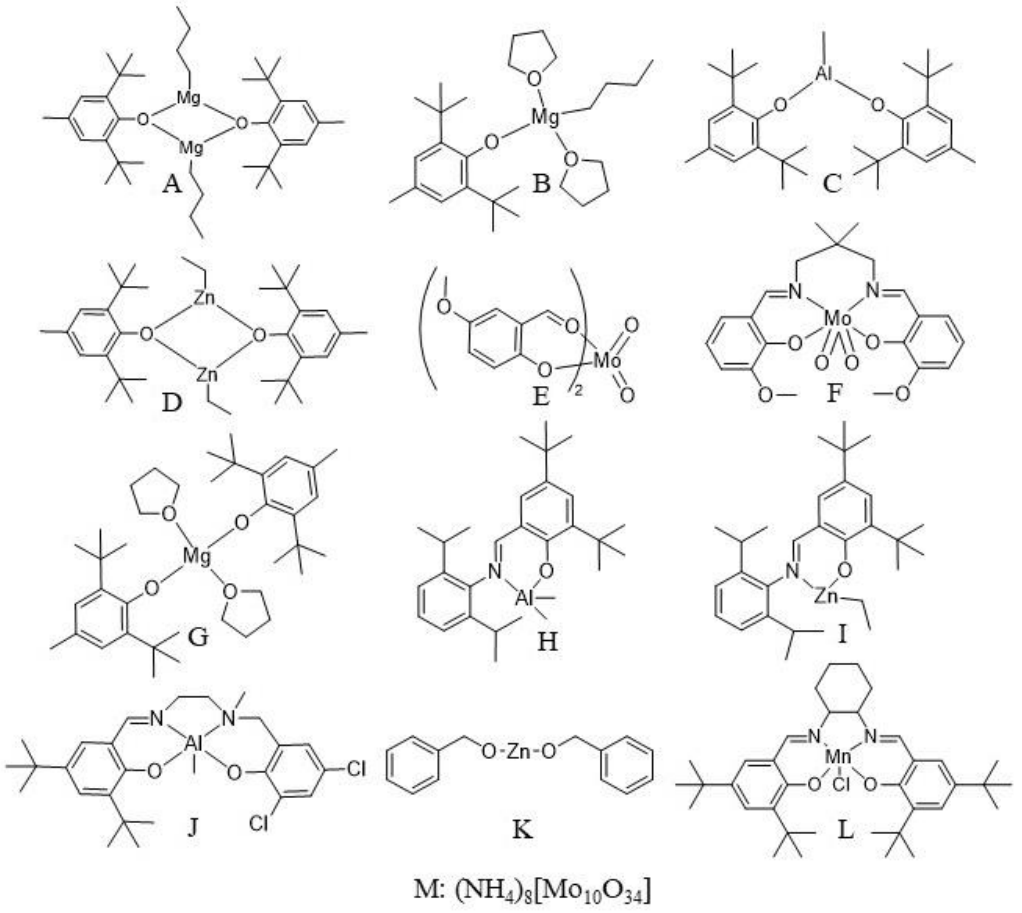

Figure 3.11. Catalysts tested for copolymerization ability

Homopolymerization reactions using these catalysts (Table 3.1) were typically clean, showing only the starting material monomer and the homopolymer, allowing for a comparison of

the allyl protons as a facile way to determine monomer conversions. We did note, however, that catalysts DPP, DBU, $Sn(OTf)_2$ and TBD often lead to broadened signals in ^1H NMR spectra making analysis difficult.

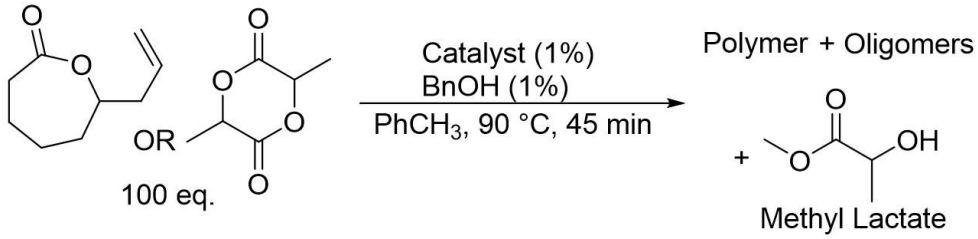

Catalyst	*Rac*-LA conversion %	6-Allyl-caprolactone conversion %
(A)	<1 (98)	>98%
(B)	<1 (99)	99%
(C)	30 (90)	53%
(D)	80 (82)	98%
(E)	9 (33)	8%
(F)	<1 (17)	1%
(G)	0 (99)	>98%
(H)	42 (99)	17%
(I)	78 (99)	91%
(J)	63 (99)	38%
(K)	88 (99)	84%
(L)	<1 (66)	<1%
(M)	<1 (98)	1%
$Sn(OTf)_2$	5 (66)	Unknown other material
DPP	Could not be determined	50%, unknown other material
DBU	Could not be determined	<1%
$MoO_2(acac)_2$	6 (9)	5%
$Sn(Oct)_2$	96 (98)	<2%
TBD	95 (98)	Could not be determined

Table 3.1. Conversion of monomers. For *rac*-LA two conversions are noted, the first is based on the total amount of PLA observed post quench relative to monomer and the second, shown in parentheses, is the modified conversion adjusted for PLA degradation to methyl lactate and oligomers post-quenching with methanol. 6-allyl caprolactone shows only conversion into its homopolymer. Acac = acetylacetonate, oct = octanoate, TBD = triazabicyclodecene, OTf = triflate, DPP = diphenylphosphate, DBU = 1,8-diazabicyclo[5.4.0]undec-7-ene

Surprisingly, upon analysis of homopolymerizations of *rac*-LA numerous catalysts yielded a mixture of products identified as PLA, lactide oligomers and methyl lactate. Initially it was unclear whether the mixture of products was due to PLA degradation upon methanol addition during reaction quenching or poor consumption of monomer under the experimental ROP conditions. Recently there has been extensive work devoted to the conversion of PLA into commodity chemicals such as alkyl lactates, leading us to consider the possibility of polymer degradation.[28] Indeed, upon stirring a sample of PLA in THF with methanol and a magnesium catalyst (1 wt%) at room temperature, methyl lactate was observed as the only product by ^{1}H NMR after 6 hr (Scheme 3.2). Furthermore, when *rac*-LA was subject to identical conditions, methyl lactate was not observed in appreciable quantities, suggesting that in the homopolymerization product mixtures methyl lactate resulted from PLA degradation and not degradation of the monomer. Thus, we hypothesize that *rac*-LA was first polymerized to PLA, but then degraded by rapid transesterification with methanol due to the Lewis Acid nature of the catalysts to yield byproducts, such as methyl lactate or oligomeric species during reaction quenching. With this information in hand, we indicate two conversions in Table 3.1, the first of which is the conversion of *rac*-LA as determined by the amount of PLA after quench with methanol. The second represents a modified conversion, which includes the total conversion of *rac*-LA into all observed species (PLA, oligomers, and methyl lactate). We found this to be an important distinction to make here as certain catalysts (e.g., A, B and D, Figure 3.10) that are

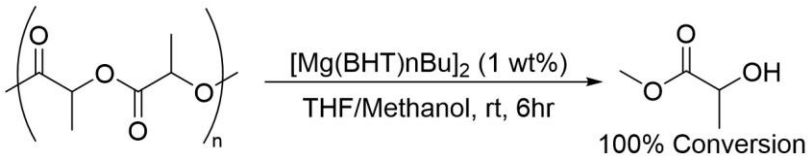

Scheme 3.2. Degradation of PLA to methyl lactate

both highly active for the polymerization of *rac*-LA and the degradation of PLA still offered a potential route to making statistical copolymers with monomer **A**.

Having identified several catalysts that show high reactivity for both *rac*-LA and **A** in homopolymerizations, we proceeded to examine their reactivities in copolymerizations with both monomers present in equal amounts (Table 3.2). The copolymerizations were set up identical to the homopolymerization procedure with a ratio of *rac*-LA: **A**: catalyst: initiator of 50:50:1:1 in toluene (1M) at 90 °C for 24 hr, with benzyl alcohol as the initiating group. As has been reported before, stark reactivity differences between the copolymerization and homopolymerization processes were observed.[9,19a,29] All catalysts showed a strong preference for lactide

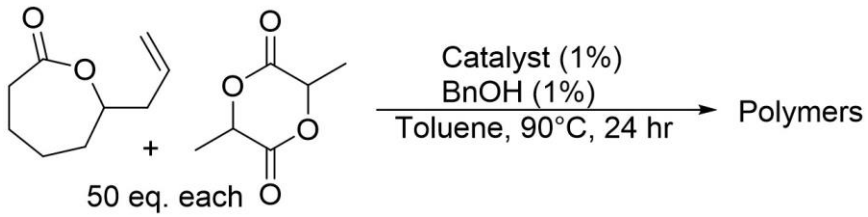

Catalyst	*Rac*-LA conversion (%)	6-Allyl caprolactone (A) conversion (%)
(A)	> 90%	<3%
(B)	> 90%	< 3%
(D)	>76%	<10%
(G)	> 90%	< 4%
(I)	74%	< 1%
(J)	< 33%	< 2%
(K)	91%	< 3%
$Sn(OTf)_2$	< 50%	< 3%
$La[N(TMS)_2]_3$	92%	< 2%
Me-TBD	> 90%	< 3%

Table 3.2. Conversion of monomers during 1:1 copolymerization between *rac*-LA and **A** using select catalysts at 1 mol%. Benzyl alcohol (1 mol%) as initiating group.

polymerization, with only small amounts of **A** being polymerized. Due to the ongoing difficulties of achieving sufficient reactivity of monomer **A**, at this point we questioned whether solution-based polymerizations were the problem and if better success may be found under neat/melt conditions (130 °C or higher).

Melt-type copolymerizations were initially performed with benzoic acid, which had recently been reported to statistically copolymerize caprolactone and lactide.[30] According to ^{1}H NMR spectroscopy data, copolymerizations between **A** and *rac*-LA showed near equal reactivity between monomers using benzoic acid at 155 °C for 24-48 hr with a 10% catalyst loading and 1% benzyl alcohol as initiator. To ensure that the two monomers were being consumed in tandem and not independent as two separate homopolymerizations, ^{13}C{^{1}H} NMR spectroscopy monitoring was employed and five different monomer feeds were tested (**A**: *rac*-LA of 9:1, 7:3, 1:1, 3:7 and 1:9). As shown in Figure 3.11, we observed distinct peak changes for linkages between the two monomers, where LA represents *rac*-LA and CL represents 6-allyl caprolactone (**A**). Our assignment of the peak linkages was based on literature reports of *rac*-LA and ε-caprolactone copolymerizations, and comparison to homopolymers of **A**.[9] PLA type peaks (LA-LA), are observed up field of 170.0 ppm while lactide monomer linked to **A** (CL-LA) peaks are found between 171.0 and 170.0 ppm. Likewise, homopolymer-like blocks of **A** (CL-CL) can be observed near 173.3 ppm, with surrounding peaks being linked to **A** carbonyls adjacent to a lactide monomer (labeled as CL-LA). We observed a strong preference for LA-LA linkages when *rac*-LA was in excess (bottom two spectra, Figure 3.12) with very little CL-CL blocks. When monomer **A** is the reagent in excess (top two spectra, Figure 3.11), the opposite result was found, wherein CL-CL linkages are preferred and LA-LA blocks are only observed as a small portion of the product. Under an equimolar feed a balanced reaction took place where CL-CL,

CL-LA and LA-LA linkages were observed at near equal ratios. Furthermore, both ^{1}H and $^{13}C\{^{1}H\}$ NMR showed residual monomer in the reaction mixtures that was present in comparable ratios to the initial monomer feed for each reaction.

Concurrent with our tests using benzoic acid, we also performed neat/melt reactions using other simple, commercially available reagents (see list in Figure 3.11). $^{13}C\{^{1}H\}$ NMR spectroscopy data showed similar levels of success for statistical copolymerizations between either **A** or **B** and *rac*-LA. We observed that **A** showed copolymer composition proportional to

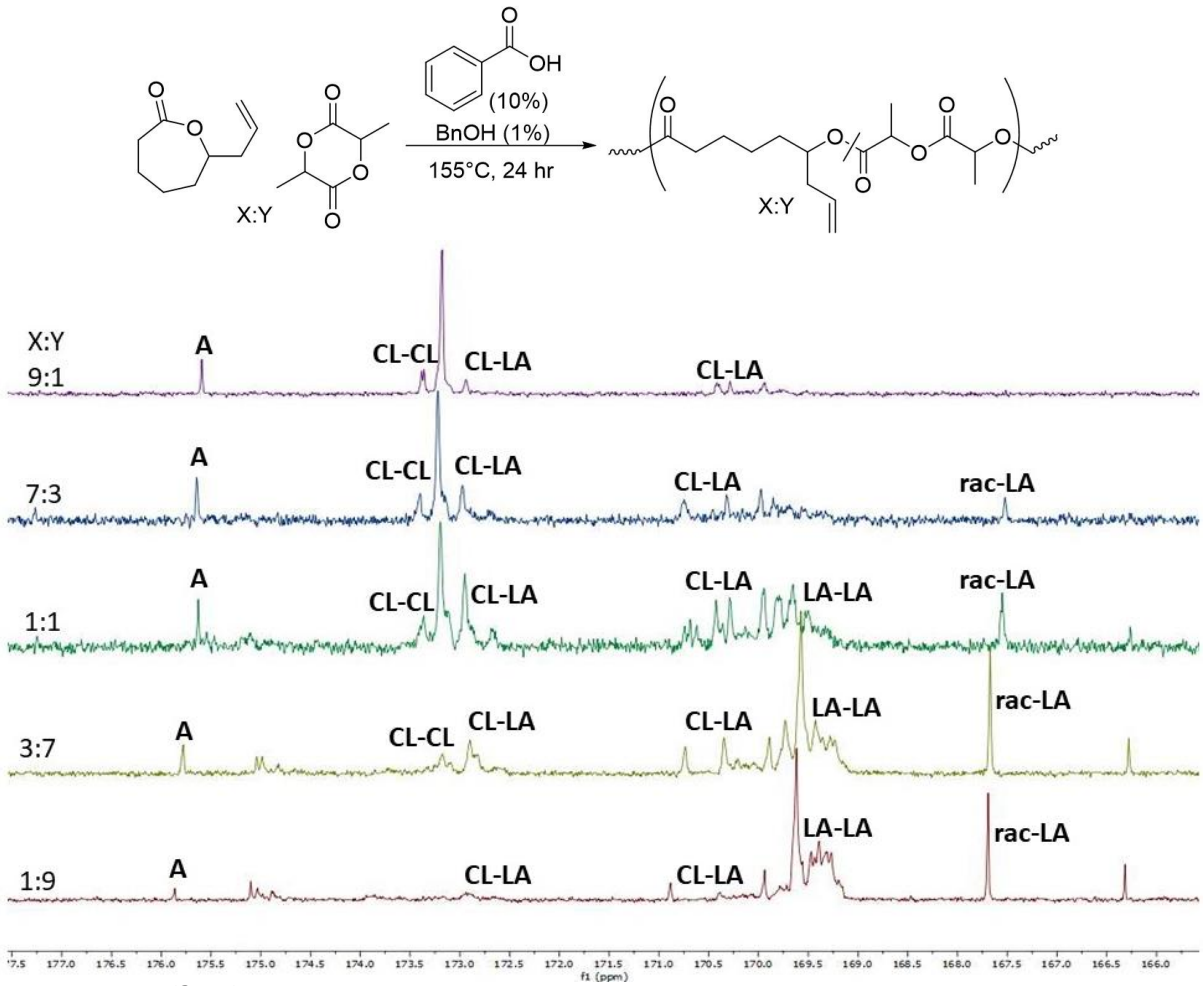

Figure 3.12. $^{13}C\{^{1}H\}$ NMR of copolymerization between **A** and *rac*-LA using benzoic acid (10%) as catalyst and benzyl alcohol (1%) as initiator. X and Y represent the ratio of **A** and lactide, respectively. CL represents **A** (6-allyl caprolactone) and LA is *rac*-LA.

the monomer feed ratio for $Al(O^{i}pr)_3$, $Zn(lactate)_2$, $BiPh_3$ and $Sn(oct)_2$ at 1% or less catalyst loadings. Monomer **B** was consumed in statistical copolymerizations with diphenyl phosphate (DPP, 5% loading), triazabicyclodecene (TBD, 5-10% loading, 48+ hr), $Al(O^{i}pr)_3$, $Zn(lactate)_2$, $BiPh_3$ and $Sn(oct)_2$. Copolymerizations with DPP, TBD and benzoic acid were slow, showing conversions of ≤50%, even after 48-72 hr with high catalyst loadings (>5%) and temperatures (135-155 °C). They also proved incapable of performing the copolymerizations at higher scales (>4 mmol), which unfortunately made their use impractical for isolating the desired polymers on a synthetically useful scale. On the other hand, although $Al(O^{i}pr)_3$, $Zn(lactate)_2$, $BiPh_3$ and $Sn(oct)_2$ showed some success in copolymerizations of monomers **A** and **B**, the reactions produced inconsistent yields and often led to the reaction medium gelling, making reproducibility an issue. Overall, even with several catalysts showing potential to make statistical copolymers, we were unable to synthesize copolymers on useful scales under readily reproducible conditions, usually obtaining a maximum of 100-200 mg of copolymer after purification by precipitation with a varied level of statistical reactivity ($^{13}C\{^{1}H\}$ NMR).

Due to issues of low conversion observed in both solution-based and neat copolymerizations and gelling under melt conditions for both **A** and **B** with *rac*-LA, we altered our approach by focusing on the monomer used instead of reaction conditions. We decided to begin with a solution-based copolymerization to avoid gelling and diffusion constraints of neat/melt polymerizations. We hypothesized that the new monomer, 3-vinyl caprolactone (**C**), would behave in a similar fashion to unfunctionalized ε-caprolactone because the steric hindrance of the smaller vinyl group (versus allyl) would be decreased at the three-position of the ε-caprolactone ring, thus avoiding disrupting carbonyl coordination, while still maintaining the same primary alkoxide in the propagation step of the coordination-insertion mechanism (*vide*

supra, Figure 3.5). According to this hypothesis, we envisioned that **C** would be suitable for preparing a statistical copolymer with *rac*-LA using known catalysts and methods in solution. Monomer **C** was synthesized in three steps from ε-caprolactone (Scheme 3.3). First, ε-caprolactone was converted into a silyl-enol ether on a 30 g (66% yield) scale by trapping the enolate generated upon reaction with lithium diisopropylamide (LDA) with chlorotrimethylsilane TMSCl).[31] A palladium catalyzed reaction utilizing allyl methyl carbonate then produced an unsaturated ε-caprolactone product, 6,7-dihydrooxepin-2(5H)-one (40 g, 89%).[32] The unsaturated ε-caprolactone is susceptible to 1,4-addition by vinylmagnesium bromide, which generated 3-vinyl caprolactone on synthetically useful yields of 1-3 g (≤45% yield). To the best of our knowledge **C** had not been synthesized previously and its purity and structure were ascertained by ^{1}H, $^{13}C\{^{1}H\}$, COSY and HSQC NMR spectroscopy (Figures 3.25-3.28).

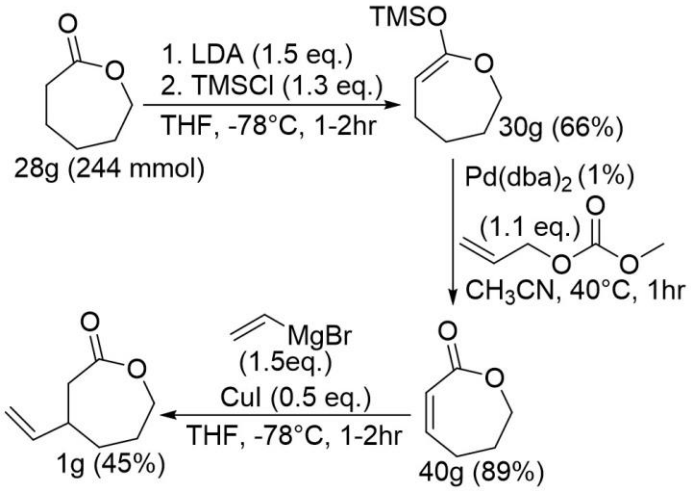

Scheme 3.3. Three step synthesis of 3-vinyl caprolactone

With **C** in hand, we initiated copolymerization studies using the bulky aluminum-salen TIPS compound initially tested for monomers **A** and **B** under the same conditions (50:50:1:1 *rac*-LA: **C**: catalyst: initiator, 1M in toluene, 90 °C, 24 hr, Figures 3.10 and 3.13). Gratifyingly, upon removal of volatiles, ^{1}H NMR analysis of the resulting copolymer showed that both *rac*-LA and

C were converted at near equal amounts. Varying the monomer feeds of *rac*-LA: **C** to 9:1, 7:3, 1:1, 3:7, and 1:9 ratios and analyzing the resulting copolymers by $^{13}C\{^{1}H\}$ NMR spectroscopy showed the copolymer makeup was dependent on the monomer feed ratio (Figure 3.14). For example, when lactide was in excess (90%), monomer triads containing 3-vinyl caprolactone (**C**) were only observed bordering lactide units (LL). Likewise, when **C** was in excess (90%), triads all contain at least one unit of **C,** and a large block of polymerized **C** is the defining characteristic. At a 1:1 ratio of **C** and *rac*-LA an even distribution of triads including **C** and *rac*-LA was observed, showing an equal likelihood for either monomer to be incorporated into the copolymer. Taken together, the relative incorporation of monomers into the copolymers being proportional to the feed ratio of the copolymerization indicated a statistical process was achieved.

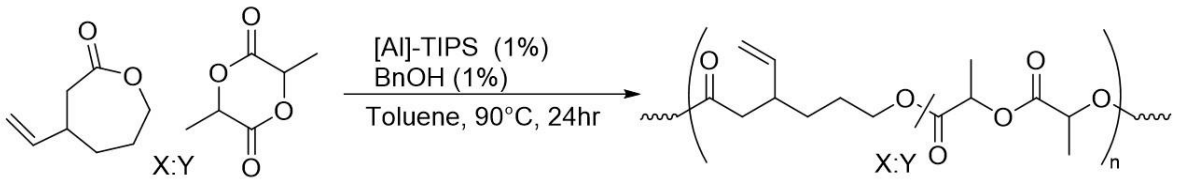

Figure 3.13. Copolymerization of **C** with lactide under optimized conditions

Having identified conditions for the statistical copolymerization of **C** with *rac*-LA, we isolated several polymers of varied levels of olefin incorporation by varying the feed ratio of the monomers but holding all other conditions constant. Monomeric ratios within the polymers were determined by the distinct ^{1}H NMR resonances for *rac*-LA and **C**. Detailed copolymer analysis (e.g., SEC) was only able to be performed on a select number of our copolymers, but good polydispersity (Đ) values (< 1.2) and controlled molecular weights were achieved when at a

100:1:1 ratio of total monomer: catalyst: initiator with the catalyst and initiator being the same (aluminum-TIPS benzyl oxide complex, Figure 3.9, Appendix D, Table D.2).

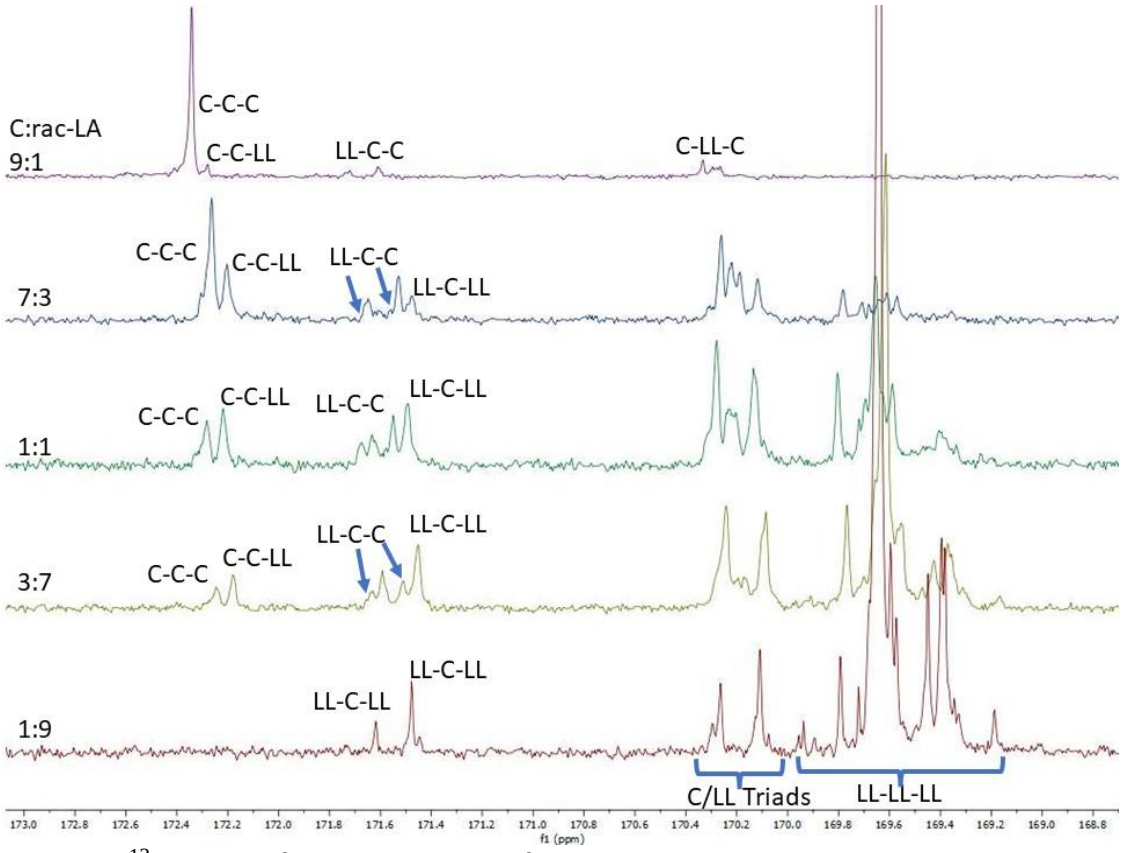

Figure 3.14. ^{13}C NMR of carbonyl region of *rac*-LA and monomer **C** copolymerizations at varied ratios

Theoretically, the maximum MW achievable under the monomer: initiator ratio (100:1) we used was ~15 kg/mol (depending on which monomer is in excess). We were interested to see if the current set of conditions would be capable of producing higher MW copolymers to maximize the number of olefins per chain, while maintaining low levels of incorporation of **C**. Thus, we made initial steps to gradually increase copolymer MW by varying the initiating alcohol (Figure 3.15). Two strategies were pursued to increase the MWs: decrease the overall loading of the Al-alkoxide (catalyst and initiator) and vary the initiating group only while keeping the concentration of Al constant (1 mol%) and starting from the Al-ethyl complex. The

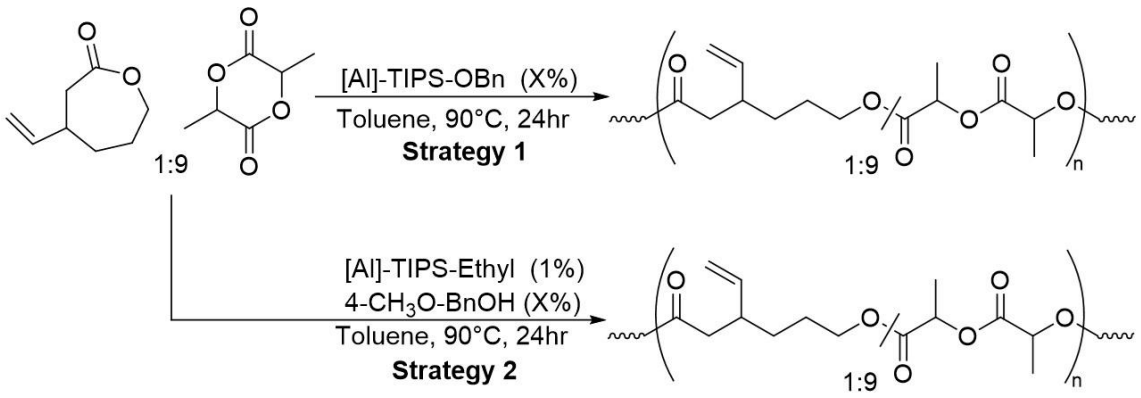

Figure 3.15. Attempts at molecular weight control of copolymers, where X represents the % of aluminum catalyst and the % of initiating benzyl alcohol.

Al-ethyl complex is the precursor material to the two Al-alkoxide catalysts seen in Figure 3.9, and it is proposed that the initiating alcohol (e.g., benzyl alcohol or 4-methoxybenzyl alcohol) first reacts at the Al-center to generate a unit of ethylene and the active Al-alkoxide catalyst. Beginning with our first strategy, we performed copolymerizations between *rac*-LA and **C** in a 9:1 molar ratio at a 2-4 mmol scale using the Al-TIPS-benzyl oxide catalyst while in toluene (1M) at 90 °C for an initial 24 hr. We found that decreasing the loading of Al-TIPS alkoxide below 1% drastically reduces the rate of reaction. For example, conversions of <20% were observed after 48 hr at an Al-TIPS-alkoxide loading of 0.5 mol%. For the second strategy, starting from a constant loading of Al in the form of Al-TIPS-ethyl at 1 mol%, but varying the initiating group, 4-methoxybenzyl alcohol, from 5% to 0.3%, a maximum MW of 30 kg/mol was observed (conventional polystyrene analysis, Table 3.3). Initiator loadings of 1%, 0.5% or 0.3% all produced copolymers with MWs near 30 kg with Đ values of 1.3. Switching initiating groups from benzyl alcohol to 4-methoxybenzyl alcohol had no discernible effect on monomer conversions but was often used because the methoxy group's ^{1}H NMR resonance at 3.80 ppm is a useful reference. At this point it is unclear why MWs observed by SEC do not match those

predicted by the initiator feed or why 30 kg/ mol appears to be the maximum MW, but we suspect catalyst decomposition plays a role, likely due to trace lactic acid or other impurities in one or both monomers.

Run	Monomer: Initiator	$M_{n,\,avg.}$ (NMR)	M_n Theory	Conventional Calibration Analysis			Yield (%)
				M_w (kg/mol)	M_n (kg/mol)	$Đ$ (M_w/M_n)	
1	20:1	4.1	2.9	9.8	6.9	1.4	49
2	100:1	16	14	27	21	1.3	58
3	200:1	36	29	30	23	1.3	64
4	300:1	48	43	30	23	1.3	67

Table 3.3. Copolymerizations of 3-vinyl caprolactone and *rac*-LA (1:9 ratio) while varying the amount of initiating alcohol and catalyst

Even with the MW of our copolymers under the present conditions (1M toluene, 90 °C, 24-48 hr) seemingly reaching a maximum around 30 kg/ mol (SEC), NMR spectroscopy still indicated a consistent statistical copolymerization was occurring in all cases. Therefore, the olefin moieties were still expected to be uniformly distributed across polymer chains and they were deemed suitable for post-polymerization functionalization reactions.

3.2.2. Post-polymerization Modifications

With statistical copolymers in hand, we set out to explore the versatility of post-polymerization reactions (Figure 3.16). For consistency, all copolymers used in the post-polymerization modification reactions were synthesized using the Al-TIPS-alkoxide at 1 mol% relative to total monomer (*rac*-LA + **C**) concentration (expected MW ~15 kg/mol). We initiated our post-polymerization reactions with thiol-ene chemistry, which is a proven method to utilize olefins as functional handles for the modification of polymers.[33] We therefore decided to begin

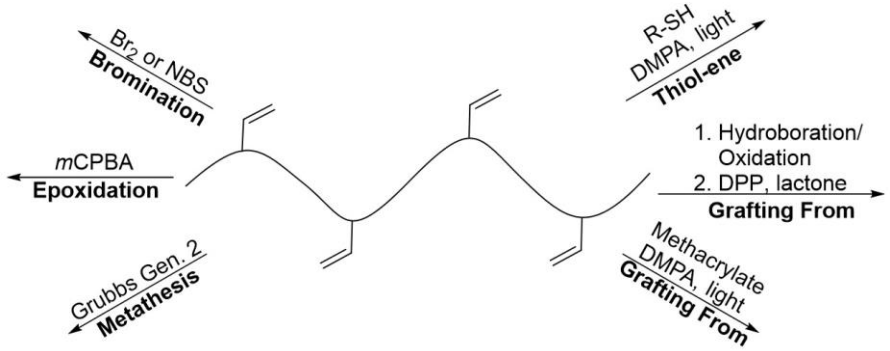

Figure 3.16. Post-polymerization modification type reactions performed and copolymers of rac-LA and **C**

our studies using a model thiol, 1-octane thiol, as a proof of concept for the thiol-ene transformation using standard conditions reported in the literature with 2,2-dimethoxy-2-phenylacetophenone (DMPA, 0.5 equivalents) as the radical initiator under ultraviolet (UV, 350-400 nm) light irradiation.[34] Ten equivalents of thiol relative to the vinyl groups of the copolymer were used while in $CHCl_3$, showing complete consumption of the vinyl groups within 1 hr (^{1}H NMR, Figure 3.16). Comparison to the starting material polymer showed that exactly one equivalent of 1-octane thiol was incorporated per vinyl group of the starting material copolymer, indicative of a successful, controlled reaction.

Following the success with a small molecule addition with 1-octane thiol, we then moved to the addition of longer chains. Poly(dimethylsiloxane) (PDMS) is a commercially available polymer that can be purchased with variable end groups or substituents throughout the polymer. Two thiol-containing derivatives were purchased from Gelest, Inc. (Figure 3.17) and subject to our thiol-ene reaction conditions. Although the presence of multiple thiol groups could potentially lead to crosslinking between polymer strands, we aimed to avoid this by using excess of the PDMS reagents (five equivalents). We were unable to ascertain whether any crosslinking had occurred due to the high molecular weights and oily nature of the PDMS reagents (MW = 7-

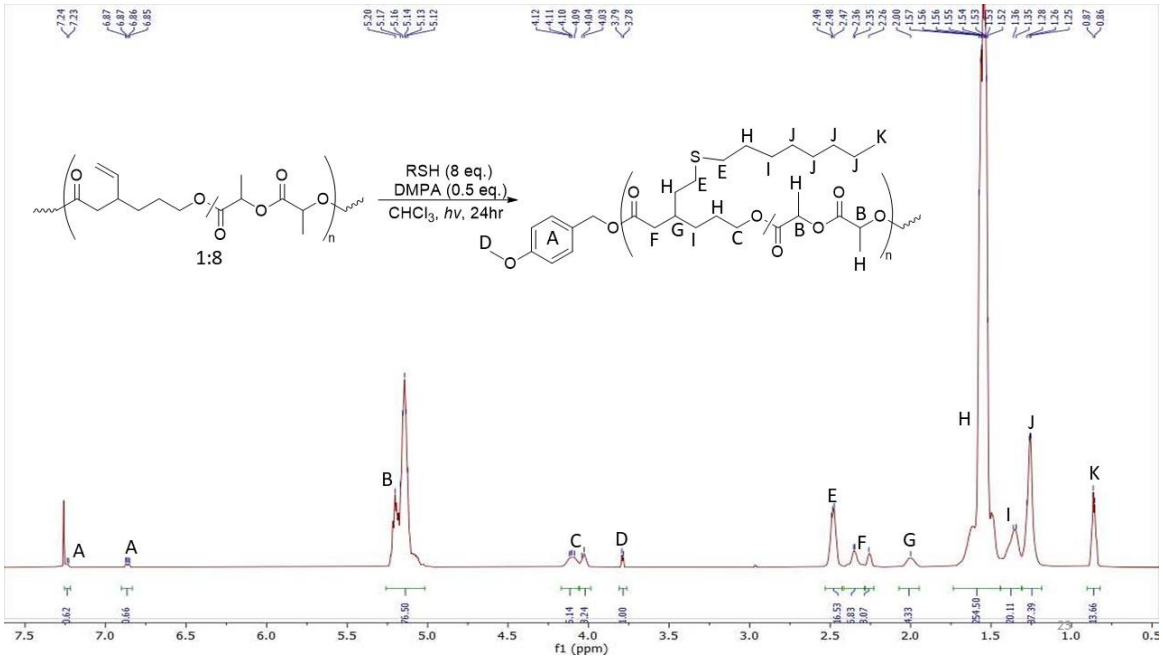

Figure 3.17. Thiol-ene reaction where R = octane, and the copolymer of **C** and rac-LA is made up of a 1:8 ratio

10 kg/mol), which led to products as fluffy white solids that were highly soluble in most organic solvents. Starting with the mercapto-terminated PDMS derivative, Figure 3.18 (left side), under UV irradiation, consumption of the vinyl group occurred within 2 hr using DMPA as the radical initiator (Figure 3.19). Precipitation of reaction mixtures into hexanes or diethyl ether readily removed excess unreacted PDMS materials, yielding a new copolymer species as a white fluffy solid (75% yield). The ^{1}H NMR spectrum of this solid contained new peaks near 0.07 ppm (^{1}H

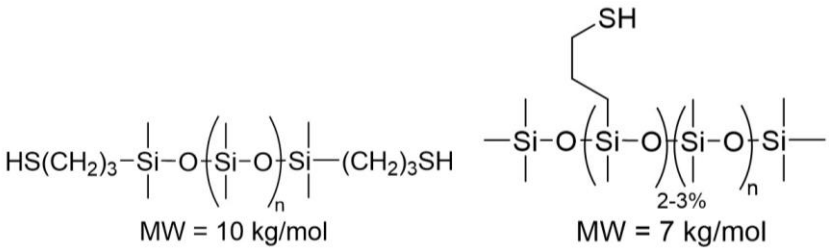

Figure 3.18 mercaptopropyl terminated PDMS and [2-3% (mercaptopropyl)methylsiloxane-dimethylsiloxane copolymer reagents

NMR), indicative of the PDMS chain. To further verify that the PDMS chain was in fact attached to the starting material copolymer diffusion-ordered spectroscopy (DOSY) NMR was performed. The data showed a single diffusion coefficient that differed from the mercapto-terminated PDMS starting material, consistent with successful attachment (Figure 3.20).

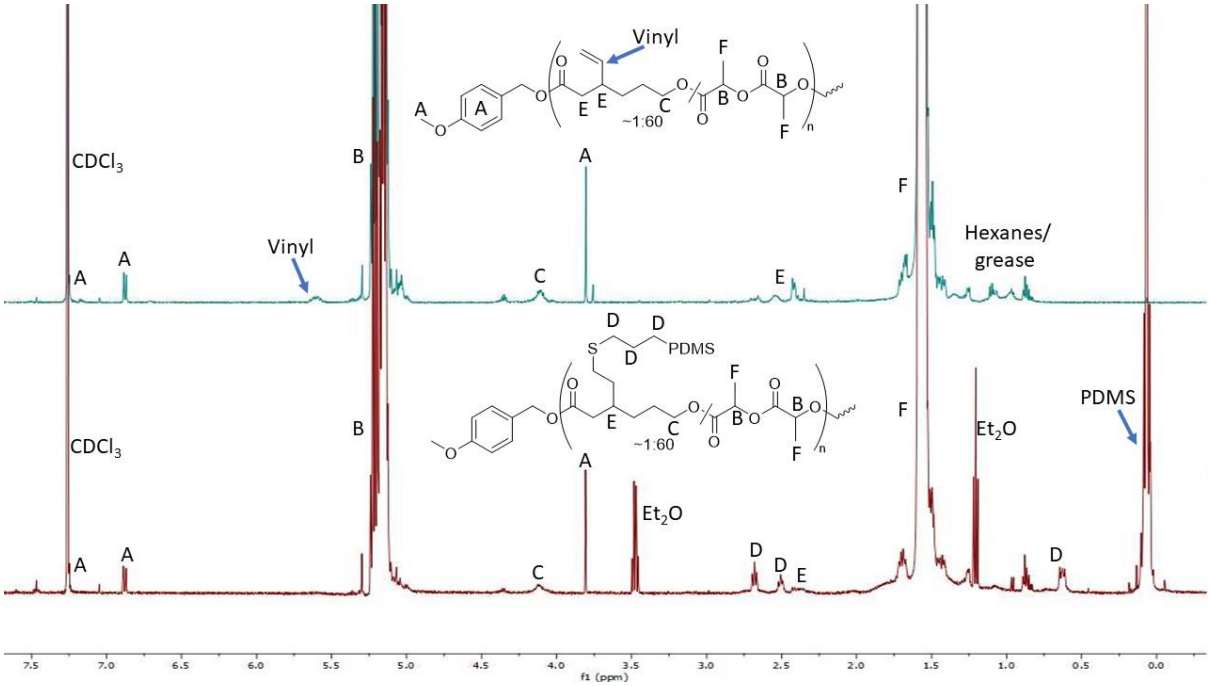

Figure 3.19. Thiol-ene reaction of copolymer with mercapto-terminated PDMS. Top) starting material copolymer. Bottom) PDMS incorporated product

With olefins being susceptible to radical chemistry, we predicted that the vinyl groups of our copolymers could be crosslinked using our now established thiol-ene methodology by using a short-chained dithiol as a crosslinker. 1,6-Hexanedithiol (0.5 equivalents relative to copolymer vinyl groups) was chosen as crosslinker in $CHCl_3$ with DMPA (0.5 equivalents) as initiator. Within 30 min of the homogeneous reaction mixture being exposed to UV light the solution became a solid mass (Figure 3.21). When the exact same reaction was performed but without the inclusion of the dithiol crosslinker, the solution still gelled and become solid, but required

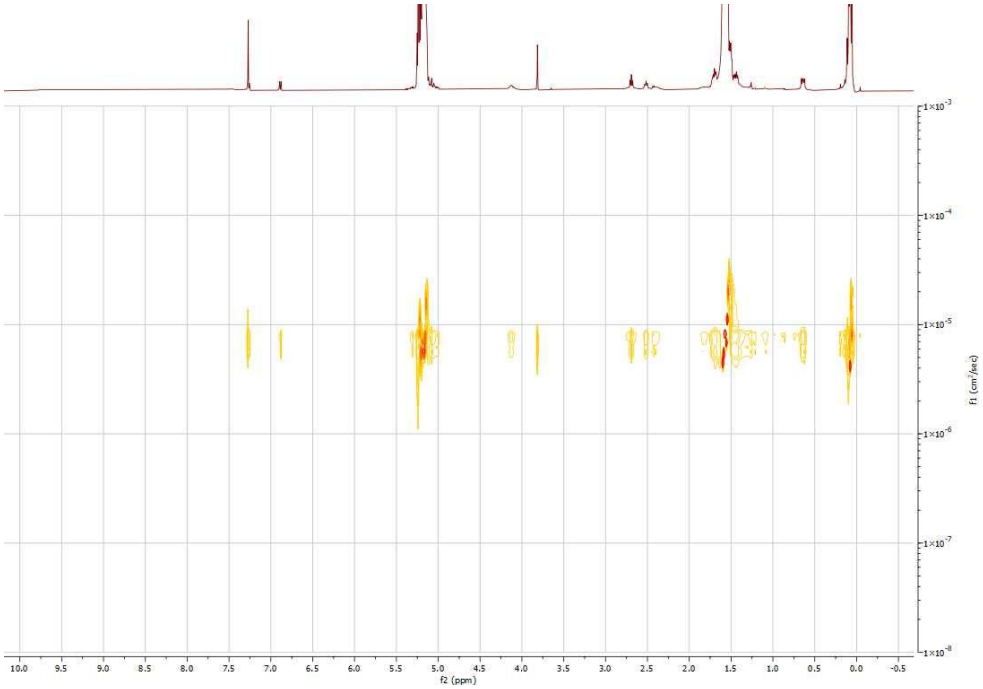

Figure 3.20. DOSY NMR of PDMS containing copolymer after thiol-ene reaction

reaction times of over 8 hr. We hypothesize that under UV light DMPA was still able to generate radicals that could react with the vinyl groups of the copolymers, leading to crosslinking events. However, crosslinking reactions were made more efficient using dithiols, which could generate more accessible thiol-radicals with DMPA leading to a faster crosslinking process. ^{1}H NMR analysis showed the disappearance of vinyl groups while maintaining other resonances in support of crosslinking. Furthermore, reaction products showed properties characteristic of crosslinked materials such as gelling/swelling with the addition of organic solvents.

Upon successful realization of polymer post-polymerization modification by thiol-ene chemistry we sought to achieve a polymer grafting-from approach, whereby a polymer chain or unit would be grown off the existing copolymer instead of added to it. Two types of grafting-from reactions were performed, a ring-opening polymerization (ROP), and a free-radical polymerization (FRP) (Scheme 3.4). To accomplish the former, we first needed to convert the

vinyl group into an alcohol, which was achieved through a hydroboration-oxidation sequence, resulting in a primary alcohol that then serves as an initiator for ROP of a cyclic ester. Alternatively, we anticipated that the vinyl group could be polymerized directly with another olefin, such as methacrylate, by photo-induced radical initiation with DMPA. Hydroboration-oxidation of the vinyl group was achieved using borane complexed to dimethyl sulfide (two equivalents) in THF, which resulted in a gelled material, similar in appearance to the previously discussed thiol-ene crosslinked polymers. Subsequent addition of excess H_2O_2 and NaOH quickly turned the gelled material back into a clear homogenous solution. Upon workup, ^{1}H NMR spectroscopy data confirmed the disappearance of the vinyl group and showed the monomer connections between LA-**C** as directly observed by protons "D" (indicating that chain-scission did not occur; Figure 3.22, top spectrum versus middle).

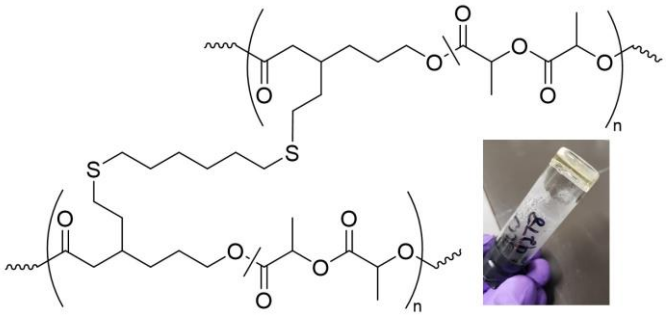

Figure 3.21. Crosslinked copolymer using 1,6-hexanedithiol as a crosslinking agent.

For grafting-from ROP reactions, the hydroxyl group-containing copolymer was combined with DPP (5%) as catalyst and ε-caprolactone (20 equivalents per hydroxyl group) in toluene (0.5-1M) and heated to 70 °C for 18 hr (Figure 3.22 bottom spectrum). Subsequent precipitations into hexanes, ether and methanol removed any residual ε-caprolactone monomer or polycaprolactone homopolymer that may have been formed by an adventitious initiator, such as water. DOSY NMR supports the existence of a single polymer chain (Figure 3.58). Having

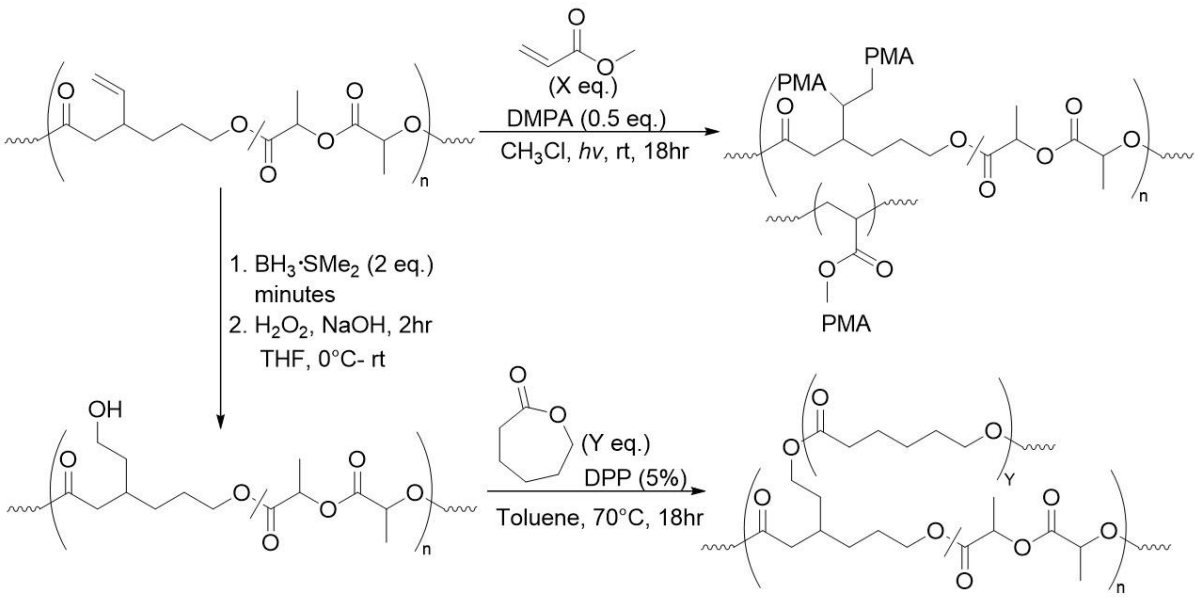

Scheme 3.4. Free-radical polymerization (FRP) of poly(3-vinyl caprolactone-co-lactide) with methacrylate (top). Hydroboration-oxidation of copolymer to convert vinyl group to primary alcohol (left). Grafting-from ring-opening polymerization (ROP) of caprolactone using the primary alcohol of the copolymer as initiator (bottom).

established a successful grafting-from ROP with ε-caprolactone the PCL chain length was then varied from the copolymer from 3-50 equivalents to demonstrate the tunability of these materials (Figure 3.23). The PCL chain, observed most clearly at 4.05 and 2.30 ppm by ^{1}H NMR, shows the expected increase in CL-CL linkages for PCL formation as the number of ε-caprolactone equivalents increased in the grafting-from ROP. At the same time the CL-LA links and PLA segments (labeled A and B in Figure 3.22) remain constant, indicating no chain scission occurred between *rac*-LA and **C**.

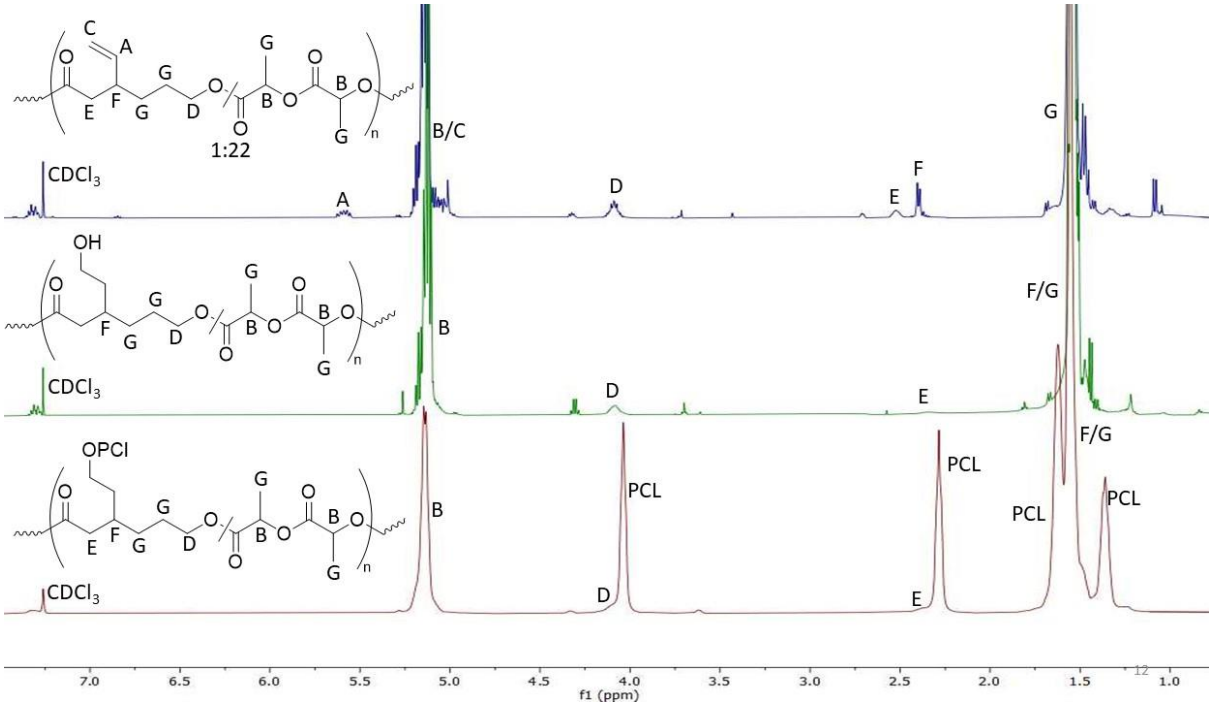

Figure 3.22. Top: Copolymer 22:1 rac-LA:**C**. Middle: Hydroboration-oxidation product. Bottom: product of grafting from reaction using DPP (5%) as catalyst and caprolactone (20 equivalents) and monomer. Note that protons A and C are found in the range off 2.20-2.45ppm but are difficult to see in the stacked spectra. See appendix for other characterization.

We also polymerized methacrylate from the vinyl group of the new copolymers, obviating the need for a hydroboration-oxidation pre-functionalization. Copolymer, combined with methacrylate (15 or 50 equivalents) and DMPA (0.5 equivalents) in $CHCl_3$, was exposed to UV light for 18 hr. ^{1}H NMR spectroscopy analysis showed disappearance of the vinyl groups from the copolymer as well as new peaks at 3.65, 2.30 and 1.95 ppm indicative of polymethacrylate (PMA, Figure 3.24). DOSY NMR analysis confirmed the PMA chain is connected to the copolymer as all signals correspond to a single diffusion coefficient (Figure 3.63).

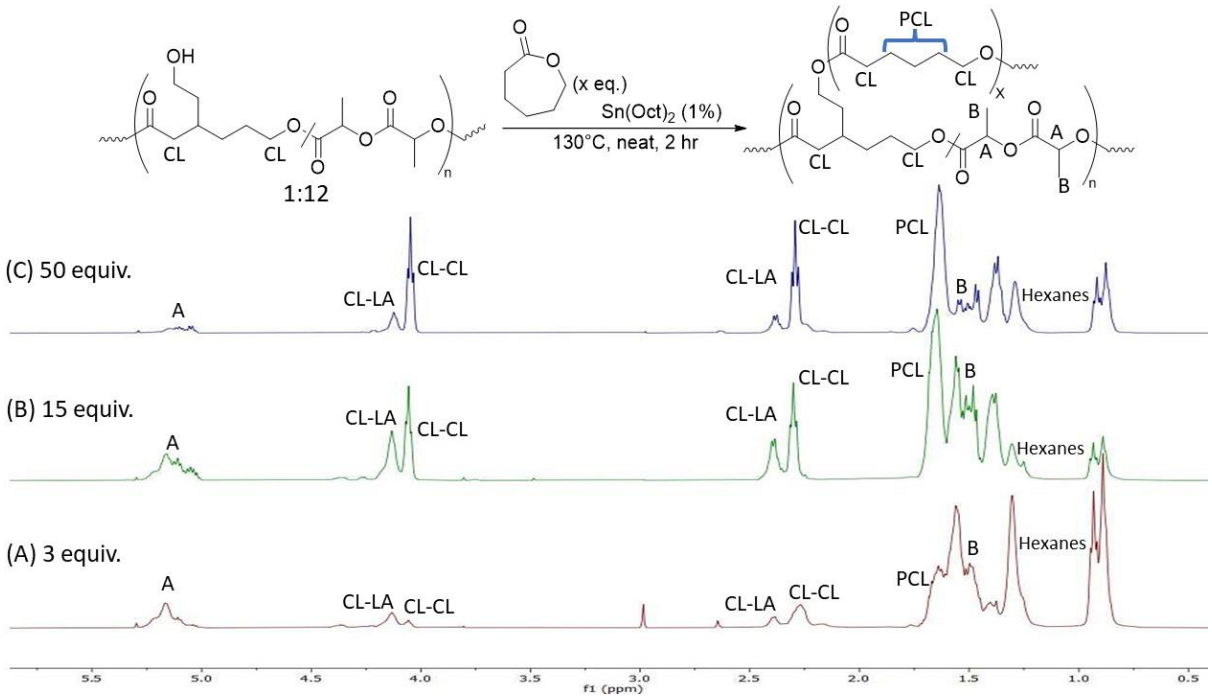

Figure 3.23. ROP graft from reactions varying caprolactone amounts. (A) three equivalents of caprolactone, (B) 15 equivalents of caprolactone, (C) 50 equivalents of caprolactone. The reactions were performed neat at 130 °C for two hr. A and B represent peaks from rac-LA polymer, CL represents peaks from caprolactone monomers. CL-LA indicates a unit of caprolactone monomer next to rac-LA whereas CL-CL indicates adjacent caprolactone units

Finally, we sought to use the vinyl group of our copolymers for metathesis reactions. Poly(ethylene glycol) (PEG) is a useful polymer and is known to have properties differing from PLA, such as its increased water solubility.[35] It was therefore of interest to see if we could incorporate a PEG chain onto the olefin-containing copolymers. Polyethylene glycol monomethyl ether (MW = 2 kg/mol) was purchased from Sigma Aldrich, and an allyl group installed through known methods by reaction with allyl bromide and KO^{t}Bu.[58] The PEG-O-allyl was then combined with copolymer in $CHCl_3$, with Grubbs generation 2 catalyst (2 mol% relative to copolymer vinyl groups) and heated to 55 °C for three days (Scheme 3.5). After numerous precipitations into methanol to separate the PEG-O-allyl starting material, ^{1}H NMR spectra of the material showed a new peak at 3.63 ppm, indicative of the ethylene units of PEG

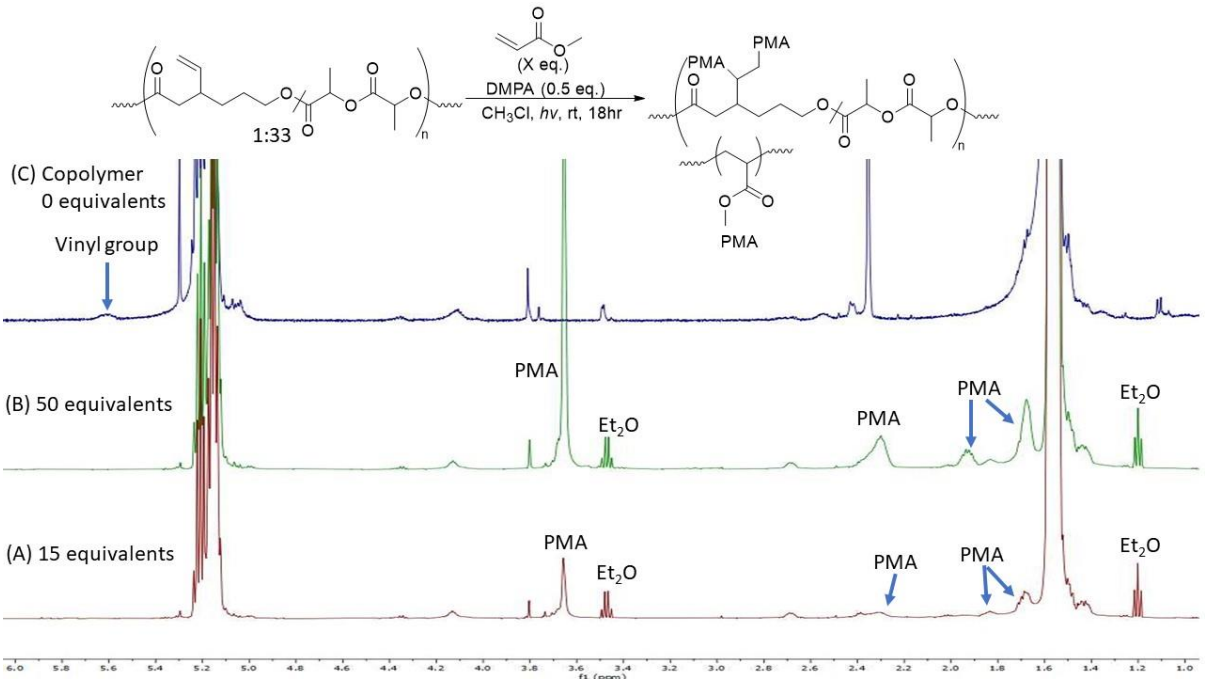

Figure 3.24. Graft from reactions using photo-initiating conditions and methacrylate. (A) 15 equivalents of methacrylate relative to vinyl group, (B) 50 equivalents of methacrylate, (C) starting material copolymer made up rac-La: 3-vinyl caprolactone (33:1)

(Experimental, Figure 3.65). Olefinic protons were still observed as expected, showing two signals at 5.46 and 5.58 ppm in a 1:3 ratio, perhaps due to an E:Z preference across the new double bond. To confirm the incorporation of PEG onto the copolymer, DOSY NMR was performed and showed a polymer chain with a single diffusion coefficient, indicating a successful metathesis reaction between our copolymer and the allyl-PEG (Figure 3.66).

Having successfully demonstrated the possibility to perform grafting-to and grafting-from reactions with our copolymers, we decided to demonstrate two other simple transformations that had previously been demonstrated on homopolymers of 6-allyl caprolactone

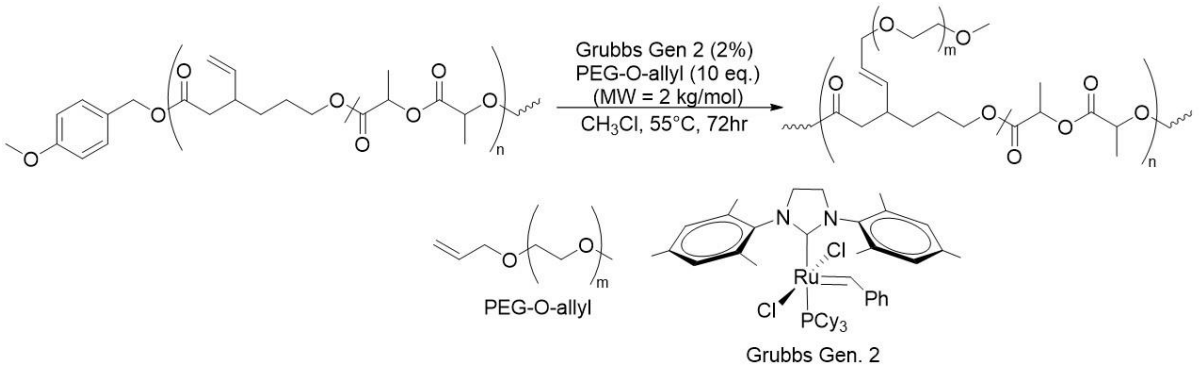

Scheme 3.5. Metathesis grafting-from reaction using polyethylene glycol monomethyl ether capped with an allyl group (PEG-O-allyl).

(**A**) and copolymers with lactide: bromination and epoxidation (Scheme 3.6).[36] Bromination of the vinyl protons occurred readily (2 hr) through addition of 1.2 equivalents of Br_2 to a solution of copolymer in $CHCl_3$. ^1H NMR spectra showed clear consumption of the vinyl group, while other ^1H resonances remained unchanged (Experimental, Figures 3.67, 3.68). Likewise, the vinyl groups of our copolymers were converted into epoxides by addition of 1.3 equivalents of *m*CPBA to a solution of copolymer in CH_2Cl_2 at room temperature and stirring for 18 hr. ^1H NMR spectra showed disappearance of the vinyl protons of the copolymer (Experimental, Figures 3.69, 3.70). ^1H NMR spectra of both bromination and epoxidation reaction products also

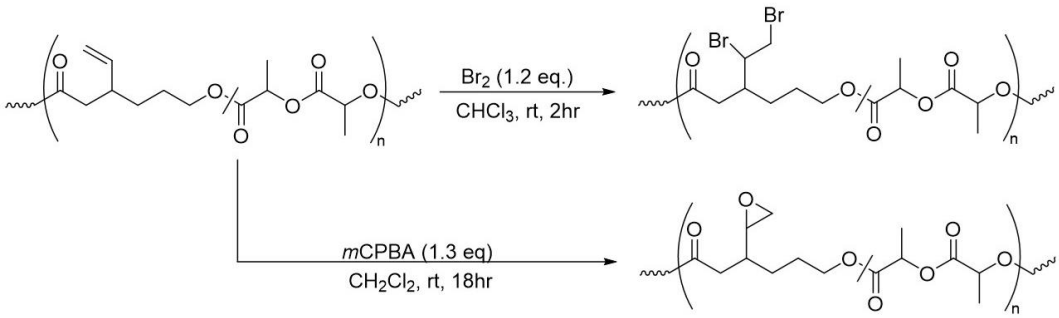

Scheme 3.6. Bromination of copolymer with Br_2 to make the dibrominated product (top). Epoxidation of copolymer with *m*CPBA (bottom)

showed new complicated signals due to the now diastereotopic proton couplings between the vinyl group and methine proton of **C**.

Although beyond the scope of this work, we anticipate that the addition of bromine to the copolymers could open the door to performing atom transfer radical polymerizations as an alternative grafting-from method or as an electrophile for nucleophilic additions. The epoxidation of the vinyl group could affect the solubilities of the copolymer depending on the ratio of monomers or it could be ring opened to an alcohol as differing way to generate an alcohol for ROP.

3.3. Conclusions and Outlook

The statistical copolymerization of *rac*-LA with either allyl or vinyl caprolactones was accomplished under various conditions. ε-Caprolactones bearing an allyl group at the 6- or 2-position (monomers **A** and **B**, respectively) proved capable of achieving statistical copolymerizations while under neat/melt conditions (135 °C+) with numerous commercially available catalysts. Unfortunately, due to the diffusion limitations and suspected tendency to crosslink allyl groups over the course of the reactions, yields and/or conversions were low and reproducibility was problematic. By placing a vinyl group at the 3-position of the ε-caprolactone ring (monomer **C**) these limitations were circumvented and solution-based conditions using a bulky aluminum-salen catalyst were identified to form statistical copolymers with *rac*-LA.

Upon achieving the desired copolymerization conditions with **C**, we successfully synthesized copolymers at various ratios of monomers to vary olefin density within the copolymer. High molecular weight copolymers were not achieved, however, with the highest MW attained being near 30 kg/mol. Post-polymerization modification reactions were performed on the copolymers including thiol-ene, metathesis, crosslinking, hydroboration-oxidation, bromination and epoxidation reactions. Grafting-from reactions also were achieved by using photo-induced radical polymerizations with methacrylate, or ROP of ε-caprolactone, using a pre-formed hydroboration-oxidation product. These methods enabled addition of different polymer chains to the parent copolymer such as polycaprolactone, polymethacrylate, poly(dimethylsiloxane) and poly(ethylene glycol).

We anticipate that this initial work, shown as a proof of concept, will inspire further improvements in the synthesis and mechanical testing of such PLA and PLACL derivatives. Future exploration could investigate the effect the density of vinyl groups on numerous aspects

of post-polymerization modifications, including crosslinking and the addition of small or large molecules to the parent copolymer. By being able to vary the number of olefins to functionalize, as well as the size and the properties of the group to be added, a highly tunable class of copolymers have been identified. Furthermore, the ability to create copolymers with very few vinyl groups (<5%) essentially enables the bio-renewability and degradability of PLA to be retained, while allowing the bulk material properties to be tuned. Mechanical testing (e.g., tensile strength, elasticity etc.) was beyond the scope of our study, but the opportunity to explore the physical characteristics of our copolymers to the users' desire will be of high interest.

One major limitation to our current copolymerization strategy was that the catalyst used was quite slow and possibly prone to degradation, which made it difficult to achieve copolymers of high molecular weight or achieve copolymers on large scale. Even under increased reaction times our system was limited to a MW of 18-30 kg/mol. Improvements upon this design or the investigation of other catalysts or conditions that avoid the pitfalls that plagued monomers **A** and **B** are likely necessary to make our copolymers of practical use. Several catalytic systems have recently been reported that could be of interest for the copolymerization of monomers **A-C** and may be suitable to addressing some of the limitations observed.[37] We also envision that the olefin group of monomers **A-C** could be further used in metathesis or radical-type polymerizations, serving a secondary role of a ROP post-polymerization modification. Taken together the present work represents a step toward the goal of finding alternatives to fossil fuel only based plastics, while potentially addressing shortcomings of PLA.

3.4. Experimental

Reagents and materials.

Anhydrous solvents, unless otherwise stated, were purchased from Fisher Scientific, degassed with argon and dried by aluminum column prior to use. All reagents purchased from commercial sources were used as received unless stated otherwise. *n*-Butyllithium (2.5M in hexanes, CAS: 109-72-8), magnesium chloride (anhydrous, >98%, CAS: 7786-30-3), paraformaldehyde (95%, CAS:30525-89-4), 2,2-dimethyl-1,3-propanediamine (99%, CAS: 7328-91-8), triethyl aluminum (93%, CAS: 97-93-8), benzyl alcohol (anhydrous, >98%, CAS:100-51-6), 4-methoxybenzyl alcohol (98%, CAS: 105-13-5), diisopropylamine (>99%, CAS: 108-18-9), chlorotrimethylsilane (>98%, CAS: 75-77-4), bis(dibenzylidineacetone)palladium(0) (CAS: 32005-36-0), copper(I) iodide (anhydrous, >99.995%, CAS:7681-65-4), vinylmagnesium bromide (1M in THF, CAS: 1826-67-1), *rac*-lactide (99%, CAS: 95-96-5), Hydrochloric acid (37%, CAS: 7647-01-0), allyl bromide (99%, CAS: 106-95-6), 1-pyrolidino-1-cyclohexene (97%, CAS: 1125-99-1), *meta*-chloroperoxybenzoicacid (mCPBA, ≤77%, CAS: 937-14-4), sodium bicarbonate (≥99.7%, CAS: 114-55-8), hexamethylphosphoramide (99%, 680-31-9) were purchased from Sigma Aldrich. Imidazole (99%, CAS: 288-32-4), dichloromethane (DCM, HPLC grade, CAS: 75-09-2), diethyl ether (HPLC grade, CAS: 60-29-7), tetrahydrofuran (THF, HPLC grade, CAS: 109-99-9), toluene (HPLC grade, CAS: 108-88-3), acetonitrile (MeCN, HPLC grade, CAS: 75-05-8), ethanol (CAS: 64-7-5) were purchased from Fisher Scientific. 2-bromophenol (98%, CAS: 95-56-7), *tert*-butyldimethylsilyl chloride (TBDMSCl, 97%, CAS: 18162-48-6), triisopropylsilyl chloride (TIPSCl, 98%, CAS: 13154-24-0), ε-caprolactone (99%, CAS: 502-44-3), allyl methyl carbonate (97%, CAS: 35466-83-2), were purchased from Oakwood Chemical.

Catalysts used were either available commercially or synthesized according to literature reports: A,[38] B,[38] C,[39] D,[40] E,[41]**Error! Bookmark not defined.** F,[42] G,[43] H,[44] I,[45] J,[46] K,[9] L,[47] M,[48] N,[49] O[50]. Deuterated solvents were purchased from Cambridge Isotopes. Nuclear magnetic resonance (NMR) spectroscopy was performed on a 500MHz Varian Unity Inova (^{1}H and ^{13}C{^{1}H}). Chemical shifts for ^{1}H NMR spectra were referenced to the residual protium in the deuterated solvent and ^{13}C NMR were referenced to the solvent itself. Before use, benzyl alcohol and ε-caprolactone were dried over calcium hydride, distilled under vacuum/argon and then stored in a nitrogen glovebox over activated 3Å molecular sieves prior to use. *Rac*-lactide was crystallized from toluene at least three times and dried under dynamic vacuum prior to use. Elemental analyses were performed by CENTC Elemental Analysis Facility, Department of Chemistry, University of Rochester, NY. For SEC data, the average molar mass values and molar mass distributions were determined by SEC using a tetrahydrofuran or chloroform mobile phase on an Agilent Infinity 1260 series HPLC system equipped with a Wyatt HELEOS-II multiangle laser light scattering detector and a Wyatt Optilab T-rEX diffractive refractive index detector through three Wyatt Stryagel HR columns at 25 °C and a flow rate of 1 mL min^{-1}. Conventional analysis reported herein is based off a polystyrene standard calibration curve. Data were provided by Elizabeth Kellstedt and Professor Marc Hillmyer at the University of Minnesota, Twin Cities.

3.4.1. Synthesis of Monomers

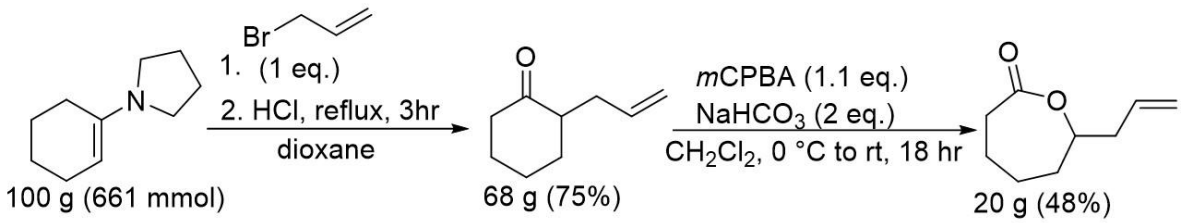

Scheme. 3.7. Two-step synthesis of 6-allyl caprolactone (monomer **A**)

Preparation of 6-allyl Caprolactone (A).

Step 1. 2-allyl cyclohexanone was prepared via literature procedure.[51] Synthesis was achieved on scales of up to 100 g (661 mmol), providing 68.1 g (75%) of product and could be carried on without purification. Product was determined by ^{1}H NMR to match that of the reported material. ^{1}H NMR (500 MHz, $CDCl_3$) δ_H 5.72-5.79 (1H, m), 4.98-5.03 (2H, m), 2.50-2.56 (1H, m), 2.26-2.38 (3H, m), 2.09-2.15 (1H, m), 2.04-2.07 (1H, m), 1.96-2.01 (1H, m), 1.83 (1H, m), 1.60-1.70 (2H, m), 1.32-1.40 ppm (1H, m).

Step 2. Baeyer-Villiger oxidation of 2-allyl caprolactone.[52] Baeyer-Villiger oxidations were successful on scales of up to 38 g (270 mmol) of 2-allyl caprolactone. Product was determined by comparison to the literature.[53] ^{1}H NMR (500 MHz, $CDCl_3$) δ_H 5.84 (1H, m), 5.13 (2H, m), 4.28 (1H, m), 2.65-2.70 (1H, m), 2.56-2.62 (1H, m), 2.45-2.52 (1H, m), 2.30-2.36 (1H, m), 1.92-1.97 (3H, m), 1.56-1.60 ppm (3H, m).

Notes: During the reaction large quantities of white solid forms, inhibiting the ability of the reaction to stir. Future work could use a mechanical stirrer. To extract as much product as possible excessive washings of the white solid were performed with dichloromethane. 3-chloro benzoic acid can be difficult to remove from the monomer but performing a vacuum distillation

after column chromatography proved successful in this regard.

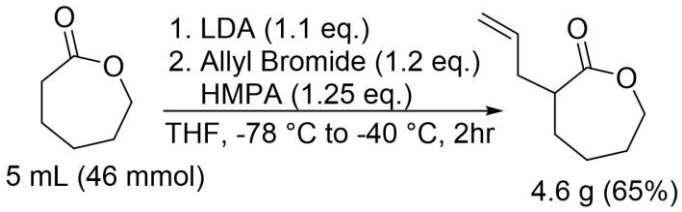

Scheme. 3.8. Synthesis of 2-allyl caprolactone (monomer **B**)

Preparation of 2-allyl Caprolactone (B).

Synthesis performed based on literature report.[54] Purification follows by column chromatography using a gradient from hexanes up to 1/10 EtOAc/hexanes (R_f = 0.12). Product determined by comparison to reported NMR data. ^{1}H NMR (500 MHz, $CDCl_3$) δ_H 5.78-5.86 (1H, m), 5.06-5.10 (2H, m), 4.20-4.31 (2H, m), 2.56-2.64 (m, 2H), 2.12-2.18 (1H, m), 1.91-2.00 (2H, m), 1.83-1.88 (1H, m), 1.68-1.78 (1H, m), 1.54-1.63 (1H, m), 1.37-1.46 ppm (1H, m).

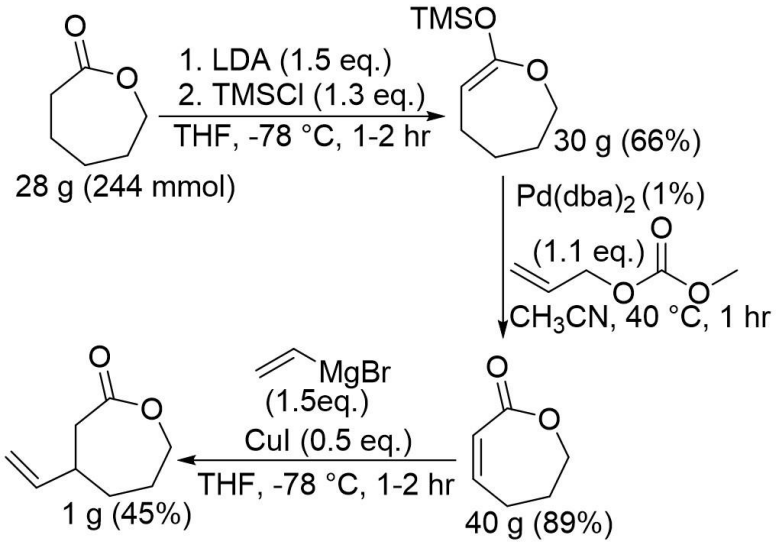

Scheme. 3.9. Three-step synthesis of 3-vinyl caprolactone (monomer **C**).

Preparation of 3-vinyl Caprolactone (C).

Trimethylsilyl ε-caprolactone enol ether. This procedure was adapted from a previous report. Note: For best success in the product purification by distillation, put the reaction mixture under vacuum (200-300 mTorr) at room temperature until it stops bubbling, meaning excess solvents and silane have been removed. Product can then be distilled at 55-60 °C, 250 mTorr (33.4 g, 50%). At the end of the distillation there are large amounts of solid/oily residue remaining Product determined by ^{1}H NMR, which matched literature reports. ^{1}H NMR (500 MHz, $CDCl_3$) δ_H 4.09 (1H, t, *J* = 5.9 Hz), 3.96 (2H, m), 1.99 (2H, quartet, *J* = 5.9 Hz), 1.80 (2H, quintet, *J* = 6.1 Hz), 1.61 (2H, quintet, *J* = 6.1 Hz), 0.19 (9H, s) ppm. ^{13}C{^{1}H} NMR δ (126 MHz, $CDCl_3$) δ_C 160.3, 83.4, 71.7, 31.5, 26.4, 23.5, 0.35 ppm.

6,7-dihydrooxepin-2(5H)-one. This procedure was altered from previous reports.[32,55] A solution of $Pd(dba)_2$ (2.01 g, 3.5 mmol, 1%) in anhydrous acetonitrile (1.0 L) was prepared within a glovebox. To this solution was added allyl methyl carbonate (43.5 mL, 383 mmol, 1.1 equivalent) in one portion via syringe, followed by the trimethylsilyl ε-caprolactone enol ether (64.8 g, 348 mmol, 1 equivalent). Upon addition the solution was immersed in an oil bath and heated to 40 °C. Upon heating, the solution will bubble vigorously as allyl methyl carbonate reacts with $Pd(dba)_2$, releasing CO_2, to form the active palladium-allyl species.[56] Once bubbling stops (<1 hour), the solution was cooled to room temperature and volatiles removed by vacuum. The dark yellow/black oil was then redissolved in diethyl ether and filtered through silica, and the filtrate concentrated to give a pale-yellow oil. Typically, no purification is needed of this compound, with the only impurity noticed being dba. (34.0 g, 87%). ^{1}H NMR (500 MHz, $CDCl_3$) δ_H 6.35 (1H, dt, J= 4.2, 12.2 Hz), 5.90 (2H, dt broad, J=2.5, 12.3Hz), 4.22 (2H, m), 2.45

(2H, m), 2.05 ppm (2H, m). $^{13}C\{^{1}H\}$ NMR δ (126 MHz, $CDCl_3$) δ_C 169.1, 143.9 (d), 121.8 (d), 37.3, 30.0, 26.9 ppm.

3-vinyl caprolactone. This procedure was adapted from previous reports for the synthesis of 3-vinyl cyclohexanone.[57] To a heterogeneous mixture of copper iodide (273 mg, 1.43 mmol, 0.08 equivalents) in anhydrous THF (21 mL) cooled to -78 °C was added a 1M solution of vinylmagnesium bromide in THF (29 mL, 29 mmol, 1.5 equivalents). The resulting dark brown/maroon solution was stirred for 10 min. Subsequently, a solution of 6,7-dihydrooxepin-2(5H)-one (2.19 g, 19.5 mmol, 1 equivalent) in THF (21 mL) was added dropwise by addition funnel over the course of 45 min. Upon complete addition the solution was then stirred an additional 30 min. A solution of saturated aqueous ammonium chloride was then added to quench the reaction as it warmed to room temperature. The aqueous layer was then separated and extracted with diethyl ether (3x50 mL), the organic layers combined and washed with water (1x 50 mL) and brine (1 x 50 mL), dried over sodium sulfate, filtered, and concentrated to give 1.79 g of crude orange oil. The crude material was purified by column chromatography on silica using ¼ ethyl acetate/hexanes (R_f = 0.20, 3:7 ethyl acetate: hexanes) yielding a faint yellow oil (999 mg, 45%). ^{1}H NMR (500 MHz, $CDCl_3$) δ_H 5.75 (1H, m), 5.04 (2H, m), 4.14-4.27 (2H, m), 2.66 (2H, m), 2.43 (1H, m), 1.97 (2H, m), 1.80 (1H, m), 1.53 ppm (1H, m). $^{13}C\{^{1}H\}$ NMR δ (126 MHz, $CDCl_3$) δ_C 174.6 ppm, 140.9, 114.4, 69.1, 39.8, 37.7, 35.0, 28.0 ppm. HRMS (ESI) *m/z*: [M+H] Calcd for $C_8H_{12}O_2H$ 141.0916; found 141.0917. [M+Na] Calcd for $C_8H_{12}O_2Na$ 163.074; found 163.0739. Elemental analysis: Theory ($C_8H_{12}O_2$): C: 68.55%, H: 8.63%. Experimental: C: 68.49%, H: 8.98%.

Notes: metallic solid crashes out over the course of the reaction as well as after quenching and it sticks around during workup sitting between the organic and aqueous phases. This solid is easily removed during drying with sodium or magnesium sulfate and filtered. Scaling up the synthesis of 3-vinyl caprolactone has proven troublesome as the crude material is difficult to purify on larger scales and significantly lower yields have been obtained (e.g., 15 g scale of 3-vinyl caprolactone led to ~18% yield). It is hypothesized that the reagent vinylmagnesium bromide may degrade over time as reagent bottles often show large amounts of solid material, presumed to be magnesium bromide.

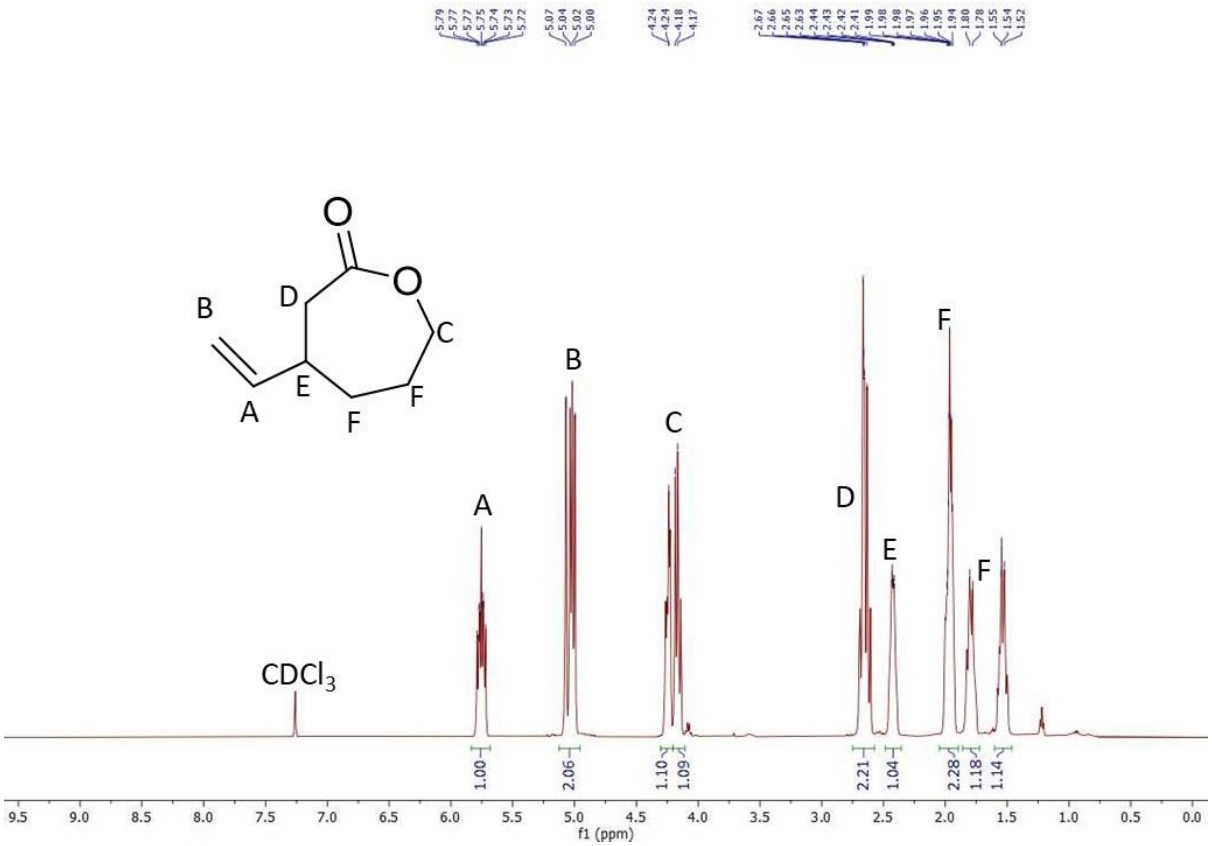

Figure. 3.25. ^{1}H NMR 3-vinyl caprolactone (**C**)

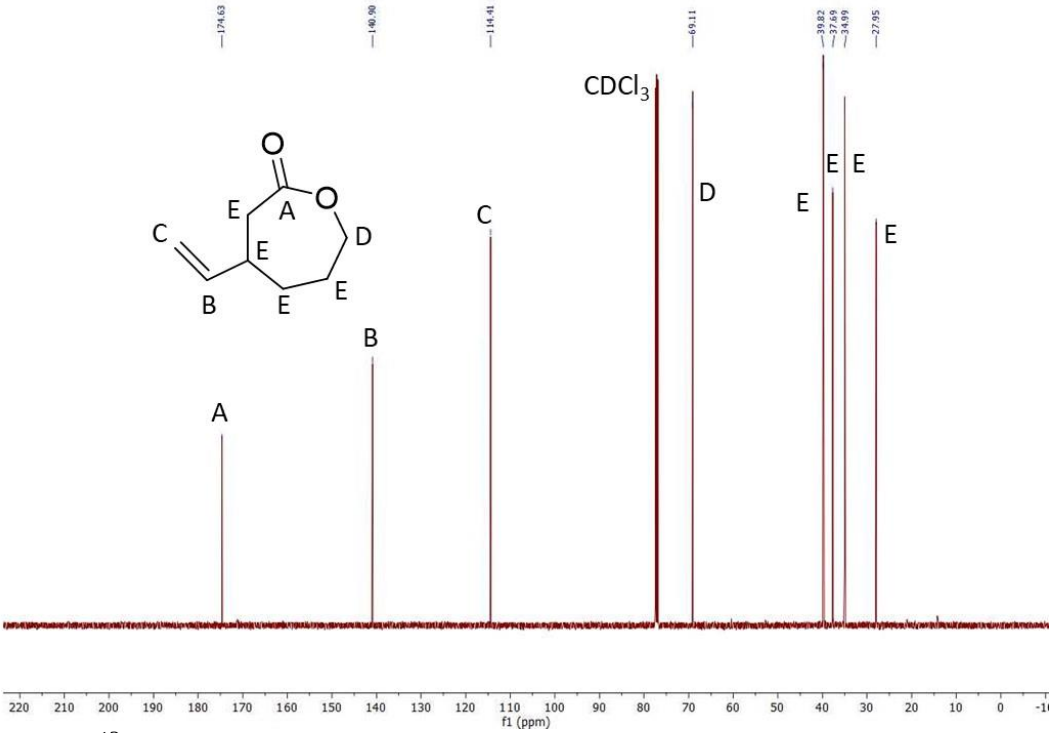

Figure. 3.26. ^{13}C NMR of 3-vinyl caprolactone (**C**)

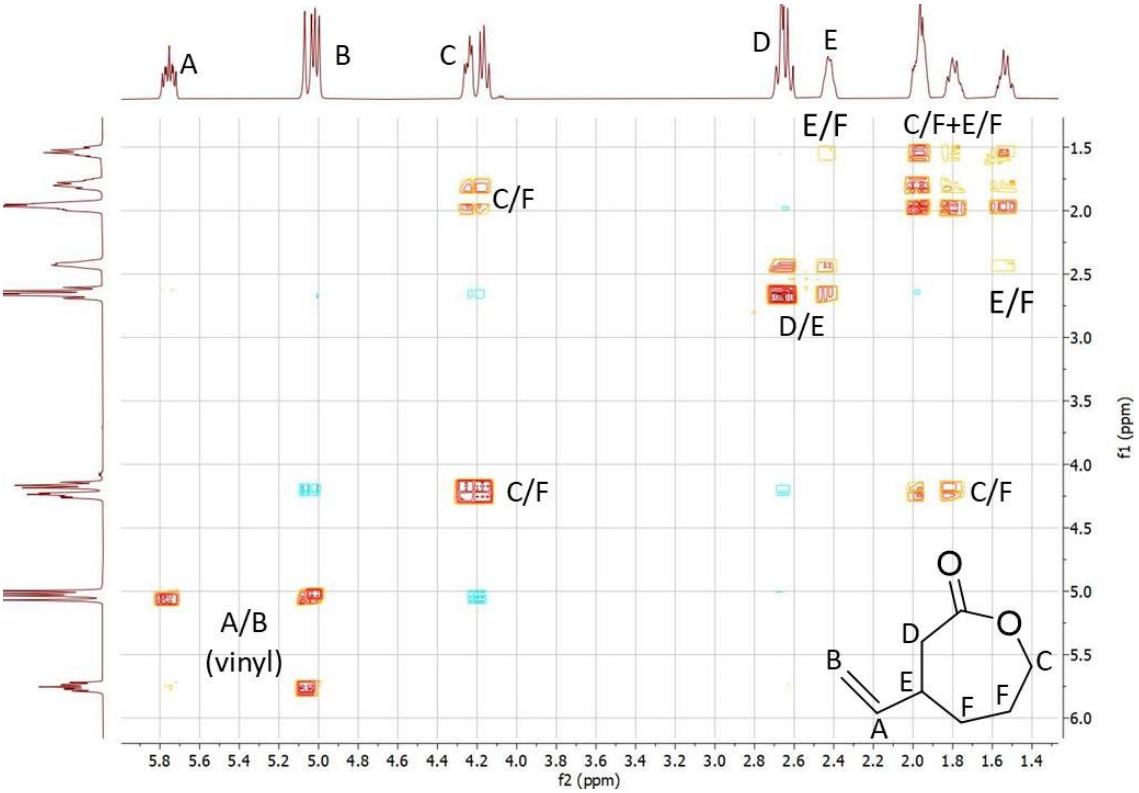

Figure. 3.27. COSY NMR 3-vinyl caprolactone (**C**). Coupled protons are labeled together.

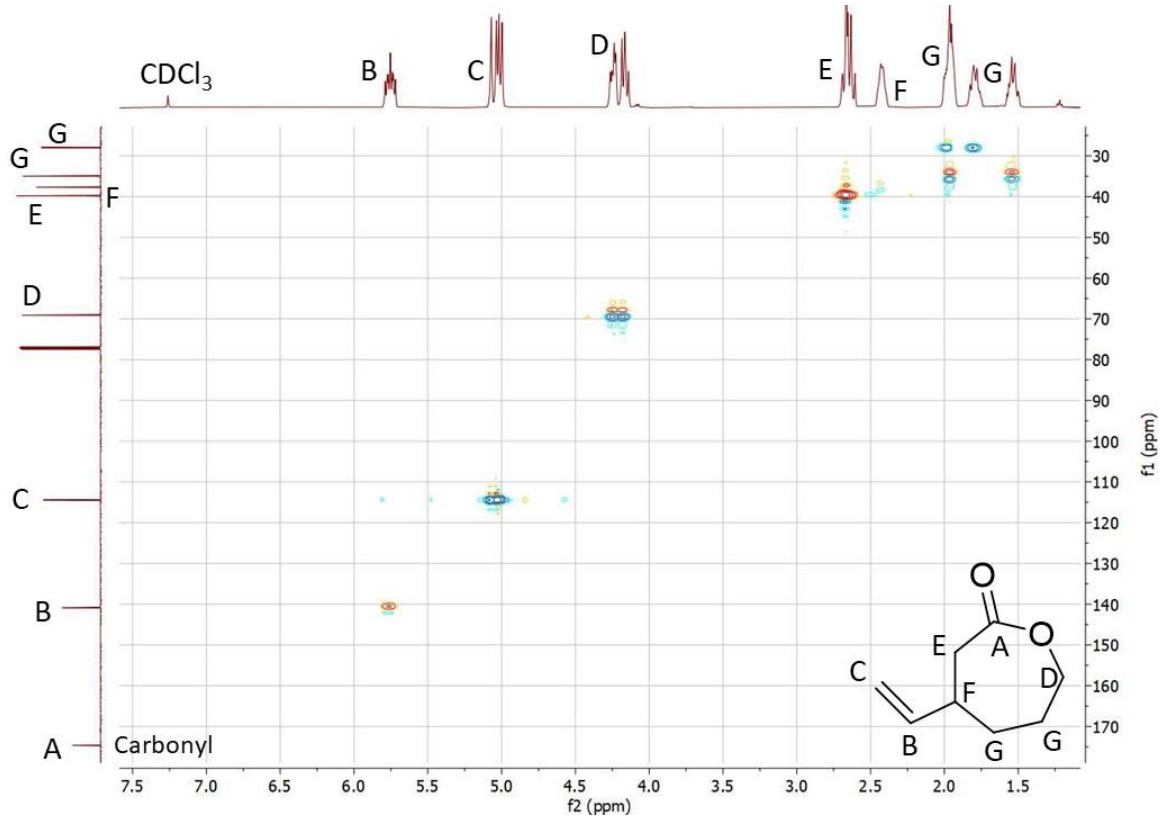

Figure. 3.28. HSQC NMR 3-vinyl caprolactone (**C**)

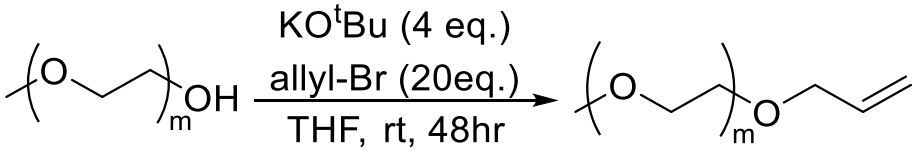

Scheme 3.10. Synthesis of poly(ethylene glycol) methyl allyl ether

Poly(ethylene glycol) methyl allyl ether. Prepared according to literature.[58] The polyethylene glycols were purchased commercially at various molecular weights and products confirmed by comparison to literature NMR.

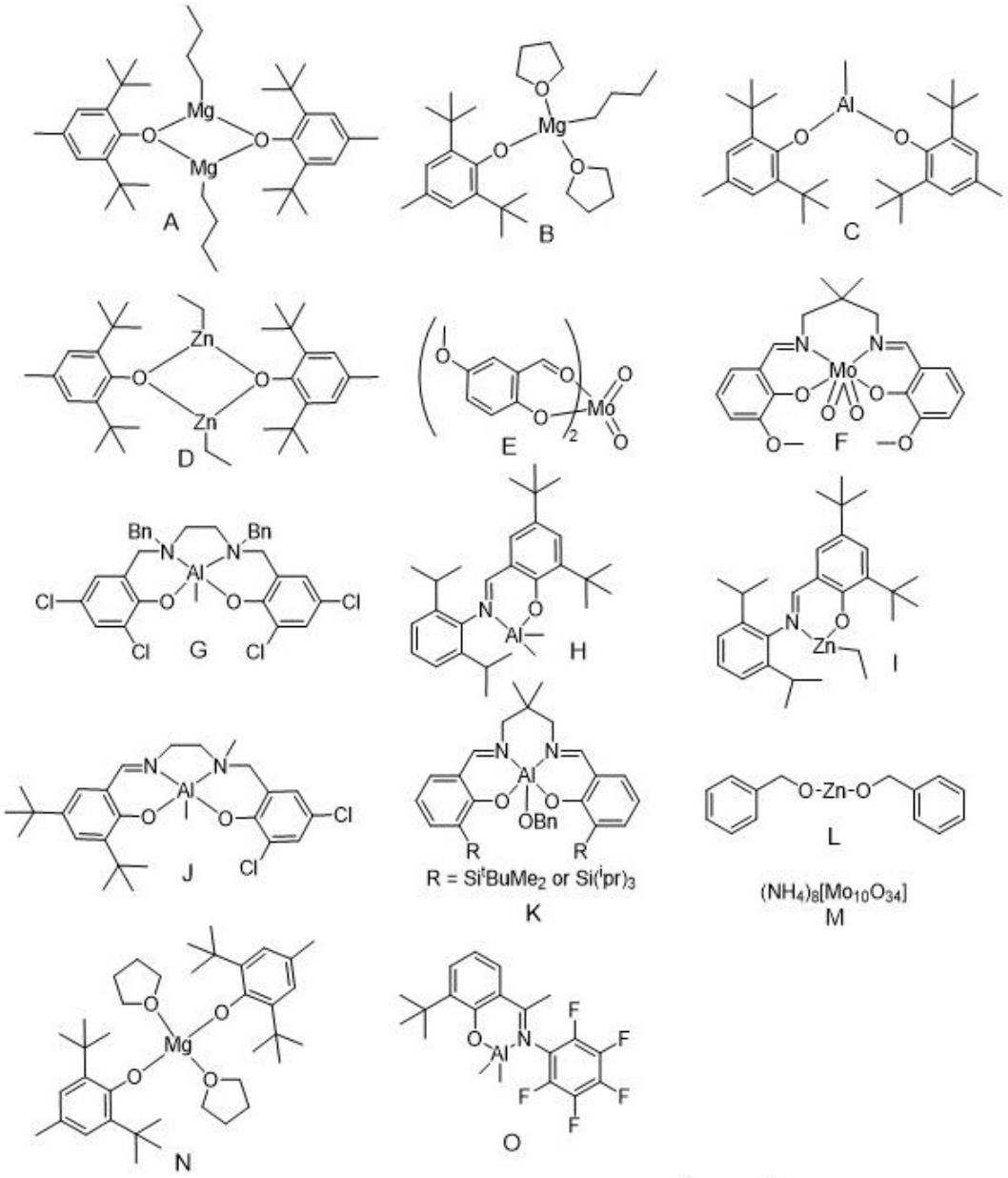

Figure. 3.29. Catalysts screened for the copolymerization of alkene-caprolactones and rac-lactide. Catalyst structures were confirmed by comparison of NMR spectra to the reported values

Synthesis of catalysts used in the screening process. All catalyst were prepared via literature methods: A,[38] B,[38] C,[39] D,[40] E,[41] F,[42] G,[43] H,[44] I,[45] J,[46] K,[9] L,[47] M,[48] N,[49] O[50]. Structures of all catalysts were confirmed via comparison to reported ^{1}H NMR values. Commercially available

catalysts were not inspected spectroscopically and were used as received from chemical suppliers.

Catalyst screening homopolymerizations. All reactions were set up in a nitrogen filled glovebox. To a 10 mL scintillation vial was added monomer, catalyst (1%), benzyl alcohol (1%) and toluene (2 mL). The mixture was then taken out of the glovebox and heated in an aluminum block preset to 90 °C for 45 min, upon which time it was cooled, quenched with methanol, volatiles removed by vacuum and the contents analyzed by ^{1}H NMR. All reactions were done as a tandem with concurrent homopolymerizations of *rac*-LA and caprolactone derivative (**A**/**B**). Catalysts that showed similar levels of conversion were then tested in copolymerization reactions.

Catalyst Screenings. In a nitrogen filled glovebox, a mixture of allyl-caprolactone and *rac*-lactide were combined in a scintillation vial. Then the catalyst of choice was added (1%), followed by benzyl alcohol as initiator (1%) and solvent if desired. The mixture was removed from the glovebox and heated in an aluminum block at the desired temperature and for the desired time. Upon completion the vial was cooled and the contents dissolved in $CDCl_3$ and analyzed by ^{1}H NMR. Promising reactions were those where similar amounts of both monomers were consumed. For such reactions a series of copolymerizations were performed simultaneously and the carbonyl region of their $^{13}C\{^{1}H\}$ NMR analyzed to determine whether the polymerization was statistical or not.

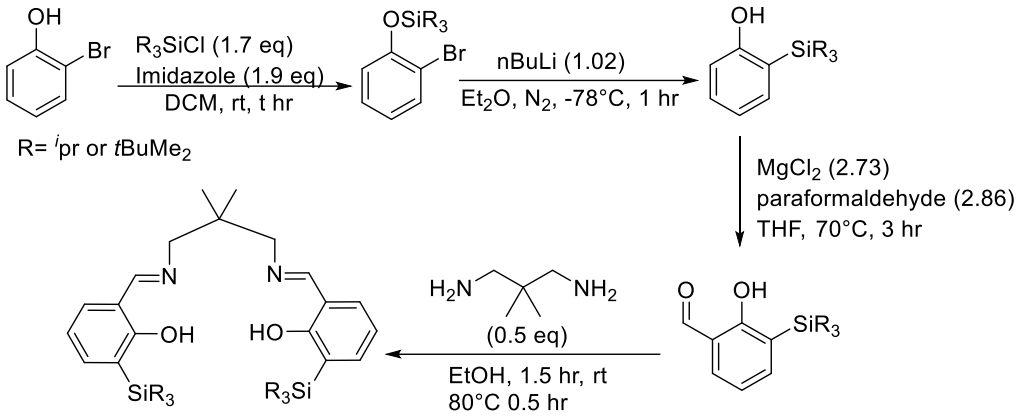

Scheme 3.11. Synthesis of salen-type ligands bearing bulky silyl groups (*tert*-butyldimethylsilyl (TBDMS) and triisopropylsilyl (TIPS))

Step 1. Silyl protection. Prepared according to literature procedure.[59] Structure confirmed by ^{1}H NMR comparison to reported values.

Step 2. Silyl shift reaction. Prepared according to literature procedure.[60] Structure confirmed by ^{1}H NMR comparison to reported values.

Step 3. Formylation: 3-(triisopropylsilyl)-2-hydroxy-benzaldehyde. Prepared according to literature procedure.[61] Structure confirmed by ^{1}H NMR comparison to reported values.

Step 4. Condensation. Prepared according to literature procedure.[61] Structure confirmed by ^{1}H NMR comparison to reported values.

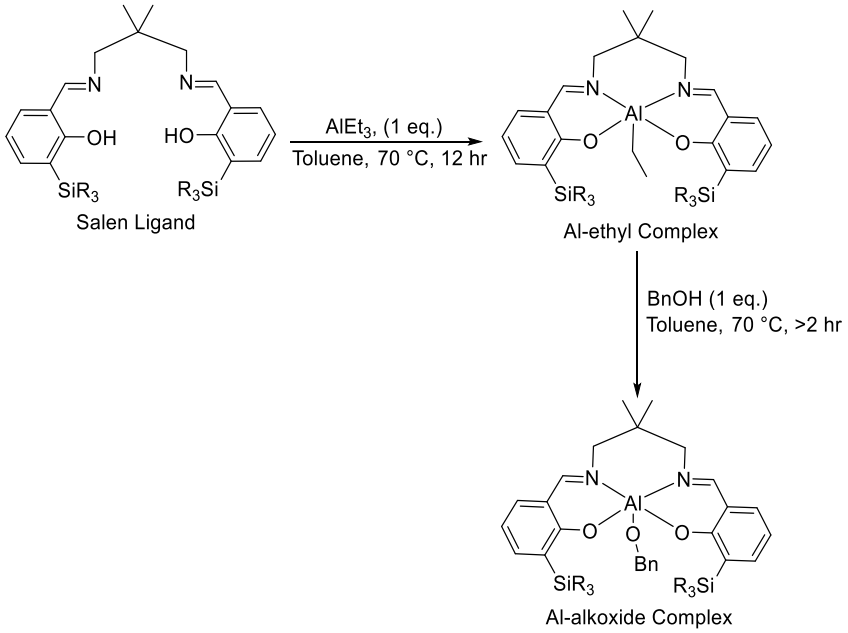

Scheme 3.12. Metalation of bulky silyl group-containing ligands with triethylaluminum to form Al-ethyl complexes followed by Al-alkoxide formation using benzyl alcohol derivatives. R represents either the TBDMS or TIPS silyl groups. Benzyl alcohol and 4-methoxy benzyl alcohol were both used to form Al-alkoxide complexes.

Metalation of Salen Ligand to form TBDMS and TIPS Salen catalysts. Prepared according to literature.[62] Note: to vary the amount of initiator when doing polymerizations, the ethyl complex was synthesized instead of the alkoxide.

3.4.2 Copolymerization Reactions

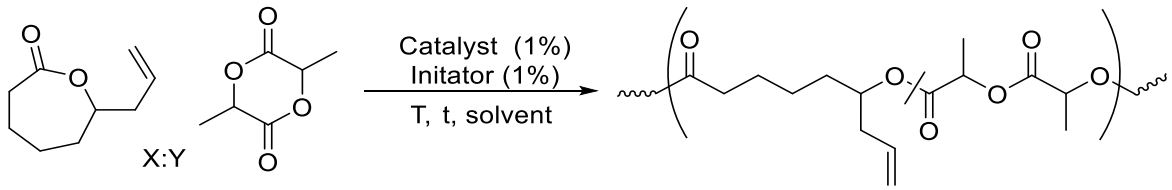

Scheme 3.13. Copolymerization reaction of 6-allyl caprolactone with rac-lactide using 1% of catalyst, 1% initiator (benzyl alcohol or 4-methoxy benzyl alcohol) under temperature (T, °C) for time (t, hr) with or without solvent (toluene)

Poly(6-allyl caprolactone-co-*rac*-LA)

Set up in a nitrogen filled glovebox. 6-allyl caprolactone (X equivalents) and *rac*-LA (Y equivalents) of desired ratio and catalyst (%) were combined within a 1-dram scintillation vial. To the mixture was added initiator (%) and toluene if they used solvent. Upon full addition of reagents, the vial was removed from the glovebox and heated within an aluminum block or oil bath preset to the desired temperature. Reactions typically went overnight (~18-20 hr) before cooling, dissolving in minimal dichloromethane and precipitating from water: methanol (1:1) to give polymer as a white solid. Yields varied based on feed ratio of the two monomers, usually 60-70% for a 5 mmol reaction. ^{1}H NMR (500 MHz, $CDCl_3$) δ_H 7.32 (5H), 5.69 (110H), 5.12-5.17 (205H), 5.02-5.09 (322H), 4.87-4.94 (114H), 4.35 (4H), 2.23-2.35 (479H),1.44-1.63 (1,130H), 1.29-1.36 ppm (256H).

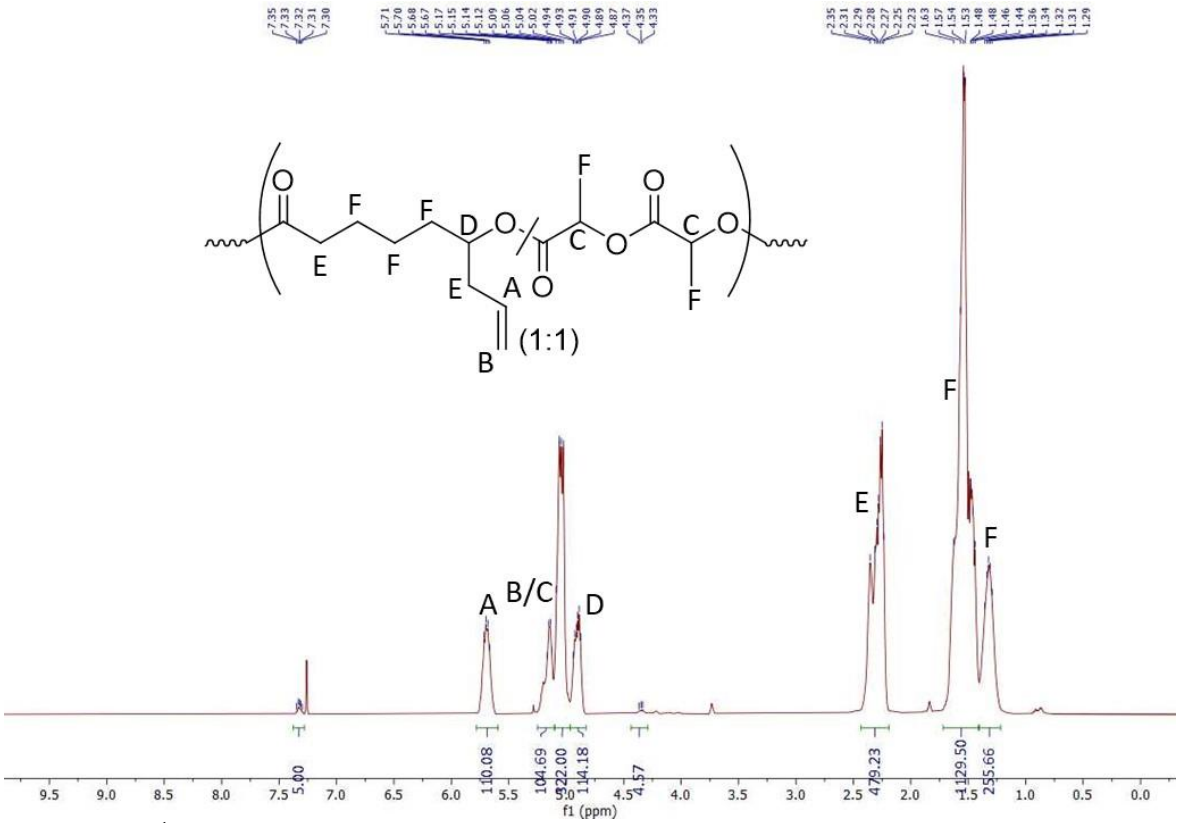

Figure 3.30. ^{1}H NMR Poly(6-allyl caprolactone-co-rac-LA) (1:1 feed ratio)

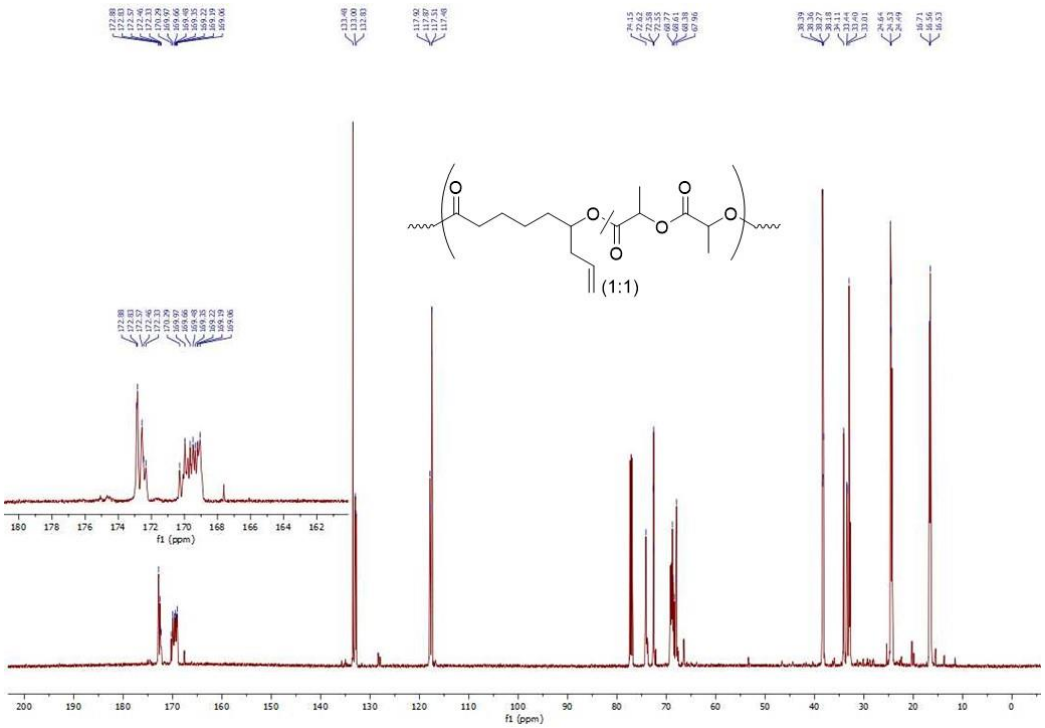

Figure 3.31. ^{13}C NMR Poly(6-allyl caprolactone-co-rac-LA) (1:1 feed ratio)

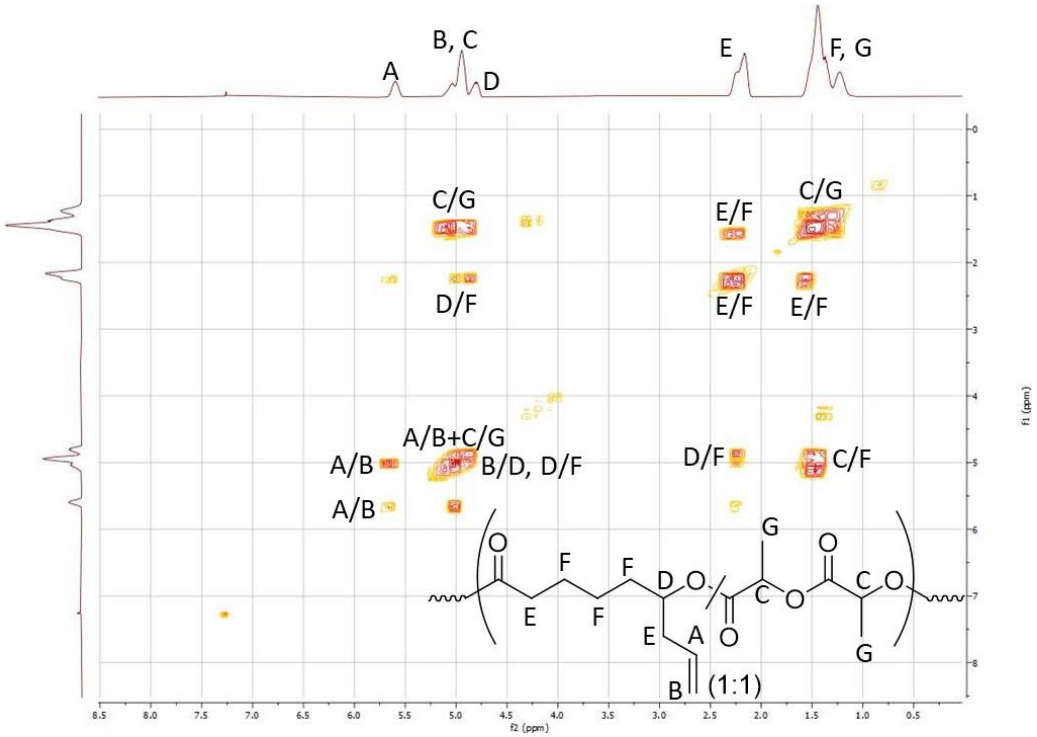

Figure. 3.32. COSY NMR Poly(6-allyl caprolactone-co-rac-LA) (1:1 feed ratio) with select proton couples labeled.

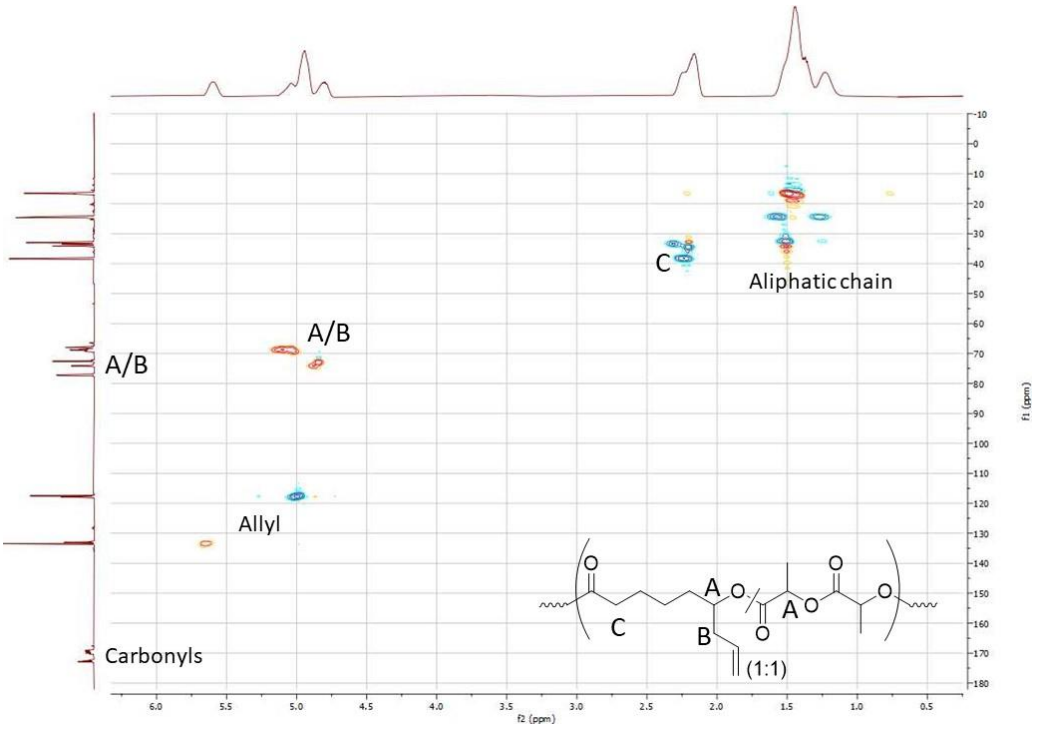

Figure. 3.33. HSQC NMR Poly(6-allyl caprolactone-co-rac-LA) (1:1 feed ratio)

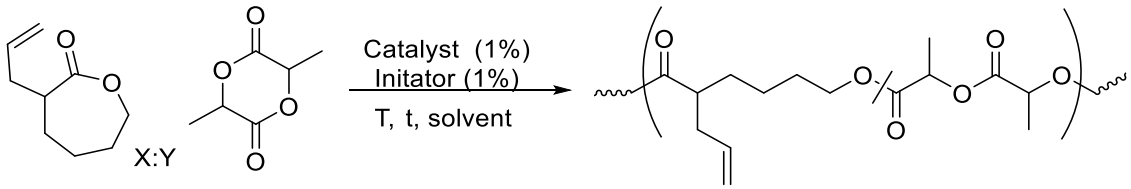

Scheme 3.14. Copolymerization reaction of 2-allyl caprolactone with *rac*-lactide using 1% of catalyst, 1% initiator (benzyl alcohol or 4-methoxy benzyl alcohol) under temperature (T, °C) for time (t, hr) with or without solvent (toluene)

Poly(2-allyl caprolactone-co-*rac*-LA)

Set up in a nitrogen filled glovebox. 2-allyl caprolactone (equiv.) and *rac*-LA (equiv.) of desired ratio and catalyst (%) were combined within a 1dram scintillation vial. To the mixture was added initiator (%) and toluene if they used solvent. Upon full addition of reagents the vial was removed from the glovebox and heated within an aluminum block or oil bath preset to the

desired temperature. Reactions typically went overnight (~18-20hr) before cooling, dissolving in minimal dichloromethane and precipitating from water: methanol (1:1). ^{1}H NMR (500 MHz, $CDCl_3$) δ_H 7.33 (5H), 5.68-5.78 (124H), 5.01-5.20 (468H), 4.35 (4H), 4.25 (5H), 4.11 (173H), 4.04 (92H), 2.48 (88H), 2.31-2.40 (182H), 2.24 (133H), 1.46-1.63 (1233H), 1.32-1.40 ppm (282H).

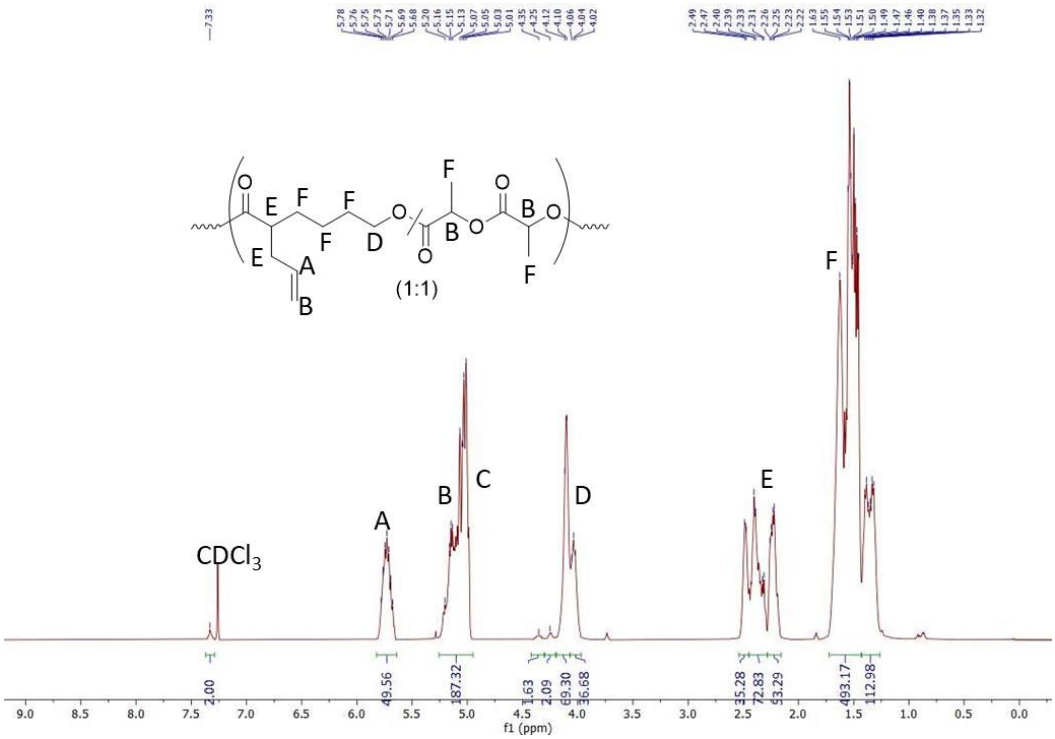

Figure 3.34. ^{1}H NMR Poly(2-allyl caprolactone-co-rac-LA) (1:1 monomer feed)

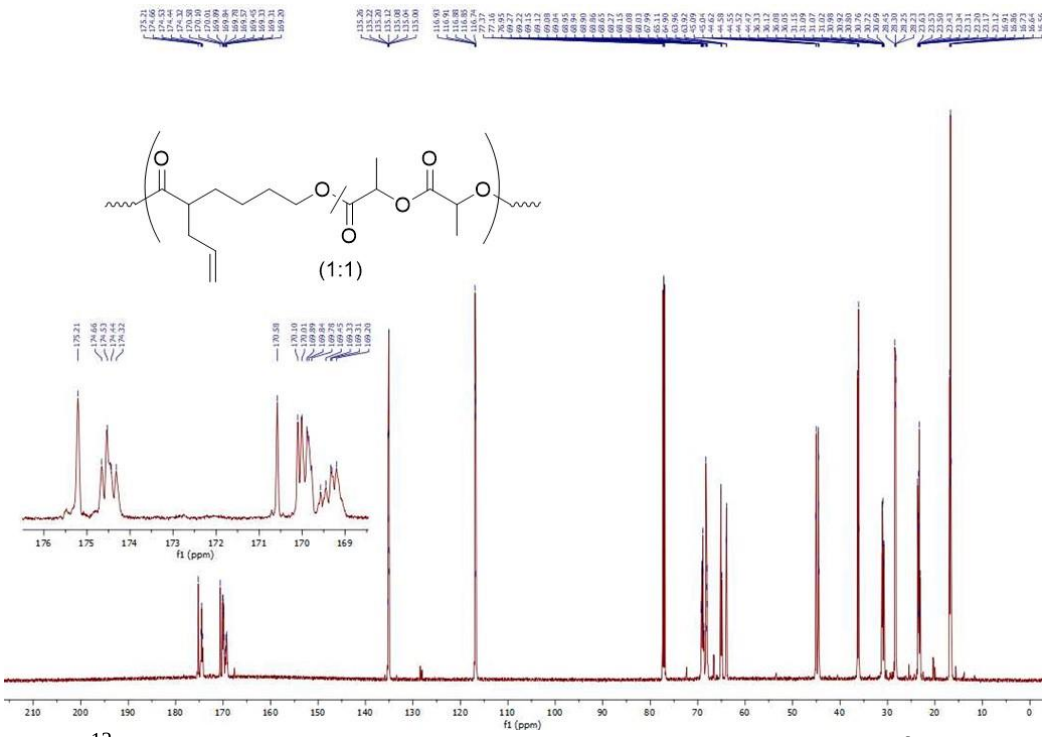

Figure 3.35. ^{13}C NMR Poly(2-allyl caprolactone-co-rac-LA) (1:1 monomer feed)

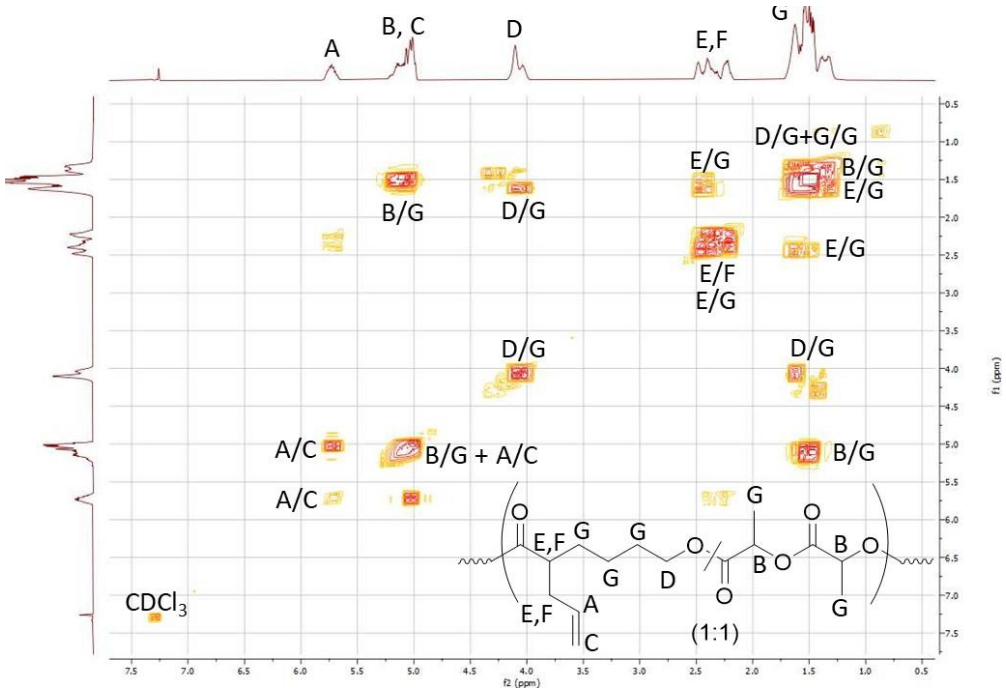

Figure 3.36. COSY NMR Poly(2-allyl caprolactone-co-rac-LA) (1:1 monomer feed). With select coupled protons

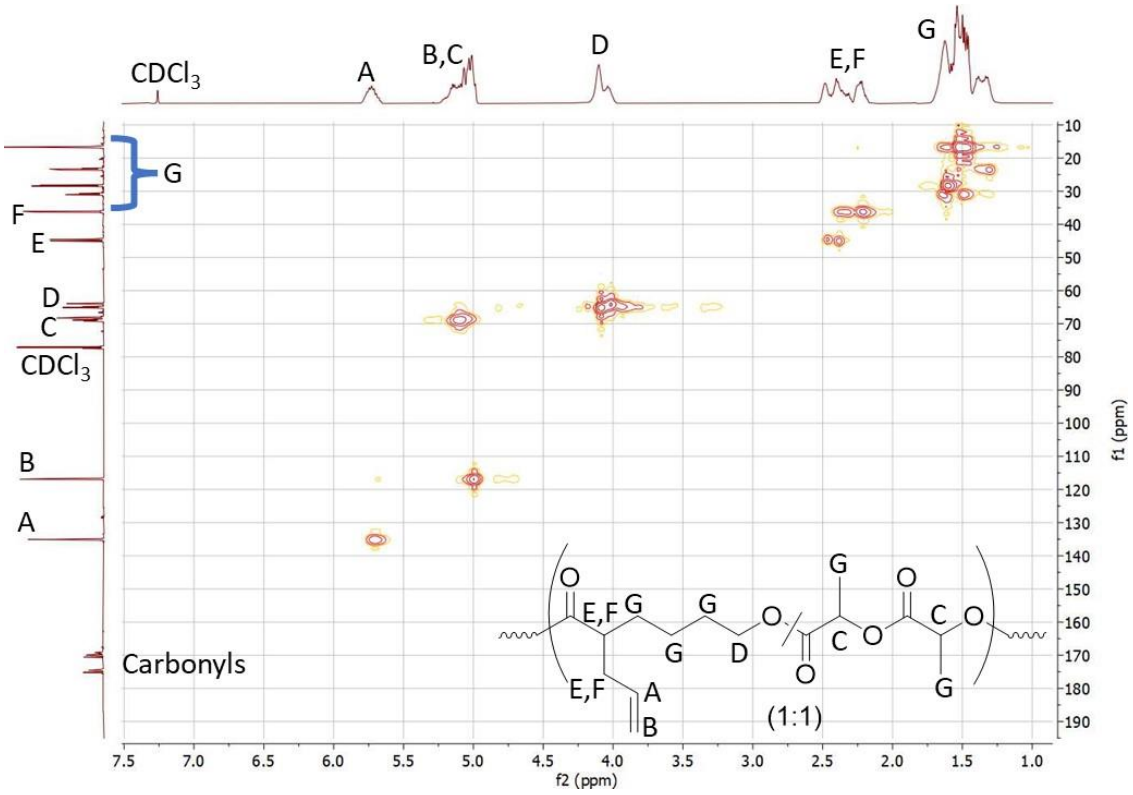

Figure 3.37. HSQC NMR Poly(2-allyl caprolactone-co-rac-LA) (1:1 monomer feed)

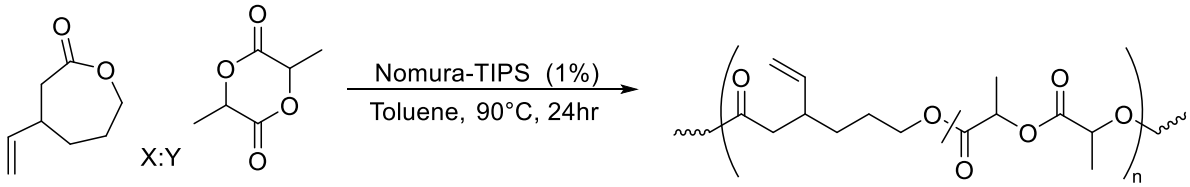

Scheme 3.15. Copolymerization of 3-vinyl caprolactone with *rac*-lactide to form poly(3-vinyl caprolactone-*stat*-*rac*-lactide).

Copolymerization of Racemic Lactide and 3-vinyl caprolactone.

As the goal was to create a polymer resembling poly(*rac*-lactide), copolymerizations were typically performed with a ratio of 9:1 *rac*-lactide:3-vinyl caprolactone to both make it resemble PLA while allowing for easy visualization of the vinyl groups by ^{1}H NMR. ^{1}H NMR (500 MHz, $CDCl_3$) δ_H 7.32 (5H), 5.58 (7H), 5.01-5.17 (160H), 4.33 (4H), 4.01-4.11 (73H), 2.51 (36H), 2.25-2.42 (73H), 1.41-1.66 (394H), 1.33 ppm (52H).

Method 1. Vial. **Example procedure (9:1 *rac*-LA: 3-vinyl caprolactone).** To a 5 mL scintillation vial within a nitrogen filled glovebox was added *rac*-lactide (519 mg, 3.8 mmol, 90 equivalents), 3-vinyl caprolactone (56 µL, 0.4 mmol, 10 equivalent) and anhydrous toluene (3.3 mL, 1M total). The mixture was heated gently with a hairdryer within the glovebox to homogenize the solution. Then a 0.05M solution of catalyst (0.7 mL, 0.04 mmol, 1%) was added, the vial sealed and immediately taken out of the glovebox and heated in an aluminum block at 90 °C for 22 hr. Upon cooling to room temperature, the polymer was precipitated from cold methanol (~4 °C). Note: for reactions that had ratios of 3-vinyl caprolactone: *rac*-lactide of 1:1 or higher using a mixture of water and methanol (1:1) improved the amount of recovered polymer, but also required a greater number of precipitations to remove unwanted monomer. As the relative proportion of alkene-caprolactone increased it proved helpful to do a subsequent precipitation from hexanes to remove any unreacted caprolactone monomer.

Method 2. Schlenk Flask. **Example procedure (9:1 *rac*-LA: 3-vinyl caprolactone).**

To a 35mL Schlenk tube within a nitrogen filled glovebox was added *rac*-lactide (519 mg, 3.6 mmol, 90 equivalents), 3-vinyl caprolactone (56 µL, 0.4 mmol, 10 equivalents) and anhydrous toluene (3.3 mL, 1M total). The flask was then taken out of the glovebox and placed in an oil bath at 90 °C to homogenize the mixture. Upon heating for roughly 10 min while stirring, a solution of catalyst (0.05M in toluene, 0.7 mL, 0.04 mmol, 1%) stored under nitrogen was added and the resulting mixture was stirred for 22 hr at 90 °C. Upon cooling to room temperature, the solution was precipitated from cold (~4°C) methanol several times, dried within a vacuum oven at 55 °C and analyzed by NMR.

Method 3. Attempt at high molecular weight. **Example procedure.**

To a 5mL scintillation vial within a nitrogen filled glovebox was added *rac*-lactide (200 mg, 1.39 mmol, 9 equivalents relative to 3-vinyl caprolactone), 3-vinyl caprolactone (23 µL, 0.15 mmol, 1 equivalent) and anhydrous toluene (1.5 mL, 1M total). The mixture was heated gently with a hairdryer within the glovebox to homogenize the solution. Then a 0.05M solution of catalyst as the ethyl complex (0.3 mL, 0.02 mmol, 1%) was added, the vial sealed and immediately taken out of the glovebox and heated in an aluminum block at 90 °C for 48 hr. Upon cooling to room temperature, the polymer was precipitated from cold methanol (~4 °C) and the polymers analyzed by NMR and SEC. Note: for reactions that had ratios of 3-vinyl caprolactone: *rac*-lactide of 1:1 or higher using a mixture of water and methanol (1:1) improved the amount of recovered polymer, but also required a greater number of precipitations to remove unwanted monomer. As the relative proportion of alkene-caprolactone increased it proved helpful to do a subsequent precipitation from hexanes to remove any unreacted caprolactone monomer.

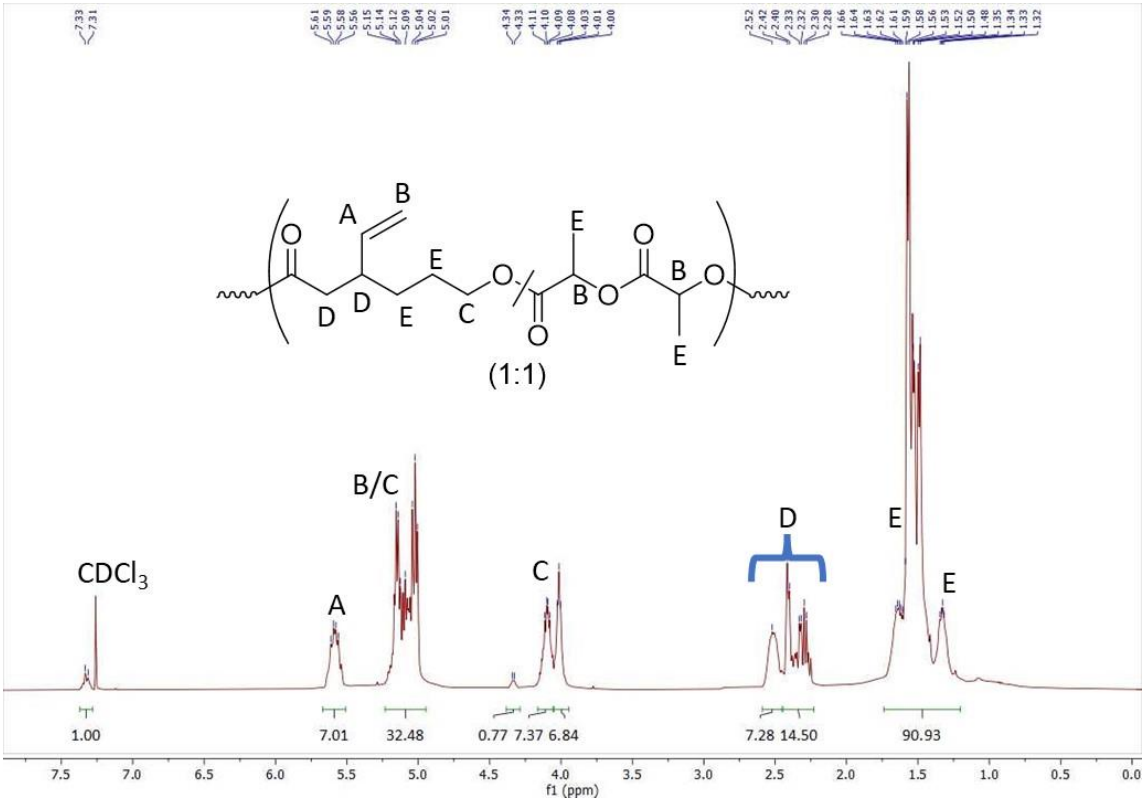

Figure. 3.38. ^{1}H NMR Poly(3-vinyl caprolactone-*stat*-rac-LA) (1:1 monomer feed)

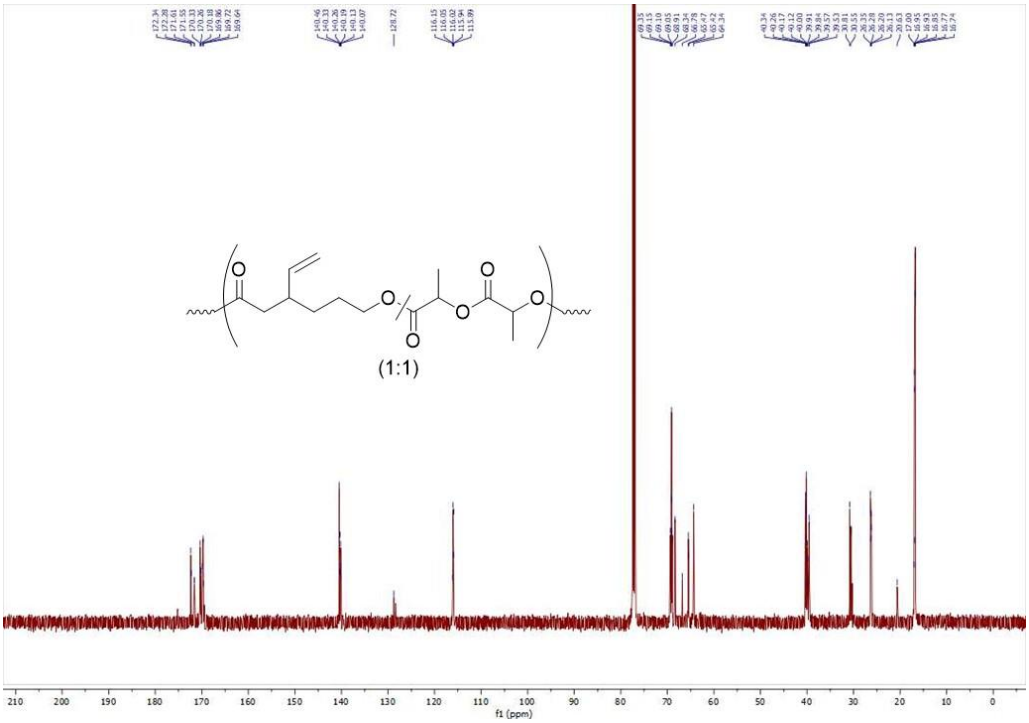

Figure 3.39. ^{13}C NMR Poly(3-vinyl caprolactone-*stat*-rac-LA) (1:1 monomer feed)

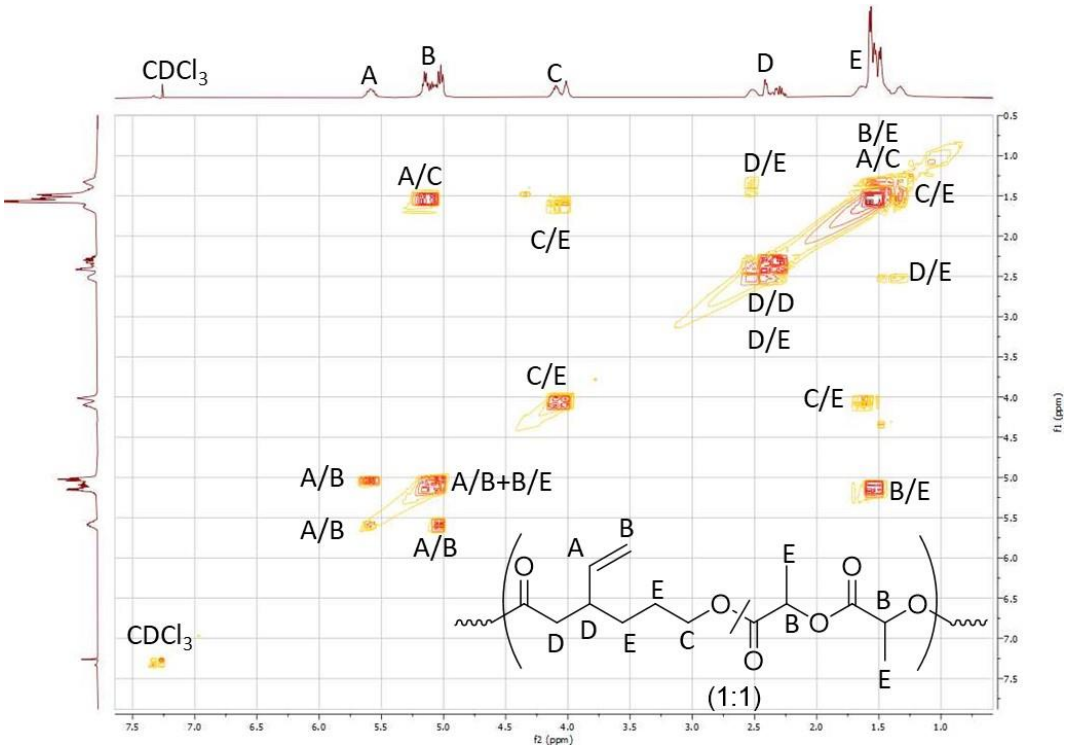

Figure 3.40. COSY NMR Poly(3-vinyl caprolactone-*stat*-rac-LA) (1:1 monomer feed). With select coupled protons labeled.

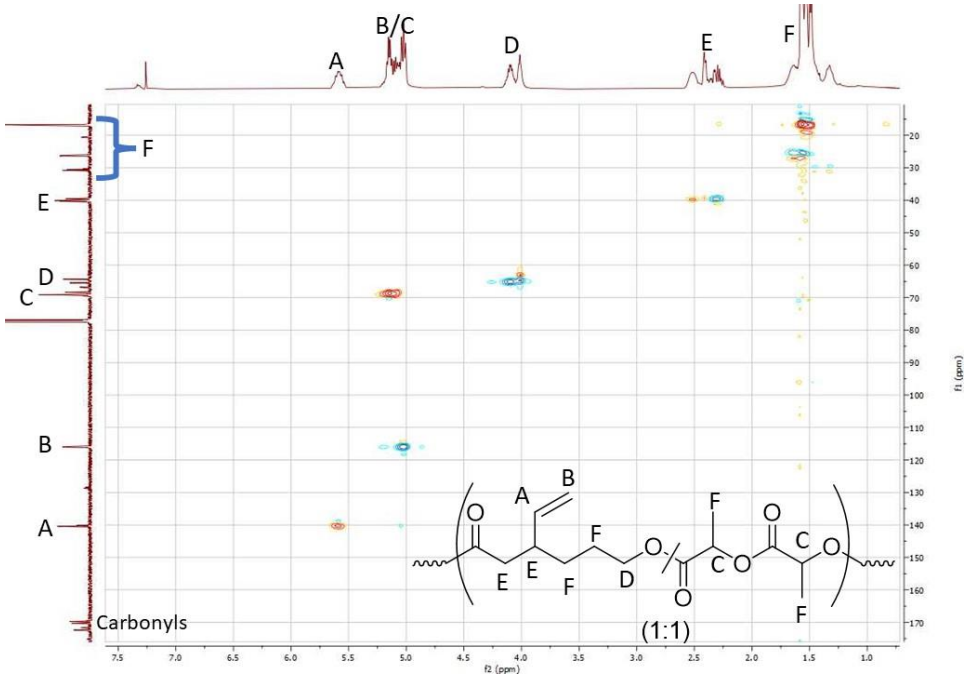

Figure 3.41. HSQC NMR Poly(3-vinyl caprolactone-*stat*-rac-LA) (1:1 monomer feed)

Poly(3-vinyl caprolactone)

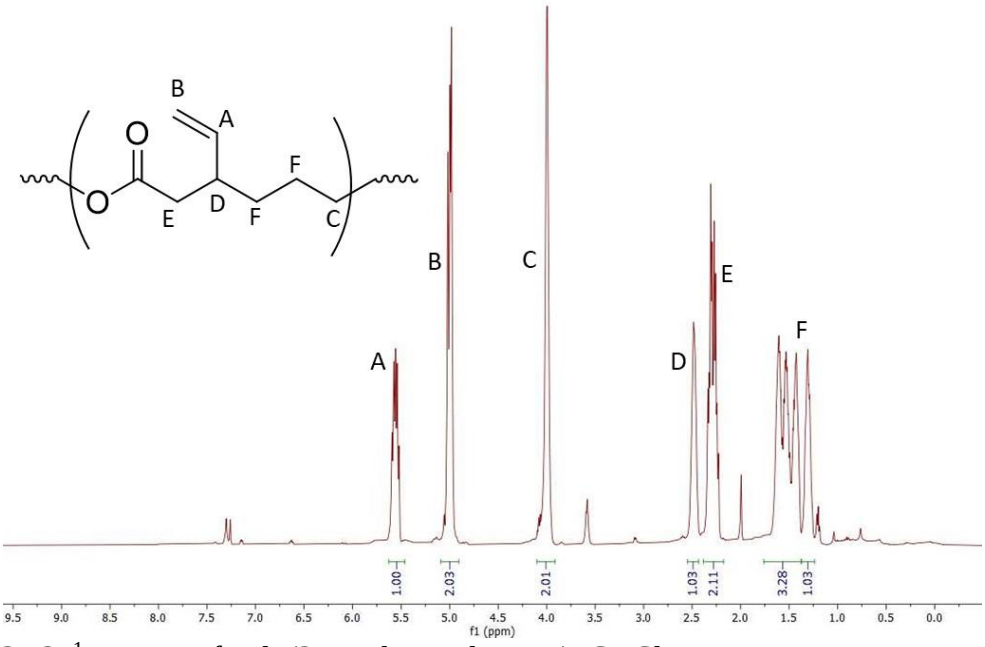

Figure 3.42. ^{1}H NMR of poly(3-vinyl caprolactone), $CDCl_3$

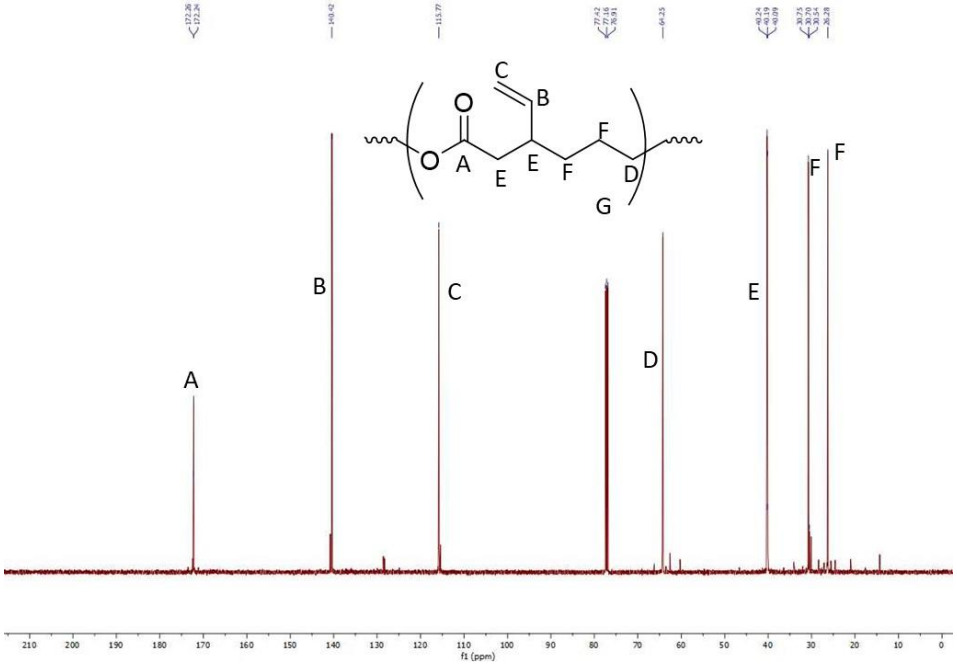

Figure 3.43. ^{13}C NMR of poly(3-vinyl caprolactone)

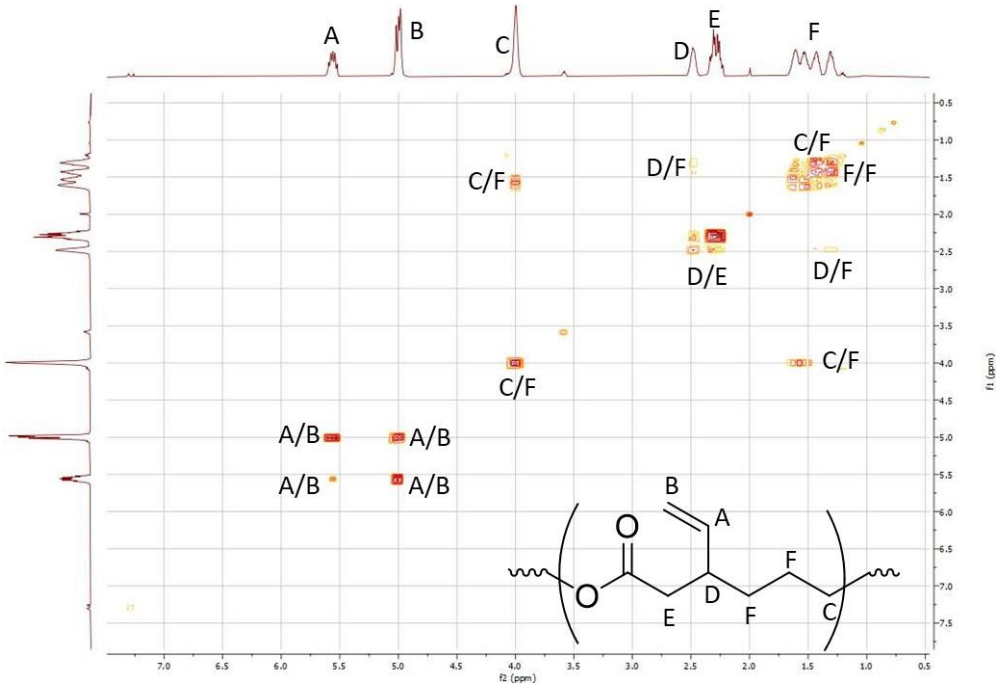

Figure 3.44. COSY NMR of poly(3-vinyl caprolactone) homopolymer with select coupled protons labeled

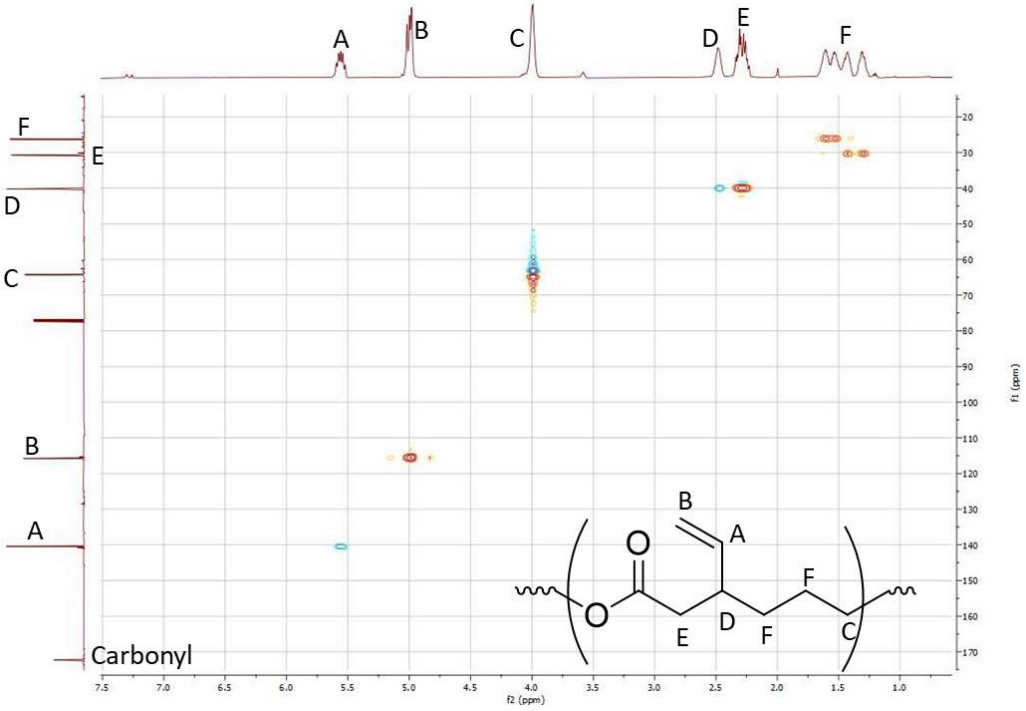

Figure 3.45. HSQC NMR of poly(3-vinyl caprolactone)

3.4.3. Copolymer Post-polymerization Modification Procedures

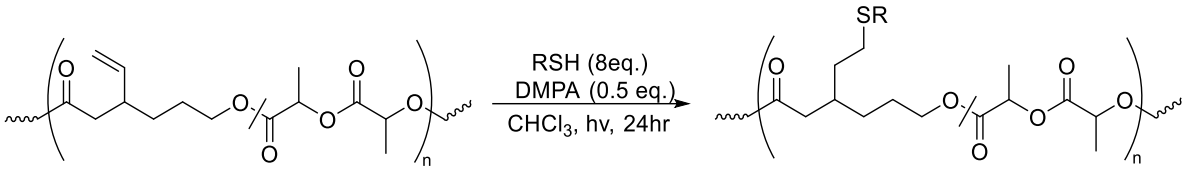

Scheme 3.16. Thiol-ene reaction of poly(3-vinyl caprolactone-stat-rac-lactide) with a thiol under photo-initiating conditions. R = alkyl group, DMPA = dimethylphenyl acetophenone.

Representative thiol-ene reaction. Example reaction with 1-octane thiol.

Copolymer (180 mg, 0.14 mmol of vinyl units, 1 equivalent) was dissolved in degassed, anhydrous, chloroform within a 5 mL scintillation vial. To this was then added thiol (240 μL, 1.4 mmol, 10 equivalents) and DMPA (18 mg, 0.07 mmol, 0.5 equivalents). The resulting homogeneous solution was stirred while surrounded by blue LED lights (365 nm) with a fan flowing overhead to avoid increasing the temperature. The mixture was allowed to stir overnight, upon which time the polymer was precipitated from cold methanol (~4 °C). Product was obtained as a white solid (73%). Example using 1-octane thiol. Other thiols used include PDMS derivatives. ^{1}H NMR (500 MHz, $CDCl_3$) δ_H 7.24 (2H), 6.86 (2H), 4.96-5.20 (211H), 4.10 (19H), 4.02 (12H), 3.78 (3H), 2.66 (16H), 2.48 (44H), 2.36 (19H), 2.25 (13H), 2.00 (18H), 1.46-1.70 (725H), 1.30-1.45 (79H), 1.27 (126H), 0.86 ppm (49H).

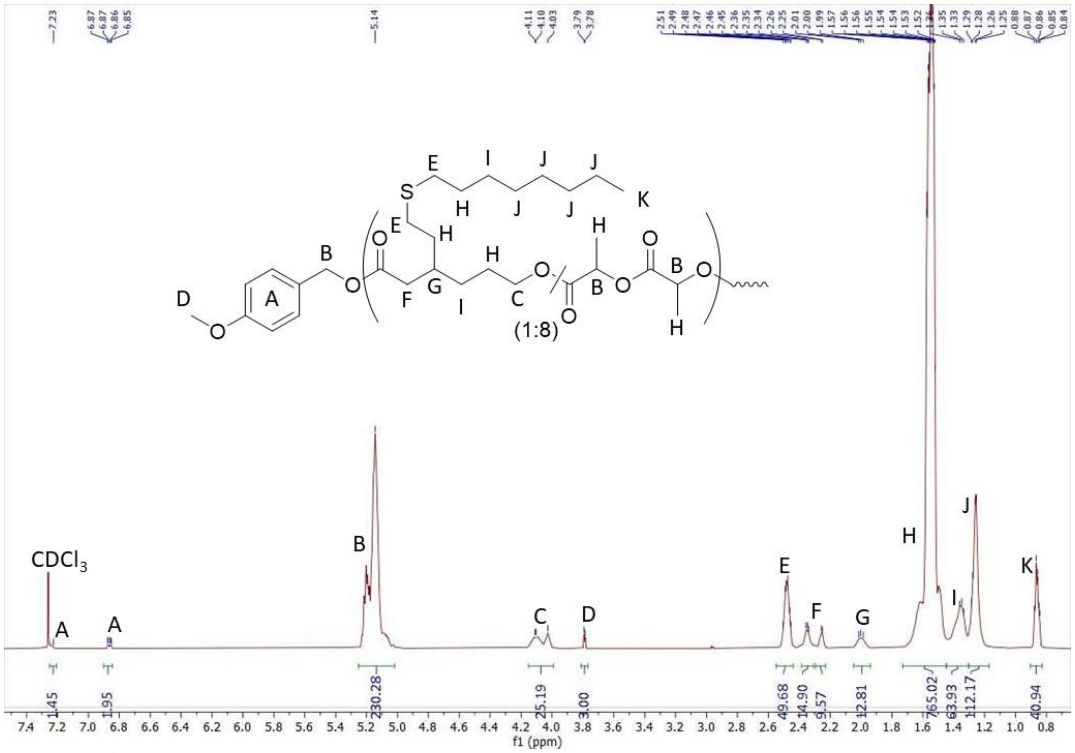

Figure 3.45. ^{1}H NMR of 3-vinyl caprolactone/rac-LA (1:8) copolymer with 1-octane thiol6

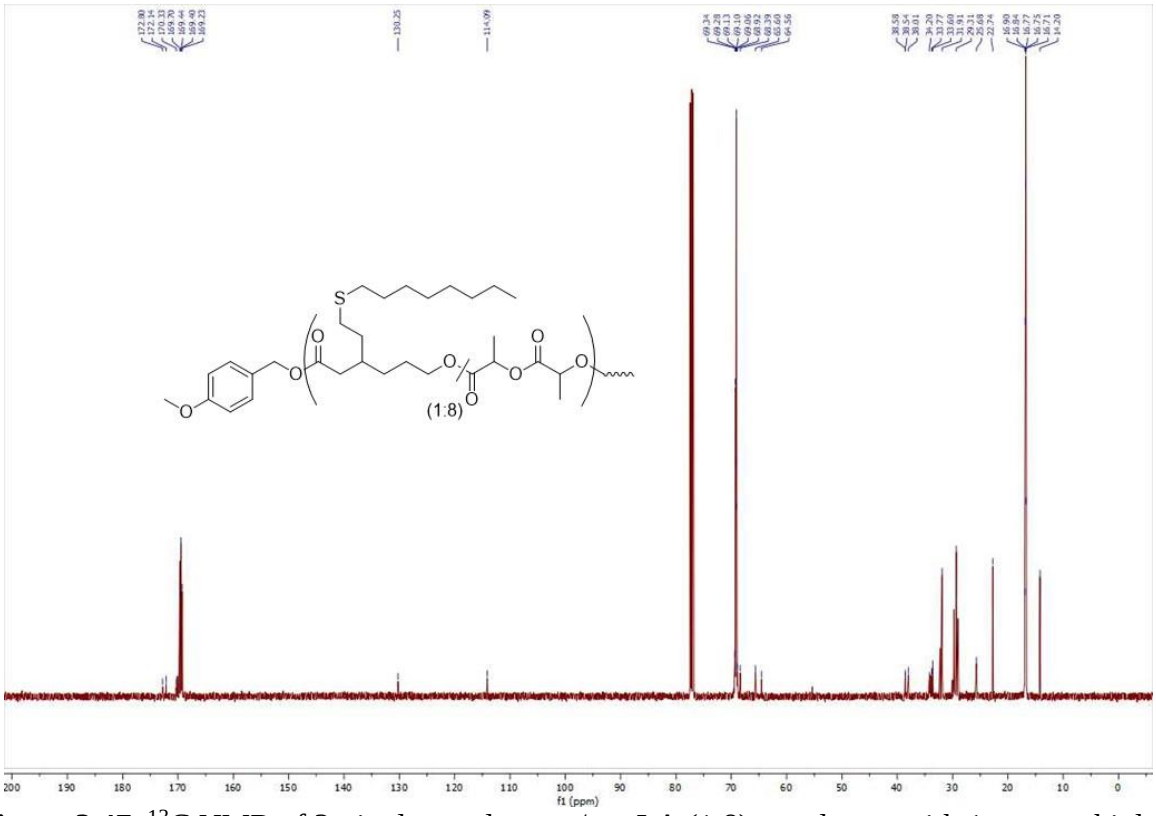

Figure 3.47. ^{13}C NMR of 3-vinyl caprolactone/rac-LA (1:8) copolymer with 1-octane thiol

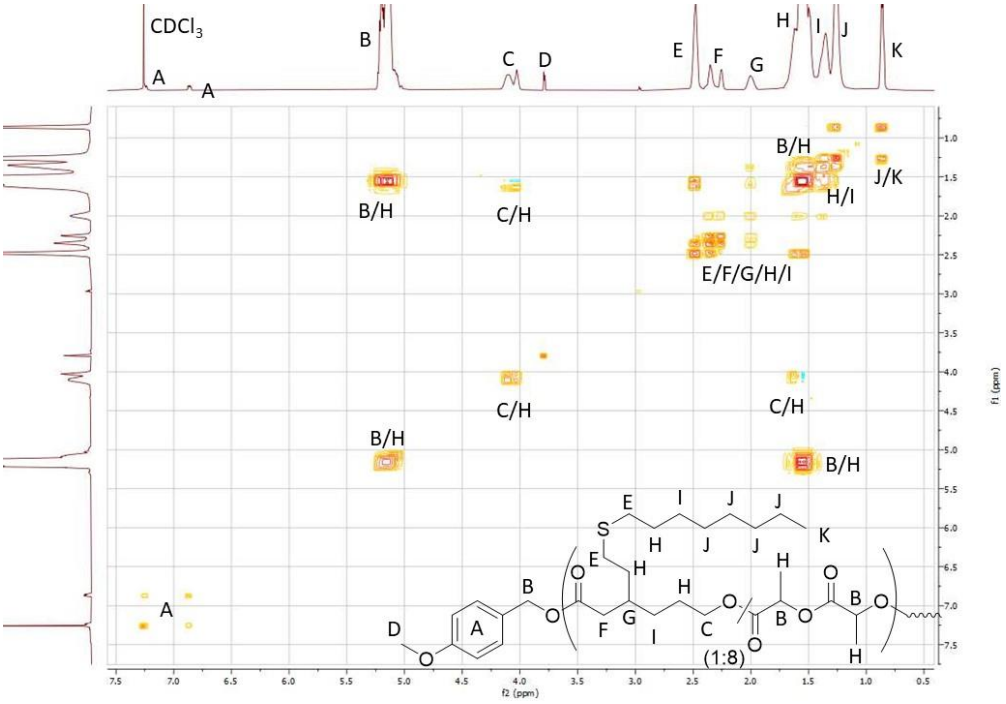

Figure 3.48. COSY NMR of 3-vinyl caprolactone/rac-LA (1:8) copolymer with 1-octane thiol

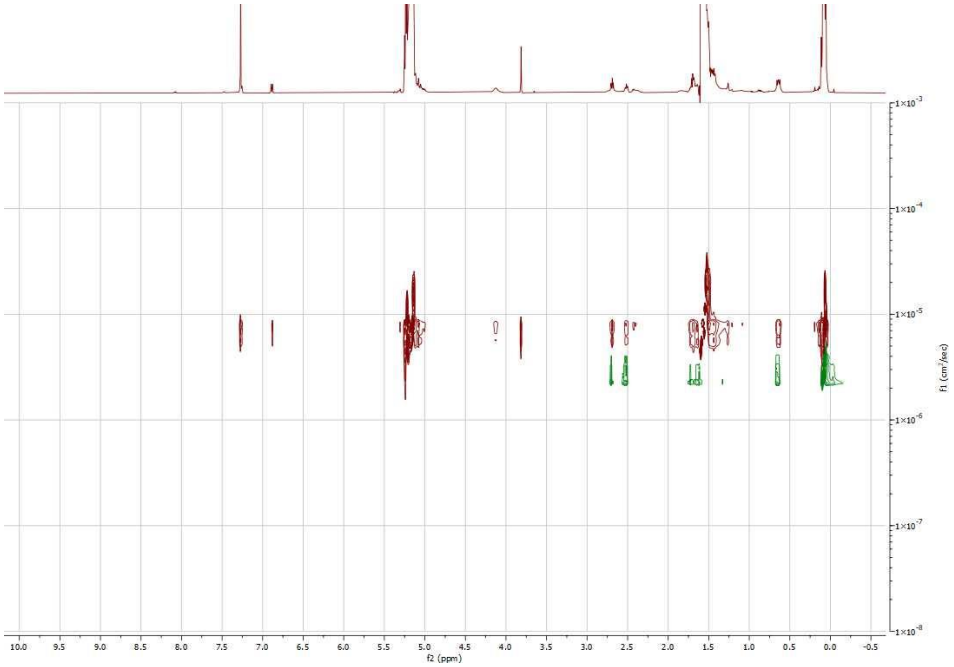

Figure 3.49. DOSY NMR of Thiol-ene of P(3-vinyl caprolactone-co-rac-LA) with mercapto-terminated PDMS (red) and mercapto-terminated PDMS reagent (green).

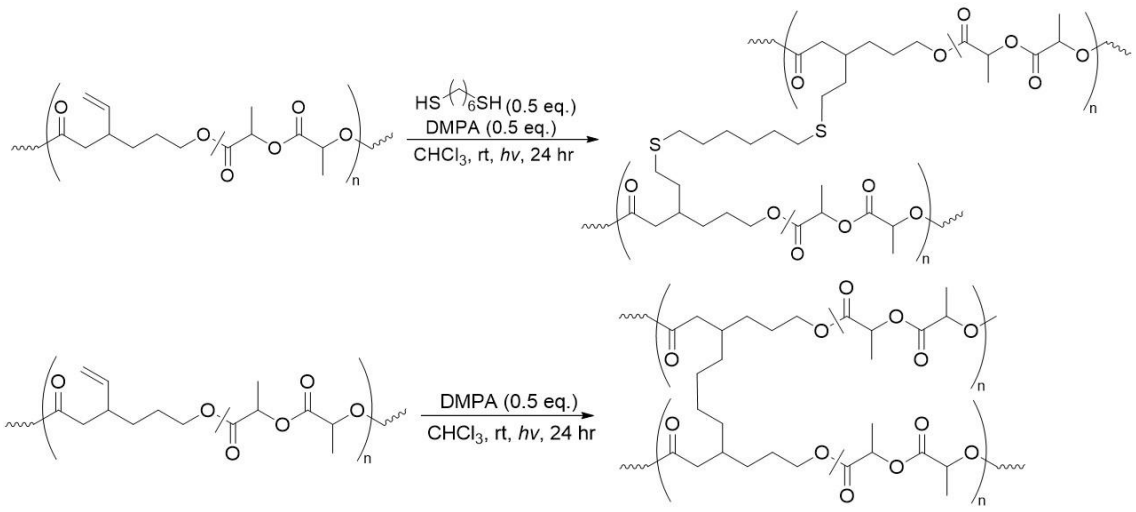

Scheme 3.17. Crosslinking reactions of poly(3-vinyl caprolactone-stat-rac-lactide) with 1,6-hexane dithiol (top) or in the absence of a thiol (bottom) under photo-initiating conditions with DMPA as a photoinitiator

Crosslinking

Crosslinking reactions were performed following the typical thiol-ene reaction procedure with the difference of using only 0.5-0.6 equivalents of dithiol. 0.25 equivalents were used for crosslinking with pentaerythritol tetrakis(3-mercaptopropionate). Alternatively, it was shown that the polymers form gels even in the absence of dithiol by simple radical crosslinking, with chloroform likely acting as a proton source. Due to the gelling of polymers, the crosslinked copolymers were insoluble in traditional organic solvents and could not be characterized by NMR spectroscopy thoroughly. We were able to make crosslinked copolymers at low olefin loadings (e.g., 28:1 *rac*-LA, 3-vinyl caprolactone) as to make the material less tough which allowed us to see the disappearance of vinyl peaks. Mechanical testing of the crosslinked polymers may be of interest in future works.

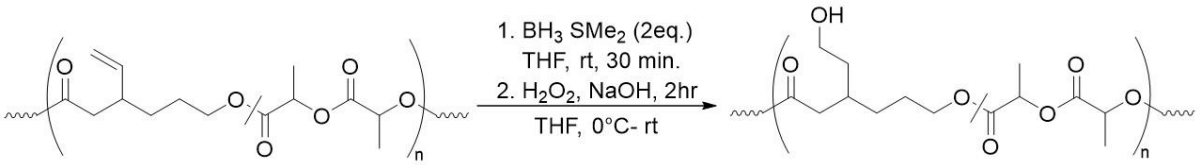

Scheme 3.18. Hydroboration-oxidation of poly(3-vinyl caprolactone-stat-rac-lactide) with borane complexed to dimethyl sulfide (step 1) followed by H_2O_2 and NaOH to convert the vinyl group into a primary alcohol.

Hydroboration-Oxidation of Copolymer.

To a solution of copolymer (380mg, 0.19 mmol of vinyl units, 1.0 equivalent) in THF (3 mL) was added borane dimethyl sulfide (36 μL, 0.38 mmol, 2.0 equivalents) at room temperature. The initially homogeneous mixture begins to gel within a minute of borane addition after which time the solution is unable to stir. After allowing to react for thirty min the solution was cooled to 0 °C and 30% aqueous hydrogen peroxide (194 μL, 10 equivalents) was added dropwise resulting in an exothermic reaction, followed by 4N aqueous NaOH (475 μL, 10 equivalents). The solution bubbled rapidly quickly turning clear, colorless, and homogeneous. The solution was stirred an additional two hr at room temperature, after which time it was diluted with saturated aqueous NH_4Cl (10 ml) and extracted with dichloromethane (4 x 4 mL). The organic layers were then combined, dried over Na_2SO_4, filtered, and concentrated to give a white solid material (~50% yield). ^{1}H NMR (500 MHz, $CDCl_3$) δ_H 7.22 (2H), 6.58 (2H), 5.12-5.19 (224H), 4.31-4.37 (14H), 4.23 (5H), 4.11 (12H), 3.97 (5H), 3.77 (3H), 3.59-3.65 (8H), 2.64-2.69 (1H), 2.62 (2H), 1.87-2.38 (9H), 1.45-1.65 (696H), 1.37-1.45 ppm (31H).

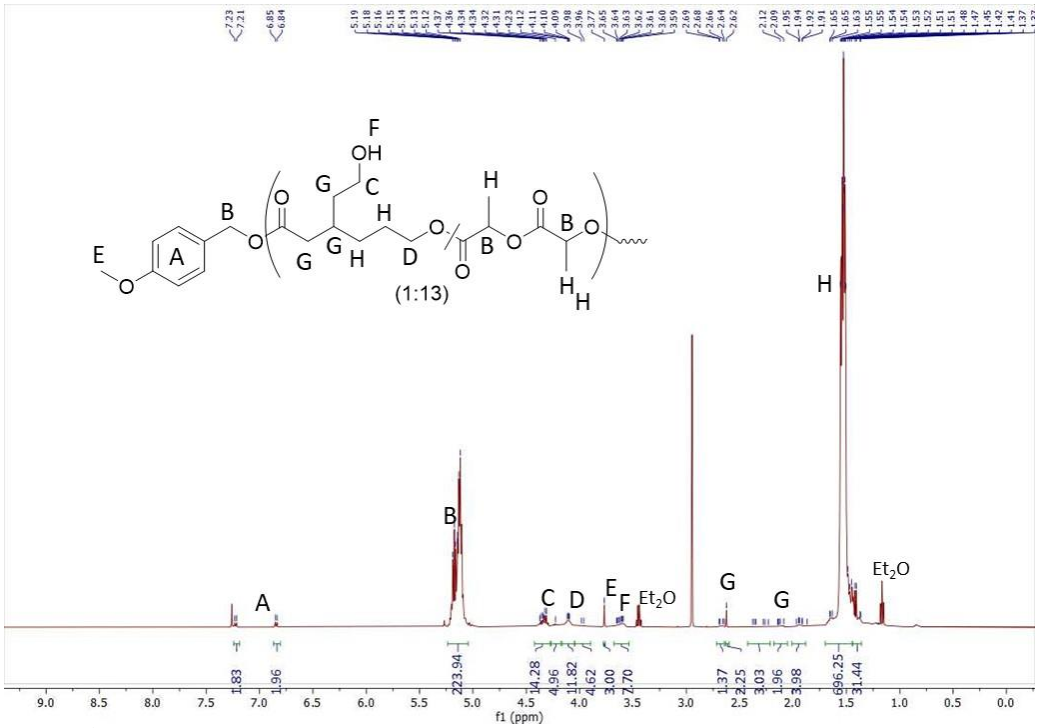

Figure 3.50. [1]H NMR hydroboration-oxidation product 3-vinyl caprolactone/rac-LA (1:13)

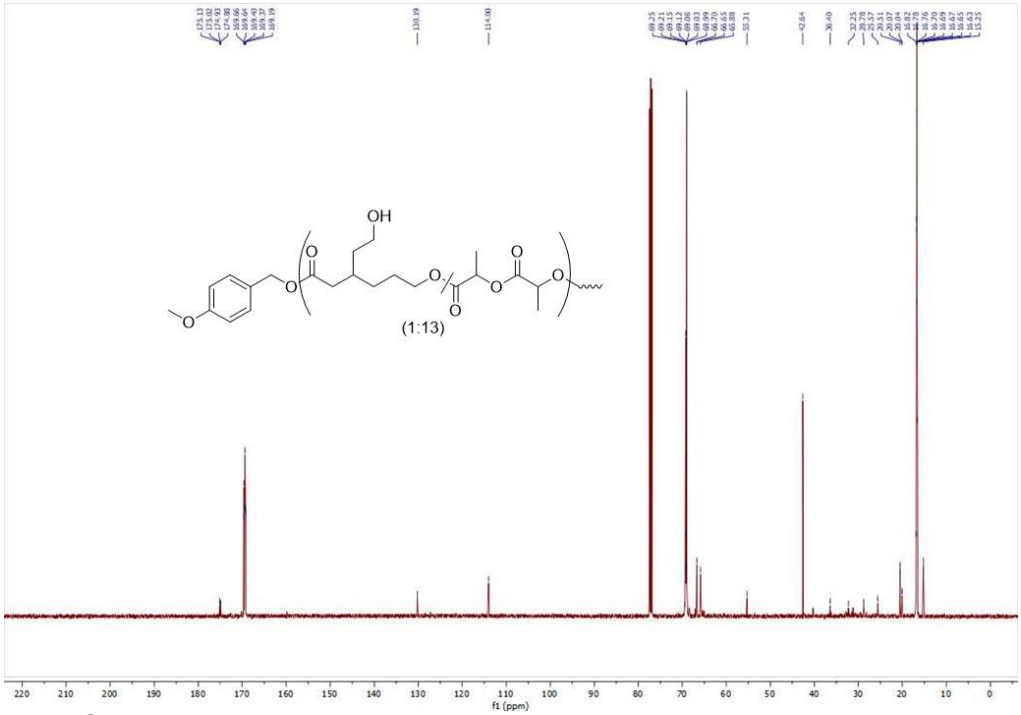

Figure 3.51. [13]C NMR hydroboration-oxidation product 3-vinyl caprolactone/rac-LA (1:13) copolymer

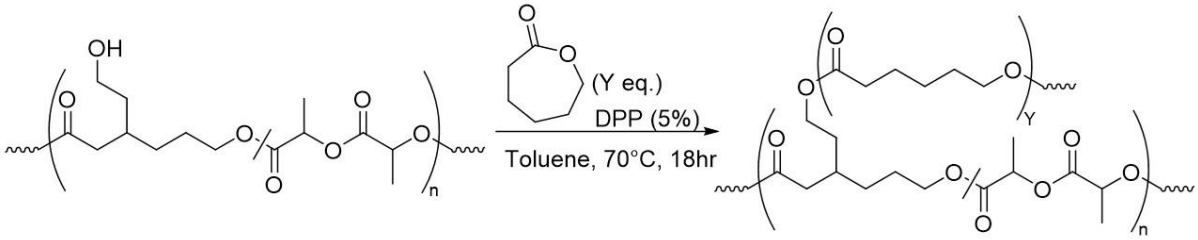

Scheme 3.19. Ring-opening polymerization grafting-from reaction with ε-caprolactone using the primary alcohol generated via hydroboration-oxidation of poly(3-vinyl caprolactone-stat-rac-lactide) as the initiator and DPP as catalyst. Y denotes the number of equivalents of caprolactone monomer used in the ROP grafting-from reaction.

Grafting-from reactions.

Grafting-from ring-opening polymerization. Example reaction.

Within a nitrogen filled glovebox, hydroxyl group containing copolymer (0.02 mmol hydroxyl units, 1.0 equivalent) was combined with DPP (2 mg, 5%) and lactone monomer (51 μL, 0.4 mmol, 20 equivalents) in a scintillation vial. Subsequently the vials were removed from the box where they were heated within an aluminum block at 70 °C for 18 hr. Upon cooling, the contents were dissolved in minimal dichloromethane and precipitated into hexanes. Other examples for ROP graft-from reactions are in appendix. ^{1}H NMR (500 MHz, $CDCl_3$) δ_H 6.87 (2H), 5.07-5.20 (209H), 4.31-4.43 (10H), 4.12 (14H), 4.05 (64H), 3.80 (3H), 2.38 (8H), 2.30 (66H), 1.44-1.64 (805H), 1.37-1.43 ppm (75H)

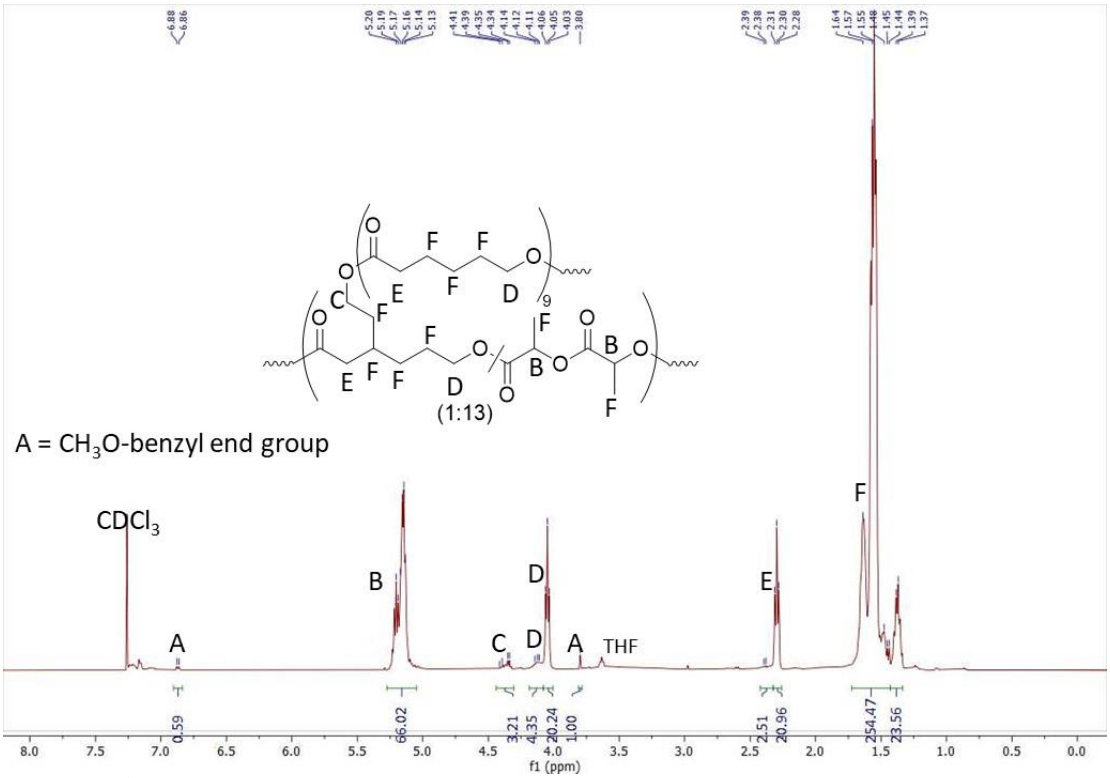

Figure 3.52. ^{1}H NMR ROP graft from reaction example. 20 equivalents of ε-caprolactone

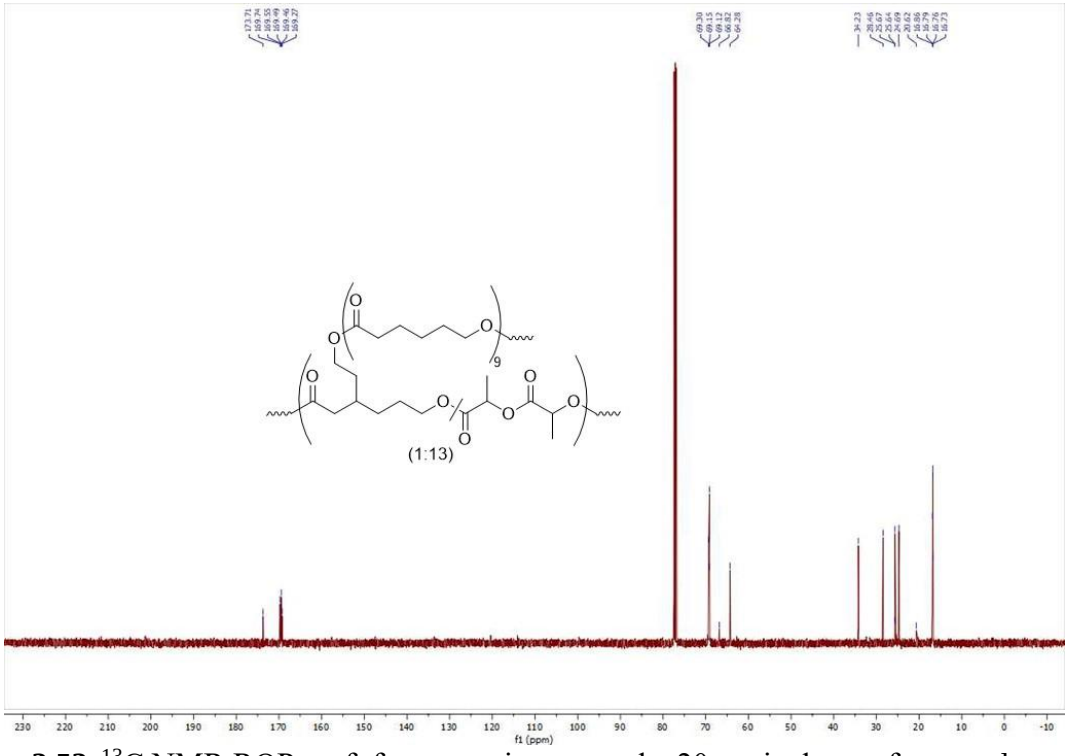

Figure 3.53. ^{13}C NMR ROP graft from reaction example. 20 equivalents of ε-caprolactone

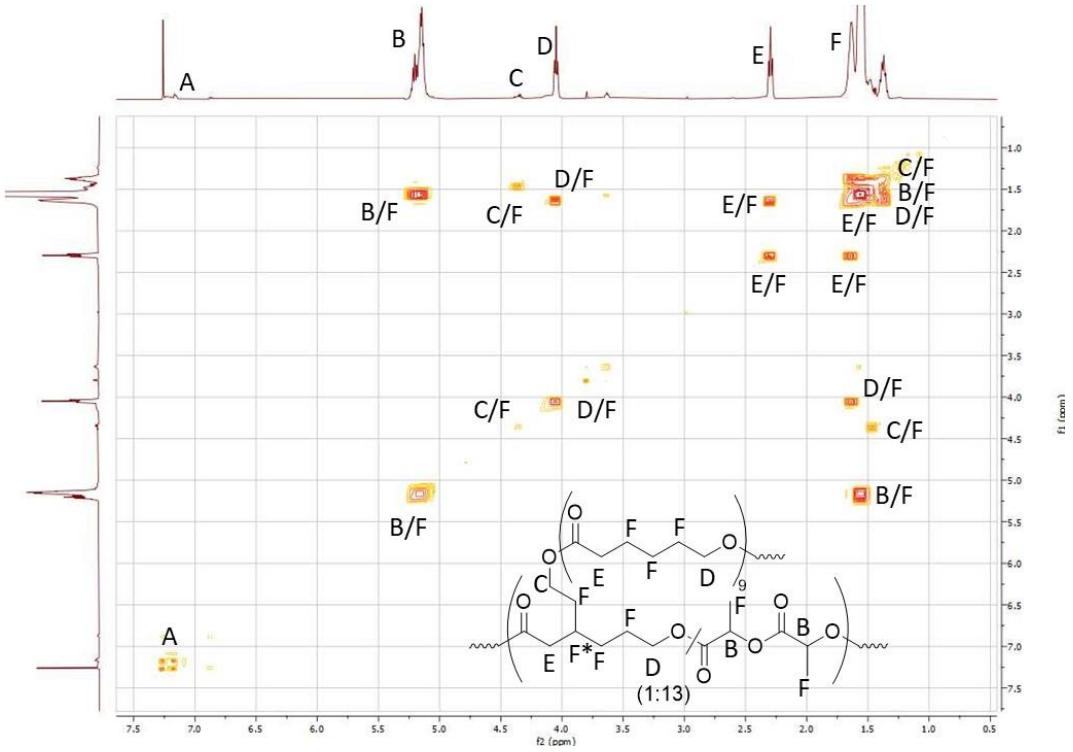

Figure 3.54. COSY NMR ROP graft from reaction. 20 equivalents of ε-caprolactone

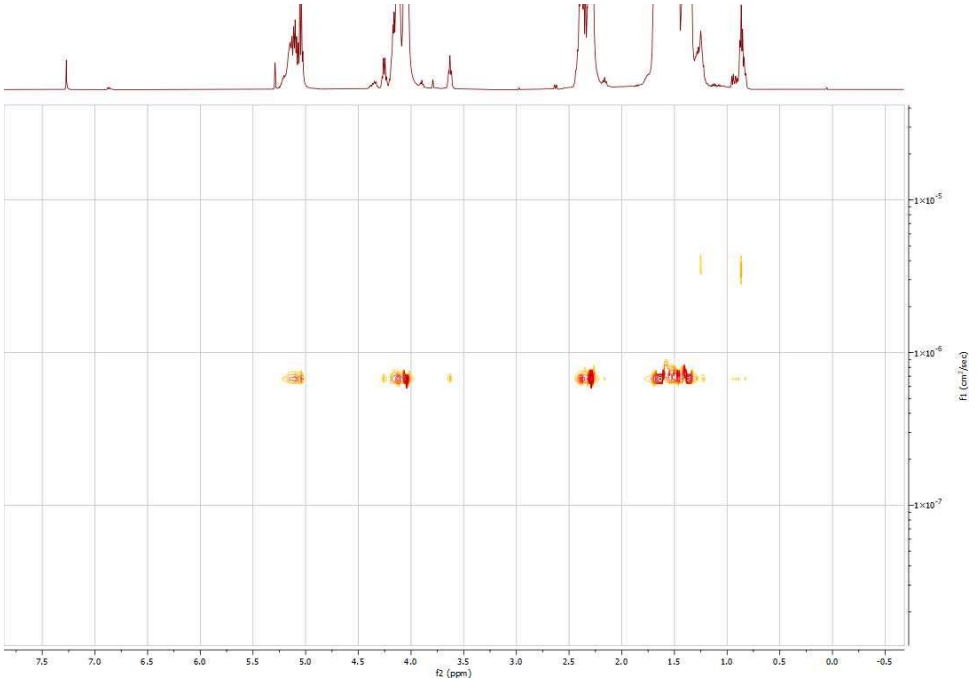

Figure 3.55. DOSY NMR ROP graft from reaction. 20 equivalents of ε-caprolactone

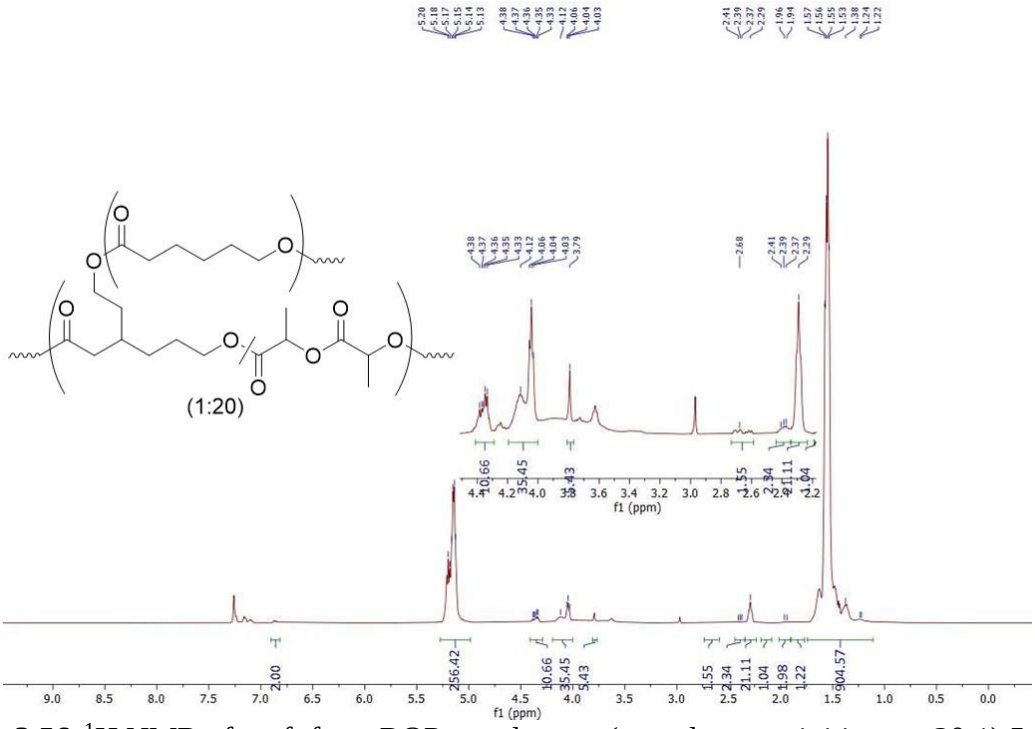

Figure 3.56. ^{1}H NMR of graft from ROP copolymers (caprolactone: initiator = 20:1) 5 equivalents caprolactone

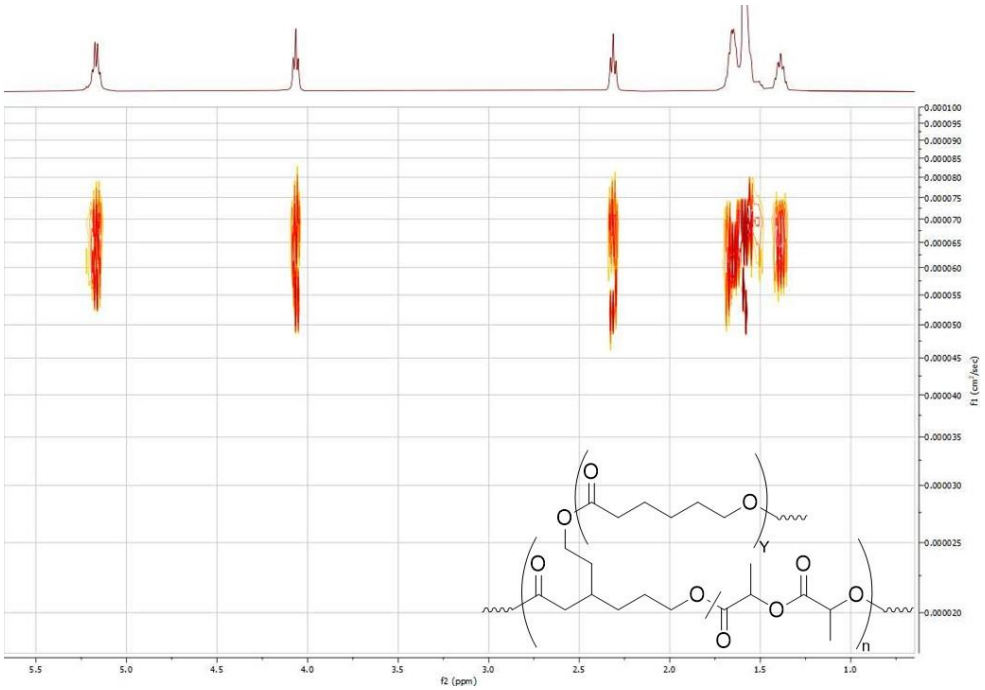

Figure 3.57. DOSY NMR of graft from ROP copolymers (caprolactone: initiator alcohol = 20:1) 20 equivalents caprolactone

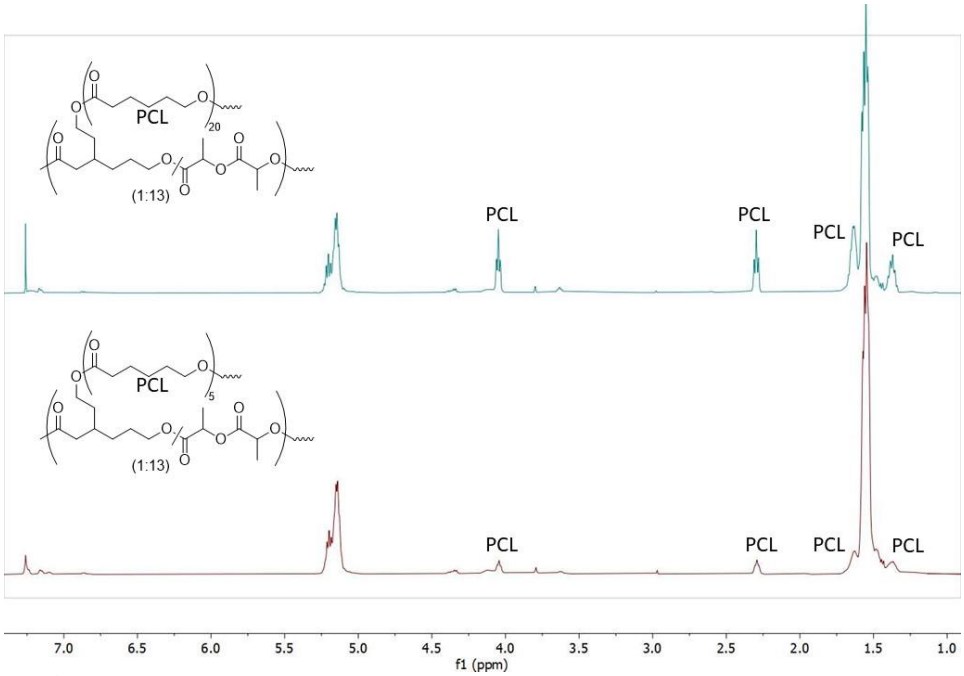

Figure 3.58. [1]H NMR grafting from radical polymerization of poly(3-vinyl caprolactone-co-lactide (1:34) with (A) 15 or (B) 50 equivalents of methacrylate. (C) is the starting material copolymer.

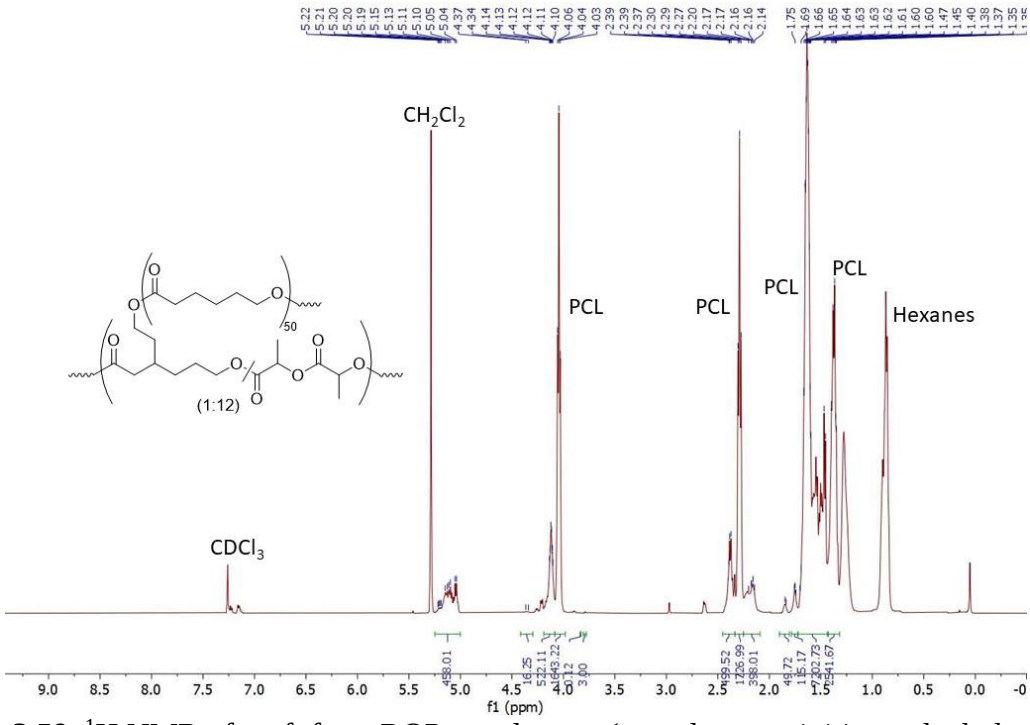

Figure 3.59. [1]H NMR of graft from ROP copolymers (caprolactone: initiator alcohol = 50:1)

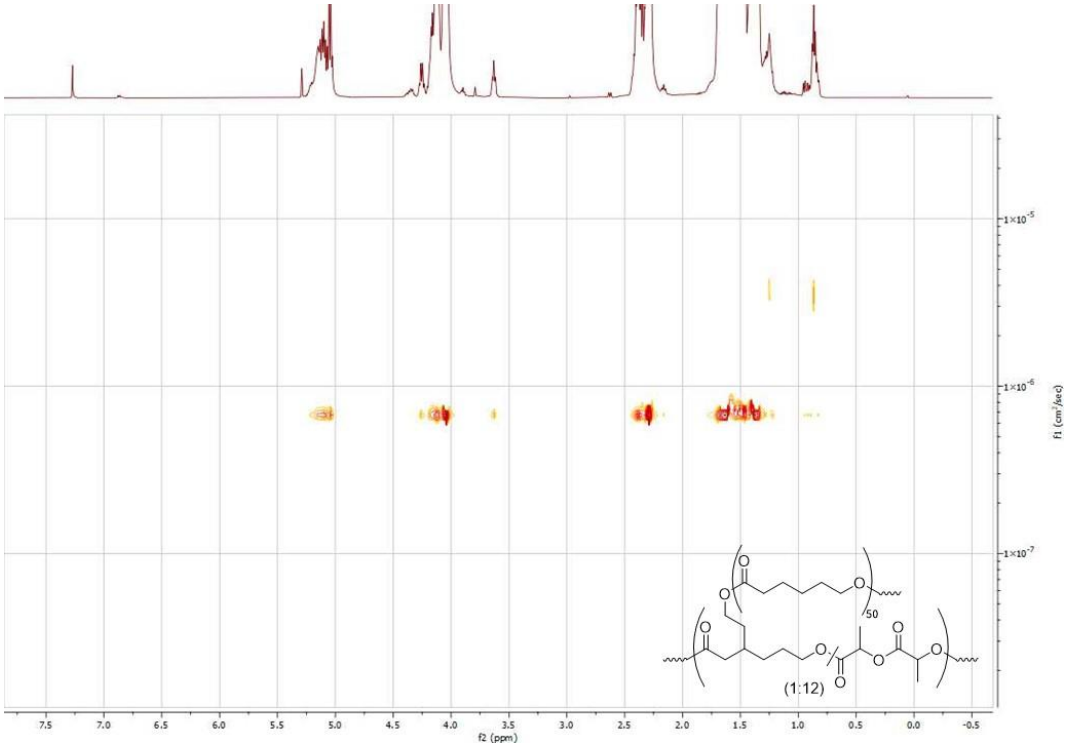

Figure 3.60. DOSY of graft from ROP copolymers (caprolactone initiator alcohol = 50:1)

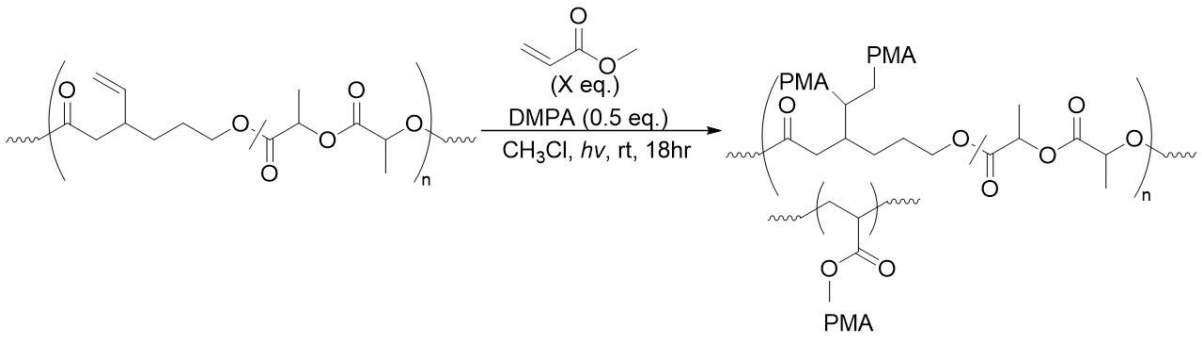

Scheme 3.20. Free-radical polymerization grafting from reaction with methacrylate with poly(3-vinyl caprolactone-stat-rac-lactide) under photo-initiating conditions with DMPA as the photo-initiator under UV light.

Grafting-from radical polymerization reactions. Example reaction

To a 10 mL vial was added a teflon stir bar, copolymer (105 mg, 0.021 mmol of vinyl groups, 1 equivalent), DMPA (6 mg, 0.01 mmol, 0.5 equivalents), anhydrous $CHCl_3$ (1 ml) and

methacrylate (94 μL, 1.0 mmol, 50 equivalents) to form a clear, colorless solution. The reaction mixture was degassed through at least three freeze, pump thaw cycles and then exposed to UV light for 18 hr while stirring. The slightly yellow solution was then precipitated into hexanes, followed by methanol to give the polymer as a white solid. Addition examples of spectra are in the appendix. ^{1}H NMR (500 MHz, $CDCl_3$) δ_H 7.24 (2H), 6.87 (2H), 5.12-5.22 (344H), 4.13 (7H), 3.80 (3), 366 (122H), 2.68 (5H), 2.25-2.43 (42H), 1.92 (18H), 1.83 (15G), 1.68 (67H), 1.42-1.58 ppm (1,146H).

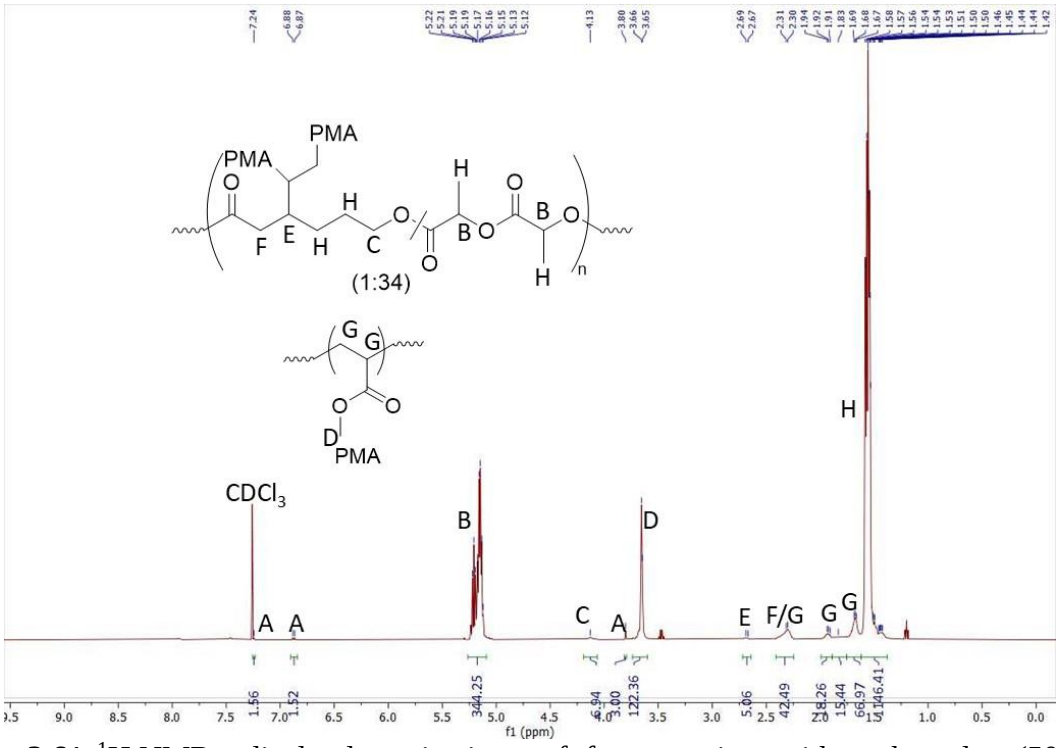

Figure 3.61. ^{1}H NMR radical polymerization graft from reactions with methacrylate (50 equivalents

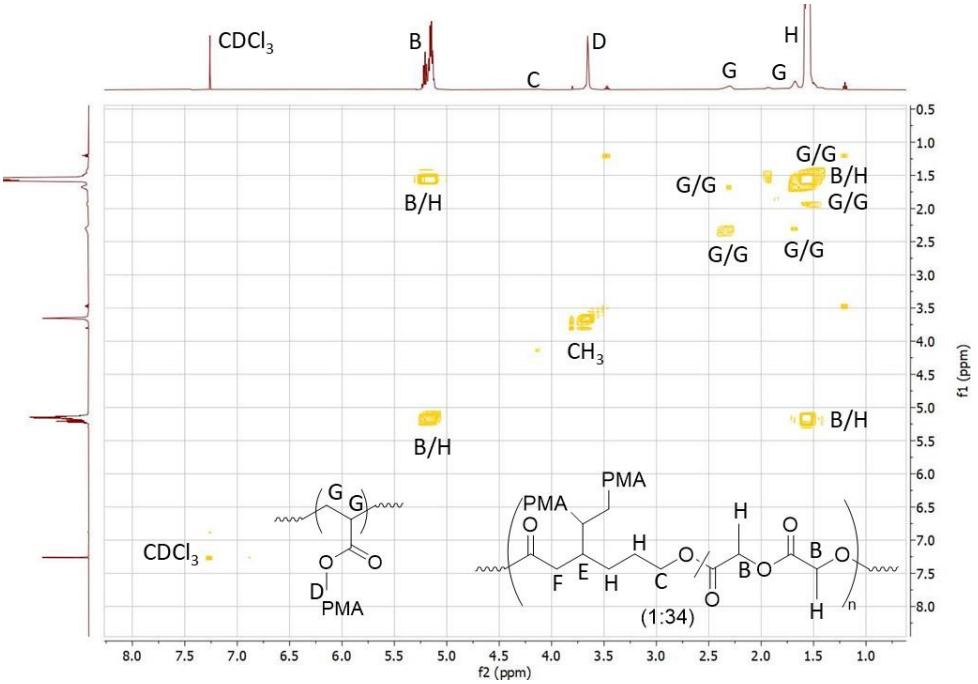

Figure 3.62. COSY NMR of radical polymerization graft from reactions with methacrylate (50 equivalents) with select coupled protons. Note: protons A, E, F are within the baseline on this intensity.

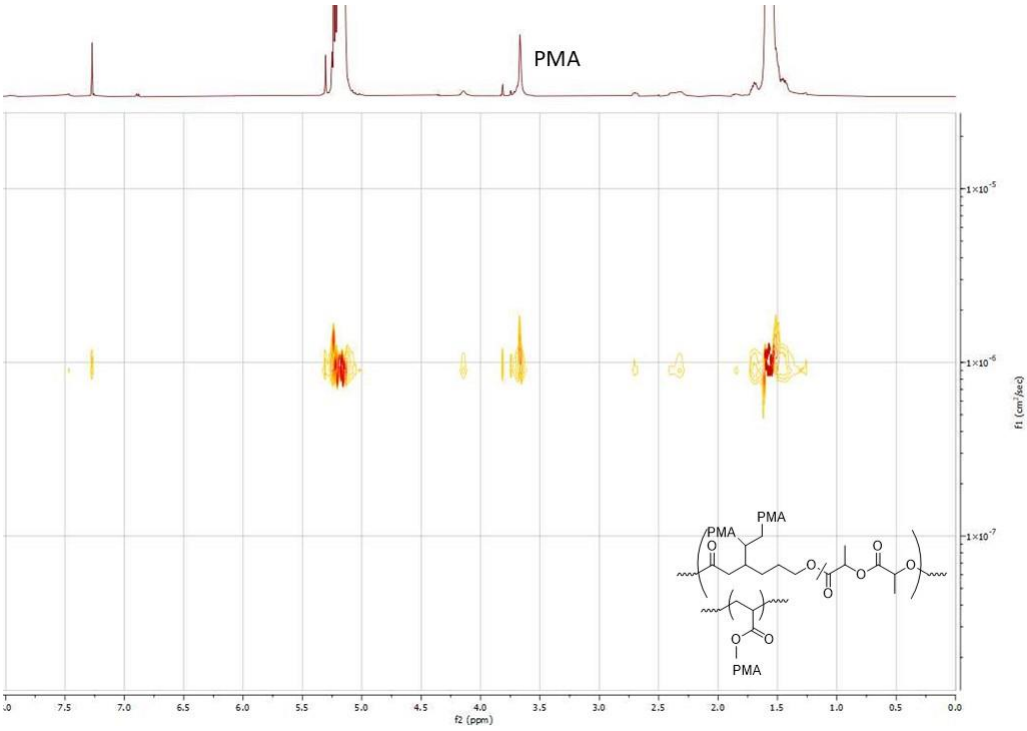

Figure 3.63. DOSY NMR of graft from radical polymerization with methacrylate under photo-initiating conditions ()

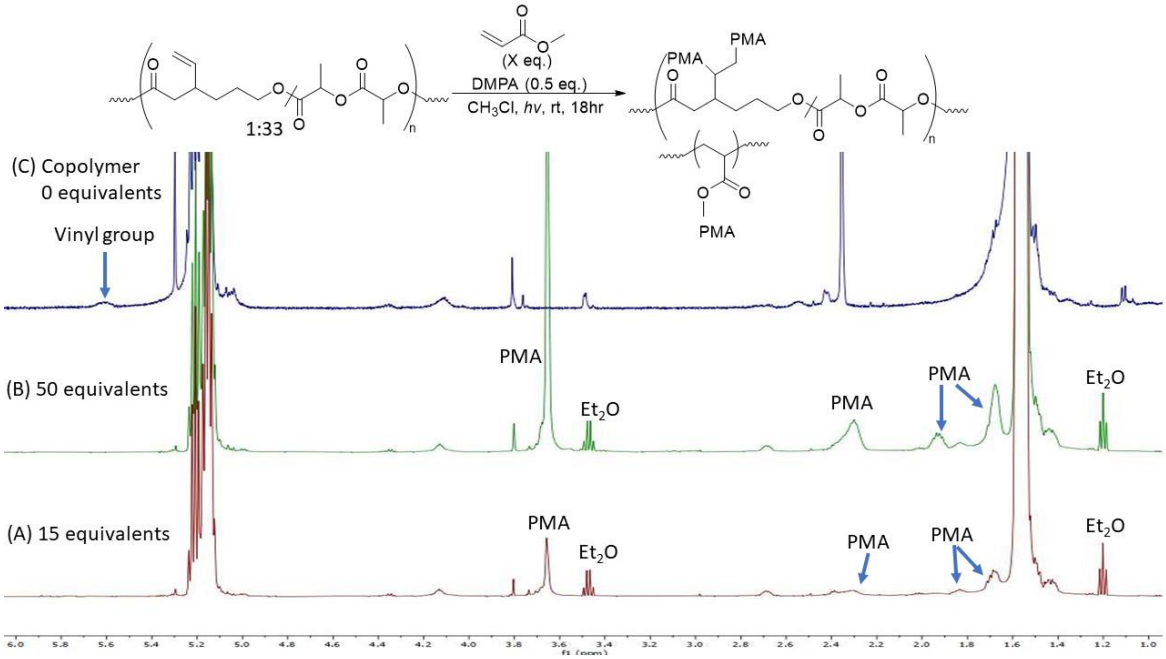

Figure 3.64. Comparison of poly(**C**-co-rac-LA) and its graft from products with methacrylate

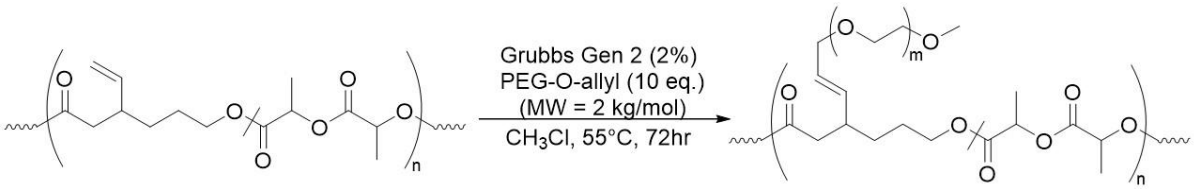

Scheme 3.21. Metathesis grafting-from reaction with monomethyl monoallyl ether polyethylene glycol and Grubbs Generation 2 catalyst

Grafting-from metathesis.

Copolymer (352 mg, 0.09 mmol vinyl groups, 1 equivalent) and monomethyl ether polyethylene glycol end capped with an allyl group (MW = 2 kg/mol, 500 mg, 0.25 mmol, 3 equivalents) were dissolved in anhydrous $CHCl_3$ (6 mL) in a 20 ml scintillation vial while in a nitrogen glovebox. Grubbs Generation 2 catalyst (3.7 mg, 0.004 mmol, 5%) was then added, the reaction vessel sealed with a septum secured by copper wire, removed from the glovebox and the mixture degassed by three freeze pump thaw cycles before heating in an oil bath at 55 °C for three days. After cooling to rt, the polymer was precipitated from methanol multiple times, the mother liquor removed, and the material dried by vacuum. ^{1}H NMR (500 MHz, $CDCl_3$) δ_H 7.24 (2H), 6.88 (2H), 5.60 (3H), 5.46 (1H), 5.01-5.19 (228H), 4.06-4.11 (9H), 3.80 (3H), 3.71-3.79 (3H), 3.64 (156H). 3.37 (2H), 2.39-2.54 (10H), 1.53-1.72 ppm (726H).

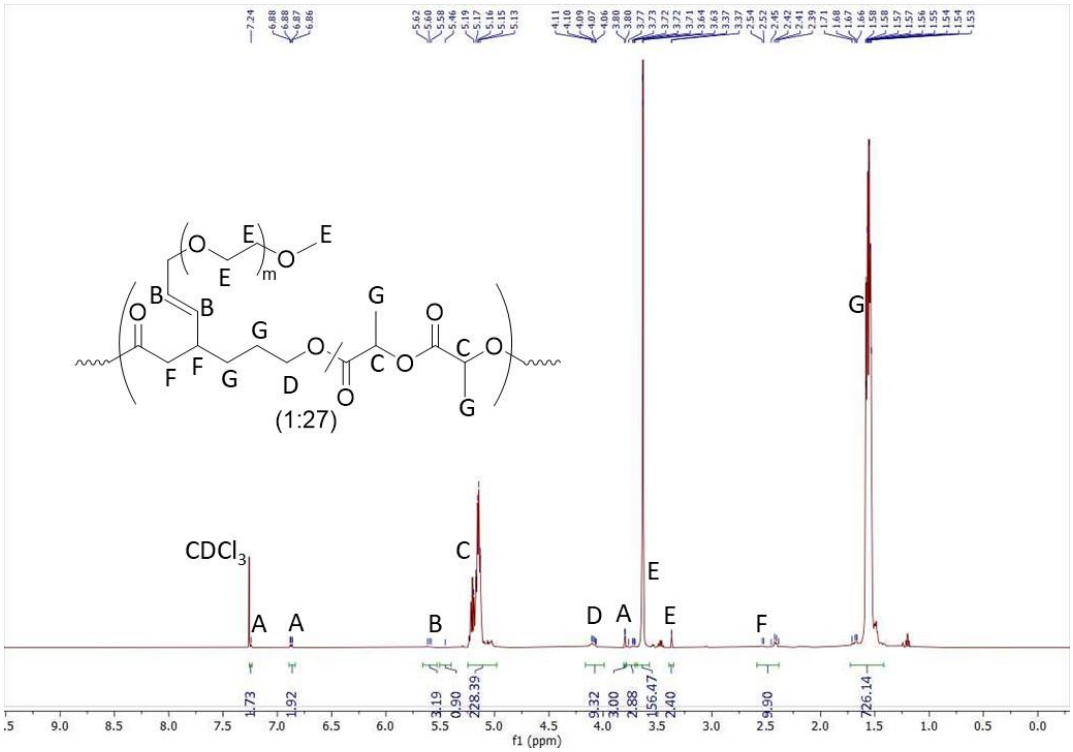

Figure 3.65. ^{1}H NMR Metathesis reaction of copolymer with PEG-O-allyl

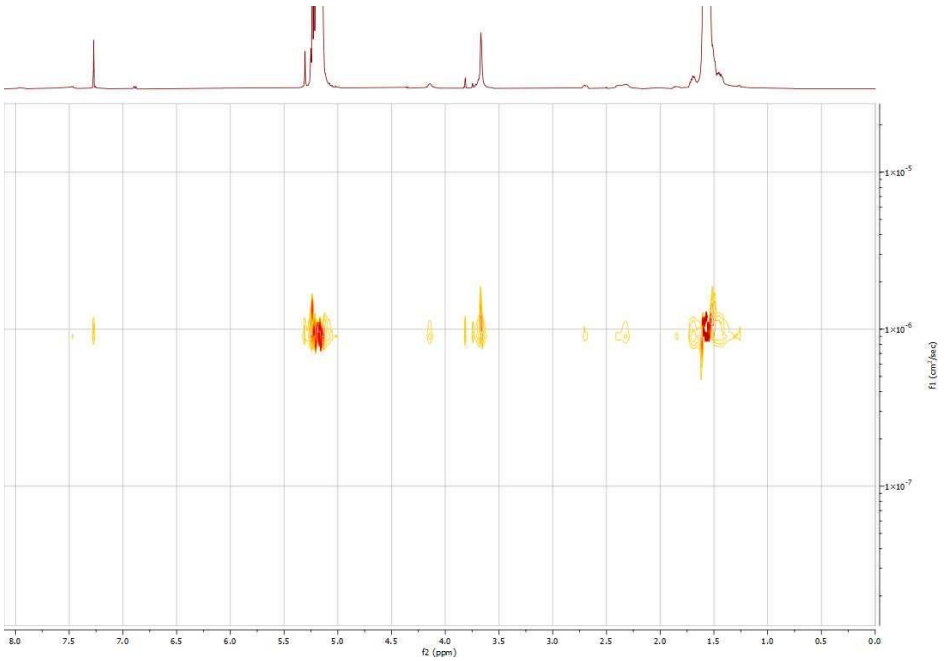

Figure 3.66. DOSY NMR of metathesis reaction between poly(3-vinyl caprolactone-co-rac-LA) with PEG-O-allyl. Sample displayed in Figure 3.55.

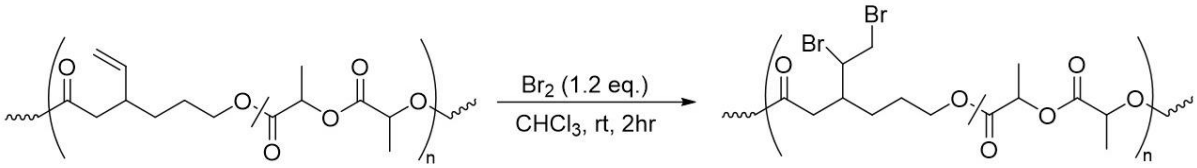

Scheme. 3.22. Bromination of poly(3-vinyl caprolactone-stat-*rac*-lactide) with elemental bromine

Bromination of copolymers

General Bromination Procedure. Poly(3-vinyl caprolactone-co-*rac*-lactide) (1:15, 225 mg, 0.1 mmol vinyl units, 1 equivalent) was dissolved in dichloromethane (0.5 mL). To the solution was added elemental bromine (6.5 µL, 0.12 mmol, 1.2 equivalents) and the now orange/brown mixture stirred for two hr at room temperature. Saturated aqueous $Na_2S_2O_3$ was then added until the solution became colorless and then 3 mL of water was added to dilute the mixture. The organics were then extracted with CH_2Cl_2 (3 x 2 mL) and the organics dried over Na_2SO_4, filtered and concentrated. The resulting white solid was dissolved in minimum CH_2Cl_2 and precipitated from diethyl ether. The reaction was successful based on the disappearance of vinyl protons. Note: Bromination and epoxidation of the vinyl groups creates a new chiral center and set of diastereomers, which dilutes the proton signal in ^{1}H NMR, making the new signals from the vinyl group difficult to assign.

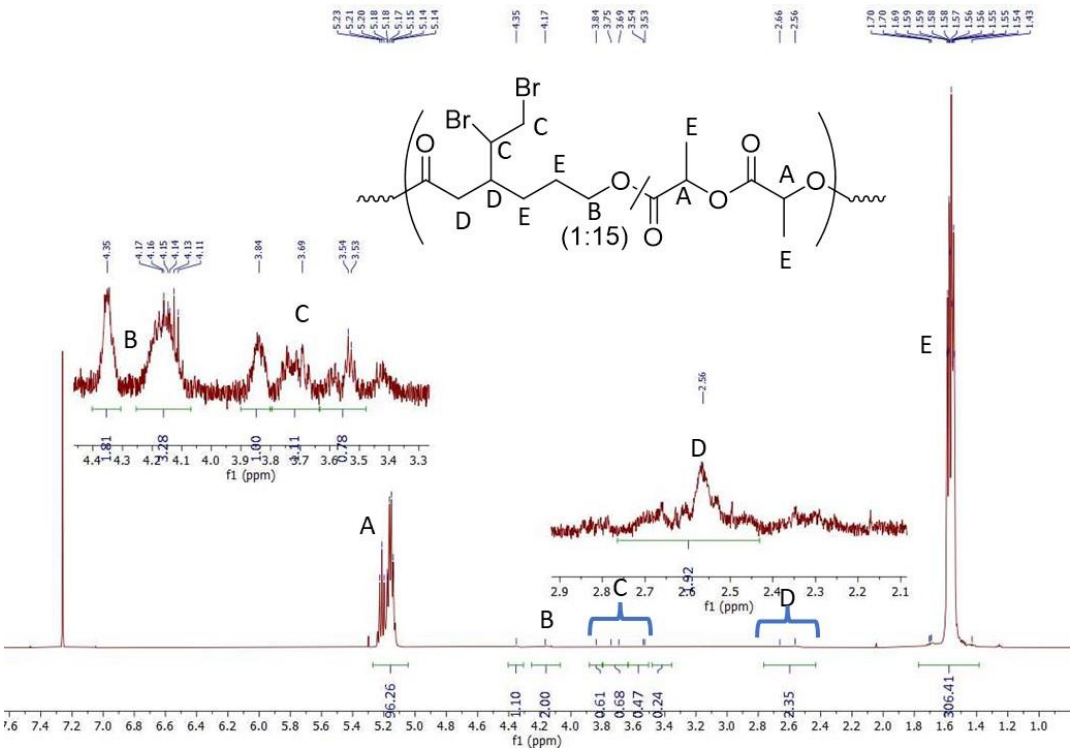

Figure 3.67. ^{1}H NMR of bromination product of poly(3-vinyl caprolactone-co-rac-lactide) (1:15). Note: peak at 4.35 ppm is attributed to the end group monomer.

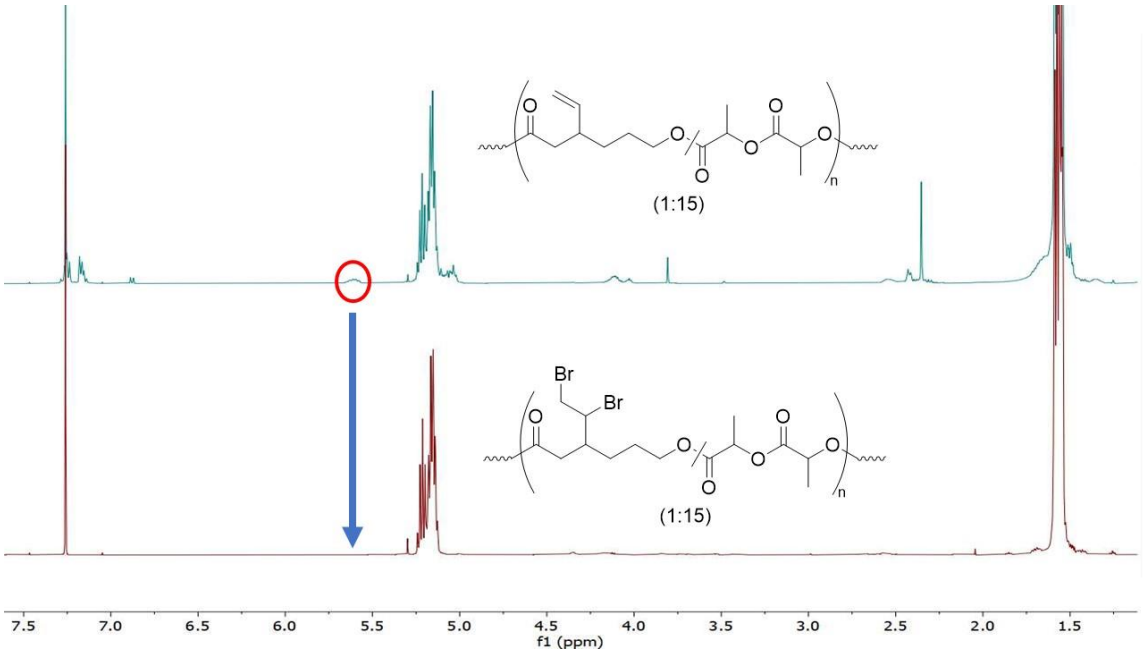

Figure 3.68. Stacked spectra of parent copolymer (top) and the brominated product (bottom) showing the disappearance of the vinyl group protons

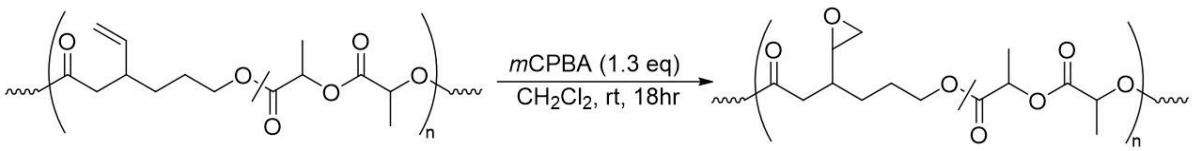

Scheme 3.23. Epoxidation of poly(3-vinyl caprolactone-stat-*rac*-lactide) using *m*CPBA

Epoxidation of copolymers

General Epoxidation Procedure. Poly(3-vinyl caprolactone-co-*rac*-lactide) (1:39, 210 mg, 0.036 mmol of vinyl units, 1 equivalent) was dissolved in 0.8 mL of CH_2Cl_2 and *m*CPBA (8.2 mg, 0.047 mmol, 1.3 equivalents) was added. The mixture was allowed to stir overnight with some white solid crashing out of solution in that time. The mixture was then filtered, the organics washed with water and brine, dried over Na_2SO_4, filtered and concentrated. The resulting white solid was dissolved in minimum CH_2Cl_2 and precipitated from diethyl ether and methanol. Reaction was successful based on the disappearance of vinyl protons.

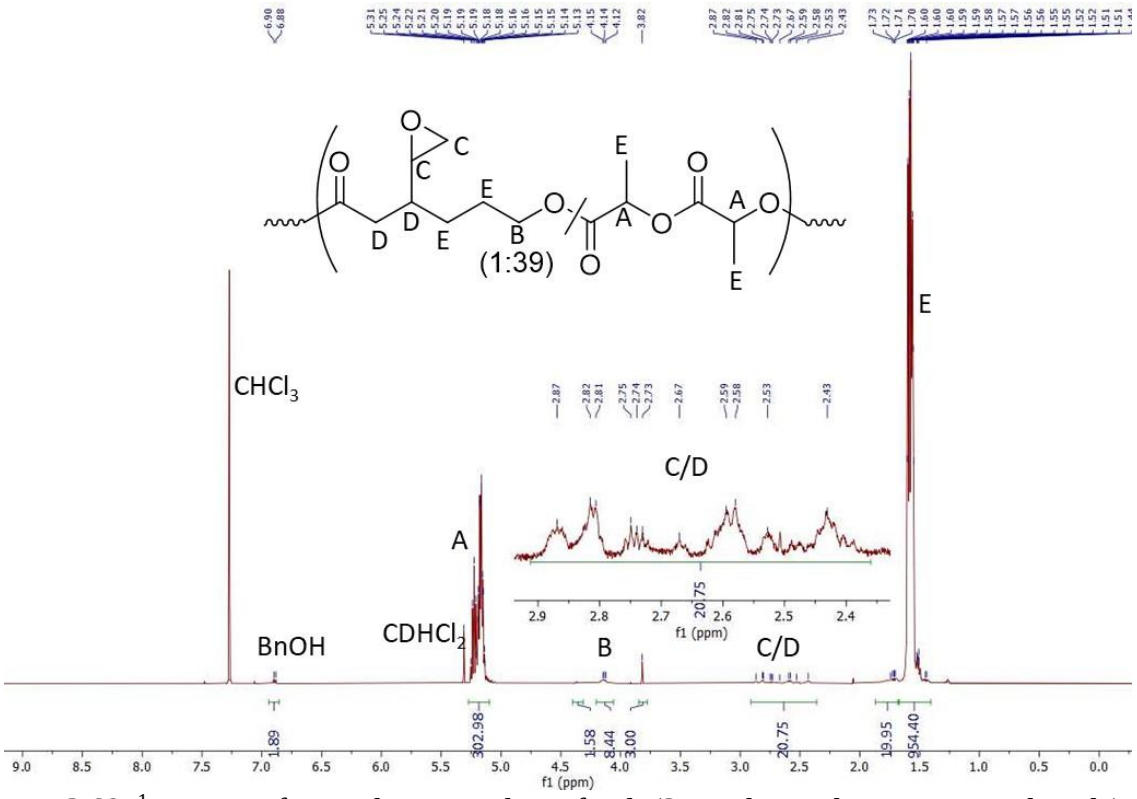

Figure 3.69. ^{1}H NMR of epoxidation product of poly(3-vinyl caprolactone-co-rac-lactide) (1:30). Complex splitting due to mixtures of chiral centers makes distinguishing protons C and D difficult.

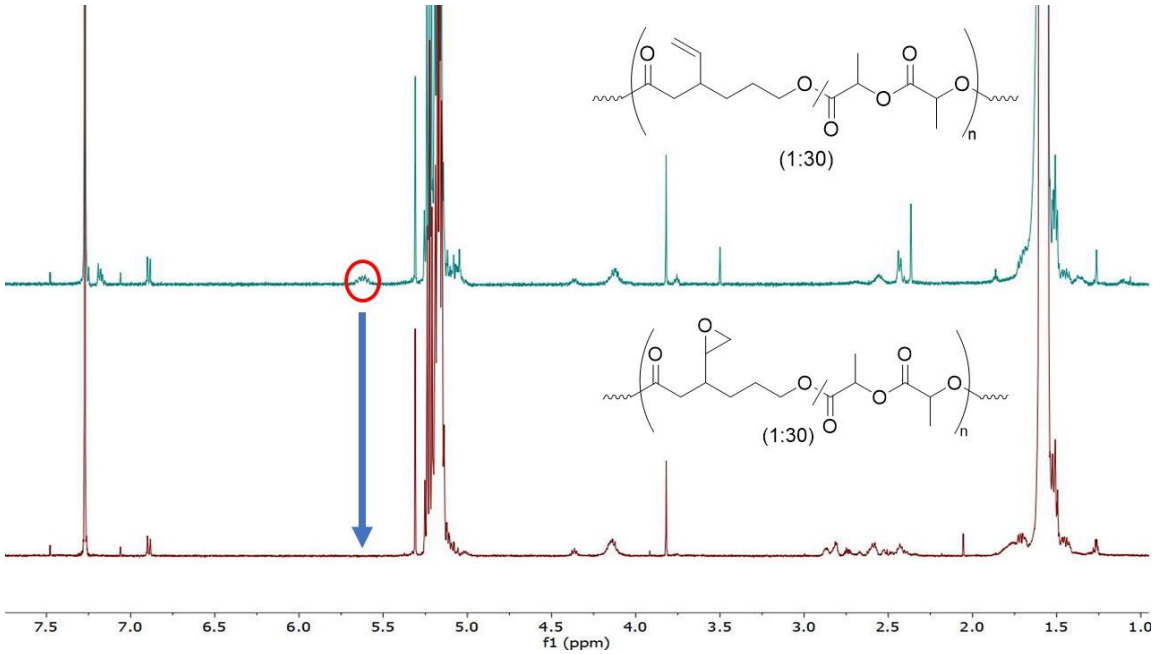

Figure 3.70. Stacked spectra of parent copolymer (top) and the epoxidized product (bottom) showing the disappearance of the vinyl group protons

3.5. References

1. Andrady, A. L.; Neal, M. A. Applications and Societal Benefits of Plastics. *Philos. Trans. R. Soc. B Biol. Sci.* **2009**, *364* (1526), 1977–1984.

2. (a) Jambeck, J.; Geyer, R.; Wilcox, C.; Siegler, T. R.; Perryman, M.; Andrady, A.; Narayan, R.; Law, K. L. Plastic Waste Inputs from Land into the Ocean. *Science (80-.* **2015**, *347* (6223), 768-. (b) Huang, J.; Veksha, A.; Chan, W. P.; Giannis, A.; Lisak, G. Chemical Recycling of Plastic Waste for Sustainable Material Management: A Prospective Review on Catalysts and Processes. *Renew. Sustain. Energy Rev.* **2022**, *154* (May 2021), 111866.

3. Henton, D. E.; Gruber, P.; Lunt, J.; Randall, J. Polylactic Acid Technology. *Adv. Mater.* **2000**, *12* (23), 1841–1846.

4. (a) Yao, K.; Tang, C. Controlled Polymerization of Next-Generation Renewable Monomers and Beyond. *Macromolecules* **2013**, *46* (5), 1689–1712. (b) Wang, F. F.; Liu, C. L.; Dong, W. S. Highly Efficient Production of Lactic Acid from Cellulose Using Lanthanide Triflate Catalysts. *Green Chem.* **2013**, *15* (8), 2091–2095. (c) Bozell, J. J.; Petersen, G. R. Technology Development for the Production of Biobased Products from Biorefinery Carbohydrates—the US Department of Energy's "Top 10" Revisited. *Green Chem.* **2010**, *12* (4), 539–555. (d) Gao, C.; Ma, C.; Xu, P. Biotechnological Routes Based on Lactic Acid Production from Biomass. *Biotechnol. Adv.* **2011**, *29* (6), 930–939. (e) Choi, S.; Song, C. W.; Shin, J. H.; Lee, S. Y. Biorefineries for the Production of Top Building Block Chemicals and Their Derivatives. *Metab. Eng.* **2015**, *28*, 223–239. (f)

Chung, H.; Yang, J. E.; Ha, J. Y.; Chae, T. U.; Shin, J. H.; Gustavsson, M.; Lee, S. Y. Bio-Based Production of Monomers and Polymers by Metabolically Engineered Microorganisms. *Curr. Opin. Biotechnol.* **2015**, *36*, 73–84.

5. Vink, E. T. H., Rábago, K. R., Glassner, D. A., & Gruber, P. R. (2003). Applications of life cycle assessment to NatureWorksTM polylactide (PLA) production. *Polymer Degradation and Stability*, *80*(3), 403–419.

6. (a) Auras, R.; Singh, P.; Singh, J. Evaluation of OPLA Polymers with Existing PET and OPS for Fresh Food Service Containers. *Pack. Technol. Sci.* **2005**, No. November 2004, 141–156. (b) Kale, G.; Auras, R.; Singh, S. P. Comparison of the Degradability of Poly(Lactide) Packages in Composting and Ambient Exposure Conditions. *Packag. Technol. Sci.* **2007**, *20* (1), 49–70. (c) Gupta, A. P.; Kumar, V. New Emerging Trends in Synthetic Biodegradable Polymers - Polylactide: A Critique. *Eur. Polym. J.* **2007**, *43* (10), 4053–4074. (d) Farah, S.; Anderson, D. G.; Langer, R. Physical and Mechanical Properties of PLA, and Their Functions in Widespread Applications — A Comprehensive Review. *Adv. Drug Deliv. Rev.* **2016**, *107*, 367–392.

7. Inkinen, S.; Hakkarainen, M.; Albertsson, A. C.; Södergård, A. From Lactic Acid to Poly(Lactic Acid) (PLA): Characterization and Analysis of PLA and Its Precursors. *Biomacromolecules* **2011**, *12* (3), 523–532.

8. (a) Shaver, M. P.; Cameron, D. J. A. Tacticity Control in the Synthesis of Poly(Lactic Acid) Polymer Stars with Dipentaerythritol Cores. *Biomacromolecules* **2010**, *11* (12), 3673–3679. (b) Sasanuma, Y.; Touge, D. Configurational Statistics of Poly(L-Lactide) and Poly(DL-Lactide) Chains. *Polymer (Guildf).* **2014**, *55* (7), 1901–1911. (c) Farah, S.;

Anderson, D. G.; Langer, R. Physical and Mechanical Properties of PLA, and Their Functions in Widespread Applications — A Comprehensive Review. *Adv. Drug Deliv. Rev.* **2016**, *107*, 367–392.

9. (a) Dechy-Cabaret, O.; Martin-Vaca, B.; Bourissou, D. Controlled Ring-Opening Polymerization of Lactide and Glycolide. *Chem. Rev.* **2004**, *104* (12), 6147–6176. (b) Albertsson, A. C.; Varma, I. K. Recent Developments in Ring Opening Polymerization of Lactones for Biomedical Applications. *Biomacromolecules* **2003**, *4* (6), 1466–1486. (c) Platel, R. H.; Hodgson, L. M.; Williams, C. K. Biocompatible Initiators for Lactide Polymerization. *Polym. Rev.* **2008**, *48* (1), 11–63. (d) Jérôme, C.; Lecomte, P. Recent Advances in the Synthesis of Aliphatic Polyesters by Ring-Opening Polymerization. *Adv. Drug Deliv. Rev.* **2008**, *60* (9), 1056–1076. (e) Wheaton, C. A.; Hayes, P. G.; Ireland, B. J. Complexes of Mg, Ca and Zn as Homogeneous Catalysts for Lactide Polymerization. *J. Chem. Soc. Dalt. Trans.* **2009**, *9226* (25), 4832–4846. (f) Jianming, R.; Anguo, X.; Hongwei, W.; Hailin, Y. Review - Recent Development of Ring-Opening Polymerization of Cyclic Esters Using Aluminum Complexes. *Des. Monomers Polym.* **2014**, *17* (4), 345–355. (g) Stanford, M. J.; Dove, A. P. Stereocontrolled Ring-Opening Polymerisation of Lactide. *Chem. Soc. Rev.* **2010**, *39* (2), 486–494. (h) Sauer, A.; Kapelski, A.; Fliedel, C.; Dagorne, S.; Kol, M.; Okuda, J. Structurally Well-Defined Group 4 Metal Complexes as Initiators for the Ring-Opening Polymerization of Lactide Monomers. *Dalt. Trans.* **2013**, *42* (25), 9007–9023. (i) Chisholm, M. H. Concerning the Ring-Opening Polymerization of Lactide and Cyclic Esters by Coordination Metal Catalysts. *Pure Appl. Chem.* **2010**, *82* (8), 1647–1662.

10. (a) Ohya, Y.; Nagahama, K. Biodegradable Polymeric Materials. *Drug Deliv. Syst.* **2008**, *23* (6), 618–626. (b) Rasal, R. M.; Janorkar, A. V.; Hirt, D. E. Poly(Lactic Acid) Modifications. *Prog. Polym. Sci.* **2010**, *35* (3), 338–356. (c) Auras, R.; Harte, B.; Selke, S. An Overview of Polylactides as Packaging Materials. *Macromol. Biosci.* **2004**, *4* (9), 835–864. (d) Källrot, M.; Edlund, U.; Albertsson, A. C. Covalent Grafting of Poly(L-Lactide) to Tune the in Vitro Degradation Rate. *Biomacromolecules* **2007**, *8* (8), 2492–2496. (e) Cong, S. Properties of Polylactic Acid Fiber Based Polymers and Their Correlation with Composition. *Proc. 2007 Int. Conf. Adv. Fibers Polym. Mater. ICAFPM* **2007**, *1*, 8–11. (f) Kaseem, M. Properties and Medical Applications of Polylactic Acid, Pol. **2014**. (g) Tyler, B.; Gullotti, D.; Mangraviti, A.; Utsuki, T.; Brem, H. Polylactic Acid (PLA) Controlled Delivery Carriers for Biomedical Applications. *Adv. Drug Deliv. Rev.* **2016**, *107*, 163–175.

11. (a) Nagarajan, V.; Mohanty, A. K.; Misra, M. Perspective on Polylactic Acid (PLA) Based Sustainable Materials for Durable Applications: Focus on Toughness and Heat Resistance. *ACS Sustain. Chem. Eng.* **2016**, *4* (6), 2899–2916. (b) Sangeetha, V. H.; Deka, H.; Varghese, T. O.; Nayak, S. K. State of the Art and Future Prospectives of Poly(Lactic Acid) Based Blends and Composites. *Polym. Compos.* **2018**, *39* (1), 81–101. (c) Yu, L.; Dean, K.; Li, L. Polymer Blends and Composites from Renewable Resources. *Prog. Polym. Sci.* **2006**, *31* (6), 576–602.

12. Koning, C.; Van Duin, M.; Pagnoulle, C.; Jerome, R. Strategies for Compatibilization of Polymer Blends. *Prog. Polym. Sci.* **1998**, *23* (4), 707–757. (b) Calandrelli, L.; Calarco, A.; Laurienzo, P.; Malinconico, M.; Petillo, O.; Peluso, G. Compatibilized Polymer

Blends Based on PDLLA and PCL for Application in Bioartificial Liver. *Biomacromolecules* **2008**, *9* (6), 1527–1534. (c) Imre, B.; Pukánszky, B. Compatibilization in Bio-Based and Biodegradable Polymer Blends. *Eur. Polym. J.* **2013**, *49* (6), 1215–1233.

13. (a) D'Hooge, D. R.; Van Steenberge, P. H. M.; Derboven, P.; Reyniers, M. F.; Marin, G. B. Model-Based Design of the Polymer Microstructure: Bridging the Gap between Polymer Chemistry and Engineering. *Polym. Chem.* **2015**, *6* (40), 7081–7096. (b) Panahi-Sarmad, M.; Abrisham, M.; Noroozi, M.; Amirkiai, A.; Dehghan, P.; Goodarzi, V.; Zahiri, B. Deep Focusing on the Role of Microstructures in Shape Memory Properties of Polymer Composites: A Critical Review. *Eur. Polym. J.* **2019**, *117* (March), 280–303. (c) Urayama, H.; Moon, S. Il; Kimura, Y. Microstructure and Thermal Properties of Polylactides with Different L- and D-Unit Sequences: Importance of the Helical Nature of the L-Sequenced Segments. *Macromol. Mater. Eng.* **2003**, *288* (2), 137–143. (d) Urayama, H.; Kanamori, T.; Kimura, Y. Microstructure and Thermomechanical Properties of Glassy Polylactides with Different Optical Purity of the Lactate Units. *Macromol. Mater. Eng.* **2001**, *286* (11), 705–713.

14. Stirling, E.; Champouret, Y.; Visseaux, M. Catalytic Metal-Based Systems for Controlled Statistical Copolymerisation of Lactide with a Lactone. *Polym. Chem.* **2018**, *9* (19), 2517–2531.

15. (a) Wedde, S.; Rommelmann, P.; Scherkus, C.; Schmidt, S.; Bornscheuer, U. T.; Liese, A.; Gröger, H. An Alternative Approach towards Poly-ε-Caprolactone through a Chemoenzymatic Synthesis: Combined Hydrogenation, Bio-Oxidations and

Polymerization without the Isolation of Intermediates. *Green Chem.* **2017**, *19* (5), 1286–1290. (b) Das, M.; Mandal, B.; Katiyar, V. Sustainable Routes for Synthesis of Poly(ε-Caprolactone): Prospects in Chemical Industries. 2020, pp 21–33.

16. Woodruff, M. A.; Hutmacher, D. W. The Return of a Forgotten Polymer - Polycaprolactone in the 21st Century. *Prog. Polym. Sci.* **2010**, *35* (10), 1217–1256.

17. (a) Bero, M.; Kasperczyk, J.; Adamus, G. Coordination Polymerization of Lactides, 3. Copolymerization of L,L-Lactide and ε-Caprolactone in the Presence of Initiators Containing Zn and Al. *Die Makromolekulare Chemie*. 1993, pp 907–912. (b Bero, M.; Kasperczyk, J.; Adamus, G. Coordination Polymerization of Lactides, 3. Copolymerization of L,L-Lactide and ε-Caprolactone in the Presence of Initiators Containing Zn and Al. *Die Makromolekulare Chemie*. 1993, pp 907–912. (c) Mosna, J.; Duda, A.; Libiszowski, J.; Penczek, S. Copolymerization of LL-Lactide at Its Living Polymer-Monomer Equilibrium with E-Caprolactone as Comonomer. *Macromolecules* **2005**, *38*, 2027–2029. (d) Duda, A.; Biela, T.; Libiszowski, J.; Penczek, S.; Dubois, P.; Mecerreyes, D.; Jérôme, R. Block and Random Copolymers of ε-Caprolactone. *Polym. Degrad. Stab.* **1998**, *59* (1–3), 215–222. (e) Vion, J. M.; Jérôme, R.; Teyssié, P.; Aubin, M.; Prud'homme, R. E. Synthesis, Characterization, and Miscibility of Caprolactone Random Copolymers. *Macromolecules* **1986**, *19* (7), 1828–1838. (f) Vanhoorne, P.; Dubois, P.; Jerome, R.; Teyssie, P. Structural Analysis of Copolyesters of E-Caprolactone and l- or D , L-Lactide Initiated by Al(OiPr)3. **1992**, *3*, 37–44. (g) Watanabe, K.; Tanaka, R.; Takada, K.; Kim, M. J.; Lee, J. S.; Tajima, K.; Isono, T.;

Satoh, T. Intramolecular Olefin Metathesis as a Robust Tool to Synthesize Single-Chain Nanoparticles in a Size-Controlled Manner. *Polym. Chem.* **2016**, *7* (29), 4782–4792.

18. Lewiński, J.; Horeglad, P.; Wójcik, K.; Justyniak, I. Chelation Effect in Polymerization of Cyclic Esters by Metal Alkoxides: Structure Characterization of the Intermediate Formed by Primary Insertion of Lactide into the Al-OR Bond of an Organometallic Initiator. *Organometallics*. 2005, pp 4588–4593.

19. (a) Jacobs, C.; Dubois, P.; Jerome, R.; Teyssie, P. Macromolecular Engineering of Polylactones and Polylactides. 5. Synthesis and Characterization of Diblock Copolymers Based on Poly-e-Caprolactone and Poly(L,L or D,L)Lactide by Aluminum Alkoxides. *Macromolecules* **1991**, *24* (11), 3027–3034. (b) Florczak, M.; Libiszowski, J.; Mosnacek, J.; Duda, A.; Penczek, S. L,L-Lactide and ε-Caprolactone Block Copolymers by a "poly(L,L-Lactide) Block First" Route. *Macromol. Rapid Commun.* **2007**, *28* (13), 1385–1391.

20. Nomura, N.; Akita, A.; Ishii, R.; Mizuno, M. Random Copolymerization of ε-Caprolactone with Lactide Using a Homosalen-Al Complex. *J. Am. Chem. Soc.* **2010**, *132* (6), 1750–1751.

21. (a) Florczak, M.; Duda, A. Effect of the Configuration of the Active Center on Comonomer Reactivities: The Case of ε-Caprolactone/L,L-Lactide Copolymerization. *Angewandte Chemie - International Edition*. 2008, pp 9088–9091. (b) Kan, C.; Ma, H. Copolymerization of L-Lactide and ϵ-Caprolactone Catalyzed by Mono-and Dinuclear Salen Aluminum Complexes Bearing Bulky 6,6′-Dimethylbipheyl-Bridge: Random and Tapered Copolymer. *RSC Adv.* **2016**, *6* (53), 47402–47409.

22. (a) Fernández, J.; Etxeberria, A.; Sarasua, J. R. Synthesis, Structure and Properties of Poly(L-Lactide-Co-ε-Caprolactone) Statistical Copolymers. *J. Mech. Behav. Biomed. Mater.* **2012**, *9*, 100–112. (b) Fernández, J.; Etxeberria, A.; Sarasua, J. R. Synthesis, Structure and Properties of Poly(L-Lactide-Co-ε-Caprolactone) Statistical Copolymers. *J. Mech. Behav. Biomed. Mater.* **2012**, *9*, 100–112. (c) Hiljanen-Vainio, M.; Karjalainen, T.; Seppälä, J. Biodegradable Lactone Copolymers. I. Characterization and Mechanical Behavior of ε-Caprolactone and Lactide Copolymers. *Journal of Applied Polymer Science*. 1996, pp 1281–1288. (d) Hiljanen-Vainio, M. P.; Orava, P. A.; Seppala, J. V. Properties of ε-Caprolactone/DL-Lactide (ε-CL/DL-LA) Copolymers with a Minor ε-CL Content. *Journal of Biomedical Materials Research*. 1997, pp 39–46. (e) Ostafinska, A.; Fortelny, I.; Nevoralova, M.; Hodan, J.; Kredatusova, J.; Slouf, M. Synergistic Effects in Mechanical Properties of PLA/PCL Blends with Optimized Composition, Processing, and Morphology. *RSC Adv.* **2015**, *5* (120), 98971–98982. (f) Fortelny, I.; Ujcic, A.; Fambri, L.; Slouf, M. Phase Structure, Compatibility, and Toughness of PLA/PCL Blends: A Review. *Front. Mater.* **2019**, *6* (August), 1–13. (g) Luyt, A. S.; Gasmi, S. Influence of Blending and Blend Morphology on the Thermal Properties and Crystallization Behaviour of PLA and PCL in PLA/PCL Blends. *J. Mater. Sci.* **2016**, *51* (9), 4670–4681. (h) Matta, A. K.; Rao, R. U.; Suman, K. N. S.; Rambabu, V. Preparation and Characterization of Biodegradable PLA/PCL Polymeric Blends. *Procedia Mater. Sci.* **2014**, *6* (Icmpc), 1266–1270. (i) Sangroniz, A.; Sangroniz, L.; Hamzehlou, S.; Río, J. del; Santamaria, A.; Sarasua, J. R.; Iriarte, M.; Leiza, J. R.; Etxeberria, A. Lactide-Caprolactone Copolymers with Tuneable Barrier Properties for Packaging Applications.

Polymer (Guildf). **2020**, *202* (February). (j) Fernández, J.; Larrañaga, A.; Etxeberría, A.; Sarasua, J. R. Effects of Chain Microstructures and Derived Crystallization Capability on Hydrolytic Degradation of Poly(l-Lactide/ε-Caprolactone) Copolymers. *Polymer Degradation and Stability*. 2013, pp 481–489. (k) Ugartemendia, J. M.; Muñoz, M. E.; Santamaria, A.; Sarasua, J. R. Supramolecular Structure, Phase Behavior and Thermo-Rheological Properties of a Poly (l-Lactide-Co-ε-Caprolactone) Statistical Copolymer. *Journal of the Mechanical Behavior of Biomedical Materials*. 2015, pp 153–163.

23. (a) Dong, Z.; Ren, Z.; Thompson, S. J.; Xu, Y.; Dong, G. Transition-Metal-Catalyzed C-H Alkylation Using Alkenes. *Chem. Rev.* **2017**, *117* (13), 9333–9403. (b) Lan, X. W.; Wang, N. X.; Xing, Y. Recent Advances in Radical Difunctionalization of Simple Alkenes. *European J. Org. Chem.* **2017**, *2017* (39), 5821–5851. (c) Beller, M.; Seayad, J.; Tillack, A.; Jiao, H. Catalytic Markovnikov and Anti-Markovnikov Functionalization of Alkenes and Alkynes: Recent Developments and Trends. *Angew. Chemie - Int. Ed.* **2004**, *43* (26), 3368–3398. (d) Zhou, F.; Li, M.; Jiang, H.; Wu, W. Recent Advances in Transformations Involving Electron-Rich Alkenes: Functionalization, Cyclization, and Cross-Metathesis Reactions. *Adv. Synth. Catal.* **2021**, *363* (21), 4841–4855.

24. (a) D. Mecerreyes, R. D. Miller, J. L. Hedrick, C. Detrembleur, R. J. Ring-opening Polymerization of 6-hydroxynon-8-enoic Acid Lactone Novel Biodegradable Copolymers Containing Allyl Pendent Groups. *J. Polym. Sci. Part A Polym. Chem.* **2000**, *38*, 870–875. (b) Campos, L. M.; Killops, K. L.; Sakai, R.; Paulusse, J. M. J.; Damiron, D.; Drockenmuller, E.; Messmore, B. W.; Hawker, C. J. Development of Thermal and Photochemical Strategies for Thiol-Ene Click Polymer Functionalization.

Macromolecules **2008**, *41* (19), 7063–7070. (c) Ritter, O. S. and H. Hyperbranched Polyesters Based on Hydroxyalkyl-Lactones via Thiol-Ene Click Reaction. *Polym Int* **2015**, *64*, 37–41. (d) Clamor, C.; Cattoz, B. N.; Wright, P. M.; O'Reilly, R. K.; Dove, A. P. Controlling the Crystallinity and Solubility of Functional PCL with Efficient Post-Polymerisation Modification. *Polym. Chem.* **2021**, *12* (13), 1983–1990. (e) Watanabe, K.; Tanaka, R.; Takada, K.; Kim, M. J.; Lee, J. S.; Tajima, K.; Isono, T.; Satoh, T. Intramolecular Olefin Metathesis as a Robust Tool to Synthesize Single-Chain Nanoparticles in a Size-Controlled Manner. *Polym. Chem.* **2016**, *7* (29), 4782–4792. (f) Silantyeva, E. A.; Willits, R. K.; Becker, M. L. Postfabrication Tethering of Molecular Gradients on Aligned Nanofibers of Functional Poly(ϵ-Caprolactone)S. *Biomacromolecules* **2019**, *20* (12), 4494–4501. (g) Campos, L. M.; Killops, K. L.; Sakai, R.; Paulusse, J. M. J.; Damiron, D.; Drockenmuller, E.; Messmore, B. W.; Hawker, C. J. Development of Thermal and Photochemical Strategies for Thiol-Ene Click Polymer Functionalization. *Macromolecules* **2008**, *41* (19), 7063–7070. (h) Pelegri-O'Day, E. M.; Paluck, S. J.; Maynard, H. D. Substituted Polyesters by Thiol–Ene Modification: Rapid Diversification for Therapeutic Protein Stabilization. *J. Am. Chem. Soc.* **2017**, *139* (3), 1145–1154. (i) Darcos, V.; Antoniacomi, S.; Paniagua, C.; Coudane, J. Cationic Polyesters Bearing Pendent Amino Groups Prepared by Thiol-Ene Chemistry. *Polym. Chem.* **2012**, *3* (2), 362–368.. (j) Pelegri-O'Day, E. M.; Bhattacharya, A.; Theopold, N.; Ko, J. H.; Maynard, H. D. Synthesis of Zwitterionic and Trehalose Polymers with Variable Degradation Rates and Stabilization of Insulin. *Biomacromolecules* **2020**, *21* (6), 2147–2154.

25. Schneiderman, D. K.; Hillmyer, M. A. Aliphatic Polyester Block Polymer Design. *Macromolecules* **2016**, *49* (7), 2419–2428.

26. (a) Vanhoorne, P.; Dubois, P.; Jerome, R.; Teyssie, P. Structural Analysis of Copolyesters of E-Caprolactone and l- or D , L-Lactide Initiated by Al(OiPr)3. *Macromolecules* **1992**, *3*, 37–44. (b) Vion, J. M.; Jérôme, R.; Teyssié, P.; Aubin, M.; Prud'homme, R. E. Synthesis, Characterization, and Miscibility of Caprolactone Random Copolymers. *Macromolecules* **1986**, *19* (7), 1828–1838. (c) Mosna, J.; Duda, A.; Libiszowski, J.; Penczek, S. Copolymerization of LL-Lactide at Its Living Polymer-Monomer Equilibrium with E-Caprolactone as Comonomer. *Macromolecules* **2005**, *38*, 2027–2029.

27. (a) Jacobs, C.; Dubois, P.; Jerome, R.; Teyssie, P. Macromolecular Engineering of Polylactones and Polylactides. 5. Synthesis and Characterization of Diblock Copolymers Based on Poly-e-Caprolactone and Poly(L,L or D,L)Lactide by Aluminum Alkoxides. *Macromolecules* **1991**, *24* (11), 3027–3034. (b) Florczak, M.; Libiszowski, J.; Mosnacek, J.; Duda, A.; Penczek, S. L,L-Lactide and ε-Caprolactone Block Copolymers by a "poly(L,L-Lactide) Block First" Route. *Macromol. Rapid Commun.* **2007**, *28* (13), 1385–1391.

28. (a) Yang, R.; Xu, G.; Lv, C.; Dong, B.; Zhou, L.; Wang, Q. Zn(HMDS)2 as a Versatile Transesterification Catalyst for Polyesters Synthesis and Degradation toward a Circular Materials Economy Approach. *ACS Sustain. Chem. Eng.* **2020**, *8* (50), 18347–18353. (b) Yang, R.; Xu, G.; Lv, C.; Dong, B.; Zhou, L.; Wang, Q. Zn(HMDS)2as a Versatile Transesterification Catalyst for Polyesters Synthesis and Degradation toward a Circular

Materials Economy Approach. *ACS Sustain. Chem. Eng.* **2020**, *8* (50), 18347–18353. (c) Román-Ramírez, L. A.; McKeown, P.; Jones, M. D.; Wood, J. Kinetics of Methyl Lactate Formation from the Transesterification of Polylactic Acid Catalyzed by Zn(II) Complexes. *ACS Omega* **2020**, *5* (10), 5556–5564. (d) Payne, J.; McKeown, P.; Driscoll, O.; Kociok-Köhn, G.; Emanuelsson, E. A. C.; Jones, M. D. Make or Break: Mg(II)-and Zn(II)-Catalen Complexes for PLA Production and Recycling of Commodity Polyesters. *Polym. Chem.* **2021**, *12* (8), 1086–1096. (e) Mckeown, P.; Kamran, M.; Davidson, M. G.; Jones, M. D.; Román-Ramírez, L. A.; Wood, J. Organocatalysis for Versatile Polymer Degradation. *Green Chem.* **2020**, *22* (12), 3721–3726. (f) Román-Ramírez, L. A.; McKeown, P.; Jones, M. D.; Wood, J. Poly(Lactic Acid) Degradation into Methyl Lactate Catalyzed by a Well-Defined Zn(II) Complex. *ACS Catal.* **2019**, *9* (1), 409–416. (g) (1) Alberti, C.; Damps, N.; Meißner, R. R. R.; Hofmann, M.; Rijono, D.; Enthaler, S. Selective Degradation of End-of-Life Poly(Lactide) via Alkali-Metal-Halide Catalysis. *Adv. Sustain. Syst.* **2020**, *4* (1), 1–9 (h) Stewart, J.; Fuchs, M.; Payne, J.; Driscoll, O.; Kociok-Köhn, G.; Ward, B. D.; Herres-Pawlis, S.; Jones, M. D. Simple Zn(Ii) Complexes for the Production and Degradation of Polyesters. *RSC Adv.* **2022**, *12* (3), 1416–1424. (i) Petrus, R.; Bykowski, D.; Sobota, P. Solvothermal Alcoholysis Routes for Recycling Polylactide Waste as Lactic Acid Esters. *ACS Catal.* **2016**, *6* (8), 5222–5235. (j) Petrus, R.; Bykowski, D.; Sobota, P. Solvothermal Alcoholysis Routes for Recycling Polylactide Waste as Lactic Acid Esters. *ACS Catal.* **2016**, *6* (8), 5222–5235. (k) Hofmann, M.; Alberti, C.; Scheliga, F.; Meißner, R. R. R.; Enthaler, S. Tin(Ii) 2-Ethylhexanoate Catalysed Methanolysis of End-of-Life Poly(Lactide). *Polym. Chem.* **2020**, *11* (15),

2625–2629. (l) Leibfarth, F. A.; Moreno, N.; Hawker, A. P.; Shand, J. D. Transforming Polylactide into Value-Added Materials. *J. Polym. Sci. Part A Polym. Chem.* **2012**, *50* (23), 4814–4822. (m) McKeown, P.; Román-Ramírez, L. A.; Bates, S.; Wood, J.; Jones, M. D. Zinc Complexes for PLA Formation and Chemical Recycling: Towards a Circular Economy. *ChemSusChem* **2019**, *12* (24), 5233–5238. (n) Santulli, F.; Lamberti, M.; Mazzeo, M. A Single Catalyst for Promoting Reverse Processes: Synthesis and Chemical Degradation of Polylactide. *ChemSusChem* **2021**, *14* (24), 5470–5475. (o) Román-Ramírez, L. A.; McKeown, P.; Shah, C.; Abraham, J.; Jones, M. D.; Wood, J. Chemical Degradation of End-of-Life Poly(Lactic Acid) into Methyl Lactate by a Zn(II) Complex. *Ind. Eng. Chem. Res.* **2020**, *59* (24), 11149–11156.. (p) Phomphrai, K.; Pracha, S.; Phonjanthuek, P.; Pohmakotr, M. Facile Alcoholysis of L-Lactide Catalysed by Group 1 and 2 Metal Complexes. *Dalt. Trans.* **2008**, No. 23, 3048–3050. (q) Cheung, E.; Alberti, C.; Enthaler, S. Chemical Recycling of End-of-Life Poly(Lactide) via Zinc-Catalyzed Depolymerization and Polymerization. *ChemistryOpen* **2020**, *9* (12), 1224–1228. (r) Alberti, C.; Enthaler, S. Depolymerization of End-of-Life Poly(Lactide) to Lactide via Zinc-Catalysis. *ChemistrySelect* **2020**, *5* (46), 14759–14763.

29. (a) C Jacobs, C.; Dubois, P.; Jerome, R.; Teyssie, P. Macromolecular Engineering of Polylactones and Polylactides. 5. Synthesis and Characterization of Diblock Copolymers Based on Poly-e-Caprolactone and Poly(L,L or D,L)Lactide by Aluminum Alkoxides. *Macromolecules* **1991**, *24* (11), 3027–3034. (b) Florczak, M.; Libiszowski, J.; Mosnacek, J.; Duda, A.; Penczek, S. L,L-Lactide and ε-Caprolactone Block Copolymers by a

"poly(L,L-Lactide) Block First" Route. *Macromol. Rapid Commun.* **2007**, *28* (13), 1385–1391.

30. (a) Mezzasalma, L.; Harrisson, S.; Saba, S.; Loyer, P.; Coulembier, O.; Taton, D. Bulk Organocatalytic Synthetic Access to Statistical Copolyesters from l -Lactide and ϵ-Caprolactone Using Benzoic Acid. *Biomacromolecules* **2019**, *20* (5), 1965–1974. (b) Mezzasalma, L.; De Winter, J.; Taton, D.; Coulembier, O. Benzoic Acid-Organocatalyzed Ring-Opening (Co)Polymerization (ORO(c)P) of l-Lactide and ϵ-Caprolactone under Solvent-Free Conditions: From Simplicity to Recyclability. *Green Chem.* **2018**, *20* (23), 5385–5396. (c) Jehanno, C.; Mezzasalma, L.; Sardon, H.; Ruipérez, F.; Coulembier, O.; Taton, D. Benzoic Acid as an Efficient Organocatalyst for the Statistical Ring-Opening Copolymerization of ϵ-Caprolactone and L -Lactide: A Computational Investigation. *Macromolecules* **2019**, *52* (23), 9238–9247.

31. Paterson, I. α-Alkylation and α-Alkylidenation of Carbonyl Compounds By O-Silylated Enolate Phenylthioalkylation. *Tetrahedron* **1988**, *44* (13), 4207–4219.

32. Minami, I.; Takahashi, K.; Shimizu, I.; Kimura, T.; Tsuji, J. New Synthetic Methods for α,β -Unsaturated Ketones, Aldehydes, Esters and Lactones by the Palladium-Catalyzed Reactions of Silyl Enol Ethers, Ketene Silyl Acetals, and Enol Acetates with Allyl Carbonates. *Tetrahedron* **1986**, *42* (11), 2971–2977.

33. (a) Matsumura, S.; Hlil, A. R.; Lepiller, C.; Gaudet, J.; Guay, D.; Shi, Z.; Holdcroft, S.; Hay, A. S. Modification of RAFT-Polymers via Thiol-Ene Reactions: A General Route to Functional Polymers and New Architectures. *J. Polym. Sci. Part A Polym. Chem.* **2008**,

46 (April), 7207–7224. (b) Lowe, A. B. Thiol-Ene "Click" Reactions and Recent Applications in Polymer and Materials Synthesis. *Polym. Chem.* **2010**, *1* (1), 17–36.

34. For examples of reports using a similar methodology see the following examples: (a) Yi, N.; Chen, T. T. D.; Unruangsri, J.; Zhu, Y.; Williams, C. K. Orthogonal Functionalization of Alternating Polyesters: Selective Patterning of (AB): N Sequences. *Chem. Sci.* **2019**, *10* (43), 9974–9980. (b) Chen, T. T. D.; Zhu, Y.; Williams, C. K. Pentablock Copolymer from Tetracomponent Monomer Mixture Using a Switchable Dizinc Catalyst. *Macromolecules* **2018**, *51* (14), 5346–5351. (c) Jones, C. H.; Chen, C. K.; Chen, M.; Ravikrishnan, A.; Zhang, H.; Gollakota, A.; Chung, T.; Cheng, C.; Pfeifer, B. A. PEGylated Cationic Polylactides for Hybrid Biosynthetic Gene Delivery. *Mol. Pharm.* **2015**, *12* (3), 846–856. (d) Campos, L. M.; Killops, K. L.; Sakai, R.; Paulusse, J. M. J.; Damiron, D.; Drockenmuller, E.; Messmore, B. W.; Hawker, C. J. Development of Thermal and Photochemical Strategies for Thiol-Ene Click Polymer Functionalization. *Macromolecules* **2008**, *41* (19), 7063–7070. (e) Pelegri-O'Day, E. M.; Paluck, S. J.; Maynard, H. D. Substituted Polyesters by Thiol–Ene Modification: Rapid Diversification for Therapeutic Protein Stabilization. *J. Am. Chem. Soc.* **2017**, *139* (3), 1145–1154. (f) Chen, C. K.; Law, W. C.; Aalinkeel, R.; Yu, Y.; Nair, B.; Wu, J.; Mahajan, S.; Reynolds, J. L.; Li, Y.; Lai, C. K.; Tzanakakis, E. S.; Schwartz, S. A.; Prasad, P. N.; Cheng, C. Biodegradable Cationic Polymeric Nanocapsules for Overcoming Multidrug Resistance and Enabling Drug-Gene Co-Delivery to Cancer Cells. *Nanoscale* **2014**, *6* (3), 1567–1572.

35. (a) Chen, J.; Spear, S. K.; Huddleston, J. G.; Rogers, R. D. Polyethylene Glycol and Solutions of Polyethylene Glycol as Green Reaction Media. *Green Chem.* **2005**, *7* (2), 64–82. (b) Corrigan, O. I.; Murphy, C. A.; Timoney, R. P. Dissolution Properties of Polyethylene Glycols and Polyethylene Glycol-Drug Systems. *Int. J. Pharm.* **1979**, *4* (1), 67–74.

36. D. Mecerreyes, R. D. Miller, J. L. Hedrick, C. Detrembleur, R. J. Ring-opening Polymerization of 6-hydroxynon-8-enoic Acid Lactone Novel Biodegradable Copolymers Containing Allyl Pendent Groups. *J. Polym. Sci. Part A Polym. Chem.* **2000**, *38*, 870–875.

37. (a) Meimoun, J.; Sutapin, C.; Stoclet, G.; Favrelle, A.; Roussel, P.; Bria, M.; Chirachanchai, S.; Bonnet, F.; Zinck, P. Lactide Lactone Chain Shuttling Copolymerization Mediated by an Aminobisphenolate Supported Aluminum Complex and Al(O IPr)3: Access to New Polylactide Based Block Copolymers. *J. Am. Chem. Soc.* **2021**, *143* (50), 21206–21210. (b) Rittinghaus, R. D.; Zenner, J.; Pich, A.; Kol, M.; Herres-Pawlis, S. Master of Chaos and Order: Opposite Microstructures of PCL-Co-PGA-Co-PLA Accessible by a Single Catalyst**. *Angew. Chemie - Int. Ed.* **2022**, *61* (11).

38. Nifant'ev, I. E.; Shlyakhtin, A. V.; Tavtorkin, A. N.; Ivchenko, P. V.; Borisov, R. S.; Churakov, A. V. Monomeric and Dimeric Magnesium Mono-BHT Complexes as Effective ROP Catalysts. *Catal. Commun.* **2016**, *87*, 106–111.

39. Maruoka, K.; Itoh, T.; Sakurai, M.; Nonoshita, K.; Yamamoto, H. Amphiphilic Reactions by Means of Exceptionally Bulky Organoaluminum Reagents. Rational Approach for

Obtaining Unusual Equatorial, Anti-Cram, and 1, 4 Selectivity in Carbonyl Alkylation. *J. Am. Chem. Soc.* **1988**, *110* (4), 3588–3597.

40. Darensbourg, D. J.; Holtcamp, M. W.; Struck, G. E.; Zimmer, M. S.; Niezgoda, S. A.; Rainey, P.; Robertson, J. B.; Draper, J. D.; Reibenspies, J. H. Catalytic Activity of a Series of Zn(II) Phenoxides for the Copolymerization of Epoxides and Carbon Dioxide. *J. Am. Chem. Soc.* **1999**, *121* (1), 107–116.

41. Maruta, Y.; Abiko, A. Random Copolymerization of ε-Caprolactone and l-Lactide with Molybdenum Complexes. *Polym. Bull.* **2014**, *71* (4), 989–999.

42. Báez, J. E.; Martínez-Richa, A. Synthesis and Characterization of Poly(ε-Caprolactone) and Copolyesters by Catalysis with Molybdenum Compounds: Polymers with Acid-Functional Asymmetric Telechelic Architecture. *Polymer (Guildf).* **2005**, *46* (26), 12118–12129.

43. Hormnirun, P.; Marshall, E. L.; Gibson, V. C.; White, A. J. P.; Williams, D. J. Remarkable Stereocontrol in the Polymerization of Racemic Lactide Using Aluminum Initiators Supported by Tetradentate Aminophenoxide Ligands. *J. Am. Chem. Soc.* **2004**, *126* (9), 2688–2689..

44. Shi, T.; Luo, W.; Liu, S.; Li, Z. Controlled Random Copolymerization of *Rac*-Lactide and ε-Caprolactone by Well-Designed Phenoxyimine Al Complexes. *J. Polym. Sci. Part A Polym. Chem.* **2018**, *56* (6), 611–617.

45. Darensbourg, D. J.; Rainey, P.; Yarbrough, J. Bis-Salicylaldiminato Complexes of Zinc. Examination of the Catalyzed Epoxide/CO2 Copolymerization. *Inorg. Chem.* **2001**, *40* (5), 986–993.

46. Pilone, A.; De Maio, N.; Press, K.; Venditto, V.; Pappalardo, D.; Mazzeo, M.; Pellecchia, C.; Kol, M.; Lamberti, M. Ring-Opening Homo- and Co-Polymerization of Lactides and ε-Caprolactone by Salalen Aluminum Complexes. *Dalt. Trans.* **2015**, *44* (5), 2157–2165.

47. Herold, R. J.; Aggarwal, S. L.; Neff, V. Mechanisms of the Reactions of Diethylzinc with Isopropanol and Water. *Can. J. Chem.* **1963**, *41* (5), 1368–1380.

48. Báez, J. E.; Martínez-Richa, A. Synthesis and Characterization of Poly(ε-Caprolactone) and Copolyesters by Catalysis with Molybdenum Compounds: Polymers with Acid-Functional Asymmetric Telechelic Architecture. *Polymer (Guildf).* **2005**, *46* (26), 12118–12129.

49. Wilson, J. A.; Hopkins, S. A.; Wright, P. M.; Dove, A. P. "Immortal" Ring-Opening Polymerization of ω-Pentadecalactone by Mg(BHT)2(THF)2. *Polym. Chem.* **2014**, *5* (8), 2691–2694.

50. Meduri, A.; Fuoco, T.; Lamberti, M.; Pellecchia, C.; Pappalardo, D. Versatile Copolymerization of Glycolide and *Rac*-Lactide by Dimethyl(Salicylaldiminato)Aluminum Compounds. *Macromolecules* **2014**, *47* (2), 534–543.

51. Özdemirhan, D.; Sarıçelik, Ö. Chemoenzymatic Route to Optically Active Dihydroxy Cyclopenta[b]Naphthalenones; Precursors for Decalin-Based Bioactive Natural Products. *Tetrahedron Asymmetry* **2017**, *28*, 118–124.

52. Just-Baringo, X.; Clark, J.; Gutmann, M. J.; Procter, D. J. Selective Synthesis of Cyclooctanoids by Radical Cyclization of Seven-Membered Lactones: Neutron

Diffraction Study of the Stereoselective Deuteration of a Chiral Organosamarium Intermediate. *Angew. Chemie - Int. Ed.* **2016**, *55* (40), 12499–12502.

53. Valerio, V.; Petkova, D.; Madelaine, C.; Maulide, N. Direct Room-Temperature Lactonisation of Alcohols and Ethers onto Amides: An "Amide Strategy" for Synthesis. *Chem. - A Eur. J.* **2013**, *19* (8), 2606–2610.

54. Molander, G. A.; Harris, C. R. Sequenced Reactions with Samarium(II) Iodide. Tandem Intramolecular Nucleophilic Acyl Substitution/Intramolecular Barbier Cyclizations. *J. Am. Chem. Soc.* **1995**, *117* (13), 3705–3716.

55. Denmark, S. E.; Gould, N. D.; Wolf, L. M. A Systematic Investigation of Quaternary Ammonium Ions as Asymmetric Phase-Transfer Catalysts. Synthesis of Catalyst Libraries and Evaluation of Catalyst Activity. *J. Org. Chem.* **2011**, *76* (11), 4260–4336.

56. Minami, I.; Tsuji, J. Dehydrogenation of Alcohols with Allyl Carbonates Catalyzed by Palladium or Ruthenium Complexes. *Tetrahedron* **1987**, *43* (17), 3903–3915.

57. Ashworth, P.; Belagali, S. L.; Casson, S.; Marczak, A.; Kocieński, P. A Method for the Chromatographic Resolution of Tetrahydropyran-2-Ones. *Tetrahedron* **1991**, *47* (47), 9939–9946.

58. Campos, L. M.; Killops, K. L.; Sakai, R.; Paulusse, J. M. J.; Damiron, D.; Drockenmuller, E.; Messmore, B. W.; Hawker, C. J. Development of Thermal and Photochemical Strategies for Thiol-Ene Click Polymer Functionalization. *Macromolecules* **2008**, *41* (19), 7063–7070.

59. Lavery, C. B.; McDonald, R.; Stradiotto, M. Efficient Palladium-Catalyzed Synthesis of Substituted Indoles Employing a New (Silanyloxyphenyl)Phosphine Ligand. *Chem. Commun.* **2012**, *48* (58), 7277–7279.

60. Nomura, N.; Ishii, R.; Yamamoto, Y.; Kondo, T. Stereoselective Ring-Opening Polymerization of a Racemic Lactide by Using Achiral Salen- and Homosalen-Aluminum Complexes. *Chem. - A Eur. J.* **2007**, *13* (16), 4433–4451.

61. Hasegawa, T.; Kishida, H.; Nomura, N. A Practical Ortho-Rearrangement of Silyl Group of Ortho-Bromophenyl Silyl Ethers Using Magnesium(0). *Tetrahedron Lett.* **2017**, *58* (5), 455–457.

Appendix A.

Directing Group Strategy for the Dual Catalytic Transesterification and Dehydrative Decarbonylation of Fatty Acid Methyl Esters

A.1 Introduction

Previous work established the potential for a dual catalytic system involving a Lewis Acid catalyst, $ZnCl_2$, that facilitated a transesterification event between a directing group, 2-pyridine methanol, and palmitic methyl ester (Figure A.1).[1] We hypothesized that upon transesterification, a second catalytic cycle takes over where $Ru_3(CO)_{12}$ in the presence of three equivalents of PCy_3 can coordinate to the pyridine group. This coordination allows Ru to become close in proximity to the acyl C-O bond of the ester and facilitate a sequence of decarbonylation, β-hydride elimination, olefin decoordination and reductive elimination, generating a mixture of olefins as well as regenerating the directing group.

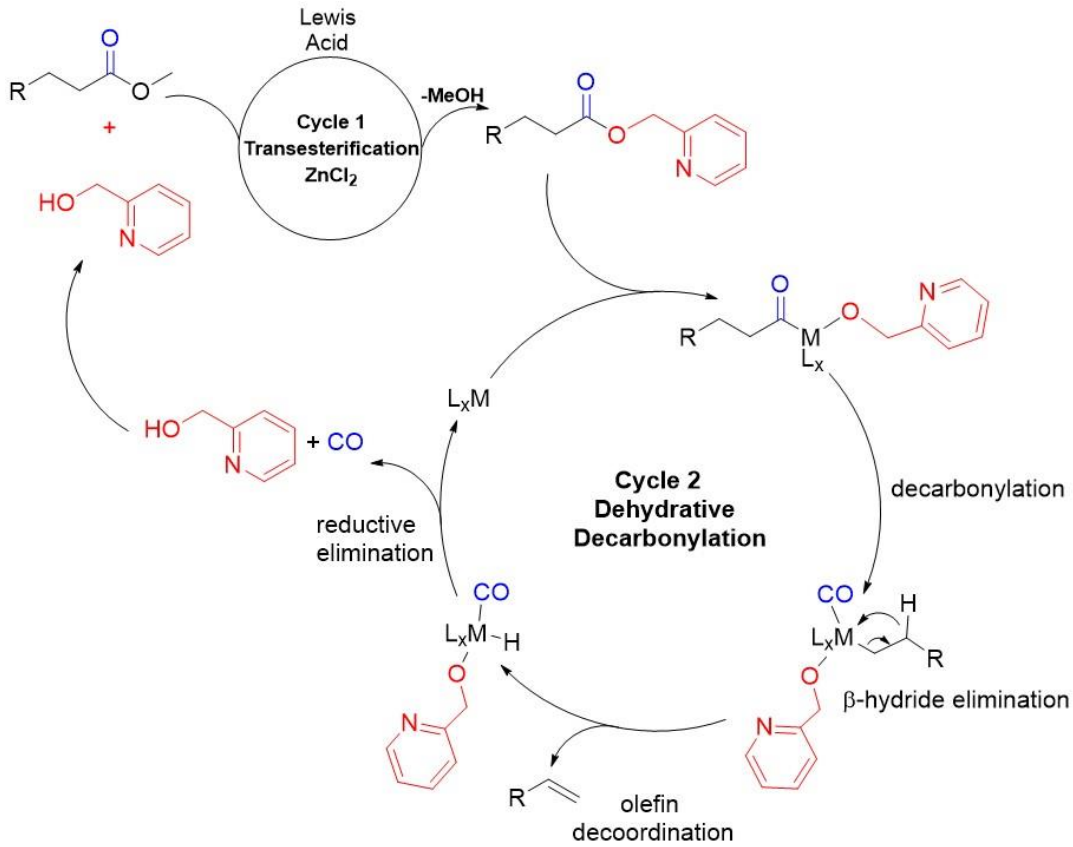

Figure A.1. Dual catalytic cycle for the conversion of fatty acid methyl esters into olefins using a tandem transesterification and dehydrative decarbonylation strategy

In the reported work, it was noted that switching from 2-pyridine methanol to benzyl alcohol resulted in no olefin formation, indicating the crucial directing group effect necessary for the reported transformation to take place. Furthermore, even at the high temperatures of the reaction (190 °C), likely necessary to remove CO from the catalyst or activate the $Ru_3(CO)_{12}$ cluster, a maximum conversion of 64% of the ester to a mixture of linear olefins was achieved. We hypothesized that changing from a monodentate directing group to a multidentate ligand would improve the overall efficiency of the dual catalytic process by enhancing the stability of the active Ru species and perhaps keeping it chelated in a more active form. We anticipated that the directing group ligand, which would have an appended alcohol, would be able to undergo transesterification with the methyl ester to generate a new directing group-ester that could subsequently undergo the dehydrative decarbonylation sequence with a bound Ru to produce the desired linear olefins (Figure A.2). In our initial report, selectivity was an issue, with no preference being observed towards the production of α-olefins. Our hypothesis was that the new

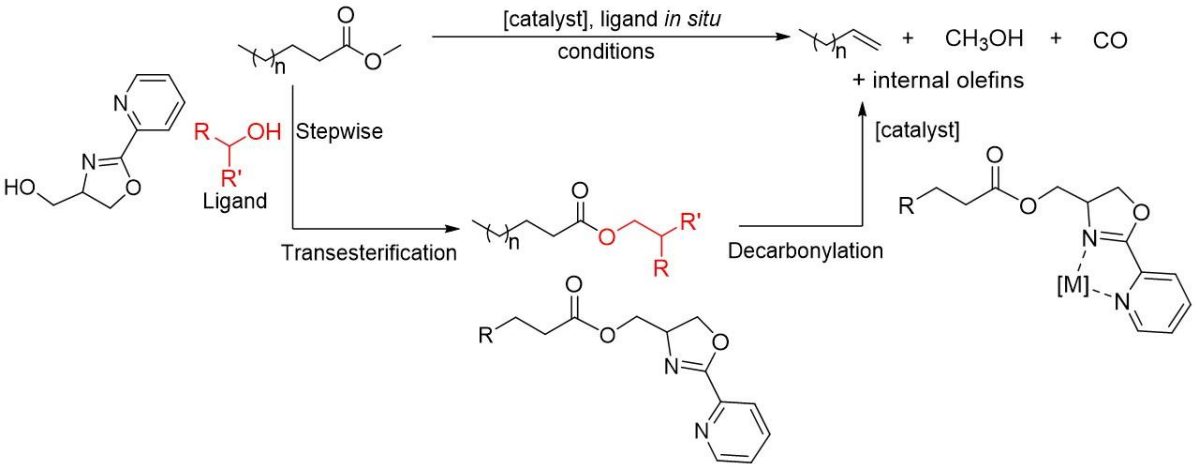

Figure A.2. Stepwise process for the conversion of fatty methyl ester into olefins by means of transesterification and decarbonylation. Alternatively, the process can occur via one step. A pyridine-oxazoline (pyrox) ligand is shown here as an example.

multidentate ligand, with its increased sterics, might provide the additional benefit of preventing the chain-walking processes that leads to a mixture of internal olefins.

We initially envisioned three different directing group ligands (**A-C**, Figure A.3). Directing group **A** is the simplest expansion of the original directing group, 2-pyridine methanol, with a second pyridine ring added to make a bidentate bipyridine (bipy) ligand. Directing group **B** is also bidentate and similar in sterics to **A**, but slightly different in electronics, with the methanol substituent, which is key to transesterification, located on an oxazoline ring in **B** but on a pyridine ring on **A**. Directing group **C** is a tridentate ligand featuring two pyridine rings linked by an amino group containing an ethanol moiety for transesterification. All three ligand structures were verified by NMR spectroscopy and compared to literature reports when applicable.

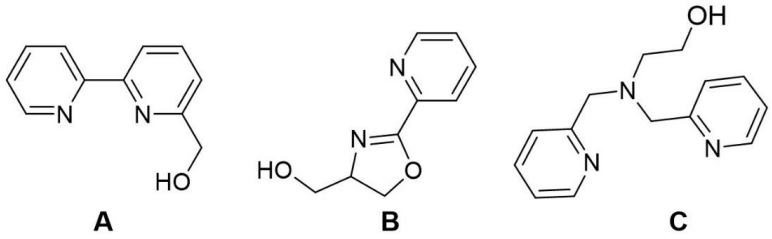

Figure A.3. Ligands used for the dual catalytic reactions

In this exploratory work we compared the catalytic decarbonylation reactions using **A-C** and 2-pyridine methanol under our reported set of conditions (DMPU, 190°C).[1] To check if either or both catalytic cycles (transesterification and decarbonylation) were improved, independent reactions were performed to prove individual steps of the catalytic cycle. Transesterification ability was examined under catalytic conditions ($ZnCl_2$, 190°C, 18 hours), as was decarbonylation starting from pre-synthesized directing group-esters of palmitic acid.

Finally, the dual catalytic process was examined using the previously established optimized conditions.[1]

A.2. Results and Discussion

For a comparison to our group's previously reported work we set out to synthesize three different directing group ligands that had been previously reported in the literature.[1,2-6] To this end we first attempted to modify a reported procedure for this cross coupling between 2-bromo-6-methylalcohol-pyridine and 2-bromopyridine with the latter being in excess to make up for its preference to perform homocouplings (Scheme A.1). Even after extensive alterations to the reaction procedures, including controlling the rate of addition of reagents by syringe pump, temperature, and ratio of pyridines very little of the desired compound was obtained (<10% isolated yield), but enough was accumulated to test its reactivity.

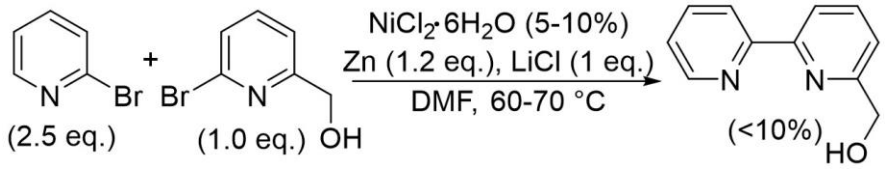

Scheme A.1. Synthesis of **A** by Ni-catalyzed cross coupling

With the difficulties for the synthesis of the desired bipyridine ligand, we also set out to synthesize a pyrOx ligand (made up of one pyridine and one oxazoline unit). Three different routes were undertaken for the synthesis of the desired pyrox ligand, two of which had been previously reported while the third is a combination of the two (Scheme A.2).[5,6] Difficulties only arose towards the end of the synthesis with the cyclization of the serine unit necessary to generate the oxazoline ring. As with the bipy ligand, the pyrOx ligand could only be obtained in

low yields by any of the attempted methods but was purified in sufficient amounts to perform reactivity studies.

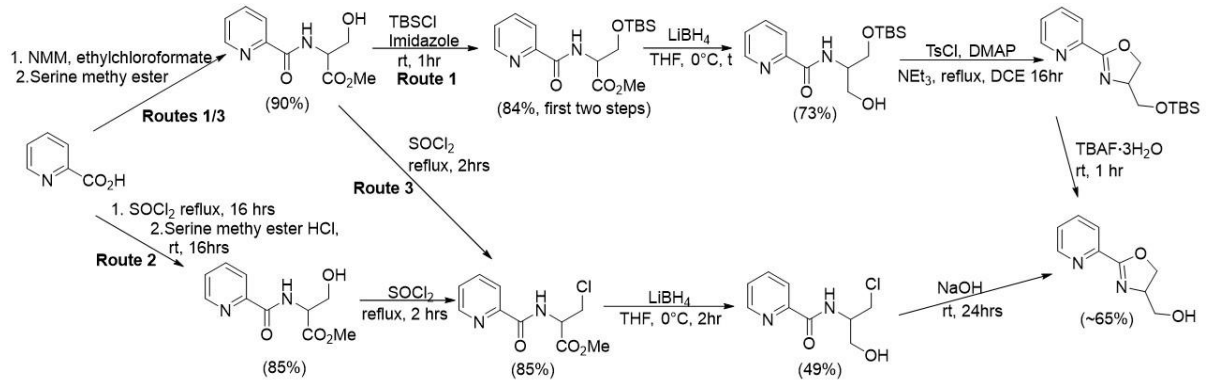

Scheme A.2. Synthesis of **B** through multi-route syntheses. Note: Cyclization with TsCl/DMAP gave only impure products and no accurate yield was obtained

Lastly, we synthesized a tridentate ligand that contained two pyridine rings bridged by an amino group. The synthesis of directing group **C** begins with a reductive amination between pyridine carboxaldehyde and 2-picolylamine. Subsequently, stirring the amino bridged pyridines with K_2CO_3 in dimethylformamide (DMF), followed by addition of 2-bromoethanol formed **C** in useable yields (20%). Alternatively, 2-(chloromethyl) pyridine could be stirred with ethanolamine and NaOH, in a mixture of CH_2Cl_2 and H_2O to form **C** in one step and more appreciable yields (66%). Both synthetic methods proved useful to obtaining enough ligand to provide comparative reactivity studies to the bipy and pyrox ligands.

Reactivity Studies.

Upon obtaining synthetically useful amounts of **A**-**C** we set out to probe the conversion of methyl palmitate to olefins through both a stepwise and dual catalytic manner for comparison to our reported system. To begin, we tested the ability of each of the ligands to perform

transesterification with the methyl ester under the reported catalytic conditions, in N-N'-dimethylpropyleneurea (DMPU) at 190 °C for 18 hours using $ZnCl_2$ (25%) as the Lewis Acid catalyst (Table A.1). The directing group was used in a 1:1 ratio with methyl palmitate to try to

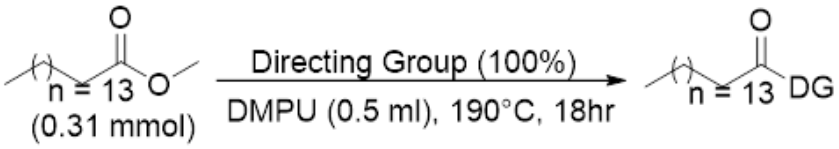

Directing Group (100%) (DG)	$ZnCl_2$ (%)	DG-ester (%)
2-pyridine methanol	25	38
2-pyridine methanol	25	44
A	25	24
A	25	36
B	25	10
B	25	8
C	0	0
C	25%	0
C	150%	0

Table A.1. Transesterification of methyl palmitate with varied DG's

get as much directing group-ester as possible. After multiple attempts, our results show that 2-pyridine methanol was far superior to **A-C**, achieving ~42% conversion to the directing group-ester, whereas **A** produces 30%, **B** (9%) and **C** showed no observable ester formation, even when increasing the amount of Lewis Acid catalyst to 150% (Table A.1).

Next, we sought to test the efficacy of the directing group-esters for the dehydrative-decarbonylation catalytic cycle. To do this we first synthesized the directing group-esters from palmitic acid using oxalyl chloride to first generate palmitoyl chloride, which then readily underwent nucleophilic attack by the alcohols of the ligands. Once isolated and their structures confirmed by ^{1}H NMR spectroscopy, they were subject to the catalytic conditions: DMPU, 190 °C, $Ru_3(CO)_{12}$ (5%) and PCy_3 (15%). Like with the transesterification reactions, the original

directing group, 2-pyridine methanol, produced olefins far better than **A**-**C**, with only **A** producing any observable olefin product (Table A.2).

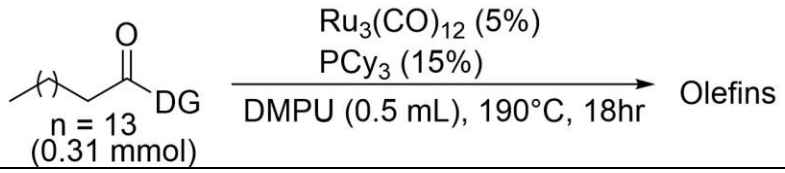

Directing Group	Olefin (%)
2-pyridine methanol*	31
2-pyridine methanol	32
2-pyridine methanol	31
A*	0
A	9
A	<2
B	0
B	0
C	0
C	0

Table A.2. Decarbonylation of pre-synthesized DG-esters under catalytic conditions
*0.24 mmol scale

As the goal of this work was to establish a new DG that could perform both the transesterification and dehydrative-decarbonylation catalytic cycles *in situ* we then performed dual catalytic reactions, only changing which directing group was used (Table A.3). After 18 hours at 190 °C Unfortunately, only when 2-pyridine methanol was used did any olefin production occur under the dual catalytic conditions, while **A** showed minor directing group-ester formation when used in stoichiometric amounts.

Although it is unclear what the nature of the Ru species is in solution as it starts as a cluster ($Ru_3(CO)_{12}$), we attempted to have the Ru ligate to **A** of 2-pyridine methanol prior to the transesterification and decarbonylation processes. $Ru_3(CO)_{12}$ was stirred with 2-pyridine methanol or **A** (1.25 equivalents per Ru atom) prior to adding methyl palmitate (Table A.4).

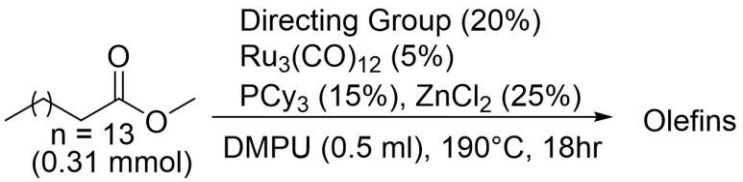

Directing Group (%)	DG-ester (%)	olefin (%)
2-pyridine methanol (20%)	N/D	29
2-pyridine methanol (20%)[a]	N/D	27
2-pyridine methanol (100%)	22	10
A (20%)	N/D	0
A (20%) [a]	N/D	0
A (100%)	16	0
B (%)	N/D	0
B (%)	N/D	0
C (%)	N/D	0 (five attempts)

Table A.3. Dual catalytic reactions performed under previously optimized conditions
[a]35ml bomb tube. N/D = not detected

Although trace amounts of olefin were produced with **A** and $Ru_3(CO)_{12}$ we once again observe that 2-pyridine methanol is superior to the multidentate directing group, which only shows trace amounts of products.

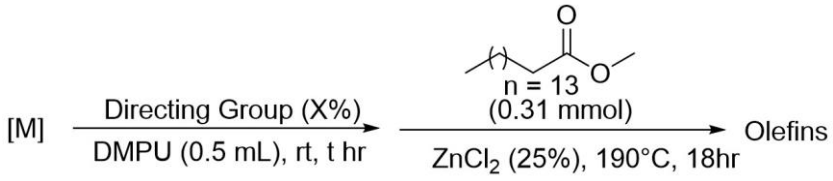

Metal (%)	Time stirred	Directing Group (X%)	Olefin Yield (%)
$Ru_3(CO)_{12}$ (5%)	0.5 hr	2-pyridine methanol (20)	13%
$Ru_3(CO)_{12}$ (5%)	0.5 hr	2-pyridine methanol (20)	13%
$Ru_3(CO)_{12}$ (5%)	0.5 hr	A (20)	<2%
$Ru_3(CO)_{12}$ (5%)	0.5 hr	A (20)	0%
$Ru_3(CO)_{12}$ (5%)	1 hr	2-pyridine methanol (30)	33
$Ru_3(CO)_{12}$ (5%)	1 hr	2-pyridine methanol (60)	21
$Ru_3(CO)_{12}$ (5%)	1 hr	A (30)	0
$Ru_3(CO)_{12}$ (5%)	1 hr	A (60)	4

Table A.4. Results of pre-stir studies.

A.3. Conclusions

Taken together our experiments clearly indicate a drastic decrease in reactivity for each of the three multidentate directing groups screened in every reaction scenario: transesterification, decarbonylation and dual catalysis. The inability to undergo transesterification is a critical failure of the system. At this point it became clear that our established dual catalytic strategy is limited in its productivity and the alteration of to a multidentate directing group would not improve upon the initial design. Ultimately, the results of our comparative work made us question the underlying mechanism to this process and what steps in the dehydrative decarbonylation cycle are most impacted by ligand design. This led us to next perform experimental investigations into a model system of hydrocinnamoyl chloride with Pd and phosphine ligands in collaboration with computational collaborators Samuel Asiedu Fosu, Riffat Parveen and Bess Vlaisavljevich at University of South Dakota (see chapter 2 for details).

A.4. Experimental

General.

All reagents were purchased from Sigma Aldrich and used as received. All reactions of directing groups were performed in an identical manner to our previous report.[1]

Synthesis of Directing Group Ligands

6-hydroxy-2-2'-bipyridine (A). The ligand was synthesized by means of different procedures due to low yields.[3,4] Methods were altered from the reported methodologies.

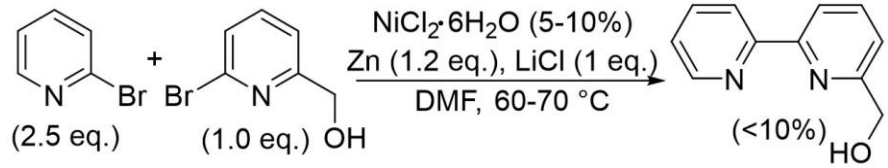

Scheme A.3. Synthesis of **A** by Ni-catalyzed cross coupling

Method 1 for Directing Group A.[3] 6-methylalcohol bipyridine was synthesized by a reported method. Alterations in reaction time, slow addition of reagents or stoichiometry could not improve yields above 10%.

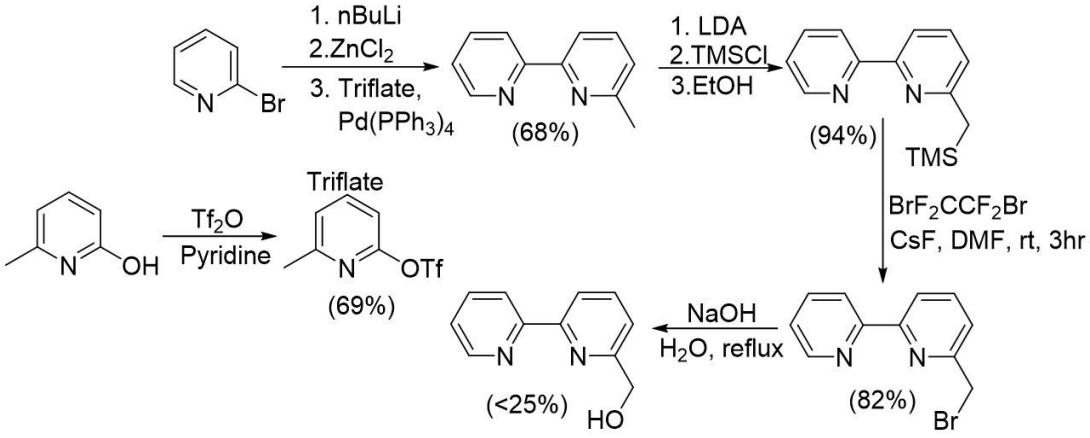

Scheme A.4. Synthesis of **A** via multistep synthesis

Method 2 for Directing group A.[4] Synthesis of 6-bromomethyl-bipyridine was accomplished by following literature procedure.[4] The hydroxylation was performed as follows. The 6-bromomethyl-bipyridine ligand was added to water with a small amount of DMF to aid in solubility. To the mixture was then added NaOH and a stir bar. The initially heterogeneous mixture was stirred at reflux for 18 hours before cooling, diluting with water and extracting the organics with dichloromethane. The combined organic layers were then dried over $MgSO_4$, filtered and volatiles removed. Product structure was confirmed by ^1H NMR comparison to literature values.[3]

Due to inconsistent yields during the cyclization step for the pyrox ligand multiple methods were explored, without a preferred route during study.[5,6] Literature methods were used for each step and products ascertained by ^1H NMR comparison to literature values. No major alterations were made to the reported procedures.

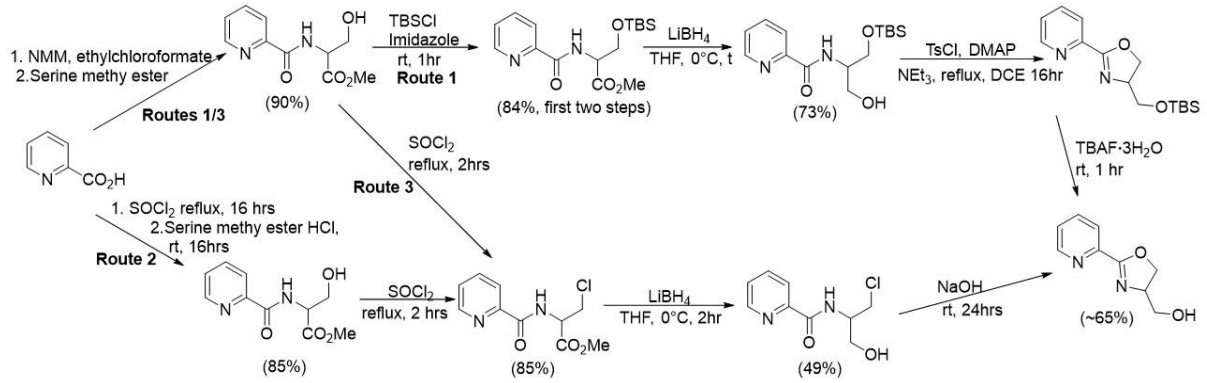

Scheme A.5. Synthesis of **B** through multi-route syntheses.

Directing Group Ligand B. Due to inconsistent yields during the cyclization step for the pyrox ligand multiple methods were explored, without a preferred route during study.[7,8] Literature

methods were used for each step and products ascertained by ^{1}H NMR comparison to literature values

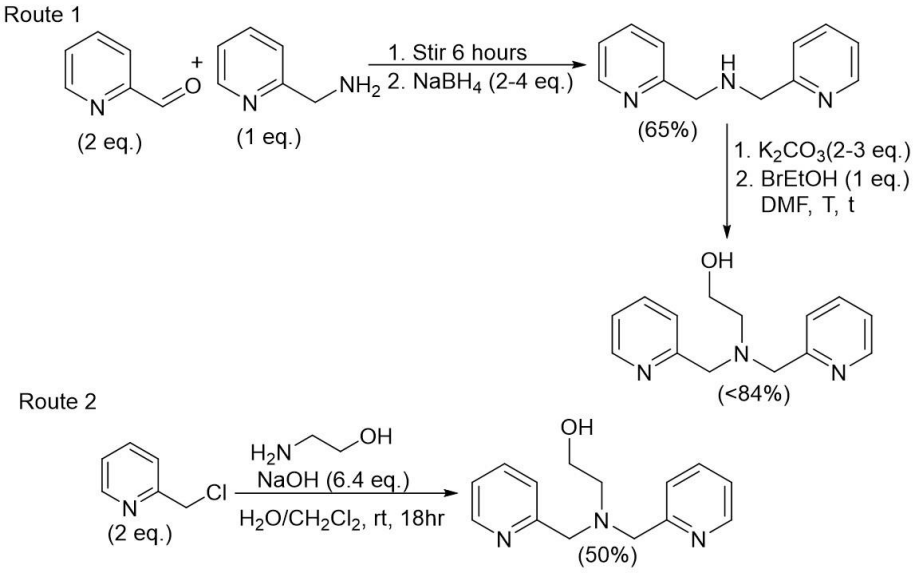

Scheme A.6. Synthesis of directing group **C** by two different routes

Directing Group Ligand C. Ligand C was synthesized using reported procedures.[6,7] Its purity and structure were ascertained through comparison to reported ^{1}H NMR data.

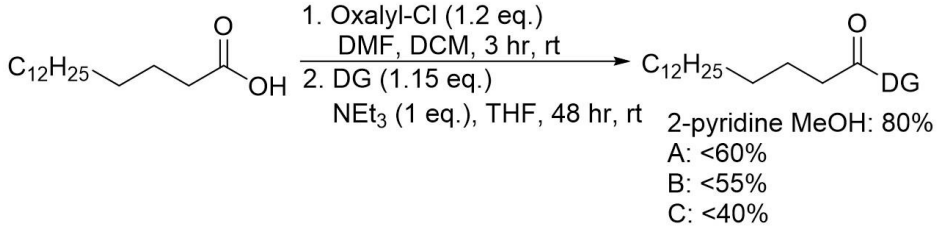

Scheme A.7. Synthesis of directing group esters

Directing Group Esters. Directing group-esters were synthesized using reported methods.[1] 2-pyridine methyl palmitate was previously reported, and we confirmed our product by comparison of ^{1}H NMR values to those reported.

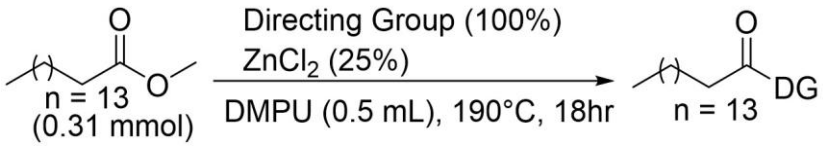

Scheme A.8. Transesterification of methyl palmitate with directing groups with $ZnCl_2$

Transesterification reactions. All transesterification reactions were performed identical to our previous report.[1]

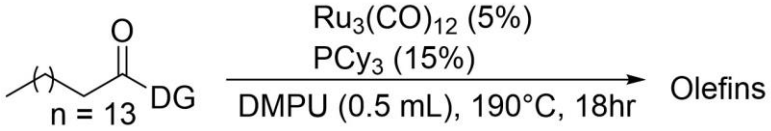

Scheme A.9. Dehydrative decarbonylation reactions starting from directing group esters

Dehydrative Decarbonylation Reactions. Decarbonylation reactions were performed as previously reported from directing group-esters and assignment of products compared to literature ^{1}H NMR values.[1]

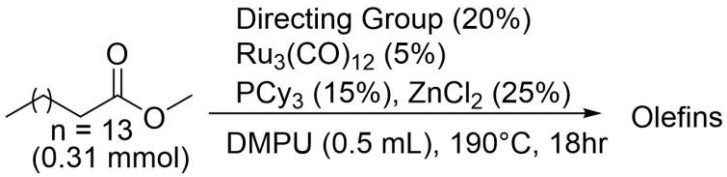

Scheme A.10. Dual catalytic conversion of methyl palmitate to olefins under catalytic conditions

Dual Catalytic Reactions. Dual catalytic reactions were performed as reported,[1] with the only change being the directing group that was used. Products were determined as comparison to reported values.[1]

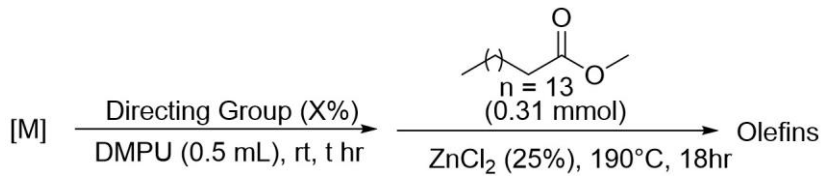

Scheme A.11. Dual catalytic conversion of methyl palmitate to olefins with metal pre-stirring of catalyst and directing group

Pre-stir Studies. For studies where the metal, $Ru_3(CO)_{12}$ or $Ni(cod)_2$, was first stirred with a directing group, the metal (0.047 mmol metal total) and directing group were stirred within a nitrogen filled glovebox in DMPU (0.5 mL) for between 0.5 and 10 hours. Subsequently $ZnCl_2$ (10.6 mg, 25 mol%) and methyl palmitate (83.8 mg, 0.31 mmol) were added and the mixtures heated at 190°C for 18 hours as had been previously reported with the dual catalytic methodology.[1]

A.5. Appendix A References

1. Fieser, M. E., Schimler, S. D., Mitchell, L. A., Wilborn, E. G., John, A., Hogan, L. T., Benson, B., LaPointe, A. M., & Tolman, W. B. (2018). Dual-catalytic decarbonylation of fatty acid methyl esters to form olefins. *Chemical Communications*, *54*(55), 7669–7672.
2. Sundaravel, K., Sankaralingam, M., Suresh, E., & Palaniandavar, M. (2011). Biomimetic iron(iii) complexes of N 3O and N 3O 2 donor ligands: Protonation of coordinated ethanolate donor enhances dioxygenase activity. *Dalton Transactions*, *40*(33), 8444–8458.
3. Liao, L. Y., Kong, X. R., & Duan, X. F. (2014). Reductive couplings of 2-halopyridines without external ligand: Phosphine-free nickel-catalyzed synthesis of symmetrical and unsymmetrical 2,2'-bipyridines. *Journal of Organic Chemistry*, *79*(2), 777–782.
4. Savage, S. A., Smith, A. P., & Fraser, C. L. (1998). Efficient synthesis of 4-, 5-, and 6-methyl-2,2'-bipyridine by a Negishi cross-coupling strategy followed by high-yield conversion to bromo- and chloromethyl-2,2'-bipyridines. *Journal of Organic Chemistry*, *63*(26), 10048–10051.
5. Schulz, M., & Christoffers, J. (2013). Synthesis of functionalized pyridine-2,6-bis(imidazolines) by ring transformation of 4-(aminomethyl)oxazoline derivatives. *European Journal of Organic Chemistry*, *4*(33), 7624–7630.
6. Schulz, M., & Christoffers, J. (2014). An unprecedented ring transformation of a 4-(aminomethyl)oxazoline derivative to a 4-(hydroxymethyl)imidazoline. *Synthesis (Germany)*, *46*(1), 81–86.

7. Schulz, M., & Christoffers, J. (2013). Synthesis of functionalized pyridine-2,6-bis(imidazolines) by ring transformation of 4-(aminomethyl)oxazoline derivatives. *European Journal of Organic Chemistry*, *4*(33), 7624–7630.

8. Schulz, M., & Christoffers, J. (2014). An unprecedented ring transformation of a 4-(aminomethyl)oxazoline derivative to a 4-(hydroxymethyl)imidazoline. *Synthesis (Germany)*, *46*(1), 81–86.

Appendix B.

Graphs and Tables for Chapter 2

Additive	Styrene Yield[a]	Other Identifiable Products
None	6%	--
AgY (Y = BF_4, SbF_6)	>99%	Hydrocinnamoyl Chloride (trace)
NaX (X = Bar^f, PF_6, SbF_6, BF_4)	>99%	Hydrocinnamoyl Chloride (trace)
$KBAr^f$	>99%	Hydrocinnamoyl Chloride (trace)
$ZnCl_2$	>99%	Hydrocinnamic Acid (trace)
$Zn(OAc)_2$	76%	22% Hydrocinnamic acid
ZnO	15%	--
Diisopropylthiourea	64%	[b]
Triazobicyclodecene (TBD)	20%	Hydrocinnamoyl chloride (trace)
$LaCl_3$	37%	Hydrocinnamoyl Chloride (trace)
Schreiner's Thiourea	3%	Messy, Hydrocinnamic acid
Thiourea	10%	[b]
$Al(O^tBu)_3$	5%	--
$Mg(OAc)_2$	11%	--

Table B.1. Reactions of complex **1.** [a]Calculated as follows:

Standard (1,3,5-trimethoxybenzene) has 9 protons corresponding to its three methyl groups at 3.76 ppm (CD_3CN) and for calculations its integration was set to 9 within the ^1H NMR spectra. This allows the denominator in the formula below to be equal to one.

$$\frac{(Integration\ of\ Styrene\ peak/\ \#\ of\ corresponding\ H's)}{(Integration\ of\ Standard/\#H's\ for\ standard)}[Standard] = [Styrene]$$

$$\frac{[Styrene]}{[Pd\ acyl]_{initial}} x\ 100 = \%\ Yield$$

Note: the two geminal protons of styrene were typically not overlapping with any other peaks, in which case their integration values were averaged for these calculations (or equivalently, the integrations were added together but then the number of protons goes from one to two leading to the same calculation).

[b]The ^1H NMR spectrum contained many overlapping peaks that we were unable to assign but suggest the formation of numerous products.

Additive	Styrene Yield[a]	Other Identifiable Products
None	0%	NA
$AgBF_4$	<5%	**2**$^+$
NaX (X = Bar^f, SbF_6)	<5%	**2**$^+$
$ZnCl_2$	8%	63% **2**$^+$
$Zn(OAc)_2$	1%	27% hydrocinnamic acid
ZnO	1%	NA
Diisopropylthiourea	3%	Hydrocinnamic acid [b]

Table B.2. Reactions of complex **2**.
[a]See above for calculation methods. [b]The ^{1}H NMR spectrum contained many overlapping peaks that we were unable to assign but suggest the formation of numerous products.

Additive	Styrene Yield[a]	Other Identifiable Products
None	0%	No Reaction
$ZnCl_2$	9%	91% **2**$^+$ remaining
$Zn(OAc)_2$	3%	>45% **2**$^+$ remaining
ZnO	0%	No reaction
Diisopropylthiourea	Trace	[b]

Table B.3. Reactions of complex **2**$^+$. [a]See above for calculation methods. [b]The ^{1}H NMR spectrum contained many overlapping peaks that we were unable to assign but suggest the formation of numerous products.

Additive	Styrene Yield[a]	Other Identifiable Products
None	0%	--
$AgBF_4$	18%	3-phenylproponal (33%), **4**$^+$ (39%), ethyl benzene (6%)
NaX (X = Bar^f, SbF_6)	14%	3-phenylproponal (30%), 4$^+$ (46%), ethyl benzene (6%)
$ZnCl_2$	45%	3-phenylproponal (53%), **4**$^+$
$Zn(OAc)_2$	25%	3-phenylproponal
ZnO	0%	No Reaction
Diisopropylthiourea	0%	No Reaction

Table B.4. Reactions of complex **3.** [a]See above for calculation methods.

Kinetic Data for Chapter 2

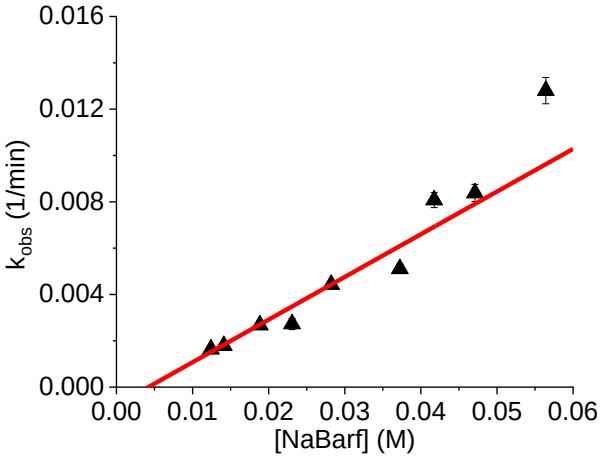

Figure B.1. k_{obs} versus [$NaBAr^f$] (M). k_{obs} values are an average of three trials. Line: y = mx+ b, m = 0.236 (0.002), b = -2.04 x 10^{-3}, R^2 = 0.939. Error values obtained through the error in individual k_{obs} values as generated through Origin Software.

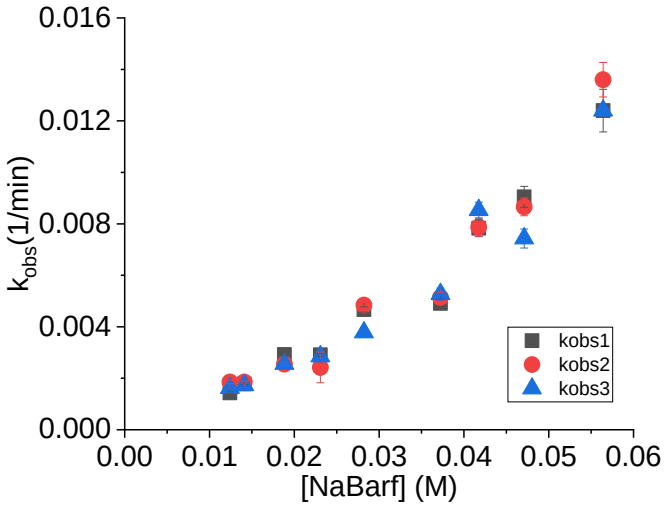

Figure B.2. All values of k_{obs} generated over three trials.

Varying Concentrations of NaBAr^f for [1] = 0.0126M

$[NaBar^f]_0 = 5.64 \times 10^{-2}M$

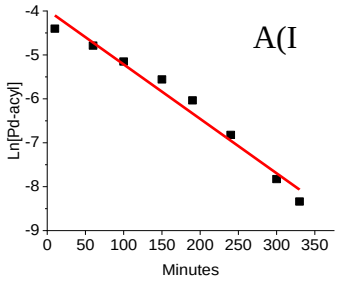

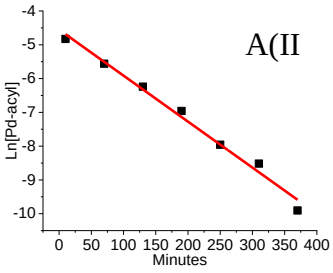

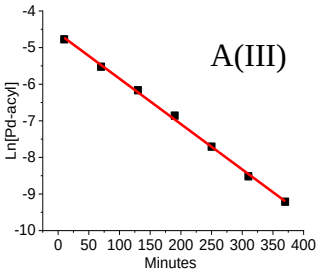

$[NaBar^f]_0 = 4.71 \times 10^{-2}M$

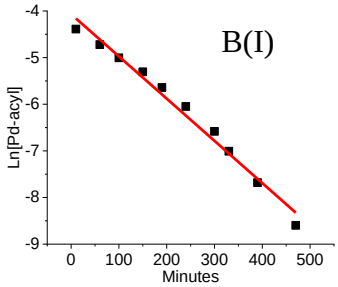

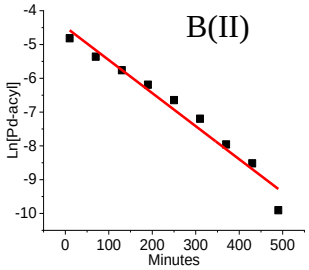

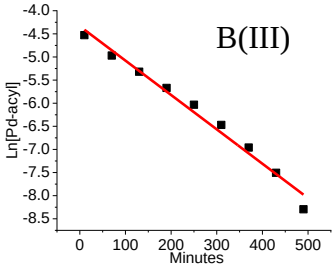

$[NaBar^f]_0 = 4.18 \times 10^{-2}M$

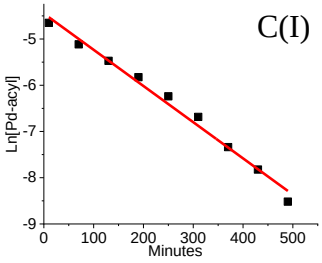

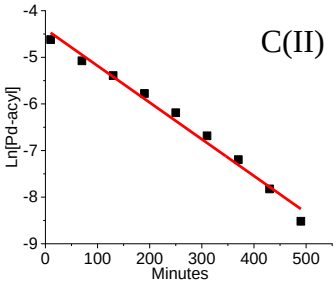

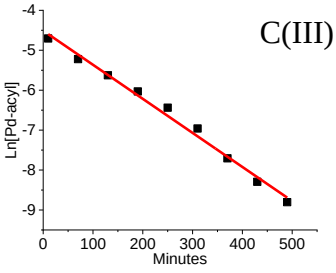

$[NaBar^f]_0 = 3.72 \times 10^{-2}M$

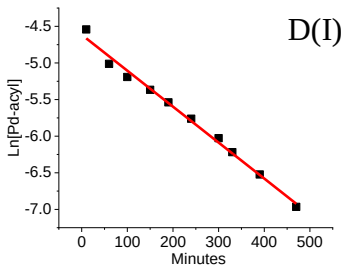

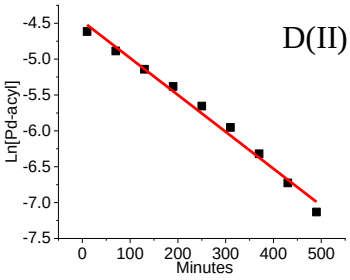

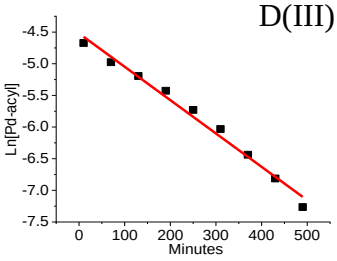

$[NaBar^f]_0 = 2.82 \times 10^{-2}M$

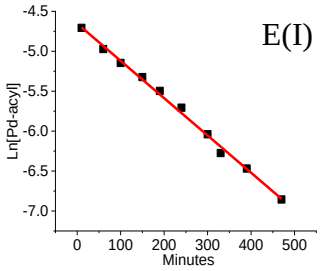

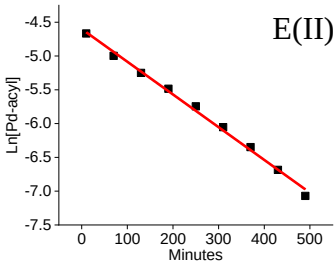

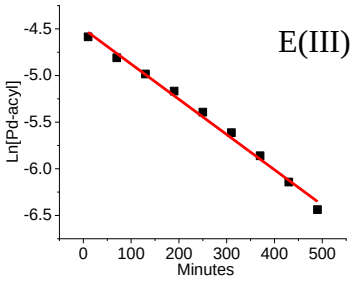

$[NaBar^f]_0 = 2.3 \times 10^{-2}M$

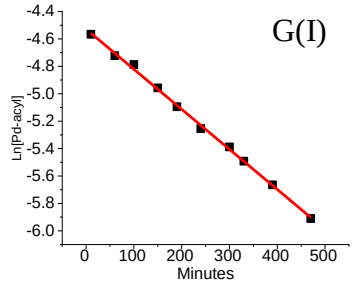

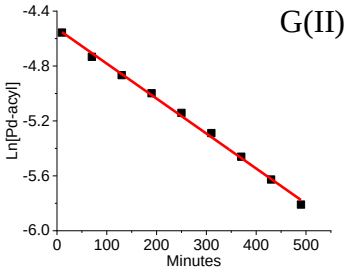

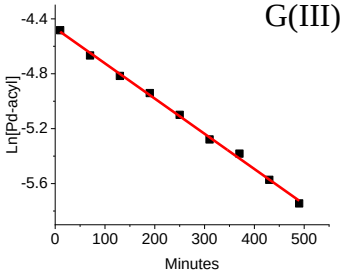

$[NaBar^f]_0 = 1.88 \times 10^{-2}M$

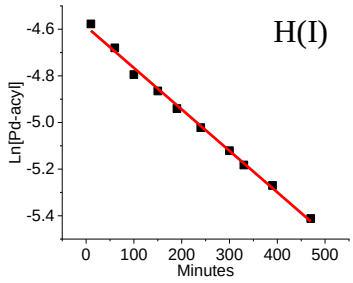

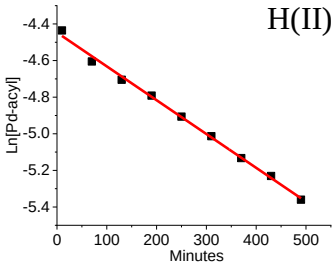

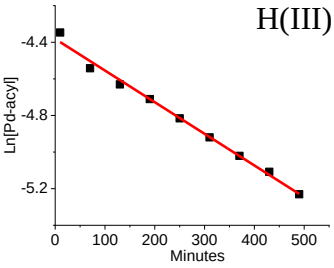

$[NaBar^f]_0 = 1.41 \times 10^{-2}M$

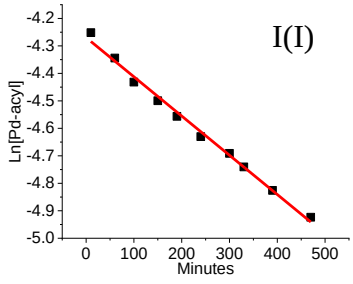

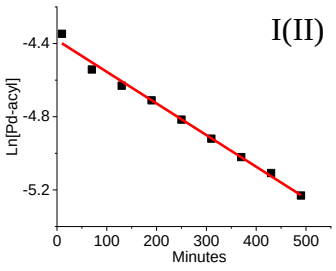

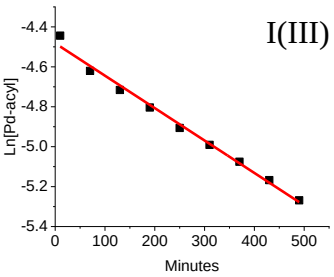

$[NaBar^f]_0 = 1.24 \times 10^{-2}M$

F(I)

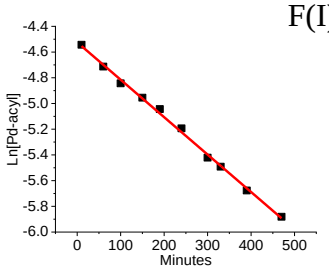

F(II)

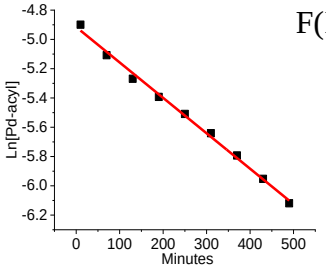

F(III)

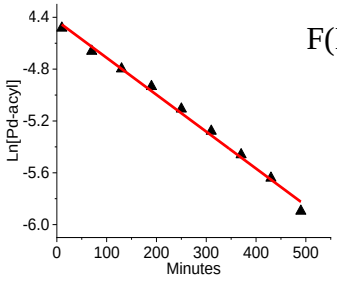

Trial	[NaBar^f] (M)[a]	Slope x 10^{-3} (k_{obs}, 1/min)	Error x 10^{-4}	R^2
A(I)	0.056	12.4	8	0.974
A(II)	0.056	13.6	7	1
A(III)	0.056	12.4	2	1
B(I)	0.047	7.83	3	0984
B(II)	0.047	7.87	4	1
B(III)	0.047	8.53	3	.983
C(I)	0.042	9.05	4	.992
C(II)	0.042	9.78	7	.989
C(III)	0.042	7.43	4	1
D(I)	0.037	4.91	2	.996
D(II)	0.037	5.14	2	.995
D(III)	0.037	5.27	2	1
E(I)	0.028	4.67	1	.998
E(II)	0.028	4.84	1	1
E(III)	0.028	3.78	1	.994
F(I)	0.023	2.91	0.5	1
F(II)	0.023	2.42	6	1
F(III)	0.023	2.85	0.9	.998
G(I)	0.019	2.92	0.4	.996
G(II)	0.019	2.55	0.5	1
G(III)	0.019	2.56	0.4	.992
H(I)	0.014	1.78	0.4	1
H(II)	0.014	1.85	0.4	.994
H(III)	0.014	1.73	0.6	.991
I(I)	0.012	1.43	0.4	1
I(II)	0.012	1.85	0.5	1
I(III)	0.012	1.62	0.6	1

Table B.5. Slopes, errors and R^2 values for kinetic studies of chloride abstraction from **1**.[a]
[a][**1**] = 0.0126M for all trials.

Appendix C.

Polymer characterization (size exclusion chromatography, distribution plots) for Chapter 3

General

The average molar mass values and molar mass distributions were determined by SEC using a tetrahydrofuran mobile phase on an Agilent Infinity 1260 series HPLC system equipped with a Wyatt HELEOS-II multiangle laser light scattering detector and a Wyatt Optilab T-rEX diffractive refractive index detector through three Wyatt Stryagel HR columns at 25 °C and a flow rate of 1 mL min^{-1}. Conventional analysis reported herein is based off a polystyrene standard calibration curve. Data were provided by Elizabeth Kellstedt and Professor Marc Hillmyer at the University of Minnesota, Twin Cities.

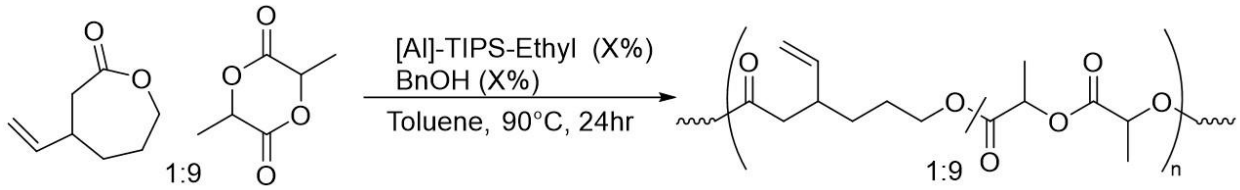

Run	Monomer: Initiator	$M_{n,\ avg.}$	M_n Theory	Conventional Calibration Analysis			Light Scattering Analysis		
				M_w (kg/mol)	M_n (kg/mol)	$Đ$ (M_w/M_n)	M_w (kg/mol)	M_n (kg/mol)	$Đ$ (M_w/M_n)
1	20:01	4.1	2.9	9.8	6.9	1.4	9.8	6.9	1.4
2	100:01:00	16	14	27	21	1.3	27	21	1.3
3	200:01:00	36	29	30	23	1.3	30	23	1.3
4	300:01:00	48	43	30	23	1.3	30	23	1.3

Table C.1. Size exclusion chromatography data for attempts at molecular weight control during the statistical copolymerization of 3-vinyl caprolactone with *rac*-lactide.

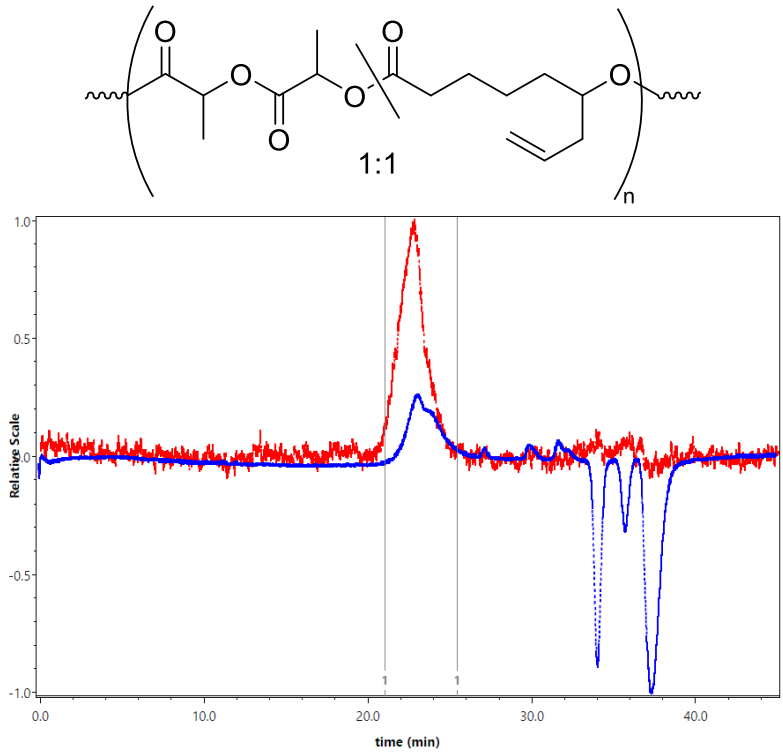

Figure C.1. SEC via light-scattering analysis of poly(6-allyl caprolactone-co-*rac*-lactide; 1:1 feed ratio). M_w = 8.0 kg/mol, M_n = 6.9 kg/mol. Polydispersity = 1.2. Red trace: light-scattering. Blue trace: differential refractive index.

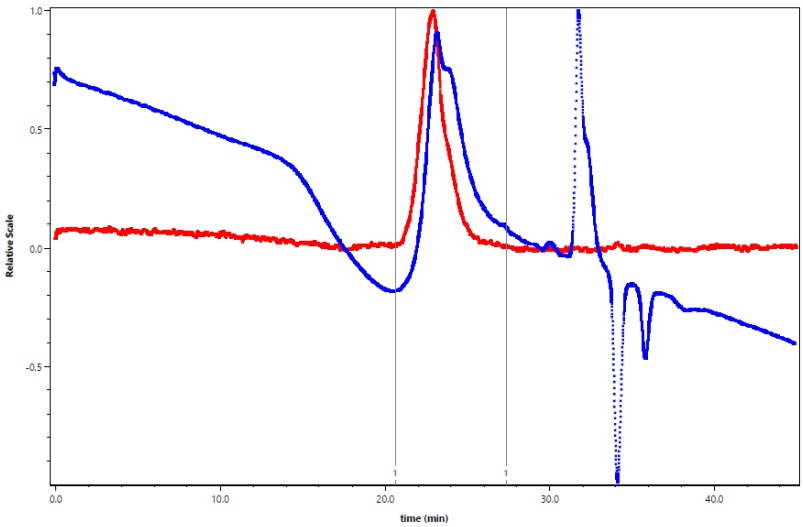

Figure C.2. SEC via conventional analysis of poly(6-allyl caprolactone-co-*rac*-lactide). M_w = 22 kg/mol, M_n = 17 kg/mol. Polydispersity = 1.3. Red trace: light-scattering. Blue trace: differential refractive index

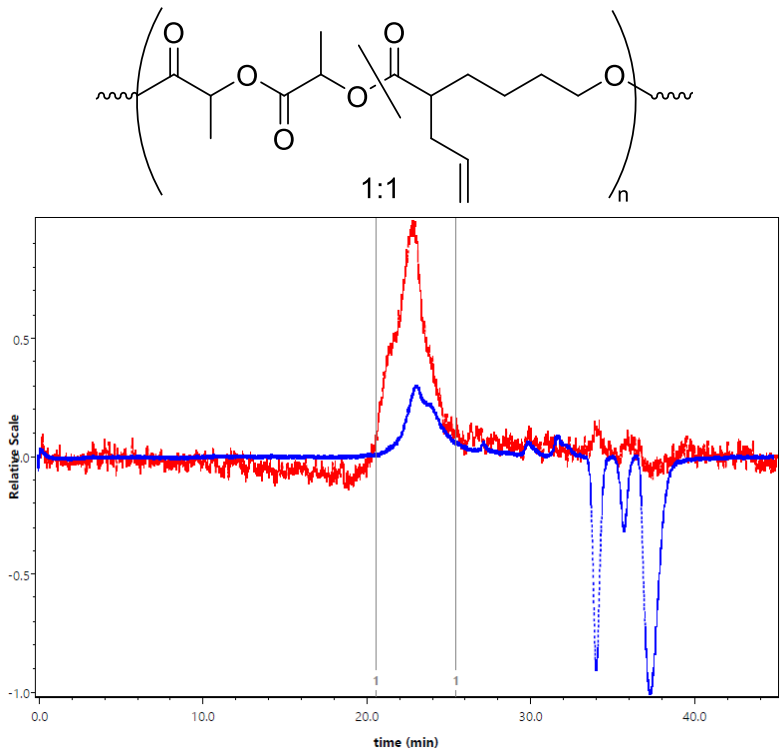

Figure C.3. SEC via conventional analysis of poly(2-allyl caprolactone-co-*rac*-lactide) (1:1) M_w = 17 kg/mol, M_n = 11 kg/mol. Polydispersity = 1.5. Red trace: light-scattering. Blue trace: differential refractive index.

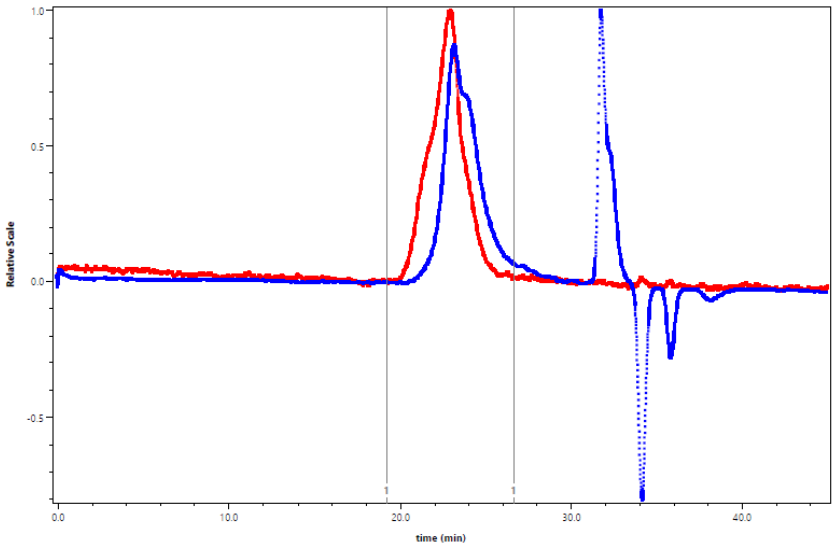

Figure C.4. SEC via light scattering analysis of poly(2-allyl caprolactone-co-*rac*-lactide). M_w = 5.9 kg/mol, M_n = 4.4 kg/mol. Polydispersity = 1.3 .Red trace: light-scattering. Blue trace: differential refractive index.

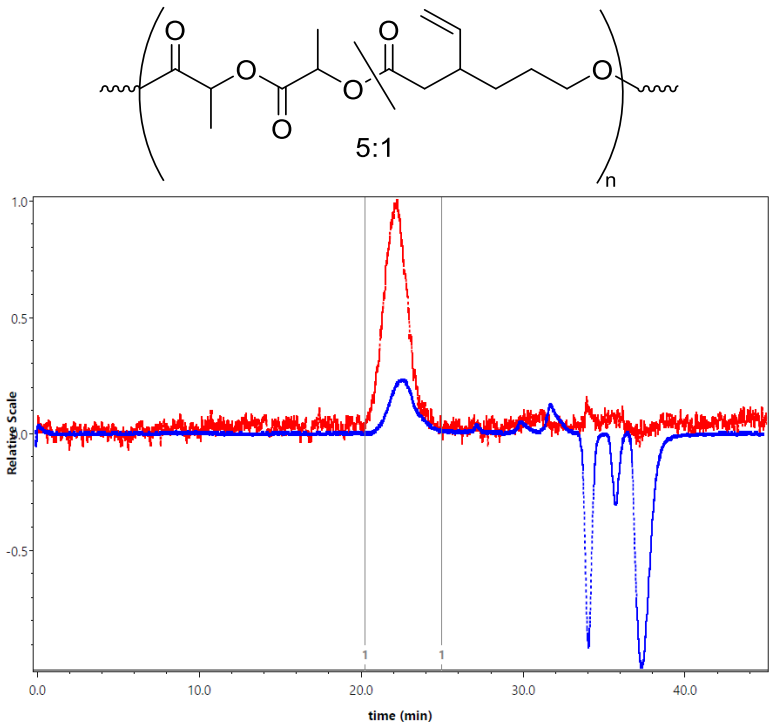

Figure C.5. SEC via conventional analysis of poly(3-vinyl caprolactone-co-*rac*-lactide) (1:5). M_w = 28 kg/mol, M_n = 18 kg/mol. Polydispersity = 1.6. Red trace: light-scattering. Blue trace: differential refractive index.

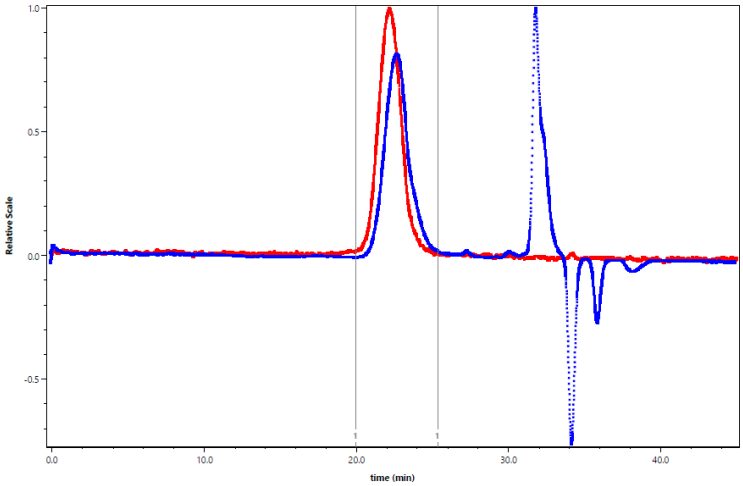

Figure C.6. SEC via light scattering analysis of poly(3-vinyl caprolactone-co-*rac*-lactide) (1:5). M_w = 6.6 kg/mol, M_n = 5.0 kg/mol. Polydispersity = 1.3. Red trace: light-scattering. Blue trace: differential refractive index

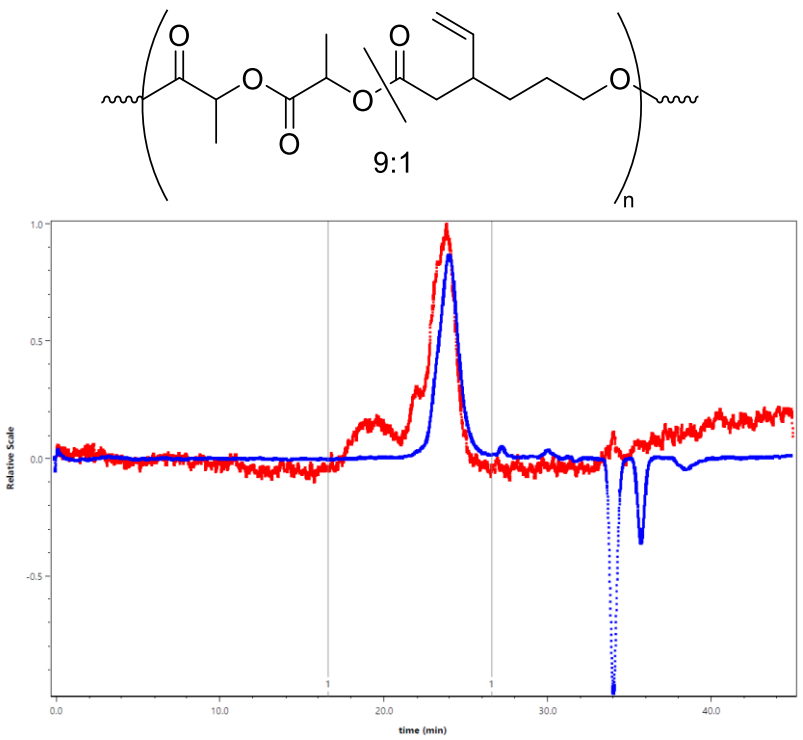

Figure C.7. SEC via light scattering analysis of poly(3-vinyl caprolactone-co-*rac*-lactide) (1:9); Monomer: Initiator = 20:1. M_w = 6.1 kg/mol, M_n = 1.1 kg/mol. Polydispersity = 1.8. Red trace: light-scattering. Blue trace: differential refractive index.

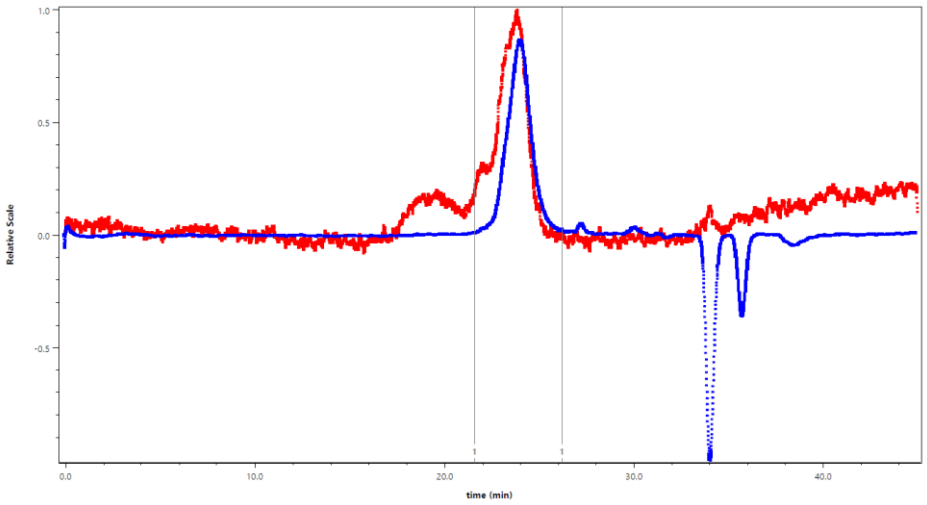

Figure C.8. SEC via conventional analysis of poly(3-vinyl caprolactone-co-*rac*-lactide) (1:9); Monomer: Initiator = 20:1. M_n = 6.9, M_w = 9.8. M_w/M_n = 1.4. Red trace: light-scattering. Blue trace: differential refractive index.

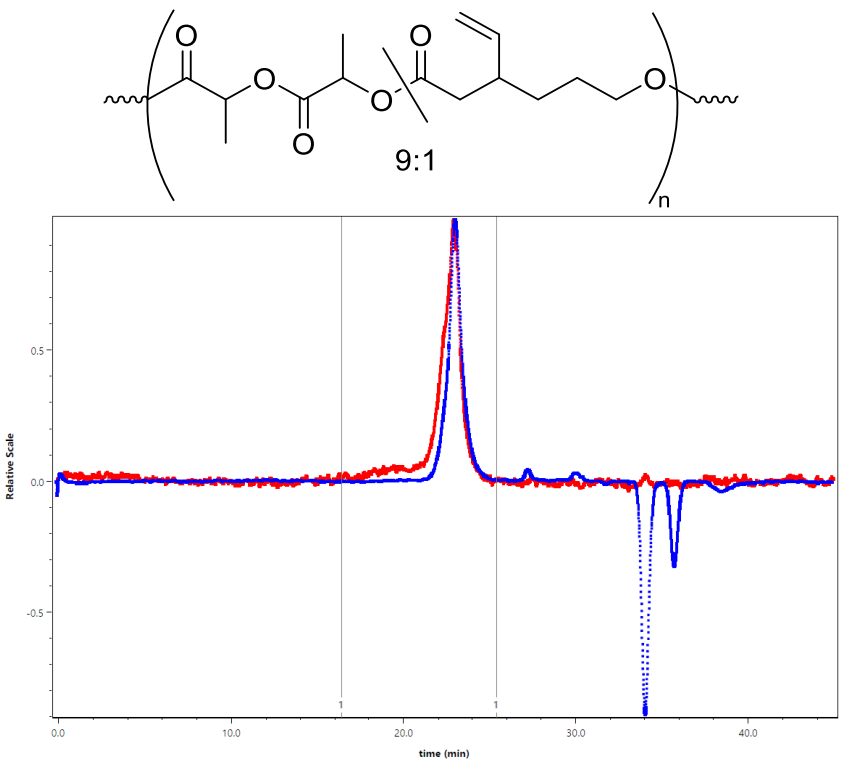

Figure C.9. SEC via light scattering analysis of poly(3-vinyl caprolactone-co-*rac*-lactide) (1:9); Monomer: Initiator = 100:1. M_w = 18 kg/mol, M_n = 13 kg/mol. Polydispersity = 1.4. Red trace: light-scattering. Blue trace: differential refractive index

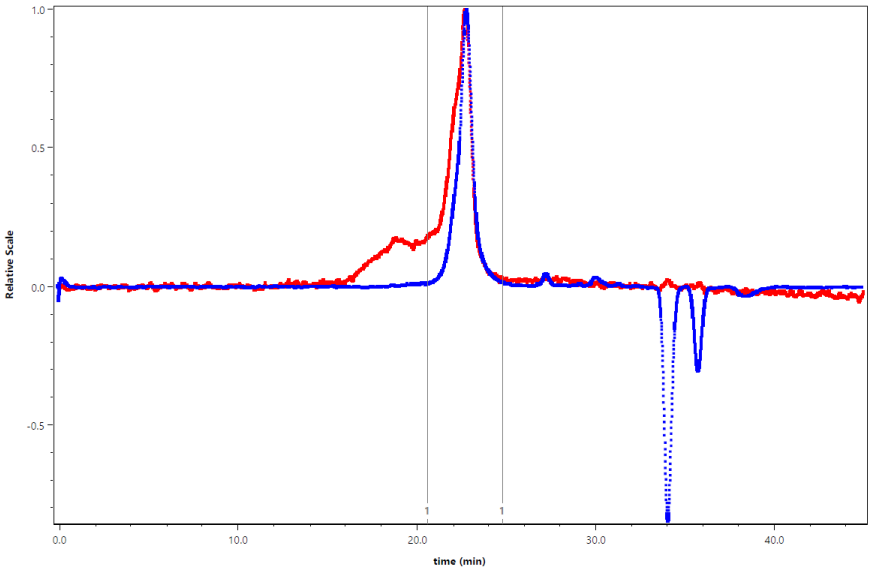

Figure C.10. SEC via conventional analysis of poly(3-vinyl caprolactone-co-*rac*-lactide) (1:9); Monomer: Initiator = 100:1. M_w = 27 kg/mol, M_n = 21 kg/mol. Polydispersity = 1.3. Red trace: light-scattering. Blue trace: differential refractive index

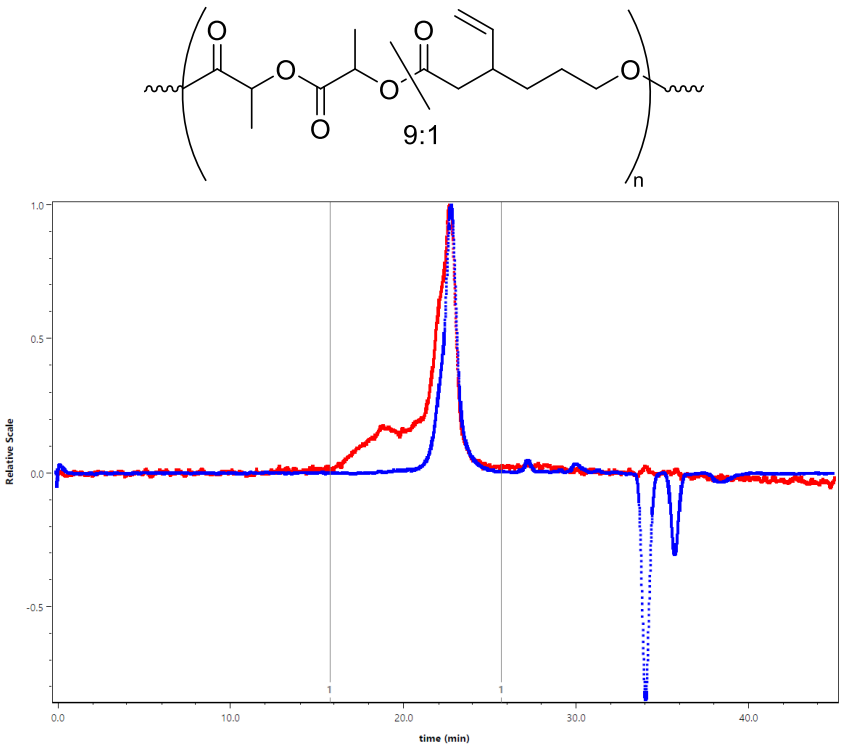

Figure C.11. SEC via light scattering analysis of poly(3-vinyl caprolactone-co-*rac*-lactide) (1:9 Monomer: Initiator = 200:1). M_w = 23 kg/mol, M_n = 15 kg/mol. Polydispersity = 1.6. Red trace: light-scattering. Blue trace: differential refractive index

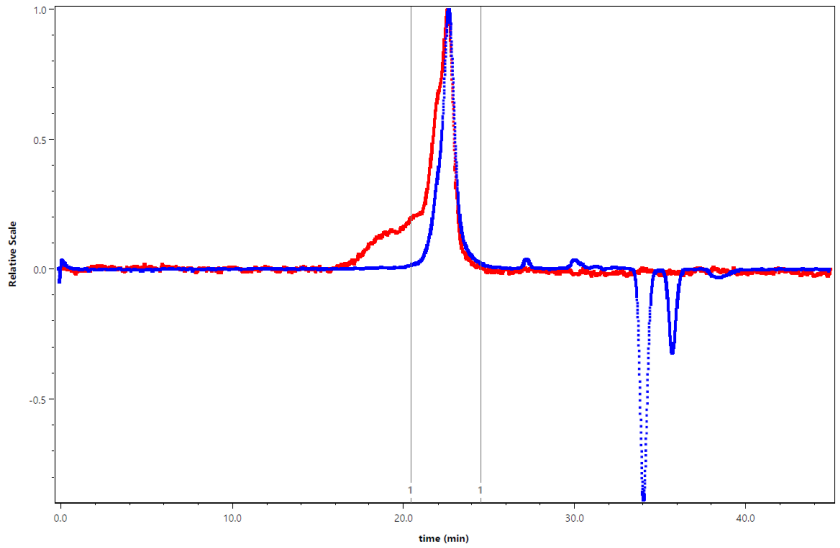

Figure C.12. SEC via conventional analysis of poly(3-vinyl caprolactone-co-*rac*-lactide) (1:9); Monomer: Initiator = 200:1). M_w = 30 kg/mol, M_n = 23 kg/mol. Polydispersity = 1.3. Red trace: light-scattering. Blue trace: differential refractive index

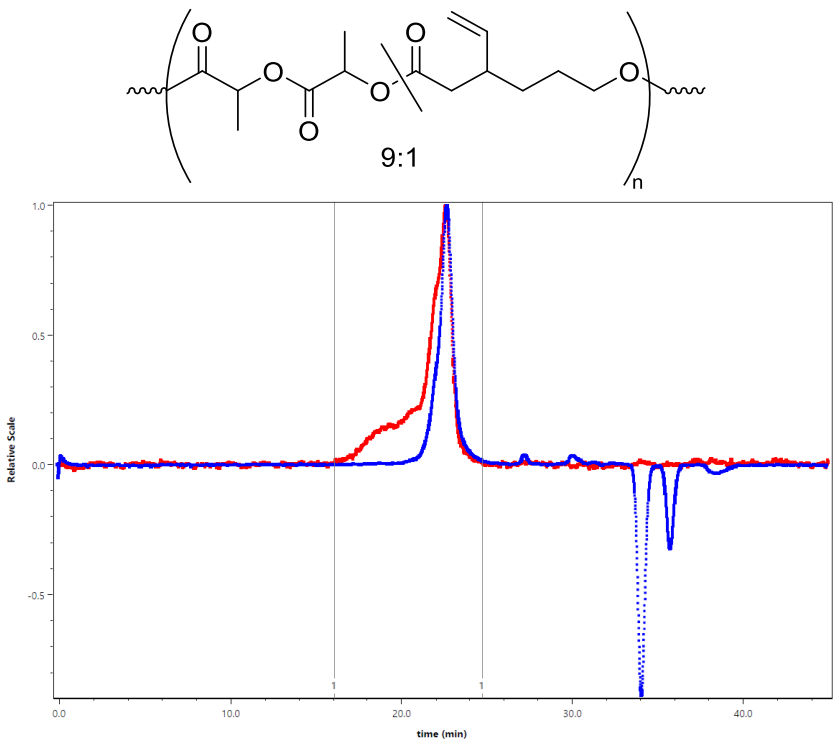

Figure C.13. SEC via light scattering analysis of poly(3-vinyl caprolactone-co-*rac*-lactide) (1:9); Monomer: Initiator = 300:1). M_w = 24 kg/mol M_n = 16 kg/mol. Polydispersity = 1.5. Red trace: light-scattering. Blue trace: differential refractive index

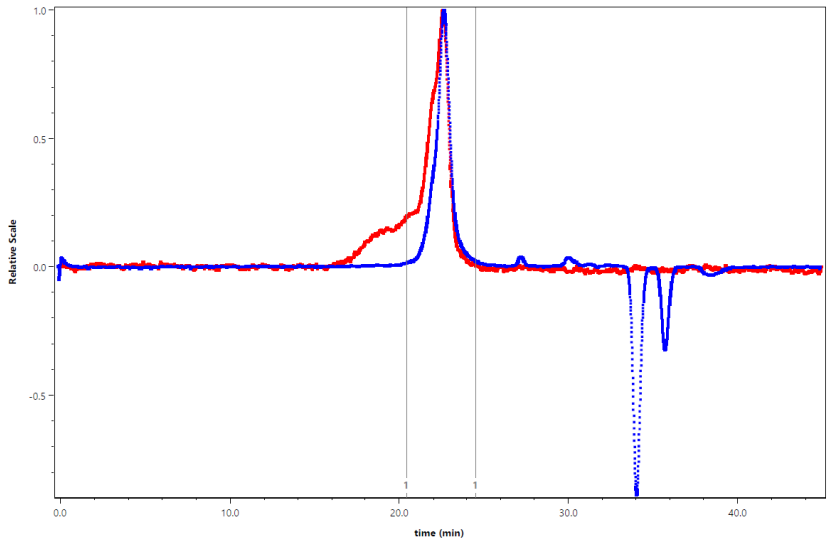

Figure C.14. SEC via conventional analysis of poly(3-vinyl caprolactone-co-*rac*-lactide) (1:9 Monomer: Initiator = 300:1). M_w = 30 kg/mol, M_n = 23 kg/mol. Polydispersity = 1.3. Red trace: light-scattering. Blue trace: differential refractive index

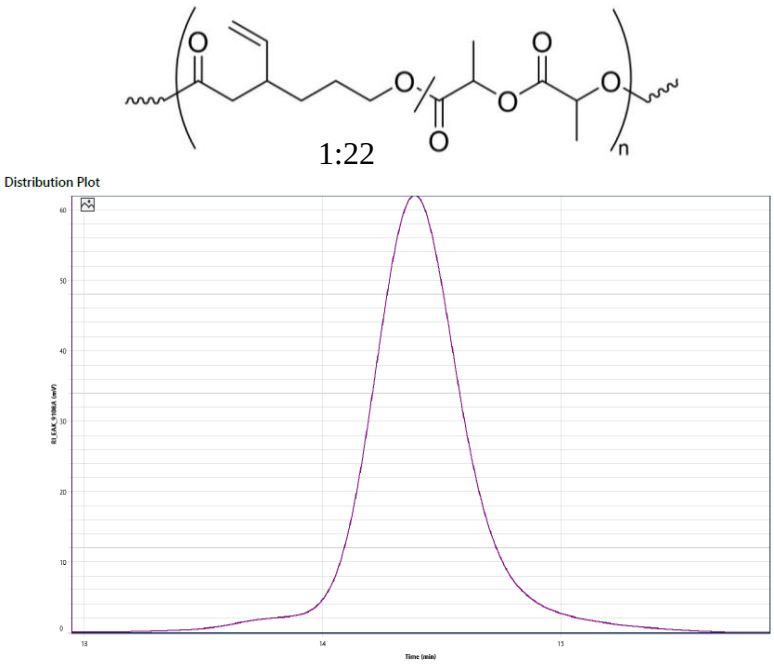

Figure C.15. Distribution Plot (poly(3-vinyl-caprolactone-co-*rac*-lactide) 1:22 **C**:*rac*-LA)

C:LA	**M_n avg (NMR)**	**Light Scattering Analysis**			**Conventional Polystyrene Analysis**		
		M_w (kg/mol)	M_n (kg/mol)	$Đ$ (M_w/M_n)	M_w (kg/mol)	M_n (kg/mol)	$Đ$ (M_w/M_n)
1:22	15	13	12	1.08	22	19	1.17
1:8	18	--	--	--	15	14	1.09

Table C.2. Size exclusion chromatography data for select poly(3-vinyl caprolactone-*rac*-lactide) copolymers

Select Copolymers and functionalizations

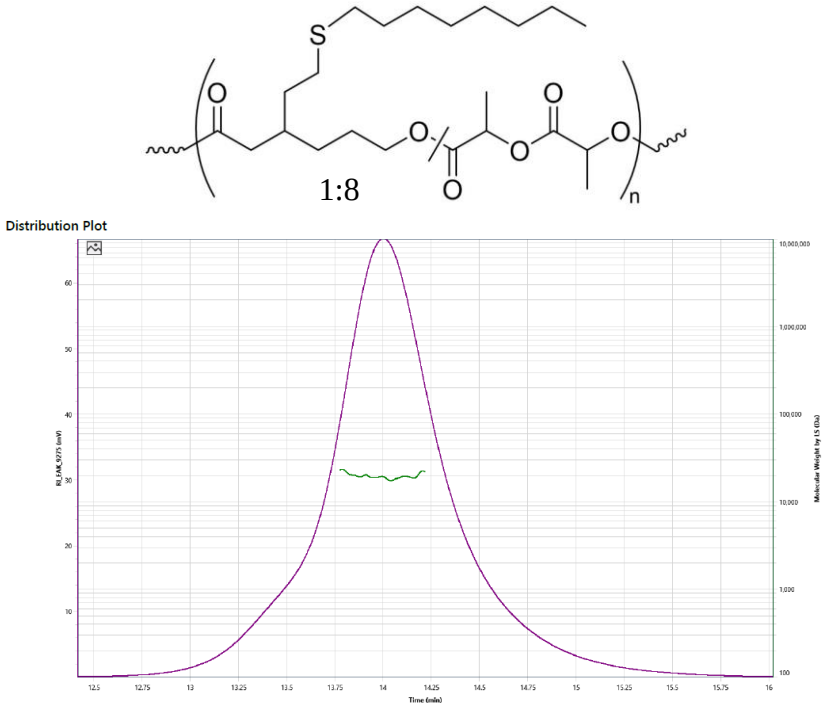

Figure C.16. Distribution plot of thiol-ene product of (poly(3-vinyl-caprolactone-co-*rac*-lactide. (**C**: rac-LA = 1:8)

M_n avg (NMR)	**Light Scattering Analysis**			**Conventional Polystyrene Analysis**		
	M_w (kg/mol)	M_n (kg/mol)	$Đ$ (M_w/M_n)	M_w (kg/mol)	M_n (kg/mol)	$Đ$ (M_w/M_n)
20	19	19	1.00	25	20	1.24

Table C.3. Size exclusion chromatography data for select poly(3-vinyl caprolactone-*rac*-lactide) copolymer functionalized by 1-octane thiol.

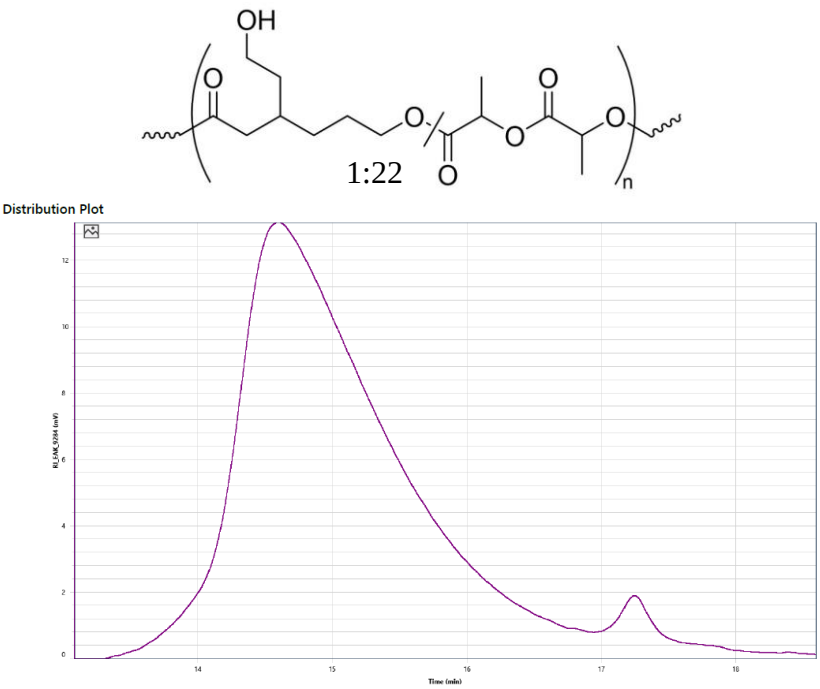

Figure C.17. Distribution plot of hydroboration-oxidation product of poly(3-vinyl-caprolactone-co-*rac*-lactide (1:22 **C**:*rac*-LA)

M_n avg (NMR)	Light Scattering Analysis			Conventional Polystyrene Analysis		
	M_w (kg/mol)	M_n (kg/mol)	$Đ$ (M_w/M_n)	M_w (kg/mol)	M_n (kg/mol)	$Đ$ (M_w/M_n)
17	--	--	--	8.8	3.3	2.68

Table C.4. Size exclusion chromatography data for select poly(3-vinyl caprolactone-*rac*-lactide) copolymers functionalized by hydroboration/oxidation.

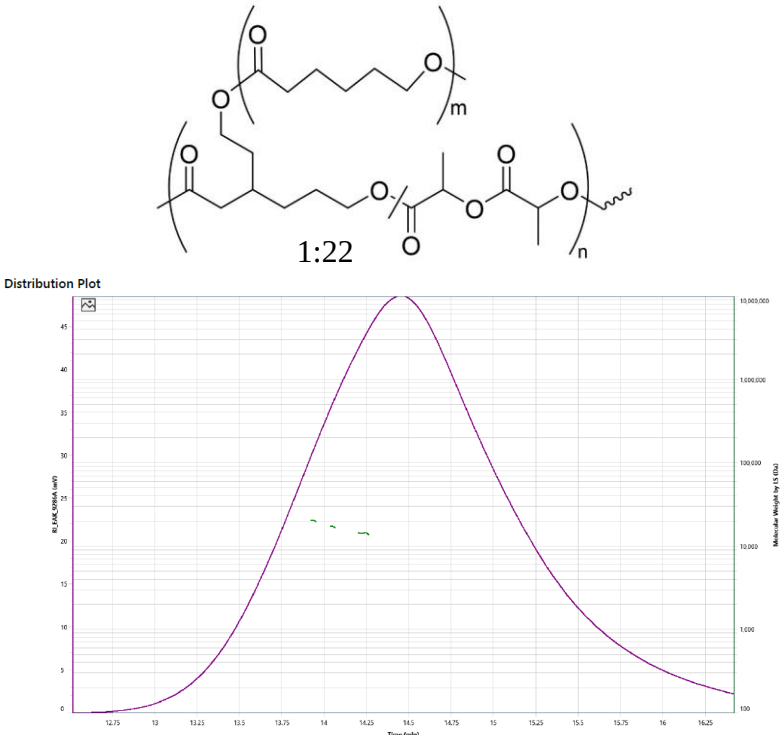

Figure C.18. Distribution plot of ROP grafting-from product (poly(3-vinyl-caprolactone-co-*rac*-lactide 1:22 **C**:*rac*-LA) 20 equivalents of caprolactone per alcohol.

M_n avg (NMR)	Light Scattering Analysis			Conventional Polystyrene Analysis		
	M_w (kg/mol)	M_n (kg/mol)	Đ (M_w/M_n)	M_w (kg/mol)	M_n (kg/mol)	Đ (M_w/M_n)
18	16	16	1.02	16	9.4	1.71

Table C.5. Size exclusion chromatography data for select poly(3-vinyl caprolactone-*rac*-lactide) copolymers functionalized by a ROP grafting from reaction with caprolactone

Appendix D.

X-ray crystallographic data

Complex 2. Hydrocinnamoyl Pd(PPh_3)$_2$ chloride

Crystal data and structure refinement for **2.**

Identification code	t12619_sq/lt/venture/TCW4000A	
Empirical formula	C_{57} H_{51} Cl O P_2 Pd	
Formula weight	955.77	
Temperature	173(2) K	
Wavelength	0.71073 Å	
Crystal system	Triclinic	
Space group	P-1	
Unit cell dimensions	a = 12.0214(6) Å	a= 78.036(2)°.
	b = 12.3727(7) Å	b= 83.797(2)°.
	c = 19.9146(11) Å	g = 61.6830(18)°.
Volume	2550.8(2) Å^3	
Z	2	
Density (calculated)	1.244 Mg/m^3	
Absorption coefficient	0.516 mm^{-1}	
F(000)	988	
Crystal size	0.189 x 0.147 x 0.122 mm^3	
Theta range for data collection	2.401 to 27.485°.	
Index ranges	-15≤h≤15, -16≤k≤16, -25≤l≤25	
Reflections collected	42750	
Independent reflections	11593 [R(int) = 0.044]	
Completeness to theta = 25.242°	99.1 %	
Absorption correction	Semi-empirical from equivalents	
Max. and min. transmission	0.9281 and 0.8714	
Refinement method	Full-matrix least-squares on F^2	
Data / restraints / parameters	11593 / 48 / 590	
Goodness-of-fit on F^2	1.097	
Final R indices [I>2sigma(I)]	R1 = 0.0312, wR2 = 0.0733	
R indices (all data)	R1 = 0.0387, wR2 = 0.0818	
Largest diff. peak and hole	0.432 and -0.323 e.Å^{-3}	

Select Bonds

Bond lengths [Å] and angles [°] for **2**

Pd(1)-C(1)	1.989(2)
Pd(1)-P(2)	2.3293(5)
Pd(1)-P(1)	2.3373(5)
Pd(1)-Cl(1)	2.4377(5)
P(1)-C(16)	1.820(2)
P(1)-C(10)	1.827(2)
P(1)-C(22)	1.8277(19)
P(2)-C(40)	1.8189(19)
P(2)-C(28)	1.8199(19)
P(2)-C(34)	1.836(2)
O(1)-C(1)	1.204(3)
C(1)-C(2)	1.513(3)
C(2)-C(3)	1.527(3)
C(2)-H(2A)	0.9900
C(2)-H(2B)	0.9900
C(3)-C(4')	1.451(7)
C(3)-C(4)	1.543(5)
C(3)-H(3A)	0.9900
C(3)-H(3B)	0.9900
C(4)-C(5)	1.3900
C(4)-C(9)	1.3900
C(5)-C(6)	1.3900
C(5)-H(5)	0.9500
C(6)-C(7)	1.3900
C(6)-H(6)	0.9500
C(7)-C(8)	1.3900
C(7)-H(7)	0.9500
C(8)-C(9)	1.3900
C(8)-H(8)	0.9500
C(9)-H(9)	0.9500
C(4')-C(5')	1.3900
C(4')-C(9')	1.3900
C(5')-C(6')	1.3900
C(5')-H(5')	0.9500
C(6')-C(7')	1.3900
C(6')-H(6')	0.9500
C(7')-C(8')	1.3900
C(7')-H(7')	0.9500
C(8')-C(9')	1.3900
C(8')-H(8')	0.9500
C(9')-H(9')	0.9500
C(10)-C(11)	1.392(3)
C(10)-C(15)	1.396(3)
C(11)-C(12)	1.388(3)
C(11)-H(11)	0.9500
C(12)-C(13)	1.376(4)
C(12)-H(12)	0.9500
C(13)-C(14)	1.374(4)
C(13)-H(13)	0.9500
C(14)-C(15)	1.387(3)
C(14)-H(14)	0.9500
C(15)-H(15)	0.9500
C(16)-C(17)	1.387(3)
C(16)-C(21)	1.392(3)
C(17)-C(18)	1.394(3)
C(17)-H(17)	0.9500
C(18)-C(19)	1.375(4)
C(18)-H(18)	0.9500
C(19)-C(20)	1.381(4)
C(19)-H(19)	0.9500
C(20)-C(21)	1.379(3)
C(20)-H(20)	0.9500
C(21)-H(21)	0.9500
C(22)-C(27)	1.391(3)
C(22)-C(23)	1.397(3)
C(23)-C(24)	1.384(3)
C(23)-H(23)	0.9500
C(24)-C(25)	1.382(3)

C(24)-H(24)	0.9500	C(44)-C(45)	1.385(3)
C(25)-C(26)	1.383(3)	C(44)-H(44)	0.9500
C(25)-H(25)	0.9500	C(45)-H(45)	0.9500
C(26)-C(27)	1.393(3)	C(1S)-C(6S)	1.353(5)
C(26)-H(26)	0.9500	C(1S)-C(2S)	1.355(5)
C(27)-H(27)	0.9500	C(1S)-H(1S)	0.9500
C(28)-C(29)	1.391(3)	C(2S)-C(3S)	1.367(5)
C(28)-C(33)	1.394(3)	C(2S)-H(2S)	0.9500
C(29)-C(30)	1.389(3)	C(3S)-C(4S)	1.392(6)
C(29)-H(29)	0.9500	C(3S)-H(3S)	0.9500
C(30)-C(31)	1.377(4)	C(4S)-C(5S)	1.373(6)
C(30)-H(30)	0.9500	C(4S)-H(4S)	0.9500
C(31)-C(32)	1.383(3)	C(5S)-C(6S)	1.368(6)
C(31)-H(31)	0.9500	C(5S)-H(5S)	0.9500
C(32)-C(33)	1.386(3)	C(6S)-H(6S)	0.9500
C(32)-H(32)	0.9500	C(7S)-C(12S)	1.347(5)
C(33)-H(33)	0.9500	C(7S)-C(8S)	1.368(5)
C(34)-C(39)	1.386(3)	C(7S)-H(7S)	0.9500
C(34)-C(35)	1.395(3)	C(8S)-C(9S)	1.373(5)
C(35)-C(36)	1.384(3)	C(8S)-H(8S)	0.9500
C(35)-H(35)	0.9500	C(9S)-C(10S)	1.396(5)
C(36)-C(37)	1.383(3)	C(9S)-H(9S)	0.9500
C(36)-H(36)	0.9500	C(10S)-C(11S)	1.352(5)
C(37)-C(38)	1.376(3)	C(10S)-H(10S)	0.9500
C(37)-H(37)	0.9500	C(11S)-C(12S)	1.354(5)
C(38)-C(39)	1.395(3)	C(11S)-H(11S)	0.9500
C(38)-H(38)	0.9500	C(12S)-H(12S)	0.9500
C(39)-H(39)	0.9500		
C(40)-C(41)	1.386(3)	C(1)-Pd(1)-P(2)	89.38(6)
C(40)-C(45)	1.398(3)	C(1)-Pd(1)-P(1)	88.37(6)
C(41)-C(42)	1.393(3)	P(2)-Pd(1)-P(1)	177.592(18)
C(41)-H(41)	0.9500	C(1)-Pd(1)-Cl(1)	175.40(6)
C(42)-C(43)	1.382(4)	P(2)-Pd(1)-Cl(1)	88.034(17)
C(42)-H(42)	0.9500	P(1)-Pd(1)-Cl(1)	94.150(17)
C(43)-C(44)	1.379(4)	C(16)-P(1)-C(10)	101.94(9)
C(43)-H(43)	0.9500	C(16)-P(1)-C(22)	104.36(9)

C(10)-P(1)-C(22)	104.16(9)	C(8)-C(7)-H(7)	120.0
C(16)-P(1)-Pd(1)	116.86(6)	C(6)-C(7)-H(7)	120.0
C(10)-P(1)-Pd(1)	117.70(7)	C(9)-C(8)-C(7)	120.0
C(22)-P(1)-Pd(1)	110.27(6)	C(9)-C(8)-H(8)	120.0
C(40)-P(2)-C(28)	107.56(9)	C(7)-C(8)-H(8)	120.0
C(40)-P(2)-C(34)	104.50(9)	C(8)-C(9)-C(4)	120.0
C(28)-P(2)-C(34)	101.42(9)	C(8)-C(9)-H(9)	120.0
C(40)-P(2)-Pd(1)	109.14(6)	C(4)-C(9)-H(9)	120.0
C(28)-P(2)-Pd(1)	112.98(6)	C(5')-C(4')-C(9')	120.0
C(34)-P(2)-Pd(1)	120.27(6)	C(5')-C(4')-C(3)	121.7(8)
O(1)-C(1)-C(2)	122.7(2)	C(9')-C(4')-C(3)	118.2(8)
O(1)-C(1)-Pd(1)	120.96(16)	C(4')-C(5')-C(6')	120.0
C(2)-C(1)-Pd(1)	116.29(14)	C(4')-C(5')-H(5')	120.0
C(1)-C(2)-C(3)	113.27(19)	C(6')-C(5')-H(5')	120.0
C(1)-C(2)-H(2A)	108.9	C(7')-C(6')-C(5')	120.0
C(3)-C(2)-H(2A)	108.9	C(7')-C(6')-H(6')	120.0
C(1)-C(2)-H(2B)	108.9	C(5')-C(6')-H(6')	120.0
C(3)-C(2)-H(2B)	108.9	C(6')-C(7')-C(8')	120.0
H(2A)-C(2)-H(2B)	107.7	C(6')-C(7')-H(7')	120.0
C(4')-C(3)-C(2)	114.6(7)	C(8')-C(7')-H(7')	120.0
C(2)-C(3)-C(4)	110.9(4)	C(7')-C(8')-C(9')	120.0
C(2)-C(3)-H(3A)	109.5	C(7')-C(8')-H(8')	120.0
C(4)-C(3)-H(3A)	109.5	C(9')-C(8')-H(8')	120.0
C(2)-C(3)-H(3B)	109.5	C(8')-C(9')-C(4')	120.0
C(4)-C(3)-H(3B)	109.5	C(8')-C(9')-H(9')	120.0
H(3A)-C(3)-H(3B)	108.1	C(4')-C(9')-H(9')	120.0
C(5)-C(4)-C(9)	120.0	C(11)-C(10)-C(15)	118.5(2)
C(5)-C(4)-C(3)	120.2(4)	C(11)-C(10)-P(1)	120.46(17)
C(9)-C(4)-C(3)	119.8(4)	C(15)-C(10)-P(1)	120.94(16)
C(4)-C(5)-C(6)	120.0	C(12)-C(11)-C(10)	120.4(2)
C(4)-C(5)-H(5)	120.0	C(12)-C(11)-H(11)	119.8
C(6)-C(5)-H(5)	120.0	C(10)-C(11)-H(11)	119.8
C(5)-C(6)-C(7)	120.0	C(13)-C(12)-C(11)	120.2(3)
C(5)-C(6)-H(6)	120.0	C(13)-C(12)-H(12)	119.9
C(7)-C(6)-H(6)	120.0	C(11)-C(12)-H(12)	119.9
C(8)-C(7)-C(6)	120.0	C(14)-C(13)-C(12)	120.1(2)

C(14)-C(13)-H(13)	120.0	C(24)-C(25)-H(25)	119.9
C(12)-C(13)-H(13)	120.0	C(26)-C(25)-H(25)	119.9
C(13)-C(14)-C(15)	120.2(3)	C(25)-C(26)-C(27)	119.9(2)
C(13)-C(14)-H(14)	119.9	C(25)-C(26)-H(26)	120.1
C(15)-C(14)-H(14)	119.9	C(27)-C(26)-H(26)	120.1
C(14)-C(15)-C(10)	120.5(2)	C(22)-C(27)-C(26)	120.25(18)
C(14)-C(15)-H(15)	119.8	C(22)-C(27)-H(27)	119.9
C(10)-C(15)-H(15)	119.8	C(26)-C(27)-H(27)	119.9
C(17)-C(16)-C(21)	119.04(19)	C(29)-C(28)-C(33)	119.17(18)
C(17)-C(16)-P(1)	120.80(15)	C(29)-C(28)-P(2)	120.51(15)
C(21)-C(16)-P(1)	120.10(15)	C(33)-C(28)-P(2)	120.31(15)
C(16)-C(17)-C(18)	119.7(2)	C(30)-C(29)-C(28)	120.3(2)
C(16)-C(17)-H(17)	120.2	C(30)-C(29)-H(29)	119.9
C(18)-C(17)-H(17)	120.2	C(28)-C(29)-H(29)	119.9
C(19)-C(18)-C(17)	120.6(2)	C(31)-C(30)-C(29)	120.1(2)
C(19)-C(18)-H(18)	119.7	C(31)-C(30)-H(30)	119.9
C(17)-C(18)-H(18)	119.7	C(29)-C(30)-H(30)	119.9
C(18)-C(19)-C(20)	119.9(2)	C(30)-C(31)-C(32)	120.1(2)
C(18)-C(19)-H(19)	120.1	C(30)-C(31)-H(31)	120.0
C(20)-C(19)-H(19)	120.1	C(32)-C(31)-H(31)	120.0
C(21)-C(20)-C(19)	119.9(2)	C(31)-C(32)-C(33)	120.3(2)
C(21)-C(20)-H(20)	120.1	C(31)-C(32)-H(32)	119.9
C(19)-C(20)-H(20)	120.1	C(33)-C(32)-H(32)	119.9
C(20)-C(21)-C(16)	120.9(2)	C(32)-C(33)-C(28)	120.1(2)
C(20)-C(21)-H(21)	119.6	C(32)-C(33)-H(33)	120.0
C(16)-C(21)-H(21)	119.6	C(28)-C(33)-H(33)	120.0
C(27)-C(22)-C(23)	119.15(18)	C(39)-C(34)-C(35)	118.47(19)
C(27)-C(22)-P(1)	118.39(14)	C(39)-C(34)-P(2)	123.85(15)
C(23)-C(22)-P(1)	122.43(15)	C(35)-C(34)-P(2)	117.67(15)
C(24)-C(23)-C(22)	120.29(19)	C(36)-C(35)-C(34)	120.9(2)
C(24)-C(23)-H(23)	119.9	C(36)-C(35)-H(35)	119.5
C(22)-C(23)-H(23)	119.9	C(34)-C(35)-H(35)	119.5
C(25)-C(24)-C(23)	120.15(19)	C(37)-C(36)-C(35)	120.2(2)
C(25)-C(24)-H(24)	119.9	C(37)-C(36)-H(36)	119.9
C(23)-C(24)-H(24)	119.9	C(35)-C(36)-H(36)	119.9
C(24)-C(25)-C(26)	120.25(19)	C(38)-C(37)-C(36)	119.4(2)

C(38)-C(37)-H(37)	120.3	C(3S)-C(2S)-H(2S)	119.9
C(36)-C(37)-H(37)	120.3	C(2S)-C(3S)-C(4S)	119.9(4)
C(37)-C(38)-C(39)	120.7(2)	C(2S)-C(3S)-H(3S)	120.1
C(37)-C(38)-H(38)	119.7	C(4S)-C(3S)-H(3S)	120.1
C(39)-C(38)-H(38)	119.7	C(5S)-C(4S)-C(3S)	118.9(4)
C(34)-C(39)-C(38)	120.3(2)	C(5S)-C(4S)-H(4S)	120.5
C(34)-C(39)-H(39)	119.8	C(3S)-C(4S)-H(4S)	120.5
C(38)-C(39)-H(39)	119.8	C(6S)-C(5S)-C(4S)	119.9(4)
C(41)-C(40)-C(45)	119.38(18)	C(6S)-C(5S)-H(5S)	120.0
C(41)-C(40)-P(2)	123.08(15)	C(4S)-C(5S)-H(5S)	120.0
C(45)-C(40)-P(2)	117.50(16)	C(1S)-C(6S)-C(5S)	120.6(4)
C(40)-C(41)-C(42)	119.8(2)	C(1S)-C(6S)-H(6S)	119.7
C(40)-C(41)-H(41)	120.1	C(5S)-C(6S)-H(6S)	119.7
C(42)-C(41)-H(41)	120.1	C(12S)-C(7S)-C(8S)	121.1(4)
C(43)-C(42)-C(41)	120.6(2)	C(12S)-C(7S)-H(7S)	119.4
C(43)-C(42)-H(42)	119.7	C(8S)-C(7S)-H(7S)	119.4
C(41)-C(42)-H(42)	119.7	C(7S)-C(8S)-C(9S)	119.4(3)
C(44)-C(43)-C(42)	119.6(2)	C(7S)-C(8S)-H(8S)	120.3
C(44)-C(43)-H(43)	120.2	C(9S)-C(8S)-H(8S)	120.3
C(42)-C(43)-H(43)	120.2	C(8S)-C(9S)-C(10S)	118.9(4)
C(43)-C(44)-C(45)	120.5(2)	C(8S)-C(9S)-H(9S)	120.6
C(43)-C(44)-H(44)	119.7	C(10S)-C(9S)-H(9S)	120.6
C(45)-C(44)-H(44)	119.7	C(11S)-C(10S)-C(9S)	119.8(4)
C(44)-C(45)-C(40)	120.1(2)	C(11S)-C(10S)-H(10S)	120.1
C(44)-C(45)-H(45)	120.0	C(9S)-C(10S)-H(10S)	120.1
C(40)-C(45)-H(45)	120.0	C(10S)-C(11S)-C(12S)	120.8(4)
C(6S)-C(1S)-C(2S)	120.5(4)	C(10S)-C(11S)-H(11S)	119.6
C(6S)-C(1S)-H(1S)	119.8	C(12S)-C(11S)-H(11S)	119.6
C(2S)-C(1S)-H(1S)	119.8	C(7S)-C(12S)-C(11S)	120.0(4)
C(1S)-C(2S)-C(3S)	120.2(4)	C(7S)-C(12S)-H(12S)	120.0
C(1S)-C(2S)-H(2S)	119.9	C(11S)-C(12S)-H(12S)	120.0

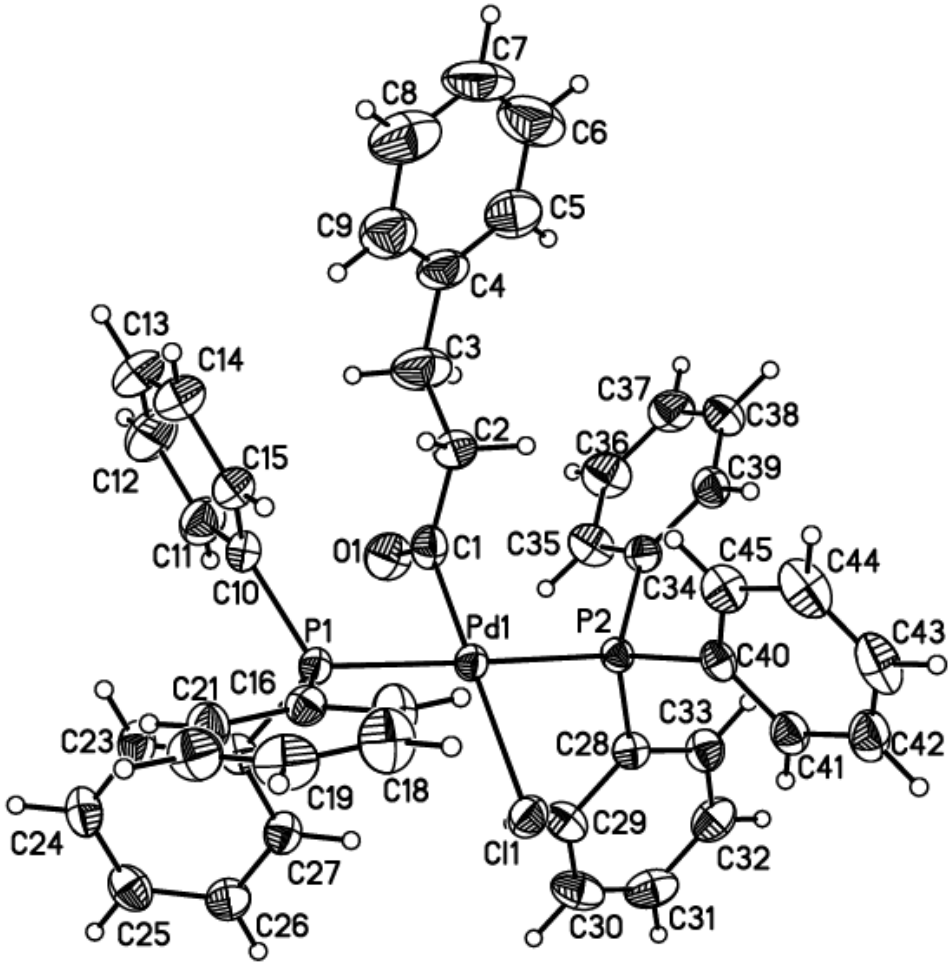

Figure D.1. Projection view with 50% probability ellipsoids- solvent atoms and disorder components omitted for clarity

Complex $2^{+}(SbF_6)$. Hydrocinnamoyl $Pd(PPh_3)_2$ acetonitrile (hexafluoroantimonate).

Crystal data and structure refinement for **$2^{+}(SbF_6)$**.

Identification code	t320	
Empirical formula	C98 H94 F12 N2 O3 P4 Pd2 Sb2	
Formula weight	2155.93	
Temperature	100(2) K	
Wavelength	0.71073 Å	
Crystal system	Triclinic	
Space group	P-1	
Unit cell dimensions	a = 11.7724(4) Å	a= 62.8619(11)°.
	b = 15.3908(5) Å	b= 77.7029(12)°.
	c = 15.5681(5) Å	g = 68.8055(12)°.
Volume	2336.47(14) $Å^3$	
Z	1	
Density (calculated)	1.532 Mg/m^3	
Absorption coefficient	1.093 mm^{-1}	
F(000)	1082	
Crystal size	0.137 x 0.085 x 0.083 mm^3	
Theta range for data collection	2.016 to 28.289°.	
Index ranges	-15<=h<=15, -20<=k<=20, -20<=l<=20	
Reflections collected	68053	
Independent reflections	11610 [R(int) = 0.0563]	
Completeness to theta = 25.242°	99.9 %	
Absorption correction	Semi-empirical from equivalents	
Max. and min. transmission	0.9010 and 0.8370	
Refinement method	Full-matrix least-squares on F^2	
Data / restraints / parameters	11610 / 21 / 571	
Goodness-of-fit on F^2	1.048	
Final R indices [I>2sigma(I)]	R1 = 0.0259, wR2 = 0.0556	
R indices (all data)	R1 = 0.0344, wR2 = 0.0584	
Extinction coefficient	n/a	
Largest diff. peak and hole	0.830 and -0.781 $e.Å^{-3}$	

Select Bonds and angles.

Bond lengths [Å] and angles [°] for **2^{+}(SbF$_6$)**.

Pd(1)-C(1)	1.9915(19)
Pd(1)-N(1)	2.1606(17)
Pd(1)-P(1)	2.3513(5)
Pd(1)-P(2)	2.3548(5)
P(1)-C(12)	1.8201(19)
P(1)-C(18)	1.8262(19)
P(1)-C(24)	1.8265(19)
P(2)-C(30)	1.815(2)
P(2)-C(36)	1.8214(19)
P(2)-C(42)	1.8257(19)
O(1)-C(1)	1.199(2)
N(1)-C(10)	1.125(3)
C(1)-C(2)	1.517(3)
C(2)-C(3)	1.532(3)
C(2)-H(2A)	0.9900
C(2)-H(2B)	0.9900
C(3)-C(4)	1.507(3)
C(3)-H(3A)	0.9900
C(3)-H(3B)	0.9900
C(4)-C(5)	1.389(3)
C(4)-C(9)	1.391(3)
C(5)-C(6)	1.379(3)
C(5)-H(5)	0.9500
C(6)-C(7)	1.380(4)
C(6)-H(6)	0.9500
C(7)-C(8)	1.380(4)
C(7)-H(7)	0.9500
C(8)-C(9)	1.390(4)
C(8)-H(8)	0.9500
C(9)-H(9)	0.9500
C(10)-C(11)	1.458(3)
C(11)-H(11A)	0.9800
C(11)-H(11B)	0.9800
C(11)-H(11C)	0.9800
C(12)-C(17)	1.394(3)
C(12)-C(13)	1.401(3)
C(13)-C(14)	1.386(3)
C(13)-H(13)	0.9500
C(14)-C(15)	1.386(3)
C(14)-H(14)	0.9500
C(15)-C(16)	1.385(3)
C(15)-H(15)	0.9500
C(16)-C(17)	1.389(3)
C(16)-H(16)	0.9500
C(17)-H(17)	0.9500
C(18)-C(23)	1.392(3)
C(18)-C(19)	1.394(3)
C(19)-C(20)	1.387(3)
C(19)-H(19)	0.9500
C(20)-C(21)	1.383(3)
C(20)-H(20)	0.9500
C(21)-C(22)	1.391(3)
C(21)-H(21)	0.9500
C(22)-C(23)	1.391(3)
C(22)-H(22)	0.9500
C(23)-H(23)	0.9500
C(24)-C(25)	1.395(3)
C(24)-C(29)	1.405(3)
C(25)-C(26)	1.388(3)
C(25)-H(25)	0.9500
C(26)-C(27)	1.389(3)
C(26)-H(26)	0.9500
C(27)-C(28)	1.388(3)
C(27)-H(27)	0.9500
C(28)-C(29)	1.388(3)
C(28)-H(28)	0.9500
C(29)-H(29)	0.9500
C(30)-C(35)	1.391(3)

C(30)-C(31)	1.393(3)	Sb(1)-F(6)	1.8763(12)
C(31)-C(32)	1.391(3)	Sb(1)-F(5)	1.8780(13)
C(31)-H(31)	0.9500	O(1S)-C(2S)	1.3211
C(32)-C(33)	1.379(3)	O(1S)-C(3S)	1.4284
C(32)-H(32)	0.9500	C(1S)-C(2S)	1.3754
C(33)-C(34)	1.385(3)	C(1S)-H(1SA)	0.9800
C(33)-H(33)	0.9500	C(1S)-H(1SB)	0.9800
C(34)-C(35)	1.389(3)	C(1S)-H(1SC)	0.9800
C(34)-H(34)	0.9500	C(2S)-H(2SA)	0.9900
C(35)-H(35)	0.9500	C(2S)-H(2SB)	0.9900
C(36)-C(41)	1.394(3)	C(3S)-C(4S)	1.2176
C(36)-C(37)	1.396(3)	C(3S)-H(3SA)	0.9900
C(37)-C(38)	1.387(3)	C(3S)-H(3SB)	0.9900
C(37)-H(37)	0.9500	C(4S)-H(4SA)	0.9800
C(38)-C(39)	1.389(3)	C(4S)-H(4SB)	0.9800
C(38)-H(38)	0.9500	C(4S)-H(4SC)	0.9800
C(39)-C(40)	1.380(3)		
C(39)-H(39)	0.9500	C(1)-Pd(1)-N(1)	178.91(7)
C(40)-C(41)	1.387(3)	C(1)-Pd(1)-P(1)	88.49(5)
C(40)-H(40)	0.9500	N(1)-Pd(1)-P(1)	91.90(5)
C(41)-H(41)	0.9500	C(1)-Pd(1)-P(2)	89.48(5)
C(42)-C(47)	1.394(3)	N(1)-Pd(1)-P(2)	90.21(5)
C(42)-C(43)	1.397(3)	P(1)-Pd(1)-P(2)	174.869(18)
C(43)-C(44)	1.385(3)	C(12)-P(1)-C(18)	104.50(9)
C(43)-H(43)	0.9500	C(12)-P(1)-C(24)	106.18(9)
C(44)-C(45)	1.390(3)	C(18)-P(1)-C(24)	103.86(9)
C(44)-H(44)	0.9500	C(12)-P(1)-Pd(1)	112.46(6)
C(45)-C(46)	1.383(3)	C(18)-P(1)-Pd(1)	111.26(6)
C(45)-H(45)	0.9500	C(24)-P(1)-Pd(1)	117.45(6)
C(46)-C(47)	1.386(3)	C(30)-P(2)-C(36)	103.99(9)
C(46)-H(46)	0.9500	C(30)-P(2)-C(42)	105.13(9)
C(47)-H(47)	0.9500	C(36)-P(2)-C(42)	105.14(9)
Sb(1)-F(3)	1.8623(14)	C(30)-P(2)-Pd(1)	115.61(6)
Sb(1)-F(2)	1.8700(14)	C(36)-P(2)-Pd(1)	105.54(6)
Sb(1)-F(4)	1.8730(13)	C(42)-P(2)-Pd(1)	119.86(6)
Sb(1)-F(1)	1.8748(13)	C(10)-N(1)-Pd(1)	178.22(18)

O(1)-C(1)-C(2)	124.36(18)	H(11A)-C(11)-H(11B)	109.5
O(1)-C(1)-Pd(1)	121.49(15)	C(10)-C(11)-H(11C)	109.5
C(2)-C(1)-Pd(1)	114.14(13)	H(11A)-C(11)-H(11C)	109.5
C(1)-C(2)-C(3)	115.45(17)	H(11B)-C(11)-H(11C)	109.5
C(1)-C(2)-H(2A)	108.4	C(17)-C(12)-C(13)	119.31(18)
C(3)-C(2)-H(2A)	108.4	C(17)-C(12)-P(1)	122.97(15)
C(1)-C(2)-H(2B)	108.4	C(13)-C(12)-P(1)	117.71(14)
C(3)-C(2)-H(2B)	108.4	C(14)-C(13)-C(12)	120.12(18)
H(2A)-C(2)-H(2B)	107.5	C(14)-C(13)-H(13)	119.9
C(4)-C(3)-C(2)	109.66(17)	C(12)-C(13)-H(13)	119.9
C(4)-C(3)-H(3A)	109.7	C(13)-C(14)-C(15)	120.13(19)
C(2)-C(3)-H(3A)	109.7	C(13)-C(14)-H(14)	119.9
C(4)-C(3)-H(3B)	109.7	C(15)-C(14)-H(14)	119.9
C(2)-C(3)-H(3B)	109.7	C(16)-C(15)-C(14)	120.09(18)
H(3A)-C(3)-H(3B)	108.2	C(16)-C(15)-H(15)	120.0
C(5)-C(4)-C(9)	118.0(2)	C(14)-C(15)-H(15)	120.0
C(5)-C(4)-C(3)	120.93(19)	C(15)-C(16)-C(17)	120.22(18)
C(9)-C(4)-C(3)	121.0(2)	C(15)-C(16)-H(16)	119.9
C(6)-C(5)-C(4)	121.3(2)	C(17)-C(16)-H(16)	119.9
C(6)-C(5)-H(5)	119.3	C(16)-C(17)-C(12)	120.10(18)
C(4)-C(5)-H(5)	119.3	C(16)-C(17)-H(17)	119.9
C(5)-C(6)-C(7)	120.2(3)	C(12)-C(17)-H(17)	119.9
C(5)-C(6)-H(6)	119.9	C(23)-C(18)-C(19)	118.94(18)
C(7)-C(6)-H(6)	119.9	C(23)-C(18)-P(1)	120.21(15)
C(6)-C(7)-C(8)	119.4(2)	C(19)-C(18)-P(1)	120.85(15)
C(6)-C(7)-H(7)	120.3	C(20)-C(19)-C(18)	120.47(19)
C(8)-C(7)-H(7)	120.3	C(20)-C(19)-H(19)	119.8
C(7)-C(8)-C(9)	120.3(2)	C(18)-C(19)-H(19)	119.8
C(7)-C(8)-H(8)	119.8	C(21)-C(20)-C(19)	120.5(2)
C(9)-C(8)-H(8)	119.8	C(21)-C(20)-H(20)	119.8
C(8)-C(9)-C(4)	120.7(2)	C(19)-C(20)-H(20)	119.8
C(8)-C(9)-H(9)	119.7	C(20)-C(21)-C(22)	119.53(19)
C(4)-C(9)-H(9)	119.7	C(20)-C(21)-H(21)	120.2
N(1)-C(10)-C(11)	179.4(3)	C(22)-C(21)-H(21)	120.2
C(10)-C(11)-H(11A)	109.5	C(23)-C(22)-C(21)	120.16(19)
C(10)-C(11)-H(11B)	109.5	C(23)-C(22)-H(22)	119.9

C(21)-C(22)-H(22)	119.9	C(35)-C(34)-H(34)	119.9
C(22)-C(23)-C(18)	120.44(19)	C(34)-C(35)-C(30)	120.02(19)
C(22)-C(23)-H(23)	119.8	C(34)-C(35)-H(35)	120.0
C(18)-C(23)-H(23)	119.8	C(30)-C(35)-H(35)	120.0
C(25)-C(24)-C(29)	118.96(18)	C(41)-C(36)-C(37)	119.06(18)
C(25)-C(24)-P(1)	120.81(15)	C(41)-C(36)-P(2)	122.49(15)
C(29)-C(24)-P(1)	120.15(15)	C(37)-C(36)-P(2)	118.39(15)
C(26)-C(25)-C(24)	120.72(19)	C(38)-C(37)-C(36)	120.49(19)
C(26)-C(25)-H(25)	119.6	C(38)-C(37)-H(37)	119.8
C(24)-C(25)-H(25)	119.6	C(36)-C(37)-H(37)	119.8
C(25)-C(26)-C(27)	119.95(19)	C(37)-C(38)-C(39)	119.9(2)
C(25)-C(26)-H(26)	120.0	C(37)-C(38)-H(38)	120.1
C(27)-C(26)-H(26)	120.0	C(39)-C(38)-H(38)	120.1
C(28)-C(27)-C(26)	119.86(19)	C(40)-C(39)-C(38)	120.0(2)
C(28)-C(27)-H(27)	120.1	C(40)-C(39)-H(39)	120.0
C(26)-C(27)-H(27)	120.1	C(38)-C(39)-H(39)	120.0
C(29)-C(28)-C(27)	120.52(19)	C(39)-C(40)-C(41)	120.5(2)
C(29)-C(28)-H(28)	119.7	C(39)-C(40)-H(40)	119.8
C(27)-C(28)-H(28)	119.7	C(41)-C(40)-H(40)	119.8
C(28)-C(29)-C(24)	119.96(19)	C(40)-C(41)-C(36)	120.1(2)
C(28)-C(29)-H(29)	120.0	C(40)-C(41)-H(41)	119.9
C(24)-C(29)-H(29)	120.0	C(36)-C(41)-H(41)	119.9
C(35)-C(30)-C(31)	119.64(18)	C(47)-C(42)-C(43)	119.00(18)
C(35)-C(30)-P(2)	118.71(15)	C(47)-C(42)-P(2)	122.89(15)
C(31)-C(30)-P(2)	121.30(15)	C(43)-C(42)-P(2)	118.09(14)
C(32)-C(31)-C(30)	119.76(19)	C(44)-C(43)-C(42)	120.57(18)
C(32)-C(31)-H(31)	120.1	C(44)-C(43)-H(43)	119.7
C(30)-C(31)-H(31)	120.1	C(42)-C(43)-H(43)	119.7
C(33)-C(32)-C(31)	120.44(19)	C(43)-C(44)-C(45)	120.14(19)
C(33)-C(32)-H(32)	119.8	C(43)-C(44)-H(44)	119.9
C(31)-C(32)-H(32)	119.8	C(45)-C(44)-H(44)	119.9
C(32)-C(33)-C(34)	120.0(2)	C(46)-C(45)-C(44)	119.40(19)
C(32)-C(33)-H(33)	120.0	C(46)-C(45)-H(45)	120.3
C(34)-C(33)-H(33)	120.0	C(44)-C(45)-H(45)	120.3
C(33)-C(34)-C(35)	120.2(2)	C(45)-C(46)-C(47)	120.92(19)
C(33)-C(34)-H(34)	119.9	C(45)-C(46)-H(46)	119.5

C(47)-C(46)-H(46)	119.5	H(1SA)-C(1S)-H(1SB)	109.5
C(46)-C(47)-C(42)	119.96(18)	C(2S)-C(1S)-H(1SC)	109.5
C(46)-C(47)-H(47)	120.0	H(1SA)-C(1S)-H(1SC)	109.5
C(42)-C(47)-H(47)	120.0	H(1SB)-C(1S)-H(1SC)	109.5
F(3)-Sb(1)-F(2)	92.11(8)	O(1S)-C(2S)-C(1S)	121.0
F(3)-Sb(1)-F(4)	90.98(8)	O(1S)-C(2S)-H(2SA)	107.1
F(2)-Sb(1)-F(4)	176.86(7)	C(1S)-C(2S)-H(2SA)	107.1
F(3)-Sb(1)-F(1)	178.34(8)	O(1S)-C(2S)-H(2SB)	107.1
F(2)-Sb(1)-F(1)	89.21(7)	C(1S)-C(2S)-H(2SB)	107.1
F(4)-Sb(1)-F(1)	87.72(7)	H(2SA)-C(2S)-H(2SB)	106.8
F(3)-Sb(1)-F(6)	88.70(6)	C(4S)-C(3S)-O(1S)	124.8
F(2)-Sb(1)-F(6)	90.56(6)	C(4S)-C(3S)-H(3SA)	106.1
F(4)-Sb(1)-F(6)	90.09(6)	O(1S)-C(3S)-H(3SA)	106.1
F(1)-Sb(1)-F(6)	90.26(6)	C(4S)-C(3S)-H(3SB)	106.1
F(3)-Sb(1)-F(5)	90.43(6)	O(1S)-C(3S)-H(3SB)	106.1
F(2)-Sb(1)-F(5)	89.08(6)	H(3SA)-C(3S)-H(3SB)	106.3
F(4)-Sb(1)-F(5)	90.31(6)	C(3S)-C(4S)-H(4SA)	109.5
F(1)-Sb(1)-F(5)	90.61(7)	C(3S)-C(4S)-H(4SB)	109.5
F(6)-Sb(1)-F(5)	179.05(6)	H(4SA)-C(4S)-H(4SB)	109.5
C(2S)-O(1S)-C(3S)	124.7	C(3S)-C(4S)-H(4SC)	109.5
C(2S)-C(1S)-H(1SA)	109.5	H(4SA)-C(4S)-H(4SC)	109.5
C(2S)-C(1S)-H(1SB)	109.5	H(4SB)-C(4S)-H(4SC)	109.5

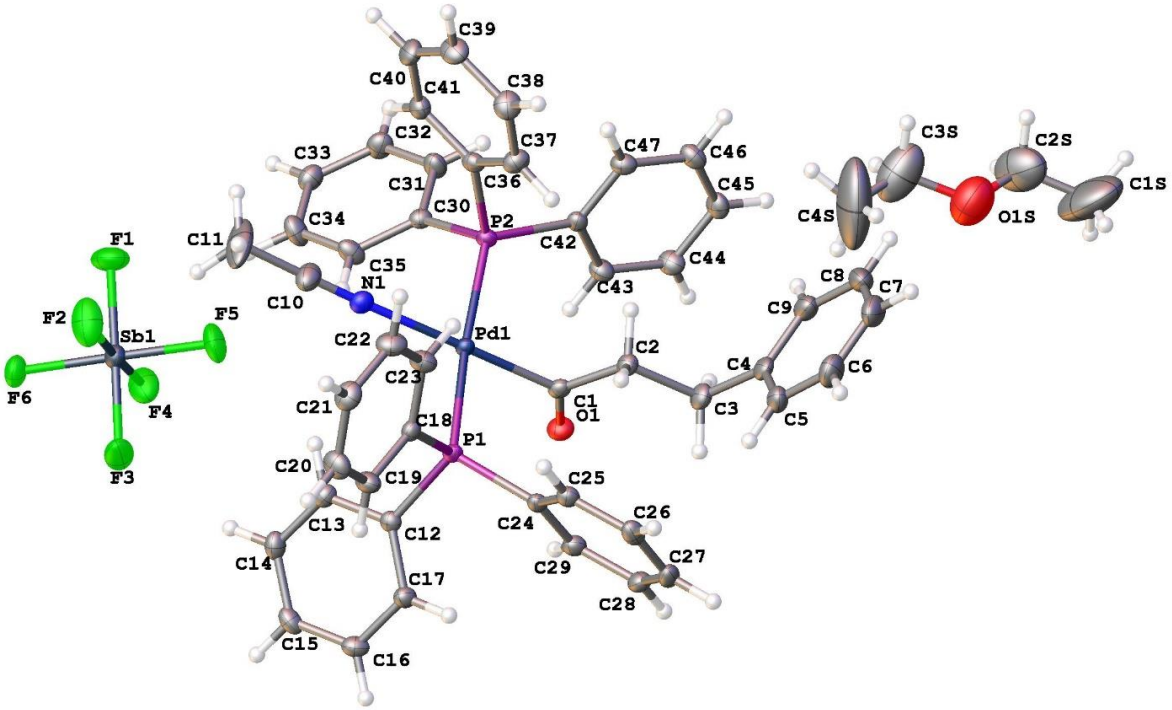

Figure D.2. Projection vie with 50% probability ellipsoids of complex $2^{+}(SbF_6)$ with a unit of diethyl either in the unit cell

Complex 3. Hydrocinnamoyl Pd(dppe) chloride

Crystal data and structure refinement for **3**

Identification code	t1020/lt/venture/TCW6068	
Empirical formula	C_{35} H_{33} Cl O P_2 Pd	
Formula weight	673.40	
Temperature	140(2) K	
Wavelength	1.54178 Å	
Crystal system	Orthorhombic	
Space group	$P2_12_12_1$	
Unit cell dimensions	a = 12.9298(6) Å	a= 90°.
	b = 14.7189(7) Å	b= 90°.
	c = 15.7117(7) Å	g = 90°.
Volume	2990.1(2) $Å^3$	
Z	4	
Density (calculated)	1.496 Mg/m^3	
Absorption coefficient	7.046 mm^{-1}	
F(000)	1376	
Crystal size	0.106 x 0.097 x 0.069 mm^3	
Theta range for data collection	4.428 to 74.709°.	
Index ranges	-15≤h≤16, -18≤k≤18, -19≤l≤19	
Reflections collected	46109	
Independent reflections	6102 [R(int) = 0.031]	
Completeness to theta = 67.679°	99.7 %	
Absorption correction	Semi-empirical from equivalents	
Max. and min. transmission	0.4259 and 0.3290	
Refinement method	Full-matrix least-squares on F^2	
Data / restraints / parameters	6102 / 0 / 361	
Goodness-of-fit on F^2	1.043	
Final R indices [I>2sigma(I)]	R1 = 0.0152, wR2 = 0.0387	
R indices (all data)	R1 = 0.0153, wR2 = 0.0387	
Absolute structure parameter	-0.0186(17)	
Largest diff. peak and hole	0.243 and -0.342 $e.Å^{-3}$	

Select Bonds and Angles.

Bond lengths [Å] and angles [°] for **3**

Pd(1)-C(1)	2.033(2)	C(13)-C(14)	1.392(3)
Pd(1)-P(2)	2.2331(5)	C(13)-H(13)	0.9500
Pd(1)-Cl(1)	2.3693(5)	C(14)-C(15)	1.390(4)
Pd(1)-P(1)	2.3956(5)	C(14)-H(14)	0.9500
P(1)-C(12)	1.821(2)	C(15)-C(16)	1.383(4)
P(1)-C(18)	1.824(2)	C(15)-H(15)	0.9500
P(1)-C(10)	1.852(2)	C(16)-C(17)	1.390(3)
P(2)-C(30)	1.817(2)	C(16)-H(16)	0.9500
P(2)-C(24)	1.821(2)	C(17)-H(17)	0.9500
P(2)-C(11)	1.835(2)	C(18)-C(23)	1.390(3)
O(1)-C(1)	1.201(3)	C(18)-C(19)	1.394(3)
C(1)-C(2)	1.519(3)	C(19)-C(20)	1.396(4)
C(2)-C(3)	1.532(3)	C(19)-H(19)	0.9500
C(2)-H(2A)	0.9900	C(20)-C(21)	1.381(4)
C(2)-H(2B)	0.9900	C(20)-H(20)	0.9500
C(3)-C(4)	1.509(3)	C(21)-C(22)	1.384(4)
C(3)-H(3A)	0.9900	C(21)-H(21)	0.9500
C(3)-H(3B)	0.9900	C(22)-C(23)	1.390(4)
C(4)-C(9)	1.389(3)	C(22)-H(22)	0.9500
C(4)-C(5)	1.393(4)	C(23)-H(23)	0.9500
C(5)-C(6)	1.387(4)	C(24)-C(29)	1.392(3)
C(5)-H(5)	0.9500	C(24)-C(25)	1.394(3)
C(6)-C(7)	1.386(4)	C(25)-C(26)	1.387(4)
C(6)-H(6)	0.9500	C(25)-H(25)	0.9500
C(7)-C(8)	1.374(4)	C(26)-C(27)	1.382(4)
C(7)-H(7)	0.9500	C(26)-H(26)	0.9500
C(8)-C(9)	1.383(4)	C(27)-C(28)	1.387(4)
C(8)-H(8)	0.9500	C(27)-H(27)	0.9500
C(9)-H(9)	0.9500	C(28)-C(29)	1.387(3)
C(10)-C(11)	1.535(3)	C(28)-H(28)	0.9500
C(10)-H(10A)	0.9900	C(29)-H(29)	0.9500
C(10)-H(10B)	0.9900	C(30)-C(35)	1.390(3)
C(11)-H(11A)	0.9900	C(30)-C(31)	1.397(3)
C(11)-H(11B)	0.9900	C(31)-C(32)	1.386(3)
C(12)-C(13)	1.396(3)		
C(12)-C(17)	1.398(3)		

C(31)-H(31)	0.9500	C(4)-C(3)-C(2)	111.6(2)
C(32)-C(33)	1.387(4)	C(4)-C(3)-H(3A)	109.3
C(32)-H(32)	0.9500	C(2)-C(3)-H(3A)	109.3
C(33)-C(34)	1.375(4)	C(4)-C(3)-H(3B)	109.3
C(33)-H(33)	0.9500	C(2)-C(3)-H(3B)	109.3
C(34)-C(35)	1.391(4)	H(3A)-C(3)-H(3B)	108.0
C(34)-H(34)	0.9500	C(9)-C(4)-C(5)	117.9(2)
C(35)-H(35)	0.9500	C(9)-C(4)-C(3)	121.6(2)
		C(5)-C(4)-C(3)	120.5(2)
C(1)-Pd(1)-P(2)	89.59(6)	C(6)-C(5)-C(4)	120.7(2)
C(1)-Pd(1)-Cl(1)	85.73(6)	C(6)-C(5)-H(5)	119.7
P(2)-Pd(1)-Cl(1)	175.27(2)	C(4)-C(5)-H(5)	119.7
C(1)-Pd(1)-P(1)	173.53(7)	C(7)-C(6)-C(5)	120.3(3)
P(2)-Pd(1)-P(1)	84.997(18)	C(7)-C(6)-H(6)	119.9
Cl(1)-Pd(1)-P(1)	99.716(19)	C(5)-C(6)-H(6)	119.9
C(12)-P(1)-C(18)	103.86(10)	C(8)-C(7)-C(6)	119.6(2)
C(12)-P(1)-C(10)	107.20(10)	C(8)-C(7)-H(7)	120.2
C(18)-P(1)-C(10)	103.81(10)	C(6)-C(7)-H(7)	120.2
C(12)-P(1)-Pd(1)	121.44(7)	C(7)-C(8)-C(9)	120.1(2)
C(18)-P(1)-Pd(1)	113.39(7)	C(7)-C(8)-H(8)	120.0
C(10)-P(1)-Pd(1)	105.73(7)	C(9)-C(8)-H(8)	120.0
C(30)-P(2)-C(24)	103.95(10)	C(8)-C(9)-C(4)	121.5(2)
C(30)-P(2)-C(11)	107.03(10)	C(8)-C(9)-H(9)	119.2
C(24)-P(2)-C(11)	105.01(10)	C(4)-C(9)-H(9)	119.2
C(30)-P(2)-Pd(1)	120.06(7)	C(11)-C(10)-P(1)	110.26(15)
C(24)-P(2)-Pd(1)	113.06(7)	C(11)-C(10)-H(10A)	109.6
C(11)-P(2)-Pd(1)	106.67(7)	P(1)-C(10)-H(10A)	109.6
O(1)-C(1)-C(2)	122.48(19)	C(11)-C(10)-H(10B)	109.6
O(1)-C(1)-Pd(1)	122.21(16)	P(1)-C(10)-H(10B)	109.6
C(2)-C(1)-Pd(1)	115.27(14)	H(10A)-C(10)-H(10B)	108.1
C(1)-C(2)-C(3)	113.7(2)	C(10)-C(11)-P(2)	108.48(15)
C(1)-C(2)-H(2A)	108.8	C(10)-C(11)-H(11A)	110.0
C(3)-C(2)-H(2A)	108.8	P(2)-C(11)-H(11A)	110.0
C(1)-C(2)-H(2B)	108.8	C(10)-C(11)-H(11B)	110.0
C(3)-C(2)-H(2B)	108.8	P(2)-C(11)-H(11B)	110.0
H(2A)-C(2)-H(2B)	107.7	H(11A)-C(11)-H(11B)	108.4

C(13)-C(12)-C(17)	119.13(19)	C(29)-C(24)-C(25)	119.1(2)
C(13)-C(12)-P(1)	116.16(16)	C(29)-C(24)-P(2)	121.41(18)
C(17)-C(12)-P(1)	124.70(16)	C(25)-C(24)-P(2)	119.50(18)
C(14)-C(13)-C(12)	120.4(2)	C(26)-C(25)-C(24)	120.3(2)
C(14)-C(13)-H(13)	119.8	C(26)-C(25)-H(25)	119.8
C(12)-C(13)-H(13)	119.8	C(24)-C(25)-H(25)	119.8
C(15)-C(14)-C(13)	119.9(2)	C(27)-C(26)-C(25)	120.3(3)
C(15)-C(14)-H(14)	120.1	C(27)-C(26)-H(26)	119.9
C(13)-C(14)-H(14)	120.1	C(25)-C(26)-H(26)	119.9
C(16)-C(15)-C(14)	120.0(2)	C(26)-C(27)-C(28)	119.8(2)
C(16)-C(15)-H(15)	120.0	C(26)-C(27)-H(27)	120.1
C(14)-C(15)-H(15)	120.0	C(28)-C(27)-H(27)	120.1
C(15)-C(16)-C(17)	120.4(2)	C(27)-C(28)-C(29)	120.2(2)
C(15)-C(16)-H(16)	119.8	C(27)-C(28)-H(28)	119.9
C(17)-C(16)-H(16)	119.8	C(29)-C(28)-H(28)	119.9
C(16)-C(17)-C(12)	120.1(2)	C(28)-C(29)-C(24)	120.3(2)
C(16)-C(17)-H(17)	119.9	C(28)-C(29)-H(29)	119.8
C(12)-C(17)-H(17)	119.9	C(24)-C(29)-H(29)	119.8
C(23)-C(18)-C(19)	119.5(2)	C(35)-C(30)-C(31)	119.2(2)
C(23)-C(18)-P(1)	118.69(17)	C(35)-C(30)-P(2)	121.65(18)
C(19)-C(18)-P(1)	121.77(19)	C(31)-C(30)-P(2)	119.01(18)
C(18)-C(19)-C(20)	119.9(2)	C(32)-C(31)-C(30)	120.5(2)
C(18)-C(19)-H(19)	120.1	C(32)-C(31)-H(31)	119.8
C(20)-C(19)-H(19)	120.1	C(30)-C(31)-H(31)	119.8
C(21)-C(20)-C(19)	120.2(2)	C(31)-C(32)-C(33)	119.6(2)
C(21)-C(20)-H(20)	119.9	C(31)-C(32)-H(32)	120.2
C(19)-C(20)-H(20)	119.9	C(33)-C(32)-H(32)	120.2
C(20)-C(21)-C(22)	120.2(2)	C(34)-C(33)-C(32)	120.4(2)
C(20)-C(21)-H(21)	119.9	C(34)-C(33)-H(33)	119.8
C(22)-C(21)-H(21)	119.9	C(32)-C(33)-H(33)	119.8
C(21)-C(22)-C(23)	120.0(3)	C(33)-C(34)-C(35)	120.2(2)
C(21)-C(22)-H(22)	120.0	C(33)-C(34)-H(34)	119.9
C(23)-C(22)-H(22)	120.0	C(35)-C(34)-H(34)	119.9
C(22)-C(23)-C(18)	120.3(2)	C(30)-C(35)-C(34)	120.1(2)
C(22)-C(23)-H(23)	119.8	C(30)-C(35)-H(35)	120.0
C(18)-C(23)-H(23)	119.8	C(34)-C(35)-H(35)	120.0

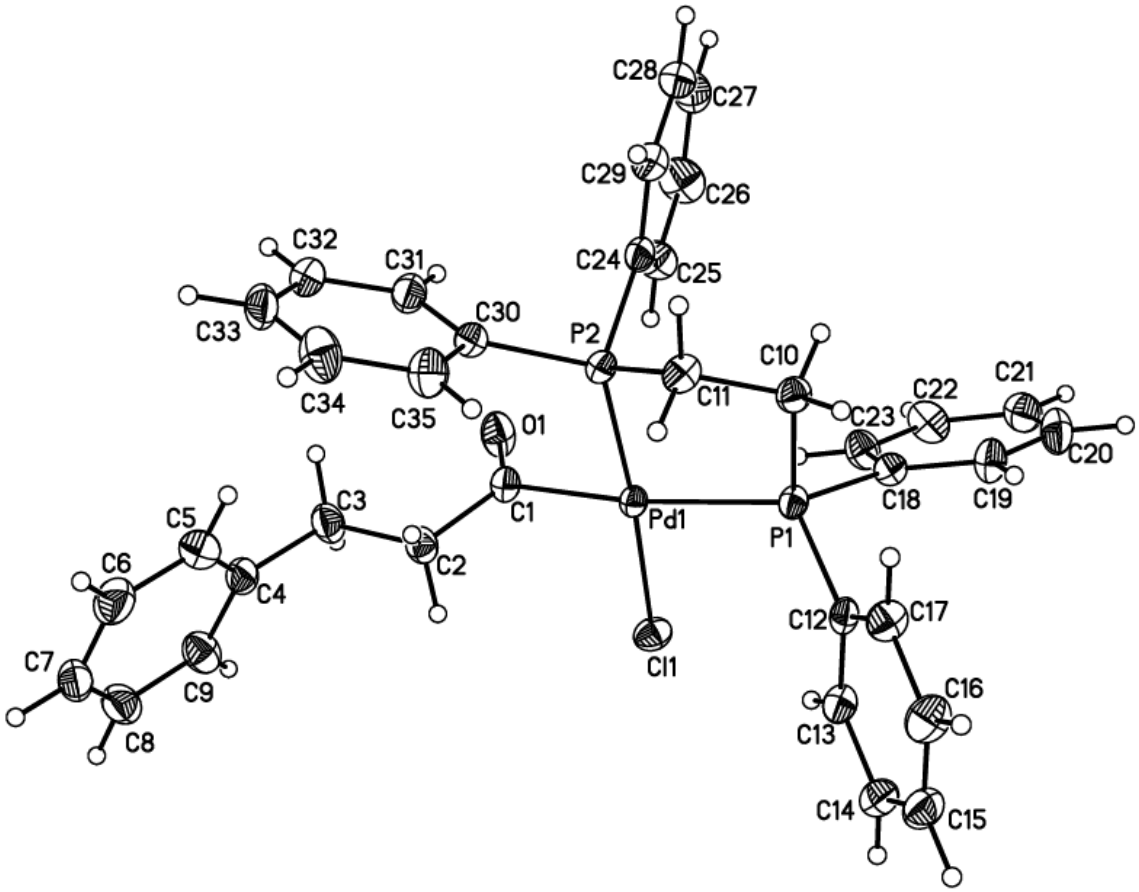

Figure D.3. Projection vie with 50% probability ellipsoids of complex 3

Appendix E.

Extra Computational/Theory details

E.1. Theory

A special thanks to Samuel Asiedu Fosu, Dr. Riffat Parveen and Professor Bess Vlaisavljevich who provided all calculations and theoretical insights.

E.1.1. Computational Details

Density Functional Theory (DFT) calculations were performed with the Gaussian 16 program package.[1] Geometry optimizations of all minima and transition states were performed using the M06-Lfunctional, [2] and the nature of all stationary points was verified by harmonic vibrational analysis. The single imaginary frequency for each transition state structure is connected to the reactants and products which was verified by following the intrinsic reaction coordinate (IRC).[3] Gibbs free energies were computed at 298.15 K. For geometry optimizations and vibrational frequencies, the def2-SV(P) basis set was used for all atoms except for Pd and Ag, where the def2-TZVP basis set and its corresponding effective core potential (ECP) were used.[4] All optimized structures were further subjected to single point calculation using def2-TZVP basis set for all atoms. Solvation effects were included using the continuum solvation model (SMD[5]) for acetonitrile in all calculations. The free energies were corrected to account for the standard state and Grimme's quasiharmonic correction was applied. In the latter correction, allo vibrational frequencies lower than 100 cm^{-1} were replaced by a value generated in the GoodVibes[6] program package using the free-rotor approximation as proposed by Grimme. Finally, the sensitivity of the energy barriers to functional choice was tested by performing single point calculations on the M06-L optimized geometries using M06-L, M06,[7] MN15,[8] and ωB97XD.[9] The def2-TZVP basis set was used for all atoms studied. The corresponding ECP was used for Pd and Ag.[10] Finally, the sensitivity of the energy barriers to functional choice was

tested by performing a subset of the calculations using M06-L, M06,[11] and ωB97XD.[12] The same basis sets and energy corrections applied to the values in the main text were included here.

E.2. Oxidative Addition (DFT)

Reaction mechanisms were computed for the oxidative addition (OA) of 3-phenylpropanoyl chloride by $Pd(P^tBu_3)_2$ and $Pd(PPh_3)_4$. The P^tBu_3 and PPh_3 Pd-acyl complexes formed as OA products are labeled **1** and **2**, respectively, as in the main text. The mechanism to form Pd-acyl complexes **1** is shown in Scheme 1 and to form **2** in Scheme 2. The analogous dppe Pd-acyl complex (**3**) is formed by ligand exchange involving **2** and dppe; therefore, no OA mechanism is presented.

The first step of the mechanism is the oxidative addition (OA) of the acyl-chloride bond in 3-phenylpropanoyl chloride (3-PPCl) on the Pd center $Pd(P^tBu_3)_2$ (Scheme S1). OA occurs via a transition state, which has a free energy barrier of 24.1 kcal/mol, affording an acyl-Pd species. To form the stable, Pd(II) resting complex **1**, a phosphine ligand is decoordinated in an exergonic process (ΔG = -13.5 kcal/mol). On the other hand, in the reaction profile with PPh_3 ligands, the formation of the square planar Pd(II) complex first requires 6.9 kcal/mol to decoordinate two phosphine ligands to form the active species, $[Pd(PPh_3)_2]$ (Scheme S2)**.** OA takes place via transition state, which has a free energy barrier of 9.2 kcal/mol (with respect to the starting species), resulting in the formation of **2** (ΔG = -19.8 kcal/mol). Lower steric hinderance by a single phosphine ligand around the Pd (II) center in **1** result in shorter Pd-CO, Pd-P and Pd-Cl bonds (1.955. 2.327 and 2.428 Å, respectively) compared to **2** (2.0, 2.371(average) and 2.542 Å respectively).

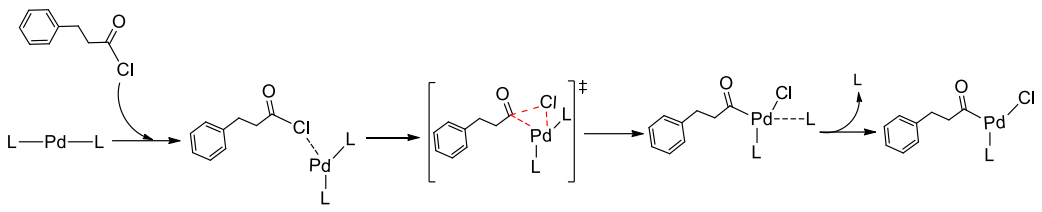

Scheme E.1. Oxidative addition steps for the reaction of 3-PPCl and $Pd(P^tBu_3)_2$ to form **1** where L= P^tBu_3.

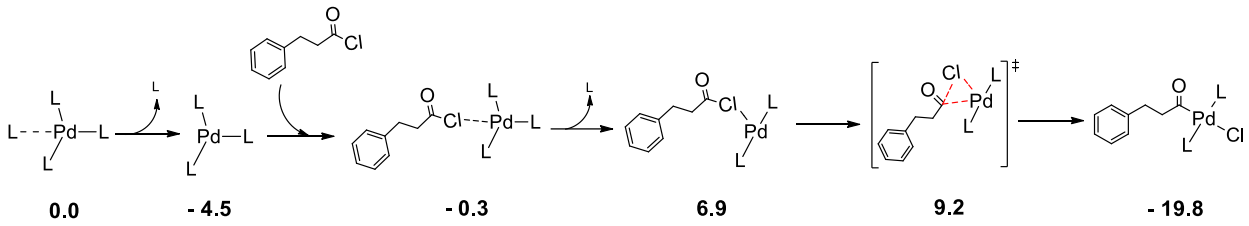

Scheme E.2. Oxidative addition steps for 3-PPCl and $Pd(PPh_3)_4$ where L= PPh_3.

E.3. Supplemental schemes for Figure 2.13

The reaction profile included in the main text presents the reactivity for **1**, **2**, and **3** in the same figure with simplified structure to be concise. The reactions pathway are shown as separate schemes here. Explicit solvent when used is shown.

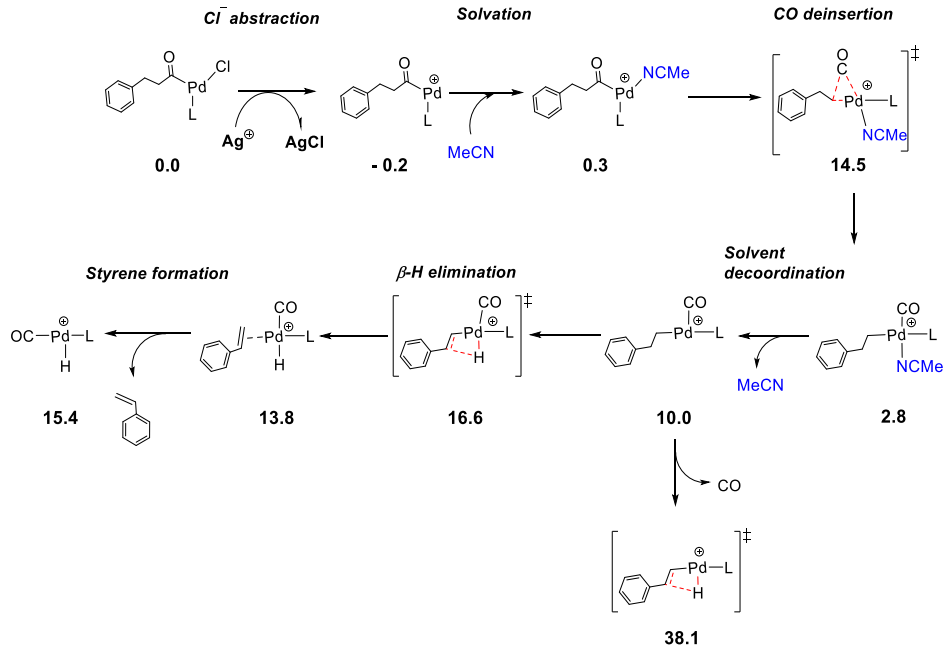

Scheme E.3. The DFT computed reaction mechanism for Pd-catalyzed CO deinsertion of 3-phenylpropionyl chloride starting from with **1** where L = P^tBu_3.

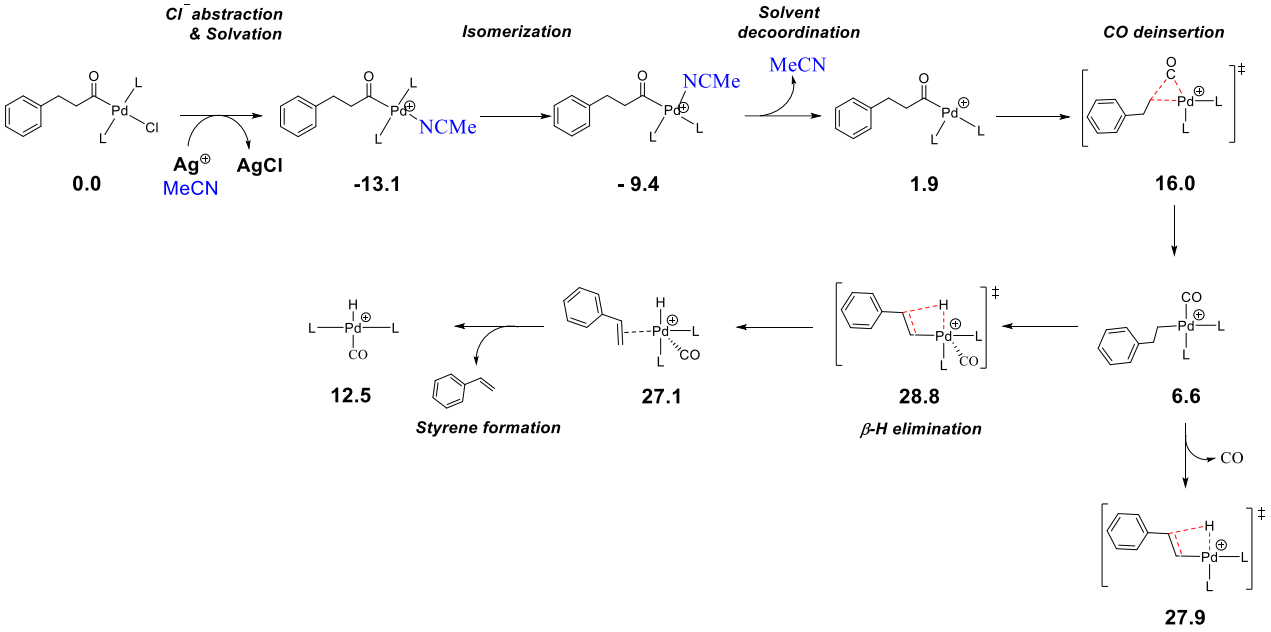

Scheme E.4. The DFT computed reaction mechanism for Pd-catalyzed CO deinsertion of 3-phenylpropionyl chloride starting from with **2** where L = PPh_3.

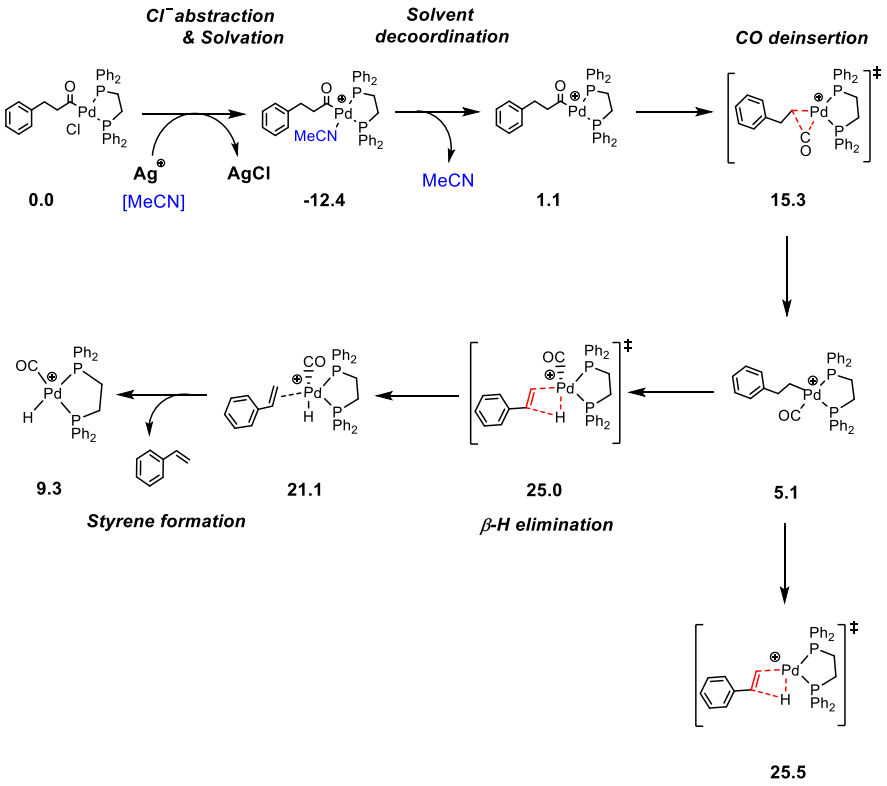

Scheme E.5. The DFT computed reaction mechanism for Pd-catalyzed CO deinsertion of 3-phenylpropionyl chloride starting from with **3** where L = dppe.

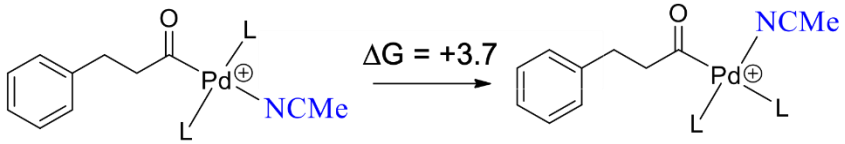

Scheme E.6. The isomerization of the solvated cationic intermediate, **2**$^{+}$, prior to CO deinsertion. ΔG in kcal/mol.

E.4. DFT optimized geometries

Selected parameters for DFT optimized geometries are included in Tables S1-S4, along with a comparison to the same parameters from X-ray crystal structures. Figure S2 includes the analogous structures with L = dppe to those in Figure 4.

Bonds	**DFT**	**Experiment**	**Difference**
Pd-P	2.327	2.295	0.032
Pd-Cl	2.428	2.337	0.091
Pd-C_{acyl}	1.955	1.947	0.008
C=O	1.198	1.186	0.012
P-Pd-Cl	168.7	162.6	6.1
P-Pd-C_{acyl}	101.7	100.7	1.0
P-Pd-C_{acyl}-O	81.6	64.9	16.7

Table E.1. Selected bond distances (Å) and angles (°) for crystal structure and corresponding DFT-optimized geometry for complex **1**.

Bonds	DFT	Experiment	Difference
Pd-P (avg.)	2.372	2.333	0.039
Pd-Cl	2.542	2.438	0.104
Pd-C_{acyl}	2.001	1.989	0.012
C=O	1.208	1.203	0.005
P1-Pd-P2	173.0	177.6	4.6
P-Pd-C_{acyl}(avg.)	90.6	88.9	1.7
P-Pd-C_{acyl}-O(avg.)	93.4	89.6	3.8

Table E.2. Selected bond distances (Å) and angles (°) for crystal structure and corresponding DFT-optimized geometry for complex **2**.

Bonds	DFT	Experiment	Difference
Pd-P1	2.463	2.396	0.067
Pd-P2	2.279	2.233	0.046
Pd-Cl	2.450	2.369	0.081
Pd-C_{acyl}	2.038	2.033	0.005
C=O	1.207	1.201	0.006
P1-Pd-C_{acyl}	174.5	173.5	1.0
P2-Pd-Cl	90.3	89.6	0.7
P2-Pd-C_{acyl}-O	89.4	86.3	3.1

Table E.3. Selected bond distances (Å) and angles (°) for crystal structure and corresponding DFT-optimized geometry for complex **3**.

Bonds	DFT	Experiment		Difference	
		($NaSbF_6$)	($AgBF_4$)	($NaSbF_6$)	($AgBF_4$)
Pd-P (avg.)	2.390	2.353	2.351	0.037	0.039
Pd-N	2.240	2.161	2.136	0.079	0.104
Pd-C_{acyl}	1.994	1.991	1.984	0.003	0.010
C=O	1.206	1.199	1.210	0.007	0.004
P1-Pd-P2	171.7	174.9	177.8	3.2	6.1
P-Pd-C_{acyl}(avg.)	91.0	89.0	89.2	2.0	1.8
P-Pd-C_{acyl}-O(avg.)	94.0	92.4	89.4	1.6	4.6

Table E.4. Selected bond distances (Å) and angles (°) for crystal structure and corresponding DFT-optimized geometry for complex $\mathbf{2}^{+}$.

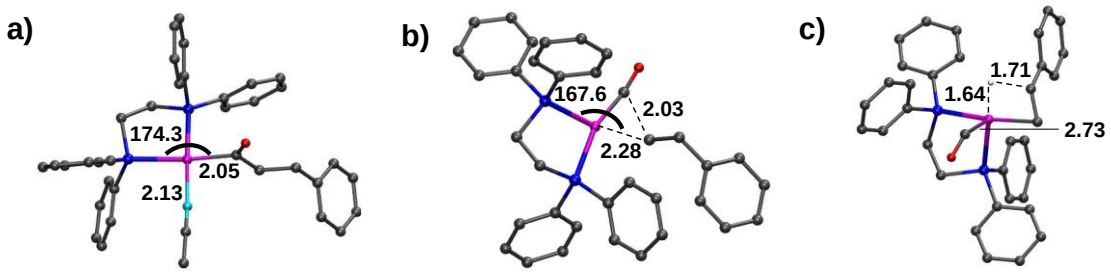

Figure E.1. DFT optimized geometries of the dppe a) solvated cationic intermediate, b) CO deinsertion transition state structure, and c) β-hydride elimination transition state structure. Bond distances are in Å and angles in degrees. Hydrogen atoms not involved in β-hydride elimination excluded for clarity. Pd in magenta, P in blue, N in cyan, O in red, C in grey.

E.5. DFT relative energies for different coordination numbers in select species.

We tested how an explicit solvent molecule or the coordination of CO to Pd effects the energies of the species in the reaction profile presented n Figure 3. Here we include additional schemes to show the relative energies.

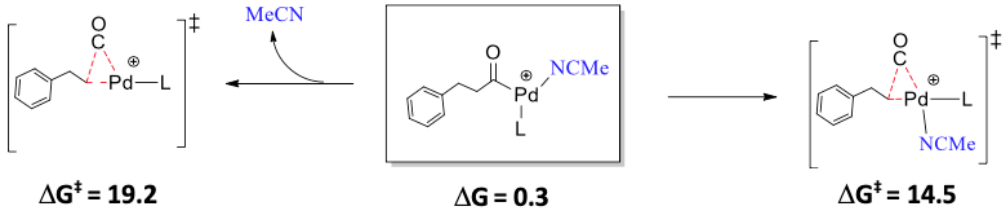

Scheme E.7. Effect of explicit solvent molecule on the CO deinsertion transition state energy barriers in P^{t}Bu$_3$ Pd-acyl complexes. Data reported with reference to **1** in the chloride abstraction pathway with Ag^+ used as halide abstraction agent. Gibbs free energy in kcal/mol.

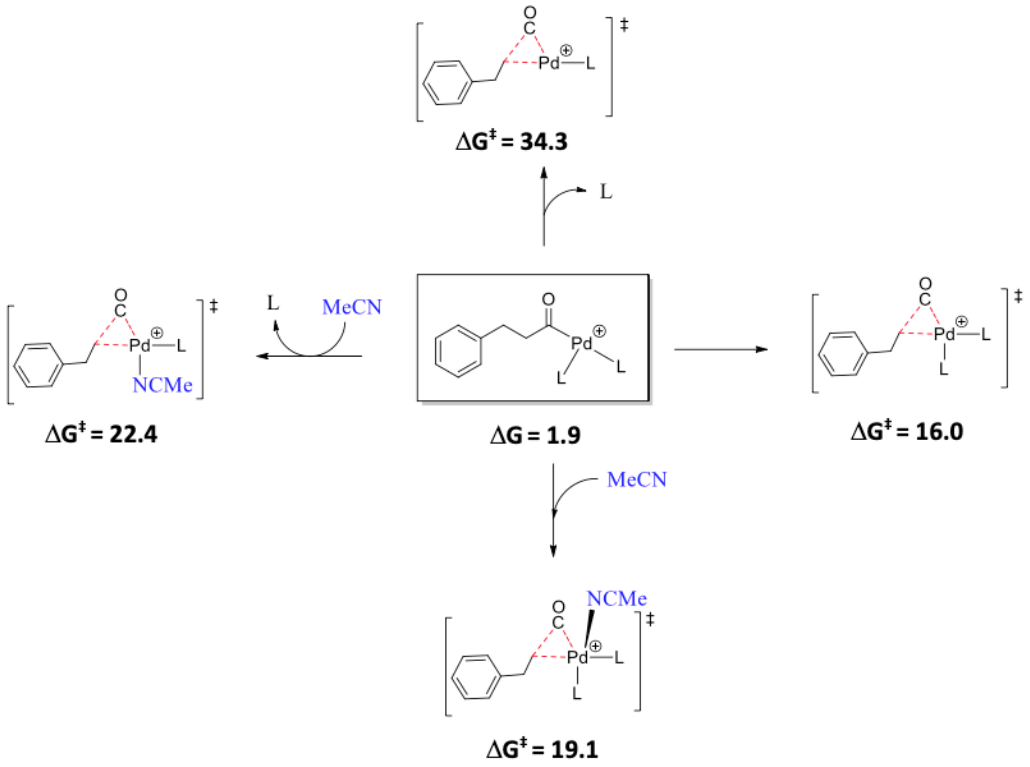

Scheme E.8. Effect of different ligand environments and explicit solvent on the CO deinsertion transition state energy barriers in PPh_3 Pd-acyl complexes. Data reported with reference to **2** in the chloride abstraction pathway with Ag^+ used as halide abstraction agent. Gibbs free energy in kcal/mol.

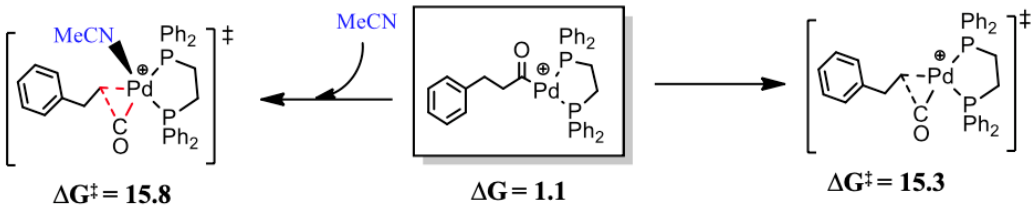

Scheme E.9. Effect of explicit solvent molecule on the CO deinsertion transition state energy barriers in dppe Pd-acyl complexes. Data reported with reference to **3** in the chloride abstraction pathway with Ag^+ used as halide abstraction agent. Gibbs free energy in kcal/mol.

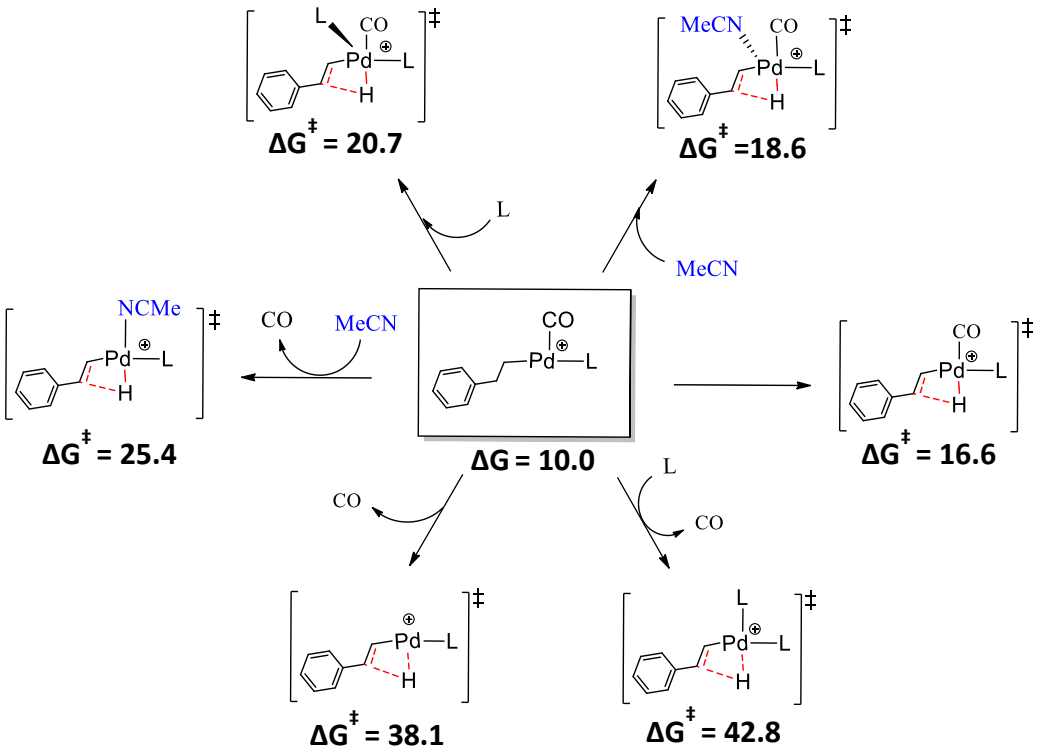

Scheme E.10. Effect of different ligand environments and explicit solvent on the β-hydride elimination transition state energy barriers in P^{t}Bu$_3$ Pd-acyl complexes. Data reported with reference to **1** in the chloride abstraction pathway with Ag^+ used as halide abstraction agent. Gibbs free energy in kcal/mol.

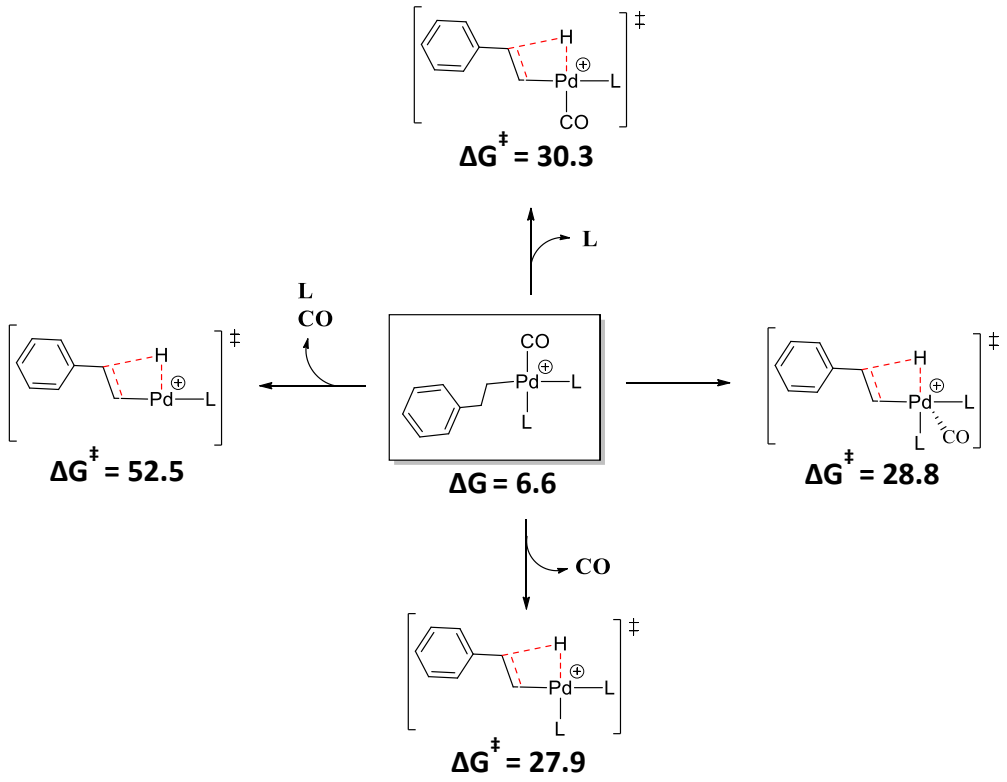

Scheme E.11. Effect of different ligand environments on β-hydride elimination transition state energy barriers in PPh_3 Pd-acyl complexes. Data reported with reference to **2** in the chloride abstraction pathway with Ag^+ used as halide abstraction agent. Gibbs free energy in kcal/mol.

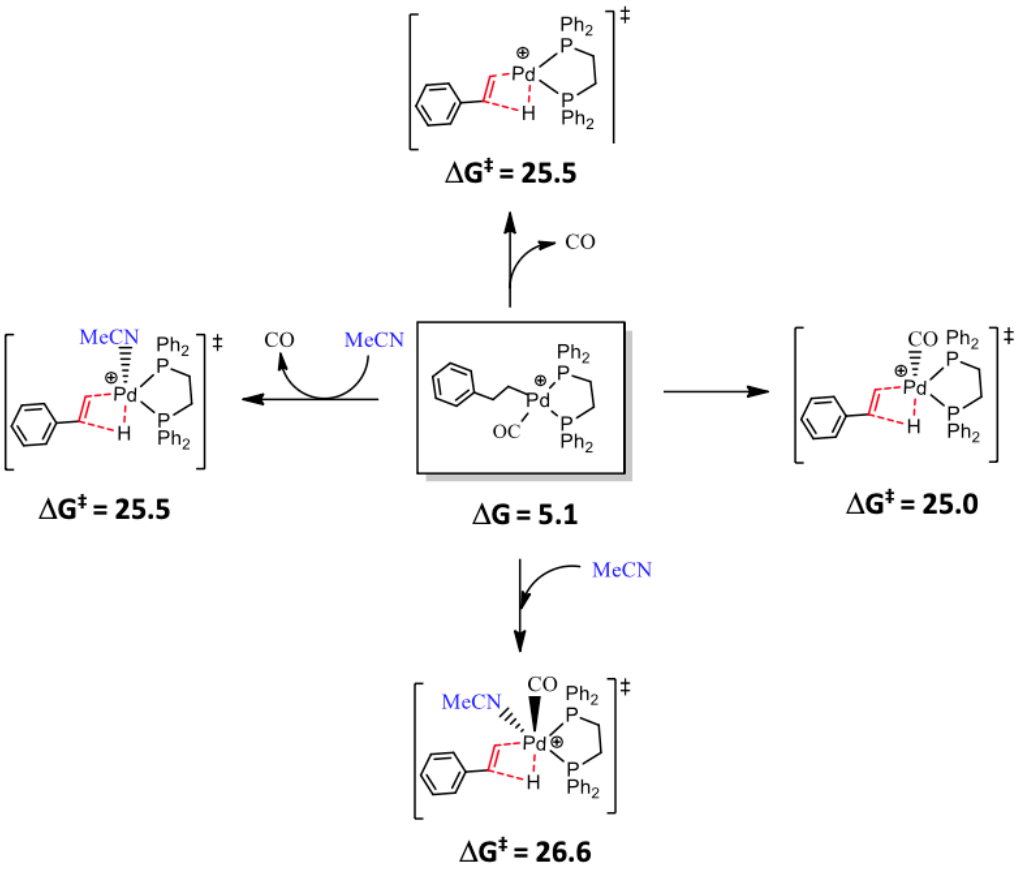

Scheme E.12. Effect of different ligand environments and explicit solvent on the β-hydride elimination transition state energy barriers in dppe Pd-acyl complexes. Data reported with reference to **3** in the chloride abstraction pathway with Ag^+ used as halide abstraction agent. Gibbs free energy in kcal/mol.

E.6. DFT functional choice

The effect of the DFT functional was tested by optimizing the geometries of **1**, its transition state (TS) for CO deinsertion, and its β-hydride elimination TS. We tested M06-L, M06, and ωB96XD. Note that while M06-L values are also included in the main text, those presented in this table do not include corrections for standard state or use the quasiharmonic approximation.

Species	M06-L	M06	ωB97XD
1	0.0	0.0	0.0
CO deinsertion TS	14.5	11.2	13.1
β-hydride elimination TS	16.6	14.3	12.7

Table E.5. Optimized geometries using different functionals for the P^{t}Bu$_3$ Pd-acyl complex (**1**). Relative Gibbs free energies in kcal/mol. The geometry was optimized with the def2-SVP basis set on light atoms and the def2-TZVP basis set on Pd and Ag (with the corresponding ECPs). but reported energies are from a single point calculation with the def2-TZVP basis set on all atoms. Ag^+ used as chloride abstracting agent. All the corrections to the energies described in the computational details are included here as well.

E.7. Coordinates and total energies for calculated structures presented in the manuscript.

The total energies for the compounds studied in this work are included in the following tables. The coordinates are provided as a single XYZ file (total energies are also included in the comment lines of this file). Compounds are identified by the figure or scheme number, reaction step number, molecular formula. The total electronic energy, total Gibbs free energy, and the Gibbs free energy that includes the standard state and quasiharmonic corrections are reported in a.u.

Figure or Scheme	Ligand (L)	Reaction Step	Molecular formula	Electronic Energy (a.u.)	Gibbs Free Energy (a.u.)	Corrected Gibbs Free Energy (a.u.)
Figure 3		1a (Therm)	$C_{21}H_{36}ClOPPd$	-1825.6840866	-1825.222384	-1825.218630
Figure 3	P^tBu_3	1	$C_{21}H_{36}ClOPPd$	-1825.7278568	-1825.263917	-1825.260223
Figure 3	P^tBu_3	2	$C_{21}H_{36}OPPd$	-1365.4592014	-1364.994147	-1364.990203
Figure 3	P^tBu_3	3	$C_{23}H_{42}NOPPd$	-1498.1101178	-1497.604897	-1497.600731
Figure 3	P^tBu_3	4	$C_{23}H_{45}NOPPd$	-1498.0858266	-1497.582658	-1497.578235
Figure 3	P^tBu_3	5	$C_{23}H_{45}NOPPd$	-1498.1062291	-1497.600252	-1497.596830
Figure 3	P^tBu_3	6	$C_{21}H_{39}OPPd$	-1365.4406092	-1364.976983	-1364.973921
Figure 3	P^tBu_3	7	$C_{21}H_{40}OPPd$	-1365.4264282	-1364.966446	-1364.963440
Figure 3	P^tBu_3	8	$C_{21}H_{40}OPPd$	-1365.4317757	-1364.970776	-1364.967772
Figure 3	P^tBu_3	9	$C_{13}H_{31}OPPd$	-1870.3996827	-1869.711141	-1869.708718
Figure 3	PPh_3	1a (Therm)	$C_{45}H_{39}ClOP_2Pd$	-3082.5690367	-3081.950676	-3081.946286
Figure 3	PPh_3	1	$C_{45}H_{39}ClOP_2Pd$	-3082.6250893	-3082.013683	-3082.004766
Figure 3	PPh_3	2	$C_{47}H_{45}NOP_2Pd$	-2755.0332415	-2754.373531	-2754.366730
Figure 3	PPh_3	3	$C_{45}H_{39}OP_2Pd$	-2622.3568859	-2621.737603	-2621.731401
Figure 3		4	$C_{45}H_{42}OP_2Pd$	-2622.3336085	-2621.713735	-2621.708962
Figure 3	PPh_3	5	$C_{45}H_{42}OP_2Pd$	-2622.3500459	-2621.728786	-2621.723914
Figure 3		6	$C_{45}H_{42}OP_2Pd$	-2622.3055552	-2621.693391	-2621.688478
Figure 3		7	$C_{45}H_{42}OP_2Pd$	-2622.3089783	-2621.695955	-2621.691206
Figure 3		8	$C_{37}H_{34}OP_2Pd$	-2312.9429853	-2312.457568	-2312.450993
Figure 3	dppe	1a(Therm)	$C_{35}H_{33}ClOP_2Pd$	-2698.221626	-2697.721871	-2697.716342
Figure 3	dppe	1	$C_{35}H_{33}ClOP_2Pd$	-2698.2749812	-2697.773427	-2697.767059
Figure 3	dppe	2	$C_{37}H_{39}NOP_2Pd$	-2370.6776903	-2370.135123	-2370.127807
Figure 3	dppe	3	$C_{35}H_{33}OP_2Pd$	-2238.0045355	-2237.501640	-2237.494961
Figure 3		4	$C_{35}H_{33}OP_2Pd$	-2237.9823872	-2237.477362	-2237.472265
Figure 3	dppe	5	$C_{35}H_{33}OP_2Pd$	-2237.9982537	-2237.493170	-2237.488593
Figure 3	dppe	6	$C_{35}H_{33}OP_2Pd$	-2237.9594285	-2237.461635	-2237.456883
Figure 3	dppe	7	$C_{35}H_{33}OP_2Pd$	-2237.9665995	-2237.467623	-2237.462994
Figure 3	dppe	8	$C_{27}H_{25}OP_2Pd$	-1928.597862	-1928.223252	-1928.218386
Figure 3	Olefin		C_8H_8	-309.3682538	-309.266377	-309.263489

Table E.6. The total energies for the Pd compounds shown in Figure 3 reported in a.u.

Figure or Scheme	Ligand (L)	Reaction Step	Molecular formula	Electronic Energy (a.u.)	Gibbs Free Energy (a.u.)	Corrected Gibbs Free Energy (a.u.)
Scheme S1	Substrate	1	C_9H_9ClO	-883.3070723	-883.188123	-883.184728
Scheme S1	$(P^tBu_3)_2Pd$	1	$C_{24}H_{54}P_2Pd$	-1756.6961709	-1756.028970	-1756.025932
Scheme S1	P^tBu_3	2	$C_{33}H_{63}ClOP_2Pd$	-2640.0131974	-2639.204479	-2639.199711
Scheme S1	P^tBu_3	3	$C_{33}H_{63}ClOP_2Pd$	-2639.9890198	-2639.175079	-2639.172271
Scheme S1	P^tBu_3	4	$C_{33}H_{63}ClOP_2Pd$	-2640.0440715	-2639.230947	-2639.227724
Scheme S1	P^tBu_3	5	$C_{12}H_{27}P$	-814.2992408	-813.974314	-813.971967
Scheme S2	$(PPh_3)_4Pd$	1	$C_{33}H_{63}ClOP_2Pd$	-4270.4812018	-4269.503834	-4269.496041
Scheme S2	PPh_3	2	$C_{18}H_{15}P$	-1035.5840214	-1035.358032	-1035.353751
Scheme S2	PPh_3	2	$C_{54}H_{45}P_3Pd$	-3234.8791114	-3234.157934	-3234.149388
Scheme S2	PPh_3	3	$C_{63}H_{54}ClOP_3Pd$	-4118.203233	-4117.334818	-4117.327437
Scheme S2	PPh_3	4	$C_{45}H_{39}ClOP_2Pd$	-3082.5841749	-3081.968359	-3081.962287
Scheme S2	PPh_3	5	$C_{45}H_{39}ClOP_2Pd$	-3082.581076	-3081.964630	-3081.958617
Scheme S3	P^tBu_3	7 (-CO)	$C_{20}H_{36}PPd$	-1252.170507	-1251.716951	-1251.713904
Scheme S4	PPh3	3	$C_{47}H_{45}NOP_2Pd$	-2755.028656	-2754.366885	-2754.360763
Scheme S4	PPh3	7 (-CO)	$C_{44}H_{39}P_2Pd$	-2509.090545	-2508.480017	-2508.474824
Scheme S5	dppe	6 (-CO)	$C_{34}H_{33}P_2Pd$	-2124.7413886	-2124.246346	-2124.240924
			CO	-113.2041433	-113.218196	-113.215178
			CH3CN	-132.6381783	-132.617229	-132.611431
			Na^+	-162.1403803	-162.154809	-162.151790
			NaCl	-622.3925648	-622.414415	-622.411405
			Ag^+	-146.9560322	-146.972638	-146.969619
			AgCl	-607.219251	-607.243006	-607.239999

Table E.7. The total energies for the Pd compounds shown in Schemes S1-S5 reported in a.u.

Molecular formula	Electronic Energy (a.u.)	Gibbs Free Energy (a.u.)	Corrected Gibbs Free Energy (a.u.)
CO	-113.2041433	-113.218196	-113.215178
CH3CN	-132.6381783	-132.617229	-132.611431
Na^+	-162.1403803	-162.154809	-162.151790
NaCl	-622.3925648	-622.414415	-622.411405
Ag^+	-146.9560322	-146.972638	-146.969619
AgCl	-607.219251	-607.243006	-607.239999

Table E.8. The total energies for the small molecules involved in the reactions reported in a.u.

E. 8. Appendix E References

1. Frisch *et al.*, Gaussian 16, Revision A.03. Gaussian, Inc., Wallingford CT, 2016.
2. (a) Dardzinski, D.; Yu, M.; Moayedpour, S.; Marom, N. Best Practices for First-Principles Simulations of Epitaxial Inorganic Interfaces. *J. Phys. Condens. Matter* **2022**, *34* (23). (b) Dardzinski, D.; Yu, M.; Moayedpour, S.; Marom, N. Best Practices for First-Principles Simulations of Epitaxial Inorganic Interfaces. *J. Phys. Condens. Matter* **2022**, *34* (23).
3. Hratchian, H. P.; Schlegel, H. B. Using Hessian Updating to Increase the Efficiency of a Hessian Based Predictor-Corrector Reaction Path Following Method. *J. Chem. Theory Comput.* **2005**, *1* (1), 61–69.
4. Weigend, F.; Ahlrichs, R. Balanced Basis Sets of Split Valence, Triple Zeta Valence and Quadruple Zeta Valence Quality for H to Rn: Design and Assessment of Accuracy. *Phys. Chem. Chem. Phys.* **2005**, *7* (18), 3297–3305.
5. Marenich, A. V.; Cramer, C. J.; Truhlar, D. G. Universal Solvation Model Based on Solute Electron Density and on a Continuum Model of the Solvent Defined by the Bulk Dielectric Constant and Atomic Surface Tensions. *J. Phys. Chem. B* **2009**, *113* (18), 6378–6396.
6. Li, Y. P.; Gomes, J.; Sharada, S. M.; Bell, A. T.; Head-Gordon, M. Improved Force-Field Parameters for QM/MM Simulations of the Energies of Adsorption for Molecules in Zeolites and a Free Rotor Correction to the Rigid Rotor Harmonic Oscillator Model for Adsorption Enthalpies. *J. Phys. Chem. C* **2015**, *119* (4), 1840–1850..

7. Zhao, Y.; Truhlar, D. G. The M06 Suite of Density Functionals for Main Group Thermochemistry, Thermochemical Kinetics, Noncovalent Interactions, Excited States, and Transition Elements: Two New Functionals and Systematic Testing of Four M06-Class Functionals and 12 Other Function. *Theor. Chem. Acc.* **2008**, *120* (1–3), 215–241.
8. Yu, H. S.; He, X.; Li, S. L.; Truhlar, D. G. MN15: A Kohn-Sham Global-Hybrid Exchange-Correlation Density Functional with Broad Accuracy for Multi-Reference and Single-Reference Systems and Noncovalent Interactions. *Chem. Sci.* **2016**, *7* (8), 5032–5051.
9. Chai, J. Da; Head-Gordon, M. Long-Range Corrected Hybrid Density Functionals with Damped Atom-Atom Dispersion Corrections. *Phys. Chem. Chem. Phys.* **2008**, *10* (44), 6615–6620.
10. Andrae, D.; Häußermann, U.; Dolg, M.; Stoll, H.; Preuß, H. Energy-Adjusted Ab Initio Pseudopotentials for the Second and Third Row Transition Elements. *Theor. Chim. Acta* **1990**, *77* (2), 123–141.
11. Zhao, Y.; Truhlar, D. G. The M06 Suite of Density Functionals for Main Group Thermochemistry, Thermochemical Kinetics, Noncovalent Interactions, Excited States, and Transition Elements: Two New Functionals and Systematic Testing of Four M06-Class Functionals and 12 Other Function. *Theor. Chem. Acc.* **2008**, *120* (1–3), 215–241..
12. Andrae, D.; Häußermann, U.; Dolg, M.; Stoll, H.; Preuß, H. Energy-Adjusted Ab Initio Pseudopotentials for the Second and Third Row Transition Elements. *Theor. Chim. Acta* **1990**, *77* (2), 123–141.